Heterogeneous materials with evolving microstructure : constitutive modeling, numerical implementation and applications.

Konstantinos Danas

Thèse présentée pour l'obtention du titre de

DOCTEUR DE L'ÉCOLE POLYTECHNIQUE

Spécialité : Mécanique

par

Konstantinos Danas

Sujet de thèse

Évolution de la microstructure dans les matériaux poreux: modélization, implémentation numérique et applications

Porous materials with evolving microstructure: constitutive modeling, numerical implementation and applications

soutenue le 5 mai 2008 devant le jury composé de :

M. Jean-Baptiste LEBLOND	*Président du jury*
M. Jean-Claude MICHEL	*Rapporteur*
M. Karam SAB	*Rapporteur*
M. Nikolaos ARAVAS	*Examinateur*
M. Michel BORNERT	*Examinateur*
M. Andreas MORTENSEN	*Examinateur*
M. Pedro PONTE CASTAÑEDA	*Directeur de thèse*

À ma famille et C.I.

Acknowledgments

This thesis was carried out at the Laboratoire de Mécanique des Solides (LMS) under the doctoral program of École Polytechnique. My thesis work was mainly funded by the mostly prestigious "Gaspard Monge" fellowship of École Polytechnique and partially by the program of scholarships for Hellenes of the Alexander S. Onassis Public Benefit Foundation.

I would like to express my gratitude to my thesis adviser and mentor Professor Pedro Ponte Castañeda for his guidance throughout my quest in the extraordinary field of mechanics and homogenization. I would like to thank him for his patience during the last four years, as well as for the tremendous amount of knowledge that he transmitted to me.

I would also like to thank my undergraduate adviser and mentor Professor Nikolaos Aravas for introducing me to the astounding field of solid mechanics and subsequently to Professor Pedro Ponte Castañeda, as well as for his inspiring teaching of mechanics which gave me the incentive to follow this field of research.

I gratefully thank Professor Jean-Baptiste Leblond for accepting to be the President of my thesis committee as well as Professor Jean-Claude Michel and Professor Karam Sab for spending their valuable time to read and report on my thesis document. In addition, I would like to express my gratitude to Professor Michel Bornert and Professor Andreas Mortensen for their enthusiasm and for accepting to participate in my thesis committee. I feel extremely honored to have had a committee of this highest scientific level.

My special thanks go to the Director M. Bernard Halphen and Assistant Director M. Claude Stolz for their support all these years of my Ph.D. thesis. I would also like to thank all the people at the LMS for their help during my stay at LMS and more generally in France.

In particular, I would like to express my deep gratitude to my colleagues and friends Professor Martin I. Idiart and Professor Oscar Lopez-Pamies, for our great philosophical and scientific discussions, which were often too loud for the rest of the people in the lab. I would also like to thank my friends and colleagues Professor Michele Brun and Michalis Agoras for the fruitful discussions in scientific, political and philosophical matters.

But above all, I am greatly indebted to my family: my parents Vasileios and Eleni and my sister Katerina for their unconditional support, encouragement and guidance over all these years. Finally, I would like to express my deepest gratitude to Charis. This work would not have been possible without her extraordinary patience, understanding, strength, and optimism.

ABSTRACT

Porous materials with evolving microstructure: Constitutive modeling, numerical implementation and applications

Konstantinos Danas
Adviser: Professor Pedro Ponte Castañeda

This work is concerned with the application of the "second-order" nonlinear homogenization procedure of Ponte Castañeda (2002) to generate estimates for the effective behavior of viscoplastic porous materials. The main concept behind this procedure is the construction of suitable variational principles utilizing the idea of a "linear comparison composite" to generate corresponding estimates for the nonlinear porous media. Thus, the main objective of this work is to propose a general constitutive model that accounts for the evolution of the microstructure and hence the induced anisotropy resulting when the porous material is subjected to finite deformations.

The model is constructed in such a way that it reproduces exactly the behavior of a "composite-sphere assemblage" in the limit of hydrostatic loadings, and therefore coincides with the hydrostatic limit of Gurson's (1977) criterion in the special case of ideal plasticity and isotropic microstructures. As a consequence, the new model improves on earlier homogenization estimates, which have been found to be quite accurate for low triaxialities but overly stiff for sufficiently high triaxialities and nonlinearities. Additionally, the estimates delivered by the model exhibit a dependence on the third invariant of the macroscopic stress tensor, which has a significant effect on the effective response of the material at moderate and high stress triaxialities.

Finally, the above-mentioned results are generalized to more complex anisotropic microstructures (arbitrary pore shapes and orientation) and general, three-dimensional loadings, leading to overall anisotropic response for the porous material. The model is then extended to account for the evolution of microstructure when the material is subjected to finite deformations. To validate the proposed model, finite element axisymmetric unit-cell calculations are performed and the agreement is found to be very good for the entire range of stress triaxialities and nonlinearities considered.

RÉSUMÉ

Évolution de la microstructure dans les matériaux poreux: modélization, implémentation numérique et applications

Konstantinos Danas
Directeur de thèse: Professeur Pedro Ponte Castañeda

Le travail de thèse porte sur l'application de la méthode non-linéaire d' homogénéisation dite du "second-ordre" de Ponte Castañeda (2002) pour estimer le comportement effectif des matériaux poreux viscoplastique. A titre de rappel, cette méthode est basée sur la construction des principes variationnels appropriés en utilisant un composite linéaire de comparaison pour produire des évaluations correspondantes à des milieux poreux non-linéaires. Ainsi, l'objectif principal de ce travail est de proposer un modèle constitutif général qui tient compte de l' évolution de la microstructure, et par conséquent, de l'anisotropie induite par l'application de déformations finies au matériau poreux.

Le modèle est construit pour reproduire exactement le comportement d'un "assemblage de sphère composites" dans la limite des chargements hydrostatiques, et coïncide donc avec la limite hydrostatique du critère de Gurson (1977) pour des matériaux poreux plastiques avec des microstructures isotropes. En conséquence, ce nouveau modèle améliore les estimations d'homogénéisation existantes, lesquelles sont satisfaisantes pour de faibles triaxialités mais excessivement raides pour des triaxialités et des non-linéarités élevées. En outre, les estimations obtenues par le modèle dépendent de la troisiéme invariable du tenseur macroscopique des contraintes, lequel porte un effet non négligeable sur la réponse effective du matériau pour de moyennes et hautes triaxialités.

De plus, les résultats cités ci-dessus ont été généralisés à des microstructures anisotropes complexes (par exemple : des microstructures avec des formes et des orientations arbitraires des pores) et à des chargements tridimensionnels, conduisant à la réponse anisotrope globale du matériau poreux. Le modèle est ensuite étendu pour tenir compte de l'évolution de la microstructure lorsque le matériau est soumis à des déformations finies. Enfin, la validation du modèle proposé a été réalisée par le biais de calculs par éléments finis sur des microstructures axisymétriques périodiques, et donnent des résultats pertinents pour l'ensemble des triaxialités et des non-linéarités envisagées.

Contents

Chapter 1

Introduction

This work is concerned with the estimation of the constitutive behavior of composite materials and particularly of porous media. A composite material is a heterogeneous material that consists of two or more different materials, called phases, with different properties. In turn, a porous material is a special type of a two-phase composite material consisting of pores (voids) and a surrounding medium, called the matrix phase. A *random* distribution of pores (microstructure) can be found in a wide variety of materials, such as sintered metals and ceramics, rocks and human bones, in sizes much smaller than the specimen under consideration. In principle, numerical techniques such as "finite element" or Fourier transform algorithms could be used to solve for the local behavior of the material, provided that the exact location of the pores in the material is known. However, in most of the cases, the only available information is the volume concentration and, possibly, the two-point probability distribution function of the voids. Furthermore, the element size used in a finite element algorithm should have the same order of magnitude as the size of the microstructure, which in turn is several orders of magnitude smaller than the size of the macroscopic material. This would make the computation very intensive in time. It is, thus, useful to develop theoretical techniques that will allow us to estimate the effective behavior of such materials in a more efficient manner.

As mentioned previously, the length scale of the inhomogeneities (microscale) is much smaller than the size of the specimen and the scale of variation of the loading conditions (macroscale). Such a heterogeneous material can be regarded as a *homogeneous* material on the macroscale, with certain "effective properties", which depend on the individual phase properties as well as on their distribution in space, i.e., the *microstructure*. In most composite materials the microstructure is too complicated to be characterized in full detail. For this reason, in most of real-life applications, the microstructure can be described only in terms of statistical partial information. A means of estimating the constitutive behavior of composite materials by making use of the available statistical information about their microstructure is provided by the "homogenization" methods. These methods have as a purpose to link the macroscopic with the microscopic scale in the most efficient manner by including as much information as it is available about the microstructure of the material.

On the other hand, it is worth mentioning that in many cases of theoretical interest, the microstructure of composite materials is *periodic*. In particular, Sanchez-Palencia (1970) derived an expression for the effective behavior of linear composites with *periodic* microstructures. In this case,

where the microstructure is deterministic, estimating the effective behavior of the composite reduces the problem to a computation of a single unit-cell provided that the phases are described by strictly convex potentials. The validity of this solution holds in the entire volume of the material except in some "boundary layer" close to the exterior surface of the medium. On the other hand, most materials of interest consist of random microstructures, whose physical properties vary not only with position $\mathbf{x}$, but also depend upon a parameter α, where α is a member of a sample space $\mathcal{A}$, over which a probability measure p is defined. However, for statistically uniform media, it is usual to make an "ergodic" hypothesis (Willis, 1981) that local configurations occur over any one specimen with the frequency with which they occur over a single neighborhood in an ensemble of specimens. Under this assumption ensemble averages may be replaced by volume averages and therefore the effective behavior of the random composite may be defined over a given volume (see also Sab (1992, 1994a)).

For linear elastic composites, there exist several methods to estimate their effective behavior. Simple estimates for the effective mechanical properties of random composites have been established dating back to the early works of Voigt (1889) and Reuss (1929), who assumed uniform strain and stress fields, respectively, over the whole composite. These estimates constitute rigorous bounds since they can be obtained from a minimum potential/complementary energy. In one of the most celebrated papers, Eshelby (1957) solved the problem of an ellipsoidal inclusion in an infinite, isotropic, elastic matrix exactly. For non-dilute porous media, Hashin (1962) has proposed an exact solution for the effective behavior of a special class of linear-elastic composites known as the composite-sphere (CSA) and composite-cylinder (CCA) assemblages, when subjected to hydrostatic loading. Hashin and Shtrikman (1962a, 1962b, 1963) (HS) introduced a new variational principle that improved considerably on the Voigt and Reuss bounds by assuming that the constituent phases are isotropically distributed in the specimen. In addition to the HS bounds, the self-consistent (SC) approximation was introduced by Hershey (1954) and Kröner (1958) in the context of elastic polycrystals and was extended to other types of elastic composites by Budiansky (1965) and Hill (1965b). A generalization of these results in terms of variational principles was proposed by Willis (1977, 1978, 1981, 1982). In particular, these principles involved information on the two-point statistics of the composite, which, in turn, led to improved estimates for more general anisotropic microstructures and "particulate" composites. By allowing the shapes of the inclusions to be different than the shapes of the spatial distribution functions, Ponte Castañeda and Willis (1995) established variational approximations for "particulate" composites with some explicit statistics that are realizable. Because of the variational character of these estimates, they are free from some of the drawbacks that other approximations exhibit such as that of Mori and Tanaka (1973), which can generate tensors of effective moduli that fail to satisfy necessary symmetry requirements.

In addition to the above described linear theories, there has been much attention given to nonlinear composites as well. The first methods for estimating the effective response of nonlinear composites were developed in the context of polycrystal plasticity. Taylor (1938) obtained simple estimates, analogous to the Voigt estimates in the linear case. Hill (1965a) proposed an incremental self-consistent method for elasto-plastic polycrystals, which triggered several other schemes (Hutchinson, 1976; Berveiller and Zaoui, 1979). Following Willis work on linear composites, Talbot and Willis

(1985) used a "linear homogeneous comparison" material to provide a generalization of the HS bounds in the context of nonlinear composites. A more general class of nonlinear homogenization methods has been introduced by Ponte Castañeda (1991) (see also Willis (1991) and Ponte Castañeda (1992)), who obtained rigorous bounds by making use — via a suitably designed variational principle — of an optimally chosen "linear comparison composite" (LCC) with the same microstructure as the nonlinear composite. Michel and Suquet (1992) for porous media and Suquet (1993) for two-phase media derived an equivalent bound independently in the context of power-law phases using Hölder-type inequalities, while Suquet (1995) made the observation that the optimal linearization in the variational bound of Ponte Castañeda (1991) is given by the "secant" moduli evaluated at the second moments of the local fields in each phase in the LCC. The connections between this method and the Talbot-Willis procedure were explored by Willis (1992) and Talbot and Willis (1992).

Because the "variational" method delivers a rigorous bound, it tends to be relatively stiff for the effective behavior of nonlinear composites. In this connection, Ponte Castañeda proposed the "tangent second-order" (Ponte Castañeda, 1996) and the "second-order" method (Ponte Castañeda, 2002a), which made use of more general types of linear comparison composites (anisotropic thermoelastic phases). While the "variational" method provides a rigorous bound, the "second-order" methods deliver stationary estimates. In fact, Ponte Castañeda and Willis (1999) showed that if the fourth-order modulus tensor of the LCC is identified with the tangent moduli of the phases evaluated at certain reference tensors, then the optimal choice of certain reference tensors is given by the first moments of the local fields in the LCC. However, this does not mean that the choice made for the modulus tensor in the LCC is optimal. On the other hand, the optimal linearization in the more recent "second-order" method, which improves significantly on the previous methods, is identified with generalized-secant moduli of the phases that depend on both the first and the second moments of the local fields. The remarkable property of the "second-order" methods is their capability of reproducing exactly the small-contrast expansion of Suquet and Ponte Castañeda (1993) to second order. The main conclusions drawn by these and other works (Ponte Castañeda and Zaidman, 1996; Ponte Castañeda and Suquet, 1998, 2001; Bornert et al., 2001; Ponte Castañeda, 2002b) is that the LCC-based methods lead to estimates that are, in general, more accurate than those resulting from the earlier methodologies mentioned above. However, all of these estimates remain overly stiff in the case of porous power-law materials when they are subjected to high triaxial loadings (Ponte Castañeda and Zaidman, 1994; Kailasam and Ponte Castañeda, 1998; Pastor and Ponte Castañeda, 2002).

In addition to the homogenization methods described previously, it is also important to mention that there is a wide range of micromechanical models and special analytic results for linear and nonlinear composites with specific microstructures, and particularly porous materials. As already mentioned previously, Eshelby (1957) solved the problem of an ellipsoidal inclusion in an infinite, isotropic, elastic matrix exactly. This work triggered numerous other attempts to obtain analytical or numerical solutions for nonlinear materials with *dilute* concentration of voids. In particular, estimating the response of a dilute, porous, nonlinear material received a lot of attention in several works. These include the studies by McClintock (1968), Rice and Tracey (1969), Budiansky et al. (1982),

Duva and Hutchinson (1984), Duva (1986), Fleck and Hutchinson (1986) and Lee and Mear (1991a, 1991b, 1992a, 1992b, 1992c). One of the drawbacks of those studies is the use of a stream function technique, which is mainly applied to problems in two-dimensions or three-dimensions provided that certain symmetries are preserved in the problem (e.g., spheroidal voids and axisymmetric loading conditions aligned with the pore symmetry axis). On the other hand, the generalization of such a technique to general three dimensional microstructures and loadings is not straightforward. A second drawback of that approach, is related with the convergence of the numerical algorithms at sufficiently high nonlinearities and triaxialities (Huang, 1991b). Nonetheless, those techniques revealed some of the complex, albeit interesting, local phenomena that are observed in the nonlinear regime.

Based on the analysis of Rice and Tracey (1969), Gurson (1977) proposed a popular model for non-dilute porous solids with ideally-plastic matrix phase by making use of the exact solution for a shell (spherical or cylindrical cavity) subjected to hydrostatic loading, together with a uniform, purely, deviatoric field. However, Gurson's model was found to violate the rigorous variational bound of Ponte Castañeda at low triaxialities. Based on those observations, Leblond et al. (1994) generalized Hashin's result in the nonlinear regime, while they improved on Gurson's model by adjusting their model to coincide with the variational bound at low triaxialities. This model has been successfully extended to spheroidal voids and axisymmetric loading conditions (aligned with the symmetry of the void) by Gologanu et al. (1993, 1994, 1997). This approach was further refined by, including the studies of Gărăjeu et al. (2000), Flandi and Leblond (2005a,b) and Monchiet et al. (2007). Nonetheless, these studies are based on prescriptions for a trial velocity field similar to the dilute stream function methods discussed earlier. For this reason, a generalization of these techniques to ellipsoidal microstructures and general loading conditions is not simple and to the best knowledge of the author there exist no results for such cases.

In addition to the classical composites described previously, it is also possible to construct heterogeneous materials made out of sequentially laminated microstructures, which admit an exact solution. The interest in composites with this type of microstructures is that, in the linear case, their effective behavior has been shown by Frankfort and Murat (1986) and Milton (2002) to agree exactly with the HS estimates, for any choice of the modulus tensors of the phases (provided that the phases are "well-ordered"). For this reason, the "exact" estimates delivered for the nonlinear sequentially laminated composites can be used to assess the accuracy of the aforementioned approximate general LCC-based models considered in this work. In contrast, nonlinear sequential laminates have received much less attention. Building on the work of deBotton and Ponte Castañeda (1992), deBotton and Hariton (2002, 2005) obtained numerically exact results for high-rank, sequential laminates under in-plane loadings. They have shown numerically that as the rank of the laminate becomes sufficiently high, the effective behavior of the composite tends to be isotropic. These results have been extended to three-dimensional microstructures by Idiart (2006). In this context, it is highly relevant to mention that Idiart (2007) has recently shown that the sequentially laminated microstructures can be used to obtain exactly the purely hydrostatic limit for porous materials with the CSA and CCA microstructure.

All the aforementioned studies are mostly oriented towards the estimation of the instantaneous

effective response of nonlinear composites. Nevertheless, viscoplastic porous composites, which is the main topic of this work, can undergo finite deformations. Therefore, their microstructure is expected to evolve in time during the deformation process. In this connection, it is worth mentioning that, Aravas (1987) has developed a numerical algorithm which was based on the Gurson model to predict the evolution of porosity under finite deformations. However, as already mentioned previously, the Gurson model is constructed for isotropic microstructures, whereas evolution of microstructure, in general, can lead to the development of anisotropy in the material, which in turn could have a significant effect on the effective response of the composite. For this reason, it is essential to complement the above-mentioned homogenization methodologies with a framework allowing the characterization of the evolution of microstructure.

In principle, the solution of the exact boundary value problem for the composite would provide all the necessary information needed to describe the evolution of microstructure. However, this procedure requires, as already mentioned in the beginning of the introduction, knowledge of the exact location of the phases and very intensive full-field numerical simulations. On the other hand, homogenization techniques are interested in establishing an estimate for the effective response of the material whose microstructure is not deterministic and therefore, in describing the evolution of the microstructure on average terms. In this connection, Ponte Castañeda and Zaidman (1994) proposed a framework for determining the evolution of "volume" and "average shape" (i.e., average shape may be identified to an ellipsoidal shape in general) of voids, by making use of the macroscopic and the phase average strain-rates delivered by the "variational" homogenization method. These results were further extended to reinforced composites by the same authors (Ponte Castañeda and Zaidman, 1996). Kailasam and Ponte Castañeda (1998) provided a more general framework in order to incorporate changes in the "average orientation" of the principal axes of the ellipsoidal voids, when the material is subjected to general boundary conditions. Building on this work, Kailasam et al. (2000) and Aravas and Ponte Castañeda (2004) proposed a "complete" constitutive model for porous metals subjected to general three-dimensional finite deformations.

In addition to these studies in the framework of homogenization, there are several studies and works concerned with evolution of microstructure in dilute and non-dilute porous materials by making use of approximate models based on spherical and spheroidal shell calculations. As already mentioned previously, the problem of evolution of a single inclusion in a nonlinear infinite matrix was studied by Budiansky et al. (1982), Fleck and Hutchinson (1986) and Lee and Mear (1994, 1999). On a separate development, Gologanu et al. (1993, 1994, 1997) (*GLD*) generalized Gurson's model to account for changes in the average shape of the voids (when voids are spheroidal). Gărăjeu et al. (2000) proposed a model that incorporated distribution effects. Recently, Flandi and Leblond (2005a, 2005b) generalized the *GLD* model in viscoplastic composites, while they obtained improved results regarding the evolution of the shape parameter. However, all these methods are constrained to spheroidal prolate or oblate voids and axisymmetric loading conditions aligned with the pore symmetry axis, and in general, it is very difficult to extended them for more general ellipsoidal microstructure and loading conditions as already mentioned previously.

The main objective of this work is to propose a general, three-dimensional model based on the

"second-order" homogenization method of Ponte Castañeda (2002a) that is capable of estimating *accurately* the effective behavior of viscoplastic porous solids, when these are subjected to finite deformations. One of the main issues that are essential in this study is the improvement of this new model relative to the earlier "variational" method for high triaxiality loading conditions, while still being able to *handle completely general loading conditions and ellipsoidal microstructures*. In summary, the goal of this study is to bridge the gap between the earlier "variational" method and the more recent "second-order" method by being able to provide accurate estimates for porous media in the entire range of loading conditions.

In the following, a brief description of the chapters of this dissertation is provided. Thus, the next chapter (Chapter 2) is concerned with the theoretical aspects of this work. The main concepts of homogenization in linear and nonlinear two-phase and porous media are discussed. Those include the definition of the *effective* or *macroscopic* behavior of a random composite material subjected to general loading conditions. In order to proceed to specific estimates for the effective behavior of the composite, it is necessary to specify first the microstructure and the local constitutive behavior of the phases. In the context of this work, the phases are described by a power-law stress potential (or dissipation potential), whereas the microstructure is considered to be "particulate". Next, we provide homogenization estimates for "particulate" two-phase composite materials, whose phases are described by linearly viscous and "thermo-viscous" constitutive laws. For this class of linear "particulate" composites, use is made of the Willis estimates (1978) (Ponte Castañeda and Willis, 1995) to obtain explicit expressions for their effective behavior, as well as the corresponding phase average and second moments of the fields. For the determination of the effective behavior of nonlinear two-phase media, we make use of the "variational" method by Ponte Castañeda (1991) and the "second-order" variational formulation by Ponte Castañeda (2002a). These variational formulations make use of an *optimized* linear comparison composite (LCC), which has the same microstructure as the nonlinear one. In turn, this allows the use of any already available homogenization method to estimate the effective behavior of the linear two-phase (or porous) medium to generate corresponding estimates for the *nonlinear* two-phase (or porous) medium. Once the LCC is defined, then we describe the "variational" and the "second-order" method in the context of particulate composite materials. In the sequel, expressions are provided for the estimation of the phase average fields, which are necessary for the determination of the evolution of the microstructure. In this connection, evolution laws are provided for the corresponding microstructural variables. Finally, the aforementioned analysis is specialized for the case of porous media with ideally-plastic matrix phase, where conditions for shear localization instabilities are also provided.

In Chapter 3, we attempt to describe briefly earlier models proposed in the context of porous materials and have been extensively used in the literature. Firstly, the well-known Gurson (1977) model is described. This model makes use of the exact solution for a shell (spherical or cylindrical cavity) under hydrostatic loadings, suitably modified, to obtain estimates for the effective behavior of solids with ideally-plastic matrix phase with isotropic or transversely isotropic distributions of porosity. Next, we describe the methodology adopted by Budiansky et al. (1982) (see also McClintock, 1968; Rice and Tracey, 1969) in the context of dilute isotropic viscoplastic porous media. This method is

based on the minimum variational principle of velocities as stated by Hill (1956). Next, the studies by Fleck and Hutchinson (1986) and Lee and Mear (1992) are briefly discussed. In these studies, the authors generalized the above mentioned method in the case of dilute porous media consisting of long cylindrical pores with elliptical cross-section. This spectral methods are concluded by describing briefly the work of Lee and Mear (1992c, 1994) in the context of dilute porous media containing spheroidal voids. On a separate development, several authors such as Gologanu et al. (1993, 1994, 1997), Leblond et al. (1994), Gărăjeu et al. (2000), Flandi and Leblond (2005) and Monchiet et al. (2007) have made an attempt to generalize the Gurson model in the case of spheroidal microstructures and axisymmetric loading conditions (aligned with the pore symmetry axis). These models are briefly discussed and several comments are made in this context. In the sequel, we describe the determination of the effective behavior of high-rank sequentially laminated porous materials as discussed by deBotton and Hariton (2002) and Idiart (2006) (see Ponte Castañeda, 1992), which constitute appropriate composite materials to access the accuracy of LCC-based homogenization methods, as already mentioned previously. Finally, we present briefly a unit-cell finite element calculation made in the context of porous media with cylindrical or spherical voids, subjected to plane-strain and axisymmetric loading conditions, respectively. These results will be used to compare the evolution of microstructure as predicted by the corresponding "second-order" and "variational" homogenization methods.

Chapter 4 constitutes the beginning of a series of chapters that are related with the application of the above mentioned methods in the context of viscoplastic porous materials. In particular, this chapter deals with the estimation of the instantaneous behavior of porous media consisting of cylindrical pores aligned in the $3-$direction and distributed randomly in the plane $1-2$, that are subjected to plane-strain loading conditions. The cross-section of the pores can be circular or elliptical, such that the overall behavior of the composite is transversely isotropic or anisotropic, respectively. Both cases are studied, while the "second-order" and "variational" estimates are compared with results derived by the models described in Chapter 3. Special attention is given on the effect of the aspect ratio on the overall behavior of the porous material. First, results are shown for the case of transversely isotropic porous media subjected to plane-strain isochoric loadings, where we study the dependence of the effective properties of the composite on the nonlinearity of the matrix phase and the volume concentration (i.e., porosity) of the voids. Next, use is made of the new "second-order" model, proposed in this thesis, to derive improved estimates for transversely isotropic porous media. In this context, the new model is compared with available estimates provided by models described in Chapter 3. Finally, the chapter concludes with the study of the instantaneous effective behavior of porous materials consisting of cylindrical voids with elliptical cross-section.

Chapter 5 is a natural continuation of Chapter 4 in the context of finite deformations. More specifically, in this chapter we make use of the results developed in the preceding chapter 4 to estimate the evolution of microstructure when the porous material is subjected to plane-strain loading conditions. The "second-order" and "variational" estimates are initially compared with dilute estimates obtained by Lee and Mear (1992b), while they are also compared with unit-cell finite element calculations for dilute concentration of voids. Moreover, it has been possible to compare the "second-order" and the

"variational" estimates with finite element predictions for simple shear loading conditions. In this case, the loading induces a change of the orientation of the principal axes of the voids, and thus the material becomes fully anisotropic in the plane. Finally, the chapter concludes with the study of possible development of instabilities in the context of porous media with ideally-plastic matrix phase. For comparison, the Gurson (1977) model is also included in this last application.

Chapter 6 deals with the instantaneous effective behavior of porous media consisting of spherical or ellipsoidal voids that are subjected to general loading conditions. The "second-order" and the "variational" methods are compared with many of the models described in Chapter 3. Initially, we provide results for isotropic dilute and non-dilute porous media subjected to isochoric and more general loading conditions, where a complete study of the effect of the nonlinearity of the matrix and the concentration of voids on the effective behavior of the composite is made. Next, an attempt is made to establish the importance of non-spherical void shapes on the instantaneous effective response of porous media, where the new "second-order" model is compared with corresponding estimates obtained by the Flandi and Leblond (2005) model. Finally, the new "second-order" model is used to study the effect of the misorientation of the voids on the macroscopic response of porous materials.

Chapter 7 is concerned with the estimation of the evolution of microstructure in porous materials with spherical or ellipsoidal voids subjected to general loading conditions. Firstly, we make an attempt to compare the new "second-order" model and the "variational" method with estimates for dilute porous media consisting of spheroidal voids delivered by Lee and Mear (1994), in the case of axisymmetric loading conditions. For further validation of the new "second-order" model, unit-cell finite element calculations are performed for various stress triaxialities and nonlinearities and are used as a test case for the homogenization methods studied in this work. Next, a thorough comparison of the nonlinear homogenization estimates, the finite element calculations and the Flandi and Leblond (2005) model is provided for a high value of the nonlinear exponent and axisymmetric loading conditions. In the sequel, the "second-order" model is used to predict the evolution of the microstructure and the effective behavior of initially anisotropic porous media with ideally-plastic matrix phase. The effect of the initial misorientation of the voids in the evolution of the microstructure and the effective behavior is examined through several loading conditions. Finally, the "second-order" model is used to predict shear localization instabilities in the context of porous media with ideally-plastic matrix phase. For comparison, corresponding estimates obtained by the "variational" method are also included.

Finally Chapter 8 provides a brief summary of the main findings of this work together with some concluding remarks, as well as some prospects for future work.

List of publications resulting from this dissertation work

1. Idiart M. I., Danas K., Ponte Castañeda P., 2006, Second-order estimates for nonlinear composites and application to isotropic constituents, *C.R. Mecanique* 334, 575–581.

2. Danas K., Idiart M. I., Ponte Castañeda P., 2008, Homogenization-based constitutive model for two-dimensional viscoplastic porous media, *C.R. Mecanique*, 336, 79–90.

3. Danas K., Idiart M. I., Ponte Castañeda P., 2008, A homogenization-based constitutive model for isotropic viscoplastic porous media, *Int. J. Solids Struct.*, 45, 3392–3409.

4. Danas K., Ponte Castañeda P., A finite-strain model for viscoplastic anisotropic porous media: I – Theory, in preparation.

5. Danas K., Ponte Castañeda P., A finite-strain model for viscoplastic anisotropic porous media: II – Applications, in preparation.

6. Danas K., Ponte Castañeda P., Porous metals with directional pores: A homogenization approach, in preparation.

7. Danas K., Ponte Castañeda P., A constitutive model for viscoplastic porous media with cylindrical voids and evolution of microstructure, in preparation.

Chapter 2

Theory

2.1 Effective behavior

This chapter deals with the determination of the "effective behavior" of two-phase viscoplastic composites, and particularly of viscoplastic porous materials with "particulate" microstructures. The framework to be developed accounts for the evolution of the microstructure, which results from the finite changes in geometry that are induced by the applied loading conditions. The main purpose of this study is to develop constitutive models for viscoplastic porous materials that are capable of handling:

- the nonlinear response of the porous medium,
- microstructural information, such as the volume fraction, the average shape and orientation of the voids,
- the evolution of microstructure,
- possible development of instabilities.

Moreover, these models need to be simple and robust enough to be easily implemented in finite element codes.

The framework that is discussed in the context of this chapter is based on the nonlinear "variational" and "second-order" homogenization methods developed by Ponte Castañeda (1991, 2002a), respectively. The main idea behind these theories is the construction of suitable variational principles that make use of a "linear comparison composite" (LCC). The theories discussed in the following will be applied to estimate the effective behavior and microstructure evolution in viscoplastic porous materials subjected to general loading conditions.

More specifically, it is convenient to discuss first the case of general two-phase heterogeneous materials, whose properties vary from point to point on a length scale that is much smaller than the scale of the specimen under consideration and the scale of variation of the applied boundary conditions. This assumption is known as the "separation of length scales" and is mainly introduced when a heterogeneous material can be regarded as a homogeneous material in the macroscopic scale with some effective properties. In addition, the region in the material, where the microstructure is considered to be statistically uniform, is called a "representative volume element" (RVE).

In this regard, we consider an RVE Ω of a two-phase heterogeneous medium with each phase occupying a sub-domain $\Omega^{(r)}$ $(r = 1, 2)$. It is convenient to introduce here the notation $\langle\cdot\rangle$ and $\langle\cdot\rangle^{(r)}$ to define volume averages over the RVE (Ω) and the phase r $(\Omega^{(r)})$, respectively. The local behavior of the phases is characterized by convex stress potentials $U^{(r)}$, such that the local behavior of the composite $U(\mathbf{x}, \boldsymbol{\sigma})$ is written as:

$$U(\mathbf{x}, \boldsymbol{\sigma}) = \sum_{r=1}^{2} \chi^{(r)}(\mathbf{x}) U^{(r)}(\boldsymbol{\sigma}) \tag{2.1}$$

where the characteristic (or distribution) functions $\chi^{(r)}$ are used to describe the distribution of the phases (i.e., the microstructure) in the current configuration. These functions take values equal to 1 if $\mathbf{x} \in \Omega^{(r)}$ and zero otherwise. It is important to remark here that for random materials, which is the focus of this study, the distribution functions $\chi^{(r)}$ are not known precisely and they can only be defined in terms of $n-$point statistics. Thus, the local constitutive behavior of the composite and the phases can be defined by the relation between the Cauchy stress $\boldsymbol{\sigma}$ and the Eulerian strain-rate $\boldsymbol{D}$ via

$$\boldsymbol{D}(\mathbf{x}) = \frac{\partial U(\mathbf{x}, \boldsymbol{\sigma})}{\partial \boldsymbol{\sigma}}, \quad \forall\, \mathbf{x} \in \Omega \quad \text{and} \quad \boldsymbol{D}^{(r)} = \frac{\partial\, U^{(r)}(\boldsymbol{\sigma})}{\partial\, \boldsymbol{\sigma}}, \quad r = 1, 2. \tag{2.2}$$

Here, the strain-rate $\boldsymbol{D}(\mathbf{x})$ is the symmetric part of the velocity gradient $\boldsymbol{L} = \nabla \mathbf{v}$ expressed in standard notation as $\boldsymbol{D} = [\nabla \mathbf{v} + (\nabla \mathbf{v})^T]/2$, whereas, for later use, we may also introduce the corresponding spin tensor $\boldsymbol{\Omega}(\mathbf{x})$ as the skew-symmetric part of this velocity gradient such that $\boldsymbol{\Omega} = [\nabla \mathbf{v} - (\nabla \mathbf{v})^T]/2$. In addition, it is useful to define the following local constitutive function

$$\begin{aligned} \mathbf{M}_t(\mathbf{x}) &= \frac{\partial \boldsymbol{D}(\mathbf{x})}{\partial \boldsymbol{\sigma}(\mathbf{x})} = \frac{\partial^2 U(\mathbf{x}, \boldsymbol{\sigma})}{\partial \boldsymbol{\sigma}\, \partial \boldsymbol{\sigma}} \quad \forall\, \mathbf{x} \in \Omega, \\ \mathbf{M}_t^{(r)} &= \frac{\partial \boldsymbol{D}^{(r)}}{\partial \boldsymbol{\sigma}^{(r)}} = \frac{\partial^2 U^{(r)}(\boldsymbol{\sigma})}{\partial \boldsymbol{\sigma}\, \partial \boldsymbol{\sigma}}, \quad r = 1, 2, \end{aligned} \tag{2.3}$$

where $\mathbf{M}_t$ is a fourth-order tensor that preserves both the minor and major symmetries and is used to describe the incremental response of the heterogeneous medium and the phases at a given instant.

Under the hypotheses of *statistical uniformity* and the aforementioned *separation of length-scales*, the effective stress potential $\widetilde{U}$ of the two-phase heterogeneous medium is defined by (Hill, 1963; Hutchinson, 1976):

$$\widetilde{U}(\overline{\boldsymbol{\sigma}}) = \min_{\sigma \in \mathcal{S}(\overline{\sigma})} \langle U(\mathbf{x}, \boldsymbol{\sigma}) \rangle = \sum_{r=1}^{2} c^{(r)} \min_{\sigma\, \epsilon\, \mathcal{S}(\overline{\sigma})} \langle U^{(r)}(\boldsymbol{\sigma}) \rangle^{(r)}, \tag{2.4}$$

where

$$\mathcal{S}\,(\overline{\boldsymbol{\sigma}}) = \{\boldsymbol{\sigma}, \mathrm{div}\boldsymbol{\sigma} = 0 \text{ in } \Omega,\ \langle \boldsymbol{\sigma} \rangle = \overline{\boldsymbol{\sigma}}\}, \tag{2.5}$$

is the set of statically admissible stresses that are compatible with the applied average stress $\overline{\boldsymbol{\sigma}}$. In this connection, the quantities $c^{(r)} = \langle \chi^{(r)} \rangle$ represent the volume fractions of the given phases and thus they satisfy the identity $\sum_{r=1}^{2} c^{(r)} = 1$. In analogy to the local constitutive behavior provided in relation (2.2), and by making use of Hill's lemma (Hill, 1963), the instantaneous relation between the average Cauchy stress, $\overline{\boldsymbol{\sigma}} = \langle \boldsymbol{\sigma} \rangle$, and the average Eulerian strain-rate, $\overline{\boldsymbol{D}} = \langle \boldsymbol{D} \rangle$, is given by

$$\overline{\boldsymbol{D}} = \frac{\partial\, \widetilde{U}}{\partial\, \overline{\boldsymbol{\sigma}}}(\overline{\boldsymbol{\sigma}}). \tag{2.6}$$

This last relation provides a constitutive law for the two-phase material at each instant in time, provided that the microstructure is known. As already mentioned in the introduction, the materials considered here can undergo finite deformations, and as a consequence their microstructure is expected to evolve in time. Thus, their effective behavior will change in time due to the changes in the microstructure. For this reason, it is important to note that for a complete description of the problem, we also need to provide relations for the evolution of the microstructure. Such expressions will be given in a later section.

On the other hand, the above-described analysis can also be made in the context of a dissipation potential $W^{(r)}(\boldsymbol{D})$, which is dual (by means of the Legendre-Fenchel transform) to the stress potential $U^{(r)}(\boldsymbol{\sigma})$ and is given by

$$W^{(r)}(\boldsymbol{D}) = \max_{\boldsymbol{\sigma}} \left\{ \boldsymbol{\sigma} \cdot \boldsymbol{D} - U^{(r)}(\boldsymbol{\sigma}) \right\}, \quad r = 1, 2 \tag{2.7}$$

such that

$$\boldsymbol{\sigma}^{(r)} = \frac{\partial W^{(r)}(\boldsymbol{D})}{\partial \boldsymbol{D}}, \quad r = 1, 2. \tag{2.8}$$

The effective behavior can then be defined in terms of the effective dissipation potential by

$$\widetilde{W}(\overline{\boldsymbol{D}}) = \min_{\boldsymbol{D} \in \mathcal{K}(\overline{\boldsymbol{D}})} = \sum_{r=1}^{2} c^{(r)} \langle W^{(r)}(\boldsymbol{D}) \rangle^{(r)}, \tag{2.9}$$

where $\mathcal{K}(\overline{\boldsymbol{D}})$ is the set of kinematically admissible strain-rate fields given by

$$\mathcal{K}(\overline{\boldsymbol{D}}) = \left\{ \boldsymbol{D} \,|\, \text{there is } \mathbf{v} \text{ where } \boldsymbol{D} = \frac{1}{2}\left[\nabla \mathbf{v} + (\nabla \mathbf{v})^T\right] \text{ in } \Omega, \ \mathbf{v} = \overline{\boldsymbol{L}}\,\mathbf{x} \text{ on } \partial\Omega \right\}. \tag{2.10}$$

Here, $\overline{\boldsymbol{L}}$ is the macroscopic velocity gradient, while the macroscopic strain-rate $\overline{\boldsymbol{D}}$ and spin $\overline{\boldsymbol{\Omega}}$ are given by

$$\overline{\boldsymbol{D}} = \frac{1}{2}\left[\overline{\boldsymbol{L}} + \overline{\boldsymbol{L}}^T\right], \qquad \text{and} \qquad \overline{\boldsymbol{\Omega}} = \frac{1}{2}\left[\overline{\boldsymbol{L}} - \overline{\boldsymbol{L}}^T\right]. \tag{2.11}$$

In turn, the effective constitutive behavior of the material is given by

$$\overline{\boldsymbol{\sigma}} = \frac{\partial \widetilde{W}}{\partial \overline{\boldsymbol{D}}}(\overline{\boldsymbol{D}}). \tag{2.12}$$

This description for the effective behavior of a heterogeneous material in terms of $\widetilde{W}$ is equivalent to the one described in relation (2.4) in terms of the effective stress potential $\widetilde{U}$. In the present work, where the focus is on porous materials, it is convenient to make use of the effective stress potential $\widetilde{U}$ instead of the dissipation potential $\widetilde{W}$, and thus no explicit results will be given for $\widetilde{W}$ in the rest of the text.

In summary, the problem of estimating the effective behavior of two-phase nonlinear composites is equivalent to that of estimating the function $\widetilde{U}$ in relation (2.4). Nonetheless, computing these functions exactly is an extremely difficult task, which would require, in general, an intensive full-field numerical simulation assuming that the exact location of the phases in the RVE is known. However, in most of the cases, the microstructure is not fully deterministic, and thus, the exact location of the phases in the RVE is not known. For this reason, in this work, we will make use of a variational homogenization technique to be discussed in the following sections.

2.2 Application to porous materials

The framework described in the previous section is general and applies to any two-phase heterogeneous medium, including the case of a two-phase porous medium, which is the main subject of this work. In this regard, we consider the RVE Ω to be a two-phase porous medium with each phase occupying a sub-domain $\Omega^{(r)}$ $(r = 1, 2)$. The vacuous phase is identified with phase 2, whereas the non-vacuous phase (i.e., matrix phase) is denoted as phase 1. For later reference, the brackets $\langle\cdot\rangle$ and $\langle\cdot\rangle^{(r)}$ are used to denote volume averages over the RVE (Ω) and the phase r $(\Omega^{(r)})$, respectively. Following definitions (2.2), the local behavior of the matrix phase is characterized by an isotropic, convex stress potential $U^{(1)} \equiv U$, such that the corresponding Cauchy stress $\boldsymbol{\sigma}$ and the Eulerian strain-rate $\boldsymbol{D}$ are related by

$$\boldsymbol{D} = \frac{\partial U(\boldsymbol{\sigma})}{\partial \boldsymbol{\sigma}}, \tag{2.13}$$

whereas the corresponding stress potential of the porous phase $U^{(2)}$ is equal to zero. Then, it follows from definition (2.4) that the effective stress potential $\widetilde{U}$ for a porous medium can be reduced to

$$\widetilde{U}(\overline{\boldsymbol{\sigma}}) = (1 - f) \min_{\sigma \,\epsilon\, \mathcal{S}(\overline{\sigma})} \langle U(\boldsymbol{\sigma})\rangle^{(1)}. \tag{2.14}$$

In this expression, $f = c^{(2)}$ and $1 - f = c^{(1)}$ are the volume fractions of the porous (i.e., porosity) and the matrix phases, respectively and

$$\mathcal{S}\,(\overline{\boldsymbol{\sigma}}) = \{\boldsymbol{\sigma}, \mathrm{div}\boldsymbol{\sigma} = 0 \text{ in } \Omega,\ \boldsymbol{\sigma}\,\mathbf{n} = \mathbf{0} \text{ on } \partial\,\Omega^{(2)},\ \langle\boldsymbol{\sigma}\rangle = \overline{\boldsymbol{\sigma}}\}, \tag{2.15}$$

is the set of statically admissible stresses that are compatible with the average stress $\overline{\boldsymbol{\sigma}}$ and zero tractions on the surface of the voids. The effective constitutive relation between the average Cauchy stress, $\overline{\boldsymbol{\sigma}} = \langle\boldsymbol{\sigma}\rangle$, and the average Eulerian strain-rate, $\overline{\boldsymbol{D}} = \langle\boldsymbol{D}\rangle$ is given by relation (2.6).

As already remarked previously, estimating the effective stress potential $\widetilde{U}$ given by (2.14) for a nonlinear porous material requires further information about the location of the phases in the RVE. For this reason, in the following subsection, we introduce the notion of a "particulate" microstructure, which is appropriate for the class of porous materials to be considered here.

2.2.1 Particulate Microstructures

In most of the cases involving random composite materials, the physical properties of the media vary not only with position $\mathbf{x}$ but also from sample to sample. In general, for the complete determination of the location of the phases and hence the microstructure, we need to specify the functions $\chi^{(r)}(\mathbf{x})$ for all $\mathbf{x}$ in Ω. However, this is not possible in most of the cases of random composites and thus the description of such materials can be achieved via $n-$point correlation functions, with n being a finite integer number. On the other hand, these random systems can be considered to be *statistically uniform* (Willis, 1982), which implies that the $n-$point correlation functions are insensitive to translations. For such media, it is usual to make an assumption of *ergodic* type, which yields that local configurations occur every any one specimen with the frequency with which they occur over a single neighborhood in an ensemble of specimens. Thus, ensemble averages can be replaced by volume

averages, and hence the one-point statistics simply provide information about the volume fraction of the phases. For instance, the porosity is defined in terms of the distribution functions by $f = \langle \chi^{(2)} \rangle$.

On the other hand, the two-, three-, or n-point statistics provide information about the relative position of the phases in Ω. In the present study, we make use of homogenization methods (Hashin and Shtrikman, 1963; Willis, 1977; Willis, 1978; Ponte Castañeda and Willis, 1995) that involve information up to two-point statistics, although there exist theories that make use of three-point statistics (Beran, 1965; Kröner, 1977; Milton, 1982; Willis, 1981), which are fairly complicated and will not be used here. To begin with, Willis (1977) proposed a general description of the microstructure in terms of the two-point correlation function, which can exhibit, for example, isotropic or ellipsoidal symmetry in the space. This formulation allowed the author to obtain bounds on the effective response of the composite, while explaining the Hashin-Shtrikman (1963) variational principle for isotropic composites in a rigorous mathematical way.

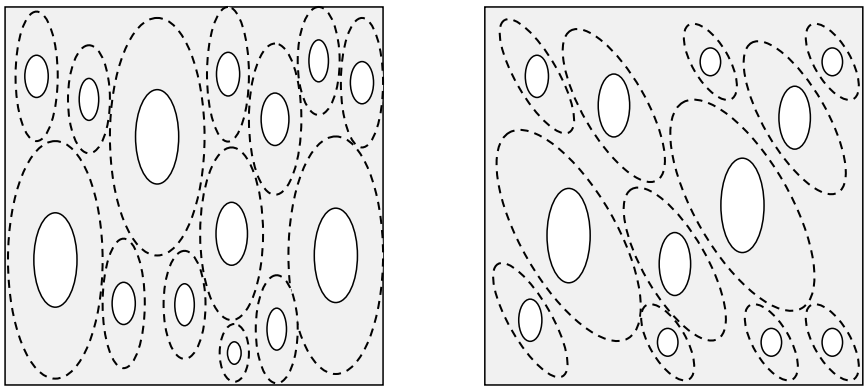

(a) (b)

Figure 2.1: Representative volume element of a "particulate" porous medium. Ellipsoidal voids distributed randomly with "ellipsoidal symmetry." The solid ellipsoids denote the voids, and the dashed ellipsoids, their distribution.

In a later work, Willis (1978) considered the case of a composite that comprises a matrix phase in which are embedded inclusions of known shapes and orientation. This description represents a "particulate" microstructure and is a generalization of the Eshelby (1956) dilute microstructure in the non-dilute regime. It is important to note that this representation is a subclass of the above-mentioned more general description (Willis, 1977) of a two-phase heterogeneous material, whose phases are simply described by the two-point correlation function. More specifically, a "particulate" composite consists of inclusions with known shapes and orientations, whereas the two-point correlation function provides information about the distribution of the centers of the inclusions. For instance, Fig. 2.1 shows schematically a representation of a "particulate" microstructure consisting of ellipsoidal inclusions (solid lines) with known shapes and orientations distributed randomly in a matrix phase with ellipsoidal symmetry (dashed ellipsoids). In the original work, Willis (1978) considered that the shape and orientation of the inclusions is the same with the shape and orientation of the distribution function, as shown in Fig. 2.1a. However, due to the heterogeneity in the strain-rate fields in the "particulate" composite, the shape of the inclusions and the shape of their distribution function

is expected, in general, to change in different proportions during the deformation process. In this connection, Ponte Castañeda and Willis (1995) generalized the study of Willis (1978) for particulate microstructures by letting the shapes of the inclusions and their distribution to have different shapes and orientation, as shown in Fig. 2.1b, and therefore to evolve in a different manner.

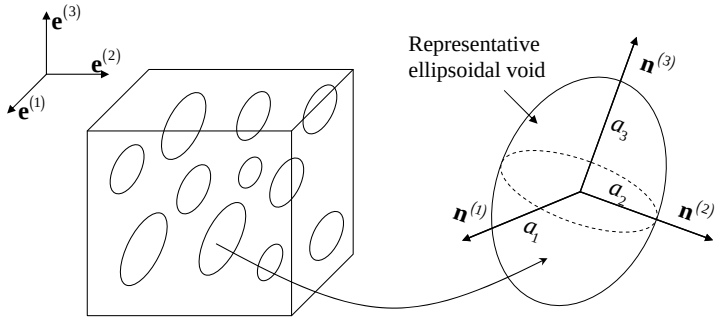

Figure 2.2: Representative ellipsoidal void.

In the following, the discussion is restricted to porous media, however, the foregoing definitions hold for any type of inclusion phase (e.g., fiber reinforced media). As already remarked in the previous paragraph, we need to define microstructural variables that describe the shape and orientation of the voids and their distribution function (Ponte Castañeda and Willis, 1995). Nevertheless, the effect of the shape and orientation of the distribution function on the effective behavior of the porous material becomes less important at low and moderate porosities (Kailasam and Ponte Castañeda, 1998), due to the fact that the contribution of the distribution function is only of order two in the volume fractions of the inclusions. Since, this work is mainly concerned with low to moderate concentrations of the voids, for simplicity, we will make the assumption, which will hold for the rest of the text, that the shape and orientation of the distribution function is identical to the shape and orientation of the voids, as shown in Fig. 2.1a, and hence it evolves in the same fashion when the material is subjected to finite deformations. The basic internal variables characterizing the state of the microstructure are:

1. the volume fraction of the voids or porosity $f = \mathcal{V}_2/\mathcal{V}$, where $\mathcal{V} = \mathcal{V}_1 + \mathcal{V}_2$ denotes the total volume, with $\mathcal{V}_1$ and $\mathcal{V}_2$ being the volume occupied by the matrix and the vacuous phase, respectively,

2. the two aspect ratios $w_1 = a_3/a_1$, $w_2 = a_3/a_2$ ($w_3 = 1$), where $2\,a_i$ with $i = 1, 2, 3$ denote the lengths of the principal axes of the representative ellipsoidal void,

3. the orientation unit vectors $\mathbf{n}^{(i)}$ ($i = 1, 2, 3$), defining an orthonormal basis set, which coincides with the principal axes of the representative ellipsoidal void.

The above set of the microstructural variables is denoted as

$$s_\alpha = \{f,\, w_1,\, w_2,\, \mathbf{n}^{(1)},\, \mathbf{n}^{(2)},\, \mathbf{n}^{(3)} = \mathbf{n}^{(1)} \times \mathbf{n}^{(2)}\}. \tag{2.16}$$

A schematic representation of the above-described microstructure is shown in Fig. 2.2. In turn, the vectors $\mathbf{n}^{(i)}$ can be described in terms of three Euler angles, which correspond to three rotations with respect to the laboratory frame axes $\mathbf{e}^{(i)}$, such that

$$\mathbf{n}^{(i)} = \boldsymbol{R}_{\psi}\, \mathbf{e}^{(i)}, \quad \text{with} \quad \boldsymbol{R}_{\psi} = \boldsymbol{R}_{\psi_3}\, \boldsymbol{R}_{\psi_2}\, \boldsymbol{R}_{\psi_1}. \tag{2.17}$$

In this expression, $\boldsymbol{R}_{\psi}$ is a proper orthogonal matrix, defined in terms of three other proper orthogonal matrices given by

$$\begin{aligned}
\boldsymbol{R}_{\psi_1} &= \begin{pmatrix} 1 & 0 & 0 \\ 0 & \cos\psi_1 & \sin\psi_1 \\ 0 & -\sin\psi_1 & \cos\psi_1 \end{pmatrix}, \\
\boldsymbol{R}_{\psi_2} &= \begin{pmatrix} \cos\psi_2 & 0 & \sin\psi_2 \\ 0 & 1 & 0 \\ -\sin\psi_2 & 0 & \cos\psi_2 \end{pmatrix}, \\
\boldsymbol{R}_{\psi_3} &= \begin{pmatrix} \cos\psi_3 & \sin\psi_3 & 0 \\ -\sin\psi_3 & \cos\psi_3 & 0 \\ 0 & 0 & 1 \end{pmatrix},
\end{aligned} \tag{2.18}$$

where ψ_1, ψ_2 and ψ_3 are three Euler angles, which denote rotation of the principal axes of the ellipsoid about the $1-$, $2-$ and $3-$ axis, respectively.

Now, the shape and orientation of the voids, as well as the shape and orientation of the two-point correlation function can be completely characterized by a symmetric second-order tensor $\boldsymbol{Z}$ introduced by Ponte Castañeda and Willis (1995) (see also Aravas and Ponte Castañeda (2004)), which is given in terms of the two aspect ratios and the three orientation vectors shown in Fig. 2.2, such that

$$\boldsymbol{Z} = w_1\, \mathbf{n}^{(1)} \otimes \mathbf{n}^{(1)} + w_2\, \mathbf{n}^{(2)} \otimes \mathbf{n}^{(2)} + \mathbf{n}^{(3)} \otimes \mathbf{n}^{(3)}, \quad \det(\boldsymbol{Z}) = w_1\, w_2. \tag{2.19}$$

Note that this assumption could be relaxed by allowing the shapes and orientation of the inclusions and of their distribution functions to be described by two different tensors $\boldsymbol{Z}$ (Ponte Castañeda and Willis, 1995). However, this more general configuration is not adopted here, for the reasons explained in the previous paragraphs.

In this class of particulate microstructures, some special cases of interest could be identified. Firstly, when $w_1 = w_2 = 1$, the resulting porous medium exhibits an overall isotropic behavior, provided that the matrix phase is also characterized by an isotropic stress potential. Secondly, if $w_1 = w_2 \neq 1$, the corresponding porous medium is transversely isotropic about the $\mathbf{n}^{(3)}-$direction, provided that the matrix phase is isotropic or transversely isotropic about the same direction. For this special configuration of the microstructure, i.e., for $w_1 = w_2 \neq 1$ with an isotropic matrix phase, several studies have been performed by several authors (Gologanu et al., 1993, 1994, 1997; Leblond et al., 1994; Gărăjeu et al. 2000; Flandi and Leblond, 2005a, 2005b; Monchiet et al., 2007).

Apart from the simple cases discussed previously, it is relevant to explore other types of particulate microstructures, which can be easily derived by appropriate specialization of the aforementioned variables s_a (Budiansky et al., 1982). In this regard, the following cases are considered:

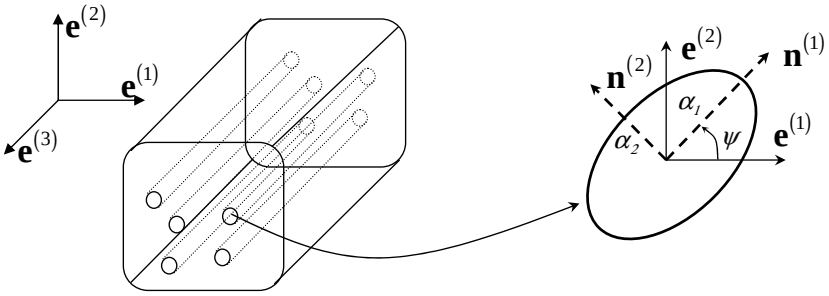

Figure 2.3: Representative ellipsoidal void in the case of cylindrical microstructures.

- $a_1 \to \infty$ or $a_2 \to \infty$ or $a_3 \to \infty$. Then, if the porosity f remains finite, the cylindrical microstructure is recovered, whereas if $f \to 0$, a porous material with infinitely thin needles is generated. Thus, the corresponding microstructural variables may be reduced to one aspect ratio w, defined appropriately (in this work we choose $a_3 \to \infty$ and hence $w = a_2/a_1$), and one angle of orientation, denoted as ψ, defined on the plane $1-2$ (see Fig. 2.3). The in-plane components of the orientation vectors are given by $\mathbf{n}^{(1)} = \cos\psi\,\mathbf{e}^{(1)} + \sin\psi\,\mathbf{e}^{(2)}$ and $\mathbf{n}^{(2)} = -\sin\psi\,\mathbf{e}^{(1)} + \cos\psi\,\mathbf{e}^{(2)}$, with $\mathbf{e}^{(1)}$ and $\mathbf{e}^{(2)}$ denoting a fixed frame of reference on the plane, as shown in Fig. 2.3.

- $a_1 \to 0$ or $a_2 \to 0$ or $a_3 \to 0$. Then, if the porosity f remains finite, the laminated microstructure is recovered (or alternatively a "porous sandwich"), whereas if $f \to 0$, a porous material with penny-shaped cracks is formed and thus the notion of density of cracks needs to be introduced. This special case will not be studied separately from the general three-dimensional case. Instead, this microstructure can be recovered when the porous material is subjected to special type of loading conditions.

To summarize, the set of the above-mentioned microstructural variables s_a provide a general three-dimensional description of a particulate porous material. It is evident that in the more general case, where the aspect ratios and the orientation of the ellipsoidal voids are such that $w_1 \neq w_2 \neq 1$ and $\mathbf{n}^{(i)} \neq \mathbf{e}^{(i)}$, the porous medium becomes highly anisotropic and estimating the effective response of such a material exactly is a real challenge. However, linear and nonlinear homogenization methods have been developed in the recent years that are capable of providing estimates and bounds for the effective behavior of such particulate composites. In the following sections, use of these techniques will be made to obtain estimates for viscoplastic porous media.

2.2.2 Constitutive behavior of the matrix phase

In order to proceed to specific results for nonlinear porous media, we need to define the constitutive relation that describes the local behavior of the matrix phase. In this regard, the matrix phase is described by an isotropic, viscoplastic stress or dissipation potential, U or W, respectively. The

general, compressible form of these potentials will be taken to be

$$U(\boldsymbol{\sigma}) = \frac{1}{2\,\kappa}\,\sigma_m^2 + \frac{\dot{\varepsilon}_o\,\sigma_o}{n+1}\left(\frac{\sigma_{eq}}{\sigma_o}\right)^{n+1} \quad \text{and} \quad W(\boldsymbol{D}) = \frac{9}{2}\,\kappa\,D_m^2 + \frac{\dot{\varepsilon}_o\,\sigma_o}{m+1}\left(\frac{D_{eq}}{\dot{\varepsilon}_o}\right)^{m+1}. \tag{2.20}$$

The scalars σ_o and $\dot{\varepsilon}_o$ denote the flow stress of the matrix phase and a reference strain-rate, while the mean and von Mises equivalent stress and strain-rate are defined by

$$\sigma_m = \frac{1}{3}\,\sigma_{ii}, \quad \sigma_{eq} = \sqrt{\frac{3}{2}\,\boldsymbol{\sigma}'\cdot\boldsymbol{\sigma}'} \quad \text{and} \quad D_m = \frac{1}{3}\,D_{ii}, \quad D_{eq} = \sqrt{\frac{2}{3}\,\boldsymbol{D}'\cdot\boldsymbol{D}'}, \tag{2.21}$$

respectively, with $i = 1, 2, 3$. The deviatoric stress $\boldsymbol{\sigma}'$ and strain-rate $\boldsymbol{D}'$ tensors are given by

$$\boldsymbol{\sigma}' = \boldsymbol{\sigma} - \sigma_m\,\boldsymbol{I}, \qquad \text{and} \qquad \boldsymbol{D}' = \boldsymbol{D} - D_m\,\boldsymbol{I}. \tag{2.22}$$

The nonlinearity of the matrix phase is introduced through $m = 1/n$, which denotes the strain-rate sensitivity parameter and takes values between 0 and 1. Note that the two limiting values $m = 1$ (or $n = 1$) and $m = 0$ (or $n \to \infty$) correspond to linear and ideally-plastic behaviors, respectively.

However, in most cases of interest, the matrix phase is incompressible, i.e., $\kappa \to \infty$, and therefore, the incompressibility limit needs to be considered in relation (2.20). The resulting stress and dissipation potentials take the simple power-law form

$$U(\boldsymbol{\sigma}) = \frac{\dot{\varepsilon}_o\,\sigma_o}{n+1}\left(\frac{\sigma_{eq}}{\sigma_o}\right)^{n+1} \quad \text{and} \quad W(\boldsymbol{D}) = \frac{\dot{\varepsilon}_o\,\sigma_o}{m+1}\left(\frac{D_{eq}}{\dot{\varepsilon}_o}\right)^{m+1}, \quad D_m = 0. \tag{2.23}$$

Note that, in this last expression, U and W are homogeneous functions of degree $n+1$ and $m+1$ in the stress $\boldsymbol{\sigma}$ and strain-rate $\boldsymbol{D}$, respectively. Use of this homogeneity property will be made in the following sections to define the effective behavior of porous materials.

2.2.3 Effective behavior of viscoplastic porous media

The effective behavior of a porous material has been defined in the general context of equation (2.14). Now, by making use of the homogeneity property of the local (incompressible) stress potential in (2.23), we can show[†] that the effective stress potential $\widetilde{U}$, in relation (2.14), is a homogeneous function of degree $n+1$ in the macroscopic stress $\overline{\boldsymbol{\sigma}}$. This property can be expressed by the following relation:

$$\widetilde{U}(\overline{\boldsymbol{\sigma}}) = \frac{\dot{\varepsilon}_o\,\sigma_o}{n+1}\widehat{h}(X_\Sigma, \overline{\boldsymbol{\sigma}}'/\overline{\sigma}_{eq};\, s_\alpha)\left(\frac{\overline{\sigma}_{eq}}{\sigma_o}\right)^{n+1}, \tag{2.24}$$

where s_α are the microstructural variables defined by (2.16), $\widehat{h}$ is a scalar function that is homogeneous of degree zero in the macroscopic stress $\overline{\boldsymbol{\sigma}}$ and X_Σ is the stress triaxiality given by

$$X_\Sigma = \frac{\overline{\sigma}_m}{\overline{\sigma}_{eq}}, \quad \overline{\sigma}_m = \overline{\sigma}_{ii}/3, \quad i = 1, 2, 3. \tag{2.25}$$

Note that when $X_\Sigma \to \infty$ the loading is purely hydrostatic such that $\overline{\boldsymbol{\sigma}} = \overline{\sigma}_m\,\boldsymbol{I}$.

In the following, we specialize this last result in two cases of interest; (a) for isotropic porous materials consisting of spherical voids (i.e., $w_1 = w_2 = 1$), and (b) for transversely isotropic porous

[†]To prove that $\widetilde{U}$ is positively homogeneous of degree $n+1$, it suffices to note that $U(\lambda\,\boldsymbol{\sigma}) = \lambda^{n+1}\,U(\boldsymbol{\sigma})$ in relation (2.14).

media consisting of cylindrical voids with circular cross-section (see Fig. 2.3) subjected to plane-strain loading conditions. In the first case, the effective stress potential $\widetilde{U}$ in (2.24) should depend on all three stress invariants and the porosity f. This implies that

$$\widetilde{U}(\overline{\boldsymbol{\sigma}}) = \frac{\dot{\varepsilon}_o\,\sigma_o}{n+1}\widehat{h}(X_\Sigma, \theta;\, f)\left(\frac{\overline{\sigma}_{eq}}{\sigma_o}\right)^{n+1}, \quad \theta = \frac{27}{2}\det\left(\frac{\overline{\boldsymbol{\sigma}}'}{\overline{\sigma}_{eq}}\right), \tag{2.26}$$

where θ is the Lode angle (see Kachanov, 1971) and is related to the third invariant of the macroscopic stress tensor.

On the other hand, the effective stress potential associated with transversely isotropic porous media consisting of aligned cylindrical voids can be further simplified for plane-strain loading by noting that it is a function of the first two invariants of the macroscopic stress tensor and the porosity f. The reason for this lies in the fact that the total energy of the material depends on the in-plane deformation modes for plane-strain loadings and therefore is independent of the determinant of $\overline{\boldsymbol{\sigma}}$ such that

$$\widetilde{U}(\overline{\boldsymbol{\sigma}}) = \frac{\dot{\varepsilon}_o\,\sigma_o}{n+1}\widehat{h}(X_\Sigma;\, f)\left(\frac{\overline{\sigma}_{eq}}{\sigma_o}\right)^{n+1}. \tag{2.27}$$

These two expressions have been introduced here since they constitute important special cases in the context of power-law materials as defined by relation (2.23).

2.2.4 Gauge function

For later reference, it is expedient to introduce here the notion of the gauge function and the *gauge factor*. Using the homogeneity of the effective stress potential $\widetilde{U}$ in $\overline{\boldsymbol{\sigma}}$ from relation (2.24), it is convenient to introduce the so-called *gauge factor* Γ_n (the subscript being used to denote dependence on the nonlinear exponent n), such that (Leblond et al., 1994)

$$\widetilde{U}(\overline{\boldsymbol{\sigma}};\, s_\alpha) = \frac{\dot{\varepsilon}_o\,\sigma_o}{n+1}\left(\frac{\Gamma_n(\overline{\boldsymbol{\sigma}};\, s_\alpha)}{\sigma_o}\right)^{n+1}. \tag{2.28}$$

It is then sufficient to study only one of the equipotential surfaces $\{\overline{\boldsymbol{\sigma}},\, \widetilde{U}(\overline{\boldsymbol{\sigma}}) = const\}$, i.e., the so-called *gauge surface* $\mathcal{P}_n$ of the porous material defined by (Leblond et al., 1994)

$$\mathcal{P}_n \equiv \left\{\overline{\boldsymbol{\Sigma}},\, \widetilde{U}(\overline{\boldsymbol{\Sigma}};\, s_\alpha) = \frac{\dot{\varepsilon}_o\,\sigma_o^{-n}}{n+1}\right\}. \tag{2.29}$$

Consequently, the value of $\widetilde{U}$ for any stress tensor $\overline{\boldsymbol{\sigma}}$ is given by (2.28), with Γ_n satisfying the relation

$$\overline{\boldsymbol{\sigma}} = \Gamma_n(\boldsymbol{\sigma};\, s_\alpha)\,\overline{\boldsymbol{\Sigma}} \qquad \text{or} \qquad \overline{\boldsymbol{\Sigma}} = \frac{\overline{\boldsymbol{\sigma}}}{\Gamma_n(\overline{\boldsymbol{\sigma}};\, s_\alpha)}. \tag{2.30}$$

Note that Γ_n is homogeneous of degree one in $\overline{\boldsymbol{\sigma}}$, and therefore $\overline{\boldsymbol{\Sigma}}$ is homogeneous of degree zero in $\overline{\boldsymbol{\sigma}}$.

In view of relation (2.29) and the definition of the gauge factor Γ_n in (2.28), it is pertinent to define the *gauge function* $\widetilde{\Phi}_n$, which provides the equation for the gauge surface via the expression

$$\overline{\boldsymbol{\Sigma}} \in \mathcal{P}_n \quad \Longleftrightarrow \quad \widetilde{\Phi}_n(\overline{\boldsymbol{\Sigma}};\, s_\alpha) = \Gamma_n(\overline{\boldsymbol{\Sigma}};\, s_\alpha) - 1 = 0. \tag{2.31}$$

The subscript n has been used to indicate that the gauge function depends explicitly on the nonlinear exponent of the matrix phase. The above definitions of the gauge surface and the gauge function

are analogous to the corresponding well known notions of the yield function and the yield surface in the context of ideal-plasticity. Such discussion is made in the following subsection, where the case of ideal-plasticity is considered separately.

Making use of the above definitions, we can redefine the stress triaxiality X_Σ in terms of $\overline{\boldsymbol{\Sigma}}$ as

$$X_\Sigma = \overline{\Sigma}_m/\overline{\Sigma}_{eq}, \qquad \overline{\Sigma}_{eq} = \sqrt{3\,\overline{\boldsymbol{\Sigma}}' \cdot \overline{\boldsymbol{\Sigma}}'/2}, \qquad \overline{\Sigma}_m = \overline{\Sigma}_{ii}/3, \qquad i = 1,2,3, \tag{2.32}$$

where $\overline{\Sigma}_m$ and $\overline{\Sigma}_{eq}$ denote the mean and equivalent part of $\overline{\boldsymbol{\Sigma}}$.

On the other hand, it follows from definitions (2.6) and (2.28) that

$$\overline{\boldsymbol{D}} = \dot{\varepsilon}_o \left(\frac{\Gamma_n(\overline{\boldsymbol{\sigma}};\, s_\alpha)}{\sigma_o}\right)^n \frac{\partial \Gamma_n(\overline{\boldsymbol{\sigma}};\, s_\alpha)}{\partial \overline{\boldsymbol{\sigma}}}, \qquad \text{or} \qquad \overline{\boldsymbol{E}} = \frac{\overline{\boldsymbol{D}}}{\dot{\varepsilon}_o \left(\Gamma_n(\overline{\boldsymbol{\sigma}};\, s_\alpha)/\sigma_o\right)^n}, \tag{2.33}$$

where $\overline{\boldsymbol{E}}$ is a suitably normalized macroscopic strain-rate that is homogeneous of degree zero in $\overline{\boldsymbol{\sigma}}$. Note that the terms $\partial\Gamma_n/\partial\overline{\boldsymbol{\sigma}}$ and $\dot{\varepsilon}_o\,(\Gamma_n/\sigma_o)^n$ in (2.33) correspond to the direction and the magnitude, respectively, of $\overline{\boldsymbol{D}}$. In turn, the strain-rate triaxiality is given by

$$X_E = \overline{E}_m/\overline{E}_{eq}, \qquad \overline{E}_{eq} = \sqrt{2\,\overline{\boldsymbol{E}}' \cdot \overline{\boldsymbol{E}}'/3}, \qquad \overline{E}_m = \overline{E}_{ii}/3, \qquad i = 1,2,3, \tag{2.34}$$

where $\overline{E}_m$ and $\overline{E}_{eq}$ denote the normalized, hydrostatic and von Mises equivalent strain-rates, while $\boldsymbol{E}'$ is the deviatoric part of the normalized strain-rate $\overline{\boldsymbol{E}}$.

2.2.5 Porous media with ideally-plastic matrix phase: general expressions

A special, albeit important, case of the above mentioned viscoplastic behavior is the one of ideal-plasticity obtained by letting $n \to \infty$ or $m \to 0$. It follows directly from relation (2.23) that the stress potential of the matrix phase is defined in the ideally-plastic limit as

$$U(\boldsymbol{\sigma}) = \begin{cases} 0, & \text{if} \quad \sigma_{eq}/\sigma_o \leq 1 \\ \infty, & \text{otherwise,} \end{cases} \tag{2.35}$$

which implies that the yield function can be expressed as

$$\Phi(\boldsymbol{\sigma}) = \sigma_{eq} - \sigma_o, \tag{2.36}$$

such that the yield surface is given by $\Phi(\boldsymbol{\sigma}) = 0$. As already expected, the matrix phase is described by the well-known von Mises yield criterion in the limit of ideal-plasticity.

Now, making use of definition (2.28) in the ideally-plastic limit, the effective stress potential $\widetilde{U}$ of the porous medium becomes (Suquet, 1983, 1993)

$$\widetilde{U}(\overline{\boldsymbol{\sigma}};\, s_\alpha) = \begin{cases} 0, & \text{if} \quad \Gamma_\infty(\overline{\boldsymbol{\sigma}};\, s_\alpha)/\sigma_o \leq 1, \\ \infty, & \text{otherwise,} \end{cases} \tag{2.37}$$

which implies that the equation describing the yield locus is

$$\Gamma_\infty(\overline{\boldsymbol{\sigma}}) = \sigma_o. \tag{2.38}$$

Note further that, by making use of the last criterion together with definition (2.30), it is readily derived that

$$\overline{\boldsymbol{\Sigma}} = \frac{\overline{\boldsymbol{\sigma}}}{\sigma_o}, \tag{2.39}$$

in the limit as $n \to \infty$. Then, it follows from (2.31), that, in the ideally-plastic limit, the gauge function may be expressed as

$$\widetilde{\Phi}_\infty(\overline{\boldsymbol{\Sigma}};\, s_\alpha) = \Gamma_\infty(\overline{\boldsymbol{\Sigma}};\, s_\alpha) - 1 = \Gamma_\infty(\overline{\boldsymbol{\sigma}}/\sigma_o;\, s_\alpha) - 1 = \widetilde{\Phi}_\infty(\overline{\boldsymbol{\sigma}}/\sigma_o;\, s_\alpha), \tag{2.40}$$

so that $\widetilde{\Phi}_\infty(\overline{\boldsymbol{\Sigma}}) = 0$ defines the corresponding gauge surface

$$\mathcal{P}_\infty \equiv \left\{\overline{\boldsymbol{\Sigma}},\, \Gamma_\infty(\overline{\boldsymbol{\Sigma}};\, s_\alpha) = 1\right\}. \tag{2.41}$$

For later use, it is convenient to define the yield criterion in terms of the macroscopic stress $\overline{\boldsymbol{\sigma}}$. This can be easily extracted from (2.40) by making use of the fact that Γ_∞ is a positively homogeneous function of degree one in its arguments, such that

$$\widetilde{\Phi}(\overline{\boldsymbol{\sigma}};\, s_\alpha) = \sigma_o\, \widetilde{\Phi}_\infty(\overline{\boldsymbol{\sigma}};\, s_\alpha) = \sigma_o\, \Gamma_\infty(\overline{\boldsymbol{\sigma}}/\sigma_o;\, s_\alpha) - \sigma_o = \Gamma_\infty(\overline{\boldsymbol{\sigma}};\, s_\alpha) - \sigma_o. \tag{2.42}$$

Thus, $\widetilde{\Phi}(\overline{\boldsymbol{\sigma}}) = 0$ is the equation describing the yield surface

$$\mathcal{P} \equiv \left\{\overline{\boldsymbol{\sigma}},\, \Gamma_\infty(\overline{\boldsymbol{\sigma}};\, s_\alpha) = \sigma_o\right\}, \tag{2.43}$$

which is nothing else but an homothetic expansion by a factor of σ_o of the gauge surface $\mathcal{P}_\infty$. In other words, the locus of the points in $\mathcal{P}_\infty$ can simply be constructed by normalizing the locus of points in $\mathcal{P}$ by σ_o (see (2.39)).

In this regard, it follows from (2.42) that the corresponding macroscopic strain-rate $\overline{\boldsymbol{D}}$ is defined by

$$\overline{\boldsymbol{D}} = \dot{\Lambda}\, \frac{\partial \widetilde{\Phi}}{\partial \overline{\boldsymbol{\sigma}}} = \dot{\Lambda}\, \frac{\partial \Gamma_\infty(\overline{\boldsymbol{\sigma}};\, s_\alpha)}{\partial \overline{\boldsymbol{\sigma}}}, \tag{2.44}$$

where $\dot{\Lambda}$ is a non-negative parameter known as the plastic multiplier to be determined by the consistency condition $\dot{\widetilde{\Phi}}$. Note that the normalized strain-rate tensor $\overline{\boldsymbol{E}}$ can be defined simply as

$$\overline{\boldsymbol{E}} = \frac{\overline{\boldsymbol{D}}}{\dot{\Lambda}} = \frac{\partial \Gamma_\infty(\overline{\boldsymbol{\sigma}};\, s_\alpha)}{\partial \overline{\boldsymbol{\sigma}}}, \tag{2.45}$$

which is in accordance with the corresponding definition in (2.33) for finite nonlinearities.

In turn, the consistency condition provides information about the incremental response of the porous material and, by making use of the fact that $\widetilde{\Phi}$ is an isotropic function of its arguments, one finds that (Dafalias, 1985)

$$\dot{\widetilde{\Phi}} = \frac{\partial \widetilde{\Phi}}{\partial \overline{\boldsymbol{\sigma}}} \cdot \overset{\triangledown}{\overline{\boldsymbol{\sigma}}} + \frac{\partial \widetilde{\Phi}}{\partial s_\alpha}\, \overset{\triangledown}{s}_\alpha = 0. \tag{2.46}$$

In this expression, the symbol $\overset{\triangledown}{()}$ has been used to denote the Jaumann rate of a given quantity, while

$$\overset{\triangledown}{s}_\alpha = \{\dot{f}, \dot{w}_1, \dot{w}_2, \overset{\triangledown}{\mathbf{n}}{}^{(1)}, \overset{\triangledown}{\mathbf{n}}{}^{(2)}, \overset{\triangledown}{\mathbf{n}}{}^{(3)}\}. \tag{2.47}$$

Here, the "dot" symbol has been used to denote time derivatives. It will be shown in a later section that the quantities $\overset{\triangledown}{s}_\alpha$ are *proportional* to the magnitude of the macroscopic strain-rate $\overline{\boldsymbol{D}}$, i.e., to

the plastic multiplier $\dot{\Lambda}$. This proportionality (considered as given here) allows us to define a scalar function, known as the Jaumann hardening rate H_J, which is independent of $\dot{\Lambda}$, via

$$\dot{\Lambda}\, H_J = -\frac{\partial \widetilde{\Phi}}{\partial s_\alpha} \overset{\triangledown}{s}_\alpha. \tag{2.48}$$

The Jaumann hardening rate is an objective measure of the geometrical softening or hardening of the porous material to be used in the prediction of instabilities in a later section. Consequently, the consistency condition in relation (2.46) can be written as

$$\dot{\widetilde{\Phi}} = \frac{\partial \widetilde{\Phi}}{\partial \boldsymbol{\sigma}} \cdot \overset{\triangledown}{\boldsymbol{\sigma}} - \dot{\Lambda}\, H_J = 0 \Rightarrow \dot{\Lambda} = \frac{1}{H_J} \frac{\partial \widetilde{\Phi}}{\partial \boldsymbol{\sigma}} \cdot \overset{\triangledown}{\boldsymbol{\sigma}}. \tag{2.49}$$

Substituting this last result in (2.44), the expression for the macroscopic strain-rate becomes

$$\overline{D}_{ij} = \frac{1}{H_J} \frac{\partial \widetilde{\Phi}}{\partial \overline{\sigma}_{ij}} \frac{\partial \widetilde{\Phi}}{\partial \overline{\sigma}_{kl}} \overset{\triangledown}{\overline{\sigma}}_{kl}. \tag{2.50}$$

This relation describes the effective constitutive behavior of a porous material with an ideally-plastic matrix phase.

To summarize, we have defined the instantaneous effective behavior of porous media in a general homogenization context making use of certain hypotheses, such as statistical uniformity and separation of length scales. Next, we have defined the notion of a "particulate" microstructure in a random composite. This definition will be used in the rest of this work to provide specific estimates for linear and nonlinear particulate porous media. In turn, the local behavior of the matrix has been assumed to follow a power-law form, which is known as a viscoplastic law. Finally, general expressions have been provided for the effective stress potential of the porous material in the nonlinear and the ideally-plastic context. In the following sections, we make use of homogenization techniques to obtain specific results on the effective behavior of linear and nonlinear porous materials.

2.3 Linearly viscous behavior

In the present study, we will make use of the "variational" (Ponte Castañeda, 1991) and the "second-order" (Ponte Castañeda, 2002a) nonlinear homogenization methods to estimate the effective behavior of viscoplastic porous media. Due to the fact that these nonlinear methods make use of available results for linearly viscous and linearly thermo-viscous porous media, it is useful here to recall briefly certain relations for linear composites. Thus, this section deals with the determination of the effective behavior of linearly viscous, two-phase composites, which are specialized later to linearly viscous porous media. The study of linearly thermo-viscous composites is made in the following section. It is worth noting here that the linearly viscous and linearly thermo-viscous materials are mathematically analogous to the linear elastic and thermo-elastic materials.

More specifically, we consider a linearly viscous composite consisting of a matrix phase identified with the label 1, and an inclusion phase identified with label 2. Now, let these phases be described by quadratic stress potentials of the form

$$U^{(r)}(\boldsymbol{\sigma}) = \frac{1}{2}\, \boldsymbol{\sigma}(\mathbf{x}) \cdot \mathbf{M}^{(r)}\, \boldsymbol{\sigma}(\mathbf{x}), \quad r = 1, 2, \quad \forall\, \mathbf{x} \in \Omega^{(r)}, \tag{2.51}$$

where $\mathbf{M}^{(r)}$ are fourth-order, positive-definite, tensors that possess both major and minor symmetries. The corresponding stress–strain-rate relation of such materials is linear and reads

$$\boldsymbol{D}^{(r)} = \frac{\partial U^{(r)}(\boldsymbol{\sigma})}{\partial \boldsymbol{\sigma}} = \mathbf{M}^{(r)}\,\boldsymbol{\sigma}^{(r)}, \quad r = 1, 2. \tag{2.52}$$

This relation can be inverted to give

$$\boldsymbol{\sigma}^{(r)} = \mathbf{L}^{(r)}\,\boldsymbol{D}^{(r)}, \quad r = 1, 2. \tag{2.53}$$

with $\mathbf{L}^{(r)} = (\mathbf{M}^{(r)})^{-1}$ denoting the viscous modulus tensor of the phases, which has both major and minor symmetries. These last relations specify completely the local behavior of the phases in the two-phase medium, whereas they are in accordance with the definitions (2.1) and (2.2).

It follows from the linearity of the problem, that the corresponding *instantaneous* effective stress potential $\widetilde{U}$ of the two-phase linear composite is also of a quadratic form and can be written as

$$\widetilde{U}(\overline{\boldsymbol{\sigma}}) = \frac{1}{2}\,\overline{\boldsymbol{\sigma}} \cdot \widetilde{\mathbf{M}}\,\overline{\boldsymbol{\sigma}}, \tag{2.54}$$

with $\widetilde{\mathbf{M}}$ being a fourth-order symmetric (both minor and major symmetries) tensor denoting the effective viscous compliance tensor of the composite. Following definition (2.6), the resulting relation between the average stress and strain-rate is given by

$$\overline{\boldsymbol{D}} = \frac{\partial \widetilde{U}(\overline{\boldsymbol{\sigma}})}{\partial \overline{\boldsymbol{\sigma}}} = \widetilde{\mathbf{M}}\,\overline{\boldsymbol{\sigma}}. \tag{2.55}$$

This relation can be inverted to yield

$$\overline{\boldsymbol{\sigma}} = \widetilde{\mathbf{L}}\,\overline{\boldsymbol{D}}, \tag{2.56}$$

with $\widetilde{\mathbf{L}} = \widetilde{\mathbf{M}}^{-1}$ denoting the effective viscous modulus tensor of the composite. For the case of two-phase *particulate* composites, where the inclusions and their distribution function have the same ellipsoidal shape and orientation, as discussed in subsection 2.2.1, the effective viscous compliance and modulus tensors, $\widetilde{\mathbf{M}}$ and $\widetilde{\mathbf{L}}$, are given by (Willis, 1978; Ponte Castañeda and Willis, 1995)

$$\widetilde{\mathbf{M}} = \mathbf{M}^{(1)} + c^{(2)}\left[c^{(1)}\,\mathbf{Q} + \left(\mathbf{M}^{(2)} - \mathbf{M}^{(1)}\right)^{-1}\right]^{-1}, \tag{2.57}$$

and

$$\widetilde{\mathbf{L}} = \mathbf{L}^{(1)} + c^{(2)}\left[c^{(1)}\,\mathbf{P} + \left(\mathbf{L}^{(2)} - \mathbf{L}^{(1)}\right)^{-1}\right]^{-1}. \tag{2.58}$$

In these expressions, $c^{(r)}$ denote the volume fractions of the phases ($r = 1$ for the matrix and $r = 2$ for the inclusions). In addition, the fourth-order microstructural tensors $\mathbf{Q}$ and $\mathbf{P}$ are related to the Eshelby (1957) and Hill (1963) polarization tensor and contain information about the shape and orientation of the inclusions and their distribution function, given by (Willis, 1978)

$$\mathbf{Q} = \frac{1}{4\pi\det(\boldsymbol{Z})}\int_{|\boldsymbol{\zeta}|=1} \widehat{\mathbf{H}}(\boldsymbol{\zeta})\,|\boldsymbol{Z}^{-1}\,\boldsymbol{\zeta}|^{-3}\,dS, \quad \text{with} \quad \widehat{\mathbf{H}} = \mathbf{L}^{(1)} - \mathbf{L}^{(1)}\,\mathbf{H}\,\mathbf{L}^{(1)}, \tag{2.59}$$

and

$$\mathbf{P} = \frac{1}{4\pi\det(\boldsymbol{Z})}\int_{|\boldsymbol{\zeta}|=1} \mathbf{H}(\boldsymbol{\zeta})\,|\boldsymbol{Z}^{-1}\,\boldsymbol{\zeta}|^{-3}\,dS. \tag{2.60}$$

Here, the tensor $\boldsymbol{Z}$ is given by relation (2.19) serving to characterize the *instantaneous* shape and orientation of the inclusions and their distribution function in this context of particulate microstructures. In addition, $H_{(ij)(kl)} = (L^{(1)}_{iakb}\zeta_a\zeta_b)^{-1}\zeta_j\zeta_l\Big|_{(ij)(kl)}$, where the brackets denote symmetrization with respect to the corresponding indices, while $\boldsymbol{\zeta}$ is a unit vector. Then, it follows from (2.59) and (2.60) that the $\mathbf{Q}$ is related to the $\mathbf{P}$ tensor through

$$\mathbf{Q} = \mathbf{L}^{(1)} - \mathbf{L}^{(1)}\,\mathbf{P}\,\mathbf{L}^{(1)}, \quad \text{since} \quad \int_{|\boldsymbol{\zeta}|=1} |\boldsymbol{Z}^{-1}\,\boldsymbol{\zeta}|^{-3}\,dS = 4\pi\,\det(\boldsymbol{Z}). \tag{2.61}$$

At this point, it is worth mentioning that both expressions (2.57) and (2.58) for $\widetilde{\mathbf{M}}$ and $\widetilde{\mathbf{L}}$, respectively, are equivalent and either of them can be used for the estimation of the instantaneous effective behavior of the linear two-phase medium (Sab, 1992). Moreover, it should be emphasized that the above Willis estimates for $\widetilde{\mathbf{M}}$ (or $\widetilde{\mathbf{L}}$) lead to uniform fields in the inclusion phase (Willis, 1978), which is consistent with the work of Eshelby (1957) in the dilute case. In fact, the Willis estimates are exact for dilute composites. On the other hand, for non-dilute media, the fields within the inclusions are, in general, non-uniform, but this "non-uniformity" is negligible (Bornert et al., 1996) provided that the inclusions are not in close proximity to each other, i.e., their volume fraction is not so large compared to the one of the matrix phase. This is an important observation that we should bear in mind when the application of these homogenization techniques is done for composites consisting of high concentrations of particles or voids. Nonetheless, the focus on this work is on porous media with low to moderate concentrations of voids, and hence the Willis procedure is expected to be sufficiently accurate in this case.

The above analysis provides a description of the instantaneous effective behavior of linearly viscous two-phase materials in terms of macroscopic measures, namely the effective stress potential $\widetilde{U}$, and the macroscopic stress $\overline{\boldsymbol{\sigma}}$ and strain-rate $\overline{\boldsymbol{D}}$. However, the homogenization theory is also capable of generating estimates for other stress and strain-rate quantities such as the first and second moments of the phase fields. In this work, the interest is mainly on the first moments of the phase fields, or equivalently, the average stress $\overline{\boldsymbol{\sigma}}^{(r)} = \langle\boldsymbol{\sigma}\rangle^{(r)}$, the average strain-rate $\overline{\boldsymbol{D}}^{(r)} = \langle\boldsymbol{D}\rangle^{(r)}$ and the average spin $\overline{\boldsymbol{\Omega}}^{(r)} = \langle\boldsymbol{\Omega}\rangle^{(r)}$ in each phase. It should be noted that the phase average strain-rate $\overline{\boldsymbol{D}}^{(r)}$ and spin $\overline{\boldsymbol{\Omega}}^{(r)}$ tensors are the symmetric and skew-symmetric parts of the phase average velocity gradient. However, in addition to the first moments, expressions can also be derived for the second-moments of the stress and strain-rate fields, which will be presented in the sequel.

In this regard, in the case of linear, two-phase materials, the estimation of the average stress and strain-rate fields is given in terms of stress and strain-rate concentration tensors by (Hill, 1963; Laws, 1973; Willis, 1981)

$$\overline{\boldsymbol{\sigma}}^{(r)} = \mathbf{B}^{(r)}\,\overline{\boldsymbol{\sigma}}, \qquad \overline{\boldsymbol{D}}^{(r)} = \mathbf{A}^{(r)}\,\overline{\boldsymbol{D}}, \tag{2.62}$$

where $r = 1, 2$. In this expression, $\mathbf{B}^{(r)}$ and $\mathbf{A}^{(r)}$ are fourth-order tensors that exhibit minor symmetry (but not necessarily major symmetry). It is important to note that the phase average stresses and strain-rates are related to the macroscopic stress and strain-rate tensor by

$$\overline{\boldsymbol{\sigma}} = \sum_{r=1}^{2} c^{(r)}\,\overline{\boldsymbol{\sigma}}^{(r)}, \qquad \overline{\boldsymbol{D}} = \sum_{r=1}^{2} c^{(r)}\,\overline{\boldsymbol{D}}^{(r)}. \tag{2.63}$$

These last relations suggest that the stress and strain-rate concentration tensors $\mathbf{B}^{(r)}$ and $\mathbf{A}^{(r)}$ should be consistent with the identities

$$\sum_{r=1}^{2} c^{(r)}\,\mathbf{B}^{(r)} = \mathbf{I}, \qquad \sum_{r=1}^{2} c^{(r)}\,\mathbf{A}^{(r)} = \mathbf{I}. \tag{2.64}$$

In addition, the phase average stress $\overline{\boldsymbol{\sigma}}^{(r)}$ and strain-rates $\overline{\boldsymbol{D}}^{(r)}$ can also be obtained by averaging the local constitutive relations (2.52) and (2.53), to obtain the following phase constitutive relations:

$$\overline{\boldsymbol{D}}^{(r)} = \mathbf{M}^{(r)}\,\overline{\boldsymbol{\sigma}}^{(r)}, \qquad \overline{\boldsymbol{\sigma}}^{(r)} = \mathbf{L}^{(r)}\,\overline{\boldsymbol{D}}^{(r)}. \tag{2.65}$$

By combining relations (2.62) and (2.65), the following relations for the macroscopic strain-rate and stress can be deduced:

$$\overline{\boldsymbol{D}} = \left\{\sum_{r=1}^{2} c^{(r)}\mathbf{M}^{(r)}\mathbf{B}^{(r)}\right\}\overline{\boldsymbol{\sigma}}, \qquad \overline{\boldsymbol{\sigma}} = \left\{\sum_{r=1}^{2} c^{(r)}\mathbf{L}^{(r)}\mathbf{A}^{(r)}\right\}\overline{\boldsymbol{D}}. \tag{2.66}$$

Now, looking at this last relation together with expressions (2.55) and (2.56), it is straightforward that the effective viscous compliance and modulus tensors $\widetilde{\mathbf{M}}$ and $\widetilde{\mathbf{L}}$ are directly related to the stress and strain-rate concentration tensors $\mathbf{B}^{(r)}$ and $\mathbf{A}^{(r)}$, respectively, through

$$\widetilde{\mathbf{M}} = \sum_{r=1}^{2} c^{(r)}\,\mathbf{M}^{(r)}\,\mathbf{B}^{(r)}, \qquad \widetilde{\mathbf{L}} = \sum_{r=1}^{2} c^{(r)}\,\mathbf{L}^{(r)}\,\mathbf{A}^{(r)}. \tag{2.67}$$

By making use of the identity (2.64), the concentration tensors $\mathbf{B}^{(r)}$ and $\mathbf{A}^{(r)}$ can be expressed in terms of $\widetilde{\mathbf{M}}$ and $\widetilde{\mathbf{L}}$, respectively, by relations

$$\begin{aligned} c^{(2)}\,\mathbf{B}^{(2)} &= \left[\mathbf{M}^{(2)} - \mathbf{M}^{(1)}\right]^{-1}\left[\widetilde{\mathbf{M}} - \mathbf{M}^{(1)}\right], \quad c^{(1)}\,\mathbf{B}^{(1)} = \mathbf{I} - c^{(2)}\,\mathbf{B}^{(2)}, \\ c^{(2)}\,\mathbf{A}^{(2)} &= \left[\mathbf{L}^{(2)} - \mathbf{L}^{(1)}\right]^{-1}\left[\widetilde{\mathbf{L}} - \mathbf{L}^{(1)}\right], \qquad c^{(1)}\,\mathbf{A}^{(1)} = \mathbf{I} - c^{(2)}\,\mathbf{A}^{(2)}. \end{aligned} \tag{2.68}$$

It is further noted that by combining relations (2.62) and (2.65), the stress and strain-rate concentration tensors are related by

$$\mathbf{A}^{(r)} = \mathbf{M}^{(r)}\mathbf{B}^{(r)}\widetilde{\mathbf{L}}, \quad \text{or} \quad \mathbf{B}^{(r)} = \mathbf{L}^{(r)}\mathbf{A}^{(r)}\widetilde{\mathbf{M}}, \quad r = 1, 2. \tag{2.69}$$

In order to complete the set of relations for the estimation of the phase average fields, corresponding expressions have been introduced by Ponte Castañeda (1997) and Kailasam and Ponte Castañeda (1998) for the evaluation of the average spin tensors $\overline{\boldsymbol{\Omega}}^{(r)}$ in each phase, such that

$$\overline{\boldsymbol{\Omega}}^{(r)} = \overline{\boldsymbol{\Omega}} - \mathbf{C}^{(r)}\,\overline{\boldsymbol{D}}, \quad \text{for} \;\; r = 1, 2. \tag{2.70}$$

In this expression, $C^{(r)}_{[ij](kl)}$ are fourth-order tensors that are skew-symmetric in the first two indices and symmetric in the last two[†], and $\overline{\boldsymbol{\Omega}}$ is the macroscopic spin tensor which is applied externally in the problem.

Following expressions (2.63), the phase average spin tensors $\overline{\boldsymbol{\Omega}}^{(r)}$ are related to the macroscopic spin tensor $\overline{\boldsymbol{\Omega}}$ through

$$\overline{\boldsymbol{\Omega}} = \sum_{r=1}^{2} c^{(r)}\,\boldsymbol{\Omega}^{(r)}, \tag{2.71}$$

[†] $A_{[ij](kl)} = (A_{ijkl} + A_{ijlk} - A_{jikl} - A_{jilk})/4$

which implies for the spin concentration tensors $\mathbf{C}^{(r)}$ that

$$\sum_{r=1}^{2} c^{(r)}\,\mathbf{C}^{(r)} = \mathbf{0}. \tag{2.72}$$

Thus using this last relation together with results provided by Ponte Castañeda (1997), it is possible to write the spin concentration tensors in terms of the strain-rate (or equivalently the stress) concentration tensors $\mathbf{A}^{(r)}$, via

$$\mathbf{C}^{(2)} = c^{(1)}\,\boldsymbol{\Pi}\left(\mathbf{L}^{(2)} - \mathbf{L}^{(1)}\right)\,\mathbf{A}^{(2)}, \quad c^{(1)}\mathbf{C}^{(1)} = -c^{(2)}\mathbf{C}^{(2)}, \tag{2.73}$$

where $\boldsymbol{\Pi}$ is a microstructural tensor related to the $\mathbf{Q}$ tensor (see (2.59)), given by

$$\boldsymbol{\Pi} = \frac{1}{4\pi\,\det(\boldsymbol{Z})}\int_{|\boldsymbol{\zeta}|=1} \check{\mathbf{H}}(\boldsymbol{\zeta})\,|\boldsymbol{Z}^{-1}\cdot\boldsymbol{\zeta}|^{-3}\,dS, \quad \check{H}_{ijkl} = \left.(L^{(1)}_{iakb}\zeta_a\zeta_b)^{-1}\zeta_j\zeta_l\right|_{[ij](kl)}. \tag{2.74}$$

The square brackets denote the skew-symmetric part of the first two indices, whereas the simple brackets define the symmetric part of the last two indices. The second-order tensor $\boldsymbol{Z}$ serves to characterize the *instantaneous* shape and orientation of the inclusions and is given by relation (2.19).

In addition to the phase average fields, it is also expedient to discuss here the determination of the second moments of the stress and the strain-rate fields. In order to make this calculation straightforward, we recall relations (2.4) and (2.54), to obtain the following expression:

$$\frac{1}{2}\overline{\boldsymbol{\sigma}}\cdot\widetilde{\mathbf{M}}\,\overline{\boldsymbol{\sigma}} = \sum_{r=1}^{2} c^{(r)}\langle\frac{1}{2}\boldsymbol{\sigma}(\mathbf{x})\cdot\mathbf{M}^{(r)}\,\boldsymbol{\sigma}(\mathbf{x})\rangle^{(r)}, \quad \forall\,\mathbf{x}\in\,\Omega^{(r)}, \tag{2.75}$$

where use of definition (2.51) has been made for the phase stress potential $U^{(r)}$. Following Ponte Castañeda and Suquet (1998) (but see also Idiart and Ponte Castañeda (2007)), the second moments of the stress fields in the linear material can be evaluated by considering the partial derivative with respect to the compliance tensors $\mathbf{M}^{(r)}$, so that

$$\langle\boldsymbol{\sigma}(\mathbf{x})\otimes\boldsymbol{\sigma}(\mathbf{x})\rangle^{(r)} = \frac{1}{c^{(r)}}\overline{\boldsymbol{\sigma}}\frac{\partial\widetilde{\mathbf{M}}}{\partial\mathbf{M}^{(r)}}\,\overline{\boldsymbol{\sigma}}, \quad \forall\,\mathbf{x}\in\,\Omega^{(r)}. \tag{2.76}$$

It is worth noting that if the fields in any of the phases are uniform, i.e., $\boldsymbol{\sigma}(\mathbf{x}) = \overline{\boldsymbol{\sigma}}^{(r)}$ for all $\mathbf{x}$ in $\Omega^{(r)}$, then $\langle\boldsymbol{\sigma}\otimes\boldsymbol{\sigma}\rangle^{(r)} = \overline{\boldsymbol{\sigma}}^{(r)}\otimes\overline{\boldsymbol{\sigma}}^{(r)}$.

As already pointed out previously, the Willis (1978) and Ponte Castañeda and Willis (1995) estimates for particulate microstructures result in uniform fields in the inclusion phase. Based on this observation, the fluctuations in the inclusion phases are zero, i.e.,

$$\langle\boldsymbol{\sigma}\otimes\boldsymbol{\sigma}\rangle^{(2)} - \overline{\boldsymbol{\sigma}}^{(2)}\otimes\overline{\boldsymbol{\sigma}}^{(2)} = \mathbf{0} \quad \text{or} \quad \boldsymbol{\sigma}(\mathbf{x}) = \overline{\boldsymbol{\sigma}}^{(2)} \quad \forall\mathbf{x}\,\in\,\Omega^{(2)}. \tag{2.77}$$

Similar expressions can also be derived for the strain-rate fluctuations by employing duality (in terms of the Legendre-Fenchel transform) and by noting that

$$\frac{1}{2}\overline{\boldsymbol{D}}\cdot\widetilde{\mathbf{L}}\,\overline{\boldsymbol{D}} = \sum_{r=1}^{2} c^{(r)}\langle\frac{1}{2}\boldsymbol{D}(\mathbf{x})\cdot\mathbf{L}^{(r)}\,\boldsymbol{D}(\mathbf{x})\rangle^{(r)}, \quad \forall\,\mathbf{x}\in\,\Omega^{(r)}. \tag{2.78}$$

Following Ponte Castañeda and Suquet (1998), the second moments of the strain-rate fields in the linear material can be evaluated by considering the partial derivative with respect to the modulus tensors $\mathbf{L}^{(r)}$, so that

$$\langle \boldsymbol{D}(\mathbf{x}) \otimes \boldsymbol{D}(\mathbf{x}) \rangle^{(r)} = \frac{1}{c^{(r)}} \overline{\boldsymbol{D}} \frac{\partial \widetilde{\mathbf{L}}}{\partial \mathbf{L}^{(r)}} \overline{\boldsymbol{D}}, \quad \forall\, \mathbf{x} \in \Omega^{(r)}. \tag{2.79}$$

As previously mentioned, the fields in the inclusion phase are uniform, as predicted by Willis (1978) and Ponte Castañeda and Willis (1995) estimates for particulate microstructures, and thus the corresponding strain-rate fluctuations in the inclusions are zero, i.e.,

$$\langle \boldsymbol{D} \otimes \boldsymbol{D} \rangle^{(2)} - \overline{\boldsymbol{D}}^{(2)} \otimes \overline{\boldsymbol{D}}^{(2)} = \mathbf{0} \quad \text{or} \quad \boldsymbol{D}(\mathbf{x}) = \overline{\boldsymbol{D}}^{(2)} \quad \forall \mathbf{x} \in \Omega^{(2)}. \tag{2.80}$$

For the same reason, the average spin $\boldsymbol{\Omega}^{(2)}$ in the inclusion phase is also uniform, which implies that

$$\boldsymbol{\Omega}(\mathbf{x}) = \overline{\boldsymbol{\Omega}}^{(2)} \quad \forall \mathbf{x} \in \Omega^{(2)}. \tag{2.81}$$

In the following subsection, we specialize the previous results for the particular case of linearly viscous porous media.

2.3.1 Linearly viscous porous media

More specifically, we consider a linear composite consisting of a matrix phase identified with the label 1, and a vacuous phase identified with label 2. The behavior of the matrix phase is described by a quadratic stress potential $U^{(1)} \equiv U$ of the form

$$U(\boldsymbol{\sigma}) = \frac{1}{2}\, \boldsymbol{\sigma} \cdot \mathbf{M}\, \boldsymbol{\sigma}, \quad \forall \mathbf{x} \in \Omega^{(1)}, \tag{2.82}$$

where $\mathbf{M}$ and $\mathbf{L} = \mathbf{M}^{-1}$ are the viscous compliance and modulus tensors of the matrix phase. In contrast, the porous phase is described by a modulus tensor $\mathbf{L}^{(2)}$ with zero eigenvalues, and a stress potential $U^{(2)} = 0$. In this connection, the instantaneous effective stress potential of the porous material is given by relation (2.54), which is recalled here for completeness to be

$$\widetilde{U}(\overline{\boldsymbol{\sigma}}) = \frac{1}{2} \overline{\boldsymbol{\sigma}} \cdot \widetilde{\mathbf{M}}\, \overline{\boldsymbol{\sigma}}, \tag{2.83}$$

where $\widetilde{\mathbf{M}}$ is the effective viscous compliance tensor of the porous medium and has both minor and major symmetries. In addition, the corresponding constitutive macroscopic law for the linearly viscous porous medium is given by (2.55) and (2.56), such that

$$\overline{\boldsymbol{D}} = \widetilde{\mathbf{M}}\, \overline{\boldsymbol{\sigma}}, \qquad \overline{\boldsymbol{\sigma}} = \widetilde{\mathbf{L}}\, \overline{\boldsymbol{D}}, \tag{2.84}$$

with $\widetilde{\mathbf{L}} = \widetilde{\mathbf{M}}^{-1}$ denoting the effective viscous modulus tensor of the linear porous medium. For the determination of the effective tensors $\widetilde{\mathbf{M}}$ or $\widetilde{\mathbf{L}}$ of the porous material, it is necessary to set $\mathbf{L}^{(2)} = \mathbf{0}$ in relation (2.57) and (2.58), respectively. The resulting expressions read

$$\widetilde{\mathbf{M}} = \mathbf{M} + \frac{f}{1-f}\, \mathbf{Q}^{-1}, \tag{2.85}$$

and

$$\widetilde{\mathbf{L}} = \mathbf{L} + f\, \left[(1-f)\, \mathbf{P} - \mathbf{M}\right]^{-1}, \tag{2.86}$$

where use of the notation $f = c^{(2)}$ is made for the volume fraction of the voids or equivalently the porosity. This implies that the volume fraction of the matrix phase is simply $c^{(1)} = 1 - f$. The microstructural tensors $\mathbf{Q}$ and $\mathbf{P}$, serving to characterize the instantaneous shape and orientation of the voids and their distribution function, are given by relations (2.59) and (2.60), respectively, where $\mathbf{L}^{(1)}$ is the viscous modulus of the matrix phase and for consistency with the notation of this subsection, it should be replaced by $\mathbf{L}$ in those expressions.

The corresponding stress and strain-rate concentration tensors $\mathbf{B}^{(r)}$ and $\mathbf{A}^{(r)}$, respectively, given by relation (2.68) simplify dramatically to

$$(1-f)\,\mathbf{B}^{(1)} = \mathbf{I}, \quad \mathbf{B}^{(2)} = \mathbf{0}, \quad (1-f)\,\mathbf{A}^{(1)} = \mathbf{M}\,\widetilde{\mathbf{L}}, \quad f\,\mathbf{A}^{(2)} = \mathbf{I} - \mathbf{M}\,\widetilde{\mathbf{L}}. \tag{2.87}$$

It follows from this result and relation (2.62) that

$$(1-f)\,\overline{\boldsymbol{\sigma}}^{(1)} = \overline{\boldsymbol{\sigma}}, \quad \overline{\boldsymbol{\sigma}}^{(2)} = \mathbf{0}. \tag{2.88}$$

This last result is consistent with the fact that the stress in the voids is zero for all $\mathbf{x}$ in $\Omega^{(2)}$. In turn, it follows from relations (2.62) and (2.87) that the phase average strain-rate in the matrix and the vacuous phase are given simply by

$$\begin{aligned} \overline{\boldsymbol{D}}^{(1)} &= \mathbf{A}^{(1)}\,\overline{\boldsymbol{D}} = \frac{1}{1-f}\mathbf{M}\,\widetilde{\mathbf{L}}\overline{\boldsymbol{D}}, \\ \overline{\boldsymbol{D}}^{(2)} &= \mathbf{A}^{(2)}\,\overline{\boldsymbol{D}} = \frac{1}{f}\left[\mathbf{I} - \mathbf{M}\,\widetilde{\mathbf{L}}\right]\,\overline{\boldsymbol{D}}. \end{aligned} \tag{2.89}$$

These expressions relate the phase average strain-rates with the macroscopic strain-rate in the linear porous medium. On the other hand, those expressions can be manipulated so that we may write the phase average strain-rates in terms of the macroscopic stress tensor $\overline{\boldsymbol{\sigma}}$. As we will see in the sections to follow, this later representation is more convenient. Thus, by making use of definitions (2.84), (2.85) and (2.87), the phase average strain-rates take the form

$$\begin{aligned} \overline{\boldsymbol{D}}^{(1)} &= \frac{1}{1-f}\mathbf{M}\,\overline{\boldsymbol{\sigma}}, \\ \overline{\boldsymbol{D}}^{(2)} &= \frac{1}{f}\,(\widetilde{\mathbf{M}} - \mathbf{M})\,\overline{\boldsymbol{\sigma}} = \frac{1}{1-f}\mathbf{Q}^{-1}\,\overline{\boldsymbol{\sigma}}. \end{aligned} \tag{2.90}$$

Finally, the phase average spin in the inclusion phase is obtained by relation (2.70), which is recalled here for completeness to be

$$\overline{\boldsymbol{\Omega}}^{(2)} = \overline{\boldsymbol{\Omega}} - \mathbf{C}^{(2)}\,\overline{\boldsymbol{D}}, \tag{2.91}$$

with $\mathbf{C}^{(2)}$ given by (2.73) after setting $\mathbf{L}^{(2)} = \mathbf{0}$ resulting in

$$\mathbf{C}^{(2)} = (f-1)\,\boldsymbol{\Pi}\,\mathbf{L}\,\mathbf{A}^{(2)} = \frac{1-f}{f}\,\boldsymbol{\Pi}\,\left(\widetilde{\mathbf{L}} - \mathbf{L}\right). \tag{2.92}$$

The fourth-order microstructural tensor $\boldsymbol{\Pi}$ is defined in expression (2.74) and is skew-symmetric with respect to the first two indices, and symmetric with respect to the last two ones. Note that by substituting (2.92) in (2.91), we obtain

$$\overline{\boldsymbol{\Omega}}^{(2)} = \overline{\boldsymbol{\Omega}} + (1-f)\,\boldsymbol{\Pi}\,\mathbf{L}\,\overline{\boldsymbol{D}}^{(2)} = \overline{\boldsymbol{\Omega}} + \boldsymbol{\Pi}\,\mathbf{L}\,\mathbf{Q}^{-1}\,\overline{\boldsymbol{\sigma}}, \tag{2.93}$$

where use of relations (2.84) and (2.85) has also been made.

2.3.2 Brief summary

In this section, we presented certain constitutive relations for two-phase, linearly viscous particulate media. We have defined the instantaneous effective behavior of the material and it has been shown that both the macroscopic properties as well as the phase average fields can be completely defined in terms of the effective viscous compliance tensor $\widetilde{\mathbf{M}}$ (or equivalently the effective viscous modulus tensor $\widetilde{\mathbf{L}}$) of the composite material. These general results for two-phase materials have been specialized to porous media, which is the main subject of this work. It is worth mentioning at this point that in the sequel use will be made of nonlinear homogenization techniques to predict the instantaneous effective behavior of nonlinear porous media. These nonlinear methods make use of results for linear composites and hence the above results will be very helpful in the sections to follow.

2.4 Linearly thermo-viscous behavior

In this section, we present constitutive relations for generalized linear two-phase materials, which are described by "thermo-viscous" stress potentials. The reason for studying such media is linked to the fact that the "second-order" nonlinear homogenization method of Ponte Castañeda (2002a), which will be used to estimate the instantaneous effective behavior of nonlinear porous media, makes use of a linearly "thermo-viscous" comparison composite. Thus, it is useful to discuss the constitutive relations that can be obtained in the context of these linear materials first. As already mentioned in the previous section, the problem of linearly "thermo-viscous" media is mathematically analogous to the one of linear "thermo-elastic" media.

In particular, let us consider a linear composite whose individual phases are described by generalized, thermo-viscous, quadratic stress potentials of the form

$$U^{(r)}(\boldsymbol{\sigma}) = \frac{1}{2}\,\boldsymbol{\sigma}(\mathbf{x}) \cdot \mathbf{M}^{(r)}\,\boldsymbol{\sigma}(\mathbf{x}) + \boldsymbol{\eta}^{(r)} \cdot \boldsymbol{\sigma}(\mathbf{x}) + \gamma^{(r)}, \quad r = 1, 2. \tag{2.94}$$

In this expression, $\mathbf{M}^{(r)}$ are fourth-order, positive-definite, tensors that have both major and minor symmetries, $\boldsymbol{\eta}^{(r)}$ are "thermal strain-rate", second-order, symmetric tensors and $\gamma^{(r)}$ are scalars related to the "specific heat" properties of the phases. The corresponding stress–strain-rate relation of such materials is linear and reads as

$$\boldsymbol{D}(\mathbf{x}) = \frac{\partial U^{(r)}(\boldsymbol{\sigma})}{\partial \boldsymbol{\sigma}} = \mathbf{M}^{(r)}\,\boldsymbol{\sigma}(\mathbf{x}) + \boldsymbol{\eta}^{(r)}, \quad \forall\, \mathbf{x} \in \Omega^{(r)}. \tag{2.95}$$

It is noted that in the case of $\boldsymbol{\eta}^{(r)} = \mathbf{0}$ and $\gamma^{(r)} = 0$, the previous case of linear viscous composites is recovered. In turn, relation (2.95) can be inverted to give

$$\boldsymbol{\sigma} = \mathbf{L}^{(r)}\,\boldsymbol{D} + \boldsymbol{\tau}^{(r)}, \qquad \boldsymbol{\tau}^{(r)} = -\mathbf{L}^{(r)}\,\boldsymbol{\eta}^{(r)}, \tag{2.96}$$

with $\mathbf{L}^{(r)} = (\mathbf{M}^{(r)})^{-1}$ denoting the viscous modulus tensor of the phases and $\boldsymbol{\tau}^{(r)}$ being a "thermal stress" second-order symmetric tensor. Then, the corresponding instantaneous effective stress potential of the linear composite is also of a quadratic form and can be written as

$$\widetilde{U}(\overline{\boldsymbol{\sigma}}) = \frac{1}{2}\,\overline{\boldsymbol{\sigma}} \cdot \widetilde{\mathbf{M}}\,\overline{\boldsymbol{\sigma}} + \widetilde{\boldsymbol{\eta}} \cdot \overline{\boldsymbol{\sigma}} + \widetilde{\gamma}. \tag{2.97}$$

In this expression, $\widetilde{\mathbf{M}}$ is the effective viscous compliance tensor of the "particulate" composite and is given by relation (2.57), which has been presented in the context of linearly viscous composites. In turn, $\widetilde{\boldsymbol{\eta}}$ is the effective "thermal strain-rate" tensor and $\widetilde{\gamma}$ denotes the effective "specific heat" of the medium. It follows from definition (2.6), that the resulting relation between the average stress and strain-rate reads

$$\overline{\boldsymbol{D}} = \frac{\partial \widetilde{U}(\overline{\boldsymbol{\sigma}})}{\partial \overline{\boldsymbol{\sigma}}} = \widetilde{\mathbf{M}}\,\overline{\boldsymbol{\sigma}} + \widetilde{\boldsymbol{\eta}}. \tag{2.98}$$

This relation can be inverted to give

$$\overline{\boldsymbol{\sigma}} = \widetilde{\mathbf{L}}\,\overline{\boldsymbol{\sigma}} + \widetilde{\boldsymbol{\tau}}, \quad \text{with} \quad \widetilde{\boldsymbol{\tau}} = -\widetilde{\mathbf{L}}\,\widetilde{\boldsymbol{\eta}}, \tag{2.99}$$

where $\widetilde{\mathbf{L}} = \widetilde{\mathbf{M}}^{-1}$ is the effective viscous modulus tensor of the two-phase medium, given by relation (2.58), and $\widetilde{\boldsymbol{\tau}}$ denotes the effective "thermal stress" tensor. The corresponding effective thermal strain-rate and stress tensors, $\widetilde{\boldsymbol{\eta}}$ and $\widetilde{\boldsymbol{\tau}}$, as well as the effective "specific heat" $\widetilde{\gamma}$ can be shown to depend on the $\widetilde{\mathbf{M}}$ (or equivalently $\widetilde{\mathbf{L}}$) and their evaluation is described in the following.

For this, it is essential to develop first relations for the phase average fields, as well as for the second moments of the fields in the composite. The estimation of the phase average stress $\overline{\boldsymbol{\sigma}}^{(r)}$, strain-rate $\overline{\boldsymbol{D}}^{(r)}$ and spin $\overline{\boldsymbol{\Omega}}^{(r)}$ is discussed next. But before that, it is worth noting that the phase average strain-rate $\overline{\boldsymbol{D}}^{(r)}$ and spin $\overline{\boldsymbol{\Omega}}^{(r)}$ denote the symmetric and skew-symmetric part of the phase average velocity gradient.

Now, the phase average stress and strain-rate fields can be written in terms of stress and strain-rate concentration tensors, so that

$$\overline{\boldsymbol{\sigma}}^{(r)} = \mathbf{B}^{(r)}\,\overline{\boldsymbol{\sigma}} + \boldsymbol{b}^{(r)}, \qquad \overline{\boldsymbol{D}}^{(r)} = \mathbf{A}^{(r)}\,\overline{\boldsymbol{D}} + \boldsymbol{a}^{(r)}, \qquad r = 1, 2. \tag{2.100}$$

Here, $\mathbf{B}^{(r)}$ and $\mathbf{A}^{(r)}$ are fourth-order tensors that exhibit minor symmetry (but not necessarily major symmetry), $\boldsymbol{b}^{(r)}$ and $\boldsymbol{a}^{(r)}$ are second-order, symmetric tensors, and $c^{(r)}$ denote the volume fractions of the phases satisfying relation $\sum_{r=1}^{2} c^{(r)} = 1$.

The phase average stress and strain-rate fields should satisfy the identity (2.63), which implies that the concentration tensors are subject to the constraints

$$\sum_{r=1}^{2} c^{(r)}\,\mathbf{B}^{(r)} = \mathbf{I}, \qquad \sum_{r=1}^{2} c^{(r)}\,\boldsymbol{b}^{(r)} = \mathbf{0}, \qquad \sum_{r=1}^{2} c^{(r)}\,\mathbf{A}^{(r)} = \mathbf{I}, \qquad \sum_{r=1}^{2} c^{(r)}\,\boldsymbol{a}^{(r)} = \mathbf{0}. \tag{2.101}$$

In addition, the phase average stress $\overline{\boldsymbol{\sigma}}^{(r)}$ and strain-rates $\overline{\boldsymbol{D}}^{(r)}$ can also be obtained by averaging the local constitutive relations (2.95) and (2.96), to obtain the following phase constitutive relations:

$$\overline{\boldsymbol{D}}^{(r)} = \mathbf{M}^{(r)}\,\overline{\boldsymbol{\sigma}}^{(r)} + \boldsymbol{\eta}^{(r)}, \qquad \overline{\boldsymbol{\sigma}}^{(r)} = \mathbf{L}^{(r)}\,\overline{\boldsymbol{D}}^{(r)} + \boldsymbol{\tau}^{(r)}. \tag{2.102}$$

Given that the phase average stress $\overline{\boldsymbol{\sigma}}^{(r)}$ and strain-rate $\overline{\boldsymbol{D}}^{(r)}$ need to satisfy (2.63), the effective

quantities in (2.97) are given by (see Ponte Castañeda, 2006)

$$\widetilde{\mathbf{M}} = \sum_{r=1}^{2} c^{(r)}\, \mathbf{M}^{(r)}\, \mathbf{B}^{(r)}, \quad \widetilde{\mathbf{L}} = \sum_{r=1}^{2} c^{(r)}\, \mathbf{L}^{(r)}\, \mathbf{A}^{(r)} \tag{2.103}$$

$$\widetilde{\boldsymbol{\eta}} = \sum_{r=1}^{2} c^{(r)}\, \boldsymbol{\eta}^{(r)}\, \mathbf{B}^{(r)}, \quad \widetilde{\boldsymbol{\tau}} = \sum_{r=1}^{2} c^{(r)}\, \boldsymbol{\tau}^{(r)}\, \mathbf{A}^{(r)}, \tag{2.104}$$

$$\widetilde{\gamma} = \sum_{r=1}^{2} c^{(r)}\, (\gamma^{(r)} + \frac{1}{2}\boldsymbol{\eta}^{(r)} \cdot \boldsymbol{b}^{(r)}). \tag{2.105}$$

Thus, the effective tensors $\widetilde{\boldsymbol{\eta}}$ and $\widetilde{\boldsymbol{\tau}}$, as well as, the effective term $\widetilde{\gamma}$ are completely determined in terms of the stress and strain-rate concentration tensors. It is interesting to note that in the special case of two-phase linearly thermo-viscous media these concentration tensors can be *completely* determined in terms of the effective compliance tensor $\widetilde{\mathbf{M}}$ (or equivalently $\widetilde{\mathbf{L}}$) due to Levin (1967) through relations

$$\begin{aligned} c^{(2)}\, \mathbf{B}^{(2)} &= -(\Delta\mathbf{M})^{-1}\, \left[\widetilde{\mathbf{M}} - \mathbf{M}^{(1)}\right], \quad c^{(1)}\, \mathbf{B}^{(1)} = \mathbf{I} - c^{(2)}\, \mathbf{B}^{(2)}, \\ c^{(2)}\, \mathbf{A}^{(2)} &= -(\Delta\mathbf{L})^{-1}\, \left[\widetilde{\mathbf{L}} - \mathbf{L}^{(1)}\right], \qquad c^{(1)}\, \mathbf{A}^{(1)} = \mathbf{I} - c^{(2)}\, \mathbf{A}^{(2)}, \end{aligned} \tag{2.106}$$

and

$$\begin{aligned} c^{(2)}\, \boldsymbol{b}^{(2)} &= -c^{(1)}\, \boldsymbol{b}^{(1)} = (\Delta\mathbf{M})^{-1} \left(\widetilde{\mathbf{M}} - \overline{\mathbf{M}}\right)\, (\Delta\mathbf{M})^{-1}\, (\Delta\boldsymbol{\eta})\,, \\ c^{(2)}\, \boldsymbol{a}^{(2)} &= -c^{(1)}\, \boldsymbol{a}^{(1)} = (\Delta\mathbf{L})^{-1} \left(\widetilde{\mathbf{L}} - \overline{\mathbf{L}}\right)\, (\Delta\mathbf{L})^{-1}\, (\Delta\boldsymbol{\tau})\,. \end{aligned} \tag{2.107}$$

In these expressions, we have made use of the notation $\Delta G = G^{(1)} - G^{(2)}$ and $\overline{G} = \sum_{r=1}^{2} c^{(r)}\, G^{(r)}$, where the set $G^{(r)} = \{\mathbf{M}^{(r)}, \mathbf{L}^{(r)}, \boldsymbol{\eta}^{(r)}, \boldsymbol{\tau}^{(r)}\}$. Making use of the above-mentioned analysis, the effective stress potential in relation (2.97) may be written in the form (Talbot and Willis, 1992)

$$\begin{aligned} \widetilde{U}(\overline{\boldsymbol{\sigma}}) = &\sum_{r=1}^{2} c^{(r)}\, \gamma^{(r)} + \overline{\boldsymbol{\eta}} \cdot \overline{\boldsymbol{\sigma}} + \frac{1}{2}\overline{\boldsymbol{\sigma}} \cdot \overline{\mathbf{M}}\, \overline{\boldsymbol{\sigma}} + \\ &+ \frac{1}{2}\, \left[\overline{\boldsymbol{\sigma}} + (\Delta\mathbf{M})^{-1}\, (\Delta\boldsymbol{\eta})\right] \cdot (\widetilde{\mathbf{M}} - \overline{\mathbf{M}})\, \left[\overline{\boldsymbol{\sigma}} + (\Delta\mathbf{M})^{-1}\, (\Delta\boldsymbol{\eta})\right]. \end{aligned} \tag{2.108}$$

In order to complete the set of expressions for two-phase, linearly thermo-viscous composites it is essential to provide estimates for the phase average spin tensors $\overline{\boldsymbol{\Omega}}^{(r)}$. For these materials, the phase average spin is written as (Ponte Castañeda, 2006)

$$\overline{\boldsymbol{\Omega}}^{(r)} = \overline{\boldsymbol{\Omega}} - \mathbf{C}^{(r)}\, \overline{\boldsymbol{D}} - \boldsymbol{\beta}^{(r)}, \quad r = 1, 2, \tag{2.109}$$

where $C^{(r)}_{[ij](kl)}$ are fourth-order spin concentration tensors that are skew-symmetric in the first two indices and symmetric in the last two[†], while $\boldsymbol{\beta}^{(r)}$ are skew-symmetric second-order tensors. The skew-symmetric second-order tensor $\overline{\boldsymbol{\Omega}}$ is the macroscopic spin (see (2.11)) and is applied externally in the problem. Next, by making use of the fact that

$$\overline{\boldsymbol{\Omega}} = \sum_{r=1}^{2} c^{(r)}\, \overline{\boldsymbol{\Omega}}^{(r)}, \tag{2.110}$$

[†] $A_{[ij](kl)} = (A_{ijkl} + A_{ijlk} - A_{jikl} - A_{jilk})/4$

it follows that

$$\sum_{r=1}^{2} c^{(r)}\,\mathbf{C}^{(r)} = \mathbf{0}, \qquad \sum_{r=1}^{2} c^{(r)}\,\boldsymbol{\beta}^{(r)} = \mathbf{0}. \tag{2.111}$$

For a two-phase composite, $\mathbf{C}^{(r)}$ is given by (2.73), whereas (Ponte Castañeda, 2006)

$$\boldsymbol{\beta}^{(2)} = c^{(1)}\,\boldsymbol{\Pi}\left[(\mathbf{L}^{(2)} - \mathbf{L}^{(1)})\,\boldsymbol{a}^{(2)} - \boldsymbol{\tau}^{(1)}\right], \qquad c^{(1)}\,\boldsymbol{\beta}^{(1)} = -c^{(2)}\,\boldsymbol{\beta}^{(1)}, \tag{2.112}$$

where $\boldsymbol{\Pi}$ and $\boldsymbol{a}^{(2)}$ have been defined by relations (2.74) and (2.107).

Finally, the second moments of the stress and strain-rate fields are given by the similar expressions presented in the context of the two-phase linearly viscous materials. In particular, the second moments of the stress fields are given by

$$\langle \boldsymbol{\sigma}(\mathbf{x}) \otimes \boldsymbol{\sigma}(\mathbf{x}) \rangle^{(r)} = \frac{1}{c^{(r)}} \frac{\partial \widetilde{U}}{\partial \mathbf{M}^{(r)}}, \quad \forall\, \mathbf{x} \in \Omega^{(r)}. \tag{2.113}$$

The second moments of the strain-rate fields can be determined in an analogous way by making use of the dual effective dissipation potential $\widetilde{W}$ defined in (2.9) in the general context of two-phase composites but will not be given here explicitly. However, the important point that should be made here is that the Willis (1978) and Ponte Castañeda and Willis (1995) estimates for particulate composites, used in this study, deliver uniform fields in the inclusion phases, and thus the corresponding stress, strain-rate and spin fluctuations in the inclusions are zero, i.e.,

$$\boldsymbol{\sigma}(\mathbf{x}) = \overline{\boldsymbol{\sigma}}^{(2)}, \quad \boldsymbol{D}(\mathbf{x}) = \overline{\boldsymbol{D}}^{(2)}, \quad \boldsymbol{\Omega}(\mathbf{x}) = \overline{\boldsymbol{\Omega}}^{(2)}, \quad \forall \mathbf{x} \in \Omega^{(2)} \tag{2.114}$$

As already stated in the previous section for linearly viscous materials, the Willis procedure for particulate media is expected to be sufficiently accurate for low to moderate concentrations of inclusions, however, special care needs to be taken when the volume fraction of the inclusion phase is large. In the present study, the interest is on porous media consisting of small concentration of voids, and hence the Willis procedure can be applied with accuracy.

2.4.1 Linearly thermo-viscous porous media

In this subsection, we specialize the results developed previously in the framework of linearly thermo-viscous porous media. In this regard, we define the porous phase ($r = 2$) by letting the eigenvalues of the relevant viscous modulus $\mathbf{L}^{(2)}$ be zero, as well as $U^{(2)} = 0$, $\boldsymbol{\eta}^{(2)} = \mathbf{0}$ and $\gamma^{(2)} = 0$. In turn, the matrix phase ($r = 1$) is described by a quadratic stress potential $U^{(1)} \equiv U$ given by

$$U(\boldsymbol{\sigma}) = \frac{1}{2}\,\boldsymbol{\sigma} \cdot \mathbf{M}\,\boldsymbol{\sigma} + \boldsymbol{\eta} \cdot \boldsymbol{\sigma} + \gamma, \tag{2.115}$$

where the superscript 1 has been removed from $\mathbf{M}$, $\boldsymbol{\eta}$ and γ for simplicity. It follows from relations (2.95) and (2.96) that the local constitutive behavior of the matrix phase is defined by

$$\boldsymbol{D}(\mathbf{x}) = \mathbf{M}\,\boldsymbol{\sigma}(\mathbf{x}) + \boldsymbol{\eta}, \qquad \boldsymbol{\sigma}(\mathbf{x}) = \mathbf{L}\,\boldsymbol{D}(\mathbf{x}) + \boldsymbol{\tau}, \qquad \forall\, \mathbf{x} \in \Omega^{(1)}, \tag{2.116}$$

with $\mathbf{L} = \mathbf{M}^{-1}$ and $\boldsymbol{\tau} = -\mathbf{L}\,\boldsymbol{\eta}$. Following result (2.97), the instantaneous effective stress potential of the porous material $\widetilde{U}$ is given by

$$\widetilde{U}(\overline{\boldsymbol{\sigma}}) = \frac{1}{2}\overline{\boldsymbol{\sigma}} \cdot \widetilde{\mathbf{M}}\,\overline{\boldsymbol{\sigma}} + \widetilde{\boldsymbol{\eta}} \cdot \overline{\boldsymbol{\sigma}} + \widetilde{\gamma}. \tag{2.117}$$

Thus, by making use of definitions (2.98) and (2.99), the corresponding effective constitutive law for the linearly thermo-viscous porous medium is given by

$$\overline{\boldsymbol{D}} = \widetilde{\mathbf{M}}\,\overline{\boldsymbol{\sigma}} + \widetilde{\boldsymbol{\eta}}, \qquad \overline{\boldsymbol{\sigma}} = \widetilde{\mathbf{L}}\,\overline{\boldsymbol{D}} + \widetilde{\boldsymbol{\tau}}, \tag{2.118}$$

with $\widetilde{\boldsymbol{\tau}} = -\widetilde{\mathbf{L}}\,\widetilde{\boldsymbol{\eta}}$. For the determination of the effective viscous compliance tensor $\widetilde{\mathbf{M}}$, it is necessary to set $\mathbf{L}^{(2)} = \mathbf{0}$ in relation (2.57), which reduces to

$$\widetilde{\mathbf{M}} = \mathbf{M} + \frac{f}{1-f}\,\mathbf{Q}^{-1}, \tag{2.119}$$

and

$$\widetilde{\mathbf{L}} = \mathbf{L} + f\,\left[(1-f)\,\mathbf{P} - \mathbf{M}\right]^{-1}, \tag{2.120}$$

for the case of porous materials. In these expressions, use of the notation $f = c^{(2)}$ is made for the volume fraction of the voids or equivalently the porosity. Accordingly, the volume fraction of the matrix phase is $c^{(1)} = 1 - f$. The tensor $\mathbf{Q}$ is given by relation (2.59), where $\mathbf{L}^{(1)}$ is the elastic modulus of the matrix phase and for consistency with the notation introduced for porous materials, should be replaced by $\mathbf{L} \equiv \mathbf{L}^{(1)}$.

The corresponding stress and strain-rate concentration tensors $\mathbf{B}^{(r)}$, $\mathbf{A}^{(r)}$, $\boldsymbol{b}^{(r)}$ and $\boldsymbol{a}^{(r)}$, given by relations (2.106) and (2.107) are simplified dramatically by setting $\mathbf{L}^{(2)} = \mathbf{0}$ such that

$$(1-f)\,\mathbf{B}^{(1)} = \mathbf{I}, \quad \mathbf{B}^{(2)} = \mathbf{0}, \quad (1-f)\,\mathbf{A}^{(1)} = \mathbf{M}\,\widetilde{\mathbf{L}}, \quad f\,\mathbf{A}^{(2)} = \mathbf{I} - \mathbf{M}\,\widetilde{\mathbf{L}}, \tag{2.121}$$

and

$$\boldsymbol{b}^{(1)} = \boldsymbol{b}^{(2)} = \mathbf{0}, \quad f\,\boldsymbol{a}^{(2)} = -(1-f)\,\boldsymbol{a}^{(1)} = \left(\mathbf{M}\,\widetilde{\mathbf{L}} - (1-f)\,\mathbf{I}\right)\,\mathbf{M}\,\boldsymbol{\tau}, \tag{2.122}$$

where it is useful to recall that $\boldsymbol{\tau} = -\mathbf{L}\,\boldsymbol{\eta}$. This last result together with relation (2.100) yields that

$$(1-f)\,\overline{\boldsymbol{\sigma}}^{(1)} = \overline{\boldsymbol{\sigma}}, \quad \overline{\boldsymbol{\sigma}}^{(2)} = \mathbf{0}, \tag{2.123}$$

which is consistent with the stress being zero in the voids for all $\mathbf{x}$ in $\Omega^{(2)}$. Next by making use of (2.121) and (2.122) and the fact that $\boldsymbol{\eta}^{(2)} = \mathbf{0}$ and $\gamma^{(2)} = 0$ for the porous phase, the corresponding effective measures $\widetilde{\boldsymbol{\eta}}$ and $\widetilde{\gamma}$, defined in (2.105), can be easily shown to reduce to

$$\widetilde{\boldsymbol{\eta}} = \boldsymbol{\eta}, \quad \widetilde{\gamma} = (1-f)\,\gamma, \tag{2.124}$$

where $\boldsymbol{\eta}$ and γ are properties of the matrix phase defined in (2.115). An equivalent expression for $\widetilde{\boldsymbol{\tau}}$ can also be obtained by

$$\widetilde{\boldsymbol{\tau}} = \widetilde{\mathbf{L}}\,\mathbf{M}\,\boldsymbol{\tau} = -\widetilde{\mathbf{L}}\,\boldsymbol{\eta}, \tag{2.125}$$

where use of the symmetries of $\widetilde{\mathbf{L}}$, $\mathbf{M}$ and $\boldsymbol{\tau} = -\mathbf{L}\,\boldsymbol{\eta}$ was made.

In turn, by making use of relations (2.100), the phase average strain-rate in the matrix and the vacuous phase are given by

$$\overline{\boldsymbol{D}}^{(1)} = \mathbf{A}^{(1)}\,\overline{\boldsymbol{D}} + \boldsymbol{a}^{(1)}, \qquad \overline{\boldsymbol{D}}^{(2)} = \mathbf{A}^{(2)}\,\overline{\boldsymbol{D}} + \boldsymbol{a}^{(2)}. \tag{2.126}$$

where the concentration tensors $\mathbf{A}^{(1)}$, $\mathbf{A}^{(2)}$, $\boldsymbol{a}^{(1)}$ and $\boldsymbol{a}^{(2)}$ are given by expressions (2.121) and (2.122), respectively. These expressions relate the phase average strain-rates with the macroscopic strain-rate in the linearly thermo-viscous porous medium. On the other hand, those expressions can be

manipulated so that the phase average strain-rates can be written in terms of the macroscopic stress tensor $\overline{\boldsymbol{\sigma}}$. As we will see in later sections, this representation is more convenient. Thus, by making use of definitions (2.118), (2.119), (2.121) and (2.122), the phase average strain-rates take the form

$$\begin{aligned}\overline{\boldsymbol{D}}^{(1)} &= \mathbf{M}\,\overline{\boldsymbol{\sigma}}^{(1)} + \boldsymbol{\eta} = \frac{1}{1-f}\mathbf{M}\,\overline{\boldsymbol{\sigma}} + \boldsymbol{\eta},\\ \overline{\boldsymbol{D}}^{(2)} &= \frac{1}{f}\left(\overline{\boldsymbol{D}} - (1-f)\,\overline{\boldsymbol{D}}^{(1)}\right) = \frac{1}{f}\left(\widetilde{\mathbf{M}} - \mathbf{M}\right)\overline{\boldsymbol{\sigma}} + \boldsymbol{\eta} = \frac{1}{1-f}\mathbf{Q}^{-1}\,\overline{\boldsymbol{\sigma}} + \boldsymbol{\eta}.\end{aligned} \tag{2.127}$$

The set of constitutive relations for the linearly thermo-viscous porous medium is concluded by providing an expression for the determination of the average spin in the voids $\overline{\boldsymbol{\Omega}}^{(2)}$, which is extracted from relation (2.109), and reads

$$\overline{\boldsymbol{\Omega}}^{(2)} = \overline{\boldsymbol{\Omega}} - \mathbf{C}^{(2)}\,\overline{\boldsymbol{D}} - \boldsymbol{\beta}^{(2)}, \tag{2.128}$$

where $\mathbf{C}^{(2)}$ is given by the corresponding result (2.92) for linearly viscous porous media, while $\boldsymbol{\beta}^{(2)}$ is determined by relation (2.112) after setting $\mathbf{L}^{(2)} = \mathbf{0}$ and $\mathbf{L}^{(1)} = \mathbf{L}$, such that

$$\boldsymbol{\beta}^{(2)} = (f-1)\,\boldsymbol{\Pi}\left(\mathbf{L}\,\boldsymbol{a}^{(2)} + \boldsymbol{\tau}\right), \tag{2.129}$$

with $\boldsymbol{a}^{(2)}$ given by (2.122), and $\boldsymbol{\Pi}$ given by (2.74). The average spin in the voids can be written alternatively as

$$\overline{\boldsymbol{\Omega}}^{(2)} = \overline{\boldsymbol{\Omega}} + (1-f)\,\boldsymbol{\Pi}\,\mathbf{L}\left(\overline{\boldsymbol{D}}^{(2)} - \boldsymbol{\eta}\right) = \overline{\boldsymbol{\Omega}} + \boldsymbol{\Pi}\,\mathbf{L}\,\mathbf{Q}^{-1}\,\overline{\boldsymbol{\sigma}}, \tag{2.130}$$

where use has been made of relations (2.126) and (2.127). By comparing this last relation to the corresponding expression (2.93) for linearly viscous porous media, we observe that the average spin in the voids is identical for linearly viscous and thermo-viscous porous media.

2.4.2 Brief summary

In this section, we presented certain constitutive relations for two-phase, linearly thermo-viscous particulate media. We have defined the instantaneous effective behavior of such materials, where it has been shown that both the macroscopic properties as well as the phase average fields can be completely defined in terms of the effective viscous compliance tensor $\widetilde{\mathbf{M}}$ of the composite material, similarly to the linearly viscous composites. These general results for two-phase thermo-viscous materials have been specialized to linearly thermo-viscous porous media. As already mentioned in the beginning of the section, the reason for studying this special type of generalized linear porous media is that in the sequel use will be made of the "second-order" (Ponte Castañeda, 2002a) nonlinear homogenization method to predict the effective behavior of nonlinear porous media. This nonlinear homogenization method makes use of results for linearly thermo-viscous composites and hence the above results will be very helpful in the sections to follow.

2.5 "Variational" method

This section is concerned with the approximate estimation of the instantaneous effective behavior of two-phase viscoplastic media, and particularly viscoplastic porous media. As already discussed in

section 2.1, estimating exactly the effective stress potential $\widetilde{U}$, defined in relation (2.14), is a very difficult task. Nevertheless, several approximate, albeit accurate, methods have been developed in the context of linear composites, as described earlier.

In this regard, Ponte Castañeda (1991, 1996, 2002a) proposed general, nonlinear homogenization methods, which are based on the construction of a "*linear comparison composite*" (LCC), with the same microstructure as the nonlinear composite. The constituent phases of the LCC are identified with appropriate linearizations of the given nonlinear phases resulting from a suitably designed variational principle. In turn, this allows the use of any already available method to estimate the instantaneous effective behavior of *linear* composites (e.g., the linear results of section 2.3) to generate corresponding estimates for *nonlinear* composites. In this section, we restrict our attention to the earlier "variational" method (Ponte Castañeda, 1991), whereas the latest more general, "second-order" homogenization method of Ponte Castañeda (2002a) will be discussed in the following section. The "tangent second-order" method (Ponte Castañeda, 1996) will not be used in this work.

It is worth noting that the following analysis will make use of the stress formulation of the problem, namely we will discuss the estimation of the instantaneous effective stress potential $\widetilde{U}$. Firstly, we will develop some general expressions in the context of two-phase materials, which will be specialized in the sequel to porous media. In fact, similar analysis may be performed in the context of the strain-rate formulation by estimating the effective dissipation potential $\widetilde{W}$ defined in (2.9). However, in this study, it is sufficient to restrict our attention to the stress formulation of the problem.

More specifically, the main idea of these homogenization methods lies in the construction of a LCC. Following definitions for linearly viscous materials in section 2.3, the corresponding phases of the LCC are characterized by quadratic stress potentials of the form (Ponte Castañeda, 1991)

$$U_L^{(r)}(\boldsymbol{\sigma};\mathbf{M}^{(r)}) = \frac{1}{2}\,\boldsymbol{\sigma}(\mathbf{x})\,\cdot\,\mathbf{M}^{(r)}\,\boldsymbol{\sigma}(\mathbf{x}), \qquad \forall\,\mathbf{x}\,\in\,\Omega^{(r)} \qquad r=1,2, \tag{2.131}$$

where, $\mathbf{M}^{(r)}$ are symmetric, fourth-order, viscous compliance tensors and the subscript L has been used to denote quantities in the LCC.

Next, "corrector" functions $V^{(r)}$ are introduced, such that:

$$V^{(r)}(\mathbf{M}^{(r)}) = \min_{\hat{\boldsymbol{\sigma}}^{(r)}} \left[U^{(r)}(\hat{\boldsymbol{\sigma}}) - U_L^{(r)}(\hat{\boldsymbol{\sigma}};\,\mathbf{M}^{(r)})\right], \tag{2.132}$$

where $\hat{\boldsymbol{\sigma}}^{(r)}$ are second-order tensors, that minimize the corrector functions $V^{(r)}$, whereas $U^{(r)}$ denotes the nonlinear stress potential of each phase, defined in (2.23). These functions, which depend on the tensors $\mathbf{M}^{(r)}$, serve to measure the nonlinearity of the phases of the original material, so that, under appropriate hypotheses, the local stress potential of the phases of the nonlinear composite may be written as:

$$U^{(r)}(\boldsymbol{\sigma}) = \sup_{\mathbf{M}^{(r)}} \left[U_L^{(r)}(\boldsymbol{\sigma};\mathbf{M}^{(r)}) + V^{(r)}(\mathbf{M}^{(r)})\right]. \tag{2.133}$$

Now, by substituting relation (2.133) in relation (2.4), the effective stress potential $\widetilde{U}$ of the nonlinear heterogeneous medium can be expressed as

$$\widetilde{U}\,(\overline{\boldsymbol{\sigma}}) = \min_{\sigma\,\epsilon\,\mathcal{S}(\overline{\sigma})} \sup_{\mathbf{M}^{(r)}(\mathbf{x})} \sum_{r=1}^{2} c^{(r)} \left\langle U_L^{(r)}(\boldsymbol{\sigma};\,\mathbf{M}^{(r)}) + V^{(r)}(\mathbf{M}^{(r)})\right\rangle^{(r)}, \tag{2.134}$$

where the brackets $\langle\cdot\rangle^{(r)}$ serve to denote volume averages over phase r and the $\mathcal{S}$ is given by relation (2.5). In this last relation, it is easily observed that the argument involved in the summation is convex in $\boldsymbol{\sigma}$ ($U_L^{(r)}$ is quadratic in $\boldsymbol{\sigma}$, and $V^{(r)}$ do not depend on $\boldsymbol{\sigma}$) and concave in $\mathbf{M}^{(r)}$. Thus, we can interchange the "min" with the "sup" operation by making use of the saddle point theorem to obtain

$$\widetilde{U}\left(\overline{\boldsymbol{\sigma}}\right) = \sup_{\mathbf{M}^{(r)}(\mathbf{x})} \left\{ \widetilde{U}_L\left(\overline{\boldsymbol{\sigma}};\, \mathbf{M}^{(r)}(\mathbf{x})\right) + \sum_{r=1}^{2} c^{(r)} \left\langle V^{(r)}(\mathbf{M}^{(r)}(\mathbf{x}))\right\rangle^{(r)} \right\}, \tag{2.135}$$

where $\widetilde{U}_L$ is the effective stress potential of a linear composite with an infinite number of phases, since the compliance tensors $\mathbf{M}^{(r)}$ are functions of the position $\mathbf{x}$ and is given by

$$\begin{aligned} \widetilde{U}_L(\overline{\boldsymbol{\sigma}}; \mathbf{M}^{(r)}) &= \min_{\sigma\, \epsilon\, \mathcal{S}(\overline{\sigma})} \sum_{r=1}^{2} c^{(r)} \left\langle U_L^{(r)}(\boldsymbol{\sigma};\, \mathbf{M}^{(r)})\right\rangle^{(r)} = \\ &= \min_{\sigma\, \epsilon\, \mathcal{S}(\overline{\sigma})} \sum_{r=1}^{2} c^{(r)} \left\langle \frac{1}{2}\, \boldsymbol{\sigma} \cdot \mathbf{M}^{(r)}\, \boldsymbol{\sigma}\right\rangle^{(r)}. \end{aligned} \tag{2.136}$$

It is interesting to note at this point that the variational principle (2.135) is equivalent to the initial variational principle (2.14), but it is still difficult to solve the optimization problem in (2.135) because of the dependence of $\mathbf{M}^{(r)}$ on the spatial variable $\mathbf{x}$. However, the main advantage of this new variational principle lies in the fact that the compliance tensors $\mathbf{M}^{(r)}(\mathbf{x})$ do not need to satisfy any constraints, apart from being positive definite, in contrast to the initial variational formulation (2.14), which requires that the stress tensor satisfy certain differential constraints defined in relation (2.5). This last observation allows us to *approximate* the variational formulation (2.135) by choosing *constant* (per phase) trial fields $\mathbf{M}^{(r)}$. A direct consequence of this is the reduction of an infinite-dimensional optimization procedure into a finite-dimensional problem. Hence, the variational principle of relation (2.135) is reduced to

$$\widetilde{U}\left(\overline{\boldsymbol{\sigma}}\right) \geq \widetilde{U}_{var}\left(\overline{\boldsymbol{\sigma}}\right) = \sup_{\mathbf{M}^{(r)}} \left\{ \widetilde{U}_L(\overline{\boldsymbol{\sigma}};\, \mathbf{M}^{(r)}) + \sum_{r=1}^{2} c^{(r)}\, V^{(r)}(\mathbf{M}^{(r)}) \right\}, \tag{2.137}$$

where the inequality has been used to denote that $\widetilde{U}_{var}$ is a lower bound (Ponte Castañeda, 1991). Then, the corrector functions $V^{(r)}$ are given by (2.132), with $\mathbf{M}^{(r)}$ being constant per phase.

Before proceeding to specific results for porous media, it is interesting to examine the optimality conditions in the context of the general two-phase material. Thus, it follows from the first optimality condition in (2.132) with respect to the tensors $\hat{\boldsymbol{\sigma}}^{(r)}$ that

$$\frac{\partial\, U^{(r)}(\hat{\boldsymbol{\sigma}})}{\partial \hat{\boldsymbol{\sigma}}} = \mathbf{M}^{(r)}\, \hat{\boldsymbol{\sigma}}^{(r)}, \quad r = 1, 2. \tag{2.138}$$

This condition has been given a physical interpretation by Suquet (1995) as a "secant-type" approximation to the nonlinear stress potential $U^{(r)}$ evaluated at a stress $\hat{\boldsymbol{\sigma}}^{(r)}$.

On the other hand, the second optimality condition with respect to $\mathbf{M}^{(r)}$ in (2.137) is not that straightforward. The reason for this is linked to the fact that the corrector functions $V^{(r)}$ are not smooth functions of $\mathbf{M}^{(r)}$, when these tensors are general, as established by Idiart and Ponte Castañeda (2006). However, for isotropic phases, where the tensors $\mathbf{M}^{(r)}$ are taken to be isotropic,

the functions $V^{(r)}$ are smooth functions of the eigenvalues of $\mathbf{M}^{(r)}$. The discussion of these optimality conditions, will not be performed in the general context of two-phase media, but instead we will discuss these issues in the particular case of porous media, which is the main subject of this work.

2.5.1 "Variational" estimates for viscoplastic porous media

More specifically, let us consider that the matrix phase is defined by a viscoplastic stress potential $U^{(1)} \equiv U$ given by (2.23), whereas the vacuous phase is described by $U^{(2)} = 0$. Then, seeking for bounds, Ponte Castañeda (1991) proposed the viscous compliance tensor $\mathbf{M}$ or, equivalently, the viscous modulus tensor $\mathbf{L}$ to be of the form

$$\mathbf{M} = \frac{1}{2\mu}\,\mathbf{K} + \frac{1}{3\kappa}\,\mathbf{J}, \qquad \mathbf{L} = (\mathbf{M})^{-1} = 2\mu\,\mathbf{K} + 3\kappa\,\mathbf{J}. \tag{2.139}$$

Here, the fourth-order tensors $\mathbf{M}$ and $\mathbf{L}$ are isotropic, μ is a shear modulus to be defined in the following, and κ is the bulk modulus of the matrix phase. Note that the nonlinear matrix phase is taken to be incompressible and hence the limit of incompressibility, i.e., $\kappa \to \infty$, will be considered later. In the last expressions $\mathbf{K}$ and $\mathbf{J}$ are the standard, fourth-order, shear and hydrostatic projection tensors, respectively, defined by

$$I_{ijkl} = \frac{1}{2}(\delta_{ik}\,\delta_{jl} + \delta_{il}\,\delta_{jk}), \quad J_{ijkl} = \frac{1}{3}\delta_{ij}\,\delta_{kl}, \quad K_{ijkl} = I_{ijkl} - J_{ijkl}, \tag{2.140}$$

with δ_{ij} denoting the Cartesian components of the standard Kronecker delta, and $\mathbf{I}$ the standard, fourth-order, identity tensor.

Making use of the above definition for $\mathbf{M}$, the stress potential U_L of the matrix phase in the LCC becomes

$$U_L(\boldsymbol{\sigma};\,\mathbf{M}) = \frac{1}{6\,\mu}\,\sigma_{eq}^2 + \frac{1}{2\,\kappa}\,\sigma_m^2. \tag{2.141}$$

It follows then from relation (2.136) and consideration of the incompressibility limit $\kappa \to \infty$ that the effective stress potential $\widetilde{U}_L$ of the porous LCC reduces to

$$\widetilde{U}_L\,(\overline{\boldsymbol{\sigma}}) = (1-f)\,\min_{\sigma\,\epsilon\,\mathcal{S}(\overline{\sigma})}\frac{1}{6\mu}\langle\sigma_{eq}^2\rangle_L^{(1)} = \frac{1}{2}\,\overline{\boldsymbol{\sigma}}\,\cdot\,\widetilde{\mathbf{M}}\,\overline{\boldsymbol{\sigma}} = \frac{1}{6\mu}\,(3\,\overline{\boldsymbol{\sigma}}\,\cdot\,\widehat{\mathbf{M}}\,\overline{\boldsymbol{\sigma}}), \tag{2.142}$$

where the subscript L is used to emphasize that the scalar σ_{eq} is associated with the stress fields in the LCC, while

$$\widehat{\mathbf{M}} = \mu\,\widetilde{\mathbf{M}}, \qquad \widetilde{\mathbf{M}} = \mathbf{M} + \frac{f}{1-f}\,\mathbf{Q}^{-1} = \frac{1}{\mu}\left(\frac{1}{2}\,\mathbf{K} + \frac{f}{1-f}\,\widehat{\mathbf{Q}}^{-1}\right). \tag{2.143}$$

Here, the effective compliance tensors $\widetilde{\mathbf{M}}$ and $\mathbf{Q}$ are homogeneous of degree -1 and 1 in the moduli μ, respectively, and hence $\widehat{\mathbf{M}}$ and $\widehat{\mathbf{Q}}$ are independent of μ (see Appendix IV). The microstructural fourth-order tensor $\mathbf{Q}$ (or $\widehat{\mathbf{Q}}$) has been defined in relation (2.59). It is noted that the incompressibility of the matrix phase requires the consideration of the limit $\kappa \to \infty$ in relation $(2.59)_2$ for the computation of $\mathbf{Q}$, which is taken with the help of the commercial package "Mathematica" (see Appendix I for more details). Note that even though the matrix phase is incompressible, the final expression for $\widetilde{\mathbf{M}}$ in relation (2.143) is compressible, since it corresponds to a porous material.

Having determined the effective behavior of the porous LCC, the effective stress potential of the viscoplastic porous material, $\widetilde{U}$, given by (2.137) for general two-phase media, simplifies to

$$\widetilde{U}_{var}\left(\overline{\boldsymbol{\sigma}}\right) = \sup_{\mu>0}\left\{\widetilde{U}_{L}\left(\overline{\boldsymbol{\sigma}};\,\mu\right) + \left(1-f\right)V\left(\mu\right)\right\}, \tag{2.144}$$

where use has been made of the notation $c^{(2)} = f$ and hence $c^{(1)} = 1-f$ to denote the volume fractions of the pores (i.e., porosity) and the matrix phase, respectively. In turn, it follows from (2.23) and (2.141) that the corrector function V associated with the matrix phase, defined in the general context of two-phase materials in (2.132), reduce to

$$V\left(\check{\boldsymbol{\sigma}},\,\mu\right) = \min_{\hat{\sigma}_{eq}}\left[\frac{\dot{\varepsilon}_o\,\sigma_o}{n+1}\left(\frac{\hat{\sigma}_{eq}}{\sigma_o}\right)^{n+1} - \frac{1}{6\,\mu}\,\hat{\sigma}_{eq}^{2}\right], \tag{2.145}$$

where $\hat{\boldsymbol{\sigma}}$ is a uniform, second-order tensor.

Then, substitution of (2.142) and (2.145) in (2.144) gives

$$\widetilde{U}_{var}\left(\overline{\boldsymbol{\sigma}}\right) = \sup_{\mu>0}\left\{\frac{1}{6\,\mu}\left(3\,\overline{\boldsymbol{\sigma}}\cdot\widehat{\mathbf{M}}\,\overline{\boldsymbol{\sigma}}\right) + \left(1-f\right)\min_{\hat{\sigma}_{eq}}\left[\frac{\dot{\varepsilon}_o\,\sigma_o}{n+1}\left(\frac{\hat{\sigma}_{eq}}{\sigma_o}\right)^{n+1} - \frac{1}{6\,\mu}\,\hat{\sigma}_{eq}^{2}\right]\right\}. \tag{2.146}$$

The first optimization condition with respect to $\hat{\sigma}_{eq}$ results in

$$\dot{\varepsilon}_o\left(\frac{\hat{\sigma}_{eq}}{\sigma_o}\right)^{n-1} = \frac{\sigma_o}{3\,\mu}, \tag{2.147}$$

where a relation between the moduli μ and the quantity $\hat{\sigma}_{eq}$ is obtained. On the other hand, it follows from (2.142), that the second optimality condition with respect to μ is expressed as

$$\sqrt{\langle\sigma_{eq}^{2}\rangle_{L}^{(1)}} = \hat{\sigma}_{eq} = \sqrt{\frac{3\,\overline{\boldsymbol{\sigma}}\cdot\widehat{\mathbf{M}}\,\overline{\boldsymbol{\sigma}}}{1-f}}, \tag{2.148}$$

where the subscript L is used to emphasize that the scalar σ_{eq} is associated with the stress fields in the LCC. In this regard, this last expression relates the quantity $\hat{\sigma}_{eq}$ to the field fluctuations of the stress fields in the LCC.

Elimination of the scalar $\hat{\sigma}_{eq}$ in (2.147) and (2.148) gives

$$\mu = \frac{\sigma_o^{n}}{3\,\dot{\varepsilon}_o}\left(\frac{1-f}{3\,\overline{\boldsymbol{\sigma}}\cdot\widehat{\mathbf{M}}\,\overline{\boldsymbol{\sigma}}}\right)^{\frac{n-1}{2}}. \tag{2.149}$$

Substituting the last results in (2.146), yields a simple expression for the effective stress potential $\widetilde{U}$, which reads (Ponte Castañeda, 1991; Willis, 1991; Michel and Suquet, 1992)

$$\widetilde{U}_{var}(\overline{\boldsymbol{\sigma}}) = \left(1-f\right)\frac{\dot{\varepsilon}_o\,\sigma_o}{n+1}\left(\frac{\hat{\sigma}_{eq}}{\sigma_o}\right)^{n+1} = \left(1-f\right)\frac{\dot{\varepsilon}_o\,\sigma_o}{n+1}\left[\frac{3\,\overline{\boldsymbol{\sigma}}\cdot\widehat{\mathbf{M}}\,\overline{\boldsymbol{\sigma}}}{\left(1-f\right)\sigma_o^{2}}\right]^{\frac{n+1}{2}}. \tag{2.150}$$

Note that the evaluation of the effective compliance tensor $\widetilde{\mathbf{M}}$ (or equivalently $\widehat{\mathbf{M}}$) introduced in expression (2.143) (or (2.85)) is essential for the computation of the effective stress potential in the last expression. In general, the computation of $\widetilde{\mathbf{M}}$ requires the numerical evaluation of surface integrals. However, it is possible to reduce these double integrals to single ones in this case (Eshelby, 1957; Mura, 1987), and sometimes to obtain fully analytical solutions. Such results will be presented

in the following sections. Furthermore, the effective stress potential $\widetilde{U}_{var}$ is a homogeneous function of degree $n+1$ in $\overline{\boldsymbol{\sigma}}$, which is consistent with the general definition for $\widetilde{U}$ in (2.28).

Furthermore, it is worth noting that, while (2.150) is a rigorous lower bound for the stress potential $\widetilde{U}$, this does not necessarily imply that the constitutive relation between the average stress $\overline{\boldsymbol{\sigma}}$ and the corresponding average strain-rate $\overline{\boldsymbol{D}}$ is also a lower bound. For this reason, the above expressions will also be regarded as "variational" estimates, where derivatives with respect to the average stress $\overline{\boldsymbol{\sigma}}$ can be considered.

Remark 2.5.1. At this point, it is useful to make the connection between the estimate (2.150) and the corresponding gauge function introduced in (2.31). Thus, from the definition of the gauge factor Γ_n in (2.28) and the estimate (2.150), it is easily derived that

$$\Gamma_n^{var}(\overline{\boldsymbol{\sigma}}) = (1-f)^{\frac{1}{1+n}}\,\hat{\sigma}_{eq}. \tag{2.151}$$

This implies that the corresponding gauge surface (see (2.29)) is described in terms of the gauge function $\widetilde{\Phi}_n^{var}$ by the following condition

$$\widetilde{\Phi}_n^{var}(\overline{\boldsymbol{\Sigma}}) = \Gamma_n^{var}(\overline{\boldsymbol{\Sigma}}) - 1 = (1-f)^{\frac{1}{1+n}}\,\hat{\sigma}_{eq}(\overline{\boldsymbol{\Sigma}}) - 1 = 0, \tag{2.152}$$

with $\overline{\boldsymbol{\Sigma}}$ denoting a normalized stress tensor that is homogeneous of degree zero in $\overline{\boldsymbol{\sigma}}$. In the next chapters, use of relation (2.152) will be made to extract relevant results for the effective behavior of isotropic and anisotropic porous media.

Next, making use of the stationarity of the estimate (2.146) with respect to the variable μ, we can determine the corresponding macroscopic strain-rate $\overline{\boldsymbol{D}}$ via

$$\overline{\boldsymbol{D}} = \widetilde{\mathbf{M}}(\mu)\,\overline{\boldsymbol{\sigma}} = \frac{1}{\mu}\,\widehat{\mathbf{M}}\,\overline{\boldsymbol{\sigma}} = \sqrt{3}\,\dot{\varepsilon}_o \left(\frac{3\,\overline{\boldsymbol{\sigma}}\cdot\widehat{\mathbf{M}}\,\overline{\boldsymbol{\sigma}}}{(1-f)\,\sigma_o^2}\right)^{\frac{n}{2}} \frac{\widehat{\mathbf{M}}\,\overline{\boldsymbol{\sigma}}}{\sqrt{\overline{\boldsymbol{\sigma}}\cdot\widehat{\mathbf{M}}\,\overline{\boldsymbol{\sigma}}}}, \tag{2.153}$$

where use of relations (2.143) and (2.149) has been made. From this last result, it is evident that the effective constitutive relation between the macroscopic stress $\overline{\boldsymbol{\sigma}}$ and strain-rate $\overline{\boldsymbol{D}}$ is nonlinear, while this nonlinearity enters through the shear modulus μ.

In order to complete the study of the "variational" method, it is necessary to provide estimates for the phase average fields in the nonlinear composite. In a recent work, Idiart and Ponte Castañeda (2006) have shown that, in the "variational" method, the phase average fields in the nonlinear composite coincide with the phase average fields in the LCC. Hence, using the relation developed in subsection 2.3.1 together with relations (2.143), the following estimates are delivered for the phase average fields in the nonlinear composite

$$\begin{aligned}
&\overline{\boldsymbol{\sigma}}^{(1)} = \overline{\boldsymbol{\sigma}}_L^{(1)} = \frac{1}{1-f}\,\overline{\boldsymbol{\sigma}}_L = \frac{1}{1-f}\,\overline{\boldsymbol{\sigma}}, \quad \overline{\boldsymbol{\sigma}}^{(2)} = \overline{\boldsymbol{\sigma}}_L^{(2)} = \mathbf{0},\\
&\overline{\boldsymbol{D}}^{(1)} = \overline{\boldsymbol{D}}_L^{(1)} = \mathbf{A}^{(1)}\,\overline{\boldsymbol{D}} = \mathbf{M}\,\overline{\boldsymbol{\sigma}}^{(1)} = \frac{1}{2\,\mu}\,\overline{\boldsymbol{\sigma}}',\\
&\overline{\boldsymbol{D}}^{(2)} = \overline{\boldsymbol{D}}_L^{(2)} = \mathbf{A}^{(2)}\,\overline{\boldsymbol{D}} = \frac{1}{f}\,(\widetilde{\mathbf{M}}-\mathbf{M})\,\overline{\boldsymbol{\sigma}} = \frac{1}{\mu\,(1-f)}\,\widehat{\mathbf{Q}}^{-1}\,\overline{\boldsymbol{\sigma}},\\
&\overline{\boldsymbol{\Omega}}^{(2)} = \overline{\boldsymbol{\Omega}}_L^{(2)} = \overline{\boldsymbol{\Omega}} - \mathbf{C}^{(2)}\,\overline{\boldsymbol{D}} = \overline{\boldsymbol{\Omega}} + (1-f)\,\boldsymbol{\Pi}\,\mathbf{L}\overline{\boldsymbol{D}}_L^{(2)} = \overline{\boldsymbol{\Omega}} + \frac{1}{\mu}\,\boldsymbol{\Pi}\,\mathbf{L}\widehat{\mathbf{Q}}^{-1}\,\overline{\boldsymbol{\sigma}},
\end{aligned} \tag{2.154}$$

where $\mathbf{A}^{(r)}$ (with $r = 1, 2$) and $\mathbf{C}^{(2)}$ are given by relations (2.87) and (2.92), respectively. In all the above expressions, use has been made of the homogeneity of the fourth order tensors $\mathbf{M}$, $\mathbf{L}$, $\mathbf{Q}$ and $\mathbf{\Pi}$ on μ (see Appendix IV for details). In turn, the second-order tensor $\overline{\boldsymbol{\Omega}}$ is the macroscopic spin tensor and is applied externally to the problem, while the incompressibility limit $\kappa \to \infty$ needs to be considered in the term $\mathbf{\Pi}\,\mathbf{L}$ (see Appendix I), which is independent of μ. It is worth noting that the work of Idiart and Ponte Castañeda (2006) does not involve the study of estimating the phase average spin in the nonlinear composite. However, based on the corresponding results for the average strain-rate $\overline{\boldsymbol{D}}^{(1)}$ or $\overline{\boldsymbol{D}}^{(2)}$, it is natural to assume that the same notion could be applied to the average spin $\overline{\boldsymbol{\Omega}}^{(2)}$.

2.6 "Second-order" method

In this section, the "second-order" homogenization method of Ponte Castañeda (2002a) is considered. This recent method makes use of a more general LCC (linear comparison composite), when compared with the above discussed "variational" method. In the context of the "second-order" method, the phases of the LCC are characterized by "thermo-viscous" quadratic stress potentials of the form defined in section 2.4, so that (Ponte Castañeda, 2002a)

$$U_L^{(r)}(\boldsymbol{\sigma}; \check{\boldsymbol{\sigma}}^{(r)}, \mathbf{M}^{(r)}) = U^{(r)}(\check{\boldsymbol{\sigma}}^{(r)}) + \frac{\partial U^{(r)}(\check{\boldsymbol{\sigma}}^{(r)})}{\partial \boldsymbol{\sigma}} \cdot (\boldsymbol{\sigma} - \check{\boldsymbol{\sigma}}^{(r)}) + \\ + \frac{1}{2}(\boldsymbol{\sigma} - \check{\boldsymbol{\sigma}}^{(r)}) \cdot \mathbf{M}^{(r)}\,(\boldsymbol{\sigma} - \check{\boldsymbol{\sigma}}^{(r)}), \tag{2.155}$$

where $U^{(r)}$ is the stress potential of each phase in the nonlinear composite, and in the present study is given by (2.23), while $\check{\boldsymbol{\sigma}}^{(r)}$ are uniform per-phase, reference stress tensors, and $\mathbf{M}^{(r)}$ are symmetric, fourth-order, compliance tensors. The subscript L is again used to denote quantities in the LCC. It is useful to remark that expression (2.155) can be identified with the corresponding one in (2.94) by letting

$$\boldsymbol{\eta}^{(r)} = \frac{\partial U^{(r)}\left(\check{\boldsymbol{\sigma}}^{(r)}\right)}{\partial \boldsymbol{\sigma}} - \mathbf{M}^{(r)}\,\check{\boldsymbol{\sigma}}^{(r)}, \\ \gamma^{(r)} = \frac{1}{2}\,\check{\boldsymbol{\sigma}}^{(r)} \cdot \mathbf{M}^{(r)}\,\check{\boldsymbol{\sigma}}^{(r)} - \frac{\partial U^{(r)}\left(\check{\boldsymbol{\sigma}}^{(r)}\right)}{\partial \boldsymbol{\sigma}} \cdot \check{\boldsymbol{\sigma}}^{(r)} + U^{(r)}(\check{\boldsymbol{\sigma}}^{(r)}). \tag{2.156}$$

Following similar procedure to the "variational" method in the previous section, it is easily shown that the effective stress potential $\widetilde{U}$ is written as

$$\widetilde{U}\,(\overline{\boldsymbol{\sigma}}) = \sup_{\mathbf{M}^{(r)}(\mathbf{x})} \left\{ \widetilde{U}_L\left(\overline{\boldsymbol{\sigma}}; \check{\boldsymbol{\sigma}}^{(r)}\,\mathbf{M}^{(r)}(\mathbf{x})\right) + \sum_{r=1}^{2} c^{(r)} \left\langle V^{(r)}(\check{\boldsymbol{\sigma}}^{(r)}, \mathbf{M}^{(r)}(\mathbf{x})) \right\rangle^{(r)} \right\}, \tag{2.157}$$

where $\widetilde{U}_L$ is the effective stress potential of a linear composite with an infinite number of phases, since the compliance tensors $\mathbf{M}^{(r)}$ are functions of the position $\mathbf{x}$ and is defined by

$$\widetilde{U}_L(\overline{\boldsymbol{\sigma}}; \check{\boldsymbol{\sigma}}^{(r)}, \mathbf{M}^{(r)}) = \min_{\sigma\,\epsilon\,\mathcal{S}(\overline{\sigma})} \sum_{r=1}^{2} c^{(r)} \left\langle U_L^{(r)}(\boldsymbol{\sigma}; \mathbf{M}^{(r)}) \right\rangle^{(r)} = \\ = \min_{\sigma\,\epsilon\,\mathcal{S}(\overline{\sigma})} \sum_{r=1}^{2} c^{(r)} \left\langle \frac{1}{2}\,\boldsymbol{\sigma} \cdot \mathbf{M}^{(r)}\,\boldsymbol{\sigma} + \boldsymbol{\eta}^{(r)} \cdot \check{\boldsymbol{\sigma}}^{(r)} + \gamma^{(r)} \right\rangle^{(r)}. \tag{2.158}$$

In turn, the corrector functions $V^{(r)}$ are defined similarly to (2.132) and they read

$$V^{(r)}(\check{\boldsymbol{\sigma}}^{(r)}, \mathbf{M}^{(r)}) = \min_{\hat{\sigma}^{(r)}} \left[U^{(r)}(\hat{\boldsymbol{\sigma}}) - U_L^{(r)}(\hat{\boldsymbol{\sigma}}; \check{\boldsymbol{\sigma}}^{(r)}\, \mathbf{M}^{(r)}) \right], \tag{2.159}$$

where $\hat{\boldsymbol{\sigma}}^{(r)}$ are second-order tensors, that minimize the corrector functions $V^{(r)}$. It is emphasized that the variational formulation defined by the last three relations in the context of the "second-order" method, namely expressions (2.157), (2.158) and (2.159) is valid for any choice of the reference stress tensor $\check{\boldsymbol{\sigma}}^{(r)}$, including the choice of $\check{\boldsymbol{\sigma}}^{(r)} = \mathbf{0}$, which leads to the "variational" method of the previous section.

As already discussed in the context of the previous section, solving the optimization problem in (2.157) is an extremely difficult task due to the dependence of $\mathbf{M}^{(r)}$ on the spatial variable $\mathbf{x}$. However, as a consequence of the fact that the compliance tensors $\mathbf{M}^{(r)}$ do not need to satisfy any constraints, apart from being positive definite, allows us to *approximate* the variational formulation (2.157) by choosing *constant* (per phase) trial fields $\mathbf{M}^{(r)}$. A direct consequence of this is the reduction of an infinite-dimensional optimization procedure into a finite-dimensional problem. Hence, the variational principle (2.157) reduces to

$$\widetilde{U}\,(\overline{\boldsymbol{\sigma}}) \geq \sup_{\mathbf{M}^{(r)}} \left\{ \widetilde{U}_L(\overline{\boldsymbol{\sigma}}; \check{\boldsymbol{\sigma}}^{(r)}\, \mathbf{M}^{(r)}) + \sum_{r=1}^{2} c^{(r)}\, V^{(r)}(\check{\boldsymbol{\sigma}}^{(r)}, \mathbf{M}^{(r)}) \right\}. \tag{2.160}$$

Note that after introducing constant per-phase compliance tensors $\mathbf{M}^{(r)}$, the estimate for $\widetilde{U}$ is approximate and thus it depends on the choice of the reference stress tensors $\check{\boldsymbol{\sigma}}^{(r)}$. The choice of these tensors will be addressed in the context of viscoplastic porous media in the following paragraphs. On the other hand, it is necessary to *emphasize* that the "variational" bound of Ponte Castañeda (1991), discussed in the previous section, (which is a special case of the one in (2.160) if we let $\check{\boldsymbol{\sigma}} = \mathbf{0}$) is the best bound that can be obtained from (2.160). Given this observation, it is then appropriate to generalize our point of view and investigate the possibility of obtaining estimates different and hopefully more accurate than the bound. This can be achieved by replacing the "sup" in relation (2.160) and the "min" in (2.159) with the more general *stationary* conditions, which implies that the effective stress potential is written as

$$\widetilde{U}_{som}\,(\overline{\boldsymbol{\sigma}}) = \operatorname*{stat}_{\mathbf{M}^{(r)}} \left\{ \widetilde{U}_L(\overline{\boldsymbol{\sigma}}; \check{\boldsymbol{\sigma}}^{(r)}\, \mathbf{M}^{(r)}) + \sum_{r=1}^{2} c^{(r)}\, V^{(r)}(\check{\boldsymbol{\sigma}}^{(r)}, \mathbf{M}^{(r)}) \right\}, \tag{2.161}$$

with $\widetilde{U}_L$ given by relation (2.158) and the corrector functions $V^{(r)}$ expressed as:

$$V^{(r)}(\check{\boldsymbol{\sigma}}^{(r)}, \mathbf{M}^{(r)}) = \operatorname*{stat}_{\hat{\sigma}^{(r)}} \left[U^{(r)}(\hat{\boldsymbol{\sigma}}^{(r)}) - U_L^{(r)}(\hat{\boldsymbol{\sigma}}^{(r)}; \check{\boldsymbol{\sigma}}^{(r)}\, \mathbf{M}^{(r)}) \right]. \tag{2.162}$$

In these relations, the stationary operation (stat) consists in setting the partial derivative of the argument with respect to the variable equal to zero, which yields a set of nonlinear algebraic equations for the variables $\hat{\boldsymbol{\sigma}}^{(r)}$ and $\mathbf{M}^{(r)}$. This last relation is valid for any two-phase nonlinear composite. In particular, it has been shown by Ponte Castañeda (2002a) that this method is exact to "second-order" in the heterogeneity contrast of the phases, which is the source of its name as "second-order" method. In contrast, the "variational" method presented in the previous section, is exact to the first

order in the heterogeneity contrast and thus is expected to deliver less accurate estimates than the "second-order" method.

The variational formulation described by the previous relations involves certain optimality (stationary) conditions. First, consider the stationary condition in (2.162), with respect to the tensor $\hat{\boldsymbol{\sigma}}^{(r)}$, which reads

$$\frac{\partial U^{(r)}(\hat{\boldsymbol{\sigma}})}{\partial \hat{\boldsymbol{\sigma}}} - \frac{\partial U^{(r)}(\check{\boldsymbol{\sigma}})}{\partial \check{\boldsymbol{\sigma}}} = \mathbf{M}^{(r)} \left(\hat{\boldsymbol{\sigma}}^{(r)} - \check{\boldsymbol{\sigma}}^{(r)}\right), \quad r = 1, 2. \tag{2.163}$$

Note that due to the multi-dimensional character of the problem as well as the fact that $V^{(r)}$ are non-convex functions of $\hat{\boldsymbol{\sigma}}$, relations (2.163) possess multiple solutions. In this connection, if $\check{\boldsymbol{\sigma}}^{(r)}$ is not equal to zero or $\hat{\boldsymbol{\sigma}}^{(r)}$, the above expression constitutes a *generalized secant-type* approximation to the nonlinear potential $U^{(r)}$, evaluated at $\hat{\boldsymbol{\sigma}}^{(r)}$ and $\check{\boldsymbol{\sigma}}^{(r)}$.

On the other hand, the second optimality condition with respect to the compliance tensor $\mathbf{M}^{(r)}$ in (2.161) is not straightforward due to the fact that, similar to the "variational" procedure of the previous section, the corrector functions $V^{(r)}$ are not smooth in $\mathbf{M}^{(r)}$ (Idiart and Ponte Castañeda, 2006). Thus, the stationary conditions cannot be obtained by direct derivation of the stress potential $\widetilde{U}$ with respect to $\mathbf{M}^{(r)}$. Even so, these optimality conditions can be satisfied partially by choosing appropriately the viscous compliance tensor $\mathbf{M}^{(r)}$, such that smoothness of the function $\widetilde{U}$ with respect to the eigenvalues of $\mathbf{M}^{(r)}$ is assured. More details on the choice of the viscous compliance tensor $\mathbf{M}^{(r)}$ are provided next, where the problem is specialized for viscoplastic porous materials.

2.6.1 "Second-order" estimates for viscoplastic porous media

In what follows, we restrict our attention to the case of nonlinear porous media, which is the main subject of this work. More specifically, for the case of porous media, the LCC is also a porous material, whose matrix phase (denoted as phase 1) is described by a generalized stress potential $U_L^{(1)} \equiv U_L$ in accord with definition (2.155), which is expressed as:

$$U_L\left(\boldsymbol{\sigma}; \check{\boldsymbol{\sigma}}, \mathbf{M}\right) = U\left(\check{\boldsymbol{\sigma}}\right) + \frac{\partial U\left(\check{\boldsymbol{\sigma}}\right)}{\partial \boldsymbol{\sigma}} \cdot \left(\boldsymbol{\sigma} - \check{\boldsymbol{\sigma}}\right) + \frac{1}{2}\left(\boldsymbol{\sigma} - \check{\boldsymbol{\sigma}}\right) \cdot \mathbf{M}\left(\boldsymbol{\sigma} - \check{\boldsymbol{\sigma}}\right), \tag{2.164}$$

where U is the stress potential of the nonlinear matrix phase, defined by (2.23), while the label 1 is omitted for simplicity, unless stated otherwise. In this last expression, $\mathbf{M}$ and $\check{\boldsymbol{\sigma}}$ are the compliance and reference tensors associated with the matrix phase. On the other hand, the vacuous phase (denoted as phase 2) is defined by a stress potential $U^{(2)} = 0$. Note that relation (2.164) can be identified with the corresponding expression (2.115) for linear "thermo-viscous" porous media by letting

$$\begin{aligned} \boldsymbol{\eta} &= \frac{\partial U\left(\check{\boldsymbol{\sigma}}\right)}{\partial \boldsymbol{\sigma}} - \mathbf{M}\,\check{\boldsymbol{\sigma}}, \\ \gamma &= \frac{1}{2}\,\check{\boldsymbol{\sigma}} \cdot \mathbf{M}\,\check{\boldsymbol{\sigma}} - \frac{\partial U\left(\check{\boldsymbol{\sigma}}\right)}{\partial \boldsymbol{\sigma}} \cdot \check{\boldsymbol{\sigma}} + U(\check{\boldsymbol{\sigma}}). \end{aligned} \tag{2.165}$$

For the purpose of this work, the reference tensor $\check{\boldsymbol{\sigma}}$ is taken to be proportional to the deviatoric macroscopic stress tensor $\overline{\boldsymbol{\sigma}}'$ so that the effective stress potential $\widetilde{U}$ of the nonlinear composite is a scalar isotropic function of the macroscopic stress tensor $\overline{\boldsymbol{\sigma}}$. The choice for the magnitude of this

tensor will be discussed in detail in a following subsection. The proportionality condition is simply written as

$$\check{\boldsymbol{\sigma}} \propto \overline{\boldsymbol{\sigma}}' \quad \Rightarrow \quad \overline{\boldsymbol{S}} = \frac{\check{\boldsymbol{\sigma}}}{\check{\sigma}_{eq}} = \frac{\overline{\boldsymbol{\sigma}}'}{\overline{\sigma}_{eq}}, \tag{2.166}$$

with $\overline{\boldsymbol{S}}$ being a second-order tensor, which is homogeneous of degree zero in $\overline{\boldsymbol{\sigma}}$ and has been introduced for convenience. In turn, for viscoplastic composites, the following choice has been proposed by Ponte Castañeda (2002b) for the compliance tensor $\mathbf{M}$ or, equivalently, for the modulus tensor $\mathbf{L}$ of the matrix phase in the LCC,

$$\mathbf{M} = \frac{1}{2\lambda}\,\mathbf{E} + \frac{1}{2\mu}\,\mathbf{F} + \frac{1}{3\kappa}\,\mathbf{J}, \qquad \mathbf{L} = (\mathbf{M})^{-1} = 2\,\lambda\,\mathbf{E} + 2\,\mu\,\mathbf{F} + 3\,\kappa\,\mathbf{J}. \tag{2.167}$$

Here, λ and μ are shear viscous moduli to be defined later, and κ is the bulk modulus of the matrix phase, while the limit of incompressibility, i.e., $\kappa \to \infty$, will be considered later. The projection tensors $\mathbf{E}$ and $\mathbf{F}$ are given by

$$\mathbf{E} = \frac{3}{2}\,\overline{\boldsymbol{S}} \otimes \overline{\boldsymbol{S}}, \quad \mathbf{F} = \mathbf{K} - \mathbf{E}, \quad \mathbf{E} + \mathbf{F} + \mathbf{J} = \mathbf{I}. \tag{2.168}$$

In the last two expressions $\mathbf{I}$, $\mathbf{K}$ and $\mathbf{J}$ are the standard, fourth-order, identity, shear and hydrostatic projection tensors, respectively, given by relation (2.140). On the other hand, $\mathbf{E}$ and $\mathbf{F}$ are motivated by the fourth-order shear eigen-tensors (Ponte Castañeda, 1996) of the tangent compliance tensor, defined as $\mathbf{M}_t = \partial^2 U(\check{\boldsymbol{\sigma}})/(\partial\boldsymbol{\sigma}\,\partial\boldsymbol{\sigma})$ (see relation (2.3)) and are such that $\mathbf{EE} = \mathbf{E}$, $\mathbf{FF} = \mathbf{F}$, $\mathbf{EF} = \mathbf{0}$. In addition, it is emphasized that even though the nonlinear matrix phase is *isotropic* (see relation (2.23)), the corresponding linearized phase in the LCC is, in general, *anisotropic*, in contrast with earlier methods, like the variational method, discussed in the previous section, where the corresponding LCC is *isotropic* (see relation (2.139)). A measure of this anisotropy is given by the ratio

$$k = \frac{\lambda}{\mu}, \tag{2.169}$$

such that $k = 1$ and $k = 0$ correspond to an isotropic and extremely anisotropic linear matrix phase.

In this regard, the effective stress potential of the porous LCC follows from relations (2.117) and (2.124), such that (Levin, 1967; Talbot and Willis, 1992):

$$\widetilde{U}_L(\overline{\boldsymbol{\sigma}}; \check{\boldsymbol{\sigma}}, \mathbf{M}) = \frac{1}{2}\,\overline{\boldsymbol{\sigma}} \cdot \widetilde{\mathbf{M}}\,\overline{\boldsymbol{\sigma}} + \boldsymbol{\eta} \cdot \overline{\boldsymbol{\sigma}} + (1-f)\,\gamma, \tag{2.170}$$

where $\boldsymbol{\eta}$ and γ are defined in (2.165), while $\widetilde{\mathbf{M}}$ is the effective compliance tensor of the linear porous medium and is defined by (2.119), which is recalled here for completeness to be

$$\widetilde{\mathbf{M}} = \mathbf{M} + \frac{f}{1-f}\,\mathbf{Q}^{-1}. \tag{2.171}$$

In this expression, $\mathbf{Q}$ is a microstructural tensor related to the Eshelby (1957) tensor given by relation (2.59). The reader is referred to section 2.4.1 for further details on the homogenization of linear thermo-viscous porous media.

At this point, it is important to mention that, because of the anisotropy of the LCC, the corresponding fourth-order tensor $\mathbf{Q}$, and therefore $\widetilde{\mathbf{M}}$ (see relation (2.171)) do not have the same eigen-tensors as the compliance tensor $\mathbf{M}$ when the microstructure is isotropic, and therefore they

cannot be written explicitly in terms of **E**, **F** and **J** (Nebozhyn and Ponte Castañeda, 1999). A direct consequence of this fact is that the deformation modes in relation (2.170) are coupled, as will be seen later. In addition, similarly to the "variational" method, incompressibility of the matrix phase requires the consideration of the limit $\kappa \to \infty$ for the computation of **Q**, which is taken with the help of the commercial package "Mathematica" (see Appendix I).

Having defined the effective behavior of the porous LCC, the corresponding "second-order" estimate for the instantaneous effective stress potential of the nonlinear porous material $\widetilde{U}$ with an incompressible matrix phase, defined for a two-phase composite in (2.161), can be shown to reduce to (Ponte Castañeda, 2002b; Idiart et al., 2006)

$$\widetilde{U}_{som}\left(\overline{\boldsymbol{\sigma}}\right) = \underset{\lambda,\,\mu}{\text{stat}} \left\{ \widetilde{U}_L\left(\overline{\boldsymbol{\sigma}}; \check{\boldsymbol{\sigma}},\, \lambda,\, \mu\right) + (1-f)\, V\left(\check{\boldsymbol{\sigma}}, \lambda,\, \mu\right) \right\}, \tag{2.172}$$

for the specific choice of **M** made in relation (2.167). In this relation, use was made of the notation $c^{(2)} = f$ and hence $c^{(1)} = 1 - f$ to express the volume fractions of the pores (i.e., porosity) and the matrix phase, respectively. In addition, the "corrector" function V is defined by

$$V\left(\check{\boldsymbol{\sigma}}, \lambda,\, \mu\right) = \underset{\hat{\sigma}}{\text{stat}} \left[U\left(\hat{\boldsymbol{\sigma}}\right) - U_L\left(\hat{\boldsymbol{\sigma}}; \check{\boldsymbol{\sigma}},\, \lambda,\, \mu\right) \right], \tag{2.173}$$

with $\hat{\boldsymbol{\sigma}}$ being a uniform, second-order tensor. By making use of the special form (2.167) of the tensor **M**, it is convenient to define two components of the tensor $\hat{\boldsymbol{\sigma}}$ that are "parallel" and "perpendicular" to the corresponding reference tensor $\check{\boldsymbol{\sigma}}$, respectively,

$$\hat{\sigma}_{||} = \sqrt{\frac{3}{2}\, \hat{\boldsymbol{\sigma}} \cdot \mathbf{E}\, \hat{\boldsymbol{\sigma}}} \quad \text{and} \quad \hat{\sigma}_{\perp} = \sqrt{\frac{3}{2}\, \hat{\boldsymbol{\sigma}} \cdot \mathbf{F}\, \hat{\boldsymbol{\sigma}}}. \tag{2.174}$$

The equivalent part of $\hat{\boldsymbol{\sigma}}$, then, reduces to

$$\hat{\sigma}_{eq} = \sqrt{\hat{\sigma}_{||}^2 + \hat{\sigma}_{\perp}^2}. \tag{2.175}$$

Before proceeding further, it is worth noting that the previous definitions (2.166), (2.167), (2.174) and (2.175), imply certain identities which are summarized as follows:

$$\begin{gathered} \hat{\boldsymbol{\sigma}} \cdot \overline{\boldsymbol{S}} = \frac{2}{3}\, \hat{\sigma}_{||}, \quad \check{\boldsymbol{\sigma}} \cdot \overline{\boldsymbol{S}} = \frac{2}{3}\, \check{\sigma}_{eq}, \\ \mathbf{E}\, \overline{\boldsymbol{\sigma}} = \overline{\boldsymbol{\sigma}}', \quad \mathbf{E}\, \check{\boldsymbol{\sigma}} = \check{\sigma}_{eq}\, \overline{\boldsymbol{S}} = \check{\boldsymbol{\sigma}}, \quad \mathbf{E}\, \hat{\boldsymbol{\sigma}} = \hat{\sigma}_{||} \overline{\boldsymbol{S}}, \\ \mathbf{F}\, \overline{\boldsymbol{\sigma}} = \mathbf{0}, \quad \mathbf{F}\, \check{\boldsymbol{\sigma}} = \mathbf{0}, \quad \mathbf{F}\, \hat{\boldsymbol{\sigma}} = \hat{\sigma}_{\perp} \overline{\boldsymbol{S}}_{\perp}, \end{gathered} \tag{2.176}$$

where $\overline{\boldsymbol{S}}_{\perp} \cdot \overline{\boldsymbol{S}} = 0$.

Now, the two stationary operations in relations (2.172) and (2.173) yield a set of nonlinear, algebraic equations for the variables λ, μ and $\hat{\boldsymbol{\sigma}}$. First of all, the optimality conditions with respect to the tensor $\hat{\boldsymbol{\sigma}}$ in (2.173), can be shown to reduce to

$$\frac{\partial U}{\partial \boldsymbol{\sigma}}(\hat{\boldsymbol{\sigma}}) - \frac{\partial U}{\partial \boldsymbol{\sigma}}(\check{\boldsymbol{\sigma}}) = \dot{\varepsilon}_o \left(\frac{\hat{\sigma}_{eq}}{\sigma_o}\right)^{n-1} \frac{\hat{\boldsymbol{\sigma}}}{\sigma_o} - \dot{\varepsilon}_o \left(\frac{\check{\sigma}_{eq}}{\sigma_o}\right)^{n-1} \frac{\check{\boldsymbol{\sigma}}}{\sigma_o} = \mathbf{M}(\hat{\boldsymbol{\sigma}} - \check{\boldsymbol{\sigma}}), \tag{2.177}$$

for power-law materials. By considering appropriate projections of this last relation in the fourth-order tensors **E** and **F**, these conditions simplify to two conditions for the scalars λ and μ, which read

$$\dot{\varepsilon}_o \left(\frac{\hat{\sigma}_{eq}}{\sigma_o}\right)^{n} \frac{\hat{\sigma}_{||}}{\hat{\sigma}_{eq}} - \dot{\varepsilon}_o \left(\frac{\check{\sigma}_{eq}}{\sigma_o}\right)^{n} = \frac{1}{3\lambda}(\hat{\sigma}_{||} - \check{\sigma}_{eq}), \quad \dot{\varepsilon}_o \left(\frac{\hat{\sigma}_{eq}}{\sigma_o}\right)^{n-1} = \frac{\sigma_o}{3\,\mu}. \tag{2.178}$$

Note that the second equation for μ in the last expression is the same with the one obtained in the context of the "variational" method, in relation $(2.149)_2$. These two last conditions can be further combined to deliver an equation for the anisotropy ratio k of the LCC, which is expediently written as

$$k \left(\frac{\hat{\sigma}_{eq}}{\check{\sigma}_{eq}} \right)^{1-n} = (k-1) \frac{\hat{\sigma}_{||}}{\check{\sigma}_{eq}} + 1. \tag{2.179}$$

An important point that should be made in the context of this last relation stems from the fact that the quantities $\hat{\sigma}_{eq}$, $\check{\sigma}_{eq}$ and $\hat{\sigma}_{||}$ are homogenous functions of degree 1 in the macroscopic stress tensor $\overline{\boldsymbol{\sigma}}$, which implies that the anisotropy ratio k depends only on the "direction" of $\overline{\boldsymbol{\sigma}}$ and not on its magnitude.

On the other hand, the scalar quantities $\hat{\sigma}_{||}$ and $\hat{\sigma}_{eq}$, defined in (2.174) and (2.175), result from the stationarity condition with respect to the scalars λ and μ in relation (2.172), such that (Ponte Castañeda, 2002a; Idiart et al., 2006)

$$\hat{\sigma}_{||} - \check{\sigma}_{eq} = \sqrt{\frac{3}{1-f} \frac{\partial \widetilde{U}_L}{\partial (2\,\lambda)^{-1}}} = \sqrt{\frac{3}{1-f} \; \langle (\boldsymbol{\sigma}_L - \check{\boldsymbol{\sigma}}) \cdot \mathbf{E} \; (\boldsymbol{\sigma}_L - \check{\boldsymbol{\sigma}}) \rangle^{(1)}} \tag{2.180}$$

and

$$\hat{\sigma}_{\perp} = \sqrt{\frac{3}{1-f} \frac{\partial \widetilde{U}_L}{\partial (2\,\mu)^{-1}}} = \sqrt{\frac{3}{1-f} \; \langle \boldsymbol{\sigma}_L \cdot \mathbf{F} \, \boldsymbol{\sigma}_L \rangle^{(1)}}. \tag{2.181}$$

The brackets $\langle \cdot \rangle^{(1)}$ denote volume averages over the matrix phase, with $\boldsymbol{\sigma}_L$ being the local stress field in the LCC. It is evident that the right-hand sides of the last two relations depend on certain traces of the field fluctuations in the LCC. In addition, it is worth mentioning that the right-hand side of the last two equations are homogeneous functions of degree zero in $\mathbf{M}$, and therefore, the quantities $\hat{\sigma}_{||}$ and $\hat{\sigma}_{\perp}$ depend on the moduli λ and μ only through the anisotropy ratio k. Thus, introducing these expressions for $\hat{\sigma}_{||}$ and $\hat{\sigma}_{\perp}$ into (2.179), we obtain a single algebraic, nonlinear equation for k, which must be solved numerically for a given choice of the reference tensor $\check{\boldsymbol{\sigma}}$. The evaluation of the two moduli, then, follows simply by noting from relations (2.169) and (2.178) that

$$\lambda = k\,\mu, \quad \text{and} \quad \mu = \frac{\sigma_o}{3\,\dot{\varepsilon}_o} \left(\frac{\hat{\sigma}_{eq}}{\sigma_o} \right)^{1-n}. \tag{2.182}$$

Finally, taking into account the stationarity conditions described previously in relations (2.179), (2.180) and (2.181), the expression (2.172) for the effective stress potential of the nonlinear porous material can be further simplified to

$$\widetilde{U}_{som}(\overline{\boldsymbol{\sigma}}) = (1-f) \left[\frac{\dot{\varepsilon}_o \sigma_o}{1+n} \left(\frac{\hat{\sigma}_{eq}}{\sigma_o} \right)^{n+1} - \dot{\varepsilon}_o \left(\frac{\check{\sigma}_{eq}}{\sigma_o} \right)^{n} \left(\hat{\sigma}_{||} - \frac{\overline{\sigma}_{eq}}{(1-f)} \right) \right], \tag{2.183}$$

where the choice for the magnitude of the reference tensor $\check{\boldsymbol{\sigma}}$ is yet to be determined as will be discussed in the following subsection. This last expression reveals the dependance of the final estimate for the effective stress potential of the nonlinear porous material on certain traces of the stress field-fluctuations in the LCC, through the quantities $\hat{\sigma}_{||}$ and $\hat{\sigma}_{eq}$. In addition, it is worth noting that the earlier "variational" method of Ponte Castañeda (1991) can be easily obtained by letting $\check{\sigma}_{eq}$ tend to zero in (2.183). This would further imply that the anisotropy ratio becomes $k = 1$ in this case (by setting $\check{\sigma}_{eq} = 0$ in (2.178)).

Remark 2.6.1. At this point, it is useful to make the connection between the estimate (2.183) and the corresponding definition for the gauge function introduced in (2.31). Thus, from the definition of the gauge factor Γ_n in (2.28) and the estimate (2.183), it is easily derived that

$$\Gamma_n^{som}(\overline{\boldsymbol{\sigma}}) = (1-f)^{\frac{1}{1+n}}\,\hat{\sigma}_{eq}\left[1-(1+n)\left(\frac{\check{\sigma}_{eq}}{\hat{\sigma}_{eq}}\right)^n\left(\frac{\hat{\sigma}_{||}}{\hat{\sigma}_{eq}}+\frac{\overline{\sigma}_{eq}}{(1-f)\,\hat{\sigma}_{eq}}\right)\right]^{\frac{1}{1+n}}, \tag{2.184}$$

This implies that the corresponding gauge surface (see (2.29)) is described in terms of the gauge function $\widetilde{\Phi}_n^{som}$ by the following condition

$$\begin{aligned}&\widetilde{\Phi}_n^{som}(\overline{\boldsymbol{\Sigma}}) = \Gamma_n^{som}(\overline{\boldsymbol{\Sigma}}) - 1 = \\ &= (1-f)^{\frac{1}{1+n}}\,\hat{\sigma}_{eq}(\overline{\boldsymbol{\Sigma}})\left[1-(1+n)\left(\frac{\check{\sigma}_{eq}(\overline{\boldsymbol{\Sigma}})}{\hat{\sigma}_{eq}(\overline{\boldsymbol{\Sigma}})}\right)^n\left(\frac{\hat{\sigma}_{||}(\overline{\boldsymbol{\Sigma}})}{\hat{\sigma}_{eq}(\overline{\boldsymbol{\Sigma}})}+\frac{\overline{\sigma}_{eq}(\overline{\boldsymbol{\Sigma}})}{(1-f)\,\hat{\sigma}_{eq}(\overline{\boldsymbol{\Sigma}})}\right)\right]^{\frac{1}{1+n}} - 1 = 0,\end{aligned} \tag{2.185}$$

with $\overline{\boldsymbol{\Sigma}}$ denoting a normalized stress tensor that is homogeneous of degree zero in $\overline{\boldsymbol{\sigma}}$. In the next chapters, use of relation (2.185) will be made to extract relevant results for the effective behavior of isotropic and anisotropic porous media.

In the sequel, we discuss the evaluation of the macroscopic average strain-rate $\overline{\boldsymbol{D}}$, initially defined in relation (2.6), which follows by differentiation of (2.172) or, equivalently, (2.183), with respect to the macroscopic stress tensor $\overline{\boldsymbol{\sigma}}$. In the present case, the resulting expression can be shown to reduce to (see details in Appendix II)

$$\overline{D}_{ij} = (\overline{D}_L)_{ij} + (1-f)\,g_{mn}\frac{\partial\check{\sigma}_{mn}}{\partial\overline{\sigma}_{ij}}. \tag{2.186}$$

Here, $\overline{\boldsymbol{D}}_L$ is the macroscopic strain-rate in the LCC given by (2.118) and (2.124), which is repeated here for completeness to be

$$\overline{\boldsymbol{D}}_L = \widetilde{\mathbf{M}}\,\overline{\boldsymbol{\sigma}} + \widetilde{\boldsymbol{\eta}}, \qquad \widetilde{\boldsymbol{\eta}} = \boldsymbol{\eta}, \tag{2.187}$$

whereas the second-order tensor $\boldsymbol{g}$ reads

$$g_{ij} = \left(\frac{1}{2\lambda}-\frac{1}{2\lambda_t}\right)\left(\hat{\sigma}_{||}-\frac{\overline{\sigma}_{eq}}{(1-f)}\right)\frac{\check{\sigma}_{ij}}{\check{\sigma}_{eq}} + \frac{f}{2(1-f)^2}\,\overline{\sigma}_{kl}\,T_{klmnij}\,\overline{\sigma}_{mn}, \tag{2.188}$$

with

$$T_{klmnij} = \left.\frac{\partial\left[Q(\check{\boldsymbol{\sigma}})\right]^{-1}_{klmn}}{\partial\check{\sigma}_{ij}}\right|_{\lambda,\,\mu}, \tag{2.189}$$

and

$$\lambda_t = \frac{\sigma_o}{3\,n\,\dot{\varepsilon}_o}\left(\frac{\check{\sigma}_{eq}}{\sigma_o}\right)^{1-n}. \tag{2.190}$$

In the context of relation (2.186), it is easily deduced that the average strain-rate $\overline{\boldsymbol{D}}$ in the nonlinear composite is not equal to the corresponding average strain-rate $\overline{\boldsymbol{D}}_L$ in the LCC. This is a direct consequence of the fact that the corresponding estimate (2.172) for the effective stress potential $\widetilde{U}_{som}$ is not fully stationary with respect to the reference stress tensor $\check{\boldsymbol{\sigma}}$.

Remark 2.6.2. In the special case of isotropic microstructures, the estimate (2.186) is coaxial but not proportional to $\overline{\boldsymbol{\sigma}}$. Indeed, the projections of the first term in (2.186) and the second term in (2.188) by the fourth-order tensor $\mathbf{F}$, defined in relation (2.168), are generally not zero. On the other hand the projections of the second term in (2.188) by the tensors $\mathbf{E}$ and $\mathbf{J}$ are always zero, namely

$$E_{pqij}\overline{\sigma}_{kl}\, T_{klmnij}\, \overline{\sigma}_{mn} = J_{pqij}\overline{\sigma}_{kl}\, T_{klmnij}\, \overline{\sigma}_{mn} = 0. \tag{2.191}$$

In summary, the "second-order" estimate (2.183) involves *two* approximations: the *linearization* of the nonlinear phases (relation (2.164)) and the *homogenization* of the LCC (relation (2.170)), where use was made of the Willis estimates (2.171). However, the estimation of the effective stress potential $\widetilde{U}_{som}$ requires a choice for the magnitude of the reference stress tensor $\check{\boldsymbol{\sigma}}$, which will be discussed in the following subsection.

2.6.2 Choices for the reference stress tensor

In this subsection, the choice of the reference stress tensor introduced in relation (2.164) is discussed. The assumption that the reference stress tensor, $\check{\boldsymbol{\sigma}}$, is proportional to the deviatoric macroscopic stress tensor $\overline{\boldsymbol{\sigma}}'$ has already been made in relation (2.166). Nonetheless, the estimate (2.183) for the effective stress potential requires a prescription for the "magnitude" of the reference stress tensor $\check{\boldsymbol{\sigma}}$, which is the main focus in this subsection.

As already discussed in prior work (Ponte Castañeda, 2002a; Idiart and Ponte Castañeda, 2005), it has not yet been possible to "optimize" the choice of the reference stress tensor. For this reason, it is necessary to prescribe a choice for the reference stress tensor $\check{\boldsymbol{\sigma}}$. The choices proposed in the earlier studies of Ponte Castañeda (2002b) and Idiart and Ponte Castañeda (2005) are summarized here as

$$\check{\boldsymbol{\sigma}} = (\overline{\boldsymbol{\sigma}}^{(1)})' = \frac{\overline{\boldsymbol{\sigma}}'}{1-f}, \tag{2.192}$$

and

$$\check{\boldsymbol{\sigma}} = \overline{\boldsymbol{\sigma}}', \tag{2.193}$$

where the prime denotes the deviatoric part of the macroscopic stress tensor $\overline{\boldsymbol{\sigma}}$. Both of these two prescriptions become zero in the purely hydrostatic loading (i.e., when $\overline{\boldsymbol{\sigma}}' = \mathbf{0}$), and thus lead exactly to the estimate delivered by the "variational" estimate of Ponte Castañeda (1991), described in the previous section, in the hydrostatic limit. However, it is known that, for isotropic porous media, the "variational" estimate is too stiff when compared to the analytical estimate obtained by the solution of the composite sphere (CSA) or cylinder (CCA) assemblages of Hashin (Hashin, 1962; Leblond et al., 1994; Gurson, 1977) subjected to pure hydrostatic loading. In this connection, it is necessary to propose a reference stress tensor, which remains non-zero in the hydrostatic limit. This procedure is described in the following paragraphs.

In this connection, it should be recalled that when the CSA or CCA are subjected to hydrostatic loading, the problem of estimating the effective behavior of the composite reduces in computing the effective behavior of an individual spherical or cylindrical hollow shell, with hydrostatic pressure

boundary conditions in the external boundary and zero traction in the internal boundary. On the other hand, there is no analytical closed-form solution for the analogous problem of ellipsoidal particulate microstructures, although in certain special cases, such as for a confocal, spheroidal shell subjected to a specific axisymmetric loading (Gologanu et al., 1993), it is possible to extract analytical solutions. This suggests the possibility of choosing a reference stress tensor that would allow the "second-order" estimate (2.183) to coincide with the analytical spherical and cylindrical analytical shell result in the hydrostatic limit, while still producing relatively accurate results for more general ellipsoidal microstructures.

From this viewpoint then and based on the analysis performed in subsection 2.2.1, we consider a particulate porous material that comprises ellipsoidal voids with aspect ratios w_1 and w_2 randomly distributed in an isotropic matrix phase. The orientation of the principal axes of the voids is described by the unit vectors $\mathbf{n}^{(i)}$ $(i = 1, 2, 3)$. In turn, the two-point correlation function of the voids, describing the relative position of the centers of the voids, has the same shape and orientation with the voids[†]. In the special case of purely hydrostatic loading, the effective stress potential $\widetilde{U}$ describing the behavior of the porous medium should not depend on the orientation vectors $\mathbf{n}^{(i)}$ $(i = 1, 2, 3)$, such that

$$\widetilde{U}(\overline{\sigma}_m\,;\, f, w_1, w_2, \mathbf{n}^{(i)}) = \widetilde{U}(\overline{\sigma}_m\,;\, f, w_1, w_2). \tag{2.194}$$

Based on this intuitive hypothesis, the proposed approximate estimate for $\widetilde{U}$ should reduce to the analytical results available in the literature, which can be recovered by considering special limiting procedures for the aspect ratios w_1 and w_2 defined in subsection 2.2.1. Those cases are itemized:

1. if $w_1 = w_2 = 1$, $\widetilde{U}$ should recover the analytical result delivered when a spherical cavity is subjected to pure hydrostatic loading.

2. if $w_1 = w_2 \to \infty$ or $w_1 = 1$ and $w_2 \to \infty$ or $w_1 \to \infty$ and $w_2 = 1$, $\widetilde{U}$ should recover the analytical result obtained when a cylindrical shell is subjected to pure hydrostatic loading.

In order to arrive at a prescription for the reference stress tensor $\check{\boldsymbol{\sigma}}$ that respects those two aforementioned conditions, it is useful first to express the effective stress potential, $\widetilde{U}$, in terms of the mean, applied macroscopic stress $\overline{\sigma}_m$ and the effective flow stress $\widetilde{\sigma}_w$ (the subscript w is used to emphasize the dependence on the aspect ratios w_1 and w_2) of the porous material, such that

$$\widetilde{U}(\overline{\boldsymbol{\sigma}}; f, w_1, w_2) = \frac{\dot{\varepsilon}_o\,\widetilde{\sigma}_w}{1+n}\left(\frac{3}{2}\frac{|\overline{\sigma}_m|}{\widetilde{\sigma}_w}\right)^{1+n}. \tag{2.195}$$

In this last expression, use has been made of the fact that the effective stress potential $\widetilde{U}$ is homogenous of degree $n+1$ in $\overline{\boldsymbol{\sigma}}$, whereas the form (2.195) implies that estimation of $\widetilde{\sigma}_w$ fully determines the effective behavior of the porous material, when subjected to hydrostatic loading conditions. It should be emphasized that there exist no exact solutions for the effective flow stress $\widetilde{\sigma}_w$ for a porous material consisting of ellipsoidal voids, except for the corresponding estimates obtained by the "variational" method, which are known to be stiff in general. However, $\widetilde{\sigma}_w$ can be computed exactly for the

[†]This analysis can be generalized to particulate porous media with ellipsoidal voids whose shape and orientation is different than the shape and orientation of their distribution function (Ponte Castañeda and Willis, 1995).

above-mentioned two microstructural configurations, i.e., for spherical voids and cylindrical voids with circular cross-section embedded in an incompressible isotropic matrix phase. In the next few paragraphs, we spell out these exact shell solutions, while comparing them with the corresponding estimates derived by the "variational" method in this case of hydrostatic loading.

In this connection, when an aggregate of an infinite hierarchy of sizes of spherical or cylindrical shells is subjected to hydrostatic loading conditions (i.e., $|X_\Sigma| \to \infty$), the corresponding effective flow stress can be computed exactly by solving the isolated shell problem, and is given by (Michel and Suquet, 1992)

$$\frac{\widetilde{\sigma}_{w=1}}{\sigma_o} = n\left(f^{-1/n} - 1\right) \quad \text{and} \quad \frac{\widetilde{\sigma}_{w\to\infty}}{\sigma_o} = \left(\frac{\sqrt{3}}{2}\right)^{\frac{1+n}{n}} \frac{\widetilde{\sigma}_{w=1}}{\sigma_o}, \tag{2.196}$$

where $\widetilde{\sigma}_{w=1}$ and $\widetilde{\sigma}_{w\to\infty}$ are the effective flow stresses of the spherical and the cylindrical shell with an incompressible matrix phase, respectively. Note that for a cylindrical shell with an incompressible isotropic matrix phase that is subjected to plane-strain loading conditions in the $3-$direction, the in-plane pressure $(\overline{\sigma}_{11}+\overline{\sigma}_{22})/2$ is identical to the three-dimensional pressure $(\overline{\sigma}_{11}+\overline{\sigma}_{22}+\overline{\sigma}_{33})/3$. This is a direct consequence of the fact that for the cylindrical shell subjected to plane-strain loading, the out-of-plane component of the stress is $\overline{\sigma}_{33} = (\overline{\sigma}_{11}+\overline{\sigma}_{22})/2$. Thus, definition (2.195) for the effective stress potential is valid for both spherical and cylindrical shells.

On the other hand, the corresponding effective flow stresses delivered by the "variational" procedure of Ponte Castañeda (1991) (VAR), for porous media containing spherical (denoted with $w = 1$) and cylindrical (denoted with $w \to \infty$) voids subjected to purely hydrostatic loading, can be shown to reduce to

$$\frac{\widetilde{\sigma}^{var}_{w=1}}{\sigma_o} = \frac{1-f}{\sqrt{f}^{\frac{1+n}{n}}} \quad \text{and} \quad \frac{\widetilde{\sigma}^{var}_{w\to\infty}}{\sigma_o} = \left(\frac{\sqrt{3}}{2}\right)^{\frac{1+n}{n}} \frac{\widetilde{\sigma}^{var}_{w=1}}{\sigma_o}. \tag{2.197}$$

Clearly, the estimates (2.196) and (2.197) delivered by the shell problem and the "variational" method, respectively, deviate significantly at low porosities. However, it is interesting to note that the effective flow stresses delivered by the shell problem and the "variational" bound satisfy the following *non-trivial* relation

$$\frac{\widetilde{\sigma}_{w\to\infty}}{\widetilde{\sigma}^{var}_{w\to\infty}} = \frac{\widetilde{\sigma}_{w=1}}{\widetilde{\sigma}^{var}_{w=1}}, \qquad \text{or} \qquad \widetilde{\sigma}_{w\to\infty} = \frac{\widetilde{\sigma}_{w=1}}{\widetilde{\sigma}^{var}_{w=1}}\,\widetilde{\sigma}^{var}_{w\to\infty}. \tag{2.198}$$

Making use now of relation (2.198) and due to lack of an analytical estimate in the case of general ellipsoidal microstructures, we make the assumption that the effective flow stress $\widetilde{\sigma}_w$ of an ellipsoidal shell with arbitrary aspect ratios w_1 and w_2 may be approximated by

$$\frac{\widetilde{\sigma}_w}{\widetilde{\sigma}^{var}_w} = \frac{\widetilde{\sigma}_{w=1}}{\widetilde{\sigma}^{var}_{w=1}} = \frac{\widetilde{\sigma}_{w\to\infty}}{\widetilde{\sigma}^{var}_{w\to\infty}}, \qquad \text{or} \qquad \widetilde{\sigma}_w = \frac{\widetilde{\sigma}_{w=1}}{\widetilde{\sigma}^{var}_{w=1}}\,\widetilde{\sigma}^{var}_w = \frac{\widetilde{\sigma}_{w\to\infty}}{\widetilde{\sigma}^{var}_{w\to\infty}}\,\widetilde{\sigma}^{var}_w, \tag{2.199}$$

where $\widetilde{\sigma}^{var}_w$ is the corresponding effective flow stress delivered by the "variational" procedure when a porous material with ellipsoidal voids of arbitrary aspect ratios w_1 and w_2 is subjected to pure hydrostatic loading. Thus, by making use of the general result for the effective stress potential in (2.150) and the definition (2.195), it is easily seen that

$$\frac{\dot{\varepsilon}_o\,\widetilde{\sigma}^{var}_w}{1+n}\left(\frac{3}{2}\frac{|\overline{\sigma}_m|}{\widetilde{\sigma}^{var}_w}\right)^{n+1} = (1-f)\,\frac{\dot{\varepsilon}_o\,\sigma_o}{n+1}\left[\frac{3\,\overline{\boldsymbol{\sigma}}\cdot\widehat{\mathbf{M}}\,\overline{\boldsymbol{\sigma}}}{(1-f)\,\sigma_o^2}\right]^{\frac{n+1}{2}}, \qquad \text{for} \qquad \overline{\boldsymbol{\sigma}} = \overline{\sigma}_m\,\boldsymbol{I}, \tag{2.200}$$

which implies that

$$\left(\frac{\widetilde{\sigma}_w^{var}}{\sigma_o}\right)^{-n} = (1-f)\left[\frac{4\,\boldsymbol{I}\cdot\widehat{\mathbf{M}}\,\boldsymbol{I}}{3\,(1-f)}\right]^{\frac{n+1}{2}}, \tag{2.201}$$

with $\widehat{\mathbf{M}}$ given by (2.143), which is not analytical for general ellipsoidal microstructures. Even so, this simple prescription may also be applied in the cases that the shape and orientation of the distribution function of the pores is not identical with the shape and orientation of the voids (Ponte Castañeda and Willis, 1995; Kailasam and Ponte Castañeda, 1998). This is a direct consequence of the fact that the "variational" method provides an estimate for general particulate microstructures as described by Ponte Castañeda and Willis (1995), and therefore the effective flow stress $\widetilde{\sigma}_w^{var}$ can be evaluated in any of these general cases.

To summarize briefly here, the main advantage of prescription (2.199) is that the estimate for $\widetilde{U}$ automatically recovers the two conditions described previously. On the other hand, it should be noted that when the porous material tends to a porous laminate (or porous "sandwich"), the "variational" estimate can be shown to be exact, i.e., the effective flow stress $\widetilde{\sigma}_w^{var}$ for such a microstructure is identically zero. This implies that (2.199) is not exact in this case, in the sense that the ratio $\widetilde{\sigma}_w/\widetilde{\sigma}_w^{var}$ should go to unity. However, it follows from $(2.199)_2$ that the absolute value for $\widetilde{\sigma}_w$ is zero and hence equal to the exact value. In this regard, the absolute error introduced by (2.199) for the determination of $\widetilde{\sigma}_w$ in this extreme case of a porous laminate is expected to be small.

Given the estimate (2.199) for the effective behavior of a porous material containing ellipsoidal voids subjected to purely hydrostatic loading, we propose the following ad-hoc choice for the reference stress tensor:

$$\check{\boldsymbol{\sigma}} = \xi\left(X_\Sigma, \overline{\boldsymbol{S}}, s_a, n\right)\overline{\boldsymbol{\sigma}}', \tag{2.202}$$

where $\overline{\boldsymbol{S}}$ is given by (2.166), s_a denotes the set of the microstructural variables defined in (2.16), n is the nonlinear exponent of the matrix phase, and

$$\xi\left(X_\Sigma, \overline{\boldsymbol{S}}\right) = \frac{1-q\,f}{1-f} + \alpha_m(\overline{\boldsymbol{S}})\,|X_\Sigma|\left(\exp\left[-\frac{\alpha_{eq}(\overline{\boldsymbol{S}})}{|X_\Sigma|}\right] + \beta\,\frac{X_\Sigma^4}{1+X_\Sigma^4}\right), \tag{2.203}$$

is a suitably chosen interpolation function. The coefficients t and β are prescribed in an ad-hoc manner to ensure the convexity of the effective stress potential and are detailed in Appendix III. The coefficients α_m and α_{eq} are, in general, functions of the microstructural variables s_a, the nonlinearity n of the matrix, the stress tensor $\overline{\boldsymbol{S}}$, but not of the stress triaxiality X_Σ. Before discussing the estimation of the coefficients α_m and α_{eq}, it is remarked that the choice (2.202) reduces to $\check{\boldsymbol{\sigma}} = \overline{\boldsymbol{\sigma}}'$ for $X_\Sigma = 0$ (see relation (2.193)), while it remains non-zero in the hydrostatic limit $|X_\Sigma| \to \infty$, in contrast with all the earlier choices proposed in the literature (Ponte Castañeda, 2002b; Idiart and Ponte Castañeda, 2005), such as the ones given by (2.192) and (2.193). It also guarantees that the effective stress potential is a homogeneous function of degree $n+1$ in the average stress $\overline{\boldsymbol{\sigma}}$ for all stress triaxialities X_Σ.

In particular, the coefficient α_m is computed such that the estimate for the effective stress potential $\widetilde{U}_{som}$, delivered by the second-order method in relation (2.183), coincides with the approximate solution for $\widetilde{U}$ in relation (2.195) in the hydrostatic limit. This condition may be written schematically

as

$$\widetilde{U}_{som} \rightarrow \widetilde{U} \quad \text{as} \quad |X_\Sigma| \rightarrow \infty \quad \Rightarrow \quad \alpha_m = \alpha_m \left(\overline{\boldsymbol{S}}, s_a, n \right), \tag{2.204}$$

which yields a nonlinear algebraic equation for α_m.

On the other hand, in order to compute the coefficient α_{eq}, an appropriate estimate for the deviatoric part of the strain-rate $\overline{\boldsymbol{D}}^{\,\prime}$ is needed in the limit as $X_\Sigma \rightarrow \pm\infty$. Note that for the general case of anisotropic microstructures, the sign (denoted as "sgn") of X_Σ matters, i.e., $\overline{\boldsymbol{D}}^{\prime}$ gets opposite values in the limits as $X_\Sigma \rightarrow +\infty$ and $X_\Sigma \rightarrow -\infty$. In addition, it is important to remark that the factor α_{eq} has to be independent of the magnitude of the macroscopic stress tensor $\overline{\boldsymbol{\sigma}}$. To ensure this, it is safe to make the following analysis with the normalized strain-rate $\overline{\boldsymbol{E}}^{\,\prime}$ (the prime denotes the deviatoric part), defined in (2.33), which is homogeneous of degree zero in $\overline{\boldsymbol{\sigma}}$ by definition.

In this regard, we first note that there exists no exact result for $\overline{\boldsymbol{E}}^{\,\prime}$ in the case of ellipsoidal voids, except for the special cases of spherical or cylindrical with circular cross-section voids and porous sandwiches, where $\overline{\boldsymbol{E}}^{\,\prime} = \boldsymbol{0}$ as $X_\Sigma \rightarrow \pm\infty$. This result is is exact for finite nonlinearities, i.e., $0 < m < 1$, while the special case of ideally-plasticity will be considered in a separate section later. On the other hand, it is emphasized that the "variational" method satisfies the above exact results, i.e., $\overline{\boldsymbol{E}}^{\,\prime}_{var} = \boldsymbol{0}$ as $X_\Sigma \rightarrow \pm\infty$. In addition, it is important to note that, for the case of hydrostatic loading, $\overline{\boldsymbol{E}}^{\,\prime}$ will be a function of the two aspect ratios w_1 and w_2, as well as the orientation vectors $\mathbf{n}^{(i)}$ $(i = 1, 2, 3)$ of the ellipsoidal void, in contrast with the effective stress potential $\widetilde{U}$, which is only a function of the two aspect ratios. This observation complicates significantly the estimation of $\overline{\boldsymbol{E}}^{\,\prime}$. However, based on the fact that, in the hydrostatic limit, $\overline{\boldsymbol{E}}^{\,\prime}_{var}$, given by (2.153), is exact in the three (including the porous sandwich) limiting cases mentioned earlier and due to absence of any other information on the computation of the deviatoric part of the strain-rate in the hydrostatic limit, the following prescription is adopted for $\overline{\boldsymbol{E}}^{\,\prime}$:

$$\overline{\boldsymbol{E}}^{\,\prime}_{som} = \frac{\overline{\boldsymbol{D}}^{\,\prime}}{\dot{\varepsilon}_o \left(\Gamma_n^{som}/\sigma_o\right)^n} \rightarrow \overline{\boldsymbol{E}}^{\,\prime}_{var} = \frac{\overline{\boldsymbol{D}}^{\,\prime}_{var}}{\dot{\varepsilon}_o \left(\Gamma_n^{var}/\sigma_o\right)^n} \quad \text{as} \quad X_\Sigma \rightarrow \pm\infty \quad \forall\, w_1,\, w_2,\, \mathbf{n}^{(i)}, \tag{2.205}$$

where Γ_n^{som} and Γ_n^{var} are the gauge factors corresponding to the "second-order" (see (2.184)) and the "variational" (see (2.151)) estimates, respectively. In addition, the above prescription guaranties that the slope of the gauge curve, as predicted by the "second-order" method will be identical to the slope of the corresponding gauge curve of the "variational" method in the hydrostatic limit.

The condition (2.205) provides an equation for the estimation of the coefficient α_{eq}, such that

$$\alpha_{eq} = \alpha_{eq} \left(\overline{\boldsymbol{S}}, s_a, n \right). \tag{2.206}$$

It should be emphasized that condition (2.205) implies that α_{eq} does not depend on the magnitude of the macroscopic stress tensor $\overline{\boldsymbol{\sigma}}$, since the terms $\overline{\boldsymbol{E}}_{som}$ and $\overline{\boldsymbol{E}}_{var}$ are homogeneous of degree zero in $\overline{\boldsymbol{\sigma}}$. While, the computation of the coefficient α_m in (2.204) needs to be performed numerically, the evaluation of α_{eq} can be further simplified to the analytical expression

$$\alpha_{eq} = \alpha_m^{-1} \left[1 + \frac{\frac{3}{2}\,\check{\sigma}_{eq}(\overline{\boldsymbol{\Sigma}})^n - \check{\sigma}_{eq}(\overline{\boldsymbol{\Sigma}})(2\,\overline{\lambda})^{-1} + \overline{d}_{||} - \overline{d}_{\,var}}{(1-f)\,\hat{\sigma}_{||}(\overline{\boldsymbol{\Sigma}})} \left(\frac{1}{2\overline{\lambda}} - \frac{1}{2\,\overline{\lambda}_t} \right)^{-1} \right]. \tag{2.207}$$

Here, use has been made of definition (2.30) for the normalized macroscopic stress tensor $\overline{\boldsymbol{\Sigma}} = \overline{\boldsymbol{\sigma}}/\Gamma_n(\overline{\boldsymbol{\sigma}})$, as well as of the fact that $\check{\sigma}_{eq}$, $\hat{\sigma}_{||}$ and $\hat{\sigma}_{eq}$ are homogeneous functions of degree one in their arguments. It is further emphasized that all the quantities involved in the above relation must be evaluated in the hydrostatic limit $X_\Sigma \to \pm\infty$, i.e., for

$$\overline{\boldsymbol{\Sigma}} = \mathrm{sgn}(X_\Sigma)\ \overline{\Sigma}_m^H\Big|_{som}\ \boldsymbol{I}, \tag{2.208}$$

where $\overline{\Sigma}_m^H\Big|_{som}$ is the corresponding normalized hydrostatic stress obtained by the "second-order" gauge function and is detailed in Appendix V.

Then, the terms in (2.207) associated with the "second-order" method are defined as

$$\overline{\lambda} = k^H\,\overline{\mu}, \qquad \overline{\mu} = \hat{\sigma}_{eq}(\overline{\boldsymbol{\Sigma}})^{1-n}/3, \qquad \overline{\lambda}_t = \frac{1}{3\,n}\,\check{\sigma}_{eq}(\overline{\boldsymbol{\Sigma}})^{1-n}, \tag{2.209}$$

and

$$\overline{d}_{||} = \frac{3}{2}\,\mathrm{sgn}(X_\Sigma)\ \overline{\Sigma}_m^H\Big|_{som}\ \overline{\boldsymbol{S}}\cdot\widetilde{\mathbf{M}}\Big|_{k=k^H,\mu=\overline{\mu}}\ \boldsymbol{I}, \tag{2.210}$$

with $\widetilde{\mathbf{M}}$ given by (2.171). Furthermore, for the computation of k^H in (2.210), it is necessary to solve the nonlinear equation for the anisotropy ratio k, defined by (2.179), in the hydrostatic limit.

On the other hand, the term $\overline{d}_{var}$ in (2.207), associated with the "variational" method, is given by

$$\overline{d}_{var} = \frac{9}{2}\,\mathrm{sgn}(X_\Sigma)\,\left(\overline{\Sigma}_m^H\Big|_{var}\right)^n\left(\frac{3\,\boldsymbol{I}\cdot\widehat{\mathbf{M}}\,\boldsymbol{I}}{1-f}\right)^{\frac{n-1}{2}}\overline{\boldsymbol{S}}\cdot\widehat{\mathbf{M}}\,\boldsymbol{I}, \tag{2.211}$$

with $\overline{\Sigma}_m^H\Big|_{var}$ denoting the corresponding normalized hydrostatic stress obtained by the "variational" gauge function, while $\widehat{\mathbf{M}}$ is given by (2.143). The evaluation of $\overline{\Sigma}_m^H\Big|_{var}$ is detailed in Appendix V.

In summary, relation (2.202), together with relations (2.204) and (2.206) (or (2.207)), completely define the reference stress tensor $\check{\boldsymbol{\sigma}}$, and thus, result (2.183) can be used to estimate the effective behavior of the viscoplastic porous material. It is important to emphasize at this point that the "second-order" procedure developed in the previous section is general enough to be able to deal with general ellipsoidal microstructures, in contrast with earlier models proposed in the literature (Gologanu et al., 1993; Leblond et al., 1994; Gărăjeu et al., 2000; Flandi and Leblond, 2005) that are constrained to spheroidal microstructures and axisymmetric loading conditions aligned with the pore symmetry axis.

2.6.3 Phase average fields

In this subsection, the focus is on estimating the average stress, strain-rate and spin in each phase of the porous material. This is necessary for the prediction of the evolution of the microstructural variables to be considered in the next section. Because of the presence of the vacuous phase the average stress tensors are trivially given by

$$(1-f)\,\overline{\boldsymbol{\sigma}}^{(1)} = \overline{\boldsymbol{\sigma}}, \qquad \overline{\boldsymbol{\sigma}}^{(2)} = \mathbf{0}. \tag{2.212}$$

On the other hand, the estimation of the average strain-rate and spin in each phase is non-trivial. As already discussed in the context of relation (2.170), use has been made of the Willis (1978)

estimates for the determination of the effective behavior of the LCC. One of the main results of this procedure is that the fields in the inclusion phase (vacuous phase in the present study) of the LCC are uniform, which can be written as $\boldsymbol{D}_L(\mathbf{x}) = \overline{\boldsymbol{D}}_L^{(2)}$ for all $\mathbf{x}$ in $\Omega^{(2)}$ in the LCC. Because of this result, the corresponding "second-order" estimate for $\overline{\boldsymbol{D}}^{(2)}$ in the nonlinear porous material also delivers uniform fields in the voids. However, the work of Idiart and Ponte Castañeda (2007) has shown that in principle $\overline{\boldsymbol{D}}^{(2)} \neq \overline{\boldsymbol{D}}_L^{(2)}$ for a general reference stress tensor $\check{\boldsymbol{\sigma}}$. On the other hand, the author is not aware of corresponding results concerning the estimation of the average spin $\overline{\boldsymbol{\Omega}}^{(2)}$ in the vacuous phase, apart from the fact that the spin is uniform in the inclusion phase of the LCC, i.e., $\boldsymbol{\Omega}_L(\mathbf{x}) = \overline{\boldsymbol{\Omega}}_L^{(2)}$, and the nonlinear composite due to the use of the Willis estimates. Regardless of any prescription for the estimation of the average strain-rate and spin in the vacuous phase, the following two relations for the macroscopic and the phase average quantities must always hold, both in the nonlinear composite and the LCC, such that

$$\overline{\boldsymbol{D}} = (1-f)\,\overline{\boldsymbol{D}}^{(1)} + f\,\overline{\boldsymbol{D}}^{(2)}, \quad \overline{\boldsymbol{D}}_L = (1-f)\,\overline{\boldsymbol{D}}_L^{(1)} + f\,\overline{\boldsymbol{D}}_L^{(2)}, \tag{2.213}$$

and

$$\overline{\boldsymbol{\Omega}} = (1-f)\,\overline{\boldsymbol{\Omega}}^{(1)} + f\,\overline{\boldsymbol{\Omega}}^{(2)}, \quad \overline{\boldsymbol{\Omega}}_L = (1-f)\,\overline{\boldsymbol{\Omega}}_L^{(1)} + f\,\overline{\boldsymbol{\Omega}}_L^{(2)}. \tag{2.214}$$

In the following, the discussion will be focused on estimating the average strain-rate and spin in the vacuous phase.

Specifically, making use of the identities (2.213) and the incompressibility of the matrix phase, the hydrostatic part of the macroscopic strain-rate $\overline{D}_m = \overline{D}_{ii}/3$ $(i = 1, 2, 3)$, and the average strain-rate in the voids, $\overline{D}_m^{(2)}$ are related through

$$\overline{D}_m^{(2)} = \frac{1}{f}\,\overline{D}_m, \quad \text{and} \quad \overline{D}_m^{(1)} = 0. \tag{2.215}$$

It is easy to verify that $\overline{D}_m^{(2)}$ cannot be equal to $(\overline{D}_m^{(2)})_L$ since $\overline{D}_m \neq (\overline{D}_m)_L$ in relation (2.186). The result (2.215) is exact and no approximations are involved.

On the other hand, the computation of the deviatoric part of the average strain-rate, $\overline{\boldsymbol{D}}^{(2)\prime}$, in the vacuous phase is non-trivial. In the work of Idiart and Ponte Castañeda (2007), the idea of computing $\overline{\boldsymbol{D}}^{(2)}$ lies in perturbing the local nonlinear phase stress potential, given by (2.23), with respect to a constant polarization type field $\boldsymbol{p}$, solve the perturbed problem through the homogenization procedure and then consider the derivative with respect to $\boldsymbol{p}$, while letting it go to zero. Consequently, the expression for the average strain-rate in the vacuous phase can be shown to be of the form

$$\overline{\boldsymbol{D}}^{(2)} = \overline{\boldsymbol{D}}_L^{(2)} - \frac{1-f}{f}\,\boldsymbol{g}\,\left.\frac{\partial \check{\boldsymbol{\sigma}}}{\partial \boldsymbol{p}}\right|_{\boldsymbol{p}\to\mathbf{0}}, \tag{2.216}$$

with $\boldsymbol{g}$ given by relation (2.188) and $\overline{\boldsymbol{D}}_L^{(2)}$ by (2.127), such that

$$\overline{\boldsymbol{D}}_L^{(2)} = \mathbf{A}^{(2)}\,\overline{\boldsymbol{D}}_L + \boldsymbol{a}^{(2)} = \frac{1}{f}\,(\widetilde{\mathbf{M}} - \mathbf{M})\,\overline{\boldsymbol{\sigma}} + \boldsymbol{\eta} = \frac{1}{1-f}\mathbf{Q}^{-1}\,\overline{\boldsymbol{\sigma}} + \boldsymbol{\eta}, \tag{2.217}$$

where $\mathbf{A}^{(2)}$, $\boldsymbol{a}^{(2)}$ and $\overline{\boldsymbol{D}}_L$ are given by relations (2.121), (2.122) and (2.187), respectively.

As already discussed previously, the evaluation of the reference stress tensor requires the computation of the effective stress potential of the shell problem. However, solving the shell problem

assuming a perturbed nonlinear potential law for the matrix phase is too complicated and probably can be achieved only by numerical calculations for general ellipsoidal microstructures. Hence, we are left with the option to evaluate the deviatoric part of $\overline{\boldsymbol{D}}^{(2)}$ approximately, while the hydrostatic part of $\overline{\boldsymbol{D}}^{(2)}$ is obtained by relation (2.215) exactly within the approximation intrinsic to the method. Thus, we set

$$\overline{\boldsymbol{D}}^{(2)\prime} = \overline{\boldsymbol{D}}_L^{(2)\prime}, \tag{2.218}$$

and attempt to get an estimate of the resulting error introduced by ignoring the second term in relation (2.216). First of all, it is important to mention that the reference stress tensor $\check{\boldsymbol{\sigma}}$ prescribed in relation (2.202) could depend on $\boldsymbol{p}$ only through the coefficients α_m and α_{eq}. This implies that relation (2.218) is exact in the low triaxiality limit $X_\Sigma = 0$, since, in this case, the reference stress tensor becomes equal to the deviatoric part of the applied macroscopic stress tensor $\overline{\boldsymbol{\sigma}}'$ and hence does not depend on $\boldsymbol{p}$ by definition. Under this observation, it is expected that prescription (2.218) is sufficiently accurate for low triaxial loadings.

Conversely, at high triaxiality loadings the error is expected to be maximum. However, estimating this error is possible only in special cases. In particular, in the cases of isotropic and transversely isotropic porous media that are subjected to pure and in-plane hydrostatic loading, respectively, the exact result reads $\overline{\boldsymbol{D}}^{(2)\prime} = \boldsymbol{0}$. It can be verified that in those cases use of relation (2.218) introduces an error less than 1% in the computation of the deviatoric part of $\overline{\boldsymbol{D}}^{(2)}$. Moreover, in this high triaxiality regime, it is expected (it will be verified in the results section) that the hydrostatic part of $\overline{\boldsymbol{D}}$, i.e., $\overline{D}_m^{(2)}$, is predominant and controls the effective behavior of the porous material. Therefore, evaluation of the average strain-rate in the inclusion from relation (2.218) is expected to be sufficiently *accurate* and *simple* for the purposes of this work.

In summary the average strain-rate tensor in the voids will be taken to be approximated by the expression

$$\overline{\boldsymbol{D}}^{(2)} = \frac{1}{f}\,\overline{D}_m\,\boldsymbol{I} + \overline{\boldsymbol{D}}_L^{(2)\prime} = \frac{1}{f}\,\overline{D}_m\,\boldsymbol{I} + \mathbf{K}\left(\frac{1}{1-f}\mathbf{Q}^{-1}\,\overline{\boldsymbol{\sigma}} + \boldsymbol{\eta}\right), \tag{2.219}$$

where $\mathbf{K}$ denotes the fourth-order shear projection tensor defined by (2.140).

Following a similar line of thought, and due to lack of results for the estimation of the phase average spin of nonlinear materials, the assumption will be made here that the average spin in the vacuous phase $\overline{\boldsymbol{\Omega}}^{(2)}$ in the nonlinear porous material can be approximated by the average spin in the pores of the LCC, $\overline{\boldsymbol{\Omega}}_L^{(2)}$. This approximation is written as

$$\overline{\boldsymbol{\Omega}}^{(2)} = \overline{\boldsymbol{\Omega}}_L^{(2)} = \overline{\boldsymbol{\Omega}} + \boldsymbol{\Pi}\,\mathbf{L}\,\mathbf{Q}^{-1}\,\overline{\boldsymbol{\sigma}}, \tag{2.220}$$

where $\overline{\boldsymbol{\Omega}}_L^{(2)}$ has already been defined in (2.130), while $\mathbf{Q}$ and $\boldsymbol{\Pi}$ are given by relation (2.59) and (2.74), respectively. Note that similar to the "variational" method, the limit of incompressibility (i.e., $\kappa \to \infty$) needs to be considered for the evaluation of the term $\boldsymbol{\Pi}\,\mathbf{L}$ (see Appendix I). Note further that expression (2.220) is identical to $(2.154)_4$ obtained for the average spin in the vacuous phase in the context of the "variational" method.

2.7 Evolution of microstructure

In the previous sections, we have made a thorough study for the determination of the instantaneous effective behavior of nonlinear porous media with particulate microstructure described by a set of internal variables denoted as $s_a = \{f, w_1, w_2, \mathbf{n}^{(1)}, \mathbf{n}^{(2)}, \mathbf{n}^{(3)} = \mathbf{n}^{(1)} \times \mathbf{n}^{(2)}\}$ as defined in subsection 2.2.1. It is helpful to recall that these microstructural variables correspond to the volume fraction of the voids or porosity f, the shape of the voids, denoted with the two aspect ratios w_1 and w_2, and the orientation of the principal axes of the representative ellipsoidal void, i.e., the orientation vectors $\mathbf{n}^{(i)}$ (with $i = 1, 2, 3$). The reader is referred to Fig. 2.2, in subsection 2.2.1, for a graphical representation of these variables.

However, viscoplastic porous materials undergo finite deformations, and as a consequence of the deformation process, the microstructure and thus the anisotropy of the material evolve. In order to complete the study of these materials, we need to provide evolution laws for each microstructural variable. As already discussed in prior work, Ponte Castañeda and Zaidman (1994), Kailasam and Ponte Castañeda (1998) and Aravas and Ponte Castañeda (2004), the homogenization theories have as a purpose to describe the effective behavior of the composite in *average* terms. For this reason, it makes sense to consider that the initially ellipsoidal voids will evolve — on "average" — to ellipsoidal voids with different shape and orientation. This consideration implies that the evolution of the shape and orientation of the pores is completely characterized by the average strain-rate and spin in the vacuous phase, which can be easily obtained as a byproduct of the homogenization methods described in the previous sections.

Consequently, we can derive evolution laws for the microstructural variables simply by making use of the kinematics of the problem. In this connection, following the work of Ponte Castañeda and Zaidman (1994) and Kailasam and Ponte Castañeda (1998) (see also Aravas and Ponte Castañeda (2004)), the evolution laws are given below:

Porosity. By making use of the incompressibility of the matrix phase, the evolution law for the porosity is obtained from the kinematical relations

$$\dot{f} = (1 - f)\overline{D}_{ii}, \quad i = 1, 2, 3, \tag{2.221}$$

where $\overline{\boldsymbol{D}}$ is evaluated from relation (2.153) for the "variational" method and (2.186) for the "second-order" method.

Aspect ratios. The evolution of the aspect ratios of the ellipsoidal void is defined by

$$\dot{w}_i = w_i \left(\mathbf{n}^{(3)} \cdot \overline{\boldsymbol{D}}^{(2)} \mathbf{n}^{(3)} - \mathbf{n}^{(i)} \cdot \overline{\boldsymbol{D}}^{(2)} \mathbf{n}^{(i)} \right) = w_i \left(\mathbf{n}^{(3)} \otimes \mathbf{n}^{(3)} - \mathbf{n}^{(i)} \otimes \mathbf{n}^{(i)} \right) \cdot \overline{\boldsymbol{D}}^{(2)}, \tag{2.222}$$

(no sum on $i = 1, 2$). The average strain-rate in the void $\overline{\boldsymbol{D}}^{(2)}$ is computed by relation (2.154) for the "variational" method and (2.219) for the "second-order" method.

Orientation vectors. The evolution of the orientation vectors $\mathbf{n}^{(i)}$ is determined by the spin of the Eulerian axes of the ellipsoidal voids, or microstructural spin $\boldsymbol{\omega}$, via

$$\dot{\mathbf{n}}^{(i)} = \boldsymbol{\omega}\, \mathbf{n}^{(i)}, \quad i = 1, 2, 3. \tag{2.223}$$

The microstructural spin $\boldsymbol{\omega}$ is related to the average spin in the void, $\overline{\boldsymbol{\Omega}}^{(2)}$, and the average strain-rate in the void, $\overline{\boldsymbol{D}}^{(2)}$, by the well-known kinematical relation (Hill, 1978; Ogden, 1984)

$$\omega_{ij}'' = \overline{\Omega}_{ij}^{(2)}'' + \frac{w_i^2 + w_j^2}{w_i^2 - w_j^2}\,\overline{D}_{ij}^{(2)}'', \qquad i \neq j, \tag{2.224}$$

where the double primes indicate components in a coordinate frame that instantaneously coincides with the principal directions of the ellipsoidal voids (i.e., with the unit vectors $\mathbf{n}^{(i)}$). The special case in which at least two of the aspect ratios are equal is discussed in detail later in this section. Now, it is convenient for the numerical implementation of expression (2.224) to refer all tensor components with respect to a fixed Cartesian coordinate system. Therefore, it is useful to express (2.224) in direct notation (Aravas and Ponte Castañeda, 2004)

$$\mathbf{n}^{(i)} \cdot \boldsymbol{\omega}\mathbf{n}^{(j)} = \mathbf{n}^{(i)} \cdot \overline{\boldsymbol{\Omega}}^{(2)}\mathbf{n}^{(j)} + \frac{w_i^2 + w_j^2}{w_i^2 - w_j^2}\,\mathbf{n}^{(i)} \cdot \overline{\boldsymbol{D}}^{(2)}\mathbf{n}^{(j)}, \quad i \neq j, \quad w_i \neq w_j, \tag{2.225}$$

with no sum over i, j. Next, writing $\boldsymbol{\omega} = (\mathbf{n}^{(i)} \cdot \boldsymbol{\omega}\,\mathbf{n}^{(j)})\mathbf{n}^{(i)}\,\mathbf{n}^{(j)}$ and $\overline{\boldsymbol{\Omega}}^{(2)} = (\mathbf{n}^{(i)} \cdot \overline{\boldsymbol{\Omega}}^{(2)}\,\mathbf{n}^{(j)})\mathbf{n}^{(i)}\,\mathbf{n}^{(j)}$ in direct notation and making use of the fact that $\overline{\boldsymbol{D}}^{(2)}$ is symmetric, which implies that

$$\mathbf{n}^{(i)} \cdot \overline{\boldsymbol{D}}^{(2)}\mathbf{n}^{(j)} = (\mathbf{n}^{(i)} \otimes \mathbf{n}^{(j)}) \cdot \overline{\boldsymbol{D}}^{(2)} = \frac{1}{2}(\mathbf{n}^{(i)} \otimes \mathbf{n}^{(j)} + \mathbf{n}^{(j)} \otimes \mathbf{n}^{(i)}) \cdot \overline{\boldsymbol{D}}^{(2)}, \tag{2.226}$$

we can express (2.224) in direct notation

$$\boldsymbol{\omega} = \overline{\boldsymbol{\Omega}}^{(2)} + \frac{1}{2} \sum_{\substack{i,j=1 \\ i\neq j \\ w_i \neq w_j}}^{3} \frac{w_i^2 + w_j^2}{w_i^2 - w_j^2} \left[(\mathbf{n}^{(i)} \otimes \mathbf{n}^{(j)} + \mathbf{n}^{(j)} \otimes \mathbf{n}^{(i)}) \cdot \overline{\boldsymbol{D}}^{(2)}\right] \mathbf{n}^{(i)} \otimes \mathbf{n}^{(j)}, \tag{2.227}$$

with $w_3 = 1$.

In turn, it is relevant to discuss the evaluation of the Jaumann rate of the orientation vectors $\mathbf{n}^{(i)}$, denoted by $\overset{\triangledown}{\mathbf{n}}{}^{(i)}$ $(i = 1, 2, 3)$. The Jaumann rate is an objective measure for the change of orientation of the voids and is related to the standard time derivative of relation (2.223) by

$$\overset{\triangledown}{\mathbf{n}}{}^{(i)} = \dot{\mathbf{n}}^{(i)} - \overline{\boldsymbol{\Omega}}\,\mathbf{n}^{(i)} = (\boldsymbol{\omega} - \overline{\boldsymbol{\Omega}})\,\mathbf{n}^{(i)}, \qquad i = 1, 2, 3, \tag{2.228}$$

where $\overline{\boldsymbol{\Omega}}$ is the macroscopic average spin applied externally in the problem. At this point, it is convenient to introduce the notion of the *plastic* spin (Dafalias, 1985), which is defined as the spin of the continuum relative to the microstructure, i.e.,

$$\boldsymbol{\Omega}^p = \overline{\boldsymbol{\Omega}} - \boldsymbol{\omega}. \tag{2.229}$$

Then, it follows from (2.228) and (2.229) that

$$\overset{\triangledown}{\mathbf{n}}{}^{(i)} = -\boldsymbol{\Omega}^p\,\mathbf{n}^{(i)} \qquad i = 1, 2, 3. \tag{2.230}$$

Remark 2.7.1. It should be mentioned that the expression (2.224) is ill-behaved for the case of a spherical void, i.e., when $w_1 = w_2 = w_3 = 1$, as well as for a spheroidal void, i.e., when $w_1 = w_2 \neq w_3 = 1$ or $w_1 \neq w_2 = w_3 = 1$ or $w_1 = w_3 = 1 \neq w_2$. In these cases, special care needs to be taken

for the computation of the spin of the Eulerian axes of the ellipsoid. More specifically, when two of the aspect ratios are equal, for instance $w_1 = w_2$, the material becomes locally transversely isotropic about the $\mathbf{n}^{(3)}-$direction, and thus the component Ω^p_{12} becomes indeterminate. Since the spin Ω^p_{12} is inconsequential in this case, it can be set equal to zero (Aravas, 1992; Aravas and Ponte Castañeda, 2004), which implies that $\omega_{12} = \overline{\Omega}_{12}$. This notion can be applied whenever the shape of the void is spheroidal, in any given orientation. Following a similar line of thought, when the voids are spherical ($w_1 = w_2 = w_3 = 1$), $\boldsymbol{\Omega}^p = \mathbf{0}$, which implies that $\overset{\triangledown}{\mathbf{n}}{}^{(i)} = 0$ and $\dot{\mathbf{n}}^{(i)} = \overline{\boldsymbol{\Omega}}\,\mathbf{n}^{(i)}$.

Remark 2.7.2. A second remark to be made in this section is that the evolution laws developed here are completely consistent with the general constitutive framework of Dafalias (1985) for anisotropic plastic solids subjected to finite deformations. The reason for this is linked to the fact that the homogenization methods provide, in a "natural" way, information about the average fields in the phases. In this regard, the present homogenization theories provide the link between general invariance considerations, such as the ones discussed by Dafalias and Rashid (1989) and Aravas (1992), and the microstructural variables which induce the development of anisotropy in the material.

2.8 Porous materials with ideally-plastic matrix phase

In this section, we specialize the homogenization results developed in sections 2.5 and 2.6, for the case of porous materials with ideally-plastic matrix phase. For this, we need to consider the limit as $n \to \infty$ or, equivalently, $m \to 0$ for the nonlinear exponent of the matrix phase in relations (2.150) and (2.183). The notion of the yield surface or yield domain has already been discussed in subsection (2.2.5) and will not be repeated here. In the following, subsections we provide specific expressions as derived by the "variational" and the "second-order" methods in the context of porous media with ideally-plastic matrix phase.

2.8.1 "Variational" estimates

Making use of definitions (2.37) and (2.42) for the effective stress potential $\widetilde{U}_{var}$ for a viscoplastic porous material, together with relation (2.150), which is repeated here for convenience

$$\widetilde{U}_{var}(\overline{\boldsymbol{\sigma}}) = (1-f)\,\frac{\dot{\varepsilon}_o\,\sigma_o}{n+1}\left(\frac{\hat{\sigma}_{eq}}{\sigma_o}\right)^{n+1} = (1-f)\,\frac{\dot{\varepsilon}_o\,\sigma_o}{n+1}\left[\frac{3\,\overline{\boldsymbol{\sigma}}\cdot\widehat{\mathbf{M}}\,\overline{\boldsymbol{\sigma}}}{(1-f)\,\sigma_o^2}\right]^{\frac{n+1}{2}}, \tag{2.231}$$

we can define the corresponding equation describing the effective yield surface of the "variational" method in the ideally-plastic limit in terms of the yield function $\widetilde{\Phi}_{var}$ via

$$\widetilde{\Phi}_{var}(\overline{\sigma};\, s_\alpha) = \hat{\sigma}_{eq}(\overline{\boldsymbol{\sigma}};\, s_\alpha) - \sigma_o = \sqrt{\frac{3\,\overline{\boldsymbol{\sigma}}\cdot\widehat{\mathbf{M}}\,\overline{\boldsymbol{\sigma}}}{(1-f)}} - \sigma_o = 0. \tag{2.232}$$

Here, $s_a = \{f, w_1, w_2, \mathbf{n}^{(1)}, \mathbf{n}^{(2)}, \mathbf{n}^{(3)} = \mathbf{n}^{(1)} \times \mathbf{n}^{(2)}\}$ is the set of the microstructural variables defined in subsection 2.2.1, while $\widehat{\mathbf{M}}$ is given by (2.143).

Remark 2.8.1. For later reference, we make a parenthesis to note that by making use of definition (2.195), the above-mentioned effective yield function $\widetilde{\Phi}_{var}$ can be written as

$$\widetilde{\Phi}_{var}(\overline{\sigma}_m;\, s_\alpha) = \frac{3}{2}|\overline{\sigma}_m| - \widetilde{\sigma}_w^{var}, \tag{2.233}$$

in the limit of purely hydrostatic loading, i.e., when $\overline{\sigma}_{eq} = 0$. In this expression, $\widetilde{\sigma}_w^{var}$ is the effective flow stress of the porous medium when subjected to purely hydrostatic loading and is given by (2.201), which reduces in the ideally plastic limit to

$$\widetilde{\sigma}_w^{var} = \left[\frac{4\,\boldsymbol{I}\cdot\widehat{\mathbf{M}}\,\boldsymbol{I}}{3\,(1-f)\,\sigma_o^2}\right]^{-\frac{1}{2}}. \tag{2.234}$$

In the simple case of spherical (denoted as $\widetilde{\sigma}_{w=1}^{var}$) and cylindrical (denoted as $\widetilde{\sigma}_{w=\infty}^{var}$) voids these effective flow stress are evaluated by considering the limit $n \to \infty$ in expression (2.197), which yields

$$\frac{\widetilde{\sigma}_{w=1}^{var}}{\sigma_o} = \frac{1-f}{\sqrt{f}} \quad \text{and} \quad \frac{\widetilde{\sigma}_{w\to\infty}^{var}}{\sigma_o} = \left(\frac{\sqrt{3}}{2}\right)\frac{\widetilde{\sigma}_{w=1}^{var}}{\sigma_o}. \tag{2.235}$$

In the following, use will be made of these results in the context of the "second-order" method to propose a reference stress tensor for porous media with an ideally-plastic matrix phase.

Remark 2.8.2. It is worth noting that by considering the ideally-plastic limit ($n \to \infty$) in (2.152), we can express the condition describing the gauge surface in terms of the corresponding gauge function $\widetilde{\Phi}_\infty^{var} = \widetilde{\Phi}_{var}/\sigma_o$ (see (2.42) for more details) via

$$\widetilde{\Phi}_\infty^{var}(\overline{\boldsymbol{\Sigma}}) = \Gamma_\infty^{var}(\overline{\boldsymbol{\Sigma}}) - 1 = \hat{\sigma}_{eq}(\overline{\boldsymbol{\Sigma}}) - 1 = 0, \tag{2.236}$$

with $\Gamma_\infty^{var} = \hat{\sigma}_{eq}$ being the associated with the "variational" method gauge factor, which is obtained by considering the limit $n \to \infty$ in (2.151), whereas $\overline{\boldsymbol{\Sigma}} = \overline{\boldsymbol{\sigma}}/\sigma_o$ (see relation (2.39)). In the next chapters, use of relation (2.236) will be made to extract relevant results for the effective behavior of isotropic and anisotropic porous media with an ideally-plastic matrix phase.

Next, the corresponding macroscopic strain-rate $\overline{\boldsymbol{D}}$ is given by differentiating the effective yield function in (2.232) with respect to $\overline{\boldsymbol{\sigma}}$, so that

$$\overline{\boldsymbol{D}} = \dot{\Lambda}\,\frac{\partial\widetilde{\Phi}_{var}}{\partial\overline{\boldsymbol{\sigma}}} = \dot{\Lambda}\,\frac{\partial\hat{\sigma}_{eq}}{\partial\overline{\boldsymbol{\sigma}}} = \dot{\Lambda}\sqrt{\frac{3}{1-f}}\,\frac{\widehat{\mathbf{M}}\,\overline{\boldsymbol{\sigma}}}{\sqrt{\overline{\boldsymbol{\sigma}}\cdot\widehat{\mathbf{M}}\,\overline{\boldsymbol{\sigma}}}}\,, \tag{2.237}$$

where $\dot{\Lambda}$ is a non-negative parameter known as the plastic multiplier computed by the consistency condition $\dot{\widetilde{\Phi}}_{var}$ defined in the general context of ideal-plasticity in (2.46). The consistency condition provides information about the incremental response of the porous medium and is expressed as

$$\dot{\widetilde{\Phi}}_{var} = \frac{\partial\widetilde{\Phi}_{var}}{\partial\overline{\boldsymbol{\sigma}}}\cdot\overset{\triangledown}{\overline{\boldsymbol{\sigma}}} + \frac{\partial\widetilde{\Phi}_{var}}{\partial s_\alpha}\,\overset{\triangledown}{s}_\alpha = 0, \tag{2.238}$$

where the symbol $\overset{\triangledown}{()}$ has been used to denote the Jaumann rate of a given quantity. In this connection, Kailasam and Ponte Castañeda (1998) and Aravas and Ponte Castañeda (2004) have shown that the

terms

$$\overset{\triangledown}{s}_\alpha = \{\dot f, \dot w_1, \dot w_2, \overset{\triangledown}{\mathbf{n}}{}^{(1)}, \overset{\triangledown}{\mathbf{n}}{}^{(2)}, \overset{\triangledown}{\mathbf{n}}{}^{(3)}\}, \tag{2.239}$$

are proportional to the plastic multiplier $\dot\Lambda$. This is a direct consequence of the fact that the phase average strain-rate $\overline{\boldsymbol{D}}^{(2)}$ and the relative spin $\overline{\boldsymbol{\Omega}}^{(2)} - \overline{\boldsymbol{\Omega}}$ (see relation (2.154)), are linear functions of the macroscopic strain-rate $\overline{\boldsymbol{D}}$, and thus of $\dot\Lambda$. To show that, we recall these expressions for the strain-rate $\overline{\boldsymbol{D}}^{(2)}$ and the spin $\overline{\boldsymbol{\Omega}}^{(2)}$, such that

$$\begin{aligned} \overline{\boldsymbol{D}}^{(2)} &= \mathbf{A}^{(2)}\,\overline{\boldsymbol{D}} = \dot\Lambda\,\mathbf{A}^{(2)}\,\frac{\partial\widetilde\Phi_{var}}{\partial\overline{\boldsymbol{\sigma}}}, \\ \overline{\boldsymbol{\Omega}}^{(2)} - \overline{\boldsymbol{\Omega}} &= -\mathbf{C}^{(2)}\,\overline{\boldsymbol{D}} = -\dot\Lambda\,\mathbf{C}^{(2)}\,\frac{\partial\widetilde\Phi_{var}}{\partial\overline{\boldsymbol{\sigma}}}, \end{aligned} \tag{2.240}$$

where $\mathbf{A}^{(2)}$ and $\mathbf{C}^{(2)}$ are strain-rate and spin concentration tensors, which are given by (2.87) and (2.92), and are independent of the macroscopic strain-rate $\overline{\boldsymbol{D}}$.

Next, it follows from (2.240) and the evolution equations for the porosity $\dot f$ in (2.221) and the aspect ratios $\dot w_1$ and $\dot w_2$ in (2.222), that

$$\dot f = (1-f)\,\overline{D}_{ii} = \dot\Lambda\,(1-f)\,\frac{\partial\widetilde\Phi_{var}}{\partial\overline{\sigma}_{ii}} = \dot\Lambda\,q_f(\overline{\boldsymbol{\sigma}};\,s_\alpha), \tag{2.241}$$

and

$$\begin{aligned} \dot w_i &= w_i\left(\mathbf{n}^{(3)}\otimes\mathbf{n}^{(3)} - \mathbf{n}^{(i)}\otimes\mathbf{n}^{(i)}\right)\cdot\overline{\boldsymbol{D}}^{(2)} = \\ &= \dot\Lambda\,w_i\left(\mathbf{n}^{(3)}\otimes\mathbf{n}^{(3)} - \mathbf{n}^{(i)}\otimes\mathbf{n}^{(i)}\right)\cdot\mathbf{A}^{(2)}\,\frac{\partial\widetilde\Phi_{var}}{\partial\overline{\boldsymbol{\sigma}}} = \dot\Lambda\,q_w^{(i)}(\overline{\boldsymbol{\sigma}};\,s_\alpha), \end{aligned} \tag{2.242}$$

with no sum on $i = 1, 2$. In the last two expressions, q_f and $q_w^{(i)}$ are smooth functions of their arguments that depend on the macroscopic stress $\overline{\boldsymbol{\sigma}}$ and the microstructural variables s_α. In turn, it follows from (2.227), (2.229) and (2.240) that the plastic spin $\boldsymbol{\Omega}^p$ can be expressed as (Aravas and Ponte Castañeda, 2004)

$$\begin{aligned} \boldsymbol{\Omega}^p &= (\overline{\boldsymbol{\Omega}} - \boldsymbol{\omega}) = \\ &= \mathbf{C}^{(2)}\,\overline{\boldsymbol{D}} - \frac{1}{2}\sum_{\substack{i,j=1\\ i\neq j\\ w_i\neq w_j}}^{3}\frac{w_i^2+w_j^2}{w_i^2-w_j^2}\left[(\mathbf{n}^{(i)}\otimes\mathbf{n}^{(j)} + \mathbf{n}^{(j)}\otimes\mathbf{n}^{(i)})\cdot\overline{\boldsymbol{D}}^{(2)}\right]\mathbf{n}^{(i)}\otimes\mathbf{n}^{(j)}, \end{aligned} \tag{2.243}$$

which implies

$$\boldsymbol{\Omega}^p = \dot\Lambda\left[\mathbf{C}^{(2)}\,\frac{\partial\widetilde\Phi_{var}}{\partial\overline{\boldsymbol{\sigma}}} - \frac{1}{2}\sum_{\substack{i,j=1\\ i\neq j\\ w_i\neq w_j}}^{3}\mathcal{X}_{(ij)}\,\mathbf{n}^{(i)}\otimes\mathbf{n}^{(j)}\right], \tag{2.244}$$

with

$$\mathcal{X}_{(ij)} = \frac{w_i^2+w_j^2}{w_i^2-w_j^2}\left[(\mathbf{n}^{(i)}\otimes\mathbf{n}^{(j)} + \mathbf{n}^{(j)}\otimes\mathbf{n}^{(i)})\cdot\mathbf{A}^{(2)}\,\frac{\partial\widetilde\Phi_{var}}{\partial\overline{\boldsymbol{\sigma}}}\right]. \tag{2.245}$$

Then, it follows from (2.228) that

$$\overset{\triangledown}{\mathbf{n}}{}^{(i)} = -\boldsymbol{\Omega}^p\,\mathbf{n}^{(i)} = \dot\Lambda\,\boldsymbol{q}_n^{(i)}\,(\overline{\boldsymbol{\sigma}};\,s_\alpha)\,\mathbf{n}^{(i)}, \quad i = 1,2,3, \tag{2.246}$$

where $\boldsymbol{q}_n^{(i)}$ are skew-symmetric, second-order tensors.

The above relations provide a complete description of the evolution equations in the ideally-plastic limit. It is straightforward then to express the Jaumann hardening rate H_J, defined in (2.48), in terms of the function q_f, $q_w^{(i)}$ and $\boldsymbol{q}_n^{(i)}$ via

$$H_J = -\frac{1}{\dot{\Lambda}}\frac{\partial\widetilde{\Phi}_{var}}{\partial s_\alpha}\overset{\triangledown}{s}_\alpha = -\frac{1}{\dot{\Lambda}}\left\{\dot{f}\frac{\partial\widetilde{\Phi}_{var}}{\partial f} + \sum_{i=1}^{2}\dot{w}_i\frac{\partial\widetilde{\Phi}_{var}}{\partial w_i} + \sum_{i=1}^{3}\frac{\partial\widetilde{\Phi}_{var}}{\partial \mathbf{n}^{(i)}}\cdot\overset{\triangledown}{\mathbf{n}}{}^{(i)}\right\} =$$
$$= -\left\{q_f\frac{\partial\widetilde{\Phi}_{var}}{\partial f} + \sum_{i=1}^{2}q_w^{(i)}\frac{\partial\widetilde{\Phi}_{var}}{\partial w_i} + \sum_{i=1}^{3}\frac{\partial\widetilde{\Phi}_{var}}{\partial \mathbf{n}^{(i)}}\cdot\boldsymbol{q}_n^{(i)}\,\mathbf{n}^{(i)}\right\}. \tag{2.247}$$

The Jaumann hardening rate is an objective measure of the geometrical softening or hardening of the porous material to be used in the prediction of instabilities in the next section. In addition, it is useful to introduce the corotational hardening rate, H_c, which is given by

$$H_c = -\frac{1}{\dot{\Lambda}}\frac{\partial\widetilde{\Phi}_{var}}{\partial s_\alpha}\overset{\circ}{s}_\alpha = -\frac{1}{\dot{\Lambda}}\left\{\dot{f}\frac{\partial\widetilde{\Phi}_{var}}{\partial f} + \sum_{i=1}^{2}\dot{w}_i\frac{\partial\widetilde{\Phi}_{var}}{\partial w_i}\right\} =$$
$$= -\left\{q_f\frac{\partial\widetilde{\Phi}_{var}}{\partial f} + \sum_{i=1}^{2}q_w^{(i)}\frac{\partial\widetilde{\Phi}_{var}}{\partial w_i}\right\}, \tag{2.248}$$

where use has been made of the fact that the rate of $\mathbf{n}^{(i)}$ corotational with the spin of the voids is

$$\overset{\circ}{\mathbf{n}}{}^{(i)} = \dot{\mathbf{n}}^{(i)} - \boldsymbol{\omega}\,\mathbf{n}^{(i)} = \mathbf{0}. \tag{2.249}$$

Then, it follows from the combination of relations (2.237), (2.247) and (2.248), that

$$\overline{D}_{ij} = \frac{1}{H_J}\frac{\partial\widetilde{\Phi}_{var}}{\partial\overline{\sigma}_{ij}}\frac{\partial\widetilde{\Phi}_{var}}{\partial\overline{\sigma}_{kl}}\overset{\triangledown}{\overline{\sigma}}_{kl} = \frac{1}{H_c}\frac{\partial\widetilde{\Phi}_{var}}{\partial\overline{\sigma}_{ij}}\frac{\partial\widetilde{\Phi}_{var}}{\partial\overline{\sigma}_{kl}}\overset{\circ}{\overline{\sigma}}_{kl}. \tag{2.250}$$

In this expression $\overset{\triangledown}{\overline{\boldsymbol{\sigma}}}$ and $\overset{\circ}{\overline{\boldsymbol{\sigma}}}$ are the Jaumann and corotational with the microstructure stress tensors, respectively defined by

$$\overset{\triangledown}{\overline{\boldsymbol{\sigma}}} = \dot{\overline{\boldsymbol{\sigma}}} + \overline{\boldsymbol{\sigma}}\,\overline{\boldsymbol{\Omega}} - \overline{\boldsymbol{\Omega}}\,\overline{\boldsymbol{\sigma}}, \qquad \text{and} \qquad \overset{\circ}{\overline{\boldsymbol{\sigma}}} = \dot{\overline{\boldsymbol{\sigma}}} + \overline{\boldsymbol{\sigma}}\,\boldsymbol{\omega} - \boldsymbol{\omega}\,\overline{\boldsymbol{\sigma}}. \tag{2.251}$$

Making use of the plastic spin $\boldsymbol{\Omega}^p$, defined in section 2.7, these two stress measures are related by

$$\overset{\triangledown}{\overline{\boldsymbol{\sigma}}} = \overset{\circ}{\overline{\boldsymbol{\sigma}}} + \overline{\boldsymbol{\sigma}}\,\boldsymbol{\Omega}^p - \boldsymbol{\Omega}^p\,\overline{\boldsymbol{\sigma}}. \tag{2.252}$$

An alternative description making use of stress measures

The previous relations provide the framework to obtain "variational" estimates in the context of porous media with ideally-plastic matrix phase. However, it is useful to discuss an alternative formulation of the above described equations by making use of the macroscopic stress $\overline{\boldsymbol{\sigma}}$ to compute the phase average strain-rate $\overline{\boldsymbol{D}}^{(2)}$ and spin $\overline{\boldsymbol{\Omega}}^{(2)}$. This alternative point of view will prove helpful in the study of the "second-order" method in the next subsection.

Starting by relation (2.231) for the effective stress potential $\widetilde{U}_{var}$ for a general nonlinear exponent n, we can write the macroscopic strain-rate as

$$\overline{\boldsymbol{D}} = \frac{\partial\widetilde{U}_{var}}{\partial\overline{\boldsymbol{\sigma}}} = (1-f)\dot{\varepsilon}_o\left(\frac{\hat{\sigma}_{eq}}{\sigma_o}\right)^n\frac{\partial\hat{\sigma}_{eq}}{\partial\overline{\boldsymbol{\sigma}}}, \tag{2.253}$$

where the terms $\partial\hat{\sigma}_{eq}/\partial\overline{\sigma}$ and $\dot{\varepsilon}_o\,(\hat{\sigma}_{eq}/\sigma_o)^n$ denote the direction and the magnitude of $\overline{\boldsymbol{D}}$. Making use of the secant condition (2.147), repeated here for completeness

$$\dot{\varepsilon}_o \left(\frac{\hat{\sigma}_{eq}}{\sigma_o}\right)^{n-1} = \frac{\sigma_o}{3\,\mu}, \tag{2.254}$$

it is easily deduced that (2.253) can be written as

$$\overline{\boldsymbol{D}} = \frac{(1-f)\,\sigma_o}{3\,\mu}\left(\frac{\hat{\sigma}_{eq}}{\sigma_o}\right)\frac{\partial\hat{\sigma}_{eq}}{\partial\overline{\boldsymbol{\sigma}}}. \tag{2.255}$$

In this expression, μ is the moduli of the matrix phase in the LCC. Now, it is emphasized that in the ideally-plastic limit ($n \to \infty$), μ is indeterminate (see (2.254)), which is consistent with the definition of the plastic multiplier $\dot{\Lambda}$ in (2.237). Thus, taking the limit $n \to \infty$ and comparing (2.237) with (2.255), one finds

$$\dot{\Lambda} = \frac{(1-f)\,\sigma_o}{3\,\mu}\left(\frac{\hat{\sigma}_{eq}}{\sigma_o}\right). \tag{2.256}$$

Obviously, when the yield condition (2.232) is not satisfied, i.e., $\hat{\sigma}_{eq} < \sigma_o$, $\mu \to \infty$ or equivalently $\dot{\Lambda} = 0$. On the other hand, when $\hat{\sigma}_{eq} = \sigma_o$, relation (2.256) becomes

$$\frac{1}{\mu} = \frac{3\,\dot{\Lambda}}{(1-f)\,\sigma_o}. \tag{2.257}$$

It follows from this relation that the moduli μ^{-1} of the LCC is directly proportional to the plastic multiplier $\dot{\Lambda}$ in the ideally-plastic limit. This result allows the direct use of relations (2.154), to estimate the phase average fields in the LCC as well as the hardening rate H_J, in (2.247) as a function of $\overline{\boldsymbol{\sigma}}$, such that

$$\overline{\boldsymbol{D}}^{(2)} = \frac{1}{1-f}\,\mathbf{Q}^{-1}\,\overline{\boldsymbol{\sigma}} = \frac{1}{\mu}\frac{1}{1-f}\,\widehat{\mathbf{Q}}^{-1}\,\overline{\boldsymbol{\sigma}} = \frac{3\,\dot{\Lambda}}{(1-f)^2}\,\widehat{\mathbf{Q}}^{-1}\,\frac{\overline{\boldsymbol{\sigma}}}{\sigma_o}, \tag{2.258}$$

and

$$\overline{\boldsymbol{\Omega}}^{(2)} - \overline{\boldsymbol{\Omega}} = \frac{1}{\mu}\,\boldsymbol{\Pi}\,\mathbf{L}\,\widehat{\mathbf{Q}}^{-1}\,\overline{\boldsymbol{\sigma}} = \frac{3\,\dot{\Lambda}}{1-f}\,\boldsymbol{\Pi}\,\mathbf{L}\,\widehat{\mathbf{Q}}^{-1}\,\frac{\overline{\boldsymbol{\sigma}}}{\sigma_o}, \tag{2.259}$$

where the fourth-order microstructural tensor $\widehat{\mathbf{Q}} = \mathbf{Q}/\mu$ and the product $\boldsymbol{\Pi}\,\mathbf{L}$ are independent of μ (see Appendix IV for derivation) and are given by relations (2.59) and (2.74) (see Appendix I), respectively. Thus, making use of (2.258) and (2.259), the functions $q_w^{(i)}$ and $q_n^{(i)}$ can be shown to be

$$\begin{aligned}\dot{w}_i &= w_i\left(\mathbf{n}^{(3)}\otimes\mathbf{n}^{(3)} - \mathbf{n}^{(i)}\otimes\mathbf{n}^{(i)}\right)\cdot\overline{\boldsymbol{D}}^{(2)} = \\ &= \dot{\Lambda}\,w_i\left(\mathbf{n}^{(3)}\otimes\mathbf{n}^{(3)} - \mathbf{n}^{(i)}\otimes\mathbf{n}^{(i)}\right)\cdot\frac{3}{(1-f)^2}\widehat{\mathbf{Q}}^{-1}\,\frac{\overline{\boldsymbol{\sigma}}}{\sigma_o} = \dot{\Lambda}\,q_w^{(i)}(\overline{\boldsymbol{\sigma}};\,s_\alpha),\end{aligned} \tag{2.260}$$

and

$$\boldsymbol{\Omega}^p = \dot{\Lambda}\left[\frac{6}{1-f}\,\boldsymbol{\Pi}\,\mathbf{L}\,\widehat{\mathbf{Q}}^{-1}\,\frac{\overline{\boldsymbol{\sigma}}}{\sigma_o} - \frac{1}{2}\sum_{\substack{i,j=1\\ i\neq j\\ w_i\neq w_j}}^{3}\mathcal{X}_{(ij)}\,\mathbf{n}^{(i)}\otimes\mathbf{n}^{(j)}\right], \tag{2.261}$$

with

$$\mathcal{X}_{(ij)} = \frac{w_i^2+w_j^2}{w_i^2-w_j^2}\left[\left(\mathbf{n}^{(i)}\otimes\mathbf{n}^{(j)} + \mathbf{n}^{(j)}\otimes\mathbf{n}^{(i)}\right)\cdot\frac{3}{(1-f)^2}\widehat{\mathbf{Q}}^{-1}\,\frac{\overline{\boldsymbol{\sigma}}}{\sigma_o}\right]. \tag{2.262}$$

Then, it follows from (2.228) that

$$\overset{\nabla}{\mathbf{n}}{}^{(i)} = -\boldsymbol{\Omega}^p\,\mathbf{n}^{(i)} = \dot{\Lambda}\,\boldsymbol{q}_n^{(i)}\,(\overline{\boldsymbol{\sigma}};\,s_\alpha)\,\mathbf{n}^{(i)}, \quad i=1,2,3. \tag{2.263}$$

The function q_f is the same as defined in (2.241). Then, following a similar procedure to the one described in the previous paragraphs, we arrive at the relation (2.247) for H_J, which is obviously independent of $\dot{\Lambda}$.

2.8.2 "Second-order" estimates

In the context of the "second-order" method the definition of the effective yield function is more complicated than in the "variational" method. The reason is that the final expression for the effective stress potential in (2.183) corresponding to general nonlinearities, i.e,

$$\widetilde{U}_{som}(\overline{\boldsymbol{\sigma}}) = (1-f)\left[\frac{\dot{\varepsilon}_o\,\sigma_o}{1+n}\left(\frac{\hat{\sigma}_{eq}}{\sigma_o}\right)^{n+1} - \dot{\varepsilon}_o\left(\frac{\check{\sigma}_{eq}}{\sigma_o}\right)^{n}\left(\hat{\sigma}_{||} - \frac{\overline{\sigma}_{eq}}{(1-f)}\right)\right], \tag{2.264}$$

cannot be written in a simple form. Thus, we need first to identify the terms that remain in the ideally-plastic limit. It can be verified from definitions (2.175) and (2.180) that

$$\hat{\sigma}_{eq} > \hat{\sigma}_{||} \geq \check{\sigma}_{eq} \geq 0. \tag{2.265}$$

Consequently, as $n \to \infty$ the second term of relation (2.264), $(\check{\sigma}_{eq}/\sigma_o)^n$, goes faster to zero than the first term $(\hat{\sigma}_{eq}/\sigma_o)^{n+1}$, provided that $\hat{\sigma}_{eq} < \sigma_o$. Then, it follows from definitions (2.37) and (2.42) that the effective yield surface may be defined in terms of the yield function $\widetilde{\Phi}_{som}$ by

$$\widetilde{\Phi}_{som}(\overline{\boldsymbol{\sigma}};\,\check{\boldsymbol{\sigma}},\,k,\,s_\alpha) = \hat{\sigma}_{eq}(\overline{\boldsymbol{\sigma}};\,\check{\boldsymbol{\sigma}},\,k,\,s_\alpha) - \sigma_o = 0, \tag{2.266}$$

where $s_a = \{f, w_1, w_2, \mathbf{n}^{(1)}, \mathbf{n}^{(2)}, \mathbf{n}^{(3)} = \mathbf{n}^{(1)} \times \mathbf{n}^{(2)}\}$ is the set of the microstructural variables defined in subsection 2.2.1, k is the anisotropy ratio in the LCC, and $\check{\boldsymbol{\sigma}}$ is the reference stress tensor given by (2.202)-(2.203). The evaluation of $\check{\boldsymbol{\sigma}}$ in the ideally-plastic limit will be detailed later in this section. On the other hand, k is determined by the solution of (2.179), which reduces to

$$(1-k)\frac{\hat{\sigma}_{||}(k)}{\check{\sigma}_{eq}} - 1 = 0, \tag{2.267}$$

in the ideally-plastic limit. Note that $\hat{\sigma}_{||}$ is a function of k given by (2.180). In addition, due to the fact that $\hat{\sigma}_{||}$ and $\check{\sigma}_{eq}$ are homogeneous functions of degree one in $\overline{\boldsymbol{\sigma}}$, the anisotropy ratio k depends only on the direction of $\overline{\boldsymbol{\sigma}}$ and not on its magnitude.

Remark 2.8.3. At this point, it is worth noting that by considering the ideally-plastic limit ($n \to \infty$) in (2.185), we can express the condition describing the gauge surface in terms of the corresponding gauge function $\widetilde{\Phi}_\infty^{som} = \widetilde{\Phi}_{som}/\sigma_o$ (see (2.42) for more details) via

$$\widetilde{\Phi}_\infty^{som}(\overline{\boldsymbol{\Sigma}}) = \Gamma_\infty^{som}(\overline{\boldsymbol{\Sigma}}) - 1 = \hat{\sigma}_{eq}(\overline{\boldsymbol{\Sigma}}) - 1 = 0, \tag{2.268}$$

with $\Gamma_\infty^{som} = \hat{\sigma}_{eq}$ being the associated with the "second-order" method gauge factor, which is obtained by considering the limit $n \to \infty$ in (2.184), whereas $\overline{\boldsymbol{\Sigma}} = \overline{\boldsymbol{\sigma}}/\sigma_o$ (see relation (2.39)). In the next

chapters, use of relation (2.268) will be made to extract relevant results for the effective behavior of isotropic and anisotropic porous media with an ideally-plastic matrix phase.

Then, the corresponding macroscopic strain-rate is obtained by differentiating the effective yield function with respect to $\overline{\boldsymbol{\sigma}}$, so that

$$\overline{\boldsymbol{D}} = \dot{\Lambda}\,\frac{\partial\widetilde{\Phi}_{som}}{\partial\overline{\boldsymbol{\sigma}}} = \dot{\Lambda}\,\frac{\partial\hat{\sigma}_{eq}}{\partial\overline{\boldsymbol{\sigma}}}, \tag{2.269}$$

where $\dot{\Lambda}$ is the plastic multiplier to be determined from the consistency condition $\dot{\widetilde{\Phi}}_{som} = 0$. The consistency condition is defined similar to the "variational" method, such that

$$\dot{\widetilde{\Phi}}_{som} = \frac{\partial\widetilde{\Phi}_{som}}{\partial\overline{\boldsymbol{\sigma}}} \cdot \overset{\triangledown}{\overline{\boldsymbol{\sigma}}} + \frac{\partial\widetilde{\Phi}_{som}}{\partial s_\alpha}\,\overset{\triangledown}{s}_\alpha = 0, \tag{2.270}$$

where the symbol $\overset{\triangledown}{()}$ has been used to denote the Jaumann rate of a given quantity. The term $\overset{\triangledown}{s}_\alpha$ can be shown to be proportional to the plastic multiplier $\dot{\Lambda}$, although it is not as simple as in the "variational" method. The difficulty arises by the fact that the average fields in the nonlinear composite are not identical to those in the LCC, as already stated in relation (2.186), where further corrections are present due to the fact that the "second-order" method is not stationary with respect to the reference stress tensor $\check{\boldsymbol{\sigma}}$.

In order to show that $\overset{\triangledown}{s}_\alpha$ is proportional to the plastic multiplier $\dot{\Lambda}$, we adopt the formulation developed at the end of the previous subsection, where we make use of the fact that the moduli μ of the matrix phase in the LCC is proportional to $\dot{\Lambda}$. To show this, we consider first the derivative in expression (2.264) with respect to $\overline{\boldsymbol{\sigma}}$, such that

$$\overline{\boldsymbol{D}} = (1-f)\,\dot{\varepsilon}_o \left(\frac{\hat{\sigma}_{eq}}{\sigma_o}\right)^n \frac{\partial\hat{\sigma}_{eq}}{\partial\overline{\boldsymbol{\sigma}}} - (1-f)\,\dot{\varepsilon}_o\,\frac{\partial}{\partial\overline{\boldsymbol{\sigma}}}\left[\left(\frac{\check{\sigma}_{eq}}{\sigma_o}\right)^n \left(\hat{\sigma}_{||} - \frac{\overline{\sigma}_{eq}}{(1-f)}\right)\right]. \tag{2.271}$$

Making use of the secant condition $(2.178)_2$, repeated here for convenience

$$\dot{\varepsilon}_o \left(\frac{\hat{\sigma}_{eq}}{\sigma_o}\right)^{n-1} = \frac{\sigma_o}{3\,\mu}, \tag{2.272}$$

and by considering the ideally-plastic limit $n \to \infty$ in the above expression, the macroscopic strain-rate reads

$$\overline{\boldsymbol{D}} = \frac{(1-f)\,\sigma_o}{3\,\mu}\left(\frac{\hat{\sigma}_{eq}}{\sigma_o}\right)\frac{\partial\hat{\sigma}_{eq}}{\partial\overline{\boldsymbol{\sigma}}}. \tag{2.273}$$

This last relation is similar to (2.255) in the context of the "variational" method. Thus, taking the limit $n \to \infty$ and comparing (2.269) with (2.273), one finds

$$\dot{\Lambda} = \frac{(1-f)\,\sigma_o}{3\,\mu}\left(\frac{\hat{\sigma}_{eq}}{\sigma_o}\right). \tag{2.274}$$

Obviously, when the yield condition (2.266) is not satisfied, i.e., $\hat{\sigma}_{eq} < \sigma_o$, $\mu \to \infty$ (from (2.254)) or equivalently $\dot{\Lambda} = 0$. On the other hand, when $\hat{\sigma}_{eq} = \sigma_o$, relation (2.274) becomes

$$\frac{1}{\mu} = \frac{3\,\dot{\Lambda}}{(1-f)\,\sigma_o}. \tag{2.275}$$

It follows from this relation that the moduli μ of the LCC is directly proportional to the plastic multiplier $\dot{\Lambda}$ in the ideally-plastic limit. It is interesting to note that this last expression for μ is identical to the one obtained in the context of the "variational" method, i.e., relation (2.257).

In the sequel, we proceed to the evaluation of the Jaumann hardening rate H_J. In order to derive an expression for H_J, it is essential to write the evolution laws for the microstructural variables in such a way that they are proportional to the plastic multiplier $\dot{\Lambda}$, or equivalently to $1/\mu$. In this regard, we first show that in the incompressibility limit $\kappa \to \infty$ the fourth-order tensors $\mathbf{M}$ and $\mathbf{L}$ are proportional to $1/\mu$ and μ and consequently to $\dot{\Lambda}$ and $1/\dot{\Lambda}$, respectively, by making use of definitions (2.167), such that

$$\mathbf{M} = \frac{1}{2\,\lambda}\,\mathbf{E} + \frac{1}{2\,\mu}\,\mathbf{F} = \frac{1}{\mu}\left(\frac{1}{2\,k}\,\mathbf{E} + \frac{1}{2}\,\mathbf{F}\right) = \frac{1}{\mu}\,\boldsymbol{\mathcal{M}}(k) \tag{2.276}$$

and

$$\mathbf{L} = 2\,\lambda\,\mathbf{E} + 2\,\mu\,\mathbf{F} = \mu\,(2\,k\,\mathbf{E} + 2\,\mathbf{F}) = \mu\,\boldsymbol{\mathcal{L}}(k). \tag{2.277}$$

In appendix IV, we show that the microstructural tensors $\mathbf{Q}$ and $\boldsymbol{\Pi}$ can also be written as

$$\mathbf{Q} = \mu\,\widehat{\mathbf{Q}}(k), \qquad \text{and} \qquad \boldsymbol{\Pi} = \frac{1}{\mu}\,\widehat{\boldsymbol{\Pi}}(k). \tag{2.278}$$

such that $\boldsymbol{\Pi}\,\mathbf{L}$ is independent of μ.

In connection with these last relations, the average strain-rate and relative spin tensors in the vacuous phase, i.e., $\overline{\boldsymbol{D}}^{(2)}$ and $\overline{\boldsymbol{\Omega}}^{(2)} - \overline{\boldsymbol{\Omega}}$, given by relations (2.219) and (2.220), respectively, can be shown to be proportional to the plastic multiplier $\dot{\Lambda}$. For this, let us recall the expression for $\overline{\boldsymbol{D}}^{(2)}$ (see relation (2.219)) in the context of ideal-plasticity, such that

$$\begin{aligned}\overline{\boldsymbol{D}}^{(2)} &= \frac{1}{f}\,\overline{D}_m\,\boldsymbol{I} + \mathbf{K}\left(\frac{1}{1-f}\mathbf{Q}^{-1}\,\overline{\boldsymbol{\sigma}} - \mathbf{M}\,\check{\boldsymbol{\sigma}}\right) = \\ &= \dot{\Lambda}\left\{\frac{1}{3\,f}\,\frac{\partial\widetilde{\Phi}_{som}}{\partial\overline{\sigma}_{ii}} + \frac{3}{1-f}\mathbf{K}\left(\frac{3}{1-f}\,\widehat{\mathbf{Q}}(k)^{-1}\,\frac{\overline{\boldsymbol{\sigma}}}{\sigma_o} - \boldsymbol{\mathcal{M}}(k)\,\frac{\check{\boldsymbol{\sigma}}}{\sigma_o}\right)\right\}.\end{aligned} \tag{2.279}$$

In this last expression, use was made of the fact that in the ideally-plastic limit $\boldsymbol{\eta} = -\mathbf{M}\,\check{\boldsymbol{\sigma}}$ (see relation (2.165)), whereas $\mathbf{K}$ denotes the fourth-order shear projection tensor defined by (2.140). In turn, the relative average spin tensor in the vacuous phase is expressed as

$$\overline{\boldsymbol{\Omega}}^{(2)} - \overline{\boldsymbol{\Omega}} = \boldsymbol{\Pi}\,\mathbf{L}\,\mathbf{Q}^{-1}\,\overline{\boldsymbol{\sigma}} = \dot{\Lambda}\,\frac{3}{1-f}\boldsymbol{\Pi}\,\mathbf{L}\,\widehat{\mathbf{Q}}(k)^{-1}\,\frac{\overline{\boldsymbol{\sigma}}}{\sigma_o}, \tag{2.280}$$

whereas the incompressibility limit $\kappa \to \infty$ needs to be considered in the term $\boldsymbol{\Pi}\,\mathbf{L}$. These relations allow us to write the evolution laws in terms of $\dot{\Lambda}$, such that

$$\dot{f} = (1-f)\,\overline{D}_{ii} = \dot{\Lambda}\,(1-f)\frac{\partial\widetilde{\Phi}_{som}}{\partial\overline{\sigma}_{ii}} = \dot{\Lambda}\,y_f(\overline{\boldsymbol{\sigma}};\check{\boldsymbol{\sigma}},\,k,\,s_\alpha), \tag{2.281}$$

and

$$\begin{aligned}\dot{w}_i &= w_i\left(\mathbf{n}^{(3)}\otimes\mathbf{n}^{(3)} - \mathbf{n}^{(i)}\otimes\mathbf{n}^{(i)}\right)\cdot\overline{\boldsymbol{D}}^{(2)} = \\ &= \dot{\Lambda}\,w_i\left(\mathbf{n}^{(3)}\otimes\mathbf{n}^{(3)} - \mathbf{n}^{(i)}\otimes\mathbf{n}^{(i)}\right)\cdot\frac{3}{1-f}\mathbf{K}\left(\frac{3}{1-f}\,\widehat{\mathbf{Q}}(k)^{-1}\,\frac{\overline{\boldsymbol{\sigma}}}{\sigma_o} - \boldsymbol{\mathcal{M}}(k)\,\frac{\check{\boldsymbol{\sigma}}}{\sigma_o}\right) = \\ &= \dot{\Lambda}\,y_w^{(i)}(\overline{\boldsymbol{\sigma}};\check{\boldsymbol{\sigma}},\,k,\,s_\alpha),\end{aligned} \tag{2.282}$$

with no sum on $i = 1, 2$. In these expressions, y_f and $y_w^{(i)}$ are smooth functions of their arguments. In turn, it follows from (2.227), (2.229) and (2.279) that the plastic spin $\boldsymbol{\Omega}^p$ can be expressed as

$$\boldsymbol{\Omega}^p = \overline{\boldsymbol{\Omega}} - \boldsymbol{\omega} = -\dot{\Lambda}\, \boldsymbol{y}_n^{(i)}\, (\overline{\boldsymbol{\sigma}}; \check{\boldsymbol{\sigma}},\, k,\, s_\alpha). \tag{2.283}$$

Then, from (2.228), one finds that

$$\overset{\triangledown}{\mathbf{n}}{}^{(i)} = \dot{\Lambda}\, \boldsymbol{y}_n^{(i)}\, (\overline{\boldsymbol{\sigma}}; \check{\boldsymbol{\sigma}},\, k,\, s_\alpha)\, \mathbf{n}^{(i)}, \tag{2.284}$$

where $\boldsymbol{y}_n^{(i)}$ are a skew-symmetric, second-order tensors given by

$$\boldsymbol{y}_n^{(i)}\, (\overline{\boldsymbol{\sigma}}; \check{\boldsymbol{\sigma}},\, k,\, s_\alpha) = \frac{3}{1-f} \boldsymbol{\Pi}\, \mathbf{L}\, \widehat{\mathbf{Q}}(k)^{-1}\, \frac{\overline{\boldsymbol{\sigma}}}{\sigma_o} + \frac{1}{2} \sum_{\substack{i,j=1 \\ i \neq j \\ w_i \neq w_j}}^{3} \mathcal{X}_{(ij)}\, \mathbf{n}^{(i)} \otimes \mathbf{n}^{(j)}, \tag{2.285}$$

with

$$\mathcal{X}_{(ij)} = \frac{w_i^2 + w_j^2}{w_i^2 - w_j^2} \left[(\mathbf{n}^{(i)} \otimes \mathbf{n}^{(j)} + \mathbf{n}^{(j)} \otimes \mathbf{n}^{(i)}) \cdot \frac{3}{1-f} \mathbf{K} \left(\frac{3}{1-f}\, \widehat{\mathbf{Q}}(k)^{-1}\, \frac{\overline{\boldsymbol{\sigma}}}{\sigma_o} - \boldsymbol{\mathcal{M}}(k)\, \frac{\check{\boldsymbol{\sigma}}}{\sigma_o} \right) \right]. \tag{2.286}$$

In summary, the functions y_f, $y_w^{(i)}$ and $\boldsymbol{y}_n^{(i)}$ are analogous to the functions q_f, $q_w^{(i)}$ and $\boldsymbol{q}_n^{(i)}$ described in the context of the "variational" method, with the difference that they also depend on the reference stress tensor $\check{\boldsymbol{\sigma}}$ and the anisotropy ratio k.

Then, it follows from (2.48), that the Jaumann hardening rate is given by

$$\begin{aligned} H_J = -\frac{1}{\dot{\Lambda}} \frac{\partial \widetilde{\Phi}}{\partial s_\alpha} \overset{\triangledown}{s}_\alpha = -\frac{1}{\dot{\Lambda}} \left\{ \dot{f} \frac{\partial \widetilde{\Phi}}{\partial f} + \sum_{i=1}^{2} \dot{w}_i \frac{\partial \widetilde{\Phi}}{\partial w_i} + \sum_{i=1}^{3} \frac{\partial \widetilde{\Phi}}{\partial \mathbf{n}^{(i)}} \cdot \overset{\triangledown}{\mathbf{n}}{}^{(i)} \right\} = \\ = -\left\{ y_f \frac{\partial \widetilde{\Phi}}{\partial f} + \sum_{i=1}^{2} y_w^{(i)} \frac{\partial \widetilde{\Phi}}{\partial w_i} + \sum_{i=1}^{3} \frac{\partial \widetilde{\Phi}}{\partial \mathbf{n}^{(i)}} \cdot \boldsymbol{y}_n^{(i)}\, \mathbf{n}^{(i)} \right\}. \end{aligned} \tag{2.287}$$

The corotational hardening rate H_c is given by

$$H_c = -\frac{1}{\dot{\Lambda}} \frac{\partial \widetilde{\Phi}}{\partial s_\alpha} \overset{\circ}{s}_\alpha = -\frac{1}{\dot{\Lambda}} \left\{ \dot{f} \frac{\partial \widetilde{\Phi}}{\partial f} + \sum_{i=1}^{2} \dot{w}_i \frac{\partial \widetilde{\Phi}}{\partial w_i} \right\} = -\left\{ y_f \frac{\partial \widetilde{\Phi}}{\partial f} + \sum_{i=1}^{2} y_w^{(i)} \frac{\partial \widetilde{\Phi}}{\partial w_i} \right\}, \tag{2.288}$$

where use has been made of relation (2.249) for the corotational rate of $\mathbf{n}^{(i)}$. Then, it follows from the combination of relations (2.269), (2.287) and (2.288), that

$$\overline{D}_{ij} = \frac{1}{H_J} \frac{\partial \widetilde{\Phi}_{som}}{\partial \overline{\sigma}_{ij}} \frac{\partial \widetilde{\Phi}_{som}}{\partial \overline{\sigma}_{kl}} \overset{\triangledown}{\overline{\sigma}}_{kl} = \frac{1}{\overset{\circ}{H}} \frac{\partial \widetilde{\Phi}_{som}}{\partial \overline{\sigma}_{ij}} \frac{\partial \widetilde{\Phi}_{som}}{\partial \overline{\sigma}_{kl}} \overset{\circ}{\overline{\sigma}}_{kl}. \tag{2.289}$$

In this expression $\overset{\triangledown}{\overline{\boldsymbol{\sigma}}}$ and $\overset{\circ}{\overline{\boldsymbol{\sigma}}}$ are the Jaumann and corotational with the microstructure stress tensors, respectively defined by relation (2.251).

Reference stress tensor. In order to conclude the present subsection, it is important to remark that for the computation of the effective yield function $\widetilde{\Phi}_{som}$ and the macroscopic strain-rate $\overline{\boldsymbol{D}}$, we need to compute the reference stress tensor $\check{\boldsymbol{\sigma}}$, as defined by (2.202). This definition for the reference stress tensor, detailed in subsection 2.6.2, is also valid in the case of ideal-plasticity. However, for

clarity, we will spell out the simplifications that can be made in this special case. Thus, making use of relation (2.195), the yield condition is expressed in terms of the effective yield function $\widetilde{\Phi}_{som}$ via

$$\widetilde{\Phi}_{som}(\overline{\sigma}_m;\, \check{\boldsymbol{\sigma}},\, f,\, w_1,\, w_2) = \frac{3}{2}\,|\overline{\sigma}_m| - \widetilde{\sigma}_w^{som} = \hat{\sigma}_{eq} - \sigma_o = 0, \tag{2.290}$$

in the case of purely hydrostatic loading, i.e., when $\overline{\sigma}_{eq} = 0$. In this expression, $\widetilde{\sigma}_w^{som}$ is the effective flow stress of the porous medium when subjected to purely hydrostatic loading, and depends on the reference stress tensor $\check{\boldsymbol{\sigma}}$. In turn, the superscript H has been used to denote quantities in the hydrostatic limit.

For the computation of $\check{\boldsymbol{\sigma}}$, we need to compute the two coefficients α_m and α_{eq}, defined in the context of relations (2.202) and (2.203), which become

$$\check{\boldsymbol{\sigma}} = \xi\left(X_\Sigma, \overline{\boldsymbol{S}}, s_a\right)\overline{\boldsymbol{\sigma}}' \tag{2.291}$$

where $\overline{\boldsymbol{S}} = \overline{\boldsymbol{\sigma}}'/\overline{\sigma}_{eq}$ is given by (2.166), s_a denotes the set of the microstructural variables defined in (2.16), n is the nonlinear exponent of the matrix phase, and

$$\xi\left(X_\Sigma, \overline{\boldsymbol{S}}\right) = \frac{1 - t\,f}{1 - f} + \alpha_m(\overline{\boldsymbol{S}})\,|X_\Sigma|\,\exp\left[-\frac{\alpha_{eq}(\overline{\boldsymbol{S}})}{|X_\Sigma|}\right], \tag{2.292}$$

is a suitably chosen interpolation function. The coefficient t is prescribed in an ad-hoc manner to ensure the convexity of the effective stress potential and is detailed in Appendix III.

The evaluation of these two scalars has been provided schematically in (2.204) and (2.206). More specifically, in order to compute α_m, first, we need to provide the analytical result of a spherical and a cylindrical shell with an ideally-plastic matrix phase subjected to purely hydrostatic loading. In this regard, the corresponding effective flow stress in this case is evaluated by considering the limit $n \to \infty$ in expression (2.196), such that

$$\frac{\widetilde{\sigma}_{w=1}}{\sigma_o} = \ln\left(\frac{1}{f}\right) \quad \text{and} \quad \frac{\widetilde{\sigma}_{w\to\infty}}{\sigma_o} = \left(\frac{\sqrt{3}}{2}\right)\frac{\widetilde{\sigma}_{w=1}}{\sigma_o}. \tag{2.293}$$

Based on the approximation introduced in relation (2.198), the effective flow stress for any combination of aspect ratios w_1 and w_2 is given by

$$\widetilde{\sigma}_w = \frac{\widetilde{\sigma}_{w=1}}{\widetilde{\sigma}_{w=1}^{var}}\,\widetilde{\sigma}_w^{var}, \tag{2.294}$$

where $\widetilde{\sigma}_w^{var}$ is the corresponding effective flow stress delivered by the "variational" procedure when a porous material with ellipsoidal voids of arbitrary aspect ratios w_1 and w_2 is subjected to purely hydrostatic loading given by (2.234) for porous media with ideally-plastic matrix phase. This result in combination with relations (2.202) and (2.204) allows the computation of the coefficient α_m from the equation

$$\widetilde{\sigma}_w^{som} = \widetilde{\sigma}_w \qquad \text{as} \qquad |X_\Sigma| \to \infty. \tag{2.295}$$

The above equation may also be expressed in terms of the yield function $\widetilde{\Phi}_{som}$ via

$$\widetilde{\Phi}_{som}(\overline{\sigma}_m;\, \check{\boldsymbol{\sigma}},\, f,\, w_1,\, w_2) = 0, \qquad \text{with} \qquad |\overline{\sigma}_m| = \frac{2}{3}\,\widetilde{\sigma}_w. \tag{2.296}$$

The previous two relations are equivalent and provide an equation for the evaluation of the factor α_m.

In turn, the coefficient α_{eq} can be computed by relation (2.207), provided that the limit $n \to \infty$ is taken, which yields

$$\alpha_{eq} = \alpha_m^{-1} \left[1 + \frac{2\, k^H \, (\overline{d}_{||} - \overline{d}_{\,var}) - \breve{\sigma}_{eq}(\overline{\boldsymbol{\sigma}})}{(1-f)\, \hat{\sigma}_{||}(\overline{\boldsymbol{\sigma}})} \right]. \tag{2.297}$$

All the quantities involved in (2.297) are evaluated in the hydrostatic limit $X_\Sigma \to \pm\infty$, i.e., for $\overline{\boldsymbol{\sigma}} = \mathrm{sgn}(X_\Sigma)\,(2\,\widetilde{\sigma}_w/3)\,\boldsymbol{I}$. In particular, $\overline{d}_{||} = \widetilde{\sigma}_w\, \overline{\boldsymbol{S}} \cdot \widehat{\mathbf{M}}(k^H)\, \boldsymbol{I}$, where $\widehat{\mathbf{M}}(k^H)$ is independent of μ and is given by

$$\widehat{\mathbf{M}}(k^H) = \boldsymbol{\mathcal{M}}(k^H) + \frac{f}{1-f}\, \widehat{\mathbf{Q}}(k^H)^{-1}, \tag{2.298}$$

in the context of the "second-order" method. Similarly, $\overline{d}_{\,var} = \widetilde{\sigma}_w^{var}\, \overline{\boldsymbol{S}} \cdot \widehat{\mathbf{M}}\, \boldsymbol{I}$, with $\widehat{\mathbf{M}}$ given by (2.143) or equivalently by (2.298) with $k^H = 1$. Furthermore, for the computation of the anisotropy ratio k^H in (2.297), it is necessary to solve the nonlinear equation (2.267), in the hydrostatic limit.

In the context of these results for the special case of porous materials with ideally-plastic matrix phase, expressions (2.206) (or (2.297)) have been assumed to continue to hold for the determination of α_{eq}, which implies that the resulting effective yield surface $\widetilde{\Phi}_{som}$ remains smooth for the entire range of the stress triaxialities. Further support for this last assumption arises from the fact that — to the best knowledge of the authors — there is no definitive numerical or experimental evidence implying the existence of a vertex in the hydrostatic limit for general isotropic or ellipsoidal microstructures (but see also Bilger et al., 2005), in contrast with transversely isotropic microstructures, where the existence of a corner may be observed in yield surfaces obtained by limit analysis procedures (Pastor and Ponte Castañeda, 2002). Note that, for the case of a vertex-like yield surface, the strain-rate $\overline{\boldsymbol{D}}$ would not be uniquely determined at the hydrostatic point.

2.8.3 Numerical implementation

In this subsection, we describe the numerical implementation of the equations developed in the context of porous media with ideally-plastic matrix phase, which are similar for the "variational" and the "second-order" method. For the "variational" method a complete numerical description of the equations has been provided by Kailasam (1998) and Aravas and Ponte Castañeda (2004) and for completeness will be repeated briefly here. On the other hand, the numerical implementation of the "second-order" equations for porous media with ideally-plastic matrix phase is presented in more detail.

First, it is essential to define the boundary conditions in the problem. For convenience, we will consider here that velocity boundary conditions are given such that

$$\mathbf{v} = \overline{\boldsymbol{L}}\, \mathbf{x}, \quad \forall\, \mathbf{x} \in \partial\Omega, \tag{2.299}$$

where $\overline{\boldsymbol{L}}$ is the macroscopic velocity gradient. The symmetric and skew-symmetric part of $\overline{\boldsymbol{L}}$ denote the macroscopic strain-rate $\overline{\boldsymbol{D}} = 1/2 \left[\overline{\boldsymbol{L}} + \overline{\boldsymbol{L}}^T \right]$ and $\overline{\boldsymbol{\Omega}} = 1/2 \left[\overline{\boldsymbol{L}} - \overline{\boldsymbol{L}}^T \right]$. Note that in the ideally-plastic limit the problem is rate-independent and thus the magnitude of $\mathbf{v}$ (or $\overline{\boldsymbol{L}}$) does not affect the

final result. Thus, we can define the total displacement $\mathbf{u}$ in terms of the velocity $\mathbf{v}$ via

$$\mathbf{u} = \mathbf{v}\, t, \qquad 0 < t < t_f, \tag{2.300}$$

where $\mathbf{v}$ is constant in time t and t_f is the total time.

In the following, the problem is solved incrementally using implicit and explicit (backward and forward Euler) schemes. First, we present the system of equations for the "variational" method, and then for the system for the "second-order" method. In the sequel, we update the values for the microstructural variables, which is the same for both methods considered here.

"Variational" method

At the beginning of the increment $t = t_j$, the known quantities are

$$\overline{\boldsymbol{D}}, \quad s_\alpha|_j\,. \tag{2.301}$$

At the end of the increment $t = t_{j+1}$, the following quantities need to be computed

$$\overline{\boldsymbol{\sigma}}_{j+1}, \quad \dot{\Lambda}_{j+1}. \tag{2.302}$$

In the general case, the total number of unknowns are 7. More specifically, the unknowns are computed by the following equations:

$$\widetilde{\Phi}_{var}(\overline{\boldsymbol{\sigma}}_{j+1};\, s_\alpha|_j) = 0, \qquad (\#1) \tag{2.303}$$

and

$$\overline{\boldsymbol{D}} = \dot{\Lambda}\, \frac{\partial \widetilde{\Phi}_{var}}{\partial \overline{\boldsymbol{\sigma}}}\bigg|_{j+1} \qquad (\#6). \tag{2.304}$$

The above set of equations is solved by using a standard Newton-Raphson technique, while the symbol # has been used to denote the number of equations.

"Second-order" method

At the beginning of the increment $t = t_j$, the known quantities are

$$\overline{\boldsymbol{D}}, \quad s_\alpha|_j\,. \tag{2.305}$$

At the end of the increment $t = t_{j+1}$, the following quantities need to be computed

$$\overline{\boldsymbol{\sigma}}_{j+1}, \quad \dot{\Lambda}_{j+1}, \quad k_{j+1}, \quad \alpha_m|_{j+1}\,, \quad k^H_{j+1}, \tag{2.306}$$

where k is the anisotropy ratio of the matrix phase in the LCC and α_m is a factor involved in the computation of the reference stress tensor $\check{\boldsymbol{\sigma}}$ given by relation (2.204). It is recalled here that for the computation of α_m, the hydrostatic limit ($|X_\Sigma| \to \infty$) needs to be considered also in the equation (2.267) for the anisotropy ratio denoted as k^H in this limiting case. Note that the number of unknowns in the more general case is 10.

More specifically, the unknowns are computed by the following equations:

$$\widetilde{\Phi}_{som}(\overline{\boldsymbol{\sigma}}_{j+1}; k_{j+1},\ \alpha_m|_{j+1}\,,\ k^H_{j+1},\ s_\alpha|_j) = 0, \qquad (\#1) \qquad (2.307)$$

$$\overline{\boldsymbol{D}} = \dot{\Lambda}\,\frac{\partial\widetilde{\Phi}_{som}}{\partial\overline{\boldsymbol{\sigma}}}\bigg|_{j+1}, \qquad (\#6) \qquad (2.308)$$

$$(1-k_{j+1})\ \hat{\sigma}_{||}\big|_{j+1} - \check{\sigma}_{eq}|_{j+1} = 0, \qquad (\#1) \qquad (2.309)$$

$$\widetilde{\sigma}^{som}_w(\alpha_m|_{j+1}\,, k^H) = \widetilde{\sigma}_w, \qquad (\#1) \qquad (2.310)$$

$$(1-k^H_{j+1})\ \hat{\sigma}^H_{||}\Big|_{j+1} - \check{\sigma}^H_{eq}\big|_{j+1} = 0, \qquad (\#1) \qquad (2.311)$$

where the superscript H has been used to denote that the relevant quantities need to be computed in the hydrostatic limit $|X_\Sigma| \to \infty$, whereas $\widetilde{\sigma}_w$ is given by (2.196). For clarity, it is worth mentioning that $\check{\boldsymbol{\sigma}} = \check{\boldsymbol{\sigma}}(\overline{\boldsymbol{\sigma}}; \alpha_m,\ s_\alpha)$ and $\hat{\sigma}_{eq}(\boldsymbol{\sigma}; \check{\boldsymbol{\sigma}},\ s_\alpha)$. Thus, all the above equations are coupled in the general case and need to be solved simultaneously.

Update of the microstructural variables

Once, the macroscopic stress $\overline{\boldsymbol{\sigma}}$ and the plastic multiplier $\dot{\Lambda}$ are known, we can update the microstructural variables $s_\alpha|_{j+1}$. Note that this step is the same for the "variational" and the "second-order" method. Then, we use an explicit scheme to update the microstructural variables by noting that the time increment is $\Delta t = t_{j+1} - t_j$, such that

$$f_{j+1} = f_j + (1-f_j)\,\overline{D}_{ii}\,\Delta t, \qquad (2.312)$$

$$w_1|_{j+1} = w_1|_j + \left(\mathbf{n}^{(3)}_j \cdot \overline{\boldsymbol{D}}^{(2)}\,\mathbf{n}^{(3)}_j - \mathbf{n}^{(1)}_j \cdot \overline{\boldsymbol{D}}^{(2)}\,\mathbf{n}^{(1)}_j\right)\Delta t \qquad (2.313)$$

$$w_2|_{j+1} = w_2|_j + \left(\mathbf{n}^{(3)}_j \cdot \overline{\boldsymbol{D}}^{(2)}\,\mathbf{n}^{(3)}_j - \mathbf{n}^{(2)}_j \cdot \overline{\boldsymbol{D}}^{(2)}\,\mathbf{n}^{(2)}_j\right)\Delta t \qquad (2.314)$$

$$\mathbf{n}^{(i)}_{j+1} = \mathbf{n}^{(i)}_j + \boldsymbol{\omega}\,\mathbf{n}^{(i)}_j\,\Delta t, \qquad i = 1,2,3. \qquad (2.315)$$

Note that in the last relation for the update of the orientation vectors $\mathbf{n}^{(i)}$, the above explicit scheme leads to non-unit vectors due to the incremental approximation introduced in the problem. This can be resolved by integrating exactly the orientation vectors $\mathbf{n}^{(i)}$ (Aravas and Ponte Castañeda, 2004), which leads to

$$\mathbf{n}^{(i)}_{j+1} = \exp(\boldsymbol{\omega})\,\mathbf{n}^{(i)}_j, \qquad i = 1,2,3. \qquad (2.316)$$

The exponential of the skew-symmetric tensor $\boldsymbol{\omega}$ is an orthogonal tensor that can be determined from the following formula, attributed to Gibbs (Cheng and Gupta, 1989)

$$\exp(\boldsymbol{\omega}) = \boldsymbol{I} + \frac{\sin x}{x}\,\boldsymbol{\omega} + \frac{1-\cos x}{x^2}\,\boldsymbol{\omega}^2, \qquad \text{with} \qquad x = \sqrt{\frac{1}{2}\,\boldsymbol{\omega}\cdot\boldsymbol{\omega}}. \qquad (2.317)$$

It is important to emphasize that the above described formulation is adequate for the purposes of this study, however, due to the explicit scheme used here, a small time increment is required. Instead, for a faster solution of the system of equations use of an implicit scheme should be made (see Aravas and Ponte Castañeda, 2004), which would allow for a larger time increment.

Finally, in many cases of interest, the applied boundary conditions are such that the stress triaxiality X_Σ is constant during the deformation process. The above mentioned system of equations can

be easily modified by imposing the constraint of constant stress triaxiality. This would imply that one of the equations associated with the flow rule, i.e., $\overline{\boldsymbol{D}} = \dot{\Lambda}\,\partial\widetilde{\Phi}/\partial\overline{\boldsymbol{\sigma}}$ needs to be replaced by the one of $X_\Sigma = const.$

2.9 Loss of ellipticity and instabilities

In this section, the main objective is to review the theoretical results needed to predict possible "shear localization" instabilities in porous materials with ideally-plastic matrix phase (Ponte Castañeda and Zaidman, 1994; Kailasam and Ponte Castañeda, 1998). First of all, we recall that in the ideally-plastic limit the matrix phase exhibits no hardening or softening. On the other hand, because of the evolution of the underlying microstructure, the corresponding porous material may exhibit geometrical hardening or softening during the deformation process. This is a direct consequence of the evolution of the microstructure. A measure of the hardening or softening effect is provided by the determination of the effective Jaumann hardening rate H_J, defined by (2.247) for the "variational" method and (2.287) for the "second-order" method, which is independent of the plastic multiplier $\dot{\Lambda}$ and is defined in terms of the rate of change of the microstructural variables by the relation

$$H_J = -\frac{1}{\dot{\Lambda}}\left\{\dot{f}\frac{\partial\widetilde{\Phi}}{\partial f} + \sum_{i=1}^{2}\dot{w}_i\frac{\partial\widetilde{\Phi}}{\partial w_i} + \sum_{j=1}^{3}\overset{\triangledown}{\mathbf{n}}{}^{(i)}\frac{\partial\widetilde{\Phi}}{\partial\mathbf{n}^{(i)}}\right\}, \tag{2.318}$$

where $\overset{\triangledown}{\mathbf{n}}{}^{(i)} = \dot{\mathbf{n}}^{(i)} - \overline{\boldsymbol{\Omega}}\,\mathbf{n}^{(i)}$ denotes the Jaumann rate of the orientation vectors $\mathbf{n}^{(i)}$. Then, the corresponding macroscopic strain-rate is given by (2.44) and is recalled here for completeness to be

$$\overline{D}_{ij} = \frac{1}{H_J}\frac{\partial\widetilde{\Phi}}{\partial\overline{\sigma}_{ij}}\frac{\partial\widetilde{\Phi}}{\partial\overline{\sigma}_{kl}}\overset{\triangledown}{\overline{\sigma}}_{kl}. \tag{2.319}$$

In this connection, it should be emphasized that even though the matrix phase is ideally-plastic, the effective behavior of the porous material is rigid-plastic. This is due to the fact that the microstructure evolves during the deformation process, and thus the porous medium may exhibit softening or hardening, which, in turn, could lead to unstable behaviors for the material.

Now, the necessary conditions for loss of ellipticity of the homogenized equations in a rigid-plastic material were given by Rice (1976). These conditions are:

1. there must be a non-deforming surface in the deformation field
2. the Jaumann hardening rate must satisfy the condition

$$H_J = \frac{1}{2}(\mathbf{u}^A\cdot\overline{\boldsymbol{\sigma}}\mathbf{u}^A - \mathbf{u}^B\cdot\overline{\boldsymbol{\sigma}}\mathbf{u}^B)|\mathbf{u}^A|^2 = H_{cr}. \tag{2.320}$$

Here, $\mathbf{u}^B$ is the normal vector to the non-deforming plane, while $\mathbf{u}^A$ is the solution of the equation

$$\frac{\partial\widetilde{\Phi}}{\partial\overline{\sigma}_{ij}} = \frac{1}{2}(u_i^A\,u_j^B + u_i^B\,u_j^A). \tag{2.321}$$

The last relation can be satisfied only if the second-order tensor $\partial\widetilde{\Phi}/\partial\overline{\sigma}_{ij}$ has at least one zero eigenvalue. It is therefore straightforward that in the case of plane-strain loading conditions the last

relation has a solution, which implies that a non-deforming plane can be found and the first of the two conditions is satisfied identically. Consequently, if the second condition is also satisfied, a possible shear localization instability may occur in the porous material.

Remark 2.9.1. It is noted here that when the loading directions are aligned with the principal axes of anisotropy (or the principal axes of the voids in the present work), condition (2.320) becomes (Rice, 1976)

$$H_J = H_{cr} = 0. \tag{2.322}$$

In the next chapters, we will study the possibility of shear localization in porous materials subjected to plane-strain loading conditions.

2.10 Concluding remarks

In this chapter, we have described a homogenization-based framework for estimating the effective behavior of nonlinear porous media subjected to general loading conditions. In particular, we have made use of the "variational" (Ponte Castañeda, 1991) and the "second-order" (Ponte Castañeda, 2002a) homogenization methods to derive estimates for random porous media. The main idea behind these methods is the construction of suitable variational principles utilizing the concept of "linear comparison composite" (LCC). These variational principles allow the conversion of available linear homogenization results into estimates for the nonlinear porous media. Next, motivated by by most applications of practical interest, these methods have been specialized to the case of porous materials with particulate microstructures and a matrix phase which is described by a power-law stress potential.

First, we have defined the notion of particulate microstructure, where we introduced the internal variables describing the volume fraction, shape and orientation of the voids. Several microstructures of practical interest have been discussed in the context of this section. As a consequence of the fact that we need to determine the effective behavior of the LCC in order to provide estimates for the nonlinear porous material, we have provided estimates for linear porous materials with particulate microstructures by making use of the Willis estimates (1977). It is worth noting, however, that more general micro-geometries could be easily considered, including multiple families of aligned pores by exploiting more general versions of the Willis (Ponte Castaneda and Willis, 1995) and Suquet (Suquet, 1990) estimates for the LCC. However, such studies will not be performed in this work.

In the sequel, we have introduced the definitions associated with a power-law material (viscoplastic behavior). In particular, we have considered that the matrix phase is described by a power-law, incompressible stress potential. Based on these definitions, we have been able to extract the form of the effective stress potential for isotropic and transversely isotropic porous materials.

Then, the "variational" (Ponte Castañeda, 1991) and the "second-order" (Ponte Castañeda, 2002a) homogenization methods have been specialized for this class of viscoplastic porous materials. In particular, it has been shown that the "variational" method, which constitutes a rigorous

lower bound for the effective stress potential (Ponte Castañeda, 1991), can be derived from the more general "second-order" method by setting the "reference" stress tensor equal to zero. However, the "variational" bound is optimal and for this reason we have considered the possibility of using the "second-order" method to obtain more general estimates, which are not bounds but are expected to be more accurate for the special type of particulate microstructures studied in the context of this work. In particular, it has been shown that when we use a more general "reference" stress tensor, the effective stress potential, predicted by the "second-order" method, depends on the certain traces of the field fluctuations in the LCC.

However, it has not yet been possible to optimize the choice of the "reference" stress tensor. In this connection, we have proposed a "reference" stress tensor which is determined in such a way that the "second-order" estimate coincides with the exact result of the composite sphere or cylinder assemblage microstructure (or equivalently with the Gurson criterion in porous solids with ideally-plastic matrix phase) under purely hydrostatic loading. This novel prescription has been generalized in the context of anisotropic microstructures by appropriate normalization of the "variational" estimate, which has been found to be too stiff at purely hydrostatic loadings. In a separate section, we have specialized the previous results in the case of porous media with ideally-plastic matrix phase.

Now, the porous media, considered in this study, are subjected to finite deformations and as a consequence the microstructure evolves in time. Thus, based on the work of Ponte Castañeda and Zaidman (1994) and Kailasam and Ponte Castañeda (1998), we have presented the relevant evolution laws for the internal microstructural variables used to describe the volume fraction, shape and orientation of the voids. In addition, we have provided the conditions for shear localization instabilities that may occur when porous media with ideally-plastic matrix phase are subjected to finite deformations.

Finally, it should be mentioned that the "second-order" method is based on a rigorous variational principle and can be used for general ellipsoidal microstructures and loading conditions. In addition, it is emphasized that the method is general enough to be capable of handling composites whose phases are described by more general constitutive laws (Lopez-Pamies and Ponte Castañeda, 2007) as opposed to the present study where the focus is on porous media with a power-law matrix phase.

2.11 Appendix I. Computation of the Q tensor

This section deals with the consideration of the incompressibility limit for the microstructural tensor $\mathbf{Q}$. In the context of the "variational" method, this computation has been performed by several authors (Kailasam, 1998; Aravas and Ponte Castañeda, 2004) and it will not be discussed here. On the other hand, in the context of the "second-order", taking the incompressibility limit in the matrix phase is not as simple as in the "variational" method. This difference is a direct consequence of the fact that in the "variational" method the viscous modulus tensor $\mathbf{L}$ of matrix phase in the LCC is isotropic and is given by (2.139), whereas in the context of the "second-order" method $\mathbf{L}$ is anisotropic and is given by (2.167). For this reason, it is very hard to consider the limit of incompressibility for a general loading, even by making use of the commercial package Mathematica. However, it has

been possible to write the components of $\mathbf{L}$ by making use of the principal loading directions. This procedure is described in the following.

Thus, in order to consider the incompressibility limit (i.e., the bulk part of the modulus tensor $\mathbf{L}^{(1)} = \mathbf{L}$ of the matrix phase $\kappa \to \infty$) in the computation of the microstructural tensor $\mathbf{Q}$ given by expression (2.59), we need to simplify the form of the modulus tensor $\mathbf{L}$, which is given by relation (2.167). In this regard, it is recalled that the the modulus tensor $\mathbf{L}$ of the matrix phase depends on the macroscopic stress tensor $\overline{\boldsymbol{\sigma}}$ through the definition of the fourth-order tensor $\mathbf{E}$ in relation (2.168). Then, it is convenient to express the components of $\mathbf{L}$ in terms of the eigenvectors of the macroscopic stress tensor $\overline{\boldsymbol{\sigma}}$. For this reason, we write the macroscopic stress tensor as

$$\overline{\boldsymbol{\sigma}} = \boldsymbol{R}\,\overline{\boldsymbol{\sigma}}_u\,\boldsymbol{R}^T. \tag{2.323}$$

In this relation, $\boldsymbol{R}$ is a proper orthogonal matrix (i.e., $\boldsymbol{R}\boldsymbol{R}^T = \boldsymbol{\delta}$, $\det(\boldsymbol{R}) = 1$ and T denotes the transpose of the matrix) and $\overline{\boldsymbol{\sigma}}_u$ is diagonal and can be evaluated by solving the following eigenvalue problem for $\overline{\boldsymbol{\sigma}}$:

$$(\overline{\boldsymbol{\sigma}} - p_i\,\boldsymbol{\delta})\,\mathbf{u}^{(i)} = 0. \tag{2.324}$$

Here, p_i and $\mathbf{u}^{(i)}$ (with $i = 1, 2, 3$) are the eigenvalues and eigenvectors of $\overline{\boldsymbol{\sigma}}$, respectively, such that

$$\overline{\boldsymbol{\sigma}}_u = \mathrm{diag}\{p_1, p_2, p_3\}, \quad \boldsymbol{R} = \{\mathbf{u}^{(1)}, \mathbf{u}^{(2)}, \mathbf{u}^{(3)}\}. \tag{2.325}$$

It is noted that for this specific analysis, the order of the eigenvalues does not affect the final result.

Having introduced the previous definition for $\overline{\boldsymbol{\sigma}}$, it is easily verified that the fourth-order, tensor $\mathbf{E}$ may be expediently expressed as

$$E_{ijkl} = R_{im}\,R_{jn}\,R_{kp}\,R_{lq}\,E^u_{mnpq}, \quad \mathbf{E}^u = \frac{3}{2}\frac{\overline{\boldsymbol{\sigma}}'_u \otimes \overline{\boldsymbol{\sigma}}'_u}{\overline{\sigma}^2_{eq}}, \tag{2.326}$$

where the "prime" denotes the deviatoric part of $\overline{\boldsymbol{\sigma}}_u$. This last result implies that the corresponding modulus tensor of the matrix phase may also be written as

$$L_{ijkl} = R_{im}\,R_{jn}\,R_{kp}\,R_{lq}\,L^u_{mnpq}, \tag{2.327}$$

where L^u_{mnpq} is given by

$$\mathbf{L}^u = \frac{1}{2\,\lambda}\,\mathbf{E}^u + \frac{1}{2\,\mu}\,\mathbf{F}^u, \qquad \mathbf{F}^u = \mathbf{K} - \mathbf{E}^u, \tag{2.328}$$

with $\mathbf{K}$ denoting the standard fourth-order shear projection tensor. The reason for this decomposition is that for a general loading, the tensor $\mathbf{L}$ is fully populated and taking the limit of incompressibility in relation $(2.59)_2$ becomes an extremely difficult task. However, the corresponding fourth-order tensor $\mathbf{L}^u$ has a diagonal form, which makes the calculation of the incompressibility limit feasible.

Next, we define the fourth-order tensor $\boldsymbol{\Gamma}$ as

$$\Gamma_{ijkl} = \frac{1}{4\pi\,\det(\boldsymbol{Z})}\int_{|\boldsymbol{\zeta}|=1} \frac{(L_{iakb}\zeta_a\zeta_b)^{-1}\zeta_j\zeta_l}{|\boldsymbol{Z}^{-1}\cdot\boldsymbol{\zeta}|^3}\,dS, \tag{2.329}$$

where $\boldsymbol{Z}$ is a second order tensor that describes the shape and orientation of the ellipsoidal voids and is given by (see (2.19))

$$\boldsymbol{Z} = w_1\,\mathbf{n}^{(1)} \otimes \mathbf{n}^{(1)} + w_2\,\mathbf{n}^{(2)} \otimes \mathbf{n}^{(2)} + \mathbf{n}^{(3)} \otimes \mathbf{n}^{(3)}, \quad \det(\boldsymbol{Z}) = w_1\,w_2, \tag{2.330}$$

with w_1 and w_2 denoting the aspect ratios of the ellipsoidal voids, whereas $\mathbf{n}^{(i)}$ $(i = 1, 2, 3)$ describing the orientation of the principal axes of the voids.

Next, it can be shown that the tensor $\mathbf{\Gamma}$ can be expressed as

$$\Gamma_{ijkl} = R_{im}\, R_{jn}\, R_{kp}\, R_{lq}\, \Gamma^u_{mnpq}, \tag{2.331}$$

with

$$\Gamma^u_{mnpq} = \frac{1}{4\pi \det(\boldsymbol{Z})} \int_{|\boldsymbol{\zeta}|=1} \frac{(L^u_{mapb}\zeta_a\zeta_b)^{-1}\zeta_j\zeta_l}{|\boldsymbol{Z}^{-1}\,\boldsymbol{R}\cdot\boldsymbol{\zeta}|^3}\, dS. \tag{2.332}$$

By making use of the fact that

$$\frac{1}{4\pi \det(\boldsymbol{Z})} \int_{|\boldsymbol{\zeta}|=1} |\boldsymbol{Z}^{-1}\cdot\boldsymbol{\zeta}|^{-3}\, dS = 1, \tag{2.333}$$

it can be shown that the tensor $\mathbf{Q}$, defined in relation (2.59), reduces to

$$\mathbf{Q} = \mathbf{L} - \mathbf{L}\,\breve{\mathbf{\Gamma}}\,\mathbf{L}, \tag{2.334}$$

where $\breve{\Gamma}_{ijkl} = (\Gamma_{ijkl} + \Gamma_{ijlk} + \Gamma_{jikl} + \Gamma_{jilk})/4$. This final result for the $\mathbf{Q}$ tensor can be shown to reduce to

$$Q_{ijkl} = R_{im}\, R_{jn}\, R_{kp}\, R_{lq}\, Q^u_{mnpq}, \quad \mathbf{Q}^u = \mathbf{L}^u - \mathbf{L}^u\,\breve{\mathbf{\Gamma}}^u\,\mathbf{L}^u, \tag{2.335}$$

where $\breve{\Gamma}^u_{ijkl} = (\Gamma^u_{ijkl} + \Gamma^u_{ijlk} + \Gamma^u_{jikl} + \Gamma^u_{jilk})/4$. This last relation allows us to express the components of $\mathbf{Q}^u$ in terms of the vectors $\mathbf{u}^{(i)}$.

The above expressions provide a way to compute the incompressibility limit $\kappa \to \infty$ by making use of the Mathematica package. Note that a direct substitution of $\mathbf{L}$ in (2.329) makes the analytical evaluation of the incompressibility limit too challenging. On the other hand, by making use of the equivalent representation (2.327) for $\mathbf{L}$ allows us to simplify the calculations considerably.

Apart from the tensor $\mathbf{Q}$, it is also necessary to compute the incompressibility limit $\kappa \to \infty$ for the combined term $\mathbf{\Pi}\,\mathbf{L}$, which is used for the computation of the average spin $\overline{\boldsymbol{\Omega}}^{(2)}$ in the vacuous phase from relations (2.154) for the "variational" method and (2.220) for the "second-order" method. The consideration of the incompressibility limit can be taken directly by considering the product $\mathbf{\Pi}\,\mathbf{L}$ without the need of using the equivalent representation (2.327) for $\mathbf{L}$. However, the resulting expressions are to cumbersome to be included here.

Once the incompressibility limit is considered in (2.332), then the corresponding integral (2.335) can be determined numerically. For this, one needs to evaluate surface integrals of the form

$$I = \int_{|\boldsymbol{\zeta}|=1} A(\boldsymbol{\zeta})\mathrm{d}S(\boldsymbol{\zeta}) = \int_{\phi=0}^{Pi} \int_{\theta=0}^{2\,\pi} A(\boldsymbol{\zeta}(\theta,\phi))\, \sin\phi\, \mathrm{d}\theta\mathrm{d}\phi, \tag{2.336}$$

where $\boldsymbol{\zeta} = \{\sin\phi\,\cos\theta, \sin\phi\,\sin\theta, \cos\phi\}$. The above integration scheme has been observed to become inadequate in terms of accuracy, when the aspect ratios become large or small, such as $w_1 = 5$ and $w_2 = 0.2$ (Aravas and Ponte Castañeda, 2004). For this reason, we write the vector $\boldsymbol{\zeta}$ in cylindrical coordinates, such that

$$\zeta_1 = \sqrt{1-z}\,\cos\theta, \quad \zeta_2 = \sqrt{1-z}\,\sin\theta, \quad \zeta_3 = z. \tag{2.337}$$

Then, the aforementioned integral I becomes

$$I = \int_{z=-1}^{1} \int_{\theta=0}^{2\,\pi} A(\boldsymbol{\zeta}(\theta, z))\, \mathrm{d}\theta \mathrm{d}z. \tag{2.338}$$

Employing the transformation $\theta(r) = (r+1)\,\pi$ in the previous expression, one finds

$$I = \pi \int_{z=-1}^{1} \int_{r=-1}^{1} A(\boldsymbol{\zeta}(\theta(r), z))\, \mathrm{d}r \mathrm{d}z. \tag{2.339}$$

This integral can be evaluated numerically by using Gauss integration of the form

$$I = \pi \sum_{i=1}^{NG} \sum_{j=1}^{NG} W_i\, W_j\, A(\boldsymbol{\zeta}(r_i, z_i)). \tag{2.340}$$

where r_i and z_i are the integration stations, W_i and W_j the corresponding weights, and NG the number of Gauss integration stations. At this point, it is important to mention that in a very recent work Masson (2008) was able to reduce the surface integral to the solution of a single one, allowing for more accurate and faster calculations of the aforementioned integrals. Unfortunately, due to the recent of this work, we were not able yet to implement this recent result in our work. Nonetheless, we expect to perform such a computation in the near future.

2.12 Appendix II. Computation of the macroscopic strain-rate

In this section, we derive the expression (2.186) for the macroscopic strain-rate tensor $\overline{\boldsymbol{D}}$. First, we recall relations (2.172) and (2.170), which describe the effective stress potential $\widetilde{U}_{som}$ of the nonlinear material and $\widetilde{U}_L$ of the LCC, respectively, and they are repeated here for convenience:

$$\widetilde{U}_{som}\left(\overline{\boldsymbol{\sigma}}\right) = \underset{\lambda,\,\mu}{\mathrm{stat}} \left\{ \widetilde{U}_L\left(\overline{\boldsymbol{\sigma}}; \check{\boldsymbol{\sigma}},\, \lambda,\, \mu\right) + (1-f)\, V\left(\check{\boldsymbol{\sigma}}, \lambda,\, \mu\right) \right\}, \tag{2.341}$$

with

$$\widetilde{U}_L(\overline{\boldsymbol{\sigma}}; \check{\boldsymbol{\sigma}}, \mathbf{M}) = (1-f) U(\check{\boldsymbol{\sigma}}) + \boldsymbol{\eta} \cdot \left(\overline{\boldsymbol{\sigma}} - (1-f)\, \check{\boldsymbol{\sigma}}\right) + \frac{1}{2}\, \overline{\boldsymbol{\sigma}} \cdot \widetilde{\mathbf{M}}\, \overline{\boldsymbol{\sigma}} - \frac{1-f}{2}\, \check{\boldsymbol{\sigma}} \cdot \mathbf{M}\, \check{\boldsymbol{\sigma}}, \tag{2.342}$$

and

$$V\left(\check{\boldsymbol{\sigma}}, \lambda,\, \mu\right) = \underset{\hat{\sigma}}{\mathrm{stat}} \left[U\left(\hat{\boldsymbol{\sigma}}\right) - U_L\left(\hat{\boldsymbol{\sigma}}; \check{\boldsymbol{\sigma}},\, \lambda,\, \mu\right) \right]. \tag{2.343}$$

Next, by making use of definition (2.167), with $\kappa \to \infty$, we can rewrite $\mathbf{M}$ as

$$\mathbf{M} = \left(\frac{1}{2\,\lambda} + \frac{1}{2\,\mu} \right) \mathbf{E} + \frac{1}{2\,\mu}\, \mathbf{K}. \tag{2.344}$$

The fourth-order tensor $\mathbf{E}$ is given by relations (2.168) and (2.166), which is recalled here for completeness, such that

$$\mathbf{E} = \frac{3}{2}\, \overline{\boldsymbol{S}} \otimes \overline{\boldsymbol{S}}, \quad \overline{\boldsymbol{S}} = \frac{\check{\boldsymbol{\sigma}}}{\check{\sigma}_{eq}}. \tag{2.345}$$

Then, it is helpful to compute the following derivative,

$$\frac{\partial E_{klmn}}{\partial \check{\sigma}_{ij}} = \frac{3}{2\,\check{\sigma}_{eq}} \left(F_{ijkl}\, \overline{S}_{mn} + F_{ijmn}\, \overline{S}_{kl} \right), \tag{2.346}$$

where $\mathbf{F} = \mathbf{K} - \mathbf{E}$ is given by (2.168).

The macroscopic strain-rate is described by relation (2.6) such that

$$\overline{\boldsymbol{D}} = \frac{\partial \widetilde{U}_{som}}{\partial \overline{\boldsymbol{\sigma}}}(\overline{\boldsymbol{\sigma}};\, \check{\boldsymbol{\sigma}}, \lambda, \mu) = \left.\frac{\partial \widetilde{U}_{som}}{\partial \overline{\boldsymbol{\sigma}}}\right|_{\check{\sigma},\lambda,\mu} + \left.\frac{\partial \widetilde{U}_{som}}{\partial \lambda}\right|_{\overline{\sigma},\,\check{\sigma},\mu} \frac{\partial \lambda}{\partial \overline{\boldsymbol{\sigma}}} + \\ + \left.\frac{\partial \widetilde{U}_{som}}{\partial \mu}\right|_{\overline{\sigma},\,\check{\sigma},\lambda} \frac{\partial \mu}{\partial \overline{\boldsymbol{\sigma}}} + \left.\frac{\partial \widetilde{U}_{som}}{\partial \check{\boldsymbol{\sigma}}}\right|_{\overline{\sigma},\lambda,\mu} \frac{\partial \check{\boldsymbol{\sigma}}}{\partial \overline{\boldsymbol{\sigma}}}. \tag{2.347}$$

This last equation requires the determination of four terms. However, the effective stress potential $\widetilde{U}_{som}$ is stationary with respect to λ and μ as a consequence of the optimality conditions in relation (2.341). This last observation implies that the second and third terms in relation (2.347) are identically zero. In contrast, the first term is associated with the macroscopic strain-rate in the LCC, such that

$$\left.\frac{\partial \widetilde{U}_{som}}{\partial \overline{\boldsymbol{\sigma}}}\right|_{\check{\sigma},\lambda,\mu} = \left.\frac{\partial \widetilde{U}_{L}}{\partial \overline{\boldsymbol{\sigma}}}\right|_{\check{\sigma},\lambda,\mu} = \widetilde{\mathbf{M}}\,\overline{\boldsymbol{\sigma}} + \boldsymbol{\eta} = \overline{\boldsymbol{D}}_L, \tag{2.348}$$

where $\widetilde{U}_L$ is given by (2.342). Hence, the only remaining term and certainly the most challenging one is the fourth term in relation (2.347). In order to proceed further it is essential to recall that the fourth-order tensor $\mathbf{E}$ depends on $\check{\boldsymbol{\sigma}}$ and hence, the last term in relation (2.347) can be further spelled out so that

$$\left.\frac{\partial \widetilde{U}_{som}}{\partial \check{\boldsymbol{\sigma}}}\right|_{\overline{\sigma},\lambda,\mu} \frac{\partial \check{\boldsymbol{\sigma}}}{\partial \overline{\boldsymbol{\sigma}}} = \left(\left.\frac{\partial \widetilde{U}_{som}}{\partial \check{\boldsymbol{\sigma}}}\right|_{\overline{\sigma},\,\mathbf{E},\,\lambda,\mu} + \left.\frac{\partial \widetilde{U}_{som}}{\partial \mathbf{E}}\right|_{\overline{\sigma},\,\check{\sigma},\lambda,\mu} \frac{\partial \mathbf{E}}{\partial \check{\boldsymbol{\sigma}}} \right) \frac{\partial \check{\boldsymbol{\sigma}}}{\partial \overline{\boldsymbol{\sigma}}}. \tag{2.349}$$

The first term of the last relation is equal to

$$\left.\frac{\partial \widetilde{U}_{som}}{\partial \check{\boldsymbol{\sigma}}}\right|_{\overline{\sigma},\,\mathbf{E},\,\lambda,\mu} = (1-f)(\mathbf{M} - \mathbf{M}_t)(\hat{\boldsymbol{\sigma}} - \frac{\overline{\boldsymbol{\sigma}}}{(1-f)}), \tag{2.350}$$

where $\mathbf{M}_t$ is a fourth-order, symmetric tensor originally defined by Ponte Castañeda (1996) and corresponds to the tangent compliance tensor:

$$\mathbf{M}_t = \frac{\partial^2 U(\check{\boldsymbol{\sigma}})}{\partial \check{\boldsymbol{\sigma}} \partial \check{\boldsymbol{\sigma}}} = \left(\frac{1}{2\,\lambda_t} + \frac{1}{2\,\mu_t}\right) \mathbf{E} + \frac{1}{2\,\mu_t}\,\mathbf{K}. \tag{2.351}$$

where λ_t is given by relation (2.190) and $\mu_t = n\,\lambda_t$. Then, with the use of relations (2.177), result (2.350) can be further simplified to

$$\left.\frac{\partial \widetilde{U}_{som}}{\partial \check{\boldsymbol{\sigma}}}\right|_{\overline{\sigma},\,\mathbf{E},\,\lambda,\mu} = (1-f)\left[\left(\frac{1}{2\,\lambda} - \frac{1}{2\,\lambda_t}\right)\left(\hat{\sigma}_{||} - \frac{\overline{\sigma}_{eq}}{1-f}\right)\overline{\boldsymbol{S}} + \right. \\ \left. + \left(\frac{1}{2\,\mu} - \frac{1}{2\,\mu_t}\right)\hat{\sigma}_{\perp}\overline{\boldsymbol{S}}_{\perp}\right] \tag{2.352}$$

where $\overline{\boldsymbol{S}}_{\perp} \cdot \overline{\boldsymbol{S}} = 0$. In turn, the second term in relation (2.349) is

$$\left.\frac{\partial \widetilde{U}_{som}}{\partial E_{klmn}}\right|_{\overline{\sigma},\,\check{\sigma},\lambda,\mu} \frac{\partial E_{klmn}}{\partial \check{\sigma}_{ij}} = \left.\frac{\partial \widetilde{U}_{L}}{\partial E_{klmn}}\right|_{\overline{\sigma},\,\check{\sigma},\lambda,\mu} \frac{\partial E_{klmn}}{\partial \check{\sigma}_{ij}} + \\ (1-f)\left.\frac{\partial V}{\partial E_{klmn}}\right|_{\overline{\sigma},\,\check{\sigma},\lambda,\mu} \frac{\partial E_{klmn}}{\partial \check{\sigma}_{ij}}. \tag{2.353}$$

The first term in this last relation follows from relation (2.342) and (2.346), such that

$$\left.\frac{\partial \widetilde{U}_L}{\partial E_{klmn}}\right|_{\overline{\sigma},\check{\sigma},\lambda,\mu} \frac{\partial E_{klmn}}{\partial \check{\sigma}_{ij}} = \left[\frac{3\left(\lambda^{-1}-\mu^{-1}\right)}{\check{\sigma}_{eq}}\left(\check{\sigma}_{kl}((1-f)\check{\sigma}_{mn}-\overline{\sigma}_{mn})+\right.\right.$$
$$\left.\left.+\frac{1}{2}\overline{\sigma}_{kl}\overline{\sigma}_{mn}\right)\left(F_{ijkl}\,\overline{S}_{mn}+F_{ijmn}\,\overline{S}_{kl}\right)\right]+\frac{f}{2\,(1-f)}\overline{\sigma}_{pq}\,\frac{\partial Q^{-1}_{pqrs}}{\partial E_{klmn}}\,\frac{\partial E_{klmn}}{\partial \check{\sigma}_{ij}}\overline{\sigma}_{rs}. \tag{2.354}$$

Note that with the use of relations (2.177) and particularly the identities $F_{ijkl}\,\overline{\sigma}_{kl}=F_{ijkl}\,\check{\sigma}_{kl}=0$, it can be easily verified that the term of the last expression in the square brackets is identically zero so that

$$\left.\frac{\partial \widetilde{U}_L}{\partial E_{klmn}}\right|_{\overline{\sigma},\check{\sigma},\lambda,\mu} \frac{\partial E_{klmn}}{\partial \check{\sigma}_{ij}} = \frac{f}{2\,(1-f)}\overline{\sigma}_{pq}\,\frac{\partial Q^{-1}_{pqrs}}{\partial \check{\sigma}_{ij}}\overline{\sigma}_{rs}. \tag{2.355}$$

In turn the second term in of relation (2.353) is

$$(1-f)\,\left.\frac{\partial V}{\partial E_{klmn}}\right|_{\overline{\sigma},\check{\sigma},\lambda,\mu} \frac{\partial E_{klmn}}{\partial \check{\sigma}_{ij}} = -\frac{\lambda^{-1}-\mu^{-1}}{2\,\check{\sigma}_{eq}}\left(\hat{\sigma}_{||}-\check{\sigma}_{eq}\right)\hat{\sigma}_{\perp}\,(\overline{S}_{\perp})_{ij}. \tag{2.356}$$

Now, combining relations (2.349),(2.352), (2.353), (2.355) and (2.356) we get

$$\left.\frac{\partial \widetilde{U}_{som}}{\partial \check{\sigma}_{ij}}\right|_{\overline{\sigma},\lambda,\mu} = (1-f)\left\{\left(\frac{1}{2\,\lambda}-\frac{1}{2\,\lambda_t}\right)\left(\hat{\sigma}_{||}-\frac{\overline{\sigma}_{eq}}{1-f}\right)\overline{S}_{ij}+\right.$$
$$\left.+\left[\left(\frac{1}{2\,\mu}-\frac{1}{2\,\mu_t}\right)-\frac{\lambda^{-1}-\mu^{-1}}{2\,\check{\sigma}_{eq}}\left(\hat{\sigma}_{||}-\check{\sigma}_{eq}\right)\right]\hat{\sigma}_{\perp}(\overline{S}_{\perp})_{ij}\right\}+$$
$$+\frac{f}{2\,(1-f)}\overline{\sigma}_{pq}\,\frac{\partial Q^{-1}_{pqrs}}{\partial \check{\sigma}_{ij}}\overline{\sigma}_{rs}. \tag{2.357}$$

Finally, making use of the secant equations (2.178) and the definitions for λ_t and μ_t in relation (2.351), it can be shown that the term proportional to $\overline{\boldsymbol{S}}_{\perp}$ is zero. Then, the last expression reduces to

$$\left.\frac{\partial \widetilde{U}_{som}}{\partial \check{\sigma}_{ij}}\right|_{\overline{\sigma},\lambda,\mu} = (1-f)\left(\frac{1}{2\,\lambda}-\frac{1}{2\,\lambda_t}\right)\left(\hat{\sigma}_{||}-\frac{\overline{\sigma}_{eq}}{1-f}\right)\overline{S}_{ij}+$$
$$+\frac{f}{2\,(1-f)}\,\overline{\sigma}_{pq}\,\frac{\partial Q^{-1}_{pqrs}}{\partial \check{\sigma}_{ij}}\overline{\sigma}_{rs}. \tag{2.358}$$

If this last relation together with expression (2.348) are plugged into relation (2.347), we recover the result (2.186).

2.13 Appendix III. Definition of the reference coefficients

The coefficients introduced in relation (2.203) are given by

$$q=\frac{1+X_{\Sigma}^4}{1+2\,q_1\,X_{\Sigma}^2+X_{\Sigma}^4}, \tag{2.359}$$

with

$$q_1=10\left(1-\left(\frac{\arctan\left(\frac{10^4 f^3}{\exp(-f)}\right)}{\pi/2}\right)^4\right), \tag{2.360}$$

and

$$\beta = \frac{2}{e}\frac{38\,m^2}{1+10\,m^2}\left(1-\left(\frac{\arctan\left(\frac{10^4 f^2}{\exp(-500 f)}\right)}{\pi/2}\right)^6\right). \tag{2.361}$$

It should be emphasized that the coefficient β becomes approximately zero for porosities larger than 1% and for very high nonlinearities (i.e., m smaller than 0.05) and hence it could be neglected in these cases.

2.14 Appendix IV. Homogeneity in the anisotropy ratio of the LCC

In this section, we prove expressions (2.278), where the fourth-order microstructural tensors $\mathbf{Q}$ and $\mathbf{\Pi}$ can be shown to be proportional to the moduli μ of the matrix phase in the LCC. The proof that follows is made in the context of the "second-order" method. However, the results obtained are also valid for the "variational" method by setting the anisotropy ratio $k = 1$. Thus, making use of definition (2.59) for $\mathbf{Q}$, we have that

$$\mathbf{Q} = \mathbf{L} - \mathbf{L}\,\mathbf{P}\,\mathbf{L}, \qquad P_{ijkl} = \frac{1}{4\pi\det(\boldsymbol{Z})}\int_{|\boldsymbol{\zeta}|=1}\frac{(L_{iakb}\zeta_a\zeta_b)^{-1}\zeta_j\zeta_l}{|\boldsymbol{Z}^{-1}\,\boldsymbol{\zeta}|^3}\,dS\Big|_{(ij)(kl)}, \tag{2.362}$$

where the tensor $\boldsymbol{Z}$ is given by relation (2.19), serving to characterize the *instantaneous* shape and orientation of the inclusions and their distribution function in this context of particulate microstructures, $\mathbf{L}$ is the modulus tensor of the matrix phase in the LCC given by (2.167) (in the context of the "second-order" method), such that

$$\mathbf{L} = 2\,\lambda\,\mathbf{E} + 2\,\mu\,\mathbf{F} = \mu\,(2\,k\,\mathbf{E} + 2\,\mathbf{F}) = \mu\,\boldsymbol{\mathcal{L}}(k), \qquad k = \frac{\lambda}{\mu}. \tag{2.363}$$

Substituting this last result in relation (2.362), the following expression is obtained:

$$P_{ijkl} = \frac{1}{4\mu\,\pi\det(\boldsymbol{Z})}\int_{|\boldsymbol{\zeta}|=1}\frac{(\mathcal{L}(k)_{iakb}\zeta_a\zeta_b)^{-1}\zeta_j\zeta_l}{|\boldsymbol{Z}^{-1}\,\boldsymbol{\zeta}|^3}\,dS\Big|_{(ij)(kl)} = \frac{1}{\mu}\,\widehat{P}_{ijkl}, \tag{2.364}$$

which in turn implies that

$$\mathbf{Q}(\lambda,\mu) = \mathbf{L} - \mathbf{L}\,\mathbf{P}\,\mathbf{L} = \mu\,\boldsymbol{\mathcal{L}}(k) - \mu\,\boldsymbol{\mathcal{L}}(k)\,\widehat{\mathbf{P}}(k)\,\boldsymbol{\mathcal{L}}(k) = \mu\,\widehat{\mathbf{Q}}(k). \tag{2.365}$$

In the case of the "variational" method, the anisotropy ratio $k = 1$ and thus $\widehat{\mathbf{Q}}$ is independent of the moduli of the matrix phase in the LCC. This last relation implies also that the effective compliance tensor $\widetilde{\mathbf{M}}$ is given by

$$\widetilde{\mathbf{M}}(\lambda,\mu) = \mathbf{M} + \frac{f}{1-f}\,\mathbf{Q}^{-1} = \frac{1}{\mu}\left(\boldsymbol{\mathcal{M}}(k) + \frac{f}{1-f}\,\widehat{\mathbf{Q}}(k)^{-1}\right) = \frac{1}{\mu}\,\widehat{\mathbf{M}}(k). \tag{2.366}$$

where $\mathbf{M} = \mathbf{L}^{-1}$ is the compliance tensor of the matrix phase in the LCC. Note that when $k = 1$, we simply recover relation (2.143).

Similarly, the tensor $\mathbf{\Pi}$ is given by (2.74), such that

$$\Pi_{ijkl} = \frac{1}{4\mu\,\pi\,\det(\boldsymbol{Z})}\int_{|\boldsymbol{\zeta}|=1}\frac{(\mathcal{L}(k)_{iakb}\zeta_a\zeta_b)^{-1}\zeta_j\zeta_l}{|\boldsymbol{Z}^{-1}\,\boldsymbol{\zeta}|^3}\,dS\bigg|_{[ij](kl)} = \frac{1}{\mu}\,\widehat{\Pi}_{ijkl}. \tag{2.367}$$

Thus, we have

$$\mathbf{\Pi}(\lambda,\mu) = \frac{1}{\mu}\,\widehat{\mathbf{\Pi}}(k). \tag{2.368}$$

Finally, it is interesting to note as well that the term $\mathbf{\Pi}\,\mathbf{L}$ is also independent of μ as a consequence of relations (2.363) and (2.368).

2.15 Appendix V. Evaluation of the hydrostatic point

In the computation of the reference stress $\check{\boldsymbol{\sigma}}$, we make use of the mean normalized stress $\overline{\mathbf{\Sigma}}_m^H$, which corresponds to the hydrostatic stress as predicted by the various methods described previously in the hydrostatic limit (the superscript H denotes that limit). More specifically, we define the quantities $\overline{\mathbf{\Sigma}}_m^H\Big|_{som}$ and $\overline{\mathbf{\Sigma}}_m^H\Big|_{var}$ in the context of relation (2.207). In this section, we spell out explicitly the expressions for the computation of these two quantities.

Thus, consider the definition of the effective stress potential $\widetilde{U}$, defined by (2.195), which is repeated here to be

$$\widetilde{U}(\overline{\boldsymbol{\sigma}};\,f,w_1,w_2) = \frac{\dot{\varepsilon}_o\,\widetilde{\sigma}_w}{1+n}\left(\frac{3}{2}\frac{|\overline{\sigma}_m|}{\widetilde{\sigma}_w}\right)^{1+n}. \tag{2.369}$$

with $\widetilde{\sigma}_w$ denoting the effective flow stress of the porous medium. The above definition holds for both the "second-order" and the "variational" method.

By contrast, consider the corresponding definition of the gauge factor (see (2.28)) such that

$$\widetilde{U}(\overline{\boldsymbol{\sigma}};\,s_\alpha) = \frac{\dot{\varepsilon}_o\,\sigma_o}{n+1}\left(\frac{\Gamma_n(\overline{\boldsymbol{\sigma}};\,s_\alpha)}{\sigma_o}\right)^{n+1}. \tag{2.370}$$

It follows then from (2.369) and (2.370) that

$$\Gamma_n(\overline{\boldsymbol{\sigma}}) = \frac{3}{2}\left(\frac{\sigma_o}{\widetilde{\sigma}_w}\right)^{\frac{n}{n+1}}|\overline{\sigma}_m|. \tag{2.371}$$

Following then the definition of the normalized stress $\overline{\mathbf{\Sigma}} = \overline{\boldsymbol{\sigma}}/\Gamma_n(\overline{\boldsymbol{\sigma}})$, one finds that

$$|\overline{\Sigma}_m| = \frac{2}{3}\left(\frac{\widetilde{\sigma}_w}{\sigma_o}\right)^{\frac{n}{n+1}} \equiv \overline{\Sigma}_m^H, \tag{2.372}$$

where H is used to emphasize that the above estimate is true for purely hydrostatic loading. Thus, the normalized mean stress $\overline{\Sigma}_m^H$ depends explicitly on the effective flow stress $\widetilde{\sigma}_w$.

Then, $\widetilde{\sigma}_w$ is given approximately by (2.199), such that

$$\widetilde{\sigma}_w = \frac{\widetilde{\sigma}_{w=1}}{\widetilde{\sigma}_{w=1}^{var}}\,\widetilde{\sigma}_w^{var}, \qquad \text{with} \qquad \frac{\widetilde{\sigma}_{w=1}}{\sigma_o} = n\left(f^{-1/n}-1\right), \qquad \frac{\widetilde{\sigma}_{w=1}^{var}}{\sigma_o} = \frac{1-f}{\sqrt{f}^{\frac{1+n}{n}}}, \tag{2.373}$$

with

$$\left(\frac{\widetilde{\sigma}_w^{var}}{\sigma_o}\right)^{-n} = (1-f)\left[\frac{4\,\boldsymbol{I}\cdot\widehat{\mathbf{M}}\,\boldsymbol{I}}{3\,(1-f)}\right]^{\frac{n+1}{2}}, \tag{2.374}$$

denoting the effective flow stress delivered by the "variational" method, while $\widehat{\mathbf{M}}$ given by (2.143), which is not analytical for general ellipsoidal microstructures.

It follows from the definition (2.372) that

$$\overline{\Sigma}_m^H\Big|_{som} = \frac{2}{3}\left(\frac{\widetilde{\sigma}_w}{\sigma_o}\right)^{\frac{n}{n+1}} \qquad \text{and} \qquad \overline{\Sigma}_m^H\Big|_{var} = \frac{2}{3}\left(\frac{\widetilde{\sigma}_w^{var}}{\sigma_o}\right)^{\frac{n}{n+1}} \tag{2.375}$$

with $\widetilde{\sigma}_w$ and $\widetilde{\sigma}_w^{var}$ given by (2.373) and (2.374), respectively.

In the special case of spherical voids, i.e., $w_1 = w_2 = 1$, $\widetilde{\sigma}_w = \widetilde{\sigma}_{w=1}$ such that

$$\overline{\Sigma}_m^H\Big|_{som} = \frac{2}{3}\left(n\left(f^{-1/n} - 1\right)\right)^{\frac{n}{n+1}} \qquad \text{and} \qquad \overline{\Sigma}_m^H\Big|_{var} = \frac{2}{3}\left(\frac{1-f}{\sqrt{f}^{\frac{1+n}{n}}}\right)^{\frac{n}{n+1}} \tag{2.376}$$

Special case of ideal-plasticity. The expressions for the special case of ideal-plasticity can be easily obtained by considering the limit $n \to \infty$ in (2.372), such that

$$|\overline{\Sigma}_m| = \frac{2}{3}\frac{\widetilde{\sigma}_w}{\sigma_o} \equiv \overline{\Sigma}_m^H. \tag{2.377}$$

Making use of (2.373) in the ideally-plastic limit and the results

$$\frac{\widetilde{\sigma}_{w=1}}{\sigma_o} = \ln\left(\frac{1}{f}\right) \qquad \text{and} \qquad \frac{\widetilde{\sigma}_{w=1}^{var}}{\sigma_o} = \frac{1-f}{\sqrt{f}}, \tag{2.378}$$

and (see equation (2.234))

$$\frac{\widetilde{\sigma}_w^{var}}{\sigma_o} = \left[\frac{4\,\boldsymbol{I}\cdot\widehat{\mathbf{M}}\,\boldsymbol{I}}{3\,(1-f)}\right]^{-\frac{1}{2}}, \tag{2.379}$$

we can readily compute $\overline{\Sigma}_m^H\Big|_{som}$ and $\overline{\Sigma}_m^H\Big|_{var}$.

Chapter 3

Other models for porous materials

The purpose of this chapter is to summarize the main features and results of other approaches for the estimation of the effective behavior of porous materials. First, we refer to the works of McClintock (1968) and Rice and Tracey (1969), who studied the problem of estimating the behavior of a porous material with an ideally-plastic matrix phase and dilute concentration of voids (these models are not discussed in detail here). These authors proposed a set of trial velocity fields based on a suitably chosen stream function, which they used to minimize a suitably constructed variational dissipation principle. Based on this idea of trial velocity fields, Gurson (1977) proposed a two-velocity field model for non-dilute porous media. In particular, the author made use of the analytical solution for a spherical (or cylindrical) hollow shell subjected to purely hydrostatic pressure to propose an approximate yield criterion for isotropic porous media.

Next, we discuss the methodology introduced by Budiansky et al. (1982) (see also Duva and Hutchinson (1984)) for dilute viscoplastic porous materials consisting of spherical and cylindrical (with circular cross-section) voids. This methodology is based on the technique introduced by McClintock (1968) and Rice and Tracey (1969) and involves a more sophisticated choice for the stream function based on an eigen-function expansion by making use of the Rayleigh-Ritz method. This technique has been extended to dilute viscoplastic porous media consisting of cylindrical voids with elliptical cross-section by Fleck and Hutchinson (1986) and Lee and Mear (1992b), as well as to spheroidal voids subjected to axisymmetric loading conditions (aligned with the pore symmetry axis) by Lee and Mear (1992c).

In the next section, we present the Leblond et al. (1994) model, which is a generalization of the Gurson model in the context of isotropic viscoplastic porous media. In addition, we discuss the extension of this last model in the case of spheroidal voids and axisymmetric loading conditions (Gologanu et al., 1993, 1994, 1997; Gărăjeu et al., 2000; Flandi and Leblond, 2005). In the following, we describe the analysis performed initially by deBotton and Hariton (2002) and later by Idiart (2006) in the context of a special class of isotropic porous materials, known as "high-rank sequential laminates." Finally, we discuss the application of the finite element method to compute the effective behavior of a cubic (periodic) or cylindrical unit cell consisting of a single void subjected to several loadings.

3.1 Gurson model

In this section, we describe briefly the Gurson (1977) model, which was developed to estimate the overall behavior of porous solids with an ideally-plastic matrix phase and cylindrical (2D) or spherical (3D) microstructures. This model makes use of the exact solution for a shell (spherical or cylindrical cavity) under hydrostatic loadings, suitably modified, to obtain estimates for the effective behavior of ideally-plastic solids with isotropic or transversely isotropic distributions of porosity.

For the case of cylindrical cavities, Gurson's yield criterion takes the form

$$\Phi^{2D}_{GUR}(\overline{\boldsymbol{\sigma}}) = \frac{\overline{\sigma}^2_{eq}}{\sigma^2_o} + 2\,f\,\cosh\left(\frac{\sqrt{3}}{2}\,\overline{\sigma}_{\gamma\gamma}\right) - 1 - f^2 = 0, \quad \gamma = 1,2 \tag{3.1}$$

while for spherical cavities

$$\Phi^{3D}_{GUR}(\overline{\boldsymbol{\sigma}}) = \frac{\overline{\sigma}^2_{eq}}{\sigma^2_o} + 2\,f\,\cosh\left(\frac{1}{2}\,\overline{\sigma}_{ii}\right) - 1 - f^2 = 0, \quad i = 1,2,3. \tag{3.2}$$

For purely hydrostatic loadings, i.e., $\overline{\sigma}_{eq} = 0$, both criteria recover the exact solution for a cylindrical or spherical shell, as defined by relation (2.293) . On the other hand, for purely deviatoric loadings, i.e., $\overline{\sigma}_m = 0$, Gurson's criterion recovers the Voigt bound (uniform strain-rate in the entire shell).

One of the main disadvantages of the Gurson model is that, it contains no information about other microstructural variables such as the shape and orientation of the voids. As we will see in the following chapters, the evolution of the shape and the orientation of the voids can cause significant geometrical softening or hardening, as opposed to the softening or hardening that the evolution of porosity may induce in the porous material. However, the Gurson model can only predict the evolution of the porosity and consequently deliver inaccurate estimates when the shape and the orientation of the voids is expected to change significantly, such as in the case of low triaxiality loading. More specifically, the expression for the corresponding hardening rate, predicted by the Gurson model, is given by

$$H_{GUR} = -(1-f)\,\frac{\partial \Phi_{GUR}}{\overline{\sigma}_{ii}}\,\frac{\partial \Phi_{GUR}}{\partial f}. \tag{3.3}$$

Thus, if the loading is such that the porosity increases, the porous medium exhibits an overall softening behavior, which can be verified by a negative hardening rate ($H_{GUR} < 0$). In contrast, when the loading causes a decrease in the porosity, the material hardens and hence the hardening rate is positive ($H_{GUR} > 0$). In the special case of pure stress or strain-rate deviatoric loadings, however, there is no change in the porosity and hence the hardening rate is identically zero ($H_{GUR} = 0$).

In summary, Gurson criterion contains information only for the volume fraction of the voids, namely the porosity f, which implies that these models are valid only for spherical or cylindrical microstructures. In this regard, Gurson's model is expected to be sufficiently good for high triaxial loadings, i.e., $\overline{\sigma}_{eq}/\sigma_o \ll 1$, where the initially cylindrical or spherical voids preserve their shape during the deformation process. However, for low triaxial loadings the shape and orientation of the voids evolve significantly resulting in a highly anisotropic behavior for the porous material. In this last case, the Gurson model is expected to be highly inaccurate.

3.2 Models for porous media with dilute concentrations

In this section, we will make an attempt to summarize the main issues of earlier studies made in the context of dilute porous media. We discuss first the methodology developed by Budiansky et al. (1982) in the context of porous media containing a spherical (or cylindrical with circular cross-section) void subjected to axisymmetric loading conditions (aligned with the void symmetry axis). Then, we discuss the extension of this method to cylindrical voids with elliptical cross-sections by Fleck and Hutchinson (1986) and Lee and Mear (1992b), and to spheroidal voids by Lee and Mear (1992c).

3.2.1 Spherical void and axisymmetric loading

To begin with, based on the early study of McClintock (1968) and Rice and Tracey (1969) in dilute porous solids with ideally-plastic matrix phase, Budiansky et al. (1982) proposed a methodology making use of the minimum principle of velocities as stated by Hill (1956), to compute the effective energy of dilute viscoplastic porous media (i.e., an infinite block Ω occupying volume $\mathcal{V}$ containing a single void $\Omega^{(2)}$ occupying volume $\mathcal{V}_2$) subjected to axisymmetric loading conditions. The matrix phase $\Omega^{(1)}$ occupies a region with volume $\mathcal{V}_1$. In this procedure, the minimum principle can be written in terms of the dissipation potential W such that

$$\mathcal{F} = \int_{\mathcal{V}_1} \left[W(\boldsymbol{D}) - W(\boldsymbol{D}^\infty) - \sigma_{ij}^\infty \, \widetilde{D}_{ij} \right] d\mathcal{V} - \int_{S_2} \sigma_{ij}^\infty \, n_j \, \widetilde{v}_i \tag{3.4}$$

where the subscripts 1 and 2 denote quantities in the matrix and the void, respectively, $\boldsymbol{D}^\infty$ is a uniform strain-rate due to $\boldsymbol{\sigma}^\infty$ in the absence of the void and

$$v_i = v_i^\infty + \widetilde{v}_i, \quad \boldsymbol{D} = \boldsymbol{D}^\infty + \widetilde{\boldsymbol{D}}, \tag{3.5}$$

with

$$\widetilde{D}_{ij} = \frac{1}{2}(\widetilde{v}_{i,j} + \widetilde{v}_{j,i}), \quad \widetilde{v}_{k,k} = 0. \tag{3.6}$$

In these expressions, $\boldsymbol{D}$ is the local strain-rate in the specimen, whereas the $\mathcal{F}$ is minimized with respect to the velocity field $\widetilde{\mathbf{v}}$. By considering the volume average in (3.5), we get

$$\overline{\boldsymbol{D}} = \boldsymbol{D}^\infty + \langle \widetilde{\boldsymbol{D}} \rangle. \tag{3.7}$$

In this regard, the Rayleigh-Ritz method is used in the sequel to generate approximate expressions for the additional velocity field $\widetilde{\mathbf{v}}$. More specifically, the authors make use of the *incompressibility* of the matrix phase and the *axisymmetric* loading to introduce a "stream function", so that

$$\widetilde{v}_r = -\frac{1}{r^2 \sin\theta} \frac{\partial \left(\chi \sin\theta\right)}{\partial \theta} \quad \text{and} \quad \widetilde{v}_\theta = \frac{1}{r} \frac{\partial \chi}{\partial r}. \tag{3.8}$$

It is worth recalling that the stream function is introduced mainly for two reasons; (i) instead of guessing a form for the two components of the velocity field $\widetilde{v}_r$ and $\widetilde{v}_\theta$, we need to provide a form for a scalar function, i.e., the stream function χ, and (ii) the above velocity fields satisfy the incompressibility condition trivially. In this regard, a form for the stream function χ can be obtained by considering an eigen-function expansion, such that

$$\chi(r,\theta) = A \, \cot\theta + \sum_{k=2,4,\ldots} P_{k,\theta}(\cos\theta) \, f_k(r), \tag{3.9}$$

where $P_k(\cos\theta)$ is the Legendre polynomial of degree k and $f_k(r) = \sum_{i=1}^{M} A_k^{(i)} r^{2-i}$. It is interesting to remark that the first term, $A\cot\theta$, generates the spherically symmetric contribution to the field. Note, however, that the notion of a stream function is mainly used in two-dimensional or three-dimensional with certain symmetries (i.e., axisymmetric symmetry) problems. In contrast to extend this technique to the cases of a general three-dimensional loading or void geometry (such as general ellipsoidal voids), which is of interest in many applications, becomes a very difficult task and so far the author is not aware of such a more general result in the context of porous materials. This is a certain limitation of this procedure, since a generalization of this methodology to more complicated microstructures and loadings is not straightforward.

Now, the associated with the stream function strain-rate fields are simply

$$\widetilde{D}_r = \widetilde{v}_{r,r},\ \widetilde{D}_\theta = \frac{1}{r}(\widetilde{v}_{\theta,\theta} + \widetilde{v}_r),\ \widetilde{D}_\phi = -\widetilde{D}_r - \widetilde{D}_\theta,\ \widetilde{D}_{r\,\theta} = \frac{1}{2}\left(\frac{1}{r}\widetilde{v}_{r,\theta} - \frac{1}{r}\widetilde{v}_\theta + \widetilde{v}_{\theta,r}\right). \tag{3.10}$$

In these expressions, the velocity and strain-rate fields depend explicitly on the amplitude factors $A_k^{(i)}$, with respect to which $\mathcal{F}$ must be minimized. Thus, the actual velocity field is approximated by the velocity field $\widetilde{v}$, described previously, in terms of the factors $A_k^{(i)}$. It is evident that the larger number of factors $A_k^{(i)}$ used, the better the approximation to the actual field will be. However, this poses numerical limitations to the solution of the problem. Nonetheless, the authors used physically based considerations — the trial velocity field $\widetilde{\mathbf{v}}$ should be able to recover the Eshelby (1957) solution in the linear case — to choose a minimal number of $A_k^{(i)}$ to include in the minimization procedure. On the other hand, Huang (1991b) has shown that the choice of the number of amplitude factors is of critical importance, particularly at high nonlinearities, where a sufficiently large number of $A_k^{(i)}$ must be used for convergence. As a consequence, he showed that the results delivered by Budiansky et al. (1982), as well as Rice and Tracey (1969), seriously underestimate the dilatation rate of the void at large stress triaxialities.

In summary, the above mentioned methodology approximates the actual field by a sum of linearly independent functions that are multiplied by certain amplitude factors. The relevant function then is minimized "numerically" with respect to these amplitude factors. In turn, it is emphasized that this technique is based on a choice of a stream function, where a special class of microstructures and loading conditions is considered. This special class of microstructures involves the cases of porous media with cylindrical voids with circular or elliptical cross-sections as we will see in the following sections, as well as porous materials consisting of spherical voids subjected to axisymmetric loading conditions (aligned with the pore symmetry axis). On the other hand, the extension of this methodology to general three-dimensional ellipsoidal microstructures and loading conditions is not straightforward, due to the fact that the stream function technique is restricted to problems with two-dimensional character, such as the ones mentioned previously. Nonetheless, these limitations do not eliminate the usefulness of such methods, which were able to predict interesting nonlinear effects to be discussed in the following chapters.

3.2.2 Cylindrical void with elliptical cross-section using conformal mapping

Building on the work of Budiansky et al. (1982) and Duva and Hutchinson (1984), Fleck and Hutchinson (1986) made an attempt to apply the methodology described previously to dilute porous media consisting of cylindrical voids with *elliptical* cross-section. In order to generalize this methodology, Fleck and Hutchinson (1986) made use of a conformal mapping technique, which allowed them to write a stream function for a void with elliptical cross-section. In order to achieve this mapping, they used a complex variable z in the physical plane and a complex variable ζ in the mapped plane (see Fig. 3.1 for details), which are related by

$$z = r\, e^{\mathrm{i}\,\theta} = x_1 + \mathrm{i}\, x_2 = R\,(\zeta + m/\zeta), \quad \zeta = \xi_1 + \mathrm{i}\,\xi_2, \tag{3.11}$$

where x_1, x_2 and r, θ are Cartesian and polar coordinates in the physical plane, and ξ_1, ξ_2 and μ, ϕ are Cartesian and polar coordinates in the mapped plane. In turn, the variables R and $m = |m|e^{\mathrm{i}\,\lambda}$ contain information about the shape and orientation of the void and are given by

$$R = \frac{a_1 + a_2}{2}, \quad |m| = \frac{a_1 - a_2}{a_1 + a_2}, \quad \lambda = 2\,\psi. \tag{3.12}$$

Here, a_1 is the length of the semi-major axis of the ellipse, a_2 is length of the semi-minor axis, and

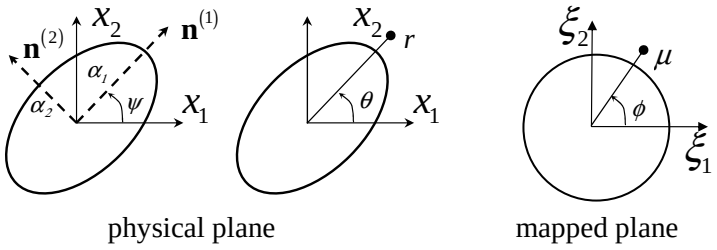

Figure 3.1: Geometry of the void and mapping from physical plane to mapped plane.

ψ is the orientation angle of the semi-major axis. The details of the geometry and the mapping are shown schematically in Fig. 3.1. Then, they defined a stream function, similar to the one defined by Budiansky et al. (1982) in relation (3.9), which is expressed as

$$\chi(r,\theta) = A\,\theta + \sum_{j=1}^{N}\sum_{k=1}^{N}\left\{A_{jk}\,\mu^{k-1}\,\sin 2j\phi + B_{jk}\,\mu^{k-1}\,\sin 2j\phi\right\}. \tag{3.13}$$

From this stream function, the authors need to compute the velocity and strain-rate fields, substitute in the minimum principle (3.4), and optimize with respect to the amplitude factors A, A_{jk} and B_{jk}. Note that the leading term $A\,\theta$ in (3.13) gives rise to the radially symmetric contribution and thus to the dilatation rate of the void.

In the following, we discuss the boundary conditions considered in that work and the connection with the homogenization estimates presented in the previous chapter. In particular, the remote field

is considered to be a state of simple shear parallel to the $\mathbf{e}^{(1)}-$direction with hydrostatic tension superimposed on the incompressible material. The remote field is then specified by the velocities

$$v_1^\infty = \dot{\gamma}\, x_2, \quad v_2^\infty = v_3^\infty = 0, \tag{3.14}$$

where $\dot{\gamma}$ is the remote shear strain-rate, and x_2 is the coordinate in the $\mathbf{e}^{(2)}-$direction. The associated non-zero components of the remote strain-rate, spin and stress are

$$D_{12}^\infty = \frac{1}{2}\,\dot{\gamma}, \quad \Omega_{12}^\infty = \frac{1}{2}\,\dot{\gamma} \tag{3.15}$$

and

$$\sigma_{11}^\infty = \sigma_{22}^\infty = \sigma_{33}^\infty = \overline{\sigma}_m, \quad \sigma_{12}^\infty = \tau. \tag{3.16}$$

The corresponding stress triaxiality defined in the work of Fleck and Hutchinson is related to the standard stress triaxiality used in this work by

$$\frac{\overline{\sigma}_m}{\tau} = \sqrt{3}\, X_\Sigma = \frac{\overline{\sigma}_m}{\overline{\sigma}_{eq}/\sqrt{3}} = \frac{\overline{\sigma}_m}{\tau/\sqrt{3}}, \tag{3.17}$$

where $\overline{\sigma}_m$ and $\overline{\sigma}_{eq}$ are the macroscopic mean and von Mises stress measures, respectively. It is also useful to relate $\dot{\gamma}$ with the remote, equivalent strain-rate D_{eq}^∞ and the equivalent macroscopic stress by noting that

$$\dot{\gamma} = \sqrt{3}\, D_{eq}^\infty = \sqrt{3}\, \overline{\sigma}_{eq}^n, \tag{3.18}$$

where n describes the nonlinearity of the matrix phase and has been introduced in relation (2.23).

In this case of a long cylindrical void the considered deformation is one of plane-strain and therefore independent of x_3. When the cylindrical void has a circular cross-section in the plane $1-2$ then the behavior of the porous medium is isotropic in this plane. However, when the aforementioned boundary conditions are applied, then the volume, shape and orientation of the void are expected to evolve in time.

More specifically, the interest is focused on the determination of the initial dilatation rate, which is related to the macroscopic strain-rate $\overline{\boldsymbol{D}}$, defined in relation (3.7), through the relation

$$\frac{\dot{\mathcal{V}}_2}{\dot{\gamma}\,\mathcal{V}_2} = \frac{\overline{D}_{\alpha\alpha}}{\sqrt{3}\, f\, D_{eq}^\infty}, \quad \alpha = 1, 2. \tag{3.19}$$

In summary, based on the work of Budiansky et al. (1982), Fleck and Hutchinson (1986) proposed a stream function by making use of a conformal mapping technique, which allowed them to obtain estimates for dilute porous materials consisting of cylindrical voids with elliptical cross-section. In the following chapters, the estimates delivered by the homogenization methods, described in the previous chapter, will be compared with the Fleck-Hutchinson results in the case of an initially cylindrical void with circular cross-section.

3.2.3 Cylindrical voids with elliptical cross-section using elliptical coordinates

In addition to the work of Fleck and Hutchinson (1986), Lee and Mear (1992b) have also studied the problem of a dilute, viscoplastic porous medium made up of an isolated cylindrical void with elliptical

cross-section. In their work, they made use of an equivalent representation of the minimum principle in terms of stress potentials, whereas they also proposed a somewhat different stream function by making use of elliptical coordinates.

More specifically, the effective stress potential of a solid containing dilute concentration of voids can be expressed as

$$\widetilde{U}(\overline{\boldsymbol{\sigma}}) = U(\overline{\boldsymbol{\sigma}}) + f\,\frac{\delta\widetilde{U}}{\delta f}, \quad \frac{\delta\widetilde{U}}{\delta f} = \frac{1}{\mathcal{A}_2}\int_{\mathcal{A}_1}\left[U(\boldsymbol{\sigma}) - U(\overline{\boldsymbol{\sigma}})\right] d\mathcal{A} - U(\overline{\boldsymbol{\sigma}}) \tag{3.20}$$

where $\mathcal{A}_2$ and $\mathcal{A}_1$ are the regions occupied by the void and the matrix phase, while U denotes the stress potential of the matrix phase and is given by relation $(2.23)_1$. It is important to note that expression (3.20) implies that the effective stress potential $\widetilde{U}$ of the porous solid has a linear correction in the concentration of the voids, i.e., the porosity f. However, we will see at the end of this section that such an expansion may have a very small range of validity for very nonlinear solids and particularly for ideally-plastic solids where such an expansion may not be valid at all (see Duva and Hutchinson, 1984). In any case, the above correction term $\delta\widetilde{U}/\delta f$ can be directly related to the minimum principle, defined previously in the context of relation (3.4), through the relation (Duva and Hutchinson, 1984; Lee and Mear, 1992b)

$$\frac{\delta\widetilde{U}}{\delta f} = W(\boldsymbol{D}^{\infty}) - \frac{\mathcal{F}_{\min}}{\mathcal{A}_2}, \tag{3.21}$$

where $\mathcal{F}_{\min}$ denotes the minimized (optimal) value of $\mathcal{F}$. Note that the volume and surface terms $\mathcal{V}_1$ and $\mathcal{S}_2$ in relation (3.4) should be replaced here by the surface and line terms $\mathcal{A}_1$ and $\mathcal{C}_2$ due to the in-plane character of the problem. For further details the reader is referred to the original work of Lee and Mear (1992b).

In order to compute the correction term $\delta\widetilde{U}/\delta f$ for porous media containing cylindrical voids with elliptical cross-section, these authors proposed a stream function in terms of elliptical coordinates (η, θ) (the η coordinate is equivalent to the radial variable in polar coordinates), such that

$$\chi = A\,\theta + \sum_{k=2,4,\ldots}\left[F_k(\eta)\,\sin k\,\theta + G_k(\eta)\,\cos k\theta\right], \tag{3.22}$$

where F_k and G_k are functions of η alone given by

$$\begin{aligned} F_k(\eta) &= \sum_{m=-1,0,1,\ldots} A_{km}\,\exp(-m\eta) \\ G_k(\eta) &= \sum_{m=-1,0,1,\ldots} B_{km}\,\exp(-m\eta). \end{aligned} \tag{3.23}$$

The reduced displacement $\widetilde{\mathbf{v}}$, defined in relation (3.5), is simply given by

$$\widetilde{v}_\eta = \frac{\alpha}{\mathcal{H}}\frac{\partial\chi}{\partial\theta}, \quad \widetilde{v}_\theta = -\frac{\alpha}{\mathcal{H}}\frac{\partial\chi}{\partial\eta}, \tag{3.24}$$

where $\mathcal{H} = \alpha\,(\cosh^2\eta - \cos^2\theta)^{1/2}$ and α is a scaling parameter related to the distance from the origin to the foci of the elliptical void. Similarly to the work of Budiansky et al. (1982), the above velocity fields are plugged in the minimum principle $\mathcal{F}$ defined in relation (3.4), where the minimization

procedure is performed with respect to the amplitude factors A, A_{km} and B_{km}, defined in (3.22) and (3.23).

In the following, we discuss the boundary conditions used by Lee and Mear (1992b) in their study. In particular, these authors imposed somewhat different boundary conditions than the ones considered by Fleck and Hutchinson (1986). More specifically, Lee and Mear studied the response of a dilute, porous solid subjected to plane-strain, traction boundary conditions. The corresponding remote stresses, that have been used, are

$$\sigma_{11}^{\infty} = S^{\infty}, \quad \sigma_{22}^{\infty} = T^{\infty}, \quad \sigma_{33}^{\infty} = \frac{1}{2}(S^{\infty} + T^{\infty}). \tag{3.25}$$

The stress triaxiality X_{Σ} may be defined as in relation (3.17) by noting that $\overline{\sigma}_m = (S^{\infty} + T^{\infty})/2$ and $\overline{\sigma}_{eq} = \sqrt{3}|S^{\infty} - T^{\infty}|/2$. It is important to note that in the case that the void has an initially circular cross-section in the plane $1-2$ then the behavior is isotropic in this plane. In this special case, the boundary conditions applied by Fleck and Hutchinson (1986), described by relation (3.16), are equivalent to the boundary conditions imposed by Lee and Mear (1992b) given by relation (3.25). The reason for this lies in the fact that the initial response of isotropic media subjected to simple or pure, in-plane shear combined with superimposed pressure is identical.

In this regard, it is essential to analyze the relevant dilatation and deviatoric quantities introduced by Lee and Mear (1992b). In particular, the Lee and Mear (LM) effective stress potential can be written in the form

$$\widetilde{U}_{LM}(\overline{\boldsymbol{\sigma}}) = (1 + f h(X_{\Sigma})) \, \frac{\dot{\varepsilon}_o \, \sigma_o}{n+1} \left(\frac{\overline{\sigma}_{eq}}{\sigma_o} \right)^{n+1}. \tag{3.26}$$

In this expression, the authors make the hypothesis that the effective stress potential $\widetilde{U}$ has a linear correction in the porosity f, and since the interest is for *dilute* porous media, only the first order term is considered.

By comparing the last expression for the effective stress potential $\widetilde{U}_{LM}$ with the corresponding expression provided by the homogenization methods in relation (2.24), it is easily deduced that

$$h(X_{\Sigma}) = \frac{1}{f}(\widehat{h}(X_{\Sigma}) - 1). \tag{3.27}$$

Then, Lee and Mear define a scalar function $P(X_{\Sigma})$, which is directly related to the dilatational rate defined in relation (3.19) by

$$P = \frac{1}{n+1} \frac{\partial h}{\partial X_{\Sigma}} = \frac{\overline{D}_{\alpha\alpha}}{f D_{eq}^{\infty}} \Rightarrow \frac{\dot{\mathcal{V}}_2}{\dot{\gamma} \, \mathcal{V}_2} = \frac{P}{\sqrt{3}}, \quad \alpha = 1, 2, \tag{3.28}$$

where D_{eq}^{∞} denotes the remote equivalent strain-rate in the absence of voids. In addition to the dilatational part of the macroscopic strain-rate, it is useful to study, as well, the deviatoric part of $\overline{\boldsymbol{D}}$. For this reason, Lee and Mear have defined the scalar function $Q(X_{\Sigma})$, which is directly related to the equivalent part of the macroscopic strain-rate $\overline{D}_{eq}$, defined in (3.7), such that

$$Q = h - X_{\Sigma} \, P = \frac{\overline{D}_{eq} - D_{eq}^{\infty}}{f \, D_{eq}^{\infty}}. \tag{3.29}$$

Making use of the last two expressions, we will be able to compare the estimates obtained by the "second-order" and the "variational" method with the "exact" numerical results of Lee and Mear (1992b) in the dilute limit.

In addition to the aforementioned analysis associated with the initial response of a dilute porous solid subjected to plane-strain loading conditions, Lee and Mear (1999) have also studied the evolution of microstructure in dilute porous viscoplastic composites subjected to the loading conditions described previously in relation (3.25). Thus, it is also relevant to compare the corresponding "second-order" estimates with the Lee and Mear (1999) predictions for the evolution of microstructure.

It is important to remark here that the authors have adopted the approximation that the void evolves through a sequence of elliptical shapes (see also Fleck and Hutchinson, 1986) during the deformation process for all nonlinearities considered. As already known, Eshelby (1957) has shown that in the context of linear porous materials, the shape of the void remains elliptical during the loading procedure. However, for nonlinear materials, the fields in the inclusions are non-uniform and thus the shape of the pores becomes in general non-elliptical. Note that in the homogenization procedures, described in the previous chapters, we make use of the average fields in the vacuous phase to compute an average *elliptical* shape for the void. On the other hand, in the technique proposed by Lee and Mear, the authors make use of information about the local velocity field provided by the stream function to compute an approximate *elliptical* void shape. More specifically, for an elliptical void with principal semi-axes a_1 and a_2 oriented at an angle ψ, as shown in Fig. 3.1, that deforms through a sequence of elliptical shapes, the velocity component normal to the void surface is given as (Fleck and Hutchinson, 1986)

$$v_\eta = \dot{\psi}(x_1\, N_2 - x_2\, N_2) + \frac{\dot{a_1}}{a_1}\, x_1\, N_1 + \frac{\dot{a_2}}{a_2}\, x_2\, N_2, \tag{3.30}$$

where N_i are the components of the unit normal to the surface of the void in the x_i system. Then, the quantities, $\dot{a_1}/a_1$, $\dot{a_2}/a_2$ and $\dot{\psi}$ are determined by three equations obtained from (3.30) by evaluating v_η (obtained from the numerical minimization of the effective stress potential (3.21)) at three points on the void boundary (e.g., the points corresponding to $\psi = 0^o$, 45^o and 90^o). Obviously, such a procedure is not the same as computing the aspect ratio of the void by making use of the average strain-rate in the vacuous phase, which is the case in the homogenization theories described in the previous chapter.

In summary, Lee and Mear (1992b) have proposed a more general stream function by making use of elliptical coordinates. In the limit that the cross-section of the void becomes circular this procedure is similar to the one followed by Budiansky et al. (1982) in the context of cylindrical voids. In addition, by making use of the above described methodology, they were able to provide results for the evolution of the microstructure under plane-strain loading conditions. These results will be compared with corresponding results obtained by the homogenization procedures, described in the previous chapter, as well as with finite element results which are discussed later in this chapter.

3.2.4 Spheroidal voids using spheroidal coordinates

This section deals with the work of Lee and Mear (1992c), who extended the previous study for cylindrical voids to porous materials consisting of spheroidal voids subjected to axisymmetric loading conditions aligned with the pore symmetry axis by making use of prolate or oblate spheroidal coordinates. In this connection, it is convenient to use the notation introduced in subsection 2.2.1 for

the description of the microstructural variables. Thus, for spheroidal voids, the corresponding aspect ratios are defined by $w_1 = a_3/a_1$ and $w_2 = a_3/a_1$, with $a_1 = a_2$. This implies that the voids can be either prolate, with aspect ratios $w_1 = w_2 > 1$, or oblate $w_1 = w_2 < 1$. The effective stress potential is given by the same expression (3.20) as in the two-dimensional case, such that

$$\widetilde{U}(\overline{\boldsymbol{\sigma}}) = U(\overline{\boldsymbol{\sigma}}) + f\,\frac{\delta\widetilde{U}}{\delta f}, \quad \frac{\delta\widetilde{U}}{\delta f} = \frac{1}{\mathcal{V}_2}\int_{\mathcal{V}_1}[U(\boldsymbol{\sigma}) - U(\overline{\boldsymbol{\sigma}})]\,d\mathcal{V} - U(\overline{\boldsymbol{\sigma}}), \tag{3.31}$$

where $\mathcal{V}_2$ and $\mathcal{V}_1$ are the regions occupied by the void and the matrix phase, while U denotes the stress potential of the matrix phase and is given by relation $(2.23)_1$. Similar to the two-dimensional case presented previously, expression (3.31) implies that the effective stress potential $\widetilde{U}$ of the porous solid has a linear correction in the concentration of the voids, i.e., the porosity f. However, we will see in the following subsection that such an expansion may have a very small range of validity for very nonlinear solids and particularly for ideally-plastic solids where such an expansion may not be valid at all (see Duva and Hutchinson, 1984). In any case, the above correction term $\delta\widetilde{U}/\delta f$ can be directly related to the minimum principle, defined previously in the context of relation (3.4), through the relation (3.21) (Duva and Hutchinson, 1984; Lee and Mear, 1992b), which takes the form

$$\frac{\delta\widetilde{U}}{\delta f} = W(\boldsymbol{D}^{\infty}) - \frac{\mathcal{F}_{\min}}{\mathcal{V}_2}, \tag{3.32}$$

for the case of spheroidal voids.

The next step in this procedure involves the definition of a stream function in terms of spheroidal coordinates (η, θ, ϕ). Then, the physical components of the velocity field $\widetilde{\mathbf{v}}$, defined by relation (3.5), are given for prolate voids by

$$\widetilde{v}_\eta = \frac{\alpha^2}{\mathcal{H}}\left\{\frac{A}{\sinh\eta} + \sum_{k=2,4,\ldots}\sum_{m=0,1,\ldots} k(k+1)\,B_{km}\,Q_m(\cosh\eta)\,P_k(\cos\theta)\right\} \tag{3.33}$$

and

$$\widetilde{v}_\theta = -\frac{\alpha^2}{\mathcal{H}}\sum_{k=2,4,\ldots}\sum_{m=1,2,\ldots} m(m+1)\,B_{km}\,Q_m(\cosh\eta)\,P_k(\cos\theta). \tag{3.34}$$

In turn, for oblate voids, the components of $\widetilde{\mathbf{v}}$ are chosen as

$$\widetilde{v}_\eta = \frac{\alpha^2}{\mathcal{H}}\left\{\frac{A}{\cosh\eta} + \sum_{k=2,4,\ldots}\sum_{m=0,1,\ldots} k(k+1)\,\mathrm{i}^{m+1}\,B_{km}\,Q_m(\mathrm{i}\sinh\eta)\,P_k(\cos\theta)\right\} \tag{3.35}$$

and

$$\widetilde{v}_\theta = -\frac{\alpha^2}{\mathcal{H}}\sum_{k=2,4,\ldots}\sum_{m=1,2,\ldots} m(m+1)\,\mathrm{i}^{m+1}\,B_{km}\,Q_m(\mathrm{i}^{m+1}\sinh\eta)\,P_k(\cos\theta). \tag{3.36}$$

In these relations,

$$\mathcal{H} = \begin{cases} \alpha\,(\sinh^2\eta + \sin^2\theta)^{1/2}, & \text{prolate voids} \\ \alpha\,(\cosh^2\eta - \sin^2\theta)^{1/2}, & \text{oblate voids,} \end{cases} \tag{3.37}$$

α is a scaling factor related to the distance from the origin to the foci of the spheroidal void, P_k are the associated Legendre functions of order one, Q_m are the associated Legendre functions (of the second kind) of order one, $\mathrm{i} = \sqrt{-1}$ is the imaginary unity, and the constants $\{A, B_{km}\}$ are the

amplitude factors with respect to which $\mathcal{F}$ (see relation (3.4)) must be minimized. It is remarked at this point that because of the symmetry of the microstructure and the axisymmetric loading, the velocity fields $\widetilde{\mathbf{v}}$ do not depend on the third coordinate ϕ. Note that if the void was ellipsoidal or misaligned with the principal loading directions, the above procedure would become too complicated, and so far there are no results for those more general cases. This is because this procedure is based on the construction of a stream function, which is a technique that is used mainly in two-dimensional problems, or three-dimensional problems with certain symmetries.

In the following, we recall the boundary conditions used by Lee and Mear (1992c) to solve the above described problem. The loading is axisymmetric about the 3−axis, such that the only non-zero components of the stress tensor are

$$\sigma_{11}^{\infty} = \sigma_{11}^{\infty} = T^{\infty}, \quad \sigma_{33}^{\infty} = S^{\infty}. \tag{3.38}$$

The stress triaxiality may be defined by

$$X_{\Sigma} = \frac{\overline{\sigma}_m}{\overline{\sigma}_{eq}}, \tag{3.39}$$

where $\overline{\sigma}_m = (S^{\infty} + 2\,T^{\infty})/3$ and $\overline{\sigma}_{eq} = |S^{\infty} - T^{\infty}|$.

In this regard, it is essential to analyze the relevant dilatation and deviatoric quantities introduced by Lee and Mear (1992c). In particular, the Lee and Mear (LM) effective stress potential can be written similarly to the two-dimensional case, so that it takes the form

$$\widetilde{U}_{LM}(\overline{\boldsymbol{\sigma}}) = (1 + f h(X_{\Sigma}))\, \frac{\dot{\varepsilon}_o\, \sigma_o}{n+1} \left(\frac{\overline{\sigma}_{eq}}{\sigma_o} \right)^{n+1}. \tag{3.40}$$

By comparing the last expression for the effective stress potential with the corresponding expression provided by the homogenization methods, in relation (2.26), it is easily deduced that

$$h(X_{\Sigma}) = \frac{1}{f}(\widehat{h}(X_{\Sigma}) - 1). \tag{3.41}$$

Then, Lee and Mear defined a scalar function $P(X_{\Sigma})$, which is directly related to the dilatational rate of the void, defined by

$$P = \frac{1}{n+1} \frac{\partial h}{\partial X_{\Sigma}} = \frac{\overline{D}_{ii}}{f D_{33}^{\infty}}, \quad i = 1, 2, 3. \tag{3.42}$$

Here, D_{33}^{∞} is the axial component of the remote strain-rate field in the absence of voids. In addition to the dilatational part of the macroscopic strain-rate, it is useful to study, as well, the deviatoric part of $\overline{\boldsymbol{D}}$. For this reason, Lee and Mear have defined the scalar function $Q(X_{\Sigma})$, which is directly related to the axial component of the deviatoric macroscopic strain-rate $\overline{D}_{33}^{\prime}$, such that

$$Q = h - X_{\Sigma}\, P = \frac{\overline{D}_{33}^{\prime} - D_{33}^{\infty}}{f\, D_{33}^{\infty}}, \tag{3.43}$$

where the prime is used to denote the deviatoric part of $\overline{\boldsymbol{D}}$. Making use of the last two expressions, we are able to compare the estimates obtained by the "second-order" and the "variational" method with "exact" numerical results in the dilute limit. Note that the above quantities P and Q depend also on the microstructural variables, such as the aspect ratios $w_1 = w_2$. Relevant comparisons between the

homogenization methods and the numerical results of this section will also be made in a following chapter.

In addition to the aforementioned analysis associated with the initial response of a dilute porous solid subjected to axisymmetric loading conditions, Lee and Mear (1994) have also studied the evolution of microstructure in dilute porous viscoplastic composites subjected to the loading conditions described previously by relation (3.38). Thus, it is also relevant to compare the corresponding homogenization estimates, described in the previous chapter, with the corresponding Lee and Mear predictions for the microstructure evolution. However, in order to determine the evolution of the pore shape, Lee and Mear have idealized the nonlinear problem by allowing the voids to remain spheroidal during the deformation process. As already explained in the previous subsection, this approximation is different than the one described in the context of the homogenization theories, where the objective is to compute an *average void shape* by making use of the average fields in the vacuous phase. As we will see in a following chapter, this idealization proposed by Lee and Mear could lead to inaccurate estimates for the evolution of the microstructural variables, including the evolution of porosity.

In summary, Lee and Mear (1994) have proposed a velocity field based on a stream function by making use of spheroidal coordinates. In the limit that the void becomes spherical this procedure is identical to the one followed by Budiansky et al. (1982) in the context of spherical voids. However, it is emphasized that this procedure is limited to spheroidal voids and axisymmetric loading conditions aligned with the pore symmetry axis. Moreover, it is based on the assumption that the effective stress potential has a linear correction in the porosity in the dilute limit. An attempt to comment on the validity of this expansion is performed in the following subsection.

3.2.5 Validity of the dilute expansion

In this section, we discuss the validity of the expansion proposed by Budiansky et al. (1982) and then used by many authors such as Duva and Hutchinson (1984), Fleck and Hutchinson (1986) and Lee and Mear (1992b). As already mentioned in the context of relation (3.20), the computation of the effective potential $\widetilde{U}$ for the porous material is based on a linear (regular) expansion in the porosity as $f \to 0$. In order to check this expansion, it is convenient to consider the analytical result obtained when a CSA or CCA (Composite-Sphere or Composite-Cylinder Assemblage) is subjected to purely hydrostatic pressure. In this case, the effective stress potential $\widetilde{U}$ can be computed analytically and is given by relations (2.195) and (2.196). In the case that $f \to 0$, a regular Taylor expansion for $\widetilde{U}$ about $f = 0$ leads to the following result

$$\widetilde{U}_{w=1}(\overline{\sigma}_m;\, f) \sim \frac{\dot{\varepsilon}_o\, \sigma_o\, n^{-n}}{n+1}\, f\, (1 + n\, f^{\frac{1}{n}} + \mathrm{o}(f^{\frac{1}{n}}))\left(\frac{3}{2}\frac{|\overline{\sigma}_m|}{\sigma_o}\right)^{n+1}. \tag{3.44}$$

In relation (3.44), the expansion is valid only if the second term $n\, f^{\frac{1}{n}}$ is smaller than the first term which is linear in f. It is obvious that as n becomes large the second term in the expansion is comparable to the first term. Hence, the range of validity of this expansion is expected to diminish to zero for high values of n. This puts into question the validity of the above discussed dilute estimates

in the limit as $n \to \infty$ for purely hydrostatic loading.

Perhaps at this point, it is interesting to note that the corresponding hydrostatic result of the "variational" method (see relation (2.197)) does not have a linear dependence on f in the dilute limit. In fact, as $f \to 0$, the corresponding "variational" result is of the form

$$\widetilde{U}^{var}_{w=1}(\overline{\sigma}_m;\, f) \sim \frac{\dot{\varepsilon}_o\, \sigma_o}{n+1}\, f^{\frac{n+1}{2}}\, (1 + f + \mathrm{o}(f)) \left(\frac{3}{2}\frac{|\overline{\sigma}_m|}{\sigma_o}\right)^{n+1}. \tag{3.45}$$

This result implies that the "variational" estimate approaches zero faster than linear and is thus in contrast with the analytical shell result. On the other hand, the "second-order" method is constructed such that it recovers the analytical shell result and therefore is consistent with the analysis made in relation (3.44).

3.2.6 Brief Summary

In summary, we described a set of methods developed in the context of dilute porous media. First, we have discussed the technique of Budiansky et al. (1982) which is based on a choice of a stream function to generate trial velocity fields for a dilute porous medium with initially spherical inclusions subjected to axisymmetric loading conditions. These trial fields are then used to minimize a suitably constructed dissipation potential. This methodology has then been extended to cylindrical voids with elliptical cross-section by Fleck and Hutchinson (1986) and Lee and Mear (1992b), as well as to spheroidal voids subjected to axisymmetric loading conditions (aligned with the pore symmetry axis). All these methods, however, are based on a choice of a stream function, and as a consequence their generalization to more complicated microstructures and loadings is not straightforward.

In addition, the stream function is chosen by using an eigen-function sequence. The number of terms that need to be used in this sequence depends on the nonlinearity of the matrix phase, as well as the stress triaxiality. It is worth noting here that Huang (1991b) has shown that as the nonlinear exponent n and the stress triaxiality increases a very large number of terms in this sequence (see for example (3.23)) is needed for the accurate estimation of the dilatational rate (e.g., (3.19)). This need for a large number of amplitude factors may be explained by the fact that the stress potential of the porous medium is assumed to have a linear correction in the porosity in the dilute limit. The range of validity of this dilute expansion, however, has been shown to diminish to zero for purely hydrostatic loading and large values of the nonlinear exponent n. Therefore, the numerical solution of the minimization problem in (3.4) is expected to become very sensitive at high nonlinearities and stress triaxialities. Note that the accurate prediction of the dilatation rate in dilute porous media constitutes an important measure of cavitation instabilities in solids (Huang et al., 1991a).

Nonetheless, the above-mentioned limitations do not eliminate the usefulness of such methods, which will be used in the following chapters to compare with the corresponding homogenization methods, described in chapter 2, for the case of dilute porous media. More specifically, comparisons will be made for the determination of the instantaneous behavior and the evolution of microstructure in dilute viscoplastic porous media consisting of cylindrical voids with elliptical cross-section subjected to plane-strain loadings, as well as of spheroidal voids subjected to axisymmetric loading conditions aligned with the pore symmetry axis.

3.3 Gurson-type generalized models

In this section, we discuss several extensions of the Gurson model that have been proposed over the years, to account for more general constitutive behaviors and porosity distributions. Partially inspired by the work of Lee and Mear (1992c, 1994), Gologanu et al. (1993,1994,1997) provided analytical expressions for the effective yield function of porous solids with ideally-plastic matrix phase by considering a spheroidal hollow shell (the spheroidal void is confocal with the external boundary of the shell) subjected to axisymmetric loadings, such that the spheroidal symmetry is preserved during the deformation process. Leblond et al. (1994) and Flandi and Leblond (2005) later extended these models to the more general case of viscoplastic porous materials. In a separate work, Gărăjeu et al. (2000) studied the case of an initially spherical void embedded in a cylindrical or spherical shell subjected to axisymmetric loading conditions. In this study, they also compared the difference between the two different shells. Recently, Monchiet et al.(2007) have proposed a model for isotropic porous materials by making use of an Eshelby-like trial velocity fields. In this work, we will provide a brief discussion of the latest Flandi and Leblond (2005) model, which will be used later to compare with the homogenization methods of the previous chapter.

Building on the work of Gologanu et al. (1993,1994,1997), Flandi and Leblond (2005) consider a spheroidal shell containing a confocal spheroidal void. In their analysis they made use of spheroidal coordinates, where they proposed trial velocity fields in order to approximate the effective stress potential of the porous material. Their trial velocity fields are based on an exact solution that can be achieved under certain axisymmetric loading conditions (see relevant work for further details). In fact, these axisymmetric loading conditions reduce to purely hydrostatic loading conditions in the limiting case of a spherical void.

In particular, two types of spheroids were considered: prolate ($w_1 = w_2 > 1$) and oblate ($w_1 = w_2 < 1$). Of course the case of $w_1 = w_2 = 1$ corresponds to a spherical void and is included as a limiting case. In addition, the applied loading is axisymmetric such that the spheroidal symmetry of the problem is preserved. In other words, by setting $w_1 = w_2 = w$, the spheroidal symmetry is preserved only if the non-zero components of the stress tensor are $\overline{\sigma}_{11} = \overline{\sigma}_{22}$ and $\overline{\sigma}_{33}$. Corresponding expressions defining the effective stress potential are given in the works by Flandi and Leblond (2005) and they will not be repeated here in detail. Nonetheless, for completeness, we include the effective yield criterion for a porous solid with ideally-plastic matrix phase, such that

$$\widetilde{\Phi}_{FL}(\overline{\boldsymbol{\sigma}}) = \frac{C}{\sigma_o^2}(\overline{\sigma}_{33} - \overline{\sigma}_{11} + \eta\,\overline{\sigma}_h) + 2\,q\,(g+1)(g+f)\cosh\left(\kappa\frac{\overline{\sigma}_h}{\sigma_o}\right) - (g+1)^2 - q^2(g+f)^2 = 0,$$
$$\overline{\sigma}_h = 2\alpha_2\overline{\sigma}_{11} + (1-\alpha_2)\overline{\sigma}_{33}. \tag{3.46}$$

In the last expression, $C = C(f,w)$, $\eta = \eta(f,w)$, $\alpha_2 = \alpha_2(w)$, $g = g(w)$ and $\kappa = \kappa(f,w)$. The above yield criterion reduces to the Gurson (1977) model in the case of purely hydrostatic loading and the "variational" method (Ponte Castañeda, 1991) for isochoric loadings. Furthermore, in expression (3.46), q is equivalent to the "q_1" parameter introduced by Tvergaard (1981) and Gurson (1977) to improve the predictions of their models with respect to numerical unit-cell results for periodic porous media. Thus, the value of $q = 1$ has been used by Flandi and Leblond for the case of a

spheroidal shell consisting of a confocal spheroidal void, whereas for a cylindrical shell, which is a rough approximation to a hexagonal shell (see Gărăjeu et al., 2000) containing a spheroidal void, the following expression has been proposed

$$q = 1 + (q_0 - 1)/\cosh S, \quad S = \ln w_1 = \ln w_2 = \ln w, \tag{3.47}$$

with $q_0 = 4/e \approx 1.47$ (Perrin and Leblond, 1990, 2000). Note that when $w = 1$ (i.e., for a spherical void), $q = q_0 = 1.47$. This value is consistent with the value of 1.5 initially proposed by Tvergaard (1981).

A first comment on expression (3.47) is that when $q_0 = 1$, the Flandi-Leblond model reproduces exactly the solution of the CSA and CCA of Hashin in the case of purely hydrostatic loading. In addition, it recovers the "variational" bound of Ponte Castañeda (1991) for purely isochoric loadings ($X_\Sigma = 0$). In this connection, this model is expected to be sufficiently accurate for the axisymmetric loadings, especially at high stress triaxialities. In contrast, for a cylindrical shell containing a spherical void, the choice $q_0 \neq 1$ is made. In this case, the resulting estimate for the effective behavior of the porous material is much softer than the CSA or CCA prediction, defined in relation (2.196), which is consistent with numerical periodic unit-cell calculations.

In summary, the above-defined effective yield function $\widetilde{\Phi}_{FL}$ depends on two microstructural variables, i.e., on the porosity f and the aspect ratio of the spheroidal voids w. For the special case of axisymmetric loading conditions aligned with the pore symmetry axis, this model has been validated against finite element calculations and has been found to deliver sufficiently accurate results for the evolution of the porosity and the aspect ratio in a wide range of stress triaxialities. However, the Flandi-Leblond model cannot be used, in general, for more complicated loading conditions such as combination of in-plane shear with superimposed pressure, because this would induce an ellipsoidal shape for the void with two different aspect ratios $w_1 \neq w_2$. In contrast, the "second-order" and the "variational" methods are based on a more rigorous homogenization procedure and thus are capable of handling general ellipsoidal microstructures and loading conditions, including the possible rotation of the anisotropy axes.

3.4 High-rank sequential laminates

In this section, we study a special class of nonlinear composites, known as "high-rank sequentially laminates", to estimate the effective behavior of isotropic viscoplastic porous media. In this context, we recall that the "second-order" and the "variational" estimates, discussed in the previous chapter, involve *two* approximations: the *linearization* of the nonlinear phases and the *homogenization* of the LCC (relation (2.170)). For the second approximation, use was made of the Willis (1998) estimates (2.171). These linear estimates are known (Frankfort and Mura, 1986; Milton, 2002) to be exact for composites with a special class of "sequentially laminated" microstructures. For this reason, *nonlinear* sequential laminates are particularly appropriate to assess the accuracy of the "second-order" method and, in general, of any LCC-based homogenization method (such as the "variational" method of Ponte Castañeda (1991)), on condition that the Willis estimates be used for the LCC. In

this section, exact results for this special class of *nonlinear* sequential laminates are provided.

A sequential laminate is an iterative construction obtained by layering laminated materials (which in turn have been obtained from lower-order lamination procedures) with other laminated materials, or directly with the homogeneous phases that make up the composite, in such a way as to produce hierarchical microstructures of increasing complexity (e.g., Milton, 2002). The *rank* of the laminate refers to the number of layering operations required to reach the final sequential laminate. Of the many possible types of sequential laminates, we restrict attention to porous sequential laminates formed by layering at every step a porous laminate with the matrix phase (denoted as phase 1).

Thus, a rank-1 laminate corresponds to a simple laminate with a given layering direction $\mathbf{n}^{(1)}$, with matrix and porous phases in proportions $1-f_1$ and f_1. In turn, a rank-2 laminate is constructed by layering the rank-1 laminate with the matrix phase, in a different layering direction $\mathbf{n}^{(2)}$, in proportions f_2 and $1-f_2$, respectively. Rank-M laminates are obtained by iterating this procedure M times, layering the rank-$(M-1)$ laminate with the matrix phase in the direction $\mathbf{n}^{(M)}$, in proportions f_M and $1-f_M$, respectively. A key point in this procedure is that the length scale of the *embedded* laminate is assumed to be much smaller than the length scale of the *embedding* laminate. This assumption allows to regard the rank-$(M-1)$ laminate in the rank-M laminate as a homogeneous phase, so that available expressions for the effective potential of simple laminates (e.g., deBotton and Ponte Castañeda, 1992) can be used at each step of the process to obtain an exact expression for the effective potential of the rank-M sequential laminate (e.g., Ponte Castañeda, 1992; deBotton and Hariton, 2002). From this construction process, it follows that the microstructure of these sequential laminates can be regarded as *random* and *particulate*, with phase 1 playing the role of the (continuous) matrix phase embedding the (discontinuous) porous phase. A distinctive feature of this very special class of porous materials is that the strain-rate and stress fields in the *inclusion* phase (in this case, the pores, denoted as phase 2) are uniform.

The effective stress potential of the resulting rank-M porous laminate can be shown to be (deBotton and Hariton, 2002; Idiart, 2006)

$$\widetilde{U}_M(\overline{\boldsymbol{\sigma}}) = \min_{\substack{w_j^{(i)} \\ \overline{\boldsymbol{\sigma}}^{(2)}=\mathbf{0}}} \sum_{i=1}^{M}(1-f_i)\left(\prod_{j=i+1}^{M} f_j\right) U^{(1)}\left(\overline{\boldsymbol{\sigma}}_i^{(1)}\right), \tag{3.48}$$

where $U^{(1)}$ is the matrix potential given by relation (2.23), and the average stress tensors in the matrix phase, $\overline{\boldsymbol{\sigma}}_i^{(1)}$ $(i=1,...M)$, and the pore phase, $\overline{\boldsymbol{\sigma}}^{(2)}$, are given by

$$\overline{\boldsymbol{\sigma}}_i^{(1)} = \overline{\boldsymbol{\sigma}} + f_i\ \mathbf{w}^{(i)} - \sum_{j=i+1}^{M}(1-f_j)\ \mathbf{w}^{(j)}, \tag{3.49}$$

$$\overline{\boldsymbol{\sigma}}^{(2)} = \overline{\boldsymbol{\sigma}} - \sum_{i=1}^{M}(1-f_i)\ \mathbf{w}^{(i)}. \tag{3.50}$$

In these expressions, the $\mathbf{w}^{(i)}$, $i=1,...,M$, are second-order tensors of the form

$$\mathbf{w}^{(i)} = w_1^{(i)}\ \mathbf{m}_1^{(i)}\otimes\mathbf{m}_1^{(i)} + w_2^{(i)}\ \mathbf{m}_2^{(i)}\otimes\mathbf{m}_2^{(i)} + w_3^{(i)}\ \mathbf{m}_1^{(i)}\otimes_s\mathbf{m}_2^{(i)}, \tag{3.51}$$

where $\mathbf{m}_1^{(i)}$ and $\mathbf{m}_2^{(i)}$ are two orthogonal vectors lying on the plane with normal $\mathbf{n}^{(i)}$, and $\otimes_s$ denotes the symmetric part of the outer product. The total porosity f in this rank-M laminate is given in

terms of the partial volume fractions f_i by

$$f = \prod_{i=1}^{M} f_i. \tag{3.52}$$

Thus, expression (3.48) requires the solution of a $3M$-dimensional convex minimization with respect to the scalar variables $w_\alpha^{(i)}$ $(i = 1, .., M,\ \alpha = 1, 2, 3)$, which, for a given set of f_i and $\mathbf{n}^{(i)}$ and macroscopic stress $\overline{\boldsymbol{\sigma}}$, can be solved numerically using standard numerical techniques. This minimization problem is constrained by the fact that the (uniform) stress in the porous phase $\overline{\boldsymbol{\sigma}}^{(2)}$, as given by (3.50), must be zero. This constraint (in the variables $w_j^{(i)}$) can be enforced in two different ways. One way is to enforce that the magnitude of the second-order tensor $\overline{\boldsymbol{\sigma}}^{(2)}$ be zero, in which case there is a single *non-linear* constraint, while a different, equivalent way is to enforce that each component of $\overline{\boldsymbol{\sigma}}^{(2)}$ be zero, in which case there are six *linear* constraints (see (3.50)). The latter approach has been found easier to implement and was therefore adopted in this work.

It is important to note that the effective behavior of the sequential laminates considered here, unlike that of typical nonlinear composites, does not depend on all the details of the microstructure, but only on partial information of it in the form of the volume fractions f_i and lamination directions $\mathbf{n}^{(i)}$. Of particular interest here are porous materials exhibiting overall *isotropic* symmetry. In general, the effective potential (3.48) will be anisotropic, even if the matrix potential is isotropic. However, appropriate lamination sequences, i.e., particular choices of f_i and $\mathbf{n}^{(i)}$, can be found such that the effective potential (3.48) tends to be isotropic as the rank M increases (deBotton and Hariton, 2002). To that end, the following lamination sequence has been adopted in this work:

$$f_i = \frac{1 - \frac{i}{M}\ (1 - f)}{1 - \frac{i-1}{M}\ (1 - f)}, \tag{3.53}$$

and

$$\mathbf{n}^{(i)} = \sin\psi_i \sin\phi_i\ \mathbf{e}_1 + \cos\psi_i \sin\phi_i\ \mathbf{e}_2 + \cos\phi_i\ \mathbf{e}_3, \tag{3.54}$$

where f is the prescribed porosity in the rank-M laminate, and the angles ψ_i and ϕ_i, which determine the i^{th} direction $(i = 1, ..., M)$ of lamination relative to a reference basis $\{\mathbf{e}_\alpha\}$, are given by

$$\begin{aligned} \phi_{j+kM_\eta} &= \arccos h_j, \quad h_j = 2\frac{j-1}{M_\eta - 1} - 1, \\ &\qquad j = 1, ..., M_\eta, \quad k = 0, ..., \eta - 1, \end{aligned} \tag{3.55}$$

$$\begin{aligned} \psi_{j+kM_\eta} &= \left(\psi_{j-1} + \frac{3.6}{\sqrt{M_\eta}}\frac{1}{\sqrt{1 - h_j^2}}\right) \bmod 2\pi, \\ &\qquad j = 2, ..., M_\eta - 1, \quad \psi_1 = \psi_{M_\eta} = 0. \end{aligned} \tag{3.56}$$

In these expressions, η and M_η are two integers such that the rank of the laminate is $M = \eta M_\eta$. The set of angles (3.55)-(3.56) corresponds to M_η lamination directions (3.54), uniformly distributed on the unit sphere (Saff et al., 1977), with η laminations for each direction. It has been verified numerically that, for this specific lamination sequence, the effective potential (3.48) becomes progressively less sensitive to the orientation of the principal axes of $\overline{\boldsymbol{\sigma}}$ as the parameters M_η and η increase, meaning that the effective potential tends to be more isotropic with increasing rank. The results provided in the next chapters correspond to $M = 1500$ with $M_\eta = 50$ and $\eta = 30$.

Finally, the macroscopic strain-rate is obtained by differentiating (3.48) with respect to $\overline{\boldsymbol{\sigma}}$. Noting that the expression is stationary with respect to the variables $w_j^{(i)}$, we have that

$$\overline{\boldsymbol{D}} = \sum_{i=1}^{M}(1-f_i)\left(\prod_{j=i+1}^{M} f_j\right)\frac{\partial U^{(1)}}{\partial \boldsymbol{\sigma}}\left(\overline{\boldsymbol{\sigma}}_i^{(1)}\right) + \boldsymbol{\lambda}^{(2)}, \tag{3.57}$$

where the second-order tensor $\boldsymbol{\lambda}^{(2)}$ is the optimal Lagrange multiplier associated with the traction-free constraint in (3.48). The expressions for the computation of the phase average quantities are not included here because they are too cumbersome to be shown here. However, a complete derivation of these results are given in the thesis of Idiart (2006).

In summary, the estimates obtained by the high-rank sequential laminates are very useful in the sense that they can be compared with the homogenization methods presented in the previous chapter and the Gurson-type models. This comparison is particularly pertinent in view of the fact that it has been recently shown (Idiart, 2007) that power-law, porous, sequential laminates with isotropic microstructures reproduce exactly the hydrostatic behavior of the composite-sphere assemblage, as described by expressions (2.196). Furthermore, as already stated in the beginning of the section, the linear estimates of Willis (1978) are exact for the high-rank sequential laminates. In this regard, comparing the "second-order" and the "variational" methods (which make use of the Willis estimates to solve the linear comparison composite) with the high-rank sequential laminates provides a good estimate for the accuracy of these homogenization theories.

3.5 *FEM* periodic solutions

One of the main objectives is to validate the "second-order" model for the case that the porous medium is subjected to large deformations. However, for reasons that have been explained in the introduction, it is extremely difficult to estimate numerically — with the finite element method (FEM) in this case — the effective behavior and the evolution of the underlying microstructure of a *random* porous material. On the other hand, it is feasible to solve the problem of a *periodic* porous material considering a unit-cell that contains a single void, as shown in Fig. 3.4. However, the random and the periodic material exhibit substantially different effective behavior except in the limit when the porosity is sufficiently small ($f \to 0$). As we will see later, for sufficiently small initial porosity, such as $f_o = 0.01\%$, the *periodic* unit-cell estimates, and thus the effective properties of the periodic composite, are independent of the prescribed tractions, velocities or periodic boundary conditions (Gilormini and Michel, 1998), which implies that the concentration of the voids is close to dilute. In this regard then, the comparison between the various models presented previously and the FEM calculations are meaningful provided that the porosity remains at low values during the deformation process. It is noted that for the FEM calculation use has been made of the commercial package Abaqus.

Note however, that in the special case of ideally-plasticity, the comparison between periodic and random porous media may not be meaningful. This is due to the possible formation of shear bands connecting the voids in the material. In this case, the interaction between the voids could be come

important even at very low porosities. To avoid these ill-conditioned cases, we will not perform comparisons between the homogenization and the FEM unit-cell results for porous solids with an ideally-plastic matrix phase.

3.5.1 Brief review of the theory for periodic composites

This subsection deals with the theoretical aspects of the periodic homogenization, where numerous studies have been performed over the past thirty years (Needleman, 1972; Sanchez-Palencia, 1974; Tartar, 1977; Bensoussan et al., 1983; Suquet, 1983; Bouchitte and Suquet, 1991). In those studies, the effective properties of the composite in the macroscopic scale are determined from geometrical and material data available from the study of a representative volume element (RVE) denoted as Ω. To make contact with the previous chapter, for random composites, these data are specified in terms of geometrical and material properties which are known only partially through $n-$point statistics, e.g., the volume fraction and the two-point correlation function (for particulate microstructure, the shape and orientation of the inclusions is also known). On the other hand, for periodic composites, the RVE is completely defined by the geometrical and material properties of a *unit-cell*, which generates by periodic repetition the whole microstructure of the composite. In this connection, the problem of estimating the effective behavior of the composite reduces in determining numerically the behavior of the unit-cell under appropriate boundary conditions to be discussed in the following.

Making use of the general definition (2.4), we introduce the effective stress potential $\widetilde{U}$ of a porous periodic medium by

$$\widetilde{U}(\overline{\boldsymbol{\sigma}}) = (1-f) \min_{\sigma \,\epsilon\, \mathcal{S}(\overline{\sigma})} \langle U(\boldsymbol{\sigma}) \rangle^{(1)}, \tag{3.58}$$

where U is the stress potential of the matrix phase, given by (2.23), $\langle \cdot \rangle^{(1)}$ denotes the volume average of a field over the matrix phase in the unit-cell and

$$\mathcal{S}\,(\overline{\boldsymbol{\sigma}}) = \{\boldsymbol{\sigma}, \mathrm{div}\boldsymbol{\sigma} = 0 \text{ in } \Omega,\ \langle \boldsymbol{\sigma} \rangle = \overline{\boldsymbol{\sigma}}, \quad \boldsymbol{\sigma}\,\mathbf{n} - \#\}, \tag{3.59}$$

is the set of statically admissible stresses that are compatible with the applied average stress $\overline{\boldsymbol{\sigma}}$. The abbreviated notation $\boldsymbol{\sigma}\,\mathbf{n} - \#$ has been used to denote that the traction is opposite in opposite sides of the RVE.

On the other hand, by using (2.9), the effective dissipation potential $\widetilde{W}$ of a periodic porous medium is defined by

$$\widetilde{W}(\overline{\boldsymbol{D}}) = \min_{\boldsymbol{D} \,\epsilon\, \mathcal{K}(\overline{\boldsymbol{D}})} = (1-f)\, \langle W(\boldsymbol{D}) \rangle^{(1)}, \tag{3.60}$$

where W is the dissipation potential of the matrix phase given by (2.23) and $\mathcal{K}(\overline{\boldsymbol{D}})$ is the set of kinematically admissible strain-rate fields given by

$$\mathcal{K}(\overline{\boldsymbol{D}}) = \left\{ \boldsymbol{D} \,|\, \boldsymbol{D} = \frac{1}{2}\left[\nabla \mathbf{v} + (\nabla \mathbf{v})^T\right] \text{ in } \Omega,\ \mathbf{v} = \overline{\boldsymbol{L}}\,\mathbf{x} + \mathbf{v}^* \text{ on } \partial\Omega,\ \mathbf{v}^* \,\# \right\}. \tag{3.61}$$

Here, $\overline{\boldsymbol{L}}$ is the macroscopic velocity gradient, while the macroscopic strain-rate $\overline{\boldsymbol{D}}$ and spin $\overline{\boldsymbol{\Omega}}$ are given by

$$\overline{\boldsymbol{D}} = \frac{1}{2}\left[\overline{\boldsymbol{L}} + \overline{\boldsymbol{L}}^T\right], \qquad \text{and} \qquad \overline{\boldsymbol{\Omega}} = \frac{1}{2}\left[\overline{\boldsymbol{L}} - \overline{\boldsymbol{L}}^T\right]. \tag{3.62}$$

In turn, $\mathbf{v}^*$ is a periodic velocity field in the sense that all the components of $\mathbf{v}^*$ take identical values on points of the boundary $\partial\Omega$ of the unit-cell, which are deduced by translation parallel to the invariance of the lattice.

As we will see in the following subsections, the above general definitions and boundary conditions are specialized for the case of a unit-cell containing a cylindrical void with initially circular cross-section subjected to plane-strain loading conditions, as well as to the case of a cylindrical unit-cell containing an initially spherical void subjected to axisymmetric loading conditions.

3.5.2 Plane-strain unit-cell: aligned loadings

First, we consider a unit-cell made up of a long cylindrical void with an initially circular cross-section in the plane $1-2$ subjected to plane-strain conditions, which implies that the problem is two-dimensional. The applied load is such that the principal axes of the void do not rotate around the $3-$axis, and thus the only non-zero components of the macroscopic stress tensor are

$$\overline{\boldsymbol{\sigma}} = \overline{\sigma}_{11}\,\mathbf{e}^{(1)} \otimes \mathbf{e}^{(1)} + \overline{\sigma}_{22}\,\mathbf{e}^{(2)} \otimes \mathbf{e}^{(2)}, \tag{3.63}$$

while the stress triaxiality is defined by

$$X_\Sigma = \frac{\overline{\sigma}_{11} + \overline{\sigma}_{22}}{\sqrt{3}\,|\overline{\sigma}_{11} - \overline{\sigma}_{22}|}. \tag{3.64}$$

Next, the unit-cell exhibits two orthogonal lines of symmetry, and thus it is sufficient to consider only one quarter of the unit-cell (Needleman, 1972; Suquet, 1987; Michel et al., 1999), as shown in Fig. 3.2. Now, consider that the quarter of the unit-cell occupies a region $0 \leq x_1 \leq a$ and $0 \leq x_2 \leq b$, where x_1 and x_2 are the coordinates in the $\mathbf{e}^{(1)}$ and $\mathbf{e}^{(2)}$ directions, respectively. This implies that the velocity field is expressed as $\mathbf{v} = \mathbf{v}(x_1, x_2)$. The applied boundary conditions must be periodic[†], as defined in (3.61), which implies that the upper and right side of the quarter of the unit-cell must remain straight during the deformation process (Suquet, 1987; Michel et al., 1999). This can be easily implemented by tying all the nodes of the right ($x_1 = a$) and top ($x_2 = b$) sides forcing them to move in parallel to a straight line. Concerning the left and bottom sides of the shell, symmetry boundary conditions are applied, i.e.,

$$v_1(0, x_2) = v_2(x_1, 0) = 0. \tag{3.65}$$

Finally, in order to apply a constant stress triaxiality loading, the components of the velocity at the top and right sides of the unit-cell need to be related at each step of the deformation process in such a way that the stress ratio $\overline{\sigma}_{11}/\overline{\sigma}_{22}$ remains constant and equal to its prescribed value. Nonetheless, this requires the construction of a subroutine which is not straightforward. On the other hand, we could make use of the fact that the porosity is small (i.e., $f_o = 0.01\%$) and thus apply constant stresses on the top and right side of the unit-cell, which would keep the stress triaxiality constant during the deformation process. It is important to emphasize that this trick cannot be used at finite porosities, such as $f_o \sim 5\%$. To ensure that the results presented in the following chapters correspond

[†]If the porosity is sufficiently small then the periodic boundary conditions and the uniform stress or strain boundary conditions deliver identical results as we will see in the following.

to the prescribed constant stress triaxiality, we compute the ratio $\overline{\sigma}_{11}/\overline{\sigma}_{22}$ at each instant in time and when this ratio deviates from its prescribed value by an error of 10^{-6}, the FEM calculation is terminated.

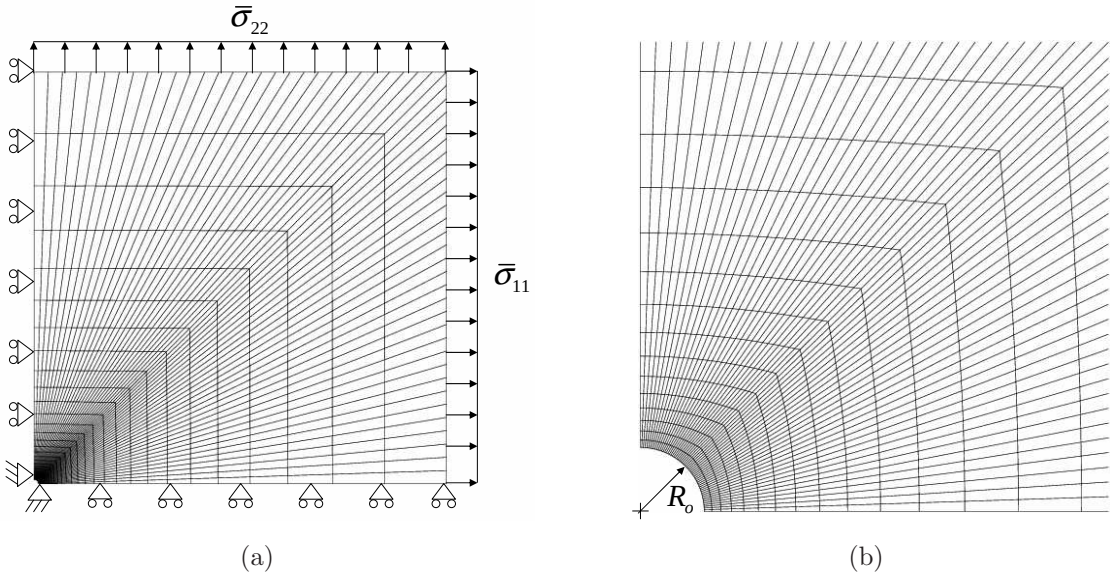

(a) (b)

Figure 3.2: Undeformed mesh for (a) plain-strain unit-cell, (b) the unit-cell near the void boundary.

Next, we describe the evaluation of the aspect ratio of the void and the porosity by making use of geometrical information provided by the FEM. More specifically, it is assumed for simplicity that the sides of the quarter specimen in Fig. 3.2 have a unit length, i.e., $a = b = 1$. Because of the geometry of the unit-cell, the radius R_o, shown in Fig. 3.2b, is computed by considering the fraction between the total surface of the unit-cell over the circular surface defined by the boundary of the void. Hence,

$$f_o = \frac{\pi R_o^2}{(2\,a) \times (2\,a)} \quad \rightarrow \quad R_o = \sqrt{\frac{4a^2 f_o}{\pi}}. \tag{3.66}$$

For convenience, Fig. 3.3 shows the boundary of the void, while on the circular segment certain nodes are shown schematically. Thus, the computation of the aspect ratio is achieved by considering the ratio of the x_2-coordinate of the node 61 over the x_1-coordinate of the node 1. It is emphasized at this point that the void is not expected to preserve an elliptical shape during the deformation process, especially in the case that the matrix phase is nonlinear. A more appropriate calculation would be to compute the average strain-rate in the void and then use equation (2.222) to determine the evolution of the aspect ratio. Such a computation has shown that in most of the cases (except in large compressive strains) the geometrical result, which makes use of the geometrical ratio of the coordinates of nodes 61 and 1, and the average result, which makes use of the average strain-rate in the void, are very close. In this regard, and for simplicity of the postprocessing of the FEM results, we will consider that the aspect ratio is given approximately by the geometrical definition.

In turn, for the evolution of porosity, we need to compute the sum of the surfaces occupied by the trapezoids produced by connecting two subsequent nodes as shown in Fig. 3.3. Then by dividing with the total surface we have the porosity at any deformed state. It is worth recalling that the surface of

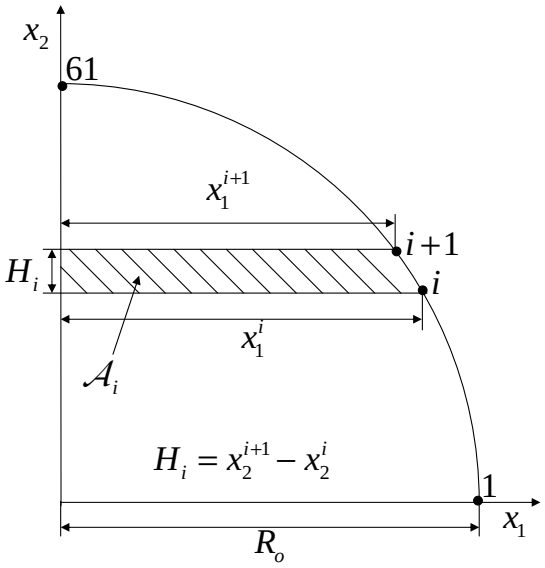

Figure 3.3: Void geometry in two-dimensions with initial radius R_o. The shaded region denotes a fraction of the total surface occupied by the void. The total surface of the void results by the sum of the surfaces of the trapezoidal shaded regions.

the trapezoid in the context of Fig 3.3 is given by

$$\mathcal{A}_i = \frac{x_1^i + x_1^{i+1}}{2}\,(x_2^{i+1} - x_2^i) \tag{3.67}$$

such that the porosity is

$$f = \frac{\sum_{i=1}^{60} \mathcal{A}_i}{\mathcal{A}_{tot}}, \tag{3.68}$$

where $\mathcal{A}_{tot}$ is the surface of the unit-cell, which can be computed by making use of the coordinates of the node that lies in the upper right corner of the cell (see Fig. 3.2).

3.5.3 Plane-strain unit-cell: simple shear loading

On the other hand, when the porous material is subjected to simple shear loading, the unit-cell does not have a line of symmetry. Thus, it is necessary to consider the whole unit-cell, as shown in Fig. 3.4. The reason for this is linked to the application of the loading condition, which is described next.

In this regard, consider that the the unit-cell occupies a region $0 \leq x_1 \leq a$ and $0 \leq x_2 \leq b$, where x_1 and x_2 are the coordinates in the $\mathbf{e}^{(1)}$ and $\mathbf{e}^{(2)}$ directions, respectively. Due to the loading, the principal axes of the void are expected to rotate around the out-of-plane axis $\mathbf{e}^{(3)}$, since during this deformation process an external macroscopic spin $\overline{\boldsymbol{\Omega}}$ is applied in the problem. In particular, consider a velocity gradient $\overline{\boldsymbol{L}}$ with the only non-zero component to be $\overline{L}_{12} = \dot{\overline{\gamma}}$, with $\dot{\overline{\gamma}}$ denoting the shear strain-rate. Consequently, the only non-zero macroscopic components of the strain-rate and spin tensors are

$$\overline{D}_{12} = \frac{1}{2}\,\dot{\overline{\gamma}}, \quad \overline{\Omega}_{12} = \frac{1}{2}\,\dot{\overline{\gamma}}. \tag{3.69}$$

The total applied shear strain is given by

$$\overline{\gamma} = \int_0^{t_f} \dot{\overline{\gamma}}\, \mathrm{d}t = 1. \tag{3.70}$$

Based on (3.61), the periodic boundary conditions in this case read as (see for example Needleman

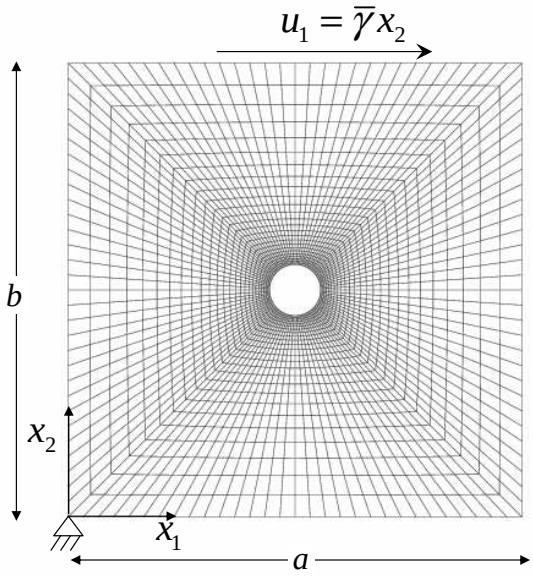

Figure 3.4: Undeformed unit-cell for simple shear loading conditions.

(1972), Suquet (1987), Michel et al. (1999))

$$\mathbf{v}(\mathbf{x}) = \overline{\boldsymbol{L}}\,\mathbf{x} + \mathbf{v}^*(\mathbf{x}), \tag{3.71}$$

where $\mathbf{v}^*(\mathbf{x})$ is a periodic velocity field that needs to be computed. However, the existing commercial packages can only provide solution for the original velocity field $\mathbf{v}$. For this reason, we define a reference point, which has a zero velocity (and displacement) $\mathbf{v}(0,0) = \mathbf{0}$ (see Aravas et al. (1995)). In the present study, the reference point is expediently chosen to be the lower left point (the axes origin). Then, by applying the periodicity condition of relation (3.71) in the left and right side of the specimen, we obtain the following conditions

$$\begin{aligned} v_i(a, x_2) &= \overline{L}_{i1}\, a + v_i^*(a, x_2), \\ v_i(0, x_2) &= \overline{L}_{i1}\, 0 + v_i^*(0, x_2). \end{aligned} \tag{3.72}$$

Then, subtraction of these two equations yields

$$v_1(a, x_2) - v_1(0, x_2) = \overline{L}_{11}\, a = 0, \quad v_2(a, x_2) - v_2(0, x_2) = \overline{L}_{21}\, a = 0. \tag{3.73}$$

Similar to the left and right sides, the same exactly procedure can be followed for the top and bottom sides, which yields the following relations

$$v_1(x_1, b) - v_1(x_1, 0) = \overline{L}_{12}\, b = \dot{\overline{\gamma}} b, \quad v_2(x_1, b) - u_2(x_1, 0) = \overline{L}_{22}\, b = 0. \tag{3.74}$$

The last four conditions together with the condition that $\mathbf{v}(0,0) = 0$ completely define the boundary conditions in the four sides of the unit-cell. It is worth noting here that for simple shear loading, we have considered an initial porosity $f_o = 1\%$, in order to have a sufficiently good mesh without the need for a large number of degrees of freedom. Moreover, because of the simple shear loading the porosity does not evolve in time and therefore, the error introduced by considering a "large" value for f_o does not get amplified during the deformation process.

In summary, the above-described unit-cells are used to compare the "second-order" and the "variational" methods with numerical finite element calculations in the context of plane-strain loading. Of course, this is not the ultimate test for these homogenization methods, however, it constitutes a significant tool to validate their estimates under several loading conditions.

3.5.4 Axisymmetric unit-cell

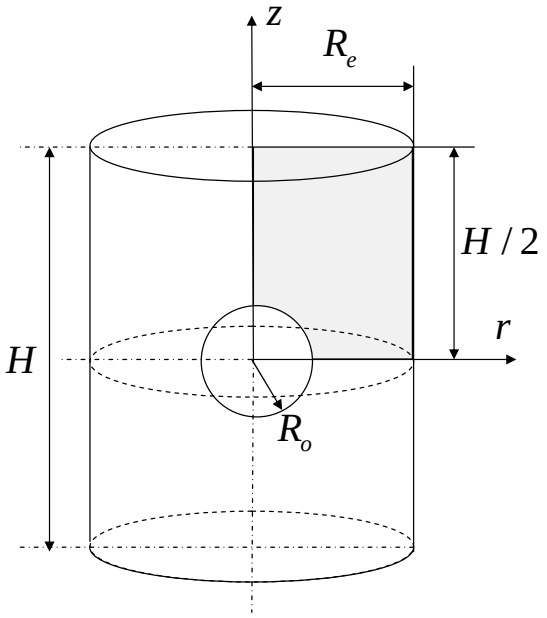

Figure 3.5: Cylindrical unit-cell with circular cross-section containing a spherical void.

In this subsection, following Bao et al. (1991), Needleman et al. (1999) and Gărăjeu et al. (2000), we consider a cylindrical cell of height H with circular cross-section of radius R_e that contains an initially spherical void of radius R_o, as shown in Fig. 3.5. This cell has been introduced as an approximation to a unit-cell of a periodic array of cylindrical cells with hexagonal cross-section. On the other hand, the applied load is axisymmetric, such that the only non-zero stress components are (see Fig. 3.6)

$$\overline{\boldsymbol{\sigma}} = \overline{\sigma}_{33}\, \mathbf{e}^{(3)} \otimes \mathbf{e}^{(3)} + \overline{\sigma}_{11}\, (\mathbf{e}^{(1)} \otimes \mathbf{e}^{(1)} + \mathbf{e}^{(2)} \otimes \mathbf{e}^{(2)}), \tag{3.75}$$

whereas the stress triaxiality is redefined as

$$X_\Sigma = \frac{\overline{\sigma}_{33} + 2\,\overline{\sigma}_{11}}{3\,|\overline{\sigma}_{33} - \overline{\sigma}_{11}|}. \tag{3.76}$$

In turn, the velocity field can be written in terms of a homogenous deformation and a periodic field $\mathbf{v}^*$, as defined in (3.61), such that

$$v_r(\mathbf{x}) = \overline{D}_{11}\, r + v_r^*(r,z), \quad v_\theta(\mathbf{x}) = 0, \quad v_z = \overline{D}_{33}\, z + v_z^*(r,z), \tag{3.77}$$

where r and z are polar coordinates introduced here for convenience.

Next, in order to approach the periodicity conditions met in the case of a cylindrical unit-cell with hexagonal cross-section, we apply the following boundary condition on the outer surface of the cylindrical unit-cell with circular cross-section:

$$v_r^*(R_e,z) = v_z^*(r,\pm H/2) = 0. \tag{3.78}$$

This implies that the unit-cell remains a cylinder with circular cross-section during the deformation process.

Note that due to the axisymmetric loading conditions and the symmetry of the unit-cell, the three-dimensional problem can be readily reduced to a two-dimensional problem, where only a cross-section (denoted with grey in Fig. 3.5) of the unit-cell needs to be considered. Then, it is convenient to introduce in-plane Cartesian coordinates x_1, x_3, such that the cross-section of the unit cell occupies a region $0 \leq x_1 \leq R_e$ and $0 \leq x_3 \leq H/2$. Then, the previous periodicity condition (3.78) can be easily implemented in ABAQUS by tying all the nodes of the right ($x_1 = R_e$) and upper ($x_3 = H/2$) side of the cross-section of the unit-cell (see Fig. 3.6) forcing them to move parallel to a straight line. On the other hand, for the left and bottom sides of the shell, symmetry boundary conditions are applied, i.e.,

$$v_1(0,x_3) = v_2(x_1,0) = 0. \tag{3.79}$$

Then, constant stresses are applied at the top and right sides of the unit-cell, whose ratio is determined by the specific choice of the stress triaxiality X_Σ. Similar to the two dimensional case, use is made of the fact that due to the small porosity considered (i.e., $f_o = 10^{-4}$), the aforementioned applied boundary conditions are appropriate in this case.

Next, the initial radius of the spherical void R_o can be computed in terms of the given porosity f_o by the following relation

$$f_o = \frac{4\,\pi R_o^3/3}{\pi\, R_e^2 * H} \quad \rightarrow \quad R_o = \left(\frac{3 f_o\, R_e^2\, H}{2}\right)^{1/3}. \tag{3.80}$$

In addition, it is useful to provide expressions for the computation of the aspect ratio and the porosity at each deformation state. For the computation of the aspect ratio, we adopt the same exactly procedure described previously, i.e., we compute w by considering the ratio x_3-coordinate of the node 61 over the x_1-coordinate of the node 1, as shown in Fig. 3.7. Note that because of the axisymmetric loading conditions and the symmetries of the problem, the initially spherical void will evolve into a spheroidal void, whose aspect ratios are equal ($w_1 = w_2 = w$).

In turn, for the evolution of porosity, we divide the volume of the void over the total volume of the cylindrical cell. The total volume of the void is equal to the sum of the independent volumes of

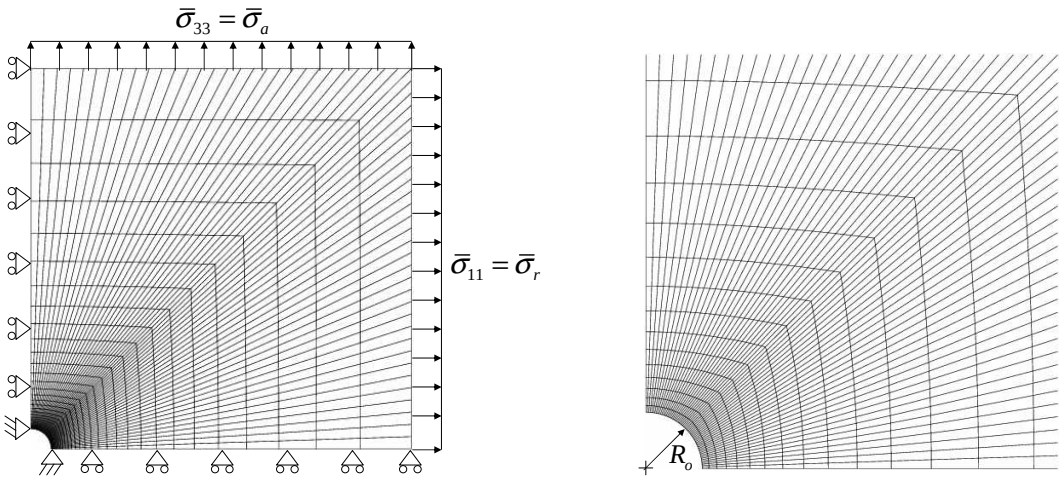

Figure 3.6: Undeformed mesh for (a) a cross-section of a cylindrical unit-cell, and (b) a cross-section of the unit-cell near the void boundary.

the truncated cones resulting from the revolution of the shaded regions around x_3-axis, as shown in Fig. 3.7. Thus, it is easily deduced that

$$\mathcal{V}_i = \pi \left(x_2^{i+1} - x_2^i\right) \frac{(x_1^i)^2 + (x_1^{i+1})^2 + x_1^{i+1}\, x_1^i}{3}, \tag{3.81}$$

such that the porosity is

$$f = \frac{\sum_{i=1}^{60} \mathcal{V}_i}{\mathcal{V}_{tot}}, \tag{3.82}$$

where $\mathcal{V}_{tot}$ is the volume of the cylindrical cell and can be computed by making use of the coordinates of the node that lies in the upper right corner of the cell (see Fig. 3.6).

In summary, the cylindrical unit-cell will be used in the following sections to provide estimates for porous media consisting of spheroidal voids. The "second-order" and "variational" methods, as well as the Flandi and Leblond (2005) model will be compared against the unit-cell FEM predictions, discussed in this section. On the other hand, in order to perform more general loading conditions, such as in-plane shear with superimposed pressure, it is necessary to consider a three-dimensional unit-cell, which complicates the calculations significantly. However, such calculations go beyond the goal of this study, and they will be possibly performed in the future.

3.6 Brief summary

In this chapter, we have made an attempt to summarize some of the many methods and models proposed over the last twenty years for viscoplastic porous materials. These models will be used to compare with the "second-order" and the "variational" methods presented in the previous chapter. It is worth emphasizing in this context that none of the methods presented in this chapter is complete enough to account for general ellipsoidal microstructures and loading conditions, in contrast with the

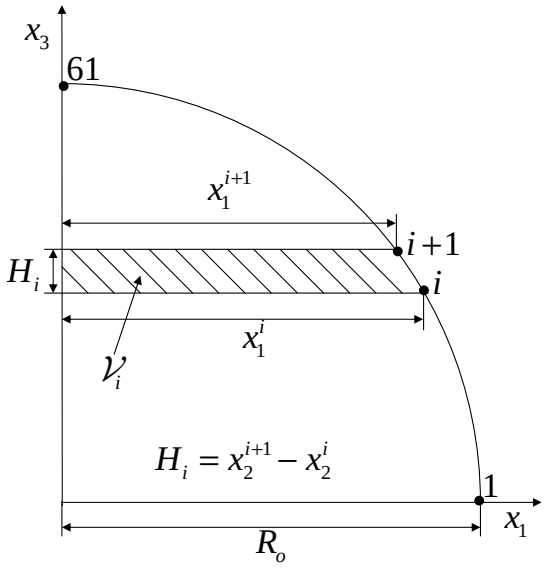

Figure 3.7: Void geometry in three-dimensions with initial radius R_o. The shaded region denotes a fraction of the total volume occupied by the spherical (or spheroidal) void. The total volume of the void is equal to the sum of the independent volumes of the truncated cones resulting from the revolution of the shaded regions around x_3-axis.

"second-order" and the "variational" methods, which are based on a general homogenization analysis and can handle general ellipsoidal pore shapes and loading condition including non-aligned loadings.

First, we discussed briefly a well-known model proposed by Gurson (1977), who made use of the exact solution for a shell (spherical or cylindrical cavity) under hydrostatic loadings, suitably perturbed, to obtain estimates for the effective behavior of ideally-plastic solids with isotropic or transversely isotropic distributions of porosity. This model has been used extensively during the last years. However, the main disadvantage of this model lies in the fact that it contains no information about the shape of the void and as we will see later, it becomes highly inaccurate at low and moderate stress triaxialities.

Next, we have presented the methodology proposed by Budiansky et al. (1982) in the context of *dilute* viscoplastic porous media consisting of spherical or cylindrical (with circular cross-section) voids, and later extended by Fleck and Hutchinson (1986) and Lee and Mear (1992b) for cylindrical voids with elliptical cross-section, as well as for spheroidal voids by Lee and Mear (1992c). This method is based on the minimum principle of velocities as stated by Hill (1956), as well as on a regular expansion of the effective stress potential of the porous medium in the dilute limit. In addition, this theory requires the choice of a stream function allowing the approximation of the actual field in terms of an approximate field consisting of a sum of linearly independent functions.

Although, this procedure is capable of extracting useful and interesting results for dilute porous materials, it may fail at very high nonlinearities and stress triaxialities. The reason for this is linked to the fact that, for purely hydrostatic loading, the expansion of the effective stress potential of a spherical shell becomes irregular in the ideally-plastic limit. A direct consequence of this result is that the range of validity of this expansion is expected to diminish to zero for high triaxiality loadings and

high nonlinearities. On the other hand, the need of this theory for a stream function poses limitations on the range of problems that can be solved. For example, it becomes too complicated to apply such a technique to estimate the effective behavior of dilute porous materials consisting of ellipsoidal voids that are subjected to general loading conditions.

In the sequel, we presented models that were inspired by the work of Gurson. Such models are numerous and is not possible to mention all of them here. In the context of this work, we have discussed briefly the studies of Gologanu et al. (1993,1994,1997), Leblond et al. (1994), Gărăjeu et al. (2000) and Flandi and Leblond (2005) (but see also Monchiet et al. (2007), Pellegrini (2002)). All of these models improve significantly on the Gurson model by being able to provide estimates for spheroidal voids subjected to axisymmetric loading conditions that are perfectly aligned with the pores symmetry axes. However, they are still not capable of handling more general ellipsoidal microstructures and loading conditions.

In a separate section, we have presented a special class of isotropic porous media with sequentially laminated microstructures for which the exact effective behavior may be computed. These materials have the distinctive feature of recovering the exact result for a shell under hydrostatic loading (Idiart, 2007), and they are in exact agreement with the Willis (1978) estimates in the linear case. For this reason, they constitute an excellent test case for the LCC-homogenization methods, such as the "second-order" and the "variational" methods considered in this study. Unfortunately, in the present work, those results are available only for isotropic and transversely isotropic porous media.

Finally, we have discussed the numerical evaluation of the effective behavior of porous materials generated by periodic repetition of unit-cells containing cylindrical (with circular cross-section) voids subjected to plane-strain loadings, as well as spherical voids subjected to axisymmetric loading conditions. Nonetheless, in order to be able to compare these numerical results for periodic porous materials with the homogenization procedures, described in the previous chapter, for random particulate porous media, it is necessary to consider a sufficiently small initial porosity so that the periodicity or the randomness of the microstructure does not affect the macroscopic response of the porous materials. Then, these unit-cells are subjected to finite deformations which has as a consequence the evolution of the underlying microstructure. Results obtained by the finite element method for the evolution of the microstructural variables (i.e., porosity, shape and orientation of the voids) as well as of the effective behavior of the porous medium will be compared with corresponding results obtained by the homogenization and the Gurson-type models described in the last two chapters.

Chapter 4

Instantaneous behavior: cylindrical voids

In the preceding chapters, we have described several homogenization and numerical models for determining the overall behavior and the evolution of the underlying microstructure in viscoplastic porous media subjected to finite deformations. In the present and subsequent chapters, these models will be used to study the behavior of porous media with specific microstructures.

In this chapter, we deal with the instantaneous response of porous materials consisting of aligned cylindrical voids in the 3−direction distributed randomly in an isotropic viscoplastic (or ideally-plastic) matrix phase subjected to plane-strain loading conditions (see Fig. 2.3). Specifically, we study the effect of the microstructure on the instantaneous response of the composite by making use of the "second-order" and the "variational" homogenization methods as well as numerical and analytical results presented briefly in the previous chapter.

For simplicity, we will consider in the rest of the chapter that the only non-zero in-plane components of the macroscopic stress tensor are $\overline{\sigma}_{11}$ and $\overline{\sigma}_{22}$, so that the equivalent and in-plane hydrostatic macroscopic stresses are defined by

$$\overline{\sigma}_{eq} = \frac{\sqrt{3}}{2}|\overline{\sigma}_{11} - \overline{\sigma}_{22}|, \quad \overline{\sigma}_m = \frac{\overline{\sigma}_{11} + \overline{\sigma}_{22}}{2}, \quad X_\Sigma = \frac{\overline{\sigma}_m}{\overline{\sigma}_{eq}}, \tag{4.1}$$

where X_Σ is the stress triaxiality defined in the context of two-dimensional, plane-strain problems.

4.1 General expressions

Before proceeding to the discussion of the results, it is useful to present first analytical expressions for the evaluation of the effective stress potential, as well as the macroscopic and phase average fields, as delivered by the "variational" and the "second-order" method. Because of the plane-strain loading, it is possible to extract analytical (or semi-analytical) expressions for the above mentioned quantities, which are presented in the following two subsections.

4.1.1 "Variational" estimates

As already discussed in the context of the "variational" method in section 2.5, the effective stress potential $\widetilde{U}_{var}$ of the porous material is given by (2.150), which is recalled here for completeness to

be

$$\widetilde{U}_{var}(\overline{\boldsymbol{\sigma}}) = (1-f)\,\frac{\dot{\varepsilon}_o\,\sigma_o}{n+1}\left(\frac{\hat{\sigma}_{eq}}{\sigma_o}\right)^{n+1} = (1-f)\,\frac{\dot{\varepsilon}_o\,\sigma_o}{n+1}\left[\frac{3\,\overline{\boldsymbol{\sigma}}\cdot\widehat{\mathbf{M}}\,\overline{\boldsymbol{\sigma}}}{(1-f)\,\sigma_o^2}\right]^{\frac{n+1}{2}}, \tag{4.2}$$

where f is the porosity, n is the nonlinear exponent of the matrix phase taking values between 1 (linear) and ∞ (ideally-plastic), while $\dot{\varepsilon}_o$ and σ_o denote a reference strain-rate and the flow stress of the matrix phase, respectively. The tensor $\widehat{\mathbf{M}}$ is related to the effective compliance tensor $\widetilde{\mathbf{M}}$ by (2.143), such that

$$\widehat{\mathbf{M}} = \mu\,\widetilde{\mathbf{M}}, \tag{4.3}$$

where μ is the shear modulus of the matrix phase in the LCC, defined by relation (2.167). It is important to note that $\widetilde{\mathbf{M}}$ is homogenous of degree -1 in μ, and hence, the tensor $\widehat{\mathbf{M}}$ and, consequently, the effective potential $\widetilde{U}_{var}$ are independent of μ.

Then, $\widetilde{\mathbf{M}}$, given by (2.85), reads

$$\widetilde{\mathbf{M}} = \frac{1}{1-f}\,\mathbf{M} + \frac{f}{1-f}\,\mathbf{G}, \quad \mathbf{G} = \mathbf{Q}^{-1} - \mathbf{M}, \quad \mathbf{M} = \frac{1}{2\,\mu}\,\mathbf{K}, \tag{4.4}$$

where $\mathbf{Q}$ is given by (2.59) for three-dimensional microstructures, $\mathbf{K}$ is the shear projection tensor given by (2.140), while the fourth-order tensor $\mathbf{G}$ has been introduced for convenience. It is interesting to note that for the case of cylindrical voids with elliptical cross-section distributed randomly in the plane, the tensor $\mathbf{Q}$, and thus $\mathbf{G}$ and $\widetilde{\mathbf{M}}$, can be evaluated analytically. In this connection, the tensor $\mathbf{G}$ can be expressed in terms of the shear modulus μ of the LCC, defined in relation (2.167), the in-plane aspect ratio w and the orientation angle ψ of the voids (see section 2.2.1 and Fig. 2.3) as follows:

$$\mathbf{G} = \frac{1}{2\,w\,\mu}\,\boldsymbol{\mathcal{G}}, \tag{4.5}$$

where the in-plane components of $\boldsymbol{\mathcal{G}}$ are given by

$$\begin{aligned} &\mathcal{G}_{1111} = w^2\,\cos(\psi)^2 + \sin(\psi)^2, \quad \mathcal{G}_{1122} = 0, \quad \mathcal{G}_{1112} = \frac{1}{2}\,(w^2-1)\sin(2\,\psi), \\ &\mathcal{G}_{2222} = \cos(\psi)^2 + w^2\,\sin(\psi)^2, \quad \mathcal{G}_{2212} = \mathcal{G}_{1112}, \quad \mathcal{G}_{1212} = 1 + w^2. \end{aligned} \tag{4.6}$$

In this last expression, use has been made of the fact that $\boldsymbol{\mathcal{G}}$ possesses both minor and major symmetry. In addition, by noting that the tensor $\mathbf{G}$ is homogeneous of degree -1 in μ, it follows from (4.3) and (4.4) that $\widehat{\mathbf{M}}$ can be expressed as

$$\widehat{\mathbf{M}} = \frac{1}{2(1-f)}\,\mathbf{K} + \frac{f}{2\,w\,(1-f)}\,\boldsymbol{\mathcal{G}}, \tag{4.7}$$

where the in-plane components of $\boldsymbol{\mathcal{G}}$ are given by (4.6).

Then, the macroscopic strain-rate $\overline{\boldsymbol{D}}$, defined by (2.153), is repeated here for completeness to be

$$\overline{\boldsymbol{D}} = \sqrt{3}\,\dot{\varepsilon}_o\left(\frac{3\,\overline{\boldsymbol{\sigma}}\cdot\widehat{\mathbf{M}}\,\overline{\boldsymbol{\sigma}}}{(1-f)\,\sigma_o^2}\right)^{\frac{n}{2}}\frac{\widehat{\mathbf{M}}\,\overline{\boldsymbol{\sigma}}}{\sqrt{\overline{\boldsymbol{\sigma}}\cdot\widehat{\mathbf{M}}\,\overline{\boldsymbol{\sigma}}}}. \tag{4.8}$$

On the other hand, the corresponding phase average strain-rate $\overline{\boldsymbol{D}}^{(2)}$ and spin $\overline{\boldsymbol{\Omega}}^{(2)}$ in the pore phase, are given by relations (2.154), such that

$$\overline{\boldsymbol{D}}^{(2)} = \frac{1}{\mu\,(1-f)}\,\widehat{\mathbf{Q}}^{-1}\,\overline{\boldsymbol{\sigma}}, \qquad \overline{\boldsymbol{\Omega}}^{(2)} = \overline{\boldsymbol{\Omega}} + \frac{1}{\mu}\,\boldsymbol{\Pi}\,\mathbf{L}\,\widehat{\mathbf{Q}}^{-1}\,\overline{\boldsymbol{\sigma}}, \tag{4.9}$$

with μ (see (2.149)) given by

$$\frac{1}{\mu} = \frac{3\,\dot{\varepsilon}_o}{\sigma_o^n}\left(\frac{3\,\overline{\boldsymbol{\sigma}}\cdot\widehat{\mathbf{M}}\,\overline{\boldsymbol{\sigma}}}{1-f}\right)^{\frac{n-1}{2}}. \tag{4.10}$$

In expression (4.9), $\overline{\boldsymbol{\Omega}}$ is the applied macroscopic spin and $\widehat{\mathbf{Q}}^{-1} = (\boldsymbol{\mathcal{G}}/w + \mathbf{K})/2$ from (4.4). On the other hand, the limit of incompressibility $\kappa \to \infty$ of the matrix phase in the LCC needs to be considered in the term $\boldsymbol{\Pi}\,\mathbf{L}$ of relation (4.9). This calculation is detailed in Appendix I.

Porous media with an ideally-plastic matrix phase. For the special case of ideally-plastic media ($n \to \infty$), the condition describing the effective yield surface is expressed in terms of the effective yield function $\widetilde{\Phi}_{var}$ (see (2.232)), via

$$\widetilde{\Phi}_{var}(\overline{\boldsymbol{\sigma}};\, f,\, w,\, \psi) = \sqrt{\frac{3\,\overline{\boldsymbol{\sigma}}\cdot\widehat{\mathbf{M}}\,\overline{\boldsymbol{\sigma}}}{1-f}} - \sigma_o = 0, \tag{4.11}$$

where the tensor $\widehat{\mathbf{M}}$ is given by (4.7). The macroscopic strain-rate $\overline{\boldsymbol{D}}$ is given by

$$\overline{\boldsymbol{D}} = \dot{\Lambda}\sqrt{\frac{3}{1-f}}\,\frac{\widehat{\mathbf{M}}\,\overline{\boldsymbol{\sigma}}}{\sqrt{\overline{\boldsymbol{\sigma}}\cdot\widehat{\mathbf{M}}\,\overline{\boldsymbol{\sigma}}}}, \tag{4.12}$$

where $\dot{\Lambda}$ is the plastic multiplier and needs to be determined by the consistency condition $\dot{\widetilde{\Phi}}_{var}$. A detailed discussion on the evaluation of $\dot{\Lambda}$ has been provided in sections 2.8.1 and 2.8.3 and is not repeated here. On the other hand, the phase average fields are given by relation (4.9), with μ given in terms of $\dot{\Lambda}$ by (2.257), recalled here to be

$$\frac{1}{\mu} = \frac{3\,\dot{\Lambda}}{(1-f)\,\sigma_o}. \tag{4.13}$$

The above expressions conclude the determination of the effective behavior, as well as of the phase average fields of the porous medium in the context of the "variational" method.

4.1.2 "Second-order" estimates

In this subsection, we present the corresponding expressions for the estimation of the effective stress potential, as well as the macroscopic strain-rate and the phase average fields, obtained by the "second-order" method, described in section 2.6.

In this connection, the effective stress potential $\widetilde{U}_{som}$ of the porous material is given by (2.183), which is repeated here for completeness:

$$\widetilde{U}_{som}(\overline{\boldsymbol{\sigma}}) = (1-f)\left[\frac{\dot{\varepsilon}_o\,\sigma_o}{1+n}\left(\frac{\hat{\sigma}_{eq}}{\sigma_o}\right)^{n+1} - \dot{\varepsilon}_o\left(\frac{\check{\sigma}_{eq}}{\sigma_o}\right)^{n}\left(\hat{\sigma}_{||} - \frac{\overline{\sigma}_{eq}}{(1-f)}\right)\right], \tag{4.14}$$

with

$$\hat{\sigma}_{eq} = \sqrt{\hat{\sigma}_{||}^2 + \hat{\sigma}_{\perp}^2}. \tag{4.15}$$

In these expressions, f is the porosity, n is the nonlinear exponent of the matrix phase taking values between 1 (linear) and ∞ (ideally-plastic), while $\dot{\varepsilon}_o$ and σ_o denote a reference strain-rate and the flow stress of the matrix phase, respectively.

For the evaluation of $\hat{\sigma}_{||}$ and $\hat{\sigma}_{\perp}$, given by (2.180), (2.181), we need to compute the effective compliance tensor $\widetilde{\mathbf{M}}$, the anisotropy ratio k of the matrix phase in the LCC and the reference stress tensor $\check{\boldsymbol{\sigma}}$.

Similar to the "variational" method, the effective compliance tensor $\widetilde{\mathbf{M}}$ is described by relation (4.4), with the $\mathbf{G}$ tensor given by

$$\mathbf{G} = \frac{1}{2\,w\,\sqrt{k}\,\mu}\,\boldsymbol{\mathcal{G}}, \tag{4.16}$$

where k is the anisotropy ratio of the matrix phase in the LCC, while $\boldsymbol{\mathcal{G}}$ is the same as in the "variational" method and is given by (4.6). Making use of the last result and restricting attention to aligned loadings (as described by (4.1)), the evaluation of the scalars $\hat{\sigma}_{||}$ and $\hat{\sigma}_{\perp}$, presented in relations (2.180) and (2.181), respectively, can be determined analytically (up to the unknown anisotropy ratio k), such that

$$\begin{aligned}\hat{\sigma}_{||} = \check{\sigma}_{eq} + \frac{\sqrt{6\,f\,\sqrt{k}}}{2(1-f)\sqrt{w}}\,\big[&(\overline{\sigma}_{11}^2+\overline{\sigma}_{22}^2)(1+w^2)+(\overline{\sigma}_{11}^2-\overline{\sigma}_{22}^2)(w^2-1)\cos(2\psi)+\\ &+2(\overline{\sigma}_{11}-\overline{\sigma}_{22}-(1-f)(\check{\sigma}_{11}-\check{\sigma}_{22}))^2\big]^{1/2},\end{aligned} \tag{4.17}$$

with $\check{\sigma}_{eq} = \sqrt{3}|\check{\sigma}_{11}-\check{\sigma}_{22}|/2$ and

$$\hat{\sigma}_{\perp} = \frac{\sqrt{6f}}{2(1-f)\sqrt{w\sqrt{k}}}\,\big[(\overline{\sigma}_{11}^2+\overline{\sigma}_{22}^2)(1+w^2)+(\overline{\sigma}_{11}^2-\overline{\sigma}_{22}^2)(w^2-1)\cos(2\psi)\big]^{1/2}. \tag{4.18}$$

In expressions (4.17) and (4.18), the anisotropy ratio k is the solution of the following nonlinear algebraic equation

$$k\,\left(\frac{\hat{\sigma}_{eq}}{\check{\sigma}_{eq}}\right)^{1-n} = (k-1)\,\frac{\hat{\sigma}_{||}}{\check{\sigma}_{eq}} + 1. \tag{4.19}$$

To complete the set of relations required for the complete evaluation of the effective stress potential, it is necessary to provide an expression for the reference stress tensor $\check{\boldsymbol{\sigma}}$. As already described in subsection 2.6.2, $\check{\boldsymbol{\sigma}}$ is defined by (2.202), such that

$$\check{\boldsymbol{\sigma}} = \xi\left(X_{\Sigma},\,\overline{\boldsymbol{S}};\,f,\,w,\,\psi,\,n\right)\overline{\boldsymbol{\sigma}}', \tag{4.20}$$

where $\boldsymbol{S} = \overline{\boldsymbol{\sigma}}'/\overline{\sigma}_{eq}$ (see (2.166)) and

$$\xi\left(X_{\Sigma},\overline{\boldsymbol{S}}\right) = \frac{1-t\,f}{1-f} + \alpha_m(\overline{\boldsymbol{S}})\,|X_{\Sigma}|\,\left(\exp\left[-\frac{\alpha_{eq}(\overline{\boldsymbol{S}})}{|X_{\Sigma}|}\right] + \beta\,\frac{X_{\Sigma}^4}{1+X_{\Sigma}^4}\right), \tag{4.21}$$

is a suitably chosen interpolation function. The coefficients t and β are prescribed in an ad-hoc manner to ensure the convexity of the effective stress potential at dilute concentrations and are detailed in Appendix III of chapter 2. In turn, the computation of the two factors $\alpha_m = \alpha_m(\overline{\boldsymbol{S}};f,w)$ and $\alpha_{eq}(\overline{\boldsymbol{S}};f,w,\psi)$ require an estimate for the effective response of the porous material subjected to hydrostatic loading conditions. The procedure for estimating these quantities has been detailed in subsection (2.6.2) in the general three dimensional case, while specific details for the two-dimensional microstructure considered in this chapter are presented in Appendix II.

In addition, the determination of the macroscopic strain-rate $\overline{\boldsymbol{D}}$, defined in (2.186) in the general context of three dimensional microstructures, has the same form in the case of cylindrical voids and

reads

$$\overline{D}_{ij} = (\overline{D}_L)_{ij} + (1-f)\, g_{mn} \frac{\partial \check{\sigma}_{mn}}{\partial \overline{\sigma}_{ij}}, \tag{4.22}$$

where $\overline{\boldsymbol{D}}_L$ is the macroscopic strain-rate in the LCC given by (2.187), such that

$$\overline{\boldsymbol{D}}_L = \widetilde{\mathbf{M}}\,\boldsymbol{\sigma} + \boldsymbol{\eta}, \qquad \text{with} \qquad \boldsymbol{\eta} = \dot{\varepsilon}_o \left(\frac{\check{\sigma}_{eq}}{\sigma_o}\right)^n - \mathbf{M}\,\check{\boldsymbol{\sigma}}, \tag{4.23}$$

where $\mathbf{M}$ is the compliance tensor of the LCC (see (2.167)) defined by

$$\mathbf{M} = \frac{1}{2\lambda}\,\mathbf{E} + \frac{1}{2\mu}\,\mathbf{F}, \qquad \mathbf{E} = \frac{3}{2}\,\overline{\boldsymbol{S}} \otimes \overline{\boldsymbol{S}}, \quad \mathbf{F} = \mathbf{K} - \mathbf{E}. \tag{4.24}$$

In turn, the second-order tensor $\boldsymbol{g}$, defined by (2.188) in the general context of three dimensional microstructures, can be shown to simplify to

$$g_{ij} = \left(\frac{1}{2\lambda} - \frac{1}{2\lambda_t}\right)\left(\hat{\sigma}_{||} - \frac{\overline{\sigma}_{eq}}{(1-f)}\right)\frac{\check{\sigma}_{ij}}{\check{\sigma}_{eq}}, \tag{4.25}$$

for the two-dimensional porous medium considered in this chapter. In (4.25), the scalars λ_t,λ and μ are given by

$$\lambda_t = \frac{\sigma_o}{3\,n}\left(\frac{\check{\sigma}_{eq}}{\sigma_o}\right)^{1-n}, \qquad \lambda = k\,\mu, \qquad \mu = \frac{\sigma_o}{3\,\dot{\varepsilon}_o}\left(\frac{\hat{\sigma}_{eq}}{\sigma_o}\right)^{1-n}. \tag{4.26}$$

On the other hand, the phase average quantities, $\overline{\boldsymbol{D}}^{(2)}$ and $\overline{\boldsymbol{\Omega}}^{(2)}$, are given by the corresponding expressions presented in section 2.6.3. For completeness, we recall these results here:

$$\overline{\boldsymbol{D}}^{(2)} = \frac{1}{f}\,\overline{D}_m\,\boldsymbol{I} + \mathbf{K}\left(\frac{1}{1-f}\mathbf{Q}^{-1}\,\overline{\boldsymbol{\sigma}} + \boldsymbol{\eta}\right), \tag{4.27}$$

and

$$\overline{\boldsymbol{\Omega}}^{(2)} = \overline{\boldsymbol{\Omega}}_L^{(2)} = \overline{\boldsymbol{\Omega}} + \boldsymbol{\Pi}\,\mathbf{L}\,\mathbf{Q}^{-1}\,\overline{\boldsymbol{\sigma}}. \tag{4.28}$$

In these expressions, $\mathbf{Q}^{-1} = \mathbf{G} + \mathbf{M}$ with $\mathbf{G}$ given by (4.16), $\mathbf{L} = \mathbf{M}^{-1}$ is the modulus tensor of the matrix phase in the LCC, given by (2.167), while the term $\boldsymbol{\Pi}\,\mathbf{L}$ requires the consideration of the incompressibility limit $\kappa \to \infty$ and is detailed in appendix I of this chapter.

Porous media with an ideally-plastic matrix phase. For the special case of ideally-plastic media ($n \to \infty$), the yield criterion may be expressed in terms of the effective yield function $\widetilde{\Phi}_{som}$, given by (2.266), via

$$\widetilde{\Phi}_{som}(\overline{\boldsymbol{\sigma}};\, \check{\boldsymbol{\sigma}}\, f,\, w,\, \psi) = \hat{\sigma}_{eq} - \sigma_o = 0, \tag{4.29}$$

where $\hat{\sigma}_{eq}$ is given by (4.15), while equation (4.19) for the anisotropy ratio k reduces to

$$(1-k)\,\hat{\sigma}_{||} - \check{\sigma}_{eq} = 0, \tag{4.30}$$

in the ideally-plastic limit. The reference stress tensor $\check{\boldsymbol{\sigma}}$ is given by the expression (4.20), while the computation of the factors α_m and α_{eq} are detailed in Appendix II.

Then, the macroscopic strain-rate $\overline{\boldsymbol{D}}$ is given in terms of the plastic multiplier $\dot{\Lambda}$ by

$$\overline{\boldsymbol{D}} = \dot{\Lambda}\,\frac{\partial \hat{\sigma}_{eq}}{\partial \overline{\boldsymbol{\sigma}}}. \tag{4.31}$$

The determination of $\dot{\Lambda}$ has been provided in sections (2.8.2) and 2.8.3 and is not repeated here. In turn, the phase average fields are given by relation (4.27) and (4.28), with μ given in terms of $\dot{\Lambda}$ by (2.275), which is recalled here for completeness to be

$$\frac{1}{\mu} = \frac{3\,\dot{\Lambda}}{(1-f)\,\sigma_o}. \tag{4.32}$$

In the following sections, we will make use of the aforementioned expressions to obtain estimates for the instantaneous effective behavior of porous media consisting of cylindrical voids that are subjected to plane-strain loading conditions.

4.2 Dilute estimates for transversely isotropic porous media

Results characterizing the behavior of dilute porous materials consisting of isolated cylindrical voids with circular cross-section subjected to plane-strain conditions are discussed in this section. In particular, the SOM and the VAR methods are compared with corresponding results obtained by the works of Fleck and Hutchinson (1986) (FH) and Lee and Mear (1992b) (LM), which have been discussed briefly in chapter 3.

Remark 4.2.1. However, before proceeding to the discussion of the results it is important to recall some observations made in the context of section 3.2, where the dilute methods of Fleck and Hutchinson (1986) and Lee and Mear (1992b) have been discussed. More specifically, these methods are based on a dilute expansion of the effective stress potential, as well as on the construction of a stream function to approximate the actual velocity field around the pore surface by making use of the Rayleigh-Ritz method. A first point that should be made is related to the fact that the range of validity of this dilute expansion diminishes to zero for purely hydrostatic loading and high nonlinearities close to the ideally plastic limit. This result is consistent with the observations made by Huang (1991b), who showed that a large number of terms in the representation of the stream function needs to be considered for convergence at high nonlinearities and stress triaxialities. In contrast, use of a small number of terms could lead to underestimation of the dilatation rate at high stress triaxialities and nonlinearities.

Remark 4.2.2. A second remark that should be made here is that Duva and Hutchinson (1984) and Duva (1986) found that the dilute methods, such as the one of Lee and Mear (1992b) under consideration here, become less accurate for small but finite concentrations of voids ($f_o \sim 10^{-2}$) at high nonlinearities and stress triaxialities. The reason for this has been attributed by the aforementioned authors to the fact that these dilute techniques are not able to take into account the interactions between voids, which may become large at high nonlinearities even when the concentration of voids is small. For this reason, the SOM and VAR estimates are obtained numerically for a very low porosity of $f_o = 10^{-6}$.

To begin with, the initial dilatation rate of an isolated void of circular cross-section is studied for an exponent $n = 5$ (or $m = 0.2$) as a function of a special measure of the stress triaxiality, denoted as $\overline{\sigma}_m/\tau = \sqrt{3}X_\Sigma$ (see (3.17)). Fig. 4.1 shows the normalized dilatation rate $\dot{\mathcal{V}}_2/(\dot{\gamma}\,\mathcal{V}_2)$ as predicted

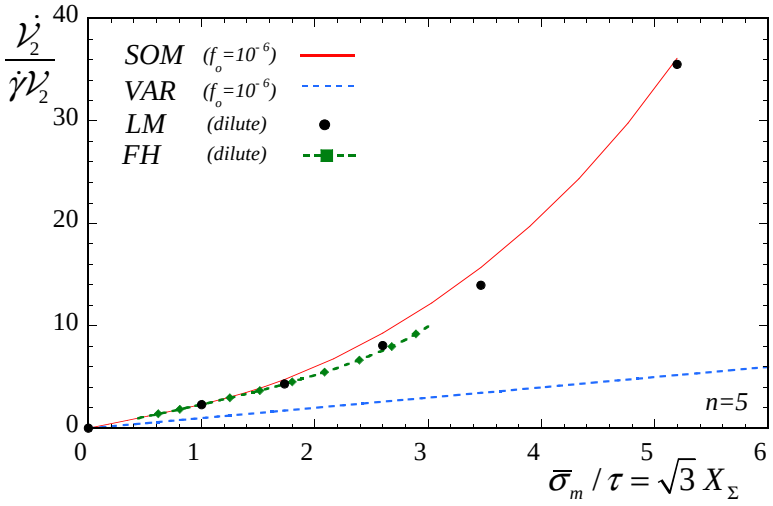

Figure 4.1: Dilatational rate for a dilute, transversely, isotropic porous medium, whose matrix phase is described by an exponent $n = 5$, predicted by the SOM. Corresponding homogenization estimates by the variational method (VAR) and numerical results by Fleck and Hutchinson (1986) (FH) and Lee and Mear (1992) (LM) are shown for comparison.

by the SOM, the VAR, the FH and the LM methods for dilute concentration of voids. A first observation that can be made in the context of Fig. 4.1 is that the VAR method underestimates significantly the dilatation rate as the stress triaxiality increases, while the SOM remains in very good agreement with the numerical FH and LM results. The improvement of the SOM over the VAR estimate is due to the fact that the SOM recovers — by construction — the analytical shell result for purely hydrostatic loadings (see subsection 2.6.2). On the other hand, it has already been shown that, in the dilute limit and for purely hydrostatic loadings, the VAR estimate is inconsistent with the analytical shell result (see equation (3.45)).

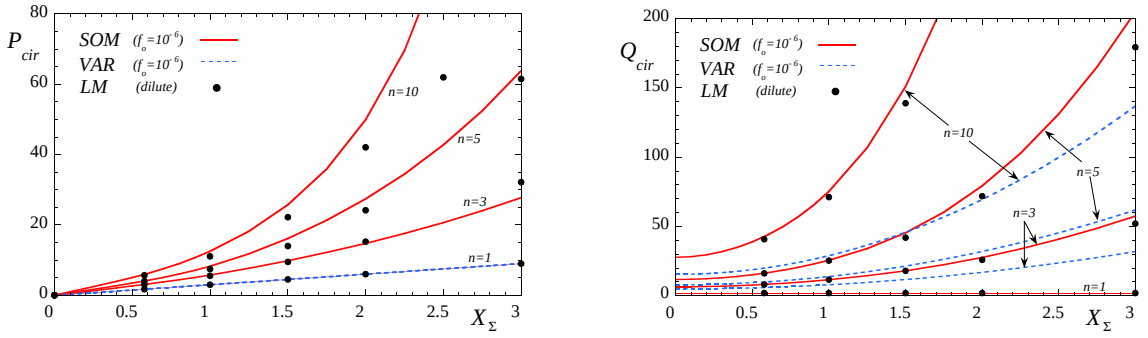

(a) (b)

Figure 4.2: Homogenization (SOM and VAR) and numerical estimates (LM) for (a) P_{cir}, which is related to the hydrostatic part of the strain-rate and (b) Q_{cir}, which is related to the deviatoric part of the strain-rate, are shown for a porous medium consisting of dilute concentration of voids with circular cross-section and matrix phase described by exponents $n = 1, 3, 5, 10$ as a function of the stress triaxiality X_Σ.

A more thorough study of the macroscopic strain-rate $\overline{\boldsymbol{D}}$ in a dilute porous medium is discussed

in Fig. 4.2, where various values for the nonlinearity exponent $n = 1, 3, 5, 10$ are considered. In this figure, P_{cir} and Q_{cir} denote measures of the hydrostatic and the deviatoric part of the strain-rate $\overline{\boldsymbol{D}}$, respectively (for further details see relations (3.28) and (3.29)), which are shown as a function of the stress triaxiality X_Σ. The main observation in the context of this figure is that both the SOM and the LM estimates are strong functions of the stress triaxiality and the nonlinearity. In addition, the SOM estimates are found to be in good agreement with the LM results, although the LM predicts lower values for both P_{cir} and Q_{cir} than the SOM method. These differences could be explained by the comments made in remark 4.2.1. On the other hand, it is emphasized that the SOM model is based on a rigorous variational principle but does not constitute an exact solution. In this regard, it could lead to overestimation of P_{cir} and Q_{cir}. Note however that for purely hydrostatic loading the SOM is exact and thus, it is expected to predict accurately the effective behavior of porous media at high stress triaxialities.

On the other hand, the VAR underestimates both the hydrostatic P_{cir} and deviatoric Q_{cir} part of the macroscopic strain-rate when compared with the SOM and the LM results. In particular, the VAR estimate for P_{cir} is independent of the nonlinearity n, such that all the estimates coincide with the $n = 1$ curve. This peculiar result can be explained by noting that the VAR estimate for P_{cir} is not linear in the porosity f in the dilute limit, as discussed in (3.45). On the other hand, the equivalent part of $\overline{\boldsymbol{D}}$ (i.e., Q_{cir}) predicted by the VAR is linear in f as $f \to 0$ (Idiart et al., 2006). However, even in this case, the VAR method still underestimates Q_{cir} when compared with corresponding estimates by the SOM and the LM methods, especially at high triaxialities and nonlinearities.

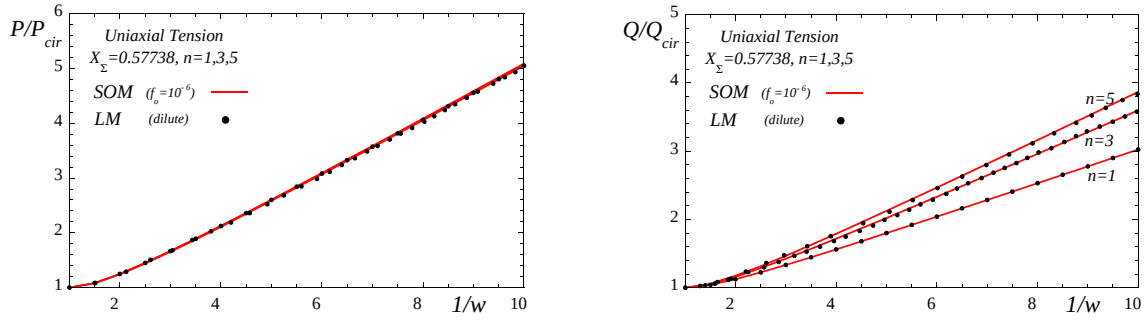

Figure 4.3: Homogenization (SOM) and numerical estimates (LM) for (a) P/P_{cir}, which is related to the hydrostatic part of the strain-rate and (b) Q/Q_{cir}, which is related to the deviatoric part of the strain-rate, are shown for a porous medium consisting of dilute concentration of voids with elliptical cross-section and matrix phase described by exponents $n = 1, 3, 5$. The results are plotted as a function of the in-plane aspect ratio $1/w$ of the elliptical voids for a uniaxial tension loading.

For completeness, Fig. 4.3 shows results for the normalized P/P_{cir} and Q/Q_{cir} for a fixed stress triaxiality $X_\Sigma = 1/\sqrt{3}$ or equivalently uniaxial tension loading, as a function of the in-plane aspect ratio $1/w$ for nonlinearities of $n = 1, 3, 5$. As already mentioned previously, the quantities P and Q are associated with the hydrostatic and deviatoric part of the macroscopic strain-rate $\overline{\boldsymbol{D}}$, respectively, whereas P_{cir} and Q_{cir} correspond to estimates for voids with circular cross-section (see definitions

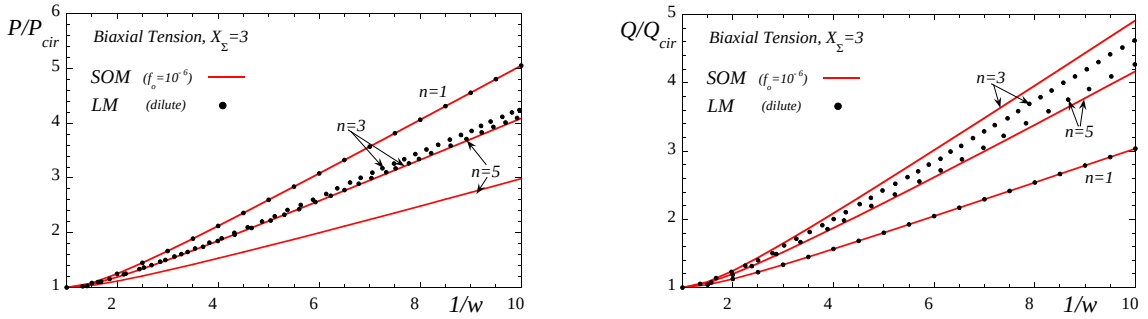

Figure 4.4: Homogenization (SOM) and numerical estimates (LM) for (a) P/P_{cir}, which is related to the hydrostatic part of the strain-rate and (b) Q/Q_{cir}, which is related to the deviatoric part of the strain-rate, are shown for a porous medium consisting of dilute concentration of voids with elliptical cross-section and matrix phase described by exponents $n = 1, 3, 5$. The results are plotted as a function of the in-plane aspect ratio $1/w$ of the elliptical voids for a biaxial tension loading with $X_\Sigma = 3$.

(3.28) and (3.29), respectively). The main observation in the context of this figure is that the SOM estimates for both P/P_{cir} and Q/Q_{cir} are in very good agreement with the corresponding LM predictions for all aspect ratios shown here[†]. In particular, we observe in Fig. 4.3a that the normalized ratio P/P_{cir} increases almost linearly with the aspect ratio $1/w$ as predicted by both the SOM and the LM methods. On the other hand, both estimates exhibit no dependence on the nonlinear exponent n, since for all the n shown here, the curves coincide.

In turn, Fig. 4.3b shows corresponding SOM and LM estimates for the normalized equivalent part of $\overline{\boldsymbol{D}}$, denoted with Q/Q_{cir}, as a function of the aspect ratio $1/w$ for a uniaxial tension loading. Similar to the previous case, the increase of Q/Q_{cir} is almost linear with respect to the in-plane aspect ratio $1/w$. In contrast to the P/P_{cir} curves, the Q/Q_{cir} estimates depend on the nonlinear exponent n, as predicted by both SOM and LM methods. Note that Q/Q_{cir} increases at higher nonlinearities for the special case of uniaxial loading. As we will see in the following figure this trend is not preserved for higher triaxial loadings.

Fig. 4.4 shows results for the normalized dilatation P/P_{cir} and deviatoric Q/Q_{cir} part of the macroscopic strain-rate $\overline{\boldsymbol{D}}$, with a fixed stress triaxiality $X_\Sigma = 3$ (biaxial tension loading), as a function of the in-plane aspect ratio $1/w$ for nonlinearities of $n = 1, 3, 5$. The main observation in the context of this figure is that the SOM and the LM predictions for Q/Q_{cir} are in better agreement than for P/P_{cir}. More specifically, we observe in Fig. 4.4a, that as the nonlinear exponent n increases, the rate of change of P/P_{cir} decreases. This trend is obtained by both the SOM and the LM method, with the first one providing a lower rate of increase for P/P_{cir} than the LM method, especially for higher values of n. It is important to emphasize though that this does not mean that the SOM underestimates P, since from Fig. 4.2a it has already been deduced that, for $n = 5$, the SOM estimate for P_{cir} lies higher than the corresponding LM prediction. However, in Fig. 4.4a, the only relevant conclusion that we can draw is that the qualitative behavior of P, as predicted by the

[†]In this case, VAR estimates are not included, since it has already been found in Fig. 4.2 that the they underestimate significantly P_{cir} and Q_{cir} and thus the comparison is not meaningful.

SOM is consistent with the LM result for any aspect ratio $1/w$. On the other hand, it is important to mention here that the SOM makes use of a prescription for the reference stress tensor, as described in subsection 2.6.2, which is related with the evaluation of the hydrostatic behavior of a porous medium consisting of cylindrical voids with arbitrary aspect ratio w. Indeed this prescription is approximate and in general it could lead to "conservative" estimates for the estimation of the dilatation rate at high stress triaxialities.

On the other hand, in Fig. 4.4b, the corresponding SOM estimate for Q/Q_{cir} is in very good agreement with the LM prediction. It is interesting to observe that the curves for $n = 3$ lie higher than the ones for $n = 5$ and $n = 1$. This interesting nonlinear behavior is captured by the SOM model, which is found to agree, at least qualitatively, with the LM predictions for the entire range of nonlinearities and aspect ratios at this high triaxial loading ($X_\Sigma = 3$). Note that in Fig. 4.3 associated with a uniaxial tension loading, such a trend was not observed.

In summary, the above results provide a first indication of the improvement of the SOM on the earlier VAR method. Furthermore, the SOM has been found to compare well with the LM results for all nonlinearities, triaxialities and aspect ratios considered here. However, it is worth noting that the accuracy of the LM results (as well as the FH results) is expected to deteriorate at high nonlinearities and stress triaxialities for the reasons explained in remark 4.2.1. This could result in an underestimation of the dilatational rate, as already observed by Huang (1991b). On the other hand, the SOM is constructed such that it recovers the exact hydrostatic solution of a CCA (composite cylinder assemblage), and as a consequence of this it is expected to be accurate at high stress triaxialities. In the sequel, we study the effective response of porous media consisting of cylindrical voids with circular (or elliptical) cross-section for finite porosities.

4.3 Effective behavior for isochoric loadings

In this section, we consider transversely isotropic porous materials that are loaded in transverse shear ($X_\Sigma = 0$). From the homogeneity of the local potential (2.23) in $\boldsymbol{\sigma}$, it follows that in the case of purely deviatoric loadings the effective stress potential can be written as

$$\widetilde{U}(\overline{\boldsymbol{\sigma}}) = \frac{\dot{\varepsilon}_o\,\widetilde{\sigma}_o}{n+1}\left(\frac{\overline{\sigma}_{eq}}{\widetilde{\sigma}_o}\right)^{n+1}, \tag{4.33}$$

where $\dot{\varepsilon}_o$ is a reference strain-rate and $\widetilde{\sigma}_o$ is the *effective flow stress* of the composite. The effective behavior is thus completely characterized by $\widetilde{\sigma}_o$. In the following, the "second-order" estimates (SOM) are compared with corresponding estimates from the high-rank sequential laminates (LAM) and the "variational" (VAR) method. Note that for isochoric loadings, the reference stress tensor, defined in subsection 2.6.2, is simply $\check{\boldsymbol{\sigma}} = \overline{\boldsymbol{\sigma}}'$.

More specifically, Fig. 4.5 presents results for the normalized effective flow stress $\widetilde{\sigma}_o/\sigma_o$ (σ_o is the flow stress of the matrix phase) as function of the strain-rate sensitivity parameter m and the porosity f. The main observation, in the context of this figure, is that the agreement of the SOM estimates with the exact LAM results is quite good, and certainly much better than the VAR estimates for all the porosities and nonlinearities considered. In addition, in Fig. 4.5b, the SOM exhibits a non-

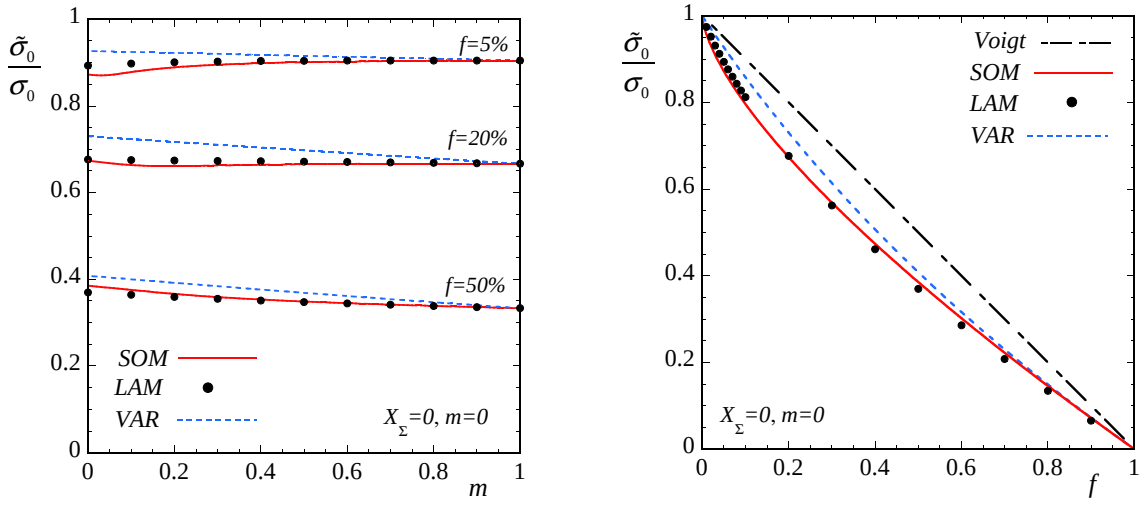

(a) (b)

Figure 4.5: Estimates and exact results for transversely, isotropic porous materials subjected to isochoric loadings ($X_\Sigma = 0$). Effective flow stress $\widetilde{\sigma}$ curves normalized by the flow stress of the matrix σ_o, (a) as a function of the strain-rate sensitivity parameter m for several porosities ($f = 5, 20, 50\%$), and (b) as a function of the porosity f in the case of an ideally-plastic matrix ($m = 0$).

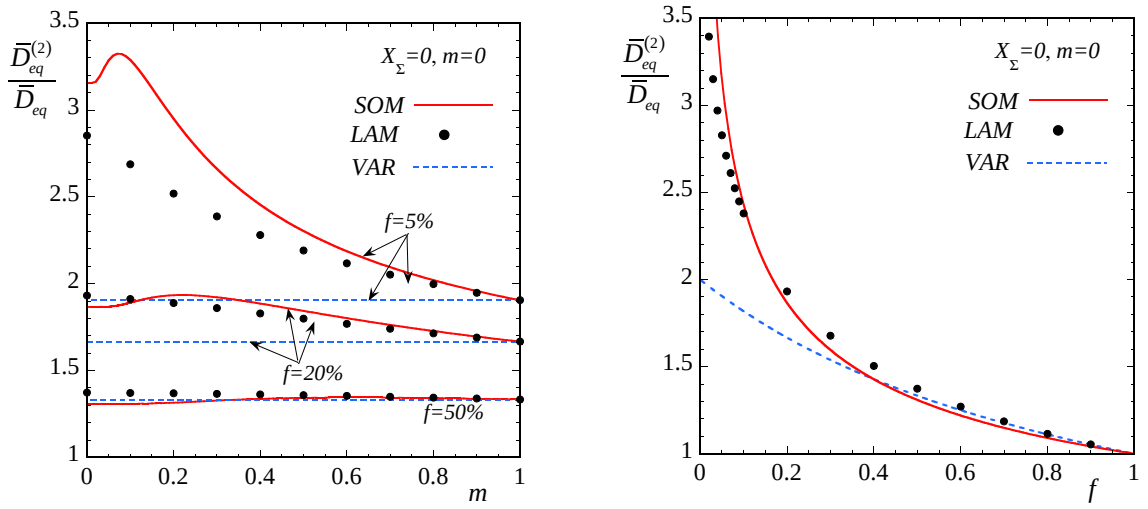

(a) (b)

Figure 4.6: Estimates and exact results for transversely, isotropic porous materials subjected to isochoric loadings ($X_\Sigma = 0$). The average equivalent strain-rate in the void $\overline{D}^{(2)}_{eq}$ normalized by the macroscopic equivalent strain-rate $\overline{D}_{eq}$ is shown, (a) as a function of the strain-rate sensitivity parameter m for several porosities ($f = 5, 20, 50\%$), and (b) as a function of the porosity f in the case of an ideally-plastic matrix ($m = 0$).

analytic behavior in the case of porous solids with ideally-plastic matrix phase when the dilute limit is considered ($\widetilde{\sigma}_o \to 1 - \frac{3}{2}\left(\frac{f}{2}\right)^{2/3}$ as $f \to 0$). In contrast, the VAR and the LAM estimates behave as $1 - af$, where $a > 0$ in the dilute limit. For completeness, the well known Voigt bound is also included in Fig. 4.5b. Of course all the models satisfy this bound. It is noted that the reason for the

big differences in behavior in this case of ideal-plasticity is that, as pointed out by Drucker (1966), this is a sensitive limit, where the exact solution corresponds to shear bands passing through the pores (see also Sab, 1994b).

Fig 4.6 shows results for the equivalent average strain-rate $\overline{D}_{eq}^{(2)}$ in the void normalized with the average equivalent strain-rate $\overline{D}_{eq}$ as function of the strain-rate sensitivity parameter m and the porosity f. In Fig 4.6a, the SOM is certainly in better agreement with the LAM estimates than the corresponding results of the VAR, although in the case of $f = 5\%$ the SOM tends to overestimate $\overline{D}_{eq}^{(2)}$. Regardless of this, it is interesting to note in Fig 4.6b that for porous media with an ideally-plastic matrix phase, both the SOM and the LAM estimates for $\overline{D}_{eq}^{(2)}$ blow up in the dilute limit, while the corresponding VAR estimates remain finite. In fact the SOM estimates behave as $\overline{D}_{eq}^{(2)}/\overline{D}_{eq} \sim f^{-1/3}$ as $f \to 0$. This is a very interesting result which illustrates the sensitivity of the first moments of the strain-rate in the void in the case of nonlinear materials.

In summary, these results illustrate that the SOM estimates are in very good agreement with the LAM results for isochoric loadings in the entire range of porosities and nonlinearities. In comparison, they are found to improve significantly on the earlier VAR method, especially for the estimation of the average strain-rate $\overline{\boldsymbol{D}}^{(2)}$ in the vacuous phase.

4.4 Gauge surfaces for cylindrical voids with circular cross-section

In order to complete the study of the effective behavior of transversely isotropic porous materials, it is necessary to include plots for the entire range of the stress triaxialities. For this reason, we specialize the more general expression for the gauge function (Leblond et al., 1994), defined in subsection 2.2.4 for ellipsoidal particulate microstructures, to the case of transversely isotropic porous media, such that

$$\widetilde{\Phi}_n(\overline{\boldsymbol{\Sigma}};\, f) = \Gamma_n(\overline{\boldsymbol{\Sigma}};\, f) - 1. \tag{4.34}$$

Here, Γ_n is the gauge factor defined by (2.151) for the "variational" method and (2.184) for the "second-order" method, whereas $\overline{\boldsymbol{\Sigma}}$ is a normalized stress tensor, defined in (2.30), that is homogeneous of degree zero in $\overline{\boldsymbol{\sigma}}$. Then, the equation $\widetilde{\Phi}_n = 0$ describes the corresponding gauge surface defined in (2.29).

In turn, the normalized, macroscopic strain-rate is given by

$$\overline{\boldsymbol{E}} = \frac{\overline{\boldsymbol{D}}}{\dot{\varepsilon}_o\, (\Gamma_n(\overline{\boldsymbol{\sigma}};\, f)/\sigma_o)^n} = \frac{\partial \Gamma_n(\overline{\boldsymbol{\sigma}};\, f)}{\partial \overline{\boldsymbol{\sigma}}}, \tag{4.35}$$

and the macroscopic stress and strain-rate triaxialities are expressed as

$$X_\Sigma = \frac{\overline{\Sigma}_m}{\overline{\Sigma}_{eq}} = \frac{\overline{\sigma}_m}{\overline{\sigma}_{eq}} \quad \text{and} \quad X_E = \frac{\overline{E}_m}{\overline{E}_{eq}} = \frac{\overline{D}_m}{\overline{D}_{eq}}, \tag{4.36}$$

where the normalized, in-plane mean stress and strain-rate are defined as $\overline{\Sigma}_m = (\overline{\Sigma}_{11} + \overline{\Sigma}_{22})/2$, $\overline{E}_m = (\overline{E}_{11} + \overline{E}_{22})/2$, and $\overline{\Sigma}_{eq}$ and $\overline{E}_{eq}$ denote the von Mises equivalent parts of the normalized stress and strain-rate, respectively.

In the sequel, the "second-order" estimates (SOM), discussed in section 2.6, are compared with corresponding results generated by the sequential laminates (LAM) described in section 3.4. In addition, these results are compared with the earlier "second-order" ($SOMS$) estimates using the simpler prescription $\check{\boldsymbol{\sigma}} = \overline{\boldsymbol{\sigma}}'$ for the reference stress tensor (see subsection 2.6.2), as well as with the "variational" estimates (VAR) and the Gurson criterion (GUR) (for the case of ideally-plastic materials). Note that Leblond et al. (1994) only considered axisymmetric loadings for the cylindrical microstructures, and therefore it was not possible to compare with their estimates for the case of plane-strain loading. However, relevant comparisons will be carried out in chapter 6 for isotropic porous media.

Fig. 4.7 shows the various estimates for the gauge surface and the corresponding macroscopic triaxialities, for moderate values of the porosity ($f = 10\%$) and nonlinearity ($m = 0.2$). The main observation in the context of this figure is that the SOM estimates proposed in this work are in very good agreement with the exact LAM results, for the entire range of the stress triaxialities. In contrast, the agreement exhibited by the $SOMS$ estimates is very good for low triaxialities, but deteriorates for sufficiently large triaxialities.

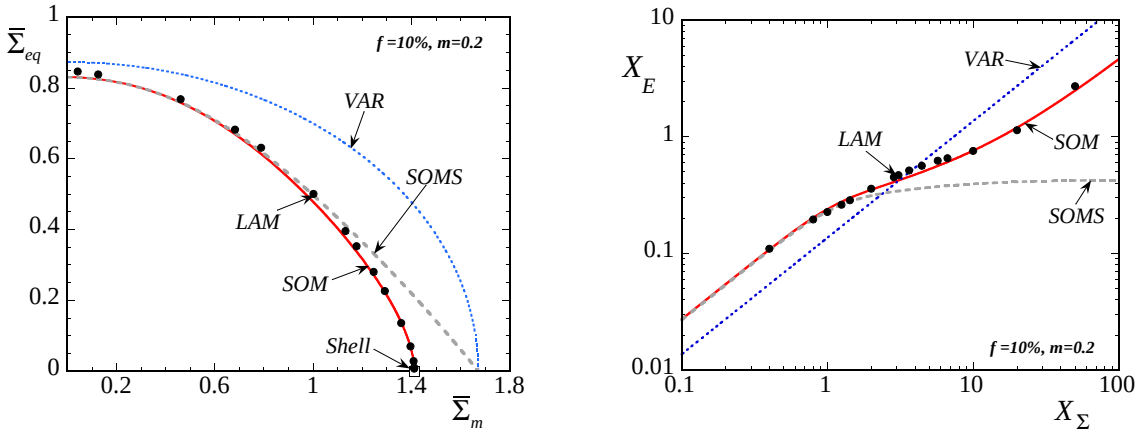

(a) (b)

Figure 4.7: (a) Gauge surfaces and (b) strain-rate - stress triaxiality plots for a transversely, isotropic porous material with porosity $f = 10\%$ and strain-rate sensitivity parameter $m = 0.2$. The SOM is compared with corresponding estimates obtained by the variational method (VAR), the high-rank sequential laminates (LAM), and the earlier second-order estimate ($SOMS$) ($\check{\boldsymbol{\sigma}} = \overline{\boldsymbol{\sigma}}'$).

In the hydrostatic limit, the SOM estimates coincide, by construction, with the exact result for CCAs, denoted by □ in Fig. 4.7a. In turn, the LAM results, which correspond to high but finite rank laminates, also tend to this exact result — further support to the fact that the LAM results should agree exactly with the hydrostatic behavior of CCAs in the limit of infinite rank has been provided by Idiart (2007). On the other hand, both the $SOMS$ curve, and the VAR estimates are found to deviate from the analytical solution (2.195) in the hydrostatic limit. Note that Fig. 4.7b shows that, although the VAR predictions for the strain-rate triaxiality X_E tend to infinity as the stress triaxiality X_Σ becomes infinite, they deviate significantly from the SOM and the LAM estimates for the entire range of the stress triaxialities. Correspondingly, the $SOMS$ curve in this figure reaches

an asymptotic value at high stress triaxialities (i.e., $\overline{D}_{eq} \neq 0$ as $|X_\Sigma| \to \infty$), which is consistent with the existence of a corner in the $\overline{\Sigma}_{eq}$-$\overline{\Sigma}_m$ plot.

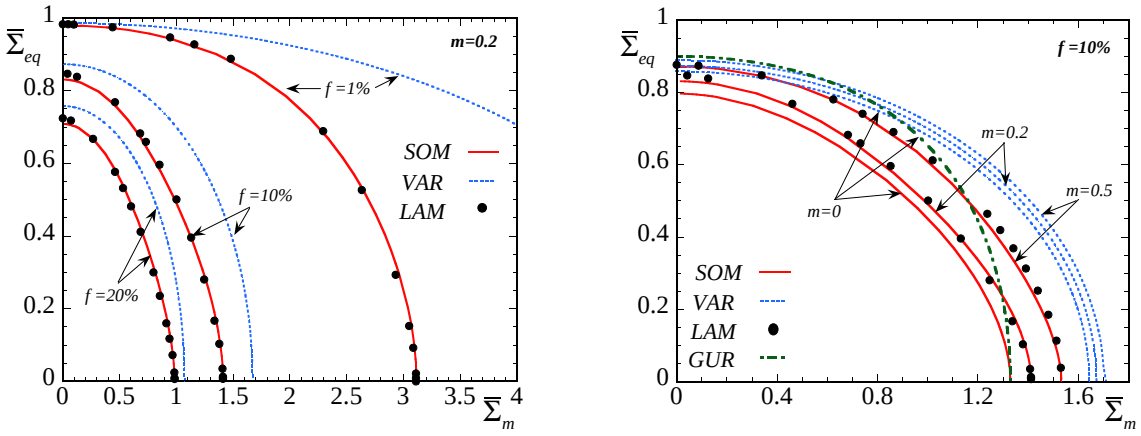

(a) (b)

Figure 4.8: SOM gauge surfaces for a transversely, isotropic porous material, as a function of (a) the porosity f for a strain-rate sensitivity parameter $m = 0.2$, and (b) the strain-rate sensitivity parameter m for a porosity $f = 10\%$. Corresponding results by the "second-order" (SOM) and the "variational" method (VAR), as well as the high-rank sequential laminates (LAM) are included for comparison. In the case of ideally-plastic matrix ($m = 0$), the Gurson criterion (GUR) is also shown.

At this point, it is worth noting that there exist evidence (Pastor and Ponte Castañeda, 2002) suggesting that the yield surface of porous materials with an ideally-plastic matrix phase may exhibit a corner on the hydrostatic axis (but see also Bilger et al. (2005)). A possible explanation for this vertex-like behavior could be the development of shear bands in the matrix phase. However, it is unrealistic to expect formation of shear bands for a porous material whose matrix phase is described by an exponent $m > 0$. For this reason, we have assumed our new gauge surfaces to be smooth on the hydrostatic axis, even in the ideally-plastic limit.

Fig. 4.8 shows effective gauge surfaces for different values of the porosity f and the strain-rate sensitivity parameter m. The gauge surfaces delivered by the SOM are in very good agreement with the LAM estimates for the entire range of $\overline{\Sigma}_{eq} - \overline{\Sigma}_m$. In particular, gauge surfaces are shown in Fig. 4.8a as functions of the porosity f for a given value of $m = 0.2$, where it is clearly observed that the VAR method significantly overestimates the resistance of the porous medium at high stress triaxialities and low porosities, when compared with the SOM and LAM estimates. However, it is worth noting that the estimate delivered by the VAR method in the hydrostatic limit improves at higher porosities (see corresponding curve for $f = 20\%$ in Fig. 4.8a). This observation is a mere consequence of the fact that the VAR estimate (2.197) approaches the exact hydrostatic solution, given by relation (2.196), at high porosities.

Fig. 4.8b shows gauge surfaces as a function of the strain-rate sensitivity parameter m for a given value of porosity $f = 10\%$. Due to numerical difficulties, LAM results are only provided for $m \geq 0.2$. Similarly to Fig. 4.8a, the SOM and the LAM estimates are in very good agreement for the entire range of macroscopic triaxialities, while the VAR estimate, albeit a rigorous upper bound,

remains too stiff as the nonlinearity of the matrix phase increases (i.e., m decreases). In addition, for the special case of ideally-plastic materials, the GUR estimate deviates significantly from the SOM estimate, despite the fact that it recovers the exact hydrostatic solution. As already anticipated, it violates the variational bound, VAR, for low stress triaxialities, in which case it tends to the Voigt bound. In any event, all the methods indicate a softening of the composite as the porosity or the nonlinearity increases, which is consistent with the contraction of the effective gauge surfaces.

4.4.1 Macroscopic strain-rates

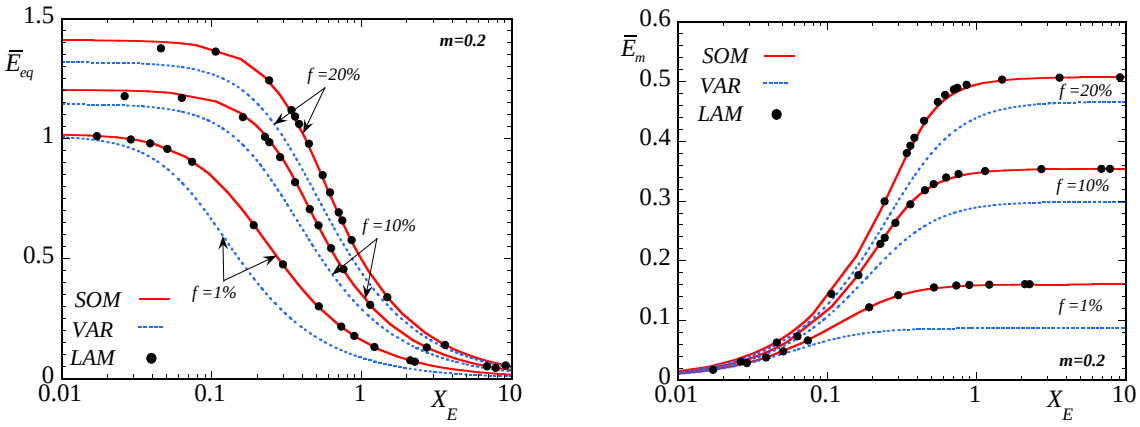

(a) (b)

Figure 4.9: Macroscopic strain-rates obtained by the SOM as a function of the porosity f and the strain-rate triaxiality X_E. (a) shows the equivalent part $\overline{E}_{eq}$ and (b) shows the hydrostatic part $\overline{E}_m$ of the macroscopic strain-rate for a strain-rate sensitivity parameter $m = 0.2$ and several porosities $f = 1, 10, 20\%$. VAR and LAM estimates are shown for comparison.

In order to complete the study of the macroscopic properties of the porous medium, Fig. 4.9 shows the two "modes" of the normalized, macroscopic strain-rate $\overline{\boldsymbol{E}}$, the equivalent ($\overline{E}_{eq}$) and the hydrostatic ($\overline{E}_m$) mode, as functions of the strain-rate triaxiality X_E and the porosity f, for a fixed value of the nonlinearity $m = 0.2$. The estimates obtained by the SOM for the modes $\overline{E}_{eq}$ and $\overline{E}_m$ are found to be quite good, when compared with the LAM estimates, for the whole range of triaxialities and porosities, considered here. On the other hand, the VAR bound underestimates $\overline{E}_{eq}$ at low triaxialities and $\overline{E}_m$ at high triaxialities, when compared with the LAM and the SOM estimates. In particular, at high triaxialities, it predicts an asymptotic value for $\overline{E}_m$ that is 40% lower than the SOM estimate (see Fig. 4.9 for $f = 1\%$) and thus, the exact result for $\overline{E}_m$ obtained by direct derivation of the exact relation (2.195) with respect to $\overline{\sigma}_m$.

Finally Fig. 4.10 shows $\overline{E}_{eq}$ and $\overline{E}_m$, as functions of the strain-rate triaxiality X_E and the nonlinearity m, for a fixed value of the porosity $f = 10\%$. Note that for the case of $m = 0$ (i.e., ideal-plasticity) the GUR estimates are also shown. The SOM estimates are in very good agreement with the LAM results for the entire range of the strain-rate triaxiality and nonlinearities considered. On the other hand, as already anticipated, the VAR method underestimates the two modes $\overline{E}_{eq}$ and $\overline{E}_m$ at low and high strain-rate triaxialities, respectively. In addition, it is further noted that,

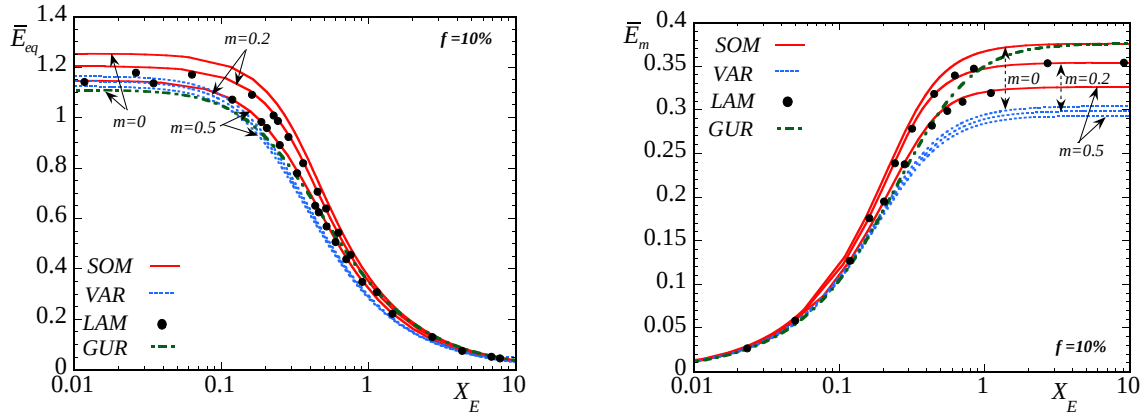

(a) (b)

Figure 4.10: Macroscopic strain-rates obtained by the SOM as a function of the strain-rate sensitivity parameter m and the strain-rate triaxiality X_E. (a) shows the equivalent part $\overline{E}_{eq}$ and (b) shows the hydrostatic part $\overline{E}_m$ of the macroscopic strain-rate for a porosity $f = 10\%$ and several exponents $m0, 0.2, 0.5$. VAR and LAM estimates are shown for comparison. In the case of ideally-plastic matrix ($m = 0$), the Gurson criterion (GUR) is also shown.

although GUR recovers by construction the analytical estimate for $\overline{E}_m$ and $\overline{E}_{eq} = 0$ in the limit of hydrostatic loading for the case of ideally-plastic materials (provided that the case of a corner in the yield surface is excluded), it is found to underestimate both of these modes of the strain-rate for moderate to low triaxialities, when compared with the SOM estimates. It should be emphasized that the accurate prediction of $\overline{E}_m$ is critical, as it controls the dilatation rate of the voids, which is even more sensitive at high triaxialities. The dilatation of the voids may lead to a significant increase of the porosity measure and eventually to the failure of the material. Therein lies the significance of the GUR model which was the first to be able to account for this effect.

In summary, the new SOM estimates are found to be in very good agreement with the LAM results for the case of transversely isotropic porous media consisting of cylindrical voids. In particular, the new prescription for the reference stress tensor, discussed in the context of section 2.6, improves significantly on earlier choices by being able to recover the exact hydrostatic shell result. On the other hand, the VAR method overestimates significantly the effective strength of the porous material and as a consequence underestimates the hydrostatic part of the strain-rate at high triaxialities.

4.5 Gauge surfaces for cylindrical voids with elliptical cross-section

In the previous section, a complete comparison has been made between the "second-order" method (SOM), the "variational" bound (VAR) and the high-rank, sequentially laminated results (LAM) in the case of transversely isotropic porous materials. In this section, we extend the predictions of the homogenization methods in the context of anisotropic microstructures. This extension is important, since the goal of this work is to propose a model that is able to approximate the effective

behavior of porous materials that are subjected to large deformations. A priori large deformations are synonymous with evolution of microstructure which in turn leads to an overall anisotropic response of the material. For a better understanding of the results that follow, it is useful to refer to Fig. 2.3 for a complete definition of the geometry of the voids.

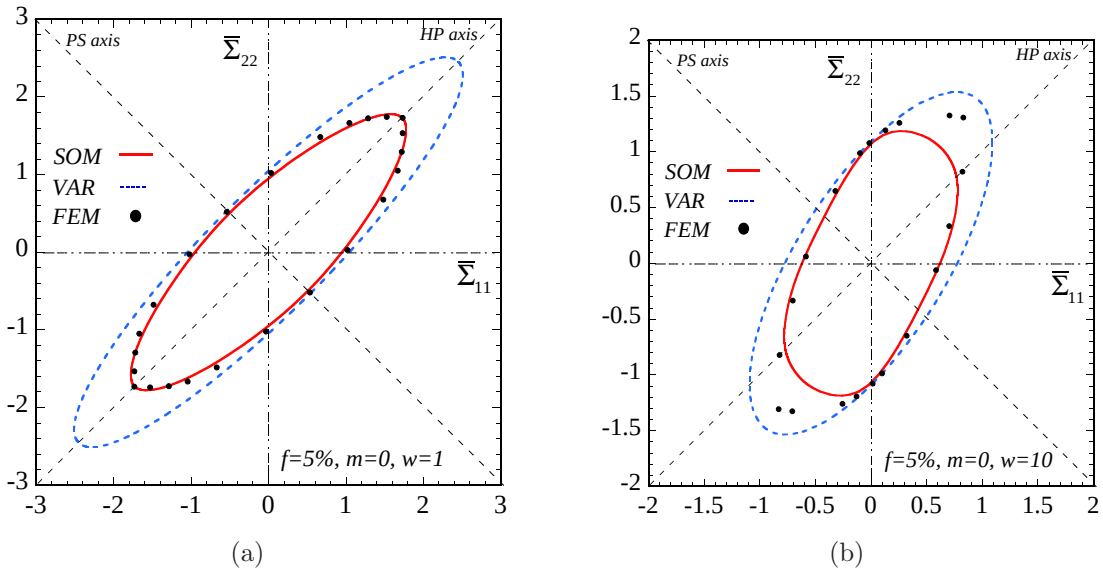

Figure 4.11: Isotropic and anisotropic gauge surfaces as predicted by the SOM, the VAR and FEM calculations for porous materials with cylindrical voids with in-plane, aspect ratio (a) $w = 1$ and (b) w=10. The matrix phase exhibits an ideally-plastic behavior ($m = 0$) and the porosity $f = 5\%$.

In this regard, Fig. 4.11 shows comparisons between the SOM, the VAR and FEM results provided by Mariani and Corigliano (2001) in the case of porous media consisting of cylindrical voids with in-plane, aspect ratio $w = 1$ and $w = 10$ and an ideally-plastic matrix phase. In the first case, the response of the composite is transversely, isotropic about the $3-$axis, whereas, in the second case, the material exhibits anisotropic behavior in the plane $1 - 2$. When $w = 1$, in Fig. 4.11a, the SOM estimates are in very good agreement with the FEM results, as already anticipated from the analysis of the previous section. The VAR estimate although quite accurate at low triaxialities, it overestimates the effective behavior of the composite at high ones. On the other hand, for $w = 10$ in Fig. 4.11b, the SOM, although quite accurate for a large section of the stress space, it becomes too soft compared to the FEM results for $\overline{\Sigma}_{22} > \overline{\Sigma}_{11} > 0$ and $\overline{\Sigma}_{22} < \overline{\Sigma}_{11} < 0$. The VAR estimate, in turn, remains stiffer than both the SOM and the FEM results in the entire stress space. It is noted that the case of $w = 10$ corresponds to a material that is highly anisotropic in the plane and, in principle, the SOM shows some of the qualitative effects of this complicated behavior. A main effect of this anisotropy is the non-standard shape of the gauge curve as determined by the SOM and the FEM results, in contrast with the VAR estimate which remains a pure ellipsoid.

Next, Fig. 4.12 and Fig. 4.13 show a set of results obtained by the SOM for three values of the porosity $f = 1, 5, 10\%$ and the aspect ratio $w = 1, 0.3, 0.1$ for a porous material with an ideally-plastic matrix phase. They are plotted in two different ways in order to highlight several effects of the anisotropy induced when the voids do not have a circular cross-section. First, in Fig. 4.12, the

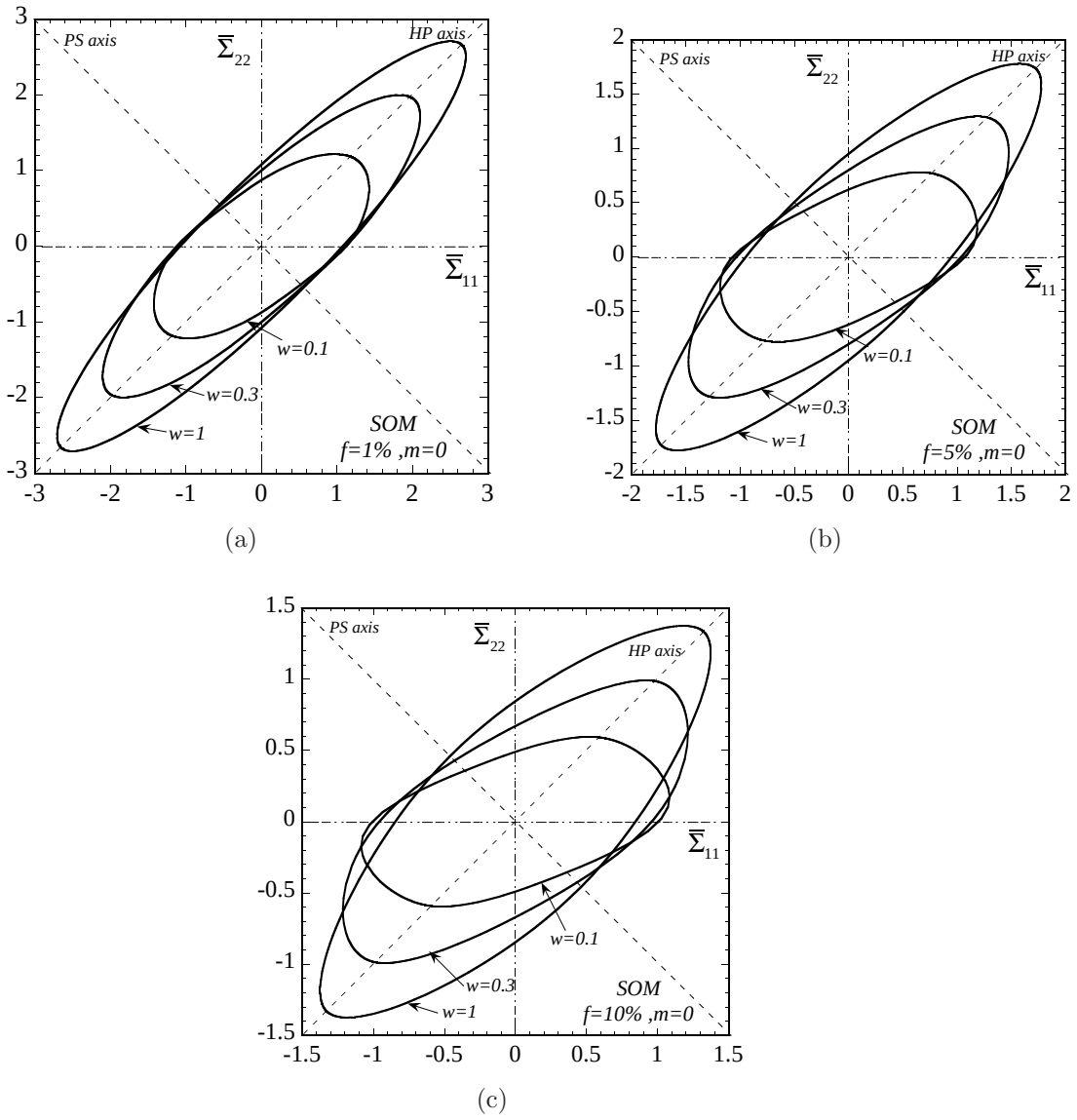

Figure 4.12: Anisotropic gauge surfaces obtained by the *SOM* for porous materials made up of cylindrical voids with in-plane, aspect ratios $w = 0.1, 0.3, 1$, and porosities (a) $f = 1\%$, (b) $f = 5\%$ and (c) $f = 10\%$. The matrix phase exhibits an ideally-plastic behavior ($m = 0$).

porosity is kept fixed and we let the aspect ratio change. For all the porosities, we observe that reduction of the aspect ratio, mainly, induces a rather significant softening of the material at high triaxiality loadings (look at the HP (hydrostatic) axis). While for $f = 1\%$, the gauge curve shrinks with the reduction of the aspect ratio without changing its shape significantly, for $f = 10\%$ in turn, the reduction of w induces a crucial distortion of the gauge curve. More specifically, for $f = 10\%$, a porous material with aspect ratio $w = 0.1$ is stiffer than the one with $w = 1$ in the $1-$direction, which of course, is intuitively expected. In contrast, the material softens in the $2-$direction as the aspect ratio decreases. Of course, the exactly opposite effect is observed when the aspect ratio increases, i.e., $w \gg 1$ (see for example Fig. 4.11b).

On the other hand, in Fig. 4.13, the aspect ratio is kept fixed, while we let the porosity change.

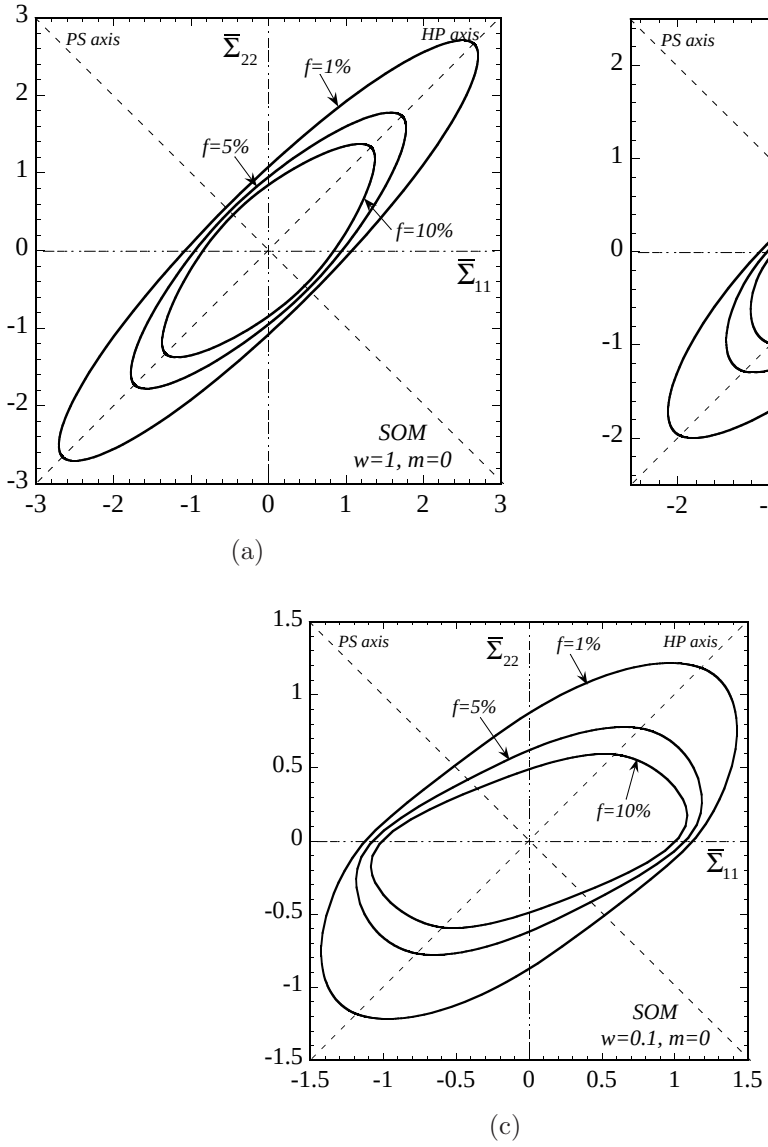

Figure 4.13: Anisotropic gauge surfaces obtained by the *SOM* for porous materials made up of cylindrical voids with porosities $f = 1, 5, 10\%$ and in-plane, aspect ratios, (a) $w = 1$, (b) $w = 0.3$ and (c) $w = 0.1$. The matrix phase exhibits an ideally-plastic behavior ($m = 0$).

As expected, in all the cases shown here, the reduction of porosity has a hardening effect on the effective behavior of the porous medium, especially at high triaxialities. It is interesting to observe, though, that in the case of $w = 0.1$ the increase of the porosity causes a very small softening effect in the direction that the voids are elongated (see Fig. 4.13c in the direction of $\overline{\Sigma}_{11}$). This is a direct consequence of the fact that while in the direction of the major axis of the elliptical void the material hardens, perpendicular to this direction the material softens (see Fig. 4.13c in the direction of $\overline{\Sigma}_{22}$). Hence, in the first case, even though the increase of the porosity induces overall softening for the composite, the elongation of the void acts against this by causing hardening in the direction of the major axis of the void. The result of this "competition" between the aspect ratio and the porosity brings about a very slight softening in the direction of the major axis of the void. On the other hand,

in the direction perpendicular to the major axis of the void the material is softer and together with the increase of the porosity, the material becomes significantly softer in this case.

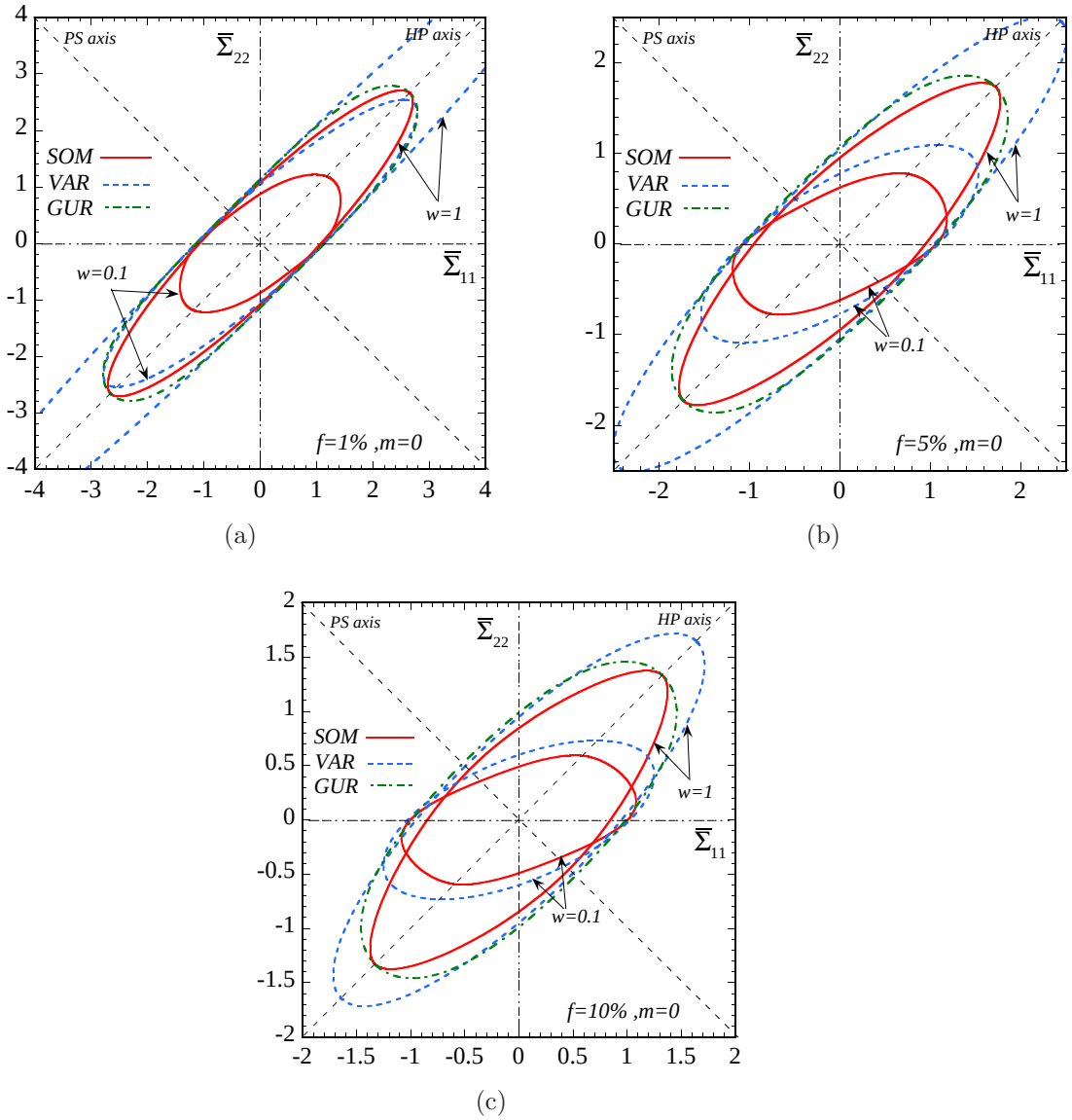

Figure 4.14: Anisotropic gauge surfaces obtained by the SOM, the VAR and the GUR models for porous materials made up of cylindrical voids with porosities $f = 1, 5, 10\%$ and in-plane, aspect ratios, $w = 1$ and $w = 0.1$. The matrix phase exhibits an ideally-plastic behavior ($m = 0$).

Finally, Fig. 4.14 compares the SOM estimates with the "variational" results (VAR) and the Gurson criterion (GUR) for three values of the porosity $f = 1, 5, 10\%$ and two values for the aspect ratio $w = 1, 0.1$. Of course, the GUR criterion contains no information about the shape of the void and hence only one curve is shown in each plot. A general comment for all the plots is that for $w = 1$ (transversely isotropic porous media) the SOM and the GUR models recover by construction the exact shell result defined by relation (2.195). In contrast, the VAR method is much stiffer than both the SOM and the GUR model at high stress triaxialities. As long as low stress triaxiality loadings are considered and still $w = 1$, the SOM and the VAR are in good agreement while the GUR model

violates slightly the VAR bound.

More specifically, a main observation in the context of Fig. 4.14a, is that for $f = 1\%$ the VAR is significantly stiffer than the SOM for both values of the aspect ratio, especially at high stress triaxialities. In turn, the deficiency of the GUR criterion to capture any information for the shape of the voids becomes obvious in this plot. While the GUR model is sufficiently accurate for circular voids and high stress triaxialities, when the aspect ratio becomes small, e.g., $w = 0.1$ in this case, the GUR predictions become overly stiff. Similar observations can also be made in the context of Fig. 4.14b and Fig. 4.14c. It is emphasized, though, that in the case of $f = 5\%$ and $f = 10\%$ the GUR estimates violate considerably the VAR bound as a consequence of not being able to include information on the shape of the voids. Consequently, the GUR model is expected to be highly inaccurate in the case of a porous material with an initially low (or high) aspect ratio.

In summary, the SOM is able to capture several features of the effective behavior of porous materials consisting of cylindrical voids with elliptical cross-section. Moreover, it is found that the aspect ratio of the voids affects significantly the response of the porous medium in all directions. In particular, the elongation of the voids can lead to geometric hardening or softening of the porous medium, which is in "competition" with the hardening or softening induced by the reduction or increase of the porosity. We will see in the following chapter how these two microstructural variables can affect the response of the porous medium when subjected to finite deformations.

4.5.1 Macroscopic strain-rates

For completeness, we present results for the macroscopic strain-rates as predicted by the SOM, the VAR and the GUR models for porous materials consisting of cylindrical voids with (circular) elliptical cross-section. Similar to the previous gauge curves, we show results for two values of the aspect ratio $w = 1, 0.1$ and a representative value of the porosity $f = 5\%$. Note that GUR curves are shown only for $w = 1$.

Fig. 4.15 shows curves for the deviatoric $\overline{E}_d = \overline{E}_{11} - \overline{E}_{22}$ and the hydrostatic $\overline{E}_m$ part of the normalized macroscopic strain-rate defined in relation (4.35) as a function of the stress triaxiality X_Σ. More specifically Fig. 4.15a shows estimates for the deviatoric part $\overline{E}_d$. The main observation in the context of this figure is the asymmetry of the $w = 0.1$ curve about the $\overline{E}_d$- and $X_\Sigma-$axes, in contrast with the $w = 1$ curve, which is completely symmetric about these axes. Note that for $w = 1$, all the models deliver a zero deviatoric strain-rate at $X_\Sigma \to \pm\infty$. Even so the GUR estimates are significantly lower than the corresponding SOM and VAR estimates in the case of $w = 1$. In turn, when $w = 0.1$, the deviatoric strain-rate, predicted by both the SOM and the VAR methods, is found to increase for low stress triaxialities, whereas it does not become zero in the purely hydrostatic limit ($X_\Sigma \to \pm\infty$). In fact, it reaches an asymptotic value for high triaxial loadings. Furthermore, it is worth to mention that, for $w = 0.1$, the deviatoric strain-rate becomes negative at sufficiently high positive stress triaxialities (i.e., $X_\Sigma \gtrsim 3$) and positive for sufficiently negative stress triaxialities (i.e., $X_\Sigma \lesssim 3$).

On the other hand, Fig. 4.15b shows results for the macroscopic mean strain-rate $\overline{E}_m$ as a function

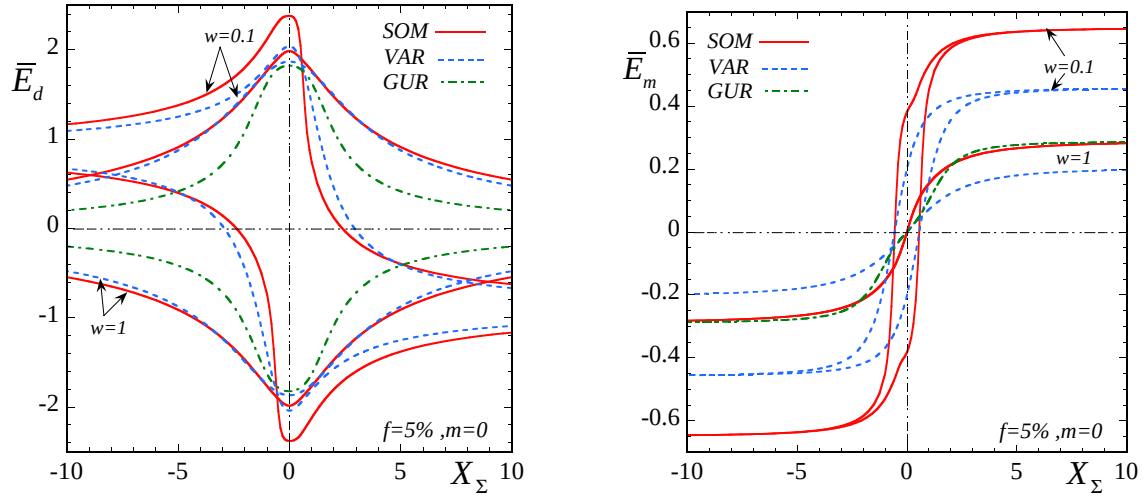

Figure 4.15: Macroscopic strain-rates obtained by the SOM as a function of the porosity f and the stress triaxiality X_Σ for two values of the aspect ratio $w = 1, 0.1$. (a) shows the deviatoric part $\overline{E}_{11} - \overline{E}_{22}$ and (b) shows the hydrostatic part $\overline{E}_m$ of the macroscopic strain-rate for an ideally-plastic matrix phase $m = 0$. VAR and GUR estimates are shown for comparison.

of the stress triaxiality X_Σ. First, we observe that the VAR method significantly underestimates $\overline{E}_m$ for both $w = 1$ and $w = 0.1$ when compared with the SOM method. Note that for $w = 1$, the SOM and the GUR models recover by construction the exact mean strain-rate obtained by a cylindrical hollow shell when subjected to purely hydrostatic loading. In addition, it is remarkable to observe such an increase of $\overline{E}_m$ in the case of $w = 0.1$. This last result highlights the importance of proposing a model that is capable of handling porous media with more general elliptical microstructures.

4.6 Concluding Remarks

In this chapter, the instantaneous effective behavior of random porous materials with cylindrical voids has been studied. The effects of the aspect ratio of the voids and the porosity on the overall response of these materials have been discussed in detail, while the "second-order" and the "variational" nonlinear homogenization methods were compared with several exact and approximate results existing in the literature.

Firstly, "second-order" estimates, obtained for a small, but finite, porosity, have been compared with earlier numerical results by Fleck and Hutchinson (1986) and Lee and Mear (1992b) for dilute porous media. This comparison revealed that the dilute estimates of Fleck and Hutchinson and Lee and Mear predict *lower* values for the dilatational rate and the deviatoric part of the strain-rate than the "second-order" model does. In addition, it is also important to refer to the work of Huang (1991b), who found that a very large number of terms needs to be considered in the Rayleigh-Ritz eigen-function expansion to achieve sufficient accuracy at high stress triaxialities and nonlinearities. A possible reason for this difficulty in obtaining convergent results could be attributed to the fact that

the range of validity of the dilute expansion for the effective stress potential of the porous medium diminishes to zero at high nonlinearities and purely hydrostatic loading. A detailed discussion about this dilute expansion has been made in subsection 3.2.5. On the other hand, the "variational" estimates have been found to underestimate significantly both the dilatation and the deviatoric part of the macroscopic strain-rate, when compared with the "second-order" and the dilute estimates of Fleck and Hutchinson and Lee and Mear.

The dilute results for transversely isotropic porous media have been supplemented by corresponding results for porous materials consisting of cylindrical voids with elliptical cross-section. In this connection, the "second-order" model was found to be in very good qualitative agreement with the Lee and Mear (1992b) results, although at high nonlinearities the quantitative agreement was less good. However, it is worth noting that, for the above mentioned reasons, the "second-order" model is expected to predict more compliant behavior for the porous material than the Lee and Mear method particularly for elliptical voids with higher aspect ratios. It is emphasized that the aforementioned work of Huang (1991b) was made for spherical voids, while no convergence studies have been performed for the case that the void is significantly elongated.

In the sequel, we have attempted to perform a thorough study of the effective behavior and the phase average strain-rate in the void as predicted by the "second-order" method, the "variational" bound and the high-rank laminate results for the case of purely deviatoric loading. The "second-order" estimates were found to be in good agreement with the laminate results, while they improved significantly on the "variational" method. A result that requires special attention in this case is the non-analytical effective behavior predicted by the "second-order" method in the dilute limit for porous media with an ideally-plastic matrix phase, and the blow-up of the average strain-rate in the voids in this case.

Next, the new "second-order" model has been studied in the case of transversely isotropic porous materials subjected to general plane-strain loading. In particular, the new "second-order" estimates were found to improve significantly on earlier estimates, particularly at high stress triaxialities where both the "variational" method and earlier versions of the "second-order" method seriously underestimated the effective response of the composite under hydrostatic loadings. The key ingredient for this improvement lies in the choice of the reference stress tensor, as already discussed in subsection 2.6.2, which allowed the "second-order" estimate to recover the analytical hydrostatic shell result. As a consequence, the "second-order" estimate for the corresponding macroscopic strain-rate, both hydrostatic and deviatoric, has also been shown to improve dramatically on the earlier "variational" result, which was found to underestimate significantly the hydrostatic part of the macroscopic strain-rate, especially at low porosities.

In the following, the "second-order" model has been extended to anisotropic microstructures, where it was illustrated that the value of the aspect ratio plays an important role in the determination of the effective behavior of anisotropic porous materials with cylindrical voids. In particular, it was found that the aspect ratio acts as a softening or a hardening mechanism, depending on the relative direction of the loading with respect to the major axis of the elliptical void. In this regard, it may cause an overall hardening to the material, even in cases that the porosity is increasing (increase of porosity

is a softening mechanism). The examples presented illustrated the subtle role that the underlying microstructure plays in the overall response of the material. Moreover, it was found that even though the Gurson criterion can be sufficiently accurate in the cases of transversely isotropic microstructures, it becomes overly stiff and thus is expected to give poor predictions when the microstructure becomes anisotropic.

Those results have been complemented with corresponding results for the macroscopic strain-rate. In this case, dramatic differences have been found between the case of cylindrical voids with circular and elliptical cross-sections. The deficiency of the Gurson model to include information about the pore shape was evident in that case. Moreover, it is important to remark that the mean macroscopic strain-rate can take very high values as the pore elongates. In this regard, it is expected that the macroscopic strain-rate takes the highest value in the case of a crack (i.e., as the aspect ratio goes to infinity or zero).

As a concluding remark of this chapter, it is worth noting that the "second-order" estimates for the instantaneous behavior of anisotropic porous materials with cylindrical voids can be used for the determination of the evolution of microstructure when the porous medium is subjected to finite deformations. In the following chapter, we will attempt to apply the results of this chapter to compute the evolution of microstructure for general plane-strain loading conditions.

4.7 Appendix I. Computation of the microstructural tensors

In this section, we give details for the computation of the microstructural tensors $\mathbf{Q}$ (or $\mathbf{P}$ from (2.60) and (2.61)) and $\mathbf{\Pi}$ in the context of porous media consisting of cylindrical voids with elliptical cross-section. For simplicity, we will present the evaluation of this tensor in the context of the "second-order" method, i.e., for a modulus tensor $\mathbf{L}$ of the matrix phase given by (2.167), recalled here for completeness

$$\mathbf{L} = 2\,\lambda\,\mathbf{E} + 2\,\mu\,\mathbf{F} + 3\,\kappa\,\mathbf{J}. \tag{4.37}$$

Then, by letting $\lambda = \mu$, $\mathbf{L}$ becomes isotropic and is the one used in the context of the "variational" method. Note that the incompressibility limit $\kappa \to \infty$ has to be considered in the computation of $\mathbf{Q}$ and $\mathbf{\Pi}$.

Now, the microstructural variables describing the shape of the voids in the plane are the aspect ratio of the elliptical void w and the orientation angle of the ψ. Thus, making use of the results of Willis (1982) for cylindrical voids, it is convenient to introduce here the tensor $\mathbf{Y}$, which is given by

$$Y_{ijkl} = \frac{w}{2\,\pi}\int_0^{2\,\pi} \frac{(L_{iakb}\,\xi_a\,\xi_b)\,\xi_j\,\xi_l}{\boldsymbol{\xi}\cdot(\boldsymbol{Z}^T\,\boldsymbol{Z})^{-1}\,\boldsymbol{\xi}}\,\mathrm{d}\phi \tag{4.38}$$

where $\xi = \{\cos\phi, \sin\phi\}$ and

$$\boldsymbol{Z} = \mathbf{n}^{(1)}\otimes\mathbf{n}^{(1)} + 1/w\,\mathbf{n}^{(2)}\otimes\mathbf{n}^{(2)}, \tag{4.39}$$

with $\mathbf{n}^{(1)} = \{\cos\psi, \sin\psi\}$ and $\mathbf{n}^{(2)} = \{-\sin\psi, \cos\psi\}$. Then, we can write the tensors $\mathbf{Q}$ and $\mathbf{\Pi}$ in terms of $\mathbf{Y}$ such that

$$\mathbf{Q} = \mathbf{L} - \mathbf{L}\,\mathbf{P}\,\mathbf{L}, \qquad \text{with} \qquad P_{ijkl} = \frac{1}{4}(Y_{ijkl} + Y_{ijlk} + Y_{jikl} + Y_{jilk}) \tag{4.40}$$

and

$$\Pi_{ijkl} = \frac{1}{4}(Y_{ijkl} + Y_{ijlk} - Y_{jikl} - Y_{jilk}). \tag{4.41}$$

The above expressions are valid for any modulus tensor $\mathbf{L}$. However, in this work, we deal with an incompressible matrix phase, which requires that $\kappa \to \infty$ in (4.37). Such a calculation could be achieved by making use of the commercial package Mathematica. First of all, taking the incompressibility limit in (4.40), one finds the result (4.5), (4.6) and (4.16), presented in the beginning of this chapter.

On the other hand, for the computation of the phase average spin in (4.28), it is necessary to evaluate the product $\mathbf{\Pi}\,\mathbf{L}$, in the limit $\kappa \to \infty$. This computation has been achieved by Mathematica but the details are too cumbersome to be reported here.

4.8 Appendix II. Evaluation of the reference stress tensor in 2D

In this section, we describe briefly the evaluation of the two factors that are present in the expression (4.20) that defines the reference stress tensor $\check{\boldsymbol{\sigma}}$, which is repeated here for completeness:

$$\check{\boldsymbol{\sigma}} = \xi\left(X_\Sigma,\, \overline{\boldsymbol{S}};\, f,\, w,\, \psi,\, n\right) \overline{\boldsymbol{\sigma}}', \tag{4.42}$$

where $\boldsymbol{S} = \overline{\boldsymbol{\sigma}}'/\overline{\sigma}_{eq}$ (see (2.166)) and

$$\xi\left(X_\Sigma, \overline{\boldsymbol{S}}\right) = \frac{1 - t\,f}{1 - f} + \alpha_m(\overline{\boldsymbol{S}})\,|X_\Sigma|\,\left(\exp\left[-\frac{\alpha_{eq}(\overline{\boldsymbol{S}})}{|X_\Sigma|}\right] + \beta\,\frac{X_\Sigma^4}{1 + X_\Sigma^4}\right), \tag{4.43}$$

is a suitably chosen interpolation function, with t and β given in Appendix III of chapter 2.

To evaluate the factor α_m, it is necessary to provide an estimate for the effective behavior of the porous material in purely hydrostatic loading. In this regard, we recall that the effective stress potential $\widetilde{U}$ of a porous material consisting of cylindrical voids, defined by (2.195), is expressed as

$$\widetilde{U}(\overline{\boldsymbol{\sigma}}; f, w) = \frac{\dot{\varepsilon}_o\,\widetilde{\sigma}_w}{1+n}\,\left(\frac{3}{2}\frac{|\overline{\sigma}_m|}{\widetilde{\sigma}_w}\right)^{1+n}. \tag{4.44}$$

For the estimation of effective flow stress $\widetilde{\sigma}_w$, we make use of the approximation proposed in relation (2.199), such that

$$\widetilde{\sigma}_w = \frac{\widetilde{\sigma}_{w\to\infty}}{\widetilde{\sigma}^{var}_{w\to\infty}}\,\widetilde{\sigma}^{var}_w, \tag{4.45}$$

where

$$\frac{\widetilde{\sigma}_{w\to\infty}}{\sigma_o} = \left(\frac{\sqrt{3}}{2}\right)^{\frac{1+n}{n}}\,n\left(f^{-1/n} - 1\right), \qquad \text{and} \qquad \frac{\widetilde{\sigma}^{var}_{w\to\infty}}{\sigma_o} = \left(\frac{\sqrt{3}}{2}\right)^{\frac{1+n}{n}}\,\frac{1-f}{\sqrt{f}^{\frac{1+n}{n}}}. \tag{4.46}$$

Here, the notation $w \to \infty$ has been used to indicate that the void has a cylindrical shape, in accordance with the general definitions introduced in subsection (2.2.1). The quantity $\widetilde{\sigma}_{w\to\infty}$ corresponds to the flow stress of a porous medium containing cylindrical voids with circular cross-section subjected to purely hydrostatic pressure. On the other hand, $\widetilde{\sigma}^{var}_{w\to\infty}$ and $\widetilde{\sigma}^{var}_w$ are the effective flow stresses of a

porous material consisting of cylindrical voids with circular and elliptical cross-section, respectively, as predicted by the "variational" method. The effective flow stress $\widetilde{\sigma}_w^{var}$ is given by (2.201) in the general case of ellipsoidal voids. However, for cylindrical voids, it can be shown to reduce to

$$\widetilde{\sigma}_w^{var} = \widetilde{\sigma}_{w\to\infty}^{var} \left(\frac{2\,w}{w^2+1} \right)^{\frac{n+1}{2\,n}} . \tag{4.47}$$

Then, the factor α_m is determined numerically by solving the following condition

$$\widetilde{U}_{som} \to \widetilde{U} \quad \text{as} \quad |X_\Sigma| \to \infty \quad \Rightarrow \quad \alpha_m = \alpha_m \left(\overline{\boldsymbol{S}}, f, w, n \right), \tag{4.48}$$

where $\widetilde{U}_{som}$ is the effective stress potential of the porous material given by (4.14), and needs to be computed in the hydrostatic limit. On the other hand, for the computation of the second factor α_{eq}, we make use of the analytical relation (2.207), which holds also for the cylindrical microstructures.

Porous media with an ideally-plastic matrix phase. For the computation of α_m and α_{eq} in the limit of ideal-plasticity, we just need to consider the limit $n \to \infty$ in the previous expressions. Thus, one finds in this limit that

$$\widetilde{\sigma}_{w\to\infty} = \frac{\sqrt{3}}{2} \log \frac{1}{f}, \qquad \text{and} \qquad \frac{\widetilde{\sigma}_{w\to\infty}^{var}}{\sigma_o} = \frac{\sqrt{3}}{2} \frac{1-f}{\sqrt{f}}, \tag{4.49}$$

and

$$\widetilde{\sigma}_w^{var} = \widetilde{\sigma}_{w\to\infty}^{var} \sqrt{\frac{2\,w}{w^2+1}}. \tag{4.50}$$

By making use of relation (4.29) (see also (2.290)), as well as of expression (4.49), the equation for the factor α_m becomes

$$\widetilde{\sigma}_w^{som} = \widetilde{\sigma}_w, \qquad \text{as} \qquad |X_\Sigma| \to \infty, \tag{4.51}$$

with $\widetilde{\sigma}_w$ given by (4.45). On the other hand, the factor α_{eq}, is determined in the ideally-plastic limit from relation (2.297), which is also valid in the case of cylindrical microstructures.

Chapter 5

Evolution of microstructure: cylindrical voids

The main objective of this chapter is to make use of the results of the previous one in order to estimate the evolution of microstructure for porous materials with cylindrical voids subjected to plane-strain loading conditions. For completeness and validation of the "second-order" model (SOM), presented in section 2.6, we study also the evolution of microstructure as predicted by the Lee and Mear (1999) (LM) method (see subsection 3.2.3), the "variational" method (VAR) (see section 2.5) and unit-cell finite element (FEM) calculations (see section 3.5). As already discussed in chapter 3, the two homogenization methods used in this work consider that the porous material consists of a random distribution of cylindrical voids aligned in the $3-$direction. On the other hand, the unit-cell calculation requires periodic boundary conditions. In this regard, the two problems, random and periodic, are not equivalent unless a sufficiently small value for the porosity is used. Note, however, that the computation of the fields in FEM becomes too cumbersome for very small porosities, since a large number of degrees of freedom needs to be used. Thus, for our problem, a porosity of $f_o = 0.01\%$ (sufficiently small) is used to perform the FEM calculations. Furthermore, it is noted that in the case of plane-strain loading, the problem reduces in estimating the in-plane effective behavior of the composite.

5.1 Evolution laws in two-dimensions

In particular, we study the problem of porous materials consisting of cylindrical voids with initially circular cross-section, subjected to plane-strain loading conditions. Due to the finite deformations, the initially circular voids evolve into elliptical ones with certain orientation in the plane. Thus, the relevant microstructural variables are the porosity f, the in-plane aspect ratio w and the in-plane orientation angle ψ. The general evolution equations presented in section 2.7, reduce here to:

Porosity. By making use of the incompressibility of the matrix phase, the evolution law for the porosity is obtained from the kinematical relations

$$\dot{f} = (1-f)\overline{D}_{\alpha\alpha}, \quad \alpha = 1,2, \tag{5.1}$$

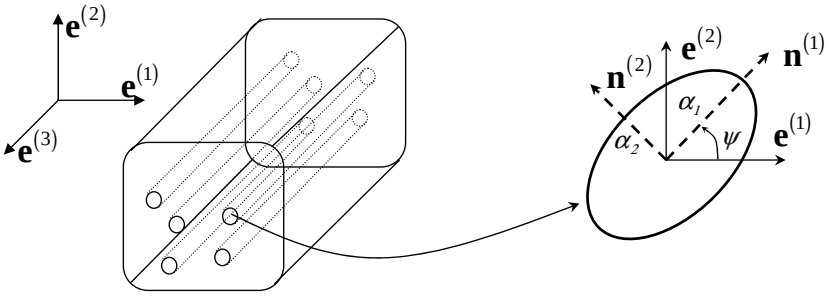

Figure 5.1: Representative ellipsoidal void in the case of cylindrical microstructures.

where $\overline{\boldsymbol{D}}$ is evaluated from relation (4.8) for the "variational" method and (4.22) for the "second-order" method.

Aspect ratio. The evolution of the in-plane aspect ratio of the void is defined by

$$\dot{w} = w\left(\mathbf{n}^{(2)} \cdot \overline{\boldsymbol{D}}^{(2)}\,\mathbf{n}^{(2)} - \mathbf{n}^{(1)} \cdot \overline{\boldsymbol{D}}^{(2)}\,\mathbf{n}^{(1)}\right) = w\left(\mathbf{n}^{(2)} \otimes \mathbf{n}^{(2)} - \mathbf{n}^{(1)} \otimes \mathbf{n}^{(1)}\right) \cdot \overline{\boldsymbol{D}}^{(2)}. \tag{5.2}$$

The average strain-rate in the void $\overline{\boldsymbol{D}}^{(2)}$ is computed by relation (4.9) for the "variational" method and (4.27) for the "second-order" method.

Orientation vectors. The evolution of the orientation vectors $\mathbf{n}^{(i)}$ (with $i = 1, 2$) is determined by the spin of the in-plane principal axes of the void, or microstructural spin $\boldsymbol{\omega}$, via

$$\dot{\mathbf{n}}^{(i)} = \boldsymbol{\omega}\,\mathbf{n}^{(i)}, \quad i = 1, 2. \tag{5.3}$$

Because of the two-dimensional character of the problem, the unit-vectors $\mathbf{n}^{(i)}$ are defined completely by the in-plane angle ψ, such that

$$\mathbf{n}^{(1)} = \cos\psi\ \mathbf{e}^{(1)} + \sin\psi\ \mathbf{e}^{(2)}, \qquad \mathbf{n}^{(2)} = -\sin\psi\ \mathbf{e}^{(1)} + \cos\psi\ \mathbf{e}^{(2)}. \tag{5.4}$$

Then, by making use of the standard notation

$$\boldsymbol{\omega} = \omega(\mathbf{e}^{(1)} \otimes \mathbf{e}^{(2)} - \mathbf{e}^{(2)} \otimes \mathbf{e}^{(1)}), \tag{5.5}$$

then the evolution law (5.3) can be replaced by the scalar expression

$$\dot{\psi} = -\omega. \tag{5.6}$$

Now, the microstructural spin $\boldsymbol{\omega}$ is related to the average spin in the void, $\overline{\boldsymbol{\Omega}}^{(2)}$, and the average strain-rate in the void, $\overline{\boldsymbol{D}}^{(2)}$, by the well-known kinematical relation (2.224) (Hill, 1978; Ogden, 1984), which takes the following form in two-dimensional problems

$$\boldsymbol{\omega} = \overline{\boldsymbol{\Omega}}^{(2)} - \frac{1}{2}\frac{1+w^2}{1-w^2}\left(\mathbf{n}^{(1)} \otimes \mathbf{n}^{(2)} + \mathbf{n}^{(2)} \otimes \mathbf{n}^{(1)}\right) \cdot \overline{\boldsymbol{D}}^{(2)}, \qquad w \neq 1. \tag{5.7}$$

The average spin tensor $\overline{\boldsymbol{\Omega}}^{(2)}$ in the pore phase is given by (4.9) for the "variational" method and by (4.28) for the "second-order" method.

Following definition (2.228) and expression (2.229) for the plastic spin (i.e., $\boldsymbol{\Omega}^p = \overline{\boldsymbol{\Omega}} - \boldsymbol{\omega}$), the Jaumann rate of the orientation vectors $\mathbf{n}^{(i)}$ is defined by

$$\overset{\triangledown}{\mathbf{n}}{}^{(i)} = -\boldsymbol{\Omega}^p\,\mathbf{n}^{(i)} \qquad i = 1, 2, 3. \tag{5.8}$$

The above definition is helpful for the computation of the Jaumann hardening rate in the context of ideal-plasticity. Note that the above evolution laws are valid for both the "variational" and the "second-order" method, while the computation of the phase average fields in the composite is the one that brings about the difference between the "variational" and the "second-order" estimates.

In the following, we study the evolution of microstructure in dilute porous media consisting of cylindrical voids with initially circular or elliptical cross-section. The Lee and Mear (1999) (LM) predictions are used as a comparison for the corresponding "second-order" (SOM) estimates. Next, we study the evolution of microstructure in porous materials subjected to loading conditions that do not induce a rotation of the principal axes of the void. In this case, we discuss the effect of the porosity and the aspect ratio on the effective response of the porous material. The results obtained by the SOM and the "variational" (VAR) methods are compared with corresponding estimates by FEM unit-cell calculations. Finally, a simple shear loading is applied. In this case, the effect of the orientation angle on the effective response of the material is studied.

5.2 Dilute porous media

In this section, we compare the evolution of the microstructure as predicted by the "second-order" method (SOM) with the Lee and Mear (1999) (LM) method presented in subsection 3.2.3 in the context of dilute porous media. The main objective of this comparison is to check the range of validity of the results obtained by the two methods. In this connection, it has been observed by Duva and Hutchinson (1984) and Duva (1986) that the dilute methods, such as the one of Lee and Mear (1999) under consideration here, cannot be used to deliver accurate estimates for small but finite concentrations of voids, particularly at high nonlinearities and stress triaxialities. The reason for this has been attributed to the fact that these dilute techniques are not able to take into account the interactions between voids, which may become large at high nonlinearities even when the concentration of voids is small. In this regard, we present results derived by the SOM method for an initial porosity $f_o = 10^{-6}$, as well as results provided by the work of Lee and Mear (1999) for dilute porous media. For validation of these two methods, we also include SOM and FEM results for small but finite porosities, e.g., $f_o = 10^{-4}$. It will be seen that the difference between the SOM results for $f_o = 10^{-6}$ and $f_o = 10^{-4}$ is negligible indicating that convergence of the SOM results is achieved.

Next, referring to Fig. 5.1, we define the loading considered in this section in terms of the remote non-zero, in-plane components of the stress tensor

$$\overline{\sigma}_{11} = T, \quad \overline{\sigma}_{22} = S, \quad \overline{\sigma}_{33} = \frac{1}{2}(S + T). \tag{5.9}$$

The $\overline{\sigma}_{33}$ takes the aforementioned value due to the fact that the matrix phase is incompressible and

the loading is plane-strain. Then, the stress triaxiality is defined in terms of S and T by

$$X_\Sigma = \frac{S+T}{\sqrt{3}\,|S-T|} = \frac{S}{|S|}\,\frac{1+T/S}{\sqrt{3}\,|1-T/S|}. \tag{5.10}$$

In the figures to follow, we use the ratio T/S as the loading parameter in the problem. The values used are $T/S = 0, 0.2, 0.4, 0.6$, which correspond to stress triaxiality $X_\Sigma = \pm 1/\sqrt{3}, 0.866, 1.347, 2.309$, respectively. Obviously, the sign of the X_Σ depends on the sign of the normalized quantity $S/|S|$. For later use, it is pertinent to define here the remote equivalent strain-rate $\dot{\varepsilon}^\infty_{eq}$ and strain in the absence of voids, which take the form

$$\dot{\varepsilon}^\infty_{eq} = \dot{\varepsilon}_o \left(\frac{\overline{\sigma}_{eq}}{\sigma_o}\right)^n, \quad \varepsilon^\infty_{eq} = \int_t \dot{\varepsilon}^\infty_{eq} \mathrm{d}t, \tag{5.11}$$

where σ_o is the flow stress of the matrix phase and $\dot{\varepsilon}_o$ is a reference strain-rate taken in the calculation to follow equal to unity.

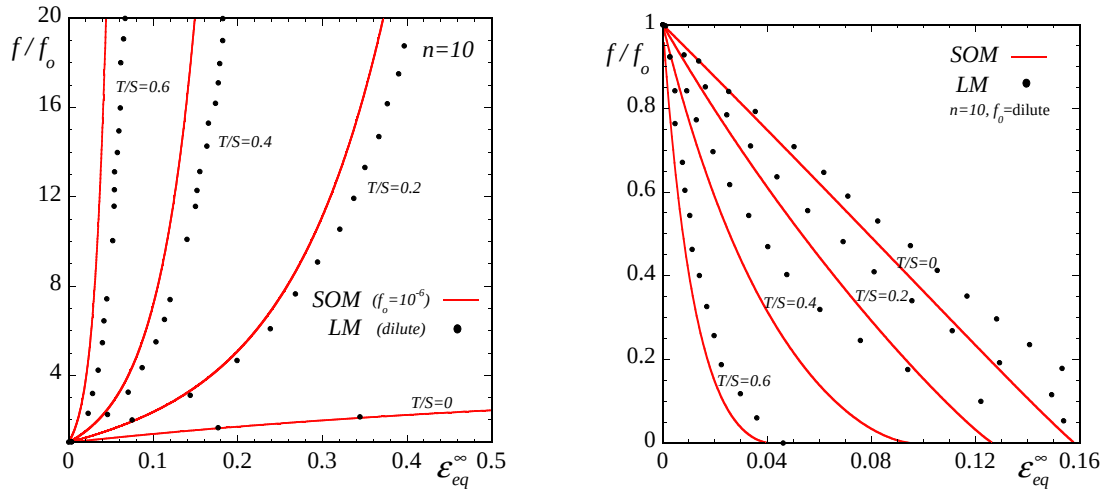

(a) (b)

Figure 5.2: Results are shown for the evolution of the normalized porosity f/f_o as a function of the remote equivalent strain ε^∞_{eq} for a dilute porous material consisting of cylindrical pores with initially circular cross-section. The matrix phase exhibits a viscoplastic behavior with an exponent $n = 10$. *SOM* and *LM* estimates are shown for (a) tensile and (b) compressive loading conditions for ratios of the in-plane stress components $T/S = 0, 0.2, 0.4, 0.6$ or $X_\Sigma = \pm 1/\sqrt{3}, 0.866, 1.347, 2.309$.

Fig. 5.2 shows results for the evolution of the normalized porosity f/f_o for several stress ratios $T/S = 0, 0.2, 0.4, 0.6$, as a function of the remote equivalent strain ε^∞_{eq} for a nonlinear exponent $n = 10$. In this figure, the *SOM* estimates are found to be in agreement with the *LM* results for all stress ratios considered. In particular, Fig. 5.2a shows results for tensile loadings, i.e., $S/|S| > 0$, where it is illustrated that by increasing the stress ratio T/S, the normalized porosity f/f_o climbs up rapidly at very high values. Here, we observe that the *LM* method is found to slightly underestimate the evolution of the porosity when compared with the *SOM* results, which is consistent with the results shown in section (4.2). In turn, Fig. 5.2b shows corresponding results for compressive loadings, i.e., $S/|S| < 0$. In this case, the voids collapse, i.e., the porosity closes down at finite strains. The strain,

where pore closure occurs, is strongly dependent on the stress triaxiality in that for a $T/S = 0.6$ the voids collapse at very low remote strain $\sim 4\%$, whereas for $T/S = 0$ pore closure occurs at a remote strain $\sim 16\%$. The results predicted by the SOM are found to be softer in comparison with the LM predictions, which is in accord with the remark made in the context of Fig. 5.2a, i.e., that the LM is stiffer at high nonlinearities.

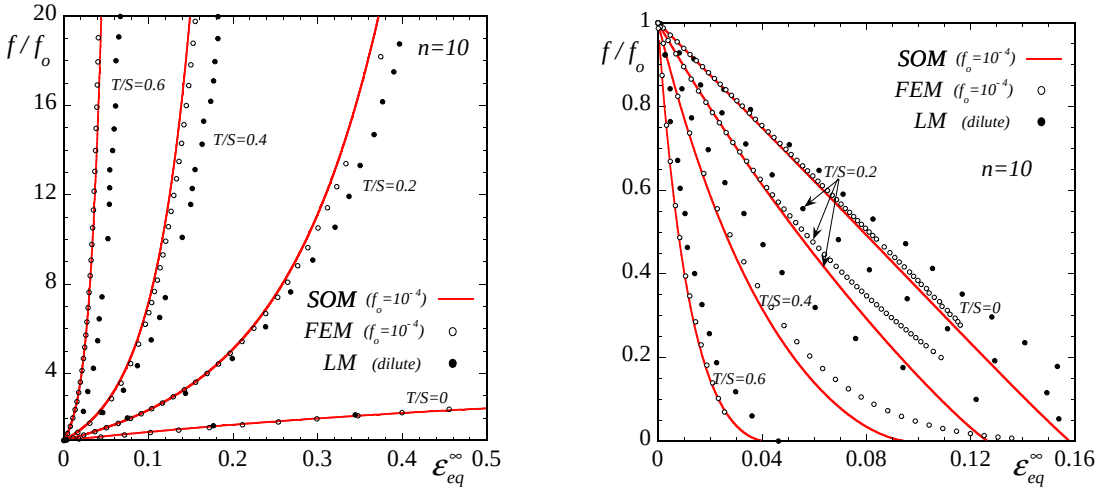

Figure 5.3: Results are shown for the evolution of the normalized porosity f/f_o as a function of the remote equivalent strain $\varepsilon^{\infty}_{eq}$ for a dilute porous material consisting of cylindrical pores with initially circular cross-section. The matrix phase exhibits a viscoplastic behavior with an exponent $n = 10$. SOM and LM estimates are shown for (a) tensile and (b) compressive loading conditions for ratios of the in-plane stress components $T/S = 0, 0.2, 0.4, 0.6$ or $X_{\Sigma} = \pm 1/\sqrt{3}, 0.866, 1.347, 2.309$.

As already stated in the introduction of this section, in order to validate further the results obtained in the previous figure, we present in Fig. 5.3 results for the evolution of the normalized porosity f/f_o as predicted by the SOM and the FEM methods for porosities $f_o = 10^{-4}$, which are "compared" with the dilute estimates of Lee and Mear. It should be noted that the SOM predictions corresponding to $f_o = 10^{-4}$ and $f_o = 10^{-6}$ did not exhibit any difference indicating that both values could be used to approximate sufficiently the dilute limit. In turn, the stress triaxialities considered here are the same used previously, i.e., $T/S = 0, 0.2, 0.4, 0.6$. First of all, we observe that the FEM results lie closer to the corresponding SOM estimates for both tensile and compressive loadings than to the LM predictions. In particular, the FEM results are more compliant than the LM estimates, which is in accordance with the observations made previously in the context of the SOM predictions. It is also important to recall here that contrary to the FEM calculations, the LM procedure assumes that the void evolves through a sequence of elliptical shapes (see also Fleck and Hutchinson, 1986) during the deformation process, which constitutes an idealization that may become rough particularly at high stress triaxialities and nonlinearities. On the other hand, in the SOM, use is made of the average fields in the vacuous phase to compute an average *elliptical* shape for the void. Obviously, all of the three procedures are different and, in general, are expected to lead to different estimates.

However, it is evident from Fig. 5.3 and the results discussed in section 4.2, that the LM procedure may underestimate slightly the effective response of dilute porous media.

5.2.1 Effect of the orientation angle

In this subsection, the SOM method is compared with the LM method for the prediction of the behavior of a dilute porous medium consisting of cylindrical voids with elliptical cross-section, whose principal axes are misaligned with the principal loading directions. For this reason, we consider a void with in-plane aspect ratio $w = 0.5$, whose semi-major axis (i.e., a_1 in Fig. 5.1) is oriented at $\psi = 22.5, 45, 67.5^o$ with respect to the $\mathbf{e}^{(1)}-$axis. The porous material is subjected to uniaxial tension and compression loading conditions with $T/S = 0$ (i.e., $X_\Sigma = \pm 1/\sqrt{3} \backsimeq \pm 0.57738$). The behavior of the matrix phase is described by a nonlinear exponent $n = 5$.

For the microstructural state described previously, Fig. 5.4 shows results for the evolution of the normalized porosity f/f_o and the orientation angle ψ as a function of the remote equivalent strain $\varepsilon_{eq}^{\infty}$, when the porous medium is subjected to uniaxial tension loading. Concerning the evolution of f/f_o, in Fig. 5.4a, both the SOM and the LM methods agree very well for the entire range of deformations considered. In particular, they both predict that when the semi-major axis of the void is initially oriented at $\psi = 22.5^o$ the porosity grows much faster than for $\psi = 45^o$ and $\psi = 67.5^o$, which is intuitively expected. In turn, Fig. 5.4b shows corresponding curves for the evolution of ψ during the deformation process. As already expected the semi-major axis of the void tends to align with the direction of the maximum principal stretch, which occurs obviously at the direction of the maximum principal stress S, i.e., at $\psi = 90^o$. It is interesting to observe that rotation of the principal axes of the void happens relatively fast, approaching the asymptotic value of $\psi = 90^o$ in $\sim 40\%$ strain.

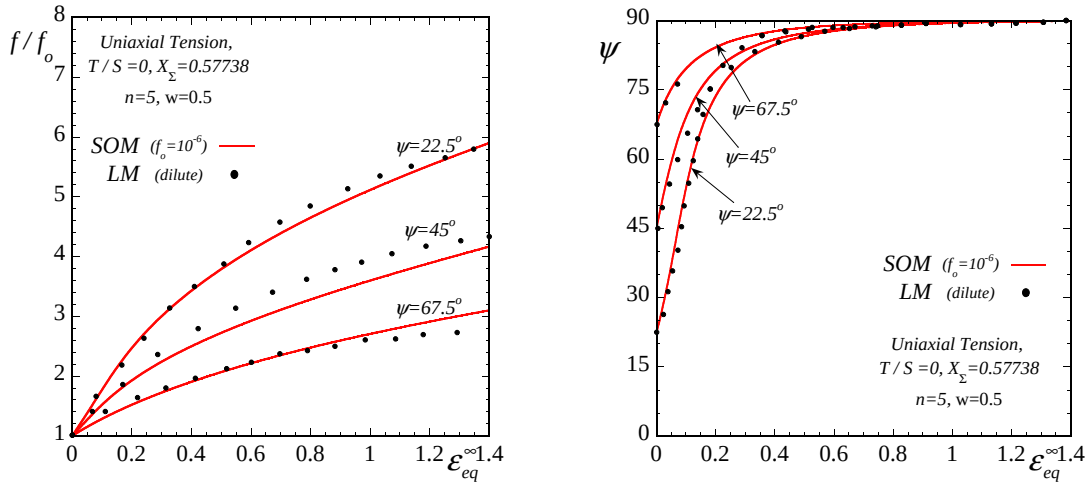

(a) (b)

Figure 5.4: Comparison of SOM with LM results are shown for the evolution of (a) the normalized porosity f/f_o and (b) the orientation angle ψ as a function of the remote equivalent strain $\varepsilon_{eq}^{\infty}$ for a dilute porous material consisting of an elliptical void with initial aspect ratio $w = 0.5$ oriented at initial angles $\psi = 22.5, 45, 67.5^o$. The matrix phase exhibits a viscoplastic behavior with an exponent $n = 5$ and the material is subjected to uniaxial tension loading, i.e., $X_\Sigma = 1/\sqrt{3}$ or $T/S = 0$ with $S/|S| > 0$.

In turn, Fig. 5.5 shows results for the evolution of the normalized porosity f/f_o and the orientation angle ψ as a function of the remote equivalent strain $\varepsilon_{eq}^{\infty}$ for a porous medium subjected to uniaxial compression loading. More specifically, in Fig. 5.5a, the SOM is found to be in good agreement with the LM results for all the angles ψ considered here. According to the observations made in the case of uniaxial tension, the porosity is found to close down faster in the case of $\psi = 22.5^o$ and slower for $\psi = 67.5^o$. On the other hand, Fig. 5.5b shows the evolution of the angle ψ as a function of $\varepsilon_{eq}^{\infty}$. As expected intuitively, the semi-major axis of the void tends to align with the $\mathbf{e}^{(1)}-$axis (i.e., $\psi = 0^o$), which is transverse to the maximum principal compressive stress. However, due to the fact that the porosity becomes zero at finite values of the remote strain $\varepsilon_{eq}^{\infty}$, the void never reaches the asymptotic value of $\psi = 0^o$ for any of the initial configurations considered here.

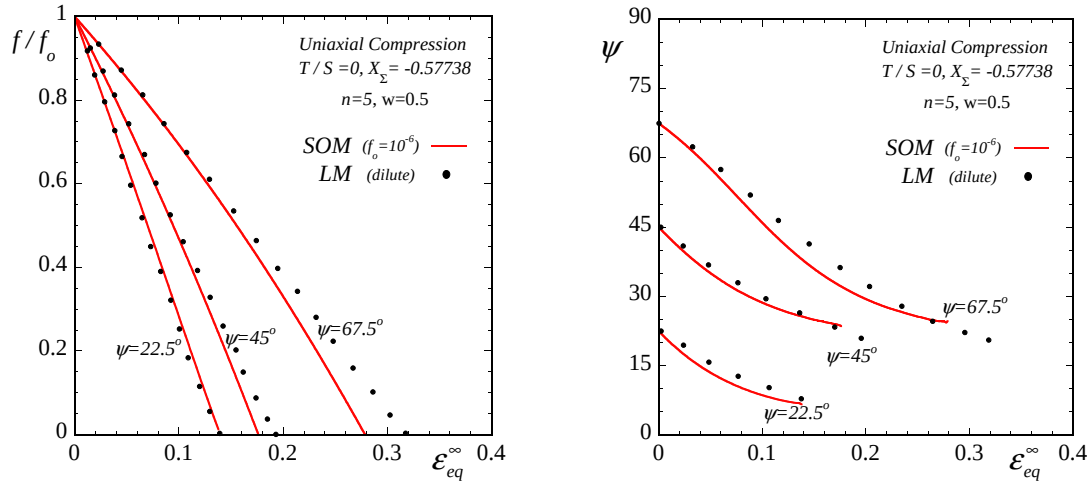

(a) (b)

Figure 5.5: Comparison of SOM with LM results are shown for the evolution of (a) the normalized porosity f/f_o and (b) the orientation angle ψ as a function of the remote equivalent strain $\varepsilon_{eq}^{\infty}$ for a dilute porous material consisting of an elliptical void with initial aspect ratio $w = 0.5$ oriented at initial angles $\psi = 22.5, 45, 67.5^o$. The matrix phase exhibits a viscoplastic behavior with an exponent $n = 5$ and the material is subjected to uniaxial compression loading, i.e., $X_\Sigma = -1/\sqrt{3}$ or $T/S = 0$ with $S/|S| < 0$.

In summary, we have shown some selective results for evolution of microstructure in dilute porous media. The SOM was compared with the LM model and it has been found to be in good agreement, particularly at lower triaxialities. On the other hand, at higher triaxialities, the LM results were found to underestimate slightly the evolution of the porosity, as already expected from the analysis made in subsection 3.2.5 and the results presented in section 4.2. Finally, the SOM has been found to predict the right evolution of the porosity and orientation angle for dilute porous media consisting of voids with initially elliptical cross-section misaligned with the principal directions of the loading. In the following sections, we validate the SOM model against FEM calculations for finite, but still small initial porosities. In addition, we include also the "variational" method, presented in section 2.5. As already explained in subsection 3.2.5, the hydrostatic part of the effective stress potential predicted by the "variational" method does not have a linear correction in the porosity f in the dilute limit and for this reason it was not meaningful to include results in this section.

5.3 Viscoplasticity

In this section, we study the problem of estimating the evolution of the microstructure and the macroscopic behavior of porous media consisting of cylindrical voids with initially circular cross-section. For the calculations performed in this section (except in subsection 5.3.4), traction boundary conditions are applied, so that the only non-zero in-plane, components of the macroscopic stress tensor are

$$\overline{\sigma}_{11} = T, \quad \overline{\sigma}_{22} = S, \quad \overline{\sigma}_{12} = 0, \quad X_\Sigma = \frac{\overline{\sigma}_{11} + \overline{\sigma}_{22}}{\sqrt{3}\,|\overline{\sigma}_{11} - \overline{\sigma}_{22}|} = \frac{S}{|S|}\,\frac{1 + T/S}{\sqrt{3}\,|1 - T/S|}, \tag{5.12}$$

where X_Σ is the stress triaxiality and is recalled here for clarity. In the figures to follow, we use the stress triaxiality X_Σ as the loading parameter in the problem. The values used are $X_\Sigma = 0, \pm 1/\sqrt{3}, 1, 5$, which correspond to stress ratio $T/S = -1, 0, 0.268, 0.793$ with $S/|S|$ being positive for tensile or negative for compressive loadings, respectively.

Provided that the major axis of the voids is aligned with the laboratory frame of reference and the principal loading axes, the only relevant microstructural variables are the porosity f and the in-plane aspect ratio $w = a_2/a_1$, with a_1 and a_2 denoting the lengths of the principal semi-axes of the ellipsoidal void (see Fig. 5.1). In turn, the orientation of the void remains fixed during the deformation process. Now, for reasons explained in subsection 3.5, the initial porosity is chosen to be $f_o = 0.01\%$. In the following subsections, we study a sequel of tensile and compressive loadings at several stress triaxialities and nonlinearities in an attempt to validate the "second-order" (SOM) method against finite-element calculations (FEM), while compare it with the earlier "variational" method (VAR).

5.3.1 Pure shear loading

Fig. 5.6 presents results for the evolution of the normalized porosity f/f_o, the aspect ratio w and the macroscopic equivalent strain-rate $\overline{D}_{eq}$ normalized by the equivalent strain-rate $\dot{\varepsilon}^\infty_{eq}$ in the absence of voids (see relation (5.11)), as a function of the macroscopic equivalent strain $\overline{\varepsilon}_{eq}$ and the nonlinearity $n = 1, 2, 4, 10$. The porous medium is subjected to pure shear loading, i.e., $X_\Sigma = 0$ or $\overline{\sigma}_{22} = -\overline{\sigma}_{11} > 0$ (or $T/S = -1$ with $S/|S| > 0$). The main observation in the context of this figure is that the SOM is in excellent agreement with the FEM for all nonlinearities considered. In contrast, the VAR estimate for the evolution of the normalized porosity f/f_o and the aspect ratio w shows no dependence on the nonlinear exponent n and coincides with the $n = 1$ curve. In addition, it underestimates significantly the normalized macroscopic strain-rate $\overline{D}_{eq}/\dot{\varepsilon}^\infty_{eq}$ especially at high nonlinearities.

More specifically, in Fig. 5.6a, it is observed that the normalized porosity f/f_o finally becomes zero at finite values of the total deformation. The value of the strain, that pore closure occurs, depends strongly on the nonlinearity of the problem, i.e., for $n = 1$ the porosity becomes zero at $\sim 58\%$ deformation, whereas for $n = 10$ the corresponding deformation is $\sim 24\%$. In addition, as the porosity approaches zero, the corresponding aspect ratio w (see Fig. 5.6b) approaches infinity, which implies that the void evolves into a crack. Note that the evolution of w depends strongly on the nonlinearity of the problem, similar to the evolution of the porosity. The macroscopic strain-rate

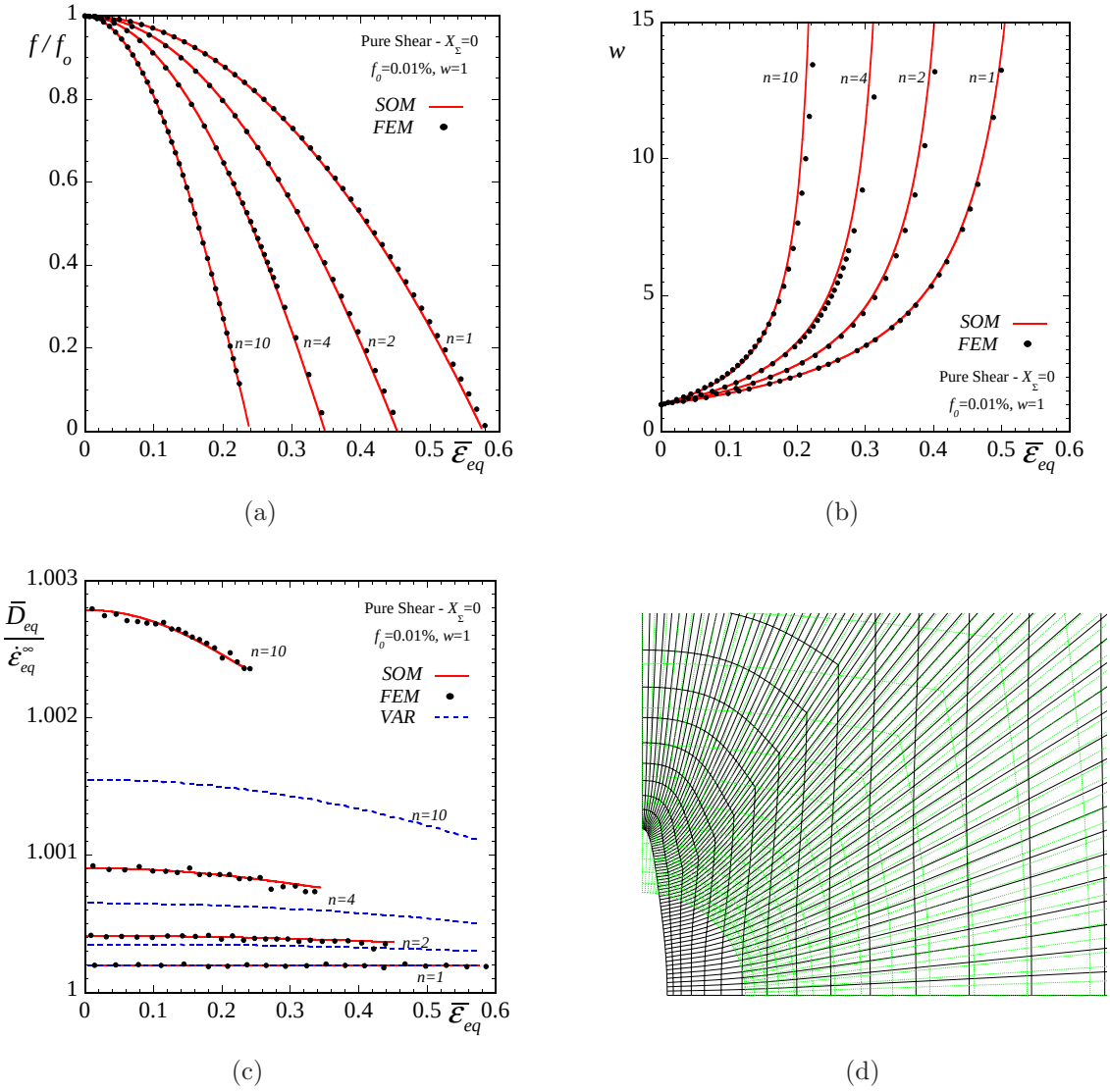

Figure 5.6: Results are shown for the evolution of the relevant microstructural and macroscopic variables for a porous material consisting of cylindrical pores with an initially, circular cross-section and porosity $f_o = 0.01\%$. The matrix phase exhibits a viscoplastic behavior with exponents $n = 1, 2, 4, 10$, while the composite is subjected to in-plane, pure shear ($X_\Sigma = 0$ or $T/S = -1$ with $S/|S| > 0$) loading conditions. SOM, FEM and VAR estimates are shown for the evolution of the (a) normalized porosity f/f_o, (b) the aspect ratio w and (c) the normalized equivalent strain-rate $\overline{D}_{eq}/\dot{\varepsilon}_{eq}$ ($\dot{\varepsilon}_{eq}$ is the corresponding remote strain-rate in the absence of voids). The VAR estimate for the evolution of the normalized porosity f/f_o and the aspect ratio w is found to be independent of the nonlinear exponent n and the corresponding predictions coincide with the $n = 1$ curves. Part (d) shows a typical deformed and undeformed FEM mesh at a given instant in time.

$\overline{D}_{eq}/\dot{\varepsilon}^{\infty}_{eq}$, in turn, is found to take higher values as the nonlinearity increases and is always greater than the corresponding remote strain-rate $\dot{\varepsilon}^{\infty}_{eq}$, as shown in Fig. 5.6c. It is obvious from this plot that the VAR method underestimates the effective behavior of the porous medium. On the other hand, the SOM method is in excellent agreement with the FEM results for all n considered here. For

visualization reasons, a plot of the initial and deformed mesh of the unit-cell is shown in Fig. 5.6d for a nonlinearity $n = 10$. In this figure, we can clearly observe the decrease of the porosity and the elongation of the pore in the direction of the maximum principal stress.

5.3.2 Tensile loadings

Uniaxial tension loading. Fig. 5.7 presents results for the evolution of the normalized porosity f/f_o, the aspect ratio w, and the normalized macroscopic axial component of the strain-rate $\overline{D}_{22}/\dot{\varepsilon}^{\infty}_{eq}$ as a function of the nonlinear exponent $n = 1, 2, 4, 10$ and the macroscopic axial strain $\overline{\varepsilon}_{22}$ for uniaxial tension (i.e., $X_\Sigma = 1/\sqrt{3}$ or $T/S = 0$ with $S/|S| > 0$). In Fig. 5.7a, the predictions of the SOM for the evolution of porosity are in very good agreement with the FEM results for all the nonlinearities considered, except for the case of $n = 10$ and large deformation $\overline{\varepsilon}_{22} > 60\%$, where a small difference between the two estimates is observed. On the other hand, the VAR estimates for f/f_o are independent of n so that all the VAR predictions coincide with the $n = 1$ curve. This implies that the VAR method underestimates the evolution of the porosity f/f_o at high nonlinearities. Furthermore, a main feature of this loading predicted by all the methods shown here, is that the porosity initially grows but finally it approaches an asymptote for sufficiently large strains. For $n = 10$ the initial porosity $f = 0.01\%$ increases four times to take a value $f \sim 0.04\%$, after 100% deformation. In turn, looking at Fig. 5.7b, the corresponding aspect ratio grows substantially for large deformations. In this case, both predictions are in good agreement up to a nonlinearity $n = 4$, whereas for $n = 10$ the SOM overestimates the evolution of w when compared with the FEM. On the other hand, the VAR estimates for w are independent of n and thus they all coinceide with the $n = 1$ curve.

In turn, the corresponding macroscopic axial strain-rate $\overline{D}_{22}/\dot{\varepsilon}^{\infty}_{eq}$ is in good agreement for all the nonlinearities, certainly in much better agreement than the corresponding VAR estimate, which tends to underestimate significantly $\overline{D}_{22}/\dot{\varepsilon}^{\infty}_{eq}$, especially at large nonlinearities. Of course all the estimates coincide for the linear case (i.e., $n = 1$). Finally, Fig. 5.7d shows undeformed and deformed meshes of the unit-cell for $n = 10$. In this figure, it is clearly observed that for this stress triaxiality $X_\Sigma = 1/\sqrt{3}$ the elongation of the pore is much more significant than the total increase of the void surface.

Biaxial tension loading with $X_\Sigma = 1$. In the previous loading conditions, the stress triaxiality was sufficiently small ($X_\Sigma < 0.6$). In Fig. 5.8, we consider a biaxial tension loading such that the stress triaxiality is $X_\Sigma = 1$ (or $T/S = 0.268$ with $S/|S| > 0$). Corresponding results for the evolution of the normalized porosity f/f_o, the aspect ratio w and the normalized macroscopic equivalent strain-rate $\overline{D}_{eq}/\dot{\varepsilon}^{\infty}_{eq}$ are shown as a function of the nonlinearity and the total equivalent strain $\overline{\varepsilon}_{eq}$. In particular, in Fig. 5.8a, the porosity f/f_o grows rapidly to high values especially at high nonlinearities. The corresponding SOM and FEM are in good agreement, while the VAR estimate is independent of the nonlinearity so that all the predictions coincide with the $n = 1$ curve. This last observation shows clearly the improvement of the SOM estimate on the earlier VAR estimates. This is a direct consequence of the fact that the SOM is constructed such that it recovers the analytical hydrostatic point predicted by a cylindrical shell subjected to hydrostatic pressure (see subsection 2.6.2). On the

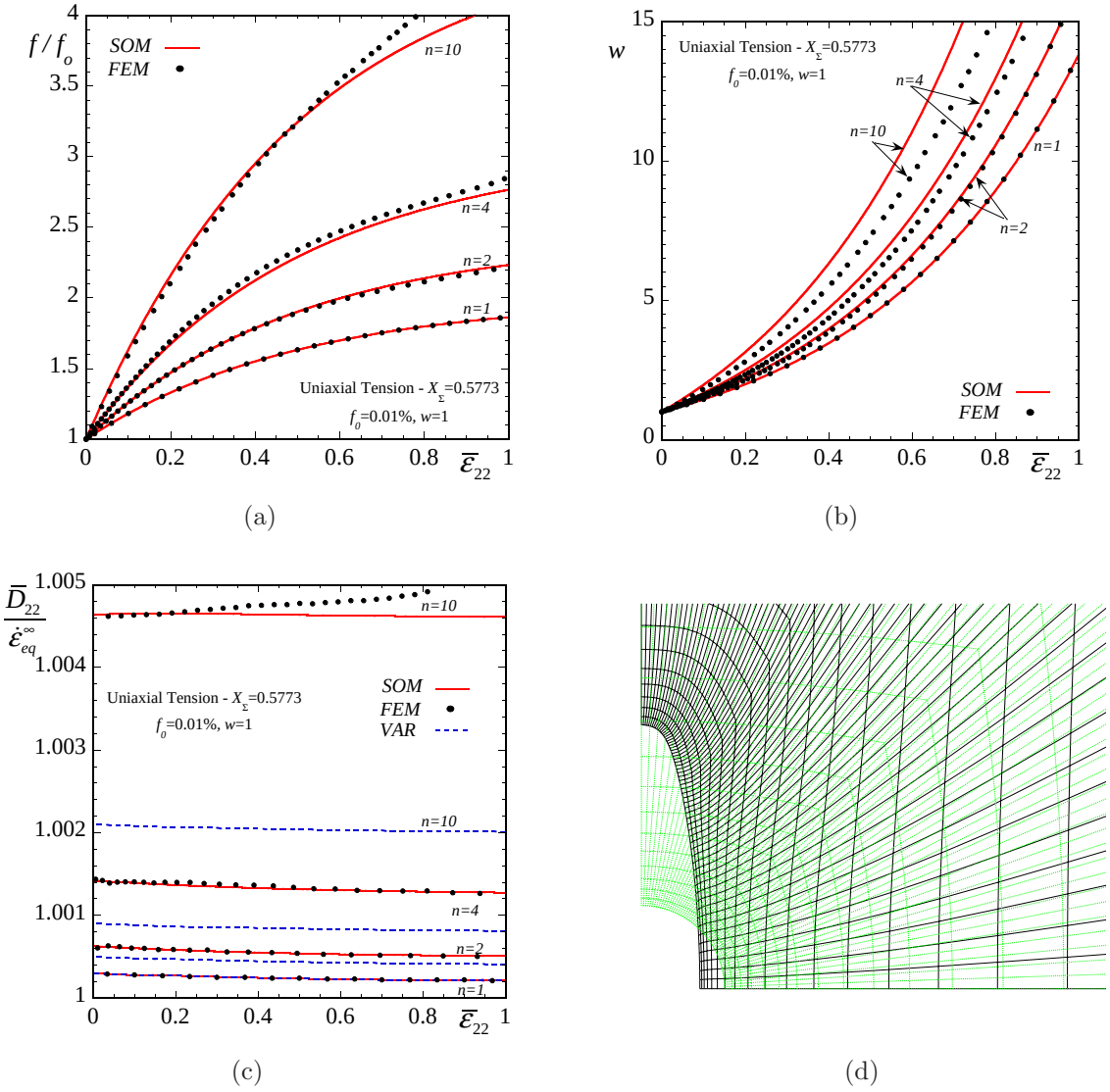

Figure 5.7: Results are shown for the evolution of the relevant microstructural and macroscopic variables for a porous material consisting of cylindrical pores with an initially, circular cross-section and porosity $f_o = 0.01\%$. The matrix phase exhibits a viscoplastic behavior with exponents $n = 1, 2, 4, 10$, while the composite is subjected to uniaxial tension ($X_\Sigma = 1/\sqrt{3}$ or $T/S = 0$ with $S/|S| > 0$) loading conditions. SOM, FEM and VAR estimates are shown for the evolution of the (a) normalized porosity f/f_o, (b) the aspect ratio w and (c) the normalized axial strain-rate $\overline{D}_{22}/\dot{\varepsilon}_{eq}$ ($\dot{\varepsilon}_{eq}$ is the corresponding remote strain-rate in the absence of voids). The VAR estimate for the evolution of the normalized porosity f/f_o and the aspect ratio w is found to be independent of the nonlinear exponent n and the corresponding predictions coincide with the $n = 1$ curves. Part (d) shows a typical deformed and undeformed FEM mesh at a given instant in time.

other hand, in Fig. 5.8b, the SOM estimates for the aspect ratio w deviate from the corresponding FEM predictions, especially at high nonlinearities (i.e., for $n = 10$). Nonetheless, this difference in the prediction of w does not affect the estimation of the normalized macroscopic strain-rate $\overline{D}_{eq}/\dot{\varepsilon}^{\infty}_{eq}$, where the SOM and the FEM are found to be in very good agreement. This last result indicates

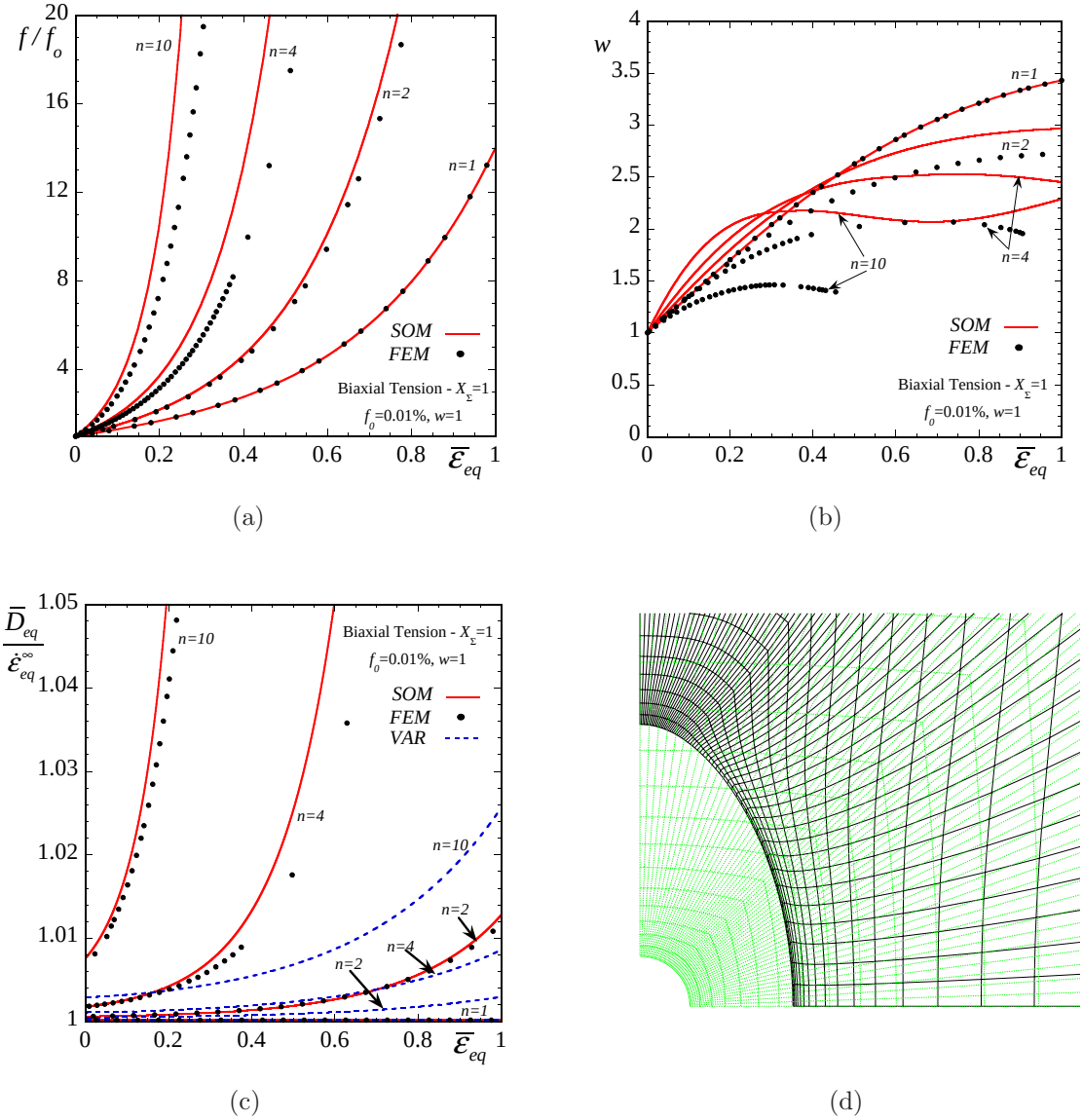

Figure 5.8: Results are shown for the evolution of the relevant microstructural and macroscopic variables for a porous material consisting of cylindrical pores with an initially, circular cross-section and porosity $f_o = 0.01\%$. The matrix phase exhibits a viscoplastic behavior with exponents $n = 1, 2, 4, 10$, while the composite is subjected to biaxial tension ($X_\Sigma = 1$ or $T/S = 0.268$ with $S/|S| > 0$) loading conditions. SOM, FEM and VAR estimates are shown for the evolution of the (a) normalized porosity f/f_o, (b) the aspect ratio w and (c) the normalized equivalent strain-rate $\overline{D}_{eq}/\dot{\varepsilon}_{eq}$ ($\dot{\varepsilon}_{eq}$ is the corresponding remote strain-rate in the absence of voids). The VAR estimate for the evolution of the normalized porosity f/f_o and the aspect ratio w is found to be independent of the nonlinear exponent n and the corresponding predictions coincide with the $n = 1$ curves. Part (d) shows a typical deformed and undeformed FEM mesh at a given instant in time.

that, for triaxiality $X_\Sigma = 1$, the macroscopic behavior of the composite is mainly controlled by the evolution of the porosity and not the one of the aspect ratio. In turn, the VAR estimate, which fails to predict well the evolution of the porosity, fails also to predict the right evolution of the macroscopic

strain-rate $\overline{D}_{eq}/\dot{\varepsilon}^{\infty}_{eq}$. Finally, Fig. 5.8d shows undeformed and deformed meshes of the unit-cell for $n = 10$. In this figure, it is clearly observed that for this stress triaxiality $X_{\Sigma} = 1$ the volume of the void increases significantly, while the aspect ratio of the void remains close to unity.

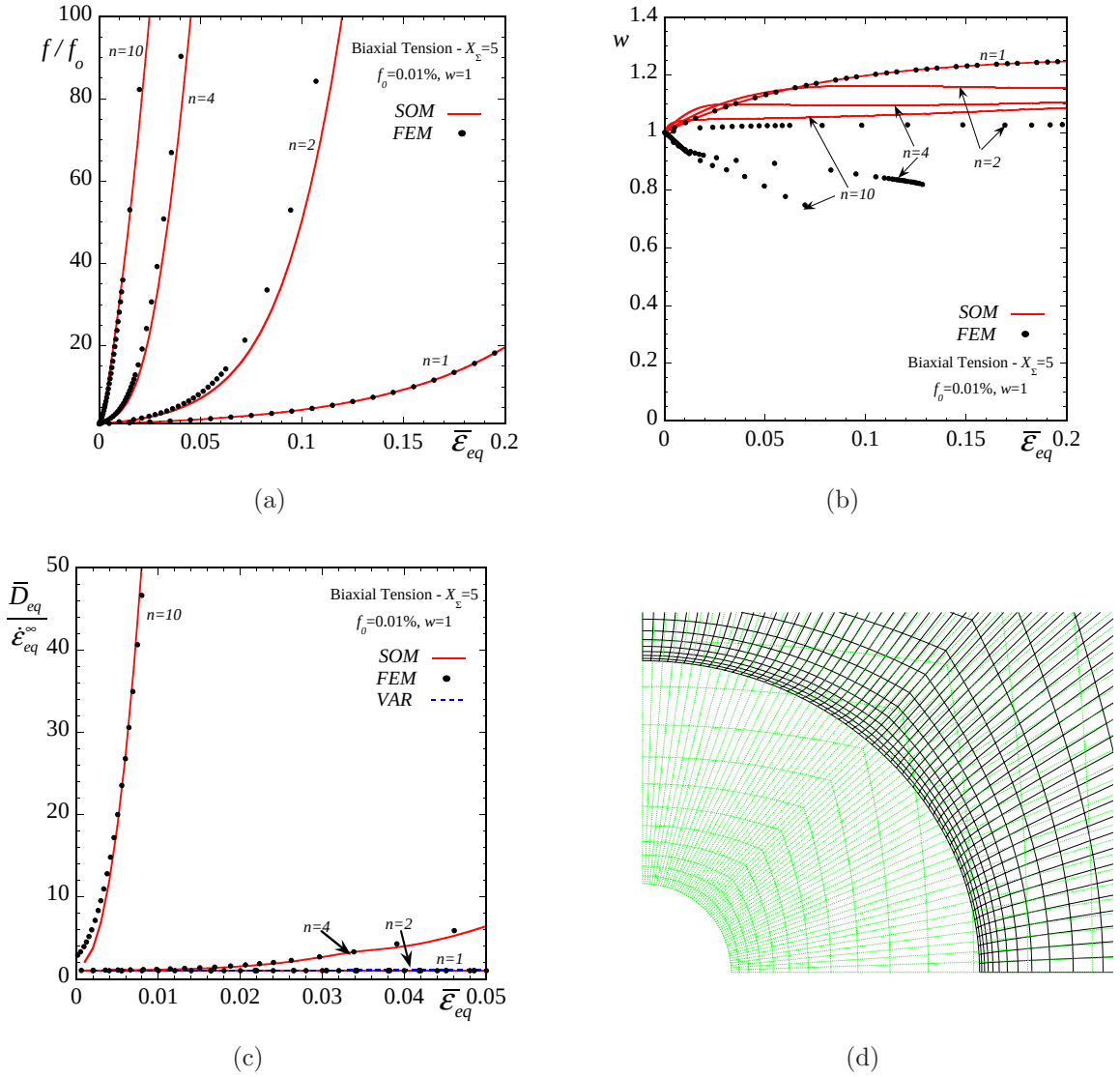

Figure 5.9: Results are shown for the evolution of the relevant microstructural and macroscopic variables for a porous material consisting of cylindrical pores with an initially, circular cross-section and porosity $f_o = 0.01\%$. The matrix phase exhibits a viscoplastic behavior with exponents $n = 1, 2, 4, 10$, while the composite is subjected to biaxial tension ($X_{\Sigma} = 5$ or $T/S = 0.793$ with $S/|S| > 0$) loading conditions. SOM, FEM and VAR estimates are shown for the evolution of the (a) normalized porosity f/f_o, (b) the aspect ratio w and (c) the normalized equivalent strain-rate $\overline{D}_{eq}/\dot{\varepsilon}_{eq}$ ($\dot{\varepsilon}_{eq}$ is the corresponding remote strain-rate in the absence of voids). The VAR estimate for the evolution of the normalized porosity f/f_o and the aspect ratio w is found to be independent of the nonlinear exponent n and the corresponding predictions coincide with the $n = 1$ curves. Part (d) shows a typical deformed and undeformed FEM mesh at a given instant in time.

Biaxial tension loading with $X_{\Sigma} = 5$. In Fig. 5.9, a high stress-triaxiality loading is applied

such that $X_\Sigma = 5$ (or $T/S = 0.793$ with $S/|S| > 0$). Corresponding results for the evolution of the normalized porosity f/f_o, the aspect ratio w and the normalized macroscopic equivalent strain-rate $\overline{D}_{eq}/\dot{\varepsilon}^{\infty}_{eq}$ are shown as a function of the nonlinearity and the total equivalent strain $\overline{\varepsilon}_{eq}$. The agreement between the SOM and the FEM is remarkable for the evolution of the normalized porosity f/f_o and the normalized macroscopic strain-rate $\overline{D}_{eq}/\dot{\varepsilon}^{\infty}_{eq}$. This is somewhat expected since, as already discussed earlier, the SOM method recovers the analytical result of a shell subjected to purely hydrostatic loading. It is interesting to note that while for $n = 1$ the porosity f becomes *twenty* times higher than the initial porosity f_o at a total strain of 20%, for $n = 10$, the porosity climbs up to *hundred* times the initial porosity f_o in just 2.5% deformation. In contrast, the VAR estimate is independent of the nonlinearity and the corresponding results coincide with the $n = 1$ curve. As a consequence, the VAR estimates fail completely to predict the evolution of f/f_o at high nonlinearities.

Looking now at Fig. 5.9b, it is observed that the SOM estimates for the aspect ratio w are not in good agreement with the FEM results, although it is evident that the aspect ratio remains very close to the unity value (i.e., the void remains almost circular) and hence is not expected to affect the macroscopic behavior of the porous material. Nonetheless, an interesting effect is observed in the context of this figure. For high nonlinearities, $n = 4, 10$, the void elongates in the transverse direction of that defined by the maximum principal loading (see Fig. 5.9d). In other words, while the maximum stress is applied in the $2-$direction, the voids elongates in the $1-$direction. This effect has been observed very early in the work of Budiansky et al. (1982) and later by Fleck and Hutchinson (1986) and Lee and Mear (1992a) in the context of dilute porous media. Since then many authors tried to model this effect with ad-hoc approximations, sometimes with success (see Flandi and Leblond (2005) for the three dimensional case). However, it is important to mention that, at high stress triaxialities, the evolution of porosity controls the effective behavior of the material, which is illustrated by the remarkable agreement between the SOM and the FEM predictions for the normalized macroscopic strain-rate $\overline{D}_{eq}/\dot{\varepsilon}^{\infty}_{eq}$ in the context of Fig. 5.9c. On the other hand, the VAR overly underestimates $\overline{D}_{eq}/\dot{\varepsilon}^{\infty}_{eq}$, so that it is not possible to distinguish the corresponding VAR curve for $n = 10$. Lastly, Fig. 5.9d shows undeformed and deformed meshes of the unit-cell for $n = 10$. In this figure, it is clearly observed that for this high stress triaxiality $X_\Sigma = 5$ the volume of the void increases significantly, while the major axis of the void elongates in the transversely ($2-$ direction) to the direction of maximum principal stress ($2-$ direction).

5.3.3 Compressive loadings

Uniaxial compression loading. Fig. 5.10 shows results for the evolution of the normalized porosity f/f_o, the aspect ratio w and the normalized macroscopic axial strain-rate $\overline{D}_{22}/\dot{\varepsilon}^{\infty}_{eq}$ as a function of the macroscopic axial strain $|\overline{\varepsilon}_{22}|$ and the nonlinearity $n = 1, 2, 4$ for uniaxial compression ($X_\Sigma = -1/\sqrt{3}$ or $T/S = 0$ with $S/|S| < 0$). More specifically, in Fig. 5.10a, the SOM predictions for the evolution of the normalized porosity f/f_o are found to be in very good agreement with the corresponding results obtained by the FEM, whereas the corresponding VAR estimates are independent of n so that all the VAR results coincide with the $n = 1$ curve. At this point, it is noted that it was not possible

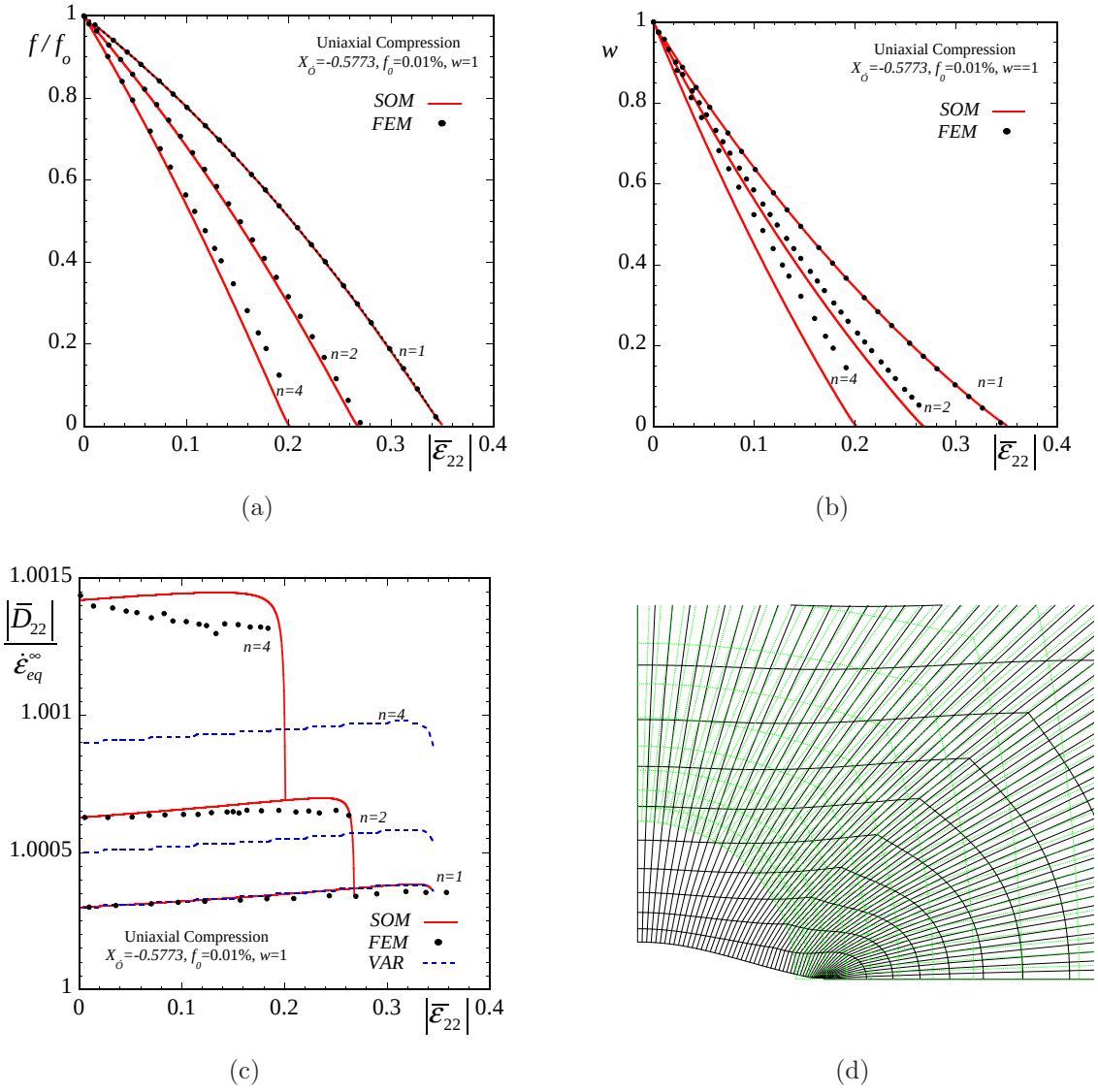

Figure 5.10: Results are shown for the evolution of the relevant microstructural and macroscopic variables for a porous material consisting of cylindrical pores with an initially, circular cross-section and porosity $f_o = 0.01\%$. The matrix phase exhibits a viscoplastic behavior with exponents $n = 1, 2, 4$, while the composite is subjected to uniaxial compression ($X_\Sigma = -1/\sqrt{3}$ or $T/S = 0$ with $S/|S| < 0$) loading conditions. SOM, FEM and VAR estimates are shown for the evolution of the (a) normalized porosity f/f_o, (b) the aspect ratio w and (c) the normalized axial strain-rate $|\overline{D}_{22}|/\dot{\varepsilon}_{eq}$ ($\dot{\varepsilon}_{eq}$ is the corresponding remote strain-rate in the absence of voids). The VAR estimate for the evolution of the normalized porosity f/f_o and the aspect ratio w is found to be independent of the nonlinear exponent n and the corresponding predictions coincide with the $n = 1$ curves. Part (d) shows a typical deformed and undeformed FEM mesh at a given instant in time.

to have good numerical accuracy with the FEM method for nonlinearities greater than $n = 4$. The reason for this is linked to the fact that as the porosity becomes smaller the void loses its concave shape and develops contact zones (see Fig. 5.10d). In this case, we do not proceed further with the FEM calculations. In fact, this is the reason that the $n = 4$ curve predicted by the FEM stops before the porosity becomes zero.

Looking now at Fig. 5.10b, the SOM slightly overestimates the decrease of the aspect ratio w when compared with the FEM. However, both methods predict a very sharp change in the aspect ratio, which finally tends to zero as the porosity becomes zero. Similar to the evolution of porosity, the VAR method underestimates the evolution of w, since it delivers results that are independent of n and thus coincide with the $n = 1$ curve.

Next, the SOM estimates for the evolution of the normalized macroscopic axial strain-rate $\overline{D}_{22}/\dot{\varepsilon}^{\infty}_{eq}$ are certainly in better agreement with the FEM, than the VAR results, while they exhibit a very abrupt change in the slope as the porosity approaches zero. This happens because the matrix phase is incompressible and therefore it cannot sustain any compressive strains as the porosity becomes zero. Next, Fig. 5.10d shows undeformed and deformed meshes of the unit-cell for $n = 4$. In this figure, it is clearly observed that total surface of the void shrinks during the deformation process, while at a certain strain the void develops contact points losing its elliptical shape. After that point, the FEM calculations are terminated since they would require to redefine the boundary conditions in order to preserve material impenetrability.

Biaxial compression loading with $X_{\Sigma} = -1$. Fig. 5.11 presents results for the evolution of the normalized porosity f/f_o, the aspect ratio w and the normalized macroscopic equivalent strain-rate $\overline{D}_{eq}/\dot{\varepsilon}^{\infty}_{eq}$ as a function of the total equivalent macroscopic strain $\bar{\varepsilon}_{eq}$ and the nonlinearity $n = 1, 2, 4$ for biaxial compression loadings ($X_{\Sigma} = -1$ or $T/S = 0.268$ with $S/|S| < 0$). For the same reasons explained in the context of Fig. 5.10, no results are presented for a nonlinear exponent $n = 10$. More specifically, in Fig. 5.11a, the SOM estimate is in quite good agreement with the FEM results for the evolution of the normalized porosity f/f_o. In addition, we observe that the porosity approaches the zero value faster than the corresponding prediction obtained in the context of the uniaxial compression loading. The corresponding VAR estimates are independent of n and thus coincide with the $n = 1$ curve. Consequently, they underestimate significantly the decrease of f/f_o at high nonlinearities.

On the other hand, the SOM estimates are not in very good quantitative agreement with the FEM results for the evolution of the aspect ratio w, as shown in Fig. 5.11b. However, it should be noted that, in the FEM, the aspect ratio w is measured by computing the geometrical ratio between the major and the minor axis of the void, based on the assumption that the void remains elliptical in shape. Now, when the porosity approaches the zero value the void does not have an elliptical cross-section and the comparison is not meaningful after this point. Even so, the corresponding estimates of the SOM for the normalized macroscopic strain-rate $\overline{D}_{eq}/\bar{\varepsilon}^{\infty}_{eq}$, in Fig. 5.11c, are in much better agreement with the FEM, certainly better than the VAR estimates. This observation indicates that the evolution of porosity f/f_o dominates over the evolution of the aspect ratio w and thus, the SOM is able to capture adequately the effective response of the porous medium for this moderate stress triaxiality. Finally, Fig. 5.11d shows undeformed and deformed meshes of the unit-cell for $n = 4$. In this figure, it is clearly observed that total surface of the void shrinks significantly during the deformation process, while the void develops contact points losing its elliptical shape, and similarly to the previous case of uniaxial compression, the FEM calculations are terminated at that point.

Biaxial compression loading with $X_{\Sigma} = -5$. Finally, the set of results for aligned loadings is completed with Fig. 5.12, where the porous material is subjected to high-triaxiality biaxial compres-

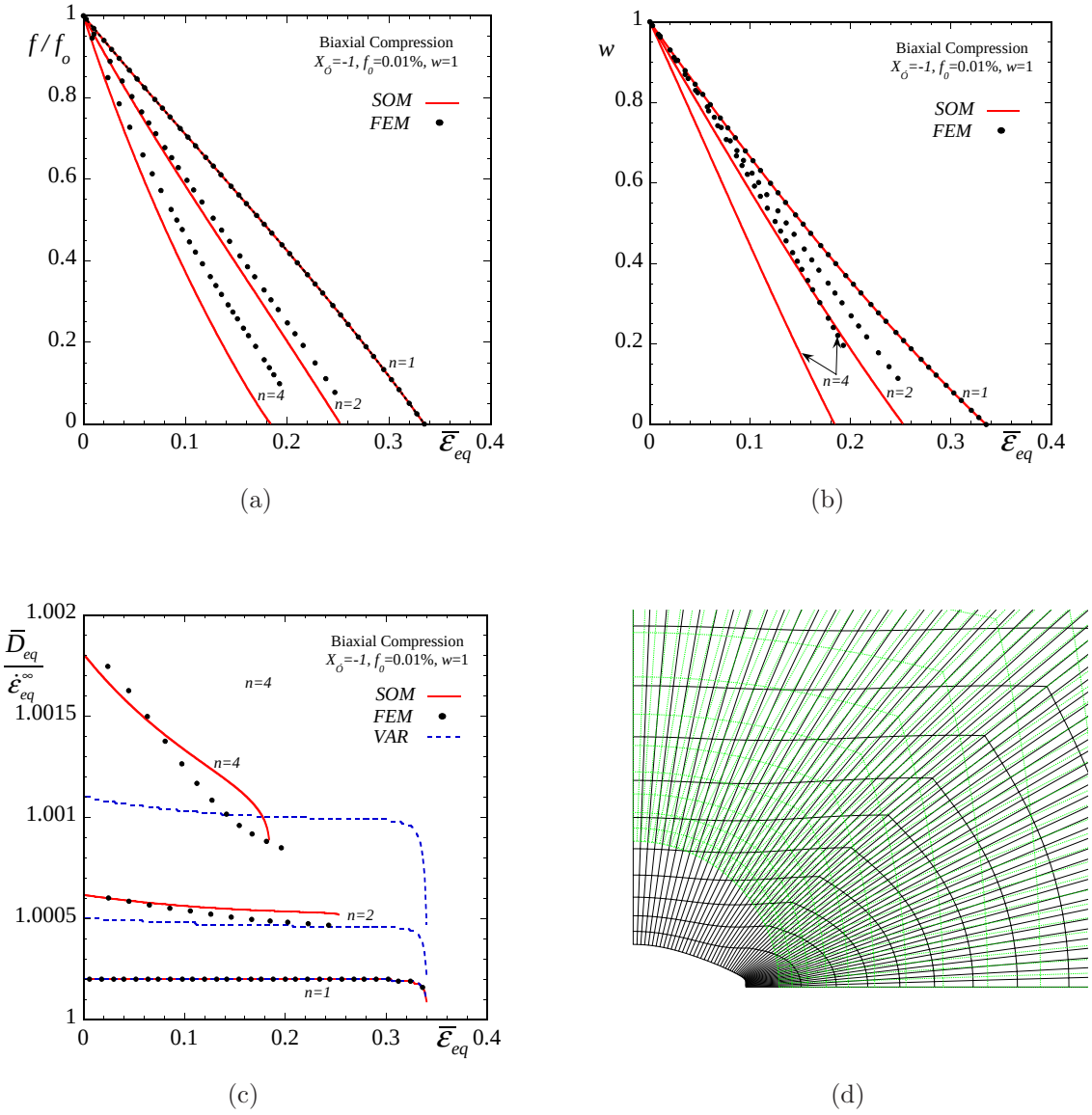

Figure 5.11: Results are shown for the evolution of the relevant microstructural and macroscopic variables for a porous material consisting of cylindrical pores with an initially, circular cross-section and porosity $f_o = 0.01\%$. The matrix phase exhibits a viscoplastic behavior with exponents $n = 1, 2, 4$, while the composite is subjected to biaxial compression ($X_\Sigma = -1$ or $T/S = 0.268$ with $S/|S| < 0$) loading conditions. SOM, FEM and VAR estimates are shown for the evolution of the (a) normalized porosity f/f_o, (b) the aspect ratio w and (c) the normalized equivalent strain-rate $\overline{D}_{eq}/\dot{\varepsilon}_{eq}$ ($\dot{\varepsilon}_{eq}$ is the corresponding remote strain-rate in the absence of voids). The VAR estimate for the evolution of the normalized porosity f/f_o and the aspect ratio w is found to be independent of the nonlinear exponent n and the corresponding predictions coincide with the $n = 1$ curves. Part (d) shows a typical deformed and undeformed FEM mesh at a given instant in time.

sion ($X_\Sigma = 5$ or $T/S = 0.793$ with $S/|S| < 0$). Similarly to the rest of the results for compression loadings, we consider here nonlinear exponents $n = 1, 2, 4$, while the corresponding predictions for the evolution of the normalized porosity f/f_o, the aspect ratio w and the normalized macroscopic

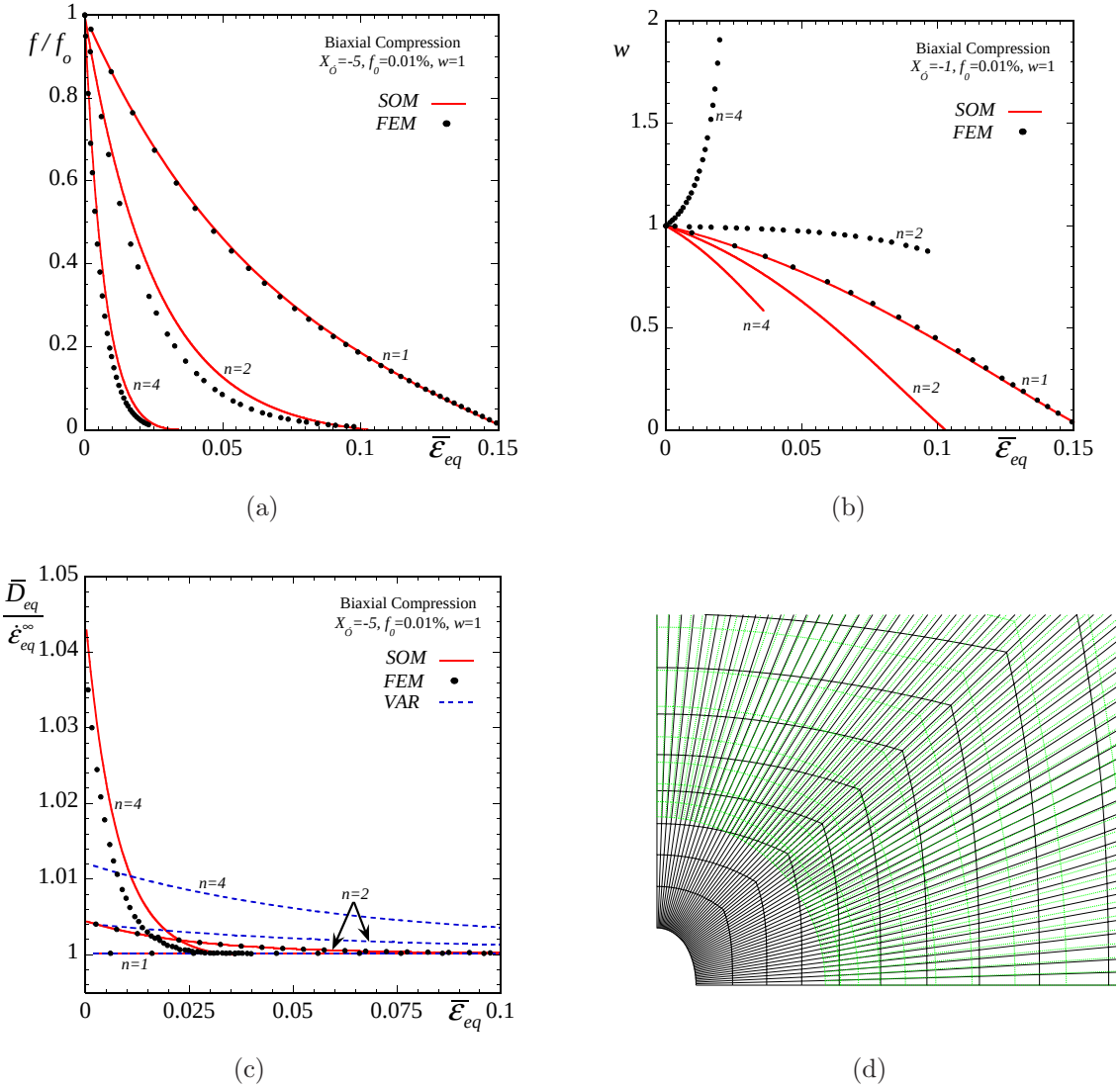

Figure 5.12: Results are shown for the evolution of the relevant microstructural and macroscopic variables for a porous material consisting of cylindrical pores with an initially, circular cross-section and porosity $f_o = 0.01\%$. The matrix phase exhibits a viscoplastic behavior with exponents $n = 1, 2, 4$, while the composite is subjected to biaxial compression ($X_\Sigma = -5$ or $T/S = 0.793$ with $S/|S| < 0$) loading conditions. SOM, FEM and VAR estimates are shown for the evolution of the (a) normalized porosity f/f_o, (b) the aspect ratio w and (c) the normalized equivalent strain-rate $\overline{D}_{eq}/\dot{\varepsilon}_{eq}$ ($\dot{\varepsilon}_{eq}$ is the corresponding remote strain-rate in the absence of voids). The VAR estimate for the evolution of the normalized porosity f/f_o and the aspect ratio w is found to be independent of the nonlinear exponent n and the corresponding predictions coincide with the $n = 1$ curves. Part (d) shows a typical deformed and undeformed FEM mesh at a given instant in time.

equivalent strain-rate $\overline{D}_{eq}/\dot{\varepsilon}^{\infty}_{eq}$ are plotted as a function of the equivalent macroscopic strain $\overline{\varepsilon}_{eq}$. The main observation in the context of Fig. 5.12a is that the SOM estimates for the porosity f/f_o are in very good agreement with the FEM results for all nonlinearities considered, whereas the VAR significantly underestimate f/f_o by being independent of n and thus coinciding with the $n = 1$ curve. In this connection, it is interesting to note that while for $n = 1$ the porosity becomes zero at strain

$\sim 15\%$, the corresponding prediction for $n = 10$ indicates that the porosity goes to zero at very low strains of the order $\sim 2.5\%$. Moreover, while f/f_o initially decreases rapidly, as it approaches the zero value, the rate of decrease of f/f_o diminishes leading to an asymptotic behavior for the evolution of the porosity.

On the other hand, the SOM estimate fails to predict qualitatively the change in the shape of the void, in Fig. 5.12b. Here, the void elongates parallel to the direction of the maximum (compressive) principal stress, as shown in Fig. 5.12d. This phenomenon is equivalent to that observed in Fig. 5.9 for high triaxiality tensile loadings, and is intuitively unexpected. However, it is remarkable to note that the evolution of the aspect ratio w has a minor effect on the prediction of the normalized equivalent macroscopic strain-rate $\overline{D}_{eq}/\dot{\varepsilon}^{\infty}_{eq}$, as shown in Fig. 5.12c. In this figure, the SOM is found to be in very good agreement with the FEM results, which clearly implies that for high-triaxiality loadings, the evolution of porosity mainly controls the effective response of the porous material. In contrast, the VAR method underestimates significantly the evolution of the $\overline{D}_{eq}/\dot{\varepsilon}^{\infty}_{eq}$, and hence, fails to predict accurately the effective behavior of the porous medium. The set of results for this loading are completed with Fig. 5.12d, which shows undeformed and deformed meshes of the unit-cell for $n = 4$. As already mentioned before, we can observe the significant growth of the porosity, and the elongation of the void towards the direction of the maximum compressive stress.

5.3.4 Simple shear loading

In the previous subsections, we studied the effects of the evolution of the porosity and the aspect ratio on the overall response of a porous material consisting of aligned cylindrical voids with initially circular cross-section subjected to biaxial loading conditions. In this subsection, we study the effective behavior of these materials when subjected to simple shear loading conditions. In this case, the in-plane principal axes of the void evolve during the deformation process. More specifically, the applied load is such that the only non-zero components of the macroscopic strain-rate and spin tensor are $\overline{D}_{12}$ and $\overline{\Omega}_{12}$, respectively. The material is subjected to total shear strain $2\,\overline{\varepsilon}_{12} = \overline{\gamma}$. For comparison, FEM results are also included, which were discussed in detail in section 3.5. Because of the applied load (isochoric loading), the porosity does not evolve during the deformation process. For numerical reasons related to the FEM calculations, the initial porosity has been chosen to be $f_o = 1\%$.

Fig. 5.13 presents results for the evolution of the orientation angle ψ and the components of the macroscopic stress tensor $\overline{\boldsymbol{\sigma}}$ as a function of the applied shear strain $\overline{\gamma}$ for various nonlinearities $n = 1, 2, 4$. Fig. 5.13a shows the evolution of the orientation angle of a void with initially circular cross-section for a nonlinear exponent $n = 4$. Because of the loading, the initial orientation of the major axis of the void lies at 45^o. As the deformation progresses, the orientation angle ψ evolves reaching a value of $\sim 32^o$ at shear strain 100%. Both the SOM and the VAR estimates are in good agreement[†] with the FEM predictions. It should also be noted that the evolution of the orientation angle ψ depends very slightly on the nonlinearity, This is the reason that we do not include graphs for other values of n. In turn, Fig. 5.13b, Fig. 5.13c and Fig. 5.13d show evolution curves for the

[†]The SOM and the VAR estimates coincide and this is the reason that the two curves are not distinguishable in Fig. 5.13a.

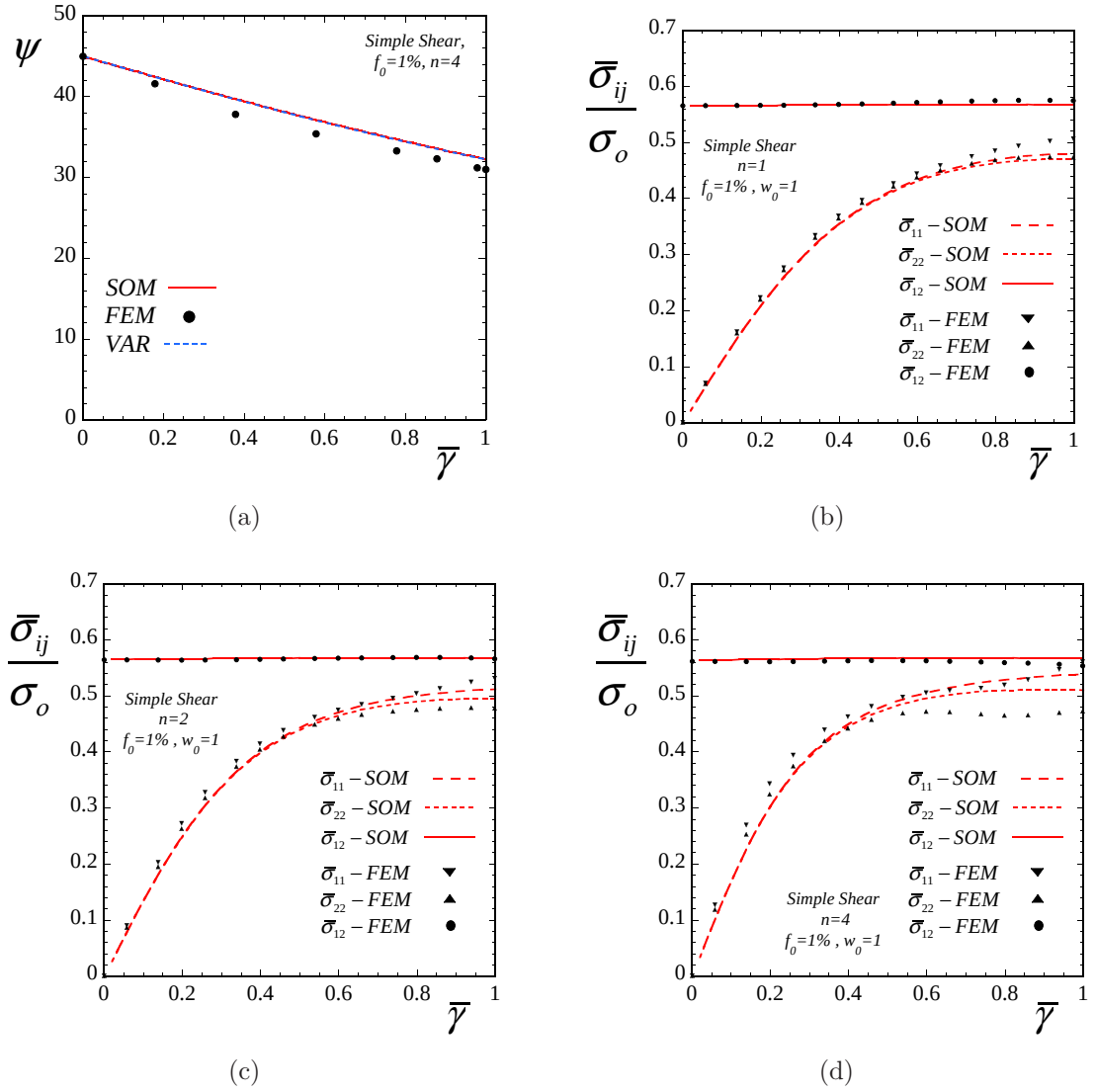

Figure 5.13: Results are shown for the evolution of the relevant microstructural and macroscopic variables for a porous material consisting of cylindrical pores with an initially, circular cross-section. The matrix phase exhibits a viscoplastic behavior with exponents $n = 1, 2, 4$, while the composite is subjected to simple shear loading ($\overline{D}_{12} > 0$ and $\overline{D}_{11} = \overline{D}_{22} = 0$) conditions. SOM and FEM estimates are shown for the evolution of the (a) orientation angle ψ (the VAR estimate coincides with the SOM curve) and the components of the macroscopic stress tensor $\overline{\boldsymbol{\sigma}}$ for (b) $n = 1$, (c) $n = 2$, and (d) $n = 4$.

macroscopic components of the stress tensor $\overline{\boldsymbol{\sigma}}$ normalized by the flow stress σ_o in the matrix phase as a function of the applied shear strain $\overline{\gamma}$ and the nonlinearity $n = 1, 2, 4$. The SOM estimates are in very good agreement with the FEM results for all the nonlinearities considered. In all the cases, the shear stress $\overline{\sigma}_{12}$ starts from a finite value, whereas $\overline{\sigma}_{11}$ and $\overline{\sigma}_{22}$ are initially zero. During the deformation process, the two components, $\overline{\sigma}_{11}$ and $\overline{\sigma}_{22}$, evolve similarly, except at sufficiently large shear strain $\overline{\gamma}$, where they start to deviate from each other. On the other hand, the shear stress $\overline{\sigma}_{12}$ remains almost unaffected by the evolution process. For clarity, in Fig. 5.14, we present various deformed states of the unit-cell for $n = 4$, whereas the undeformed initial mesh is shown in

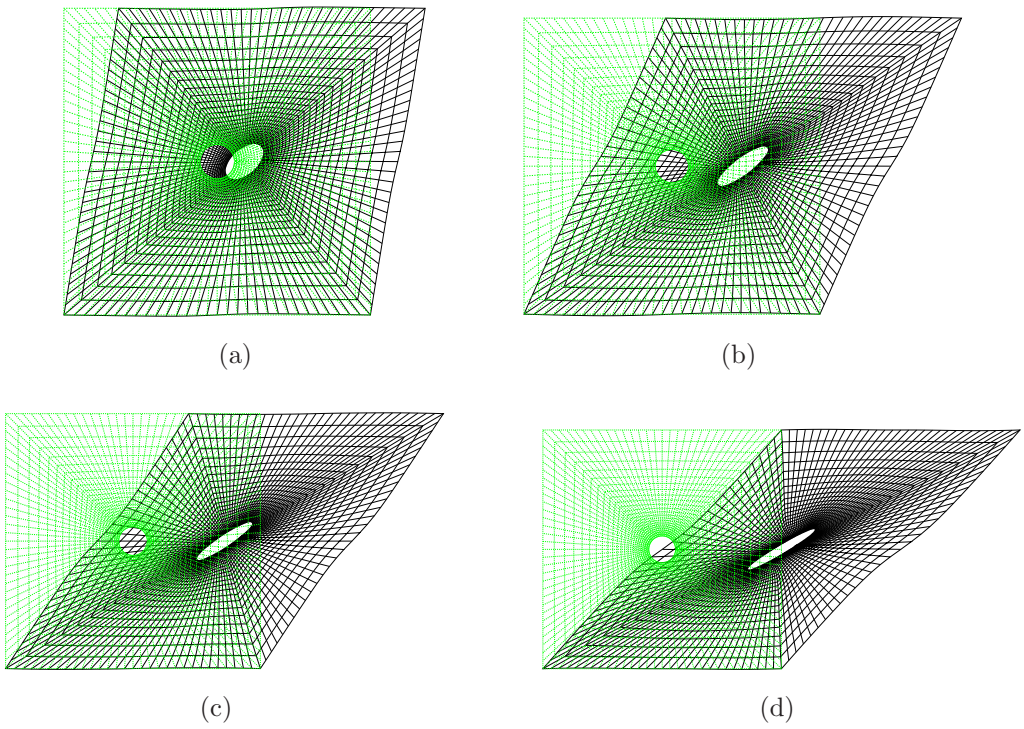

Figure 5.14: Contour plots for simple shear loading at various shear strains $\overline{\gamma}$.

the background for comparison. In this figure, it is obvious that the principal axes of the void evolve with the increase of the shear strain $\overline{\gamma}$.

5.3.5 Brief summary

In this subsection, we summarize the main results obtained in this section. First of all, the SOM is found to be in very good agreement with the FEM results for the majority of the loadings, nonlinearities and stress triaxialities considered. Furthermore, it is found to improve significantly on the earlier VAR method particularly at high stress triaxialities, where the VAR method fails to predict accurately the evolution of the porosity and consequently the evolution of the effective behavior of the porous material. This is a direct consequence of the fact that the SOM model is constructed such that it recovers the analytical result obtained when a composite-cylinder assemblage is subjected to purely hydrostatic loading conditions.

Next, it is worth noting that the SOM is also capable of predicting with sufficient accuracy the evolution of the aspect ratio (shape of the void) at low triaxialities. On the other hand, it is not in good agreement with the FEM predictions for the evolution of the aspect ratio at high stress triaxialities. In this case, the FEM results confirm the observation made initially by Budiansky et al. (1982), and later by Fleck and Hutchinson (1986) and Lee and Mear (1992b) in the context of dilute porous media, where it was found that at sufficiently high triaxialities and nonlinearities, the void elongates in a direction that is transverse to the maximum macroscopic principal stretching. This counterintuitive result however, was found to have a minor effect on the overall response of the porous medium. This can be easily explained by noting that the evolution of porosity is much more significant

than the corresponding evolution of the aspect ratio at high stress triaxialities. As a consequence, the evolution of the porosity controls the effective behavior of the porous material. In this connection, the SOM is found to predict accurately the evolution of the porosity and consequently the effective behavior of the porous material during the deformation process.

Finally, the SOM estimates are compared with FEM and VAR results for the evolution of the orientation angle of the voids and the macroscopic stress, when the porous material is subjected to simple shear loading conditions. It is worth noting that — to the knowledge of the author — the SOM and the VAR methods are the only available methods in the literature, apart from the FEM method, to be able to provide estimates for *non-dilute* porous media consisting of cylindrical voids with elliptical cross-section, that are subjected to general plane-strain loading conditions.

5.4 Ideal plasticity

In this section, we consider porous materials with an ideally-plastic matrix phase consisting of cylindrical voids aligned in the 3−direction with initially circular cross-section subjected to plane-strain loading conditions. As already discussed in section 2.9, these materials can lose ellipticity and thus become unstable. For simplicity, we will consider loadings that do not induce a change in the orientation of the principal axes of the voids (but see Kailasam and Ponte Castañeda, 1998). The reason for this is that the computation of the effective Jaumann hardening rate, H_J, introduced in relation (2.318) can be simplified considerably, since in this case the Jaumann rates and the standard time derivatives of the relevant quantities coincide.

"Variational" method. Thus following the analysis presented in subsection 2.8.1 for ideally-plastic materials, the Jaumann hardening rate, delivered by the "variational" method (VAR), is written as

$$H_J = H = -\left\{ q_f \frac{\partial \widetilde{\Phi}_{var}}{\partial f} + q_w \frac{\partial \widetilde{\Phi}_{som}}{\partial w} \right\}, \tag{5.13}$$

where $\widetilde{\Phi}_{var}$ is the effective yield condition defined in (4.11). In turn, the functions q_f and q_w are given by

$$q_f(\overline{\boldsymbol{\sigma}};\, f,\, w) = (1-f)\, \frac{\partial \widetilde{\Phi}_{var}}{\partial \overline{\sigma}_{jj}}, \qquad j = 1, 2, \tag{5.14}$$

and

$$q_w(\overline{\boldsymbol{\sigma}};\, f,\, w) = w \left(\mathbf{n}^{(2)}\, \mathbf{n}^{(2)} - \mathbf{n}^{(1)}\, \mathbf{n}^{(1)} \right) \cdot \frac{3}{(1-f)^2}\, \widehat{\mathbf{Q}}^{-1}\, \frac{\overline{\boldsymbol{\sigma}}}{\sigma_o}, \tag{5.15}$$

where $\widehat{\mathbf{Q}}^{-1} = (\boldsymbol{\mathcal{G}}/w + \mathbf{K})/2$ with $\boldsymbol{\mathcal{G}}$ given by (4.6). Note that the use of $\mathbf{n}^{(i)}$ is somewhat redundant in the sense that we considered that the principal axes of the voids are aligned with the axes of the laboratory frame, i.e., $\mathbf{n}^{(1)} = \mathbf{e}^{(1)}$ and $\mathbf{n}^{(2)} = \mathbf{e}^{(2)}$.

"Second-order" method. Next following the analysis presented in subsection 2.8.2 for ideally-plastic materials, the Jaumann hardening rate, delivered by the "second-order" method (SOM), is written as

$$H_J = H = -\left\{ y_f \frac{\partial \widetilde{\Phi}_{som}}{\partial f} + y_w \frac{\partial \widetilde{\Phi}_{som}}{\partial w} \right\}. \tag{5.16}$$

where $\widetilde{\Phi}_{som}$ is the effective yield condition defined in (4.29). In turn, the functions y_f and y_w are given by

$$y_f(\overline{\boldsymbol{\sigma}};\, f,\, w) = (1-f)\,\frac{\partial \widetilde{\Phi}_{som}}{\partial \overline{\sigma}_{jj}}, \qquad j = 1, 2, \tag{5.17}$$

and

$$y_w(\overline{\boldsymbol{\sigma}};\, f,\, w) = w\left(\mathbf{n}^{(2)}\,\mathbf{n}^{(2)} - \mathbf{n}^{(1)}\,\mathbf{n}^{(1)}\right)\cdot\frac{3}{1-f}\mathbf{K}\left(\frac{3}{1-f}\,\widehat{\mathbf{Q}}(k)^{-1}\,\frac{\overline{\boldsymbol{\sigma}}}{\sigma_o} - \boldsymbol{\mathcal{M}}(k)\,\frac{\check{\boldsymbol{\sigma}}}{\sigma_o}\right), \tag{5.18}$$

where

$$\widehat{\mathbf{Q}}^{-1} = \frac{1}{2w\,\sqrt{k}}\boldsymbol{\mathcal{G}} + \boldsymbol{\mathcal{M}}(k), \qquad \boldsymbol{\mathcal{M}} = \frac{1}{2\,k}\mathbf{E} + \frac{1}{2}\mathbf{F}, \tag{5.19}$$

with $\boldsymbol{\mathcal{G}}$ given by (4.6) and $\mathbf{E}$ and $\mathbf{F}$ by (4.24). The evaluation of k has been described in the context of relation (4.30). Similar to the previous case, the principal axes of the voids are considered to be aligned with the axes of the laboratory frame, i.e., $\mathbf{n}^{(1)} = \mathbf{e}^{(1)}$ and $\mathbf{n}^{(2)} = \mathbf{e}^{(2)}$.

Finally, the sufficient conditions for shear localization are given by relations (2.320) and (2.321). The first condition is related to the determination of the critical hardening rate H_{cr}. In the case of aligned, plane-strain loading considered in this section, the critical hardening rate can be shown to be $H_{cr} = 0$ (Rice, 1976). The second condition (2.321) simply yields that there should exist a non-deforming surface in the deformation field. Because of the plane-strain character of the problem this is trivially satisfied. Hence, the only condition sufficient for shear localization is the zero hardening rate, $H = 0$. In the next two subsections, we will study the possibility of shear localization in the cases of fixed strain-rate and stress triaxiality, respectively.

5.4.1 Applied strain-rate triaxiality

The applied in-plane load is such that the only non-zero components of the strain-rate tensor are

$$\overline{D}_{11} \neq 0, \quad \overline{D}_{22} \neq 0. \tag{5.20}$$

In the following, it is convenient to assume without any loss of generality that $|\overline{D}_{22}| > |\overline{D}_{11}|$. Then, making use of the definitions for the mean and equivalent macroscopic strain-rate, $\overline{D}_m$ and $\overline{D}_{eq}$, and the strain-rate triaxiality, X_E, which are recalled here for completeness

$$\overline{D}_{eq} = \frac{|\overline{D}_{11} - \overline{D}_{22}|}{\sqrt{3}}, \quad \overline{D}_m = \frac{\overline{D}_{11} + \overline{D}_{22}}{2}, \quad X_E = \frac{\overline{D}_m}{\overline{D}_{eq}}, \tag{5.21}$$

we can rewrite the components of the strain-rate tensor as

$$\overline{D}_{11} = \left(X_E - \rho\frac{\sqrt{3}}{2}\right)\overline{D}_{eq}, \quad \overline{D}_{22} = \left(X_E + \rho\frac{\sqrt{3}}{2}\right)\overline{D}_{eq}, \quad \overline{D}_{eq} = 1. \tag{5.22}$$

In the last expression, $\overline{D}_{eq}$ and X_E are externally applied in the problem and $\rho = \pm 1$ such that the condition $|\overline{D}_{22}| > |\overline{D}_{11}|$ is always true. In the sequel, we discuss the evolution of microstructure and the possible instabilities in the porous medium for given values of the strain-rate triaxiality, X_E, as predicted by the "second-order" method (SOM), the "variational" method (VAR) and the Gurson model (GUR).

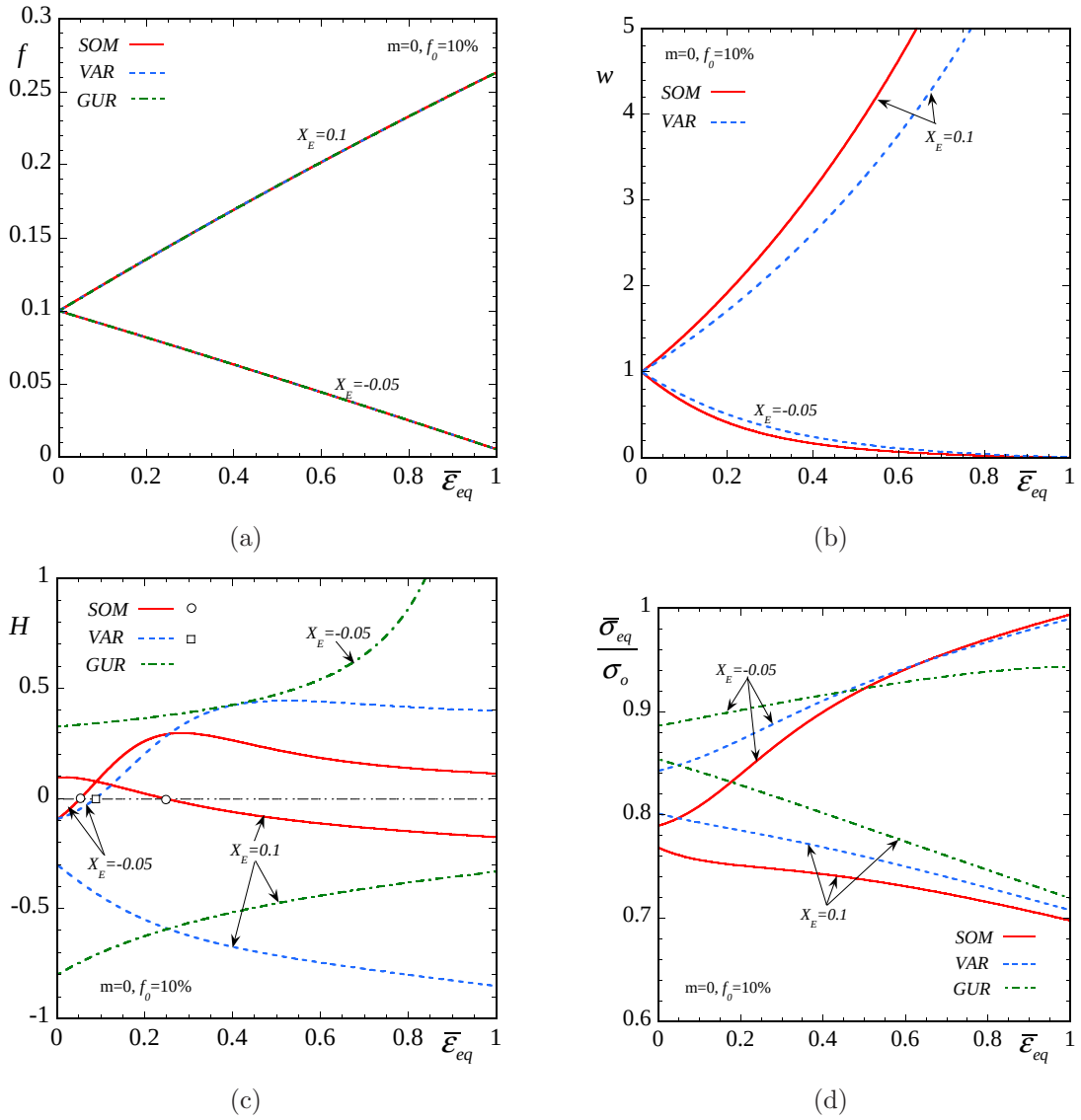

Figure 5.15: Results are shown for the evolution of the relevant microstructural and macroscopic variables for a porous material consisted of cylindrical pores with an initially, circular cross-section and porosity $f_o = 10\%$. The matrix phase exhibits an ideally-plastic behavior, while the composite is subjected to biaxial tension and compression loading conditions with fixed strain-rate triaxiality, $X_E = -0.05, 0.1$. SOM, VAR and GUR (Gurson, 1977) estimates are shown for the evolution of the (a) porosity f, (b) the aspect ratio w, (c) the hardening rate H and (d) the normalized, macroscopic equivalent stress $\overline{\sigma}_{eq}/\sigma_o$ (σ_o denotes the flow stress of the matrix phase) of the composite as a function of the macroscopic, equivalent strain $\overline{\varepsilon}_{eq}$. In (c) the symbols $\circ$ and $\square$ denote the loss of stability for the porous medium as predicted by the SOM and the VAR, respectively.

Fig. 5.15 shows evolution curves for the porosity f, the aspect ratio w, the hardening rate H and the macroscopic equivalent stress $\overline{\sigma}_{eq}$ normalized by the flow stress of the matrix phase σ_o as a function of the strain-rate triaxiality X_E and the total equivalent strain-rate $\overline{\varepsilon}_{eq}$ for a porous material consisting of cylindrical voids with circular cross-section and initial porosity $f_o = 10\%$. For completeness, the SOM is compared with corresponding estimates obtained by the VAR and the

GUR models. Two values of the strain-rate $X_E = -0.05, 0.1$ are chosen to study the instability conditions described above. More specifically, Fig. 5.15a shows evolution curves for the porosity f as predicted by the three models considered here. In this case that the loading is strain-controlled and the matrix phase is incompressible, all the methods deliver exactly the same evolution for the porosity. On the other hand, in Fig. 5.15b, the corresponding evolution of the aspect ratio is different for the various methods. Of course, the GUR model does not include any information about the shape of the voids and therefore, no curve is shown here. In contrast, the SOM predicts a higher rate of change in the aspect ratio w, when compared with the corresponding VAR estimate in both cases of X_E considered. In particular, for $X_E = 0.1$ the ellipsoidal void elongates in the direction of the maximum principal loading, i.e., for $X_E = 0.1$, $\overline{D}_{22} > \overline{D}_{11}$ the aspect ratio grows in the $2-$direction implying that $w > 1$. Consequently, the evolution of the aspect ratio w acts as a hardening mechanism during the deformation process in both methods, whereas in the case of the SOM this hardening effect is stronger than in the VAR method. On the other hand, the porosity f also grows inducing a softening in the overall behavior of the composite. These two mechanisms, i.e., the hardening effect induced by the growth of the aspect ratio w and the softening caused by the growth of the porosity f are in competition. Looking at Fig. 5.15c the curves for $X_E = 0.1$, we observe that for the SOM estimate the hardening effect caused by the growth of the aspect ratio w dominates initially over the softening mechanism of the porosity growth until a total strain of $\sim 25\%$, where the hardening rate H crosses zero. This point, denoted with a circle on the graph, corresponds to a possible instability of the material. On the other hand, in the VAR method and certainly in the GUR model, the softening effect induced by the growth of the porosity f is dominant and the corresponding curves for H never cross zero. This has as a consequence that both the VAR and the GUR models do not predict instability for strain-rate triaxiality $X_E = 0.1$. Fig. 5.15d in turn shows the corresponding stress curves where for $X_E = 0.1$ the SOM predicts a lower value for $\overline{\sigma}_{eq}$ than both the VAR and the GUR results. Of course, GUR model is the stiffest of the three models in this case and predicts higher stress values.

Similar observations can be made in the context of Fig. 5.15 for $X_E = -0.05$. In this case the material is subjected to compression in the $2-$direction and, therefore, the void elongates in the $1-$direction (i.e., $w < 1$). While the material softens in the $2-$direction, (i.e., in the direction of the maximum (absolute) principal loading) due to the change of the aspect ratio w, the overall porosity f is decreasing which induces hardening in the material. In this case, both the SOM and the VAR exhibit an initial softening due to the elongation of w in the $1-$direction, which is observed by the initial negative hardening rate H, in Fig. 5.15c. Nonetheless, the corresponding SOM and the VAR estimates for H cross zero and become positive (i.e., the medium hardens) at a critical total strain $\overline{\varepsilon}_{eq} \sim 10\%$, which indicates a possible point of instability (the SOM becomes unstable earlier than the VAR). In contrast, the GUR model predicts hardening as a consequence of the decreasing porosity and never loses stability.

This procedure, described above, can be repeated for the entire range of strain-rate triaxialities, i.e., $X_E \in (-\infty, \infty)$. In this regard, Fig. 5.16 summarizes results for the critical equivalent strain-rate $\overline{\varepsilon}^{cr}_{eq}$ for loss of stability as a function of the strain-rate triaxiality in the case of a porous medium with

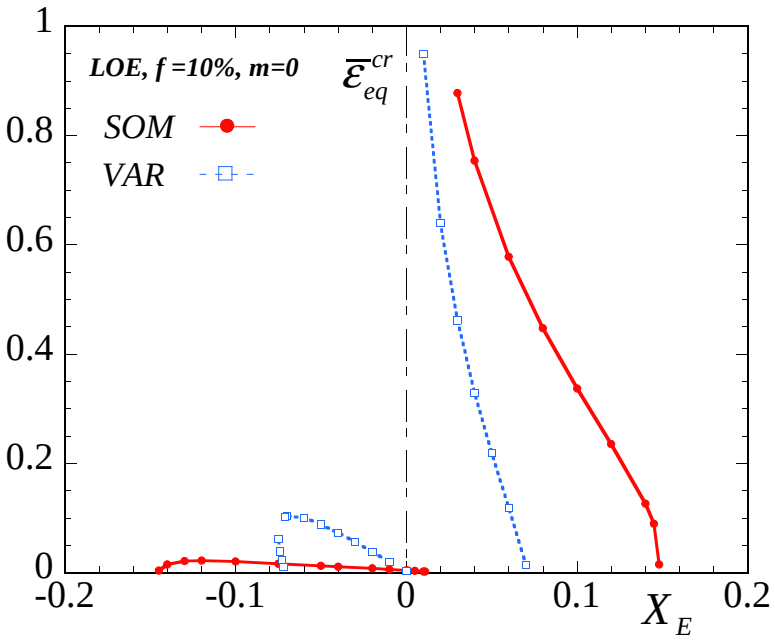

Figure 5.16: Macroscopic onset-of-failure curves as predicted by the SOM and VAR calculations, for an initially transversely, isotropic porous medium with ideally-plastic matrix phase and initial porosity $f_o = 10\%$. The plot shows the critical equivalent strain $\overline{\varepsilon}^{cr}_{eq}$ as a function of the applied strain-rate triaxiality X_E.

cylindrical voids and initial porosity $f_o = 10\%$. The main observation in the context of this figure is that for negative strain-rate triaxialities, the SOM is more unstable than the corresponding VAR method. In contrast, for positive X_E, the VAR method becomes unstable earlier than the SOM. Furthermore, it is shown that instabilities occur at low strain-rate triaxialities, where the shear strains are dominant over the dilatational strains.

In summary, it is important to mention that based on the analysis made in the context of finite nonlinearities in the previous section, the SOM is expected to predict more accurately the evolution of porosity and aspect ratio when compared with the VAR method and consequently be more accurate in determining instabilities in porous media. Nonetheless, both methods exhibit a similar qualitative behavior, while they improve substantially on the GUR model by being capable of capturing the effects of the void shape, which has been shown to be very significant in the prediction of instabilities in ideally-plastic solids.

5.4.2 Applied stress triaxiality

In this subsection, we study the possible development of shear localization in porous media with an ideally-plastic matrix phase consisting of cylindrical voids with initially circular cross-section subjected to plane-strain loading with fixed stress triaxiality X_Σ during the deformation process. Similarly to the previous case, the only non-zero components of the strain-rate and stress tensor are $\overline{D}_{11}$, $\overline{D}_{22}$, $\overline{\sigma}_{11}$ and $\overline{\sigma}_{22}$, respectively. The mean and equivalent strain-rates, $\overline{D}_m$ and $\overline{D}_{eq}$ and the strain-rate triaxiality, X_E, are defined by relation (5.21), whereas the corresponding stress quantities

are recalled here to be

$$\overline{\sigma}_{eq} = \frac{\sqrt{3}}{2}|\overline{\sigma}_{11} - \overline{\sigma}_{22}|, \quad \overline{\sigma}_m = \frac{\overline{\sigma}_{11} + \overline{\sigma}_{22}}{2}, \quad X_\Sigma = \frac{\overline{\sigma}_m}{\overline{\sigma}_{eq}}. \tag{5.23}$$

The applied load is such that the condition $|\overline{\sigma}_{22}| > |\overline{\sigma}_{11}|$ is always satisfied during the deformation process. Then making use of definitions (5.23), we could write the stress components in terms of the stress triaxiality X_Σ and the equivalent stress $\overline{\sigma}_{eq}$, such that

$$\overline{\sigma}_{11} = \left(X_\Sigma - \rho\frac{1}{\sqrt{3}}\right)\overline{\sigma}_{eq}, \quad \overline{\sigma}_{22} = \left(X_\Sigma + \rho\frac{1}{\sqrt{3}}\right)\overline{\sigma}_{eq}. \tag{5.24}$$

Here, $\rho = \pm 1$ such that the condition $|\overline{\sigma}_{22}| > |\overline{\sigma}_{11}|$ is always true. It is further noted that $\overline{\sigma}_{eq}$ is the unknown of the problem, which is computed such that $\overline{D}_{eq} = 1$. In turn, the stress triaxiality X_Σ is given. Because of the plane-strain loading the only sufficient condition for instability is $H = 0$, similarly to the previous case of the fixed strain-rate triaxiality X_E.

Fig. 5.17 shows evolution curves for the porosity f, the aspect ratio w, the hardening rate H and the equivalent stress $\overline{\sigma}_{eq}$ normalized by the flow stress in the matrix phase σ_o as a function of the stress triaxiality ($X_\Sigma = -0.1, 0.5$) and the macroscopic strain $\overline{\varepsilon}_{eq}$ for initial porosity $f_o = 10\%$. Since the stress triaxiality remains fixed during the deformation process, the strain-rate triaxiality is expected to change in time. As a consequence, the corresponding predictions of the SOM, the VAR and the GUR model for the evolution of the porosity are different. In Fig. 5.17a, for $X_\Sigma = 0.5$, the SOM and the VAR methods predict initially an increase in the porosity, which later decreases to zero (at sufficiently high strain not shown here). In contrast, the GUR model predicts a continuously increasing porosity during the deformation, which has as a consequence the softening of the porous material. In order to have a complete view of the softening or hardening of the material as predicted by the SOM and the VAR methods, it is necessary to study, as well, the evolution of the aspect ratio w, in Fig. 5.17b. For $X_\Sigma = 0.5$, w is greater than unity for both the SOM and the VAR, which implies that the porous medium hardens in the direction of the maximum principal stress, i.e., in the $2-$direction. This hardening is in contrast with the softening induced by the initial increase of the porosity.

However, as we observe in Fig. 5.17c, the SOM predicts initially softening, which is translated to a negative hardening rate H, whereas the VAR estimate predicts initially hardening, indicated by the positive H. In the sequel the SOM estimate for the hardening rate H becomes positive, which implies that H crosses zero at a critical equivalent strain $\overline{\varepsilon}_{eq} \sim 10\%$ and consequently the material becomes unstable at this point, in contrast to the corresponding VAR estimate, which remains positive during the deformation and therefore does not satisfy the condition for shear localization. On the contrary, the GUR model predicts softening during the deformation process and hence exhibits a behavior that is substantially different than the SOM and the VAR. Finally, Fig. 5.17d shows that the equivalent stress $\overline{\sigma}_{eq}$ as predicted by the SOM is lower than the corresponding estimates obtained by the VAR and the GUR models, which implies that the SOM predicts, at least initially, a much softer response for the porous medium. In large deformations, however, the SOM predicts a rapid decrease in the porosity and hence a significant hardening for the composite.

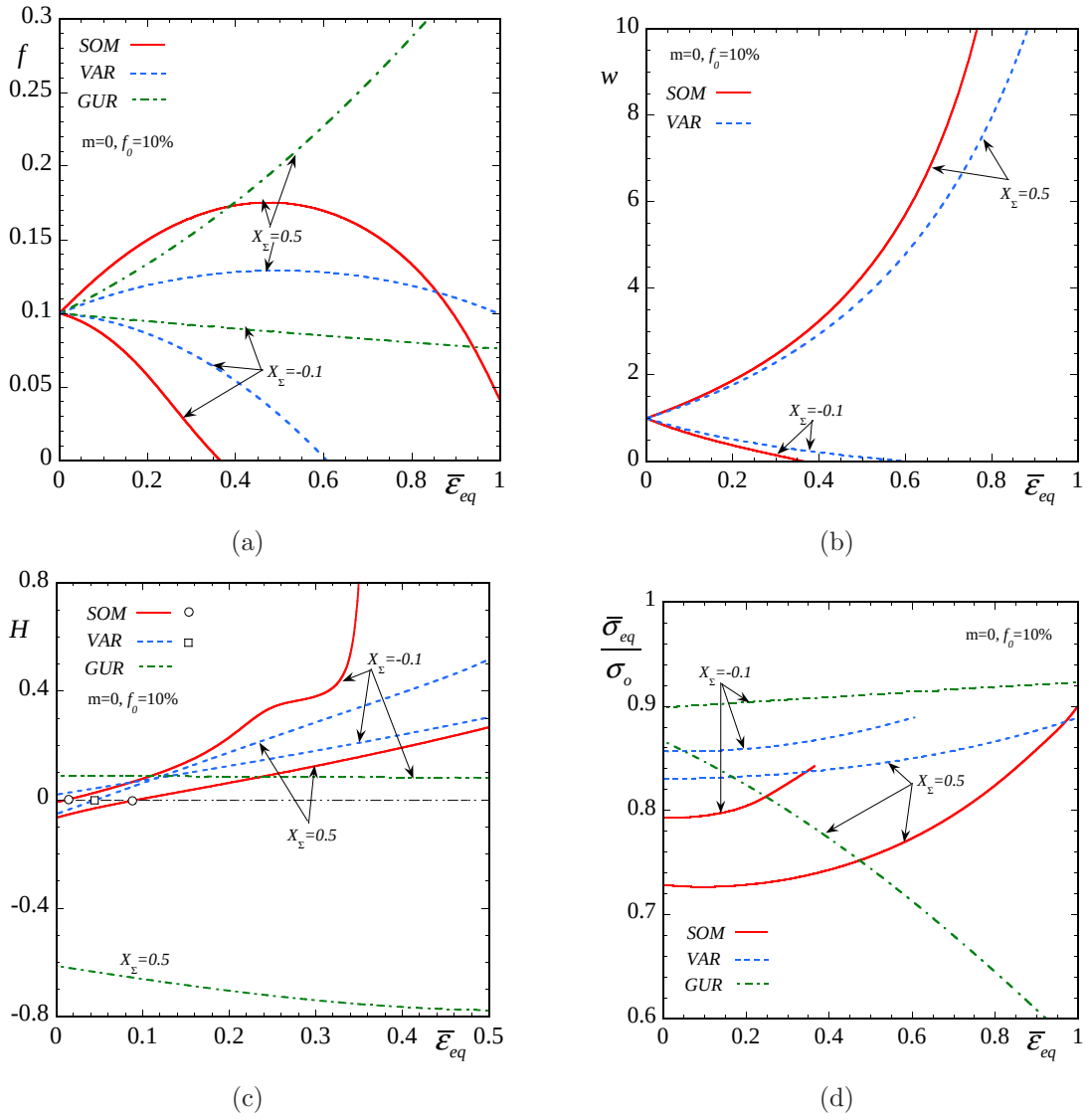

Figure 5.17: Results are shown for the evolution of the relevant microstructural and macroscopic variables for a porous material consisted of cylindrical pores with an initially, circular, in-plane cross-section and initial porosity $f_o = 10\%$. The matrix phase exhibits an ideally-plastic behavior, while the composite is subjected to biaxial tension and compression loading conditions with fixed stress triaxiality, $X_\Sigma = -0.1, 0.5$. SOM, VAR and GUR (Gurson, 1977) estimates are shown for the evolution of the (a) porosity f, (b) the aspect ratio w, (c) the hardening rate H and (d) the normalized, macroscopic equivalent stress $\overline{\sigma}_{eq}/\sigma_o$ (σ_o denotes the flow stress of the matrix phase) of the composite as a function of the macroscopic, equivalent strain $\overline{\varepsilon}_{eq}$. In (c) the symbols ∘ and □ denote the loss of stability for the porous medium as predicted by the SOM and the VAR, respectively.

Similar to the previous case, the SOM and the VAR methods exhibit a very different behavior than the corresponding GUR model for an applied stress triaxiality $X_\Sigma = -0.1$. While, the SOM and the VAR methods predict a decrease in the porosity, as shown in Fig. 5.17a, the corresponding GUR estimate for f remains almost constant during the deformation process. In addition, both the SOM and the VAR estimates exhibit a sharp decrease in the aspect ratio, $w < 1$, which induces a softening

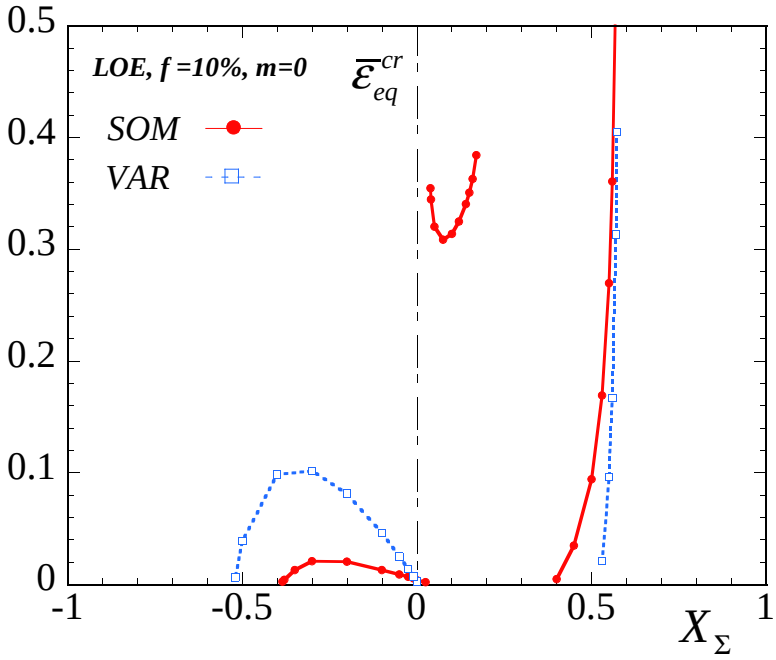

Figure 5.18: Macroscopic onset-of-failure curves as predicted by the SOM and VAR calculations, for an initially transversely, isotropic porous medium with ideally-plastic matrix phase and initial porosity $f_o = 10\%$. The plot shows the critical equivalent strain $\overline{\varepsilon}^{cr}_{eq}$ as a function of the applied stress triaxiality X_Σ.

in the direction of the maximum (absolute) principal stress ($|\overline{\sigma}_{22}| > |\overline{\sigma}_{11}|$ with $\overline{\sigma}_{22} < 0$) as shown in Fig. 5.17b. Looking now at the corresponding estimates for the hardening rate H in Fig. 5.17c, both the SOM and the VAR exhibit softening initially, while at a finite strain they become unstable (see the points where H crosses zero). On the other hand, the GUR model predicts slight hardening for the porous medium and as already anticipated it never becomes unstable for this loading. It is worth mentioning at this point that for the case of aligned loading, the GUR model can give a hardening rate equal to zero only in the case of isochoric loadings, i.e., $X_\Sigma = 0$ or $X_E = 0$.

Finally, Fig. 5.18 shows a map of the critical strains $\overline{\varepsilon}^{cr}_{eq}$ for loss of stability, as determined by the SOM and the VAR methods for the entire range of the stress triaxialities X_Σ. In the context of this figure, it is obvious that according to the SOM and the VAR estimates the material is unstable for a wide range of stress triaxialities. In particular, the SOM and the VAR estimates exhibit several differences especially at positive stress triaxialities where the VAR estimates become unstable just in a small vicinity of X_Σ, close to uniaxial tension loading conditions. In contrast the SOM estimates has a small branch of unstable behavior at stress triaxialities $0 \lesssim X_\Sigma \lesssim 0.3$. It is remarkable to note that there is a sharp transition (see both the SOM and the VAR lines close to $X_\Sigma = 0.5$), where the material passes from loadings that induce hardening ($0.3 \lesssim X_\Sigma \lesssim 0.5$) to ones that predict softening ($X_\Sigma \gtrsim 0.5$). This transition region lies closely to the uniaxial tension loading (i.e., $X_\Sigma = 0.57735$), while it is interesting to note that none of the two methods loses stability for this loading. In turn, for negative triaxialities, the SOM is more unstable at lower critical strains, while the VAR becomes unstable at higher values of $\overline{\varepsilon}^{cr}_{eq}$. In overall, it is observed that, similarly to the case of fixed strain-rate triaxialities X_E, instabilities may occur when the porous medium is subjected to low stress triaxiality

loadings, where the shear strains are expected to dominate over the corresponding dilatational strains.

5.5 Concluding Remarks

In this chapter, we have studied the evolution of microstructure in porous media consisting of cylindrical voids with initially circular or elliptical cross-section. The "second-order" estimates have been compared with the Lee and Mear (1999) results, finite element unit-cell calculations and the earlier "variational" predictions for a wide range of stress triaxialities and nonlinearities. It has been found that the "second-order" model improves significantly on the earlier "variational" method by giving much better agreement with the corresponding Lee and Mear and finite element calculations. The improvement was dramatic at higher stress triaxialities, where it was already known (Ponte Castañeda and Zaidman, 1994; Kailasam and Ponte Castañeda, 1998) that the "variational" method is overly stiff and thus underestimates significantly the evolution of the porosity.

More specifically, the "second-order" estimates were found to be in good agreement with the Lee and Mear (1999) results, for the entire range of stress triaxialities considered. However, it should be remarked that the Lee and Mear *dilute* results were found to underestimate slightly the evolution of the porosity at high stress triaxialities, when compared with the corresponding "second-order" estimates for very small but finite porosity $f_o = 10^{-6}$. To validate further this observation, we have included finite element, unit-cell results for a porosity $f_o = 10^{-4}$. It should be noted that the "second-order" predictions corresponding to $f_o = 10^{-4}$ and $f_o = 10^{-6}$ did not exhibit any difference indicating that both values could be used to approximate sufficiently the dilute limit. In this connection, the finite element results have been found to lie closer to the "second-order" estimates, leading to the conclusion that the Lee and Mear results underestimate slightly the evolution of the porosity at high stress triaxialities and nonlinearities.

To understand the difference in the predictions of the various models it was necessary to recall that Lee and Mear (see also Fleck and Hutchinson, 1986) make the assumption that the void evolves through a sequence of elliptical shapes during the deformation process, which is not the case in the finite element calculations where the void can take non-elliptical shapes. On the other hand, the "second-order" model, which is based on an homogenization procedure, makes use of the *average* fields in the vacuous phase to compute an *average elliptical* shape for the void. In this regard then, the accuracy of the "second-order" model is related to the estimation of the average fields in the porous material. Obviously, this procedure is different than the one adopted by Lee and Mear who solve the problem locally. Moreover, it is also important to mention that, according to Huang (1991b), in the method used by Lee and Mear to predict the evolution of microstructure in dilute porous media, a very large number of terms needs to be considered in the Rayleigh-Ritz eigen-function expansion to achieve sufficient accuracy at high stress triaxialities and nonlinearities. In this regard, the author believes that these two aforementioned observations could explain the fact that the Lee and Mear technique predicts lower values for the evolution of porosity, while the "second-order" model is able to predict with sufficient accuracy the evolution of porosity and thus be in closer agreement with the finite element results.

In the sequel, both the "second-order" and the Lee and Mear (1999) methods were found to be in good agreement for the prediction of the evolution of the porosity and the orientation angle of a void with initially elliptical cross-section, misaligned with the principal loading directions, when the porous medium is subjected to uniaxial tension or compression loading. In addition, the principal axes of the void evolved with a tendency to align themselves with the principal loading directions, which is intuitively expected, at least for the loadings considered here. In this connection, the "second-order" model was found to predict both qualitatively and quantitatively the evolution of the axes of anisotropy (or equivalently the principal axes of the voids) for tensile and compressive loadings.

Next, the "second-order" estimates were compared with corresponding results obtained by the finite-element and the "variational" method. The improvement of the "second-order" method over the "variational" method was dramatic at higher stress triaxialities. For instance, at a stress triaxiality $X_\Sigma = 5$ (biaxial tension) the "second-order" method and the finite element results predict that the porosity can increase up to *hundred* times the initial porosity at a strain of $\sim 2.5\%$, whereas the corresponding "variational" estimate delivers an increase in the porosity that is negligible at this strain. On the other hand, for a stress triaxiality $X_\Sigma = -5$ (biaxial compression), the porosity approaches the zero value at a strain of $\sim 15\%$ as determined by the "variational" method, in contrast to the corresponding "second-order" and finite element estimates that predict zero porosity at a strain value of $\sim 2.5\%$. A second remark in the context of this set of results is associated with the evolution of the shape of the voids (or the evolution of the in-plane aspect ratio). In this case, it has been found that the evolution of the aspect ratio is expected to affect significantly the effective behavior of the porous material at low stress triaxialities, since for such loadings the void evolves rapidly in a crack shape. For this case of low stress triaxialities, the "second-order" model has been found to provide fairly accurate estimates for the evolution of the aspect ratio when compared with finite element results for all the range of the nonlinearities considered.

On the other hand, at high stress triaxialities and nonlinearities, the "second-order" method has been shown to be in disagreement with the corresponding finite element results for the evolution of the aspect ratio. In this particular case, the finite element results confirm the observation made initially by Budiansky et al. (1982), and later by Fleck and Hutchinson (1986) and Lee and Mear (1992b,1999) in the context of dilute porous media, where it was found that the void elongates in a direction that is transverse to the maximum macroscopic principal stretching at sufficiently high triaxialities and nonlinearities. This counterintuitive result however, was found to have a minor effect on the overall response of the porous medium. The reason for this lies in the fact that at high stress triaxialities the evolution of porosity controls the effective behavior of the porous medium. Consequently, the "second-order" method, which predicts accurately the evolution of porosity at high stress triaxialities, is also capable of predicting with remarkable accuracy the macroscopic strain-rates and thus the effective response of the porous medium.

In the sequel, the "second-order" method has been compared with corresponding finite element results and "variational" estimates in the case of simple shear loading conditions. The main result in the context of this case, is that both the "second-order" and the "variational" methods predict with sufficient accuracy the evolution of the orientation angle of the elliptical void during the deformation

process, when compared with corresponding finite element results. Furthermore, the "second-order" estimates for the macroscopic stress tensor have been found to be in very good agreement with the corresponding finite element predictions for all the nonlinearities considered. It is worth noting that — to the best knowledge of the author — the "second-order" and the "variational" methods are the only available methods in the literature, apart from numerical techniques (such as the finite element or FFT methods), to be able to provide estimates for *non-dilute* porous media consisting of cylindrical voids with elliptical cross-section, that are subjected to general plane-strain loading conditions.

Finally, the "second-order" model has been used to predict possible development of instabilities in porous media with an ideally-plastic matrix phase. The "variational" method and the Gurson criterion have also been used for comparison. The main observation in the context of this section was that the porosity and the aspect ratio of the void may have opposite effects on the macroscopic behavior of the porous material and as a consequence they lead to possible development of instabilities. However, at large strain-rate or stress triaxialities the evolution of the porosity dominates over the the change of the aspect ratio and hence instability is unlikely to occur. Furthermore, the "second-order" and the "variational" methods were shown to have similar qualitative behavior as far as the prediction of instabilities is concerned. However, the "second-order" method has been shown to predict more accurately the evolution of the porosity and the aspect ratio in the case of finite nonlinearities and thus is expected to deliver more accurate results than the "variational" method in the case of porous media with an ideally-plastic matrix phase, particularly for the prediction of shear localization instabilities. On the contrary, the Gurson model does not involve any information on the shape of the voids and thus was incapable of predicting unstable behaviors except in the case of purely isochoric loadings ($X_\Sigma = 0$) where it delivers zero hardening during the deformation process. However, even in this case, the Gurson model is expected to be highly inaccurate, since for isochoric loadings the change in the shape of the void is significant.

Chapter 6

Instantaneous behavior: spherical and ellipsoidal voids

This chapter deals with the instantaneous effective behavior of porous materials consisting of ellipsoidal voids distributed randomly in the specimen. First, the study will be focused on isotropic porous materials made out of spherical voids. The "second-order" estimates (SOM) of Ponte Castañeda (2002a), discussed in section 2.6, will be compared with corresponding results obtained by the "variational" method (VAR) of Ponte Castañeda (1991), discussed in section 2.5, the Lee and Mear (1992c) method for dilute porous media methods, the high-rank sequential laminates (LAM) and the Leblond et al. (1994) (LPS) model – as well as the Flandi and Leblond, (2005) (FL) – for a wide range of nonlinearities and loadings (see chapter 3 for these last models). In the sequel, we will consider anisotropic porous materials consisting of ellipsoidal voids initially aligned with the loading directions. A thorough study of the effect of the pore shape on the effective behavior of the porous material will be attempted. Finally, this chapter will be concluded with corresponding estimates for the effective behavior of anisotropic porous media whose microstructure is misaligned with the loading directions.

6.1 General expressions

In this section, we provide expressions as explicit as possible for the computation of the effective stress potential as determined by the "variational" method, described in section (2.5) and the "second-order" method, described in section (2.6).

6.1.1 "Variational" method

In this subsection, we recall the main expressions for the estimation of the effective stress potential $\widetilde{U}_{var}$ as presented in section (2.5). Thus, it follows from equation (2.150)

$$\widetilde{U}_{var}(\overline{\boldsymbol{\sigma}}) = (1-f)\,\frac{\dot{\varepsilon}_o\,\sigma_o}{n+1}\left(\frac{\hat{\sigma}_{eq}}{\sigma_o}\right)^{n+1} = (1-f)\,\frac{\dot{\varepsilon}_o\,\sigma_o}{n+1}\left[\frac{3\,\overline{\boldsymbol{\sigma}}\cdot\widehat{\mathbf{M}}\,\overline{\boldsymbol{\sigma}}}{(1-f)\,\sigma_o^2}\right]^{\frac{n+1}{2}}, \tag{6.1}$$

where f is the porosity, n is the nonlinear exponent of the matrix phase taking values between 1 (linear) and ∞ (ideally-plastic), while $\dot{\varepsilon}_o$ and σ_o denote a reference strain-rate and the flow stress

of the matrix phase, respectively. The tensor $\widehat{\mathbf{M}}$ is related to the effective compliance tensor $\widetilde{\mathbf{M}}$ by (2.143), such that

$$\widehat{\mathbf{M}} = \mu\,\widetilde{\mathbf{M}}, \qquad \widetilde{\mathbf{M}} = \mathbf{M} + \frac{f}{1-f}\,\mathbf{Q}^{-1} = \frac{1}{\mu}\left(\frac{1}{2}\,\mathbf{K} + \frac{f}{1-f}\,\widehat{\mathbf{Q}}^{-1}\right). \tag{6.2}$$

Here, the effective compliance tensors $\widetilde{\mathbf{M}}$ and $\mathbf{Q}$ are homogeneous of degree -1 and 1 in the moduli μ, respectively, and hence $\widehat{\mathbf{M}}$ and $\widehat{\mathbf{Q}}$ are independent of μ (see Appendix IV of chapter 2). The microstructural fourth-order tensor $\mathbf{Q}$ (or $\widehat{\mathbf{Q}}$) has been defined in relation (2.59) and its calculation is detailed in Appendix I of chapter 2.

Next, the corresponding macroscopic strain-rate $\overline{\boldsymbol{D}}$ is given by (see (2.153))

$$\overline{\boldsymbol{D}} = \widetilde{\mathbf{M}}(\mu)\,\overline{\boldsymbol{\sigma}} = \frac{1}{\mu}\,\widehat{\mathbf{M}}\,\overline{\boldsymbol{\sigma}} = \sqrt{3}\,\dot{\varepsilon}_o\left(\frac{3\,\overline{\boldsymbol{\sigma}}\cdot\widehat{\mathbf{M}}\,\overline{\boldsymbol{\sigma}}}{(1-f)\,\sigma_o^2}\right)^{\frac{n}{2}}\frac{\widehat{\mathbf{M}}\,\overline{\boldsymbol{\sigma}}}{\sqrt{\overline{\boldsymbol{\sigma}}\cdot\widehat{\mathbf{M}}\,\overline{\boldsymbol{\sigma}}}}. \tag{6.3}$$

In order to complete the study of the "variational" method, it is necessary to provide estimates for the phase average fields in the nonlinear composite. These estimates have been presented in section 2.5 and are presented here for completeness:

$$\overline{\boldsymbol{D}}^{(2)} = \frac{1}{\mu\,(1-f)}\,\widehat{\mathbf{Q}}^{-1}\,\overline{\boldsymbol{\sigma}}, \qquad \overline{\boldsymbol{\Omega}}^{(2)} = \overline{\boldsymbol{\Omega}} + \frac{1}{\mu}\,\boldsymbol{\Pi}\,\mathbf{L}\,\widehat{\mathbf{Q}}^{-1}\,\overline{\boldsymbol{\sigma}}. \tag{6.4}$$

In all the above expressions, use has been made of the homogeneity of the fourth order tensors $\mathbf{M}$, $\mathbf{L}$, $\mathbf{Q}$ and $\boldsymbol{\Pi}$ on μ (see Appendix IV of chapter 2 for details). In turn, the second-order tensor $\overline{\boldsymbol{\Omega}}$ is the macroscopic spin tensor and is applied externally to the material. On the other hand, the incompressibility limit $\kappa \to \infty$ needs to be considered before evaluating numerically the term $\boldsymbol{\Pi}\,\mathbf{L}$. Similar to the two-dimensional case discussed in the previous two chapters, the methodology of computing this limit is described in Appendix I of chapter 2.

Porous media with an ideally-plastic matrix phase. For the special case of ideally-plastic media ($n \to \infty$), the yield criterion is given in terms of the effective yield function $\widetilde{\Phi}_{var}$ (see (2.232)), such that

$$\widetilde{\Phi}_{var}(\overline{\boldsymbol{\sigma}};\, s_\alpha) = \sqrt{\frac{3\,\overline{\boldsymbol{\sigma}}\cdot\widehat{\mathbf{M}}\,\overline{\boldsymbol{\sigma}}}{1-f}} - \sigma_o = 0, \tag{6.5}$$

where the tensor $\widehat{\mathbf{M}}$ is given by (6.2). The macroscopic strain-rate $\overline{\boldsymbol{D}}$ becomes

$$\overline{\boldsymbol{D}} = \dot{\Lambda}\sqrt{\frac{3}{1-f}}\,\frac{\widehat{\mathbf{M}}\,\overline{\boldsymbol{\sigma}}}{\sqrt{\overline{\boldsymbol{\sigma}}\cdot\widehat{\mathbf{M}}\,\overline{\boldsymbol{\sigma}}}}, \tag{6.6}$$

where $\dot{\Lambda}$ is the plastic multiplier and needs to be determined by the consistency condition $\dot{\widetilde{\Phi}}_{var}$. A detailed discussion on the evaluation of $\dot{\Lambda}$ has been provided in sections 2.8.1 and 2.8.3 and is not repeated here. On the other hand, the phase average fields are given by relation (4.9), with μ given in terms of $\dot{\Lambda}$ by (2.257), recalled here to be

$$\frac{1}{\mu} = \frac{3\,\dot{\Lambda}}{(1-f)\,\sigma_o}. \tag{6.7}$$

The above expressions conclude the determination of the effective behavior, as well as of the phase average fields of the porous medium in the context of the "variational" method.

6.1.2 "Second-order" method

Expressions as explicit as possible for the computation of the effective stress potential $\widetilde{U}_{som}$, defined in the context of the "second-order" method by relation (2.183) are provided in this subsection. For convenience we recall this result here, which reads

$$\widetilde{U}_{som}(\overline{\boldsymbol{\sigma}}) = (1-f)\left[\frac{\dot{\varepsilon}_o\,\sigma_o}{1+n}\left(\frac{\hat{\sigma}_{eq}}{\sigma_o}\right)^{n+1} - \dot{\varepsilon}_o\left(\frac{\check{\sigma}_{eq}}{\sigma_o}\right)^{n}\left(\hat{\sigma}_{||} - \frac{\overline{\sigma}_{eq}}{(1-f)}\right)\right]. \tag{6.8}$$

In this last expression, $\overline{\sigma}_{eq}$ is applied externally in the problem, while the determination of $\check{\sigma}_{eq}$ has been extensively discussed in subsection 2.6.2 and is recalled for completeness in the following paragraphs. In turn, the stress measures $\hat{\sigma}_{||}$ and $\hat{\sigma}_{eq}$ have been defined in relations (2.174) (or (2.180)) and (2.175), respectively. For the determination of these variables, it is necessary to compute the two partial derivatives $\partial\widetilde{U}_L/\partial(2\,\lambda)^{-1}$ and $\partial\widetilde{U}_L/\partial(2\,\mu)^{-1}$, where $\widetilde{U}_L$ is the effective stress potential in the linear comparison composite (LCC) defined by relation (2.170), and λ and μ are the moduli of the compliance tensor $\mathbf{M}$, defined in relation (2.167). Making use of these definitions, it is possible to write

$$\hat{\sigma}_{||} = \check{\sigma}_{eq} + \sqrt{\check{\sigma}_{eq}^2 + \frac{\overline{\sigma}_{eq}^2}{1-f} - \frac{2\,\check{\sigma}_{eq}\,\overline{\sigma}_{eq}}{1-f} - \frac{3\,f}{(1-f)^2}\,\overline{\boldsymbol{\sigma}}\,\mathbf{Q}^{-1}\,\frac{\partial\mathbf{Q}}{\partial\lambda^{-1}}\,\mathbf{Q}^{-1}\,\overline{\boldsymbol{\sigma}}}, \tag{6.9}$$

and

$$\hat{\sigma}_{\perp} = \sqrt{-\frac{3\,f}{(1-f)^2}\,\overline{\boldsymbol{\sigma}}\,\mathbf{Q}^{-1}\,\frac{\partial\mathbf{Q}}{\partial\mu^{-1}}\,\mathbf{Q}^{-1}\,\overline{\boldsymbol{\sigma}}}, \tag{6.10}$$

with

$$\hat{\sigma}_{eq} = \sqrt{\hat{\sigma}_{||}^2 + \hat{\sigma}_{\perp}^2}. \tag{6.11}$$

In the previous two expressions, $\mathbf{Q}$ is a microstructural tensor defined by relation (2.59). In general, this tensor involves the computation of surface (double) integrals and cannot be written in analytical form. For some special cases, though, it is possible to solve the integrals (see Mura, 1987; Ponte Castañeda and Zaidman, 1994), but explicit expressions will not be supplied here since they correspond only to some very special cases, such as the one that the matrix phase in the LCC is isotropic and the voids are spherical or spheroidal in shape. On the contrary, in the context of the "second-order" method the matrix phase in the LCC is anisotropic, which has as a consequence the non-analyticity of the integrals. Even so, the above expressions can be easily evaluated numerically with sufficient accuracy. In addition, the aforementioned expressions require a prescription for the reference stress tensor $\check{\boldsymbol{\sigma}}$. The determination of $\check{\boldsymbol{\sigma}}$ has been extensively discussed in subsection (2.6.2), whereas the definition of $\check{\boldsymbol{\sigma}}$ is given for completeness

$$\check{\boldsymbol{\sigma}} = \xi\left(X_\Sigma, \overline{\boldsymbol{S}}, s_a, n\right)\overline{\boldsymbol{\sigma}}', \tag{6.12}$$

where $\overline{\boldsymbol{S}} = \overline{\boldsymbol{\sigma}}'/\overline{\sigma}_{eq}$, $s_a = \{f,\, w_1,\, w_2,\, \mathbf{n}^{(1)},\, \mathbf{n}^{(2)},\, \mathbf{n}^{(3)} = \mathbf{n}^{(1)} \times \mathbf{n}^{(2)}\}$ denotes the set of the microstructural variables, n is the nonlinear exponent of the matrix phase, and

$$\xi\left(X_\Sigma, \overline{\boldsymbol{S}}\right) = \frac{1-t\,f}{1-f} + \alpha_m(\overline{\boldsymbol{S}})\,|X_\Sigma|\left(\exp\left[-\frac{\alpha_{eq}(\overline{\boldsymbol{S}})}{|X_\Sigma|}\right] + \beta\,\frac{X_\Sigma^4}{1+X_\Sigma^4}\right), \tag{6.13}$$

is a suitably chosen interpolation function. The coefficients t and β are detailed in Appendix III of chapter 2. On the other hand, the factors α_m and α_{eq} are, in general, functions of the microstructural

variables s_a, the nonlinearity n of the matrix, the stress tensor $\overline{\boldsymbol{S}}$, but not of the stress triaxiality X_Σ. The determination of these factors has been discussed in detail in subsection (2.6.2) and is not repeated here.

In turn, the macroscopic strain-rate $\overline{\boldsymbol{D}}$ is given by (2.186)), and is recalled here to be

$$\overline{D}_{ij} = (\overline{D}_L)_{ij} + (1-f)\, g_{mn} \frac{\partial \check{\sigma}_{mn}}{\partial \overline{\sigma}_{ij}}. \tag{6.14}$$

Here, $\overline{\boldsymbol{D}}_L$ is the macroscopic strain-rate in the LCC given by (2.118) and (2.124), such that

$$\overline{\boldsymbol{D}}_L = \widetilde{\mathbf{M}}\, \overline{\boldsymbol{\sigma}} + \widetilde{\boldsymbol{\eta}}, \qquad \widetilde{\boldsymbol{\eta}} = \boldsymbol{\eta}, \tag{6.15}$$

whereas the second-order tensor $\boldsymbol{g}$ reads as

$$g_{ij} = \left(\frac{1}{2\lambda} - \frac{1}{2\lambda_t}\right)\left(\hat{\sigma}_{||} - \frac{\overline{\sigma}_{eq}}{(1-f)}\right)\frac{\check{\sigma}_{ij}}{\check{\sigma}_{eq}} + \frac{f}{2(1-f)^2}\,\overline{\sigma}_{kl}\, T_{klmnij}\, \overline{\sigma}_{mn}, \tag{6.16}$$

with

$$T_{klmnij} = \left.\frac{\partial\, [Q(\check{\boldsymbol{\sigma}})]^{-1}_{klmn}}{\partial \check{\sigma}_{ij}}\right|_{\lambda,\,\mu}, \tag{6.17}$$

and

$$\lambda_t = \frac{\sigma_o}{3\, n\, \dot{\varepsilon}_o}\left(\frac{\check{\sigma}_{eq}}{\sigma_o}\right)^{1-n}. \tag{6.18}$$

Next, the phase average fields in the vacuous phase, i.e., the average strain-rate $\overline{\boldsymbol{D}}^{(2)}$ and spin $\overline{\boldsymbol{\Omega}}^{(2)}$, are recalled. In particular, $\overline{\boldsymbol{D}}^{(2)}$ has been defined by (2.219)

$$\overline{\boldsymbol{D}}^{(2)} = \frac{1}{f}\,\overline{D}_m\, \boldsymbol{I} + \frac{1}{(1-f)\,\mu}\mathbf{K}\,\widehat{\mathbf{Q}}(k)^{-1}\,\overline{\boldsymbol{\sigma}} + \boldsymbol{\eta}, \tag{6.19}$$

where $\mathbf{Q}$ is given by (2.59) (see details in Appendix I of chapter 2), $\mathbf{K}$ denotes the fourth-order shear projection tensor defined by (2.140), while use has been made of the fact that $\boldsymbol{\eta}$ is a deviatoric second-order tensor, such that $\mathbf{K}\,\boldsymbol{\eta} = \boldsymbol{\eta}$.

On the other hand, $\overline{\boldsymbol{\Omega}}^{(2)}$ has been given by (2.220), such that

$$\overline{\boldsymbol{\Omega}}^{(2)} = \overline{\boldsymbol{\Omega}} + \frac{1}{\mu}\,\boldsymbol{\Pi}\,\mathbf{L}\,\widehat{\mathbf{Q}}(k)^{-1}\,\overline{\boldsymbol{\sigma}}, \tag{6.20}$$

where $\boldsymbol{\Pi}$ is given by relation (2.60). Note that, similar to the "variational" method, the incompressibility limit $\kappa \to \infty$ needs to be considered before evaluating numerically the term $\boldsymbol{\Pi}\,\mathbf{L}$. The methodology of computing this limit is described in Appendix I of this chapter.

Porous media with an ideally-plastic matrix phase. For the special case of ideally-plastic media ($n \to \infty$), the yield criterion is written in terms of the effective yield function $\widetilde{\Phi}_{som}$ (see (2.266)), such that

$$\widetilde{\Phi}_{som}(\overline{\boldsymbol{\sigma}};\, \check{\boldsymbol{\sigma}}\, s_\alpha) = \hat{\sigma}_{eq} - \sigma_o = 0, \tag{6.21}$$

where $\hat{\sigma}_{eq}$ is given by (6.11), while the equation (4.19) for the anisotropy ratio k reduces to

$$(1-k)\,\hat{\sigma}_{||} - \check{\sigma}_{eq} = 0, \tag{6.22}$$

in the ideally-plastic limit. The reference stress tensor $\check{\boldsymbol{\sigma}}$ is given by the expression (6.12), while the computation of the factors α_m and α_{eq} are detailed in subsection (2.8.2).

Then, the macroscopic strain-rate $\overline{\boldsymbol{D}}$ is given in terms of the plastic multiplier $\dot{\Lambda}$ by

$$\overline{\boldsymbol{D}} = \dot{\Lambda}\,\frac{\partial \hat{\sigma}_{eq}}{\partial \overline{\boldsymbol{\sigma}}}. \tag{6.23}$$

The determination of $\dot{\Lambda}$ has been provided in sections (2.8.2) and 2.8.3 and is not repeated here. In turn, the phase average fields are given by relation (6.19) and (6.20), with μ expressed in terms of $\dot{\Lambda}$ by (see (2.275))

$$\frac{1}{\mu} = \frac{3\,\dot{\Lambda}}{(1-f)\,\sigma_o}. \tag{6.24}$$

The above expressions are used to describe the instantaneous effective behavior of porous media consisting of general ellipsoidal microstructures subjected to general loading conditions. In the following sections, we will make use of the aforementioned expressions to obtain estimates for the instantaneous effective behavior of porous media consisting of cylindrical voids that are subjected to plane-strain loading conditions.

6.2 Dilute estimates for transversely isotropic porous media

Results characterizing the behavior of dilute porous materials consisting of isolated spherical or spheroidal voids subjected to axisymmetric loading conditions are discussed in this section. In particular, the "second-order" (SOM) and the "variational" (VAR) methods are compared with corresponding results obtained by the work of Lee and Mear (1992c) (LM), which have been discussed briefly in chapter 3 (see subsection 3.2.4). It is important to note here that the SOM and VAR results are obtained numerically for a porosity $f_o = 10^{-6}$. Next, we define the loading considered in this section in terms of the remote non-zero components of the stress tensor:

$$\overline{\sigma}_{11} = \overline{\sigma}_{22} = T, \quad \overline{\sigma}_{33} = S. \tag{6.25}$$

Then, the stress triaxiality is defined in terms of S and T by

$$X_\Sigma = \frac{S+2\,T}{3\,|S-T|} = \frac{S}{|S|}\,\frac{1+2\,T/S}{3\,|1-T/S|}. \tag{6.26}$$

In the figures to follow, we use the ratio T/S as the loading parameter in the problem. The values used are $T/S = 0, 0.2, 0.4, 0.6, 0.7$, which correspond to stress triaxiality $X_\Sigma = \pm 1/3, 0.583, 1, 1.833, 2.667$, respectively. Obviously, the sign of the X_Σ depends on the sign of the normalized quantity $S/|S|$.

To begin with, Fig. 6.1 shows results for the dilatation rate P_{sph} and the deviatoric part of the axial strain-rate Q_{sph} as a function of the stress triaxiality X_Σ and the nonlinearity $n = 1, 3, 5, 10$. The quantities P_{sph} and Q_{sph} have been detailed in relations (3.42) and (3.43), respectively. Particularly in Fig. 6.1a, we observe that the SOM is in good agreement with the LM results for all the nonlinearities and triaxialities considered here, although the LM results are found to underestimate the dilatation rate at high nonlinearities. This is in accordance with the results of section 4.2 for cylindrical microstructures. A possible reason for this underestimation of the hydrostatic and deviatoric part of $\overline{\boldsymbol{D}}$ has been discussed in remark 4.2.1. More specifically, these methods are based on a dilute expansion of the effective stress potential, as well as on the construction of a stream function

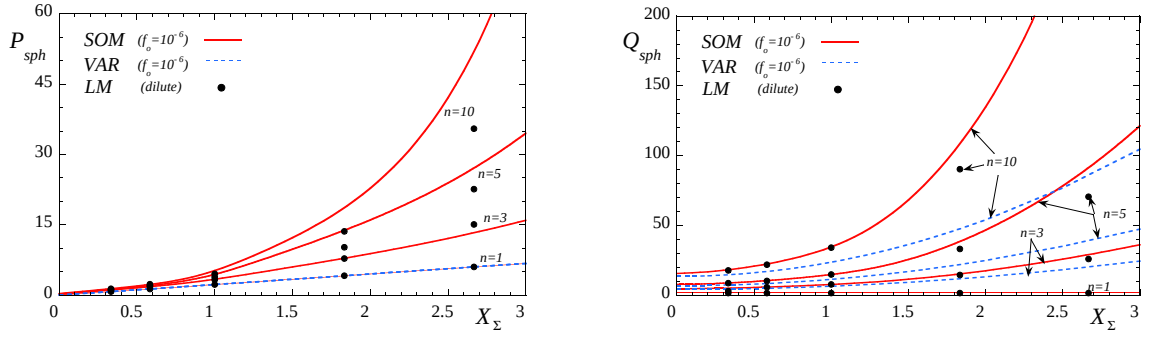

(a) (b)

Figure 6.1: Homogenization (SOM and VAR) and numerical estimates (LM) for (a) P_{sph}, which is related to the hydrostatic part of the strain-rate and (b) Q_{sph}, which is related to the deviatoric part of the strain-rate, are shown for a porous medium consisting of dilute concentration of spherical voids ($f_o = 10^{-6}$ for SOM and VAR) with matrix phase described by exponents $n = 1, 3, 5, 10$ as a function of the stress triaxiality X_Σ.

to approximate the actual velocity field around the pore surface by making use of the Rayleigh-Ritz method. A first point to be made is related to the fact that the range of validity of this dilute expansion diminishes to zero for purely hydrostatic loading and high nonlinearities close to the ideally plastic limit (see subsection 3.2.5). In addition, this result is consistent with the observations made by Huang (1991b), who showed that a large number of terms in the representation of the stream function needs to be considered for convergence at high nonlinearities and stress triaxialities.

In contrast, the VAR method underestimates significantly the dilatation rate P_{sph}, partially due to the fact that it fails to recover the analytical shell result in hydrostatic loading, as well as the fact that for hydrostatic loadings the VAR estimate does not have a linear correction in the porosity f in the dilute limit. This last observation has been extensively discussed in subsection 3.2.5. In turn, Fig. 6.1b shows corresponding results for the deviatoric part of the axial strain-rate Q_{sph}. The agreement of the SOM and the LM results is good for all nonlinearities and triaxialities considered here, whereas the VAR method completely fails to follow the rate of change of Q_{sph} with increasing stress triaxiality. Obviously, all the curves coincide in the linear case, i.e., $n = 1$. This indicates that with increasing nonlinearity the determination of the behavior of dilute porous media becomes very sensitive on the stress triaxiality, and therein lies the difficulty in obtaining numerically accurate results with the stream function technique, as discussed by Huang et al. (1991b).

Having discussed the behavior of dilute isotropic porous media, we extend this study to dilute porous media consisting of spheroidal voids with prolate or oblate shapes subjected to axisymmetric loading conditions aligned with the pore symmetry axis. In particular, Fig. 6.2 and Fig. 6.3 show results for the normalized ratio of the dilatation rate P/P_{sph} and the deviatoric axial strain-rate Q/Q_{sph} as a function of the aspect ratio w of the spheroidal voids, whereas the nonlinearity of the matrix is $n = 10$. Note that in this case, VAR estimates are not included, since they have already been found to be too stiff for isotropic porous materials and, thus, the comparison of the aforementioned ratios is not meaningful.

More specifically, Fig. 6.2 shows results for P/P_{sph} and Q/Q_{sph} for porous media consisting of

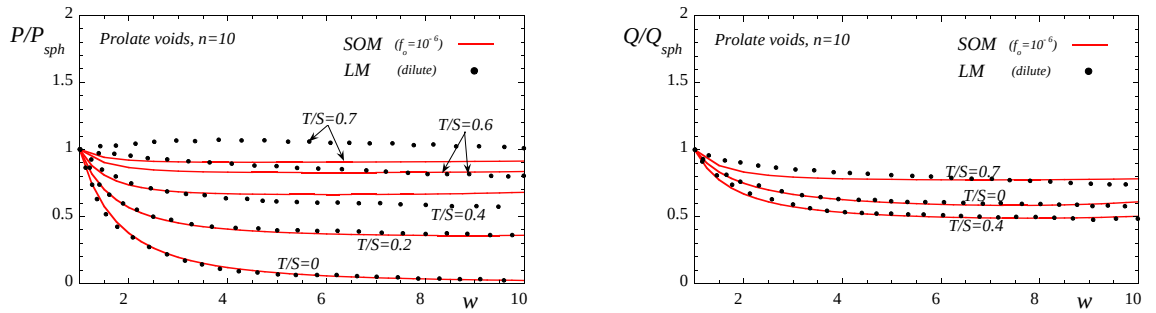

(a) (b)

Figure 6.2: Homogenization (SOM and VAR) and numerical estimates (LM) for (a) P/P_{sph}, which is related to the hydrostatic part of the strain-rate and (b) Q/Q_{sph}, which is related to the deviatoric part of the axial strain-rate $\overline{\boldsymbol{D}}'_{33}$, are shown for a porous medium consisting of dilute concentration of prolate voids ($f_o = 10^{-6}$ for SOM and VAR). The matrix phase is described by an exponent $n = 10$. The results are plotted as a function of the aspect ratio w of the spheroidal voids for axisymmetric tensile loadings with stress ratio $T/S = 0, 0.2, 0.4, 0.6, 0.7$. For clarity between the Q/Q_{sph} curves, the ratios $T/S = 0, 0.4, 0.7$ are not included.

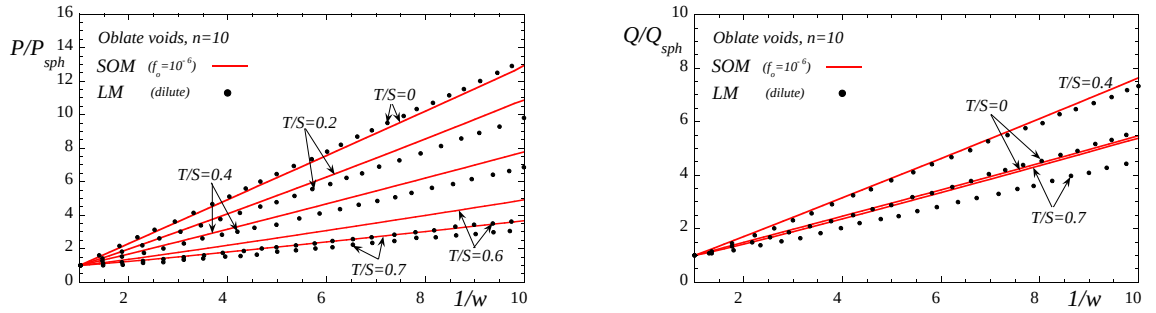

(a) (b)

Figure 6.3: Homogenization (SOM and VAR) and numerical estimates (LM) for (a) P/P_{sph}, which is related to the hydrostatic part of the strain-rate and (b) Q/Q_{sph}, which is related to the deviatoric part of the axial strain-rate $\overline{\boldsymbol{D}}'_{33}$, are shown for a porous medium consisting of dilute concentration of oblate voids ($f_o = 10^{-6}$ for SOM and VAR). The matrix phase is described by an exponent $n = 10$. The results are plotted as a function of the aspect ratio $1/w$ of the spheroidal voids for axisymmetric tensile loadings with stress ratio $T/S = 0, 0.2, 0.4, 0.6, 0.7$. For clarity between the Q/Q_{sph} curves, the ratios $T/S = 0, 0.4, 0.7$ are not included.

prolate voids subjected to axisymmetric loading conditions with stress ratios $T/S = 0, 0.2, 0.4, 0.6, 0.7$ as a function of the aspect ratio w of the spheroidal voids. The main observation in the context of this figure, is that the SOM is in good agreement with the LM results for all the stress triaxialities and aspect ratios shown here. In Fig. 6.2a, the SOM estimates for P/P_{sph} is in excellent agreement with the corresponding LM results, particularly at low and moderate triaxialities, i.e., $T/S = 0, 0.2, 0.4$. In contrast, for higher stress triaxialities ($T/S = 0.6, 0.7$), the SOM is found to underestimate slightly the ratio P/P_{sph}, when compared with the LM results. However, this does not mean that the SOM underestimates the value P, since we have already seen in Fig. 6.1, that the LM delivers a much

lower value for P_{sph} at high triaxialities.

In turn, Fig. 6.2b shows results for Q/Q_{sph}, where the SOM is found to be in excellent agreement with the LM results for all stress triaxialities T/S and aspect ratios w shown. For clarity of the curves, the values $T/S = 0.2, 0.6$ have not been included. It is also important to emphasize that in Fig. 6.2b, we observe a clear trend in the Q/Q_{sph} curves, in that the corresponding estimates for $T/S = 0$ lie higher than the corresponding results for $T/S = 0.4$ and lower that the ones for $T/S = 0.7$. This is an effect observed at high nonlinearities, which certainly is not met in the linear case, which is not included here[‡]. This last observation suggests that the SOM is able to capture adequately very strong nonlinear effects as the one discussed previously.

This section is concluded with corresponding results for dilute porous media with oblate spheroidal voids. Fig. 6.3 shows results for the dilatation rate P/P_{sph} and the deviatoric axial strain-rate Q/Q_{sph} as a function of the aspect ratio of the oblate void $1/w$. The porous medium is subjected to axisymmetric loading conditions with stress ratio $T/S = 0, 0.2, 0.4, 0.6, 0.7$, whose matrix phase is described by a nonlinear exponent $n = 10$. The main observation in the context of this figure is that the SOM is in relatively good agreement with the LM predictions, particularly for low and moderate stress triaxialities. In Fig. 6.3a, we observe that as the stress triaxiality increases the rate of change of the dilatation rate P/P_{sph} decreases. The SOM is seen to overestimate the value of P/P_{sph} at high triaxialities and high aspect ratios. This may be due to the prescription of the reference stress tensor involved in the SOM method, as described in subsection 2.6.2, which is related with the evaluation of the hydrostatic behavior of a porous medium consisting of spheroidal (or more generally ellipsoidal) voids with arbitrary aspect ratio w. Indeed this prescription is approximate and in general it could lead to "conservative" estimates for the estimation of the dilatation rate at high stress triaxialities.

On the other hand, Fig. 6.3b shows corresponding estimates for the deviatoric axial strain-rate Q/Q_{sph} as a function of the aspect ratio $1/w$ for stress ratios $T/S = 0, 0.4, 0.7$. The values $T/S = 0.2, 0.6$ are not included for clarity of the rest of the curves. Similarly to the curves for P/P_{sph}, the SOM estimates for Q/Q_{sph} are in very good agreement for low and moderate triaxialities $T/S = 0, 0.4$, while the overestimate the rate of change of Q/Q_{sph} at higher ones. Note, however, the trend observed in the context of this figure, where the curve for $T/S = 0$ lies lower than the one for $T/S = 0.4$ and higher than the corresponding curve for $T/S = 0.7$. This trend is an effect of the high nonlinearity considered here ($n = 10$), and has already been observed for prolate voids.

In a nutshell, the SOM is found to improve significantly on the VAR method by being in good agreement with the LM results for all the nonlinearities and stress triaxialities considered here.

6.3 Isotropic porous media under isochoric loadings

For consistency with the two-dimensional results presented in chapter 4, we present results on the effective behavior of isotropic porous media subjected to isochoric loading conditions. For completeness, we consider two distinct values for the Lode angle $\theta = 0, \pi/6$, which is related to the third invariant of the macroscopic stress tensor, as defined by $(6.30)_2$. Results are obtained by making

[‡]The reader is referred in the original work of Lee and Mear (1992c) for details on the linear case.

use of the "second-order" method (SOM), the "variational" method (VAR) and the sequentially laminated microstructures (LAM), discussed in section 3.4. In addition, the well-known Voigt bound is also shown whenever applicable. At this point, it is important to note that, for isochoric loadings, the reference stress tensor $\breve{\boldsymbol{\sigma}}$, discussed in subsection (2.6.2), reduces to $\breve{\boldsymbol{\sigma}} = \overline{\boldsymbol{\sigma}}'$ (the prime denotes the deviatoric part of a second-order tensor). Moreover, it is emphasized that by making use of the homogeneity of the local potential (2.23) in $\boldsymbol{\sigma}$, it follows that in the case of purely deviatoric loadings the effective stress potential can be written as

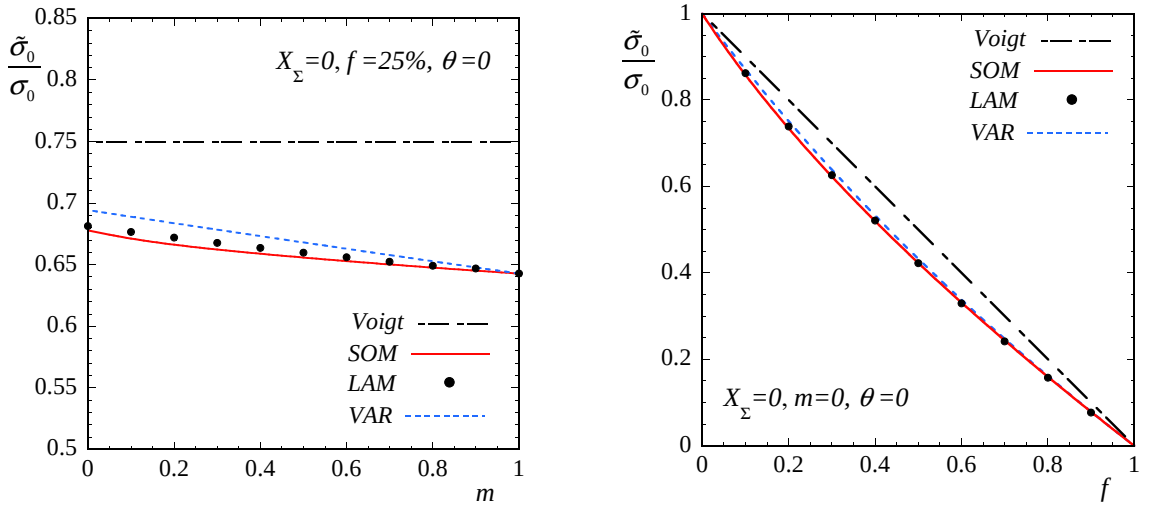

(a) (b)

Figure 6.4: Estimates and exact results for isotropic porous materials subjected to isochoric axisymmetric loadings ($X_\Sigma = 0$ and $\theta = 0$). Effective flow stress $\widetilde{\sigma}$ curves normalized by the flow stress of the matrix σ_o are shown, (a) as a function of the strain-rate sensitivity parameter m for porosity ($f = 25\%$), and (b) as a function of the porosity f in the case of an ideally-plastic matrix ($m = 0$).

$$\widetilde{U}(\overline{\boldsymbol{\sigma}}) = \frac{\dot{\varepsilon}_o\, \widetilde{\sigma}_o(\theta)}{n+1} \left(\frac{\overline{\sigma}_{eq}}{\widetilde{\sigma}_o(\theta)} \right)^{n+1}, \tag{6.27}$$

where $\widetilde{\sigma}_o$ is the *effective flow stress* of the composite and, in general, depends on the third invariant of the macroscopic stress tensor, which is denoted here with the Lode angle θ, defined by $(6.30)_2$.

More specifically, Fig. 6.4 presents results for the normalized effective flow stress $\widetilde{\sigma}_o/\sigma_o$ (σ_o is the flow stress of the matrix phase) as function of the strain-rate sensitivity parameter m and the porosity f for an axisymmetric loading, i.e., for a Lode angle $\theta = 0$. The main observation in the context of this figure is that the SOM is in good agreement with the LAM results, and certainly much better than the VAR estimates for all the porosities and nonlinearities considered. Obviously, the Voigt bound is much stiffer and hence is much less accurate. Fig. 6.4a shows corresponding results for $\widetilde{\sigma}_o/\sigma_o$ as a function of the strain-rate sensitivity parameter m for a porosity $f = 25\%$. In this figure, the SOM improves on the VAR estimates by being in much better agreement with the LAM results, even though it tends to be slightly softer than the rest of the methods. In turn, Fig. 6.4b shows corresponding results for $\widetilde{\sigma}_o/\sigma_o$ as a function of the porosity f for an ideally-plastic matrix ($m = 0$). Here, we observe that both the SOM and the LAM estimates satisfy the VAR bound

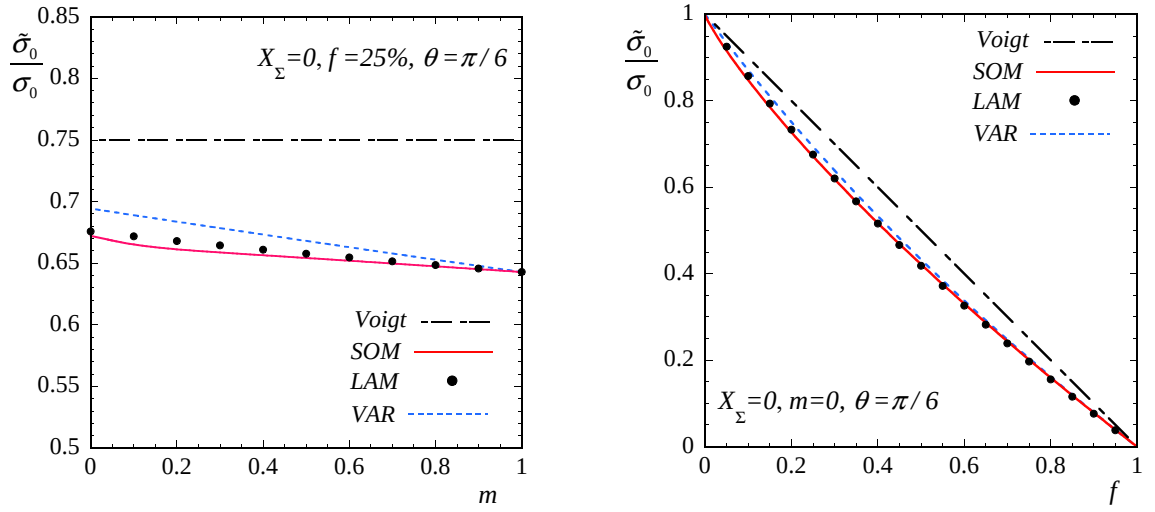

Figure 6.5: Estimates and exact results for isotropic porous materials subjected to isochoric in-plane shear loadings ($X_\Sigma = 0$ and $\theta = \pi/6$). Effective flow stress $\widetilde{\sigma}$ curves normalized by the flow stress of the matrix σ_o are shown, (a) as a function of the strain-rate sensitivity parameter m for porosity ($f = 25\%$), and (b) as a function of the porosity f in the case of an ideally-plastic matrix ($m = 0$).

in the entire range of the porosities. Note, however, that in this case all the methods — except the Voigt bound — are in quite good agreement for the entire range of the porosities considered. Nonetheless, it is remarked that all the methods — except the Voigt bound — are expected to be sufficiently accurate in the entire range of nonlinearities and porosities when the material is subjected to isochoric axisymmetric loading conditions.

For completeness, Fig. 6.5 shows corresponding results for the normalized effective flow stress $\widetilde{\sigma}_o/\sigma_o$ (σ_o is the flow stress of the matrix phase) as a function of the strain-rate sensitivity parameter m and the porosity f for in-plane shear loading, i.e., for a Lode angle $\theta = \pi/6$. Note that, while the SOM and the LAM depend on all the three invariants of the macroscopic stress tensor, the VAR method depends only on the first two invariants, i.e., on the mean $\overline{\Sigma}_m$ and the equivalent $\overline{\Sigma}_{eq}$ macroscopic stress tensor, and thus is independent of the Lode angle θ. By comparing the corresponding results for axisymmetric loading, presented in Fig. 6.4 with the estimates for in-plane shear in Fig. 6.5, we observe that, for isochoric loadings, both the SOM and the LAM estimates depend only slightly on θ and hence the observations made in the previous figure for $\theta = 0$ apply also in this case of $\theta = \pi/6$.

Fig. 6.6 presents results for the average equivalent strain-rate in the void $\overline{D}^{(2)}_{eq}$ normalized by the macroscopic equivalent strain-rate $\overline{D}_{eq}$ as a function of the strain-rate sensitivity parameter m (part (a)) and the porosity f (part (b)) for a Lode angle $\theta = 0$ (axisymmetric shear loading). In particular, in Fig. 6.6a, we observe that $\overline{D}^{(2)}_{eq}/\overline{D}_{eq}$ is not a strong function of the m for the given porosity $f = 25\%$. The corresponding SOM improves on the VAR by being in good agreement with the LAM estimates for the entire range of the nonlinearities. In turn, the VAR estimate is found to be independent of the nonlinearity m and thus underestimate the average strain-rate in the pores.

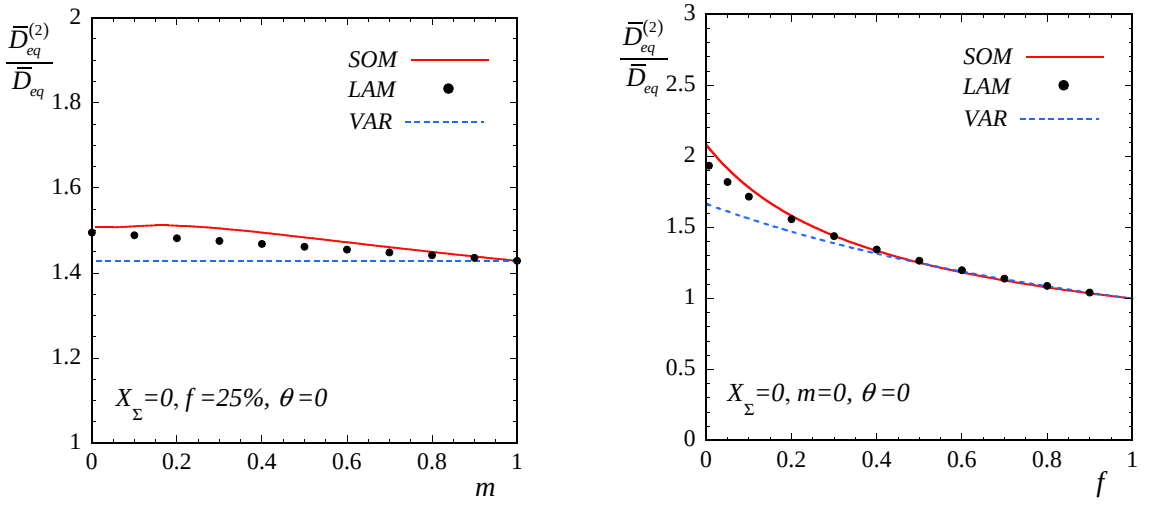

(a) (b)

Figure 6.6: Estimates and exact results for transversely, isotropic porous materials subjected to isochoric axisymmetric loadings ($X_\Sigma = 0$ and $\theta = 0$). The average equivalent strain-rate in the void $\overline{D}^{(2)}_{eq}$ normalized by the macroscopic equivalent strain-rate $\overline{D}_{eq}$ is shown, (a) as a function of the strain-rate sensitivity parameter m for porosity ($f = 25\%$), and (b) as a function of the porosity f in the case of an ideally-plastic matrix ($m = 0$).

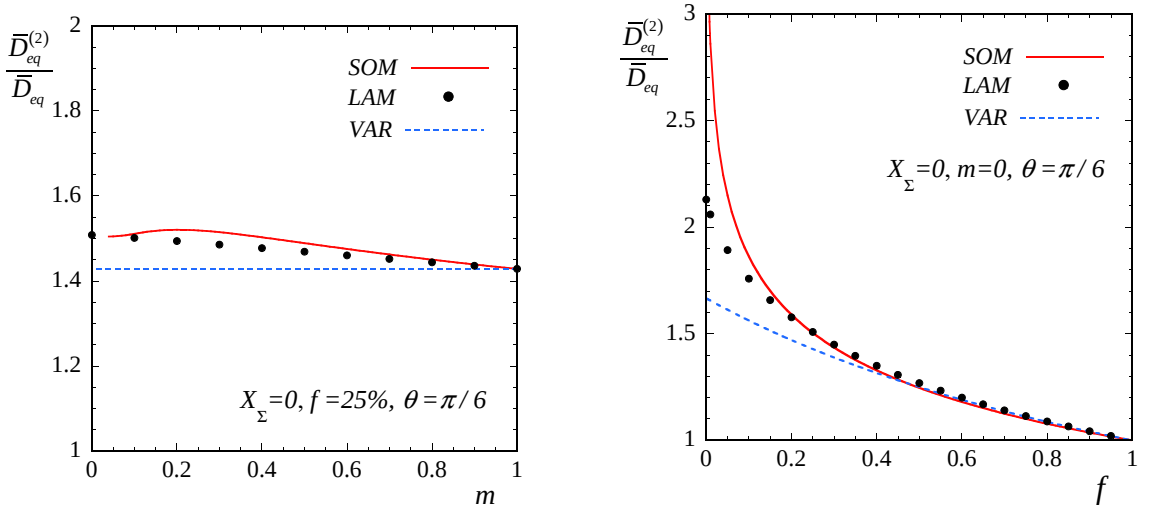

(a) (b)

Figure 6.7: Estimates and exact results for transversely, isotropic porous materials subjected to isochoric in-plane shear loadings ($X_\Sigma = 0$ and $\theta = \pi/6$). The average equivalent strain-rate in the void $\overline{D}^{(2)}_{eq}$ normalized by the macroscopic equivalent strain-rate $\overline{D}_{eq}$ is shown, (a) as a function of the strain-rate sensitivity parameter m for porosity ($f = 25\%$), and (b) as a function of the porosity f in the case of an ideally-plastic matrix ($m = 0$).

Looking now at Fig. 6.6b, it is evident that the SOM is in much better agreement with the LAM than the corresponding VAR, particularly for low and moderate porosities ($f \lesssim 0.2$). It is further remarked that the maximum difference between the SOM-LAM estimates and the VAR predictions

is observed for $m = 0$.

Fig. 6.7 presents corresponding results for the normalized average equivalent strain-rate in the void $\overline{D}^{(2)}_{eq}/\overline{D}_{eq}$ as a function of the strain-rate sensitivity parameter m (part (a)) and the porosity f (part (b)) for a Lode angle $\theta = \pi/6$ (in-plane shear loading). More specifically, in part (a), the SOM still remains in good agreement with the LAM estimates for the entire range of nonlinearities m, in contrast with the VAR estimate, which shows no dependence on the nonlinearity. Note that the VAR estimates do not depend on the Lode angle θ and hence they are identical to those presented in Fig. 6.6. On the other hand, Fig. 6.7b shows corresponding results for $\overline{D}^{(2)}_{eq}/\overline{D}_{eq}$ as a function of the porosity f for an ideally-plastic matrix. Here, it is interesting to observe that the SOM estimate is found to increase significantly at sufficiently small porosities, whereas the LAM estimates deliver a lower value for dilute concentrations. In this context, the VAR is found to underestimate significantly the corresponding estimate for $\overline{D}^{(2)}_{eq}/\overline{D}_{eq}$ when compared with the SOM and the LAM method. Note that the dependance of the SOM and the LAM methods on the third invariant of the macroscopic stress tensor $\overline{\boldsymbol{\sigma}}$, or equivalently on the Lode angle θ is more evident in the plots for the $\overline{D}^{(2)}_{eq}/\overline{D}_{eq}$.

In summary, the SOM method is found to improve on the earlier VAR method by being in much better agreement with the LAM estimates for the determination of the effective behavior of isotropic porous materials subjected to isochoric loading conditions. Moreover, the SOM and the LAM estimates for the normalized effective flow stress $\widetilde{\sigma}_o/\sigma_o$ of the porous material depend on all three invariants of the macroscopic stress tensor $\overline{\boldsymbol{\sigma}}$, although only slightly on the third invariant, denoted here with the Lode angle θ. In contrast, the VAR predictions depend only on the first two invariants, i.e., on the mean $\overline{\Sigma}_m$ and equivalent $\overline{\Sigma}_{eq}$ macroscopic stress. In this connection, it is interesting to remark that the corresponding SOM estimates for the average strain-rate in the void exhibit a much stronger dependence on the Lode angle, particularly at dilute concentrations, whereas the corresponding LAM estimates depend slightly on θ. In the next section, we will examine the behavior of isotropic porous materials under general loading conditions.

6.4 Isotropic porous media under general loading conditions

This section presents results on the effective behavior and the macroscopic strain-rate fields of isotropic, power-law, porous materials, delivered by the second-order method (SOM), when the choice (2.202) for the reference stress tensor is made. The predictions of the model proposed in this work are compared with corresponding results generated by high-rank sequential laminates (LAM) described in section 3.4. For completeness, the SOM estimates are also compared with the earlier variational bound (Ponte Castañeda, 1991) (VAR), the most recent Leblond-Perrin-Suquet (LPS) model (Leblond et al., 1994; Flandi and Leblond, 2005), which reduces to the model of Gologanu et. al. (1993) in the ideally-plastic limit, and the Gurson model (GUR) (1977) (for ideally-plastic media). This comparison is particularly pertinent in view of the fact that it has been recently shown (Idiart, 2007) that power-law, porous, sequential laminates with isotropic microstructures reproduce exactly the hydrostatic behavior of the composite-sphere assemblage, as described by expressions (2.196).

6.4.1 The gauge function for isotropic porous media

Before proceeding to the discussion of the results, it is necessary to recall the gauge function in the three-dimensional isotropic case. The definition of the gauge function is given for a general microstructure in (2.31). For isotropic porous media, the corresponding effective stress potential $\widetilde{U}$ depends only on the three principal values of the stress tensor $\overline{\boldsymbol{\sigma}}$ and the representation of the gauge surface lies in the three-dimensional space defined by the three principal directions of $\overline{\boldsymbol{\sigma}}$. Note that in the more general anisotropic case, the effective stress potential of the porous medium depends on all of the six components of the stress tensor $\overline{\boldsymbol{\sigma}}$, and this case will be discussed later. Thus, from (2.31), the gauge function is given by

$$\widetilde{\Phi}_n(\overline{\boldsymbol{\Sigma}};\, f) = \Gamma_n(\overline{\boldsymbol{\Sigma}};\, f) - 1, \tag{6.28}$$

where Γ_n is the gauge factor defined in (2.28), and is given by (2.151) for the "variational" method and (2.184) for the "second-order" method, whereas $\overline{\boldsymbol{\Sigma}}$ is an appropriately normalized stress tensor that is homogeneous of degree zero in $\overline{\boldsymbol{\sigma}}$. Thus, the gauge function is a positively homogeneous function of degree zero in the macroscopic stress $\overline{\boldsymbol{\sigma}}$, and is such that $\widetilde{\Phi}_n = 0$ defines the corresponding gauge surface defined by (2.29).

Using standard definitions for the stress measures, the normalized macroscopic stress tensor $\overline{\boldsymbol{\Sigma}}$ is written relative to its principal axes as

$$\overline{\boldsymbol{\Sigma}} = \overline{\Sigma}_m\, \boldsymbol{I} + \overline{\Sigma}_{eq}\, \overline{\boldsymbol{S}} = \mathrm{diag}\{\overline{\Sigma}_1, \overline{\Sigma}_2, \overline{\Sigma}_3\}. \tag{6.29}$$

The stress quantities $\overline{\Sigma}_m = \overline{\Sigma}_{ii}/3$ and $\overline{\Sigma}_{eq}$ are the normalized macroscopic mean and von Mises equivalent stress, respectively, $\boldsymbol{I}$ is the identity tensor, $\overline{\boldsymbol{S}} = \overline{\boldsymbol{\Sigma}}^{\,\prime}/\overline{\Sigma}_{eq}$ is a normalized stress tensor (see also relation (2.166)) with $\overline{\boldsymbol{\Sigma}}^{\,\prime}$ denoting the stress deviator, while $\overline{\Sigma}_i$ with $i = 1, 2, 3$ denote the three principal values of the normalized macroscopic stress tensor $\overline{\boldsymbol{\Sigma}}$. Making use of the previous notation, it is pertinent to define the following stress invariants

$$X_\Sigma = \frac{\overline{\Sigma}_m}{\overline{\Sigma}_{eq}}, \quad \cos(3\theta) = \frac{27}{2}\det(\overline{\boldsymbol{S}}). \tag{6.30}$$

The first is the stress triaxiality, and the second is the Lode angle (see also Kachanov, 1971) in stress space, which is related to the third invariant of the macroscopic stress tensor. The values $\theta = N\pi/3$ and $\theta = (2\,N + 1)\pi/6$, with N being a positive integer, correspond to axisymmetric and simple shear loading conditions, respectively. Relation $(6.30)_2$ may then be inverted so that, relative to its principal axes, $\overline{\boldsymbol{S}}$ is represented in terms of the Lode angle θ through

$$\overline{\boldsymbol{S}} = \frac{2}{3}\,\mathrm{diag}\left\{-\cos\left(\theta + \frac{\pi}{3}\right), -\cos\left(\theta - \frac{\pi}{3}\right), \cos\left(\theta\right)\right\}. \tag{6.31}$$

Thus, the applied normalized stress tensor $\overline{\boldsymbol{\Sigma}}$ is defined in terms of the three stress invariants, $\overline{\Sigma}_m$, $\overline{\Sigma}_{eq}$ and θ. Overall isotropy of the material implies then that Φ_n in relation (6.28) can be expediently written as

$$\widetilde{\Phi}_n(\overline{\boldsymbol{\Sigma}}) = \phi_n(\overline{\Sigma}_1, \overline{\Sigma}_2, \overline{\Sigma}_3) = \widehat{\phi}_n(\overline{\Sigma}_m, \overline{\Sigma}_{eq}, \theta), \tag{6.32}$$

where ϕ_n is a symmetric function of its arguments. At this point, it is also important to mention that as a consequence of definition (2.23) for the matrix phase, the overall response of the porous material is insensitive to the sign of $\overline{\boldsymbol{\Sigma}}$. This condition may be expressed as $\widetilde{\Phi}_n(\overline{\boldsymbol{\Sigma}}) = \widetilde{\Phi}_n(-\overline{\boldsymbol{\Sigma}})$.

Based now on definition (6.32), it is convenient to define two cross-sections of the gauge surface in order to study in detail the effective response of the porous material. One cross-section of the gauge surface may be defined by considering $\theta = const.$ This cross-section lies on a plane which is described by the Cartesian coordinates $\overline{\Sigma}_{eq}$ and $\overline{\Sigma}_m$, which is also known as the meridional plane. In turn, an alternative cross-section of the gauge surface may be considered on a plane defined by a constant hydrostatic pressure, i.e. $\overline{\Sigma}_m = const.$ This projection is equivalent to the standard deviatoric $\Pi-$plane (or else octahedral plane) in the theory of plasticity. The polar coordinates on this plane are $r = \sqrt{2/3}\,\overline{\Sigma}_{eq}$ and the Lode angle θ, respectively. For convenience, in-plane Cartesian coordinates may also be defined (Lubliner, (1990)) by using definitions (6.29) and (6.31), such that

$$x = \frac{2\overline{\Sigma}_3 - \overline{\Sigma}_1 - \overline{\Sigma}_2}{\sqrt{6}} = \sqrt{\frac{2}{3}}\overline{\Sigma}_{eq}\cos(\theta) \tag{6.33}$$

and

$$y = \frac{\overline{\Sigma}_1 - \overline{\Sigma}_2}{\sqrt{2}} = \sqrt{\frac{2}{3}}\overline{\Sigma}_{eq}\sin(\theta). \tag{6.34}$$

On the other hand, the macroscopic strain-rate and strain-rate triaxiality measures recalled here to be

$$\overline{\boldsymbol{E}} = \frac{\overline{\boldsymbol{D}}}{\dot{\varepsilon}_o\ (\Gamma_n(\overline{\boldsymbol{\sigma}};f)/\sigma_o)^n} = \frac{\partial\Gamma_n(\overline{\boldsymbol{\sigma}};f)}{\partial\overline{\boldsymbol{\sigma}}}, \quad X_E = \frac{\overline{E}_m}{\overline{E}_{eq}}, \tag{6.35}$$

where the normalized, mean strain-rate is defined as, $\overline{E}_m = \overline{E}_{ii}/3$, whereas $\overline{E}_{eq}$ denotes the von Mises equivalent part of the normalized strain-rate, defined in terms of the deviatoric strain-rate tensor $\boldsymbol{E}'$ as $\overline{E}_{eq} = \sqrt{\frac{2}{3}\,\overline{\boldsymbol{E}}'\cdot\overline{\boldsymbol{E}}'}$.

In summary, the previous definitions allow us to study in an efficient and complete manner the effective response of isotropic porous media subjected to general loading conditions.

6.4.2 Gauge surfaces for isotropic porous media

Before proceeding to the discussion of the results, it is useful to introduce first the material and loading parameters used in the plots that follow. The present study is focused on high nonlinearities such as $m = 0.1$ and $m = 0$ (i.e., ideally-plastic materials) and small to moderate porosities, $f = 1, 5, 10\%$. Results for porosity levels below 1% — relevant to ductile fracture — have not been included in the present section due to difficulties encountered in the numerical computation of the *LAM* values. In contrast, it is emphasized that *SOM* estimates have been obtained for small and dilute porosities and have already been reported in the section 6.2. It is noted, however, that the conclusions drawn below are expected to remain valid at those porosity levels.

As already discussed in the previous section, the *SOM* and the *LAM* models depend on all the three invariants of the macroscopic stress tensor (i.e., on $\overline{\Sigma}_m$, $\overline{\Sigma}_{eq}$ and θ) introduced in relations (6.30) and (6.32). For completeness, gauge curves are shown for three representative values of the Lode angle, $\theta = 0,\ \pi/4,\ \pi/2$. The value $\theta = 0$ is associated with an axisymmetric shear loading. In

turn, the value $\theta = \pi/2$ denotes a simple shear loading condition, whereas $\theta = \pi/4$ corresponds to a combination of axisymmetric and simple shear loading. It is emphasized that the rest of the models (VAR, LPS and GUR) depend only on the first two invariants, i.e., on $\overline{\Sigma}_m$ and $\overline{\Sigma}_{eq}$.

Fig. 6.8 shows effective gauge curves in the $\overline{\Sigma}_m - \overline{\Sigma}_{eq}$ plane (or meridional plane) for a fixed nonlinearity $m = 0.1$. In Fig. 6.8a the various models are compared for axisymmetric loadings ($\theta = 0$) and a typical porosity $f = 5\%$. The main result in the context of this figure is that the SOM estimates are in very good agreement with the LAM predictions for the entire range of the stress triaxialities ($X_\Sigma \in (-\infty, \infty)$), while both models recover the exact effective response of a hollow shell subjected to pure hydrostatic loading, described by relation (2.195) and (2.196). The fact that the LAM results should agree exactly with the hydrostatic behavior of CSAs in the limit of infinite rank has been shown rigorously in (Idiart, 2007). Furthermore, the SOM improves "significantly" on the earlier VAR estimate, which in spite of being in good agreement with the LAM results at low triaxialities, it is found to be too stiff at high triaxialities. Indeed, for the given porosity $f = 5\%$, the VAR method predicts that the effective response of the porous material is almost 50% stiffer than the exact shell result, when subjected to pure hydrostatic loading. It can be easily verified by comparing relations (2.196) and (2.197), that the VAR estimate deviates significantly from the analytical shell result for small porosities. On the other hand, the LPS model, even though exact in the hydrostatic loading, it deviates from the LAM results for moderate to high triaxialities (i.e., approximately $1 \leq X_\Sigma \leq 10$). In contrast, the LPS model coincides — by construction — with the VAR bound for isochoric loadings ($X_\Sigma = 0$).

Figs. 6.8b, 6.8c, 6.8d, show gauge curves for three different Lode angles, $\theta = 0, \pi/4, \pi/2$, and porosities, $f = 1, 5, 10\%$. With these graphs, we verify the very good correlation between the SOM and the LAM estimates for the whole range of stress triaxialities, porosities and Lode angles shown here. Furthermore, it is interesting to note that for $\theta = 0$ and $\theta = \pi/4$, the predicted gauge curves of both the SOM and the LAM are found to be slightly "asymmetric" about the $\overline{\Sigma}_{eq}$-axis, in contrast with the case of $\theta = \pi/2$, where the SOM and the LAM curves are completely symmetric. This "asymmetry" is a direct consequence of the coupling between the three invariants (i.e., $\overline{\Sigma}_m$, $\overline{\Sigma}_{eq}$, θ) in the expression for the gauge function introduced in relation (6.32). While the SOM and the LAM curves exhibit this particularly interesting behavior, the VAR and the LPS model show a lack of this asymmetric effect about the $\overline{\Sigma}_{eq}$-axis. This is a direct consequence of the fact that the VAR and the LPS models involve no dependence on the third invariant of the macroscopic stress tensor, and thus they cannot capture this effect, which, as will be seen later, can become non negligible at high stress triaxialities.

More specifically, in the case of axisymmetric loading ($\theta = 0$) (see Fig. 6.8b), the SOM and the LAM estimates are found to be slightly stiffer in the negative pressure regime ($\overline{\Sigma}_m < 0$), while the converse is observed when $\theta = \pi/4$ (see Fig. 6.8c), i.e., the porous material is stiffer in the positive pressure regime ($\overline{\Sigma}_m > 0$). On the other hand, for $\theta = \pi/2$ (see Fig. 6.8d), the corresponding gauge curves are completely symmetric about the $\overline{\Sigma}_{eq}$-axis. This can be explained by noting that in the case of $\theta = \pi/2$, the term $\det(\overline{\boldsymbol{\Sigma}}'/\overline{\Sigma}_{eq}) = 0$, which has the implication that the gauge function becomes an even function of the mean macroscopic stress, and therefore is independent of the sign of $\overline{\Sigma}_m$. In

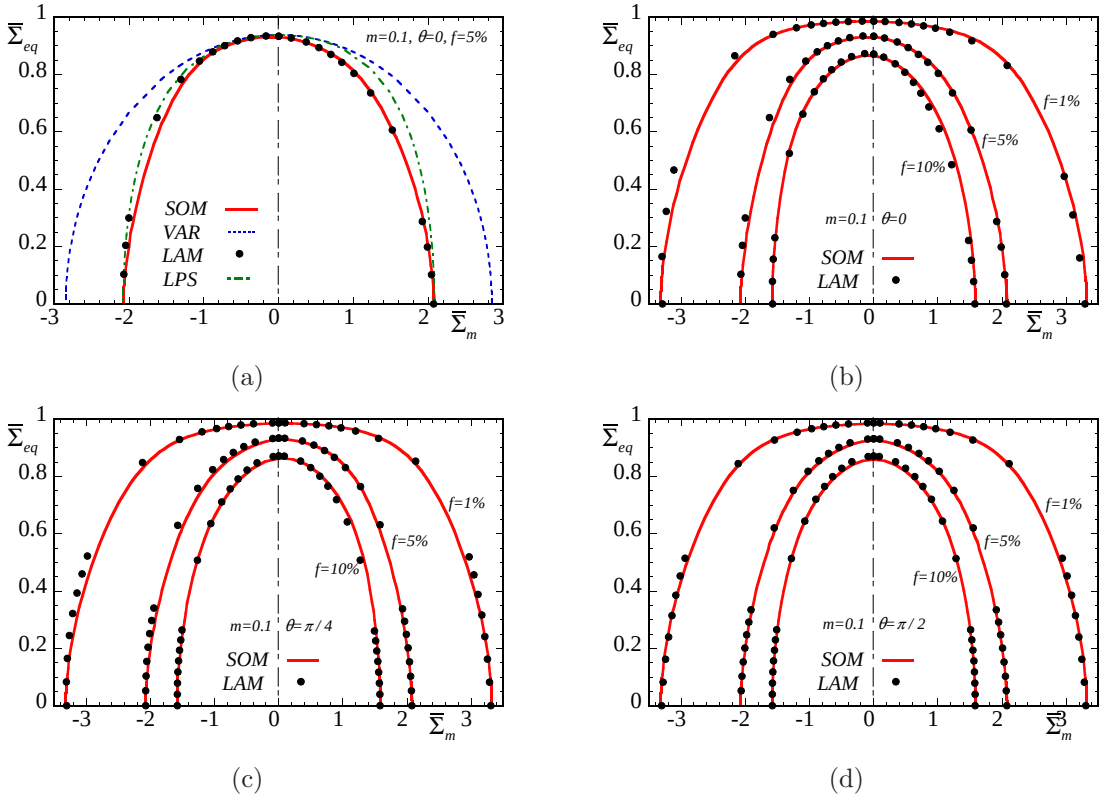

Figure 6.8: Gauge surfaces (on the $\overline{\Sigma}_m - \overline{\Sigma}_{eq}$ plane) for isotropic, porous materials as predicted by the SOM, the high-rank sequential laminates LAM, the VAR and the recently updated Leblond-Perrin-Suquet (1994) (LPS) model by Flandi and Leblond (2005) as a function of the porosity and the Lode angle θ (θ is directly related to the third invariant of the macroscopic stress tensor $\overline{\mathbf{\Sigma}}$). The strain-rate sensitivity of the matrix phase is $m = 0.1$. (a) shows gauge surfaces as predicted by the aforementioned models for a porosity $f = 5\%$ and Lode angle $\theta = 0$ (axisymmetric loading). The rest of the graphs show gauge surfaces for several porosities $f = 1, 5, 10\%$ and (b) $\theta = 0$, (c) $\theta = \pi/4$ (combination of in-plane shear and axisymmetric loading), and (d) $\theta = \pi/2$ (in-plane shear–pressure loading) as predicted by the SOM and the exact LAM results.

contrast, for $\theta = 0$ and $\theta = \pi/4$, the term $\det(\overline{\mathbf{\Sigma}}'/\overline{\Sigma}_{eq})$ is not zero and hence the gauge function is not an even function of $\overline{\Sigma}_m$. In addition, it is important to remark that the observed asymmetry of the SOM and the LAM gauge curves about the $\overline{\Sigma}_{eq}$-axis is more pronounced at moderate porosities ($f = 10\%$) than small ones ($f = 1\%$), as can be seen in Figs. 6.8b, 6.8c, 6.8d.

The special case of porous materials with an ideally-plastic matrix phase is studied next. Specifically, gauge (or yield) surfaces ($m = 0$) are shown in Fig. 6.9 for a fixed porosity $f = 5\%$ and $\theta = 0, \pi/2$. Here, the GUR model is also included, whereas LAM estimates are not available for this case due to numerical difficulties. The main observation in the context of this figure is that even though all but the VAR estimate recover the analytical hydrostatic point, the SOM exhibits a softer behavior than the LPS and the GUR models at moderate and high stress triaxialities. In addition, similar to Fig. 6.8, an interesting effect of the presence of the third invariant is the asymmetry of the gauge curve predicted by the SOM about the $\overline{\Sigma}_{eq}$-axis, in the case of $\theta = 0$, as shown in Fig. 6.9a. In this case, the SOM estimates are found to be slightly stiffer in the negative pressure

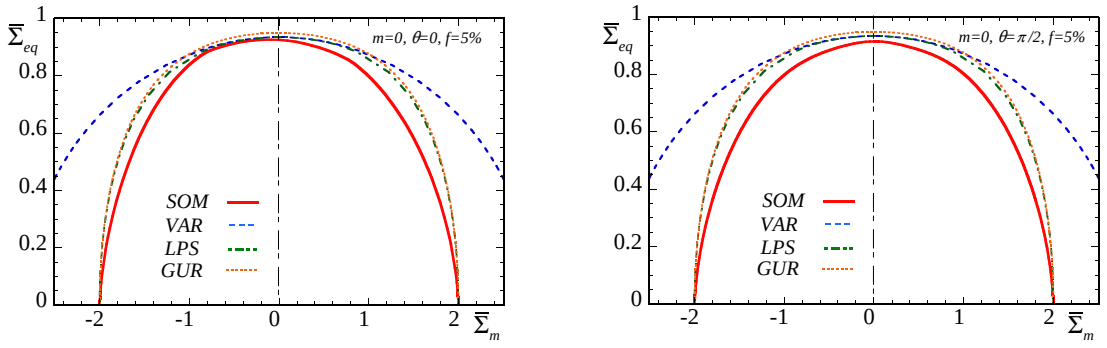

(a) (b)

Figure 6.9: Gauge surfaces (on the $\overline{\Sigma}_m - \overline{\Sigma}_{eq}$ plane) for isotropic, porous materials as predicted by the SOM, the VAR, the Gurson model (GUR) and the recently updated Leblond-Perrin-Suquet (1994) (LPS) model by Flandi and Leblond (2005) as a function of the porosity and the Lode angle θ(θ is directly related to the third invariant of the macroscopic stress tensor $\overline{\boldsymbol{\Sigma}}$). The matrix phase exhibits an ideally-plastic behavior $m = 0$. The graphs show gauge surfaces for porosity $f = 5\%$ and (a) $\theta = 0$, (b) $\theta = \pi/2$ as predicted by the aforementioned models.

regime ($\overline{\Sigma}_m < 0$) than in the positive pressure regime ($\overline{\Sigma}_m > 0$). On the contrary, for $\theta = \pi/2$, the corresponding gauge curve is symmetric about the $\overline{\Sigma}_{eq}$-axis, since in this case $\det(\overline{\boldsymbol{\Sigma}}'/\overline{\Sigma}_{eq}) = 0$. Furthermore, it is emphasized that the GUR model violates, as already anticipated, the VAR bound at low triaxialities. To amend this drawback of the GUR model at low triaxialities, the LPS model was constructed such that it recovers the VAR bound for isochoric loadings (i.e., $X_\Sigma = 0$), while it lies very close to the GUR model for moderate and high triaxialities.

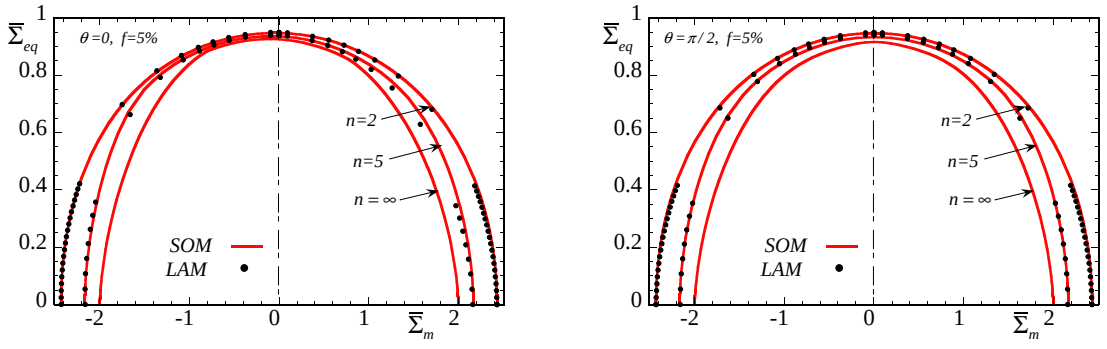

(a) (b)

Figure 6.10: Gauge surfaces (on the $\overline{\Sigma}_m - \overline{\Sigma}_{eq}$ plane) for isotropic, porous materials as predicted by the SOM and the high-rank sequential laminates LAM as a function of the nonlinear exponent and the Lode angle θ (θ is directly related to the third invariant of the macroscopic stress tensor $\overline{\boldsymbol{\Sigma}}$). The porosity takes the typical value $f = 5\%$. In particular, this figure shows gauge surfaces as predicted by the aforementioned models for nonlinear exponents $n = 2, 5, \infty\%$ and Lode angle (a) $\theta = 0$ and (b) $\theta = \pi/2$ (in-plane shear–pressure loading).

For completeness, Fig. 6.10 shows SOM and LAM gauge surfaces for nonlinear exponents $n = 2, 5, \infty$ and a typical porosity $f = 5\%$. Part (a) of this figure corresponds to Lode angle $\theta = 0$ and

part (b) to $\theta = \pi/2$. The main observation in the context of this figure is that both SOM and LAM gauge surfaces are functions of the nonlinear exponent, as already expected, while the dependence on n becomes somewhat stronger at higher stress triaxialities. In addition, it is observed that the effect of the third invariant of the macroscopic stress tensor on the effective response of the porous medium, indicated by the slight asymmetry of the gauge curves about the $\overline{\Sigma}_{eq} - axis$, diminishes at low nonlinearities, i.e., $n = 2$. This is expected since in the purely linear case ($n = 1$) there is no effect of the Lode angle.

In summary, the previous analysis made in the context of Fig. 6.8, Fig. 6.9 and Fig. 6.10 shows that the effective response of the porous material as predicted by the SOM and the LAM models exhibits somewhat softer behavior when compared with the estimates obtained by the LPS and the GUR models. In addition, the SOM and the LAM estimates depend on the third invariant of the macroscopic stress tensor $\overline{\boldsymbol{\Sigma}}$, in contrast with the rest of the models (VAR, LPS and GUR) that depend only on the first two invariants of $\overline{\boldsymbol{\Sigma}}$. Similar observations have been made by Shtern et al. (2002a,b) in the context of unit-cell, porous media, who introduced the effect of the third invariant of the macroscopic stress tensor in a somewhat ad-hoc manner.

For a better understanding of the effect of the third invariant on the effective response of the porous material, we need to study an alternative cross-section of the gauge surface, as shown in Fig. 6.11 for a fixed porosity $f = 10\%$ and strain-rate sensitivity parameter $m = 0.1$. This cross-section lies on the deviatoric or $\Pi-$plane which is defined (see subsection 6.4.1) by considering constant mean stresses $\overline{\Sigma}_m = 0$ and $\overline{\Sigma}_m = 0.99\overline{\Sigma}_m^H$ (with $\overline{\Sigma}_m^H$ denoting the mean stress delivered by the analytical shell result for a given porosity and nonlinearity, given in Appendix V of Chapter 2). The origin of these two graphs corresponds to zero deviatoric macroscopic stress $\overline{\boldsymbol{\Sigma}}'$, while $\overline{\Sigma}_1'$, $\overline{\Sigma}_2'$ and $\overline{\Sigma}_3'$ are the three principal values of $\overline{\boldsymbol{\Sigma}}'$.

Fig. 6.11a thus presents the deviatoric cross-sections of the gauge surface obtained by the SOM, the LAM and the LPS models for $\overline{\Sigma}_m = 0$. It is recalled that for isochoric loadings, the LPS model is identical to the VAR bound. In this figure, all the methods give very similar predictions for all θ. However, in order to understand further these results, it is useful to recall that overall isotropy of the porous material together with the fact that the corresponding effective gauge function in relation (6.32) is insensitive to the sign of $\overline{\boldsymbol{\Sigma}}$ (see subsection 6.4.1) yields the continuous and the dotted symmetry lines on the Π-plane (see Fig. 6.11a). This implies that the whole gauge curve may be constructed by considering stress states in any one of the twelve ($\pi/6$) segments defined by the continuous and dotted lines, which can be easily verified for all the models shown in Fig. 6.11a. However, because of the fact that the SOM and the LAM estimates depend slightly on θ in this case of isochoric loadings, the corresponding gauge curves do not form a perfect circular arc at the interval $0 < \theta < \pi/6$. On the other hand, the LPS (and the VAR) model, which is independent of θ, does form a circle with radius $r = \sqrt{2/3}\,\overline{\Sigma}_{eq}$.

Considering now the second set of gauge curves in Fig. 6.11b, it is observed that the shape of the curves delivered by the SOM and the LAM models no longer conform to the above-mentioned $\pi/6$-symmetry. This is because in this case the origin corresponds to zero deviatoric stresses, while the total stress at this point is $\overline{\boldsymbol{\Sigma}} = \overline{\Sigma}_m \boldsymbol{I}$ with $\boldsymbol{I}$ denoting the identity tensor. For this reason, the

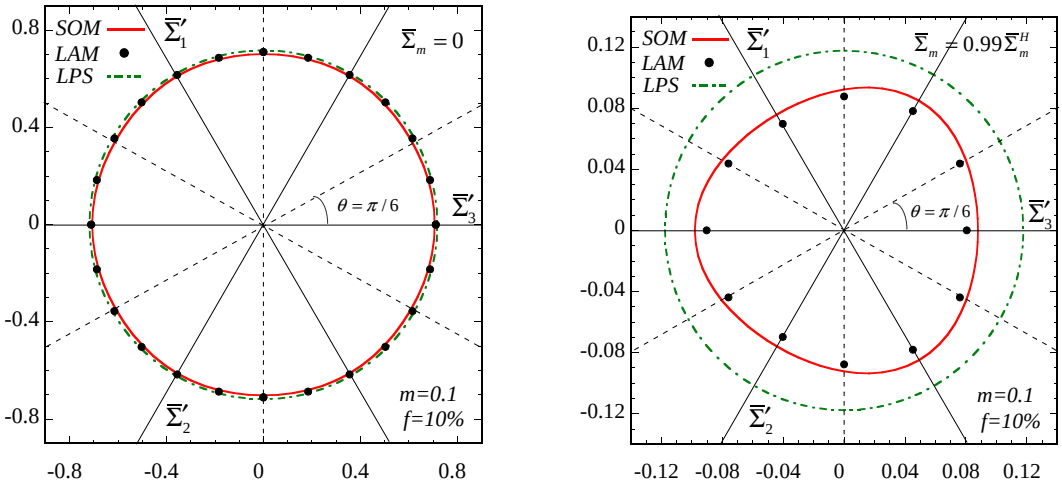

Figure 6.11: Cross-sections of the gauge surface on the deviatoric plane (or $\Pi-$plane) for $f = 10\%$ and matrix phase with exponent $m = 0.1$. The cross-sections are defined by: (a) a constant pressure $\overline{\Sigma}_m = 0$, and (b) a constant pressure $\overline{\Sigma}_m = 0.99\overline{\Sigma}^H_m$ (with $\overline{\Sigma}^H_m$ denoting the mean stress delivered by the analytical hollow shell result subjected to purely hydrostatic loading).

dotted lines no longer form axes of symmetry, since the corresponding gauge function in relation (6.32) is insensitive to the sign of $\overline{\boldsymbol{\Sigma}}$ and not the sign of the deviatoric stress $\overline{\boldsymbol{\Sigma}}'$. On the other hand, isotropy of the porous material still requires that the continuous lines form axes of symmetry. This last observation implies that the shape of the gauge curve is determined by each of the "six" $(\pi/3)$ segments formed by the continuous lines. Evidently, all the gauge curves shown in Fig. 6.11b comply to this requirement. However, as a result of the dependence on the third invariant, the shape of the *SOM* and *LAM* cross-sections is substantially different from that of the *LPS* model which is a perfect circle. The importance of this difference in shape stems from the fact that the normal to the gauge surface prescribes the macroscopic direction of flow.

Before proceeding to the discussion of the corresponding macroscopic strain-rates, it is worth mentioning that McElwain et al. (2006) have recently obtained numerical estimates (with the finite element method) for the effective behavior of *periodic*, porous media with an ideally-plastic matrix phase for high porosities ($f > 20\%$). In particular, the resulting gauge curves have — in qualitative terms — the same shape as the one obtained by the *SOM* and the *LAM* in Fig. 6.11b, while they also remark the inaccuracy of the models that make use of only the first two invariants of the macroscopic stress tensor.

6.4.3 Macroscopic strain-rates

For completeness, estimates for the macroscopic equivalent and mean strain-rates, $\overline{E}_{eq}$ and $\overline{E}_m$, respectively, are presented in this subsection. Thus, Fig 6.12 shows estimates for the macroscopic equivalent strain-rate $\overline{E}_{eq}$ as a function of the porosity and the stress triaxiality X_Σ, for a fixed value of $\theta = 0$ (i.e., axisymmetric loads) and strain-rate sensitivity parameter $m = 0.1$. In particular,

Fig 6.12a compares the macroscopic equivalent strain-rate estimates obtained by the various models for a porosity, $f = 5\%$. In this case, all the methods are shown to be in good agreement at low stress triaxialities, while they are all somewhat different from the LAM results with increasing stress triaxiality. The SOM estimates are in better agreement with the LAM results in the positive triaxiality regime, whereas for negative triaxialities the LPS estimates lie closer to the LAM results, for this particular choice of the porosity and nonlinearity. In turn, the VAR estimates differ significantly from the LAM results at moderate triaxialities. Note that, by definition, all the methods deliver zero equivalent strain-rate in the hydrostatic limit ($|X_\Sigma| \to \infty$). In turn, in Fig 6.12b, the SOM estimates are compared with the LAM estimates for two different porosities, $f = 1, 10\%$. In this figure, a clear trend is observed for both the SOM and the LAM curves at low stress triaxialities, where $\overline{E}_{eq}$ takes higher values at larger porosities, while no such pattern could be observed at higher triaxialities. Nonetheless, the SOM remains in good agreement with the LAM results for the whole range of triaxialities and porosities considered here.

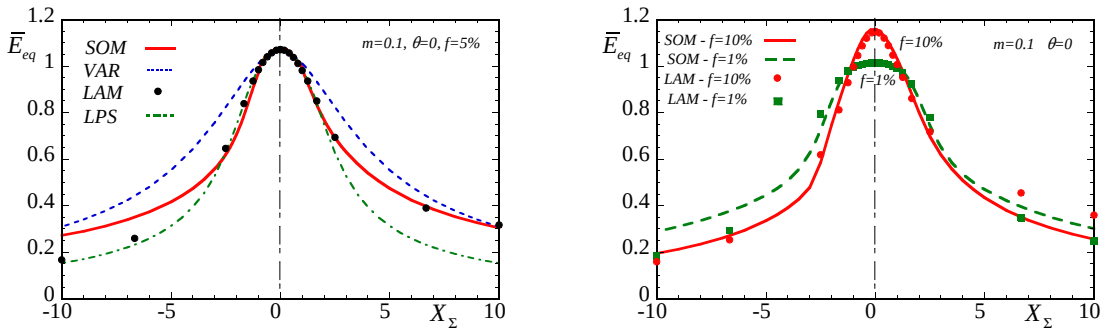

(a) (b)

Figure 6.12: Results for the suitably-normalized, equivalent macroscopic strain-rate $\overline{E}_{eq}$ as a function of the stress triaxiality X_Σ as determined by the SOM, the high-rank, sequential laminates (LAM), the VAR and the recently updated Leblond-Perrin-Suquet (1994) (LPS) model by Flandi and Leblond (2005). (a) compares the various models in the case of $f = 5\%$, Lode angle $\theta = 0$ and strain-rate sensitivity parameter $m = 0.1$, and (b) shows predictions by the SOM and the LAM for porosities $f = 1, 10\%$ and Lode angle $\theta = 0$.

Next, Fig. 6.13 shows estimates for the mean (hydrostatic) macroscopic strain-rate $\overline{E}_m$ as a function of the porosity and the stress triaxiality X_Σ, for a fixed value of $\theta = 0$ (i.e., axisymmetric loads) and strain-rate sensitivity parameter $m = 0.1$. The SOM and the LAM results are in very good agreement for the whole range of the stress triaxialities and porosities shown here. Particularly, in Fig 6.13a, the SOM is found to improve significantly on the earlier "variational" bound VAR, which severely underestimates the macroscopic mean strain-rate at high triaxialities. The LPS model is also in good agreement with the LAM results, although at moderate triaxialities it tends to be slightly stiffer than the SOM estimates. In addition, Fig. 6.13b shows that the SOM estimates are in excellent agreement with the LAM results for all the porosities considered.

Lastly, it should be emphasized from Figs. 6.12 and 6.13 that the equivalent part of the macroscopic strain-rate, $\overline{E}_{eq}$, is predominant over the corresponding hydrostatic part, $\overline{E}_m$, at low triaxialities, and

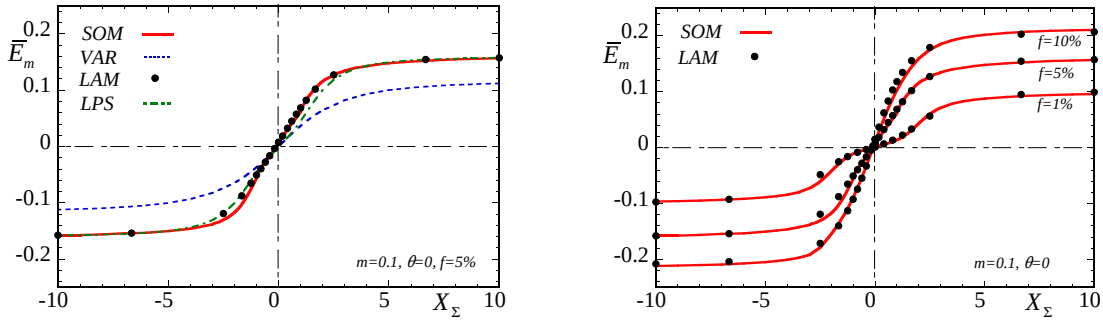

(a) (b)

Figure 6.13: Results for the suitably-normalized, mean macroscopic strain-rate $\overline{E}_m$ as a function of the stress triaxiality X_Σ as determined by the SOM, the high-rank, sequential laminates (LAM), the VAR and the recently updated Leblond-Perrin-Suquet (1994) (LPS) model by Flandi and Leblond (2005). (a) compares the various models in the case of $f = 5\%$, Lode angle $\theta = 0$ and strain-rate sensitivity parameter $m = 0.1$, and (b) shows predictions by the SOM and the LAM for porosities $f = 1, 5, 10\%$ and Lode angle $\theta = 0$.

therefore controls the effective response of the porous material in this regime. For the case of low triaxialities, the SOM is found to be in good agreement with the LAM estimates as discussed in the context of Fig. 6.12. In turn, the hydrostatic part of the macroscopic strain-rate, $\overline{E}_m$, dominates over the corresponding equivalent part, $\overline{E}_{eq}$, in the high-triaxiality regime, where the SOM is also found to be in excellent agreement with the LAM, while improving significantly on the earlier VAR estimates. These two observations together suggest that the SOM should be able to predict accurately the effective response of the porous material for the entire range of the stress triaxialities, porosities and nonlinearities.

6.5 Anisotropic porous media

The main objective of this section is to study the effective behavior of anisotropic porous materials in the most simplified way possible. In general, the behavior of such a material depends on all microstructural variables $s_a = \{f, w_1, w_2, \mathbf{n}^{(1)}, \mathbf{n}^{(2)}, \mathbf{n}^{(3)} = \mathbf{n}^{(1)} \times, \mathbf{n}^{(2)}\}$, where w_1 and w_2 are the two aspect ratios defining the shape of the ellipsoidal void, while the vectors $\mathbf{n}^{(i)}$ (with $i = 1, 2, 3$) denote the orientation of the principal axes of the voids. Furthermore, the effective behavior of an anisotropic porous material is a function of all six components of the macroscopic stress tensor $\overline{\boldsymbol{\sigma}}$. However, it would be to complicated to extract useful conclusions, if we considered the most general state of microstructure and loading conditions. For this reason, only a few configurations, albeit representative ones, will be considered in the sequel.

To begin with, it is useful to recall the general definition of the gauge factor and gauge function, introduced in relations (2.28) and (2.31), respectively, which are recalled here for completeness to be

$$\widetilde{U}(\overline{\boldsymbol{\sigma}};\, s_\alpha) = \frac{\dot{\varepsilon}_o\, \sigma_o}{n+1} \left(\frac{\Gamma_n(\overline{\boldsymbol{\sigma}};\, s_\alpha)}{\sigma_o} \right)^{n+1}, \tag{6.36}$$

and

$$\widetilde{\Phi}_n(\overline{\boldsymbol{\Sigma}};\, s_\alpha) = \Gamma_n(\overline{\boldsymbol{\Sigma}};\, s_\alpha) - 1, \tag{6.37}$$

such that $\widetilde{\Phi}_n = 0$ defines the gauge surface (see (2.29)), whereas $\overline{\boldsymbol{\Sigma}}$ is an appropriately normalized stress tensor (see (2.30)) that is homogeneous of degree zero in $\overline{\boldsymbol{\sigma}}$.

Next, consider that the principal directions of the macroscopic stress tensor $\overline{\boldsymbol{\sigma}}$ (or $\overline{\boldsymbol{\Sigma}}$) are aligned with a fixed Cartesian laboratory frame of reference defined by the three unit vectors $\mathbf{e}^{(i)}$ (with $i = 1, 2, 3$). Then, the normalized macroscopic stress tensor $\overline{\boldsymbol{\Sigma}}$ can be written in terms of its three principal values $\overline{\Sigma}_1$, $\overline{\Sigma}_2$, $\overline{\Sigma}_3$, or, equivalently, in terms of the principal values of the deviatoric stress tensor, i.e., $\overline{\Sigma}_1'$, $\overline{\Sigma}_2'$, $\overline{\Sigma}_3'$ and the mean stress $\overline{\Sigma}_m$, such that

$$\overline{\boldsymbol{\Sigma}} = \overline{\Sigma}_m \boldsymbol{I} + \overline{\Sigma}_1' \mathbf{e}^{(1)} \otimes \mathbf{e}^{(1)} + \overline{\Sigma}_2' \mathbf{e}^{(2)} \otimes \mathbf{e}^{(2)} + \overline{\Sigma}_3' \mathbf{e}^{(3)} \otimes \mathbf{e}^{(3)}, \tag{6.38}$$

with

$$\overline{\Sigma}_m = (\overline{\Sigma}_1 + \overline{\Sigma}_2 + \overline{\Sigma}_3)/3 \qquad \text{and} \qquad \overline{\Sigma}_1' + \overline{\Sigma}_2' + \overline{\Sigma}_3' = 0. \tag{6.39}$$

Based now on definition (6.37) and similar to the isotropic case discussed in the previous section, it is convenient to define two cross-sections of the gauge surface in order to study in detail the effective response of the anisotropic porous material. One cross-section of the gauge surface may be defined by considering that the direction of the deviatoric stress tensor $\overline{\boldsymbol{\Sigma}}'$ is fixed or, equivalently, that the ratio between two eigenvalues of $\overline{\boldsymbol{\Sigma}}'$ is constant (the third eigenvalue is then computed by (6.39)). This cross-section lies on a plane which is described by the Cartesian coordinates $\overline{\Sigma}_{eq}$ and $\overline{\Sigma}_m$, which is also known as the *meridional plane*.

In turn, an alternative cross-section of the gauge surface may be considered on a plane defined by a constant hydrostatic pressure, i.e. $\overline{\Sigma}_m = const$. This projection is equivalent to the standard deviatoric $\Pi-$plane (or else octahedral plane) in the theory of plasticity. In this case of anisotropic microstructures, the Lode angle θ (see relation (6.30)) can still be used, similar to the case of isotropic microstructures discussed in the previous section. In this connection, in-plane Cartesian coordinates may be defined (Lubliner, (1990)) by using definitions (6.29) and (6.31), such that

$$x = \frac{2\overline{\Sigma}_3 - \overline{\Sigma}_1 - \overline{\Sigma}_2}{\sqrt{6}} = \sqrt{\frac{3}{2}}\overline{\Sigma}_3' = \sqrt{\frac{2}{3}}\overline{\Sigma}_{eq}\cos(\theta), \tag{6.40}$$

and

$$y = \frac{\overline{\Sigma}_1 - \overline{\Sigma}_2}{\sqrt{2}} = \frac{\overline{\Sigma}_1' - \overline{\Sigma}_2'}{\sqrt{2}} = \sqrt{\frac{2}{3}}\overline{\Sigma}_{eq}\sin(\theta). \tag{6.41}$$

It is emphasized that the above representation in terms of the quantities $\overline{\Sigma}_m$, $\overline{\Sigma}_{eq}$ and θ is a direct consequence of the fact that we work in the space of principal stresses, and thus the complete stress tensor may be expressed in terms of the three principal stresses or, equivalently, in terms of the three quantities $\overline{\Sigma}_m$, $\overline{\Sigma}_{eq}$ and θ.

Next, we introduce the microstructural configurations to be studied in this work, which are shown schematically in Fig. 6.14. In the first case (a), we consider prolate spheroidal voids with aspect ratios $w_1 = w_2 = 5$, whose major (symmetry) axis is aligned with the $\mathbf{n}^{(3)}-$direction. The second configuration, in Fig. 6.14b considers oblate spheroidal voids with aspect ratios $w_1 = w_2 = 0.2$, whose minor (symmetry) axis is aligned with the $\mathbf{n}^{(3)}-$direction. As a third case (c), we consider a third microstructural configuration, which involves ellipsoidal voids with two different aspect ratios $w_1 = a_3/a_1 = 5$ and $w_2 = a_3/a_1 = 0.2$, whose major axis is aligned with the $\mathbf{n}^{(2)}$-direction and the

minor axis with $\mathbf{n}^{(1)}-$direction. This last case has been introduced to emphasize the importance of having a model that is capable of handling more general ellipsoidal microstructures.

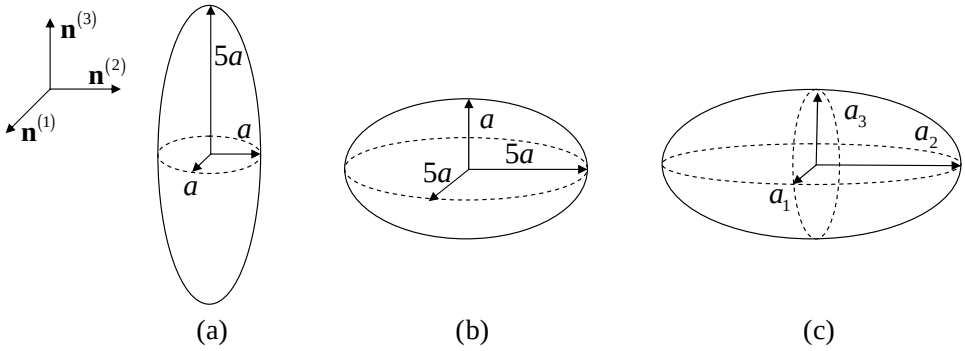

Figure 6.14: Void shapes in the frame of reference defined by the vectors $\mathbf{n}^{(i)}$ which define the orientation of the principal axes of the voids. Three configurations are considered: a) prolate voids with aspect ratios $w_1 = w_2 = 5$, b) oblate voids with aspect ratios $w_1 = w_2 = 0.2$ and c) ellipsoidal voids with aspect ratios $w_1 = 5$ and $w_2 = 0.2$.

Finally, it is essential to study the effect of the orientation of the three previous microstructural configurations with respect to the loading directions. For instance, if the principal directions of the ellipsoidal voids, i.e., $\mathbf{n}^{(i)}$, do not coincide with the principal loading directions $\mathbf{e}^{(i)}$, then the overall behavior of the composite is fully anisotropic, while the microstructure is also expected to spin during the deformation process.

In this regard, it is convenient to introduce, here, the standard notation used to describe the orientation of a vector in space in terms of the unit vectors $\mathbf{e}^{(i)}$ (with $i = 1, 2, 3$) denoting a fixed Cartesian frame of reference. Thus, let us consider an arbitrary unit vector $\mathbf{u}$ such that

$$\mathbf{u} = x_1\,\mathbf{e}^{(1)} + x_2\,\mathbf{e}^{(2)} + x_3\,\mathbf{e}^{(3)} \qquad \text{with} \qquad \sqrt{\mathbf{u}\cdot\mathbf{u}} = \sqrt{x_1^2 + x_2^2 + x_3^2} = 1. \tag{6.42}$$

Then, we consider twelve possible orientations of this vector $\mathbf{u}$ relative to the base vectors $\mathbf{e}^{(i)}$, which

Table 6.1: Orientation convention

Cases	x_1	x_2	x_3	Cases	x_1	x_2	x_3
$(1\,0\,0)$	1	0	0	$(1\,\bar{1}\,0)$	$1/\sqrt{2}$	$-1/\sqrt{2}$	0
$(0\,1\,0)$	0	1	0	$(0\,0\,\bar{1})$	0	0	-1
$(0\,0\,1)$	0	0	1	$(0\,\bar{1}\,0)$	0	-1	0
$(1\,1\,0)$	$1/\sqrt{2}$	$1/\sqrt{2}$	1	$(\bar{1}\,0\,1)$	$-1/\sqrt{2}$	0	$1/\sqrt{2}$
$(1\,0\,1)$	$1/\sqrt{2}$	0	$1/\sqrt{2}$	$(0\,1\,\bar{1})$	0	$1/\sqrt{2}$	$-1/\sqrt{2}$
$(0\,1\,1)$	0	$1/\sqrt{2}$	$1/\sqrt{2}$	$(0\,\bar{1}\,1)$	0	$-1/\sqrt{2}$	$1/\sqrt{2}$

are summarized in Table 6.1 employing the standard notation that has been widely used to describe the slip direction of single crystals. The above notation will be used to describe the orientation of the principal axes of the voids in the following paragraphs.

As already discussed in subsection 2.2.1, the orientation of the principal axes of the voids is completely defined by the unit vectors $\mathbf{n}^{(i)}$ (with $i = 1, 2, 3$), which can be written in terms of the unit vectors $\mathbf{e}^{(i)}$ (with $i = 1, 2, 3$) by using relation (2.17) such that

$$\mathbf{n}^{(i)} = \boldsymbol{R}_{\psi}\, \mathbf{e}^{(i)}, \quad \text{with} \quad \boldsymbol{R}_{\psi} = \boldsymbol{R}_{\psi_3}\, \boldsymbol{R}_{\psi_2}\, \boldsymbol{R}_{\psi_1}, \tag{6.43}$$

where $\boldsymbol{R}_{\psi}$ is a proper orthogonal matrix, defined in terms of three other proper orthogonal matrices given by

$$\begin{aligned}
\boldsymbol{R}_{\psi_1} &= \begin{pmatrix} 1 & 0 & 0 \\ 0 & \cos\psi_1 & \sin\psi_1 \\ 0 & -\sin\psi_1 & \cos\psi_1 \end{pmatrix}, \\
\boldsymbol{R}_{\psi_2} &= \begin{pmatrix} \cos\psi_2 & 0 & \sin\psi_2 \\ 0 & 1 & 0 \\ -\sin\psi_2 & 0 & \cos\psi_2 \end{pmatrix}, \\
\boldsymbol{R}_{\psi_3} &= \begin{pmatrix} \cos\psi_3 & \sin\psi_3 & 0 \\ -\sin\psi_3 & \cos\psi_3 & 0 \\ 0 & 0 & 1 \end{pmatrix},
\end{aligned} \tag{6.44}$$

where ψ_1, ψ_2 and ψ_3 are three Euler angles, which denote rotation of the principal axes of the ellipsoid about the $1-$, $2-$ and $3-$ axis, respectively. It is important to emphasize that the order of rotation in (6.43) matters. For instance, assume that initially $\mathbf{n}^{(3)}$ coincides with $\mathbf{e}^{(3)}$. Then, in order to rotate the vector $\mathbf{n}^{(3)}$ in the $(1\,\bar{1}\,0)$ direction, we need to use the values $\psi_1 = 0^o$ – $\psi_2 = 90^o$ – $\psi_3 = -45^o$ in expression (6.43). Hence, the above relations provide the tools to treat in a complete manner the orientation of the voids with respect to the fixed frame of reference defined by the unit vectors $\mathbf{e}^{(i)}$.

In the following paragraphs, we present gauge curves as predicted by the "second-order" (SOM), the "variational" (VAR) and the Flandi and Leblond (2005) (FL) methods for the various loading conditions and microstructural configurations described previously. Nevertheless, we include only selective results derived by the "variational" method, although this method is capable of handling the more general ellipsoidal microstructures and loading conditions considered here. The reason for this is linked to the fact that it has already been found that the "variational" method is too stiff for isotropic microstructures, and certainly is expected to be to stiff for anisotropic microstructures as well. Thus, for a better presentation of the results to follow, we will include "variational" curves only in special cases.

6.5.1 Aligned loadings

This subsection deals with the determination of the effective behavior of porous materials consisting of voids with prolate, oblate or ellipsoidal shapes, as shown in Fig. 6.14, whose principal axes (or equivalently $\mathbf{n}^{(i)}$ with $i = 1, 2, 3$) coincide with the principal loading directions and therefore with $\mathbf{e}^{(i)}$. In addition, these materials are subjected to two types of loading conditions, which are expressed as

$$\overline{\boldsymbol{\Sigma}} = \overline{\Sigma}_m\, \boldsymbol{I} + \frac{T}{3}\,(-\mathbf{e}^{(1)} \otimes \mathbf{e}^{(1)} - \mathbf{e}^{(2)} \otimes \mathbf{e}^{(2)} + 2\,\mathbf{e}^{(3)} \otimes \mathbf{e}^{(3)}), \quad (AXS) \tag{6.45}$$

and

$$\overline{\boldsymbol{\Sigma}} = \overline{\Sigma}_m \, \boldsymbol{I} + \frac{T}{\sqrt{3}} (\mathbf{e}^{(1)} \otimes \mathbf{e}^{(1)} - \mathbf{e}^{(2)} \otimes \mathbf{e}^{(2)}), \quad (PS), \tag{6.46}$$

where T can be either positive or negative with $|T| = \overline{\Sigma}_{eq}$, while $\overline{\Sigma}_m$ denotes the mean stress. The corresponding stress triaxiality is simply defined as

$$X_\Sigma = \frac{\overline{\Sigma}_m}{|T|}. \tag{6.47}$$

The first of the two stress states, given by (6.45), is an axisymmetric loading, denoted as AXS, with the maximum stress component in the $3-$direction. The second stress state given by (6.46) is a combination of in-plane (plane $1-2$) shear loading with superimposed pressure $\overline{\Sigma}_m$, denoted as PS. Due to the fact that the porous material is anisotropic, different loading conditions with the same stress triaxiality X_Σ would certainly result in different effective behaviors. In this connection, there are two questions that need to be answered. The first one is related to the effect of the void shape on the effective behavior of the porous medium for a given loading. The second question is linked to the effect of the loading conditions on the effective behavior of the porous material for a given void shape. An attempt to provide an answer to these two issues will be made in what follows.

Note further that if an axisymmetric loading of the form (6.45) is applied in the case of prolate or oblate voids (see Fig. 6.14), whose symmetry axis is aligned with the maximum absolute principal stress, which is the case in this subsection, the composite exhibits a transversely isotropic response about the $3-$axis, provided that the behavior of the matrix phase is isotropic. Those two microstructural states, i.e., prolate and oblate voids together with the loading condition (6.45) has also been studied by Flandi and Leblond (2005) (FL) in their model and their estimates will be included in this study for comparison with the corresponding "second-order" (SOM) predictions. Note, however, that if the second loading condition (6.46) is considered, the porous medium will exhibit an orthotropic behavior. For this last case, Flandi and Leblond have proposed an extension of their model to arbitrary stress states. However, this generalization has not been validated by the authors and corresponding results will only be shown in subsection (6.5.3), where we study the effective behavior of the porous medium on the deviatoric planes. Finally, when the void is ellipsoidal in shape (see Fig. 6.14c) with two different aspect ratios, the porous material exhibits an orthotropic response and hence, only the SOM model will be shown for this case.

More specifically, Fig. 6.15 shows gauge curves, as predicted by the SOM and FL model, on the plane $\overline{\Sigma}_m - T$, for a porous material consisting of prolate and oblate voids (see Fig. 6.14) subjected to the axisymmetric loading conditions defined by (6.45). Fig. 6.15a is concerned with prolate voids with aspect ratios $w_1 = w_2 = 5$, while the nonlinear exponent of the matrix phase is $m = 0.2$ (or $n = 5$). The SOM and the FL estimates are found to be in good agreement for all the porosities $f = 1, 5, 10\%$ considered. On the other hand, in Fig. 6.15b, which involves gauge curves for oblate voids with aspect ratios $w_1 = w_2 = 0.2$, the SOM and the FL models give different estimates, especially near the purely hydrostatic loading (i.e., $T \to 0$), where the SOM is found to be more conservative than the corresponding FL estimate. This difference may be partially due to the approximation introduced in the context of the SOM for the computation of the hydrostatic point, in relation

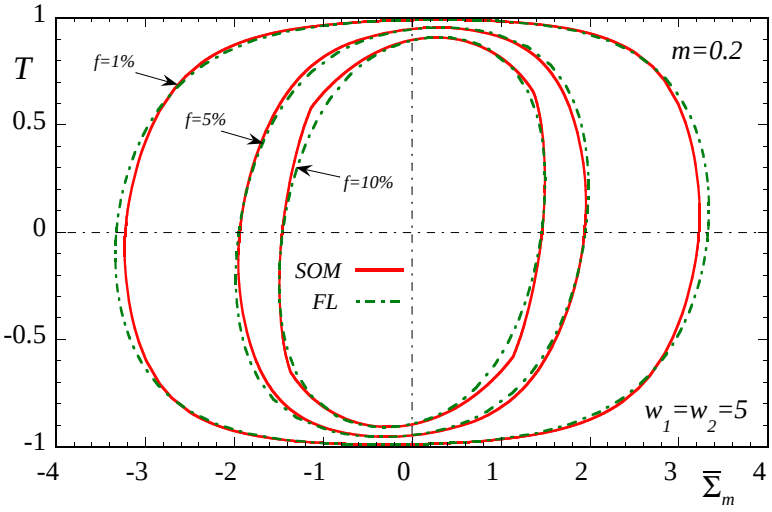

(a)

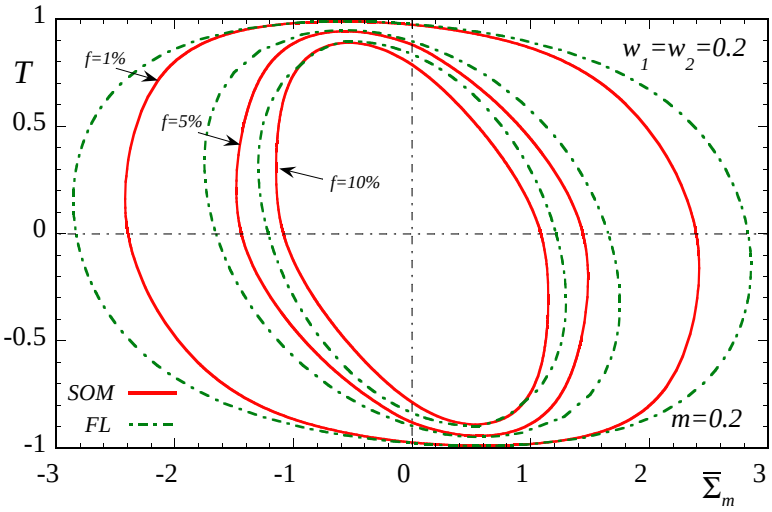

(b)

Figure 6.15: Gauge surfaces on the $\overline{\Sigma}_m - T$ plane (T denotes a measure of the deviatoric stress $\overline{\boldsymbol{\Sigma}}'$, such that $|T| = \overline{\Sigma}_{eq}$) for anisotropic, porous materials made up of spheroidal voids ($w_1 = w_2$) that are subjected to axisymmetric loading conditions aligned with the pore symmetry axis. Comparisons between the SOM and Flandi and Leblond (2005) (FL) model are included. The matrix phase is described by an exponent $m = 0.2$ ($n = 5$), while three values of porosity, $f = 1, 5, 10\%$ are used. The plots correspond to (a) $w_1 = w_2 = 5$ (prolate voids), and (b) $w_1 = w_2 = 0.2$ (oblate voids).

(2.198) for any given shape of the voids. On the other hand, the FL model is based on a hollow shell model consisting of two confocal spheroids (see Flandi and Leblond, (2005)), which certainly does not constitute a random, porous material, but rather a rough approximation for such a composite. For a more consistent comparison of the SOM estimates, numerical results for *random* porous media need to be obtained. However, determining the effective behavior of such materials is a very difficult task and such estimates are not yet available in the literature.

In the following, we study the three different microstructural configurations introduced previously

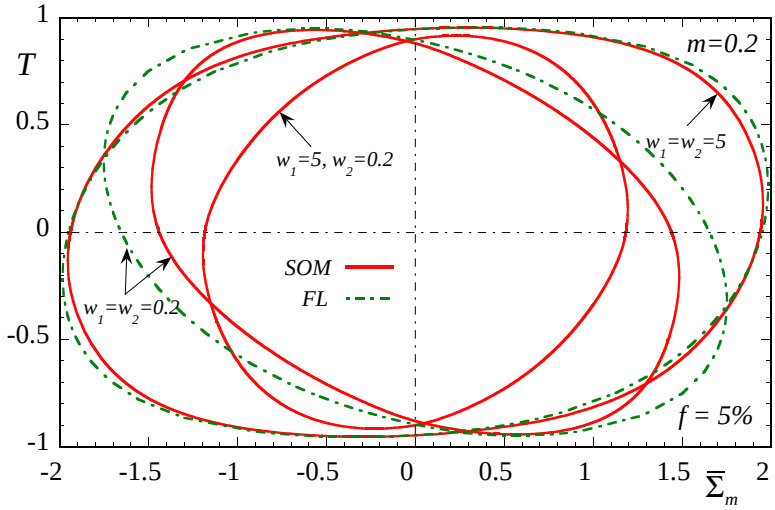

Figure 6.16: Gauge surfaces on the $\overline{\Sigma}_m - T$ plane (T denotes a measure of the deviatoric stress $\overline{\mathbf{\Sigma}}'$, such that $|T| = \overline{\Sigma}_{eq}$) for anisotropic, porous materials made up of spheroidal ($w_1 = w_2$) and ellipsoidal ($w_1 \neq w_2$) voids subjected to axisymmetric (about the 3−axis) loading conditions. The matrix phase is described by an exponent $m = 0.2$ ($n = 5$), while the porosity is $f = 5\%$. The graph shows gauge surfaces as predicted by the SOM and the Flandi-Leblond (2005) models for $w_1 = w_2 = 5$ (prolate), $w_1 = w_2 = 0.2$ (oblate) and $w_1 = 5, w_2 = 0.2$ (general ellipsoids).

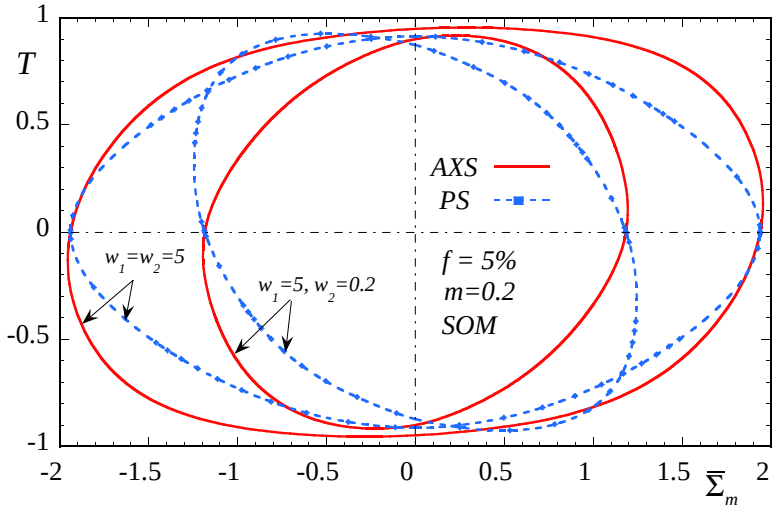

Figure 6.17: Gauge surfaces on the $\overline{\Sigma}_m - T$ plane (T denotes a measure of the deviatoric stress $\overline{\mathbf{\Sigma}}'$, such that $|T| = \overline{\Sigma}_{eq}$) for anisotropic, porous materials made up of spheroidal ($w_1 = w_2$) and ellipsoidal ($w_1 \neq w_2$) voids subjected to axisymmetric (AXS) and a combination of in-plane ($1-2$ plane) pure shear–pressure (PS) loadings. The matrix phase is described by an exponent $m = 0.2$ ($n = 5$), while the porosity is $f = 5\%$. The graph shows gauge surfaces as predicted by the SOM model for $w_1 = w_2 = 5$ (prolate) and $w_1 = 5, w_2 = 0.2$ (general ellipsoids).

for a porous medium with nonlinear exponent $m = 0.2$ (or $n = 5$) and porosity $f = 5\%$ that is subjected to axisymmetric loading conditions defined by (6.45). In particular, Fig. 6.16 shows corresponding gauge curves for spheroidal and ellipsoidal voids with aspect ratios $w_1 = w_2 = 5$

(prolate), $w_1 = w_2 = 0.2$ (oblate) and $w_1 = 5$, $w_2 = 0.2$ (general ellipsoid). For the prolate and oblate case the FL model is also included. However, for the general ellipsoidal voids only SOM estimates are available. The main observation in the context of this figure is that the effective behavior of the porous material is substantially different in all three cases considered here. Indeed, it is found that the porous medium with ellipsoidal voids ($w_1 = 5$-$w_2 = 0.2$) is softer than the one with oblate voids ($w_1 = w_2 = 0.2$) for stress states lying in the second ($T > 0$ and $\overline{\Sigma}_m < 0$) and the fourth ($T < 0$ and $\overline{\Sigma}_m > 0$) quadrant, while it is softer than the corresponding medium with prolate voids ($w_1 = w_2 = 5$) for all stress states shown in this figure.

This last example illustrates that ellipsoidal and spheroidal voids lead to very different effective behaviors. Thus, although the FL method has been shown to provide accurate estimates for the effective behavior of porous materials with spheroidal voids subjected to axisymmetric loading conditions, it is evident that it cannot be used to handle the cases of more general anisotropic porous media containing ellipsoidal voids. In contrast, the SOM model is based on a rigorous variational principle and thus is able to provide estimates for more general ellipsoidal microstructures. However, as already stated above, further validation of the SOM is needed in these general cases.

In the following, an attempt is made to examine the effect of the two different loading conditions, defined by relations (6.45) (AXS) and (6.46) (PS), on the effective behavior of anisotropic porous media. Fig. 6.17 shows only SOM gauge curves for two different microstructural configurations; (a) for prolate voids with aspect ratio $w_1 = w_2 = 5$ and (b) for general ellipsoidal voids with aspect ratios $w_1 = 5$ and $w_2 = 0.2$. It is remarkable, although expected, to observe that the type of loading has significant effects on the effective behavior of anisotropic porous media. More specifically, the effective response of a porous medium consisting of prolate voids is much softer when subjected to PS loading than AXS loading. Moreover, the corresponding PS curve for prolate voids is symmetric about the $T-$ and $\overline{\Sigma}_m-$axis, in contrast with the AXS curve, which exhibits no symmetry. The effect of the loading is even more dramatic in the case of ellipsoidal voids ($w_1 = 5$, $w_2 = 0.2$). In this case the PS and AXS loadings deliver a completely "reverse" effective behavior for the porous material. Note further that the gauge curves corresponding to the two different loadings coincide in the hydrostatic point, as they should be. However, the slope of the gauge curve at this point is totally different. This is in complete agreement with the physical intuition, and certainly a necessary requirement for any other general constitutive model that may be proposed in the future.

6.5.2 Shear–Pressure planes for misaligned microstructures

In this subsection, we consider the same loading conditions described by relations (6.45) and (6.46), whereas the principal axes of the voids are allowed to be misaligned with the loading principal directions. For convenience, the figures that follow are supplemented with a table indicating the orientation of the vectors $\mathbf{n}^{(i)}$ (with $i = 1, 2, 3$) with respect to the fixed Cartesian frame of reference defined by the unit vectors $\mathbf{e}^{(i)}$ (with $i = 1, 2, 3$). The notation to be used in the sequel has already been introduced in Table (6.1) for an arbitrary unit vector $\mathbf{u}$.

Prolate voids. Starting from Fig. 6.18, we consider porous media containing prolate voids with

aspect ratios $w_1 = w_2 = 5$ subjected to axisymmetric loading conditions given by (6.45), while the major (symmetry) axis of the voids, which is aligned with $\mathbf{n}^{(3)}$, is oriented at four different directions identified with the labels 1_p, 2_p, 3_p and 4_p, which are itemized in Table 6.2. In particular, Fig. 6.18a shows that the effective behavior of the porous material is affected by the orientation of the microstructure, particularly in the first and the fourth quadrant. Although, this effect does not seem to be so strong in overall, we will see in the next subsection that this effect is quite significant, when we consider a different cross-section of the gauge curve on the $\Pi-$plane. In fact, the largest difference is observed between the gauge curves corresponding to 1_p and 2_p, where the pore symmetry axis lies in two directions orthogonal to each other (see Table 6.2). On the other hand, an interesting observation in the context of this figure is that because of the symmetry of the microstructure and the loading, the corresponding curves for 3_p and 4_p coincide, as they should be, since the material exhibits certain invariance properties due to the fact that the void has a spheroidal shape. Note further that the effective behavior of a porous material consisting of spheroidal voids with a circular cross-section in the $1-2$ plane subjected to axisymmetric loading conditions (in the $3-$direction with $\overline{\Sigma}_{11} = \overline{\Sigma}_{22}$), as is the case here, is invariant under rotations of the voids about the $3-$axis.

In turn, Fig. 6.18b, shows corresponding gauge curves for in-plane shear—pressure loading, defined by relation (6.46). In this case the effect of the orientation of the microstructure seems to be less important on the overall behavior of the material. However, it is worth noting that due to the loading the response of the material is substantially different from the previous case, discussed in Fig. 6.18a. This can be easily deduced by noting that, unlike the previous case, the curves corresponding to 3_p and 4_p do not coincide, whereas, the 1_p curve is completely symmetric about the $T-$ and $\overline{\Sigma}_m-$axes. These observations imply that the porous material exhibits very different behaviors under various loading conditions, as already expected.

Table 6.2: Prolate voids: Orientation of principal axes

Cases	$\mathbf{n}^{(1)}$	$\mathbf{n}^{(2)}$	$\mathbf{n}^{(3)}$	ψ_1	ψ_2	ψ_3
1_p	–	–	$(0\,0\,1)$	0^o	0^o	0^o
2_p	–	–	$(0\,1\,0)$	90^o	0^o	0^o
3_p	–	–	$(0\,1\,1)$	-45^o	0^o	0^o
4_p	–	–	$(1\,0\,1)$	0^o	45^o	0^o

Oblate voids. Fig. 6.19a shows corresponding gauge curves for porous media containing oblate voids with aspect ratios $w_1 = w_2 = 0.2$ subjected to axisymmetric loading conditions given by (6.45), while the minor (symmetry) axis of the voids, which is aligned with $\mathbf{n}^{(3)}$, is oriented at four different directions identified with the labels 1_o, 2_o, 3_o and 4_o, which are itemized in Table 6.3. The main observation in the context of this figure is that the orientation of oblate voids has a very important effect on the macroscopic behavior of the porous medium when subjected to axisymmetric loading conditions. Note the difference in the gauge curves corresponding to 1_o and 2_o cases, where the material shows a completely "reverse" behavior. On the other hand, because of the symmetry of the microstructure and the loading conditions the 3_o and 4_o curves coincide, similar to the prolate case.

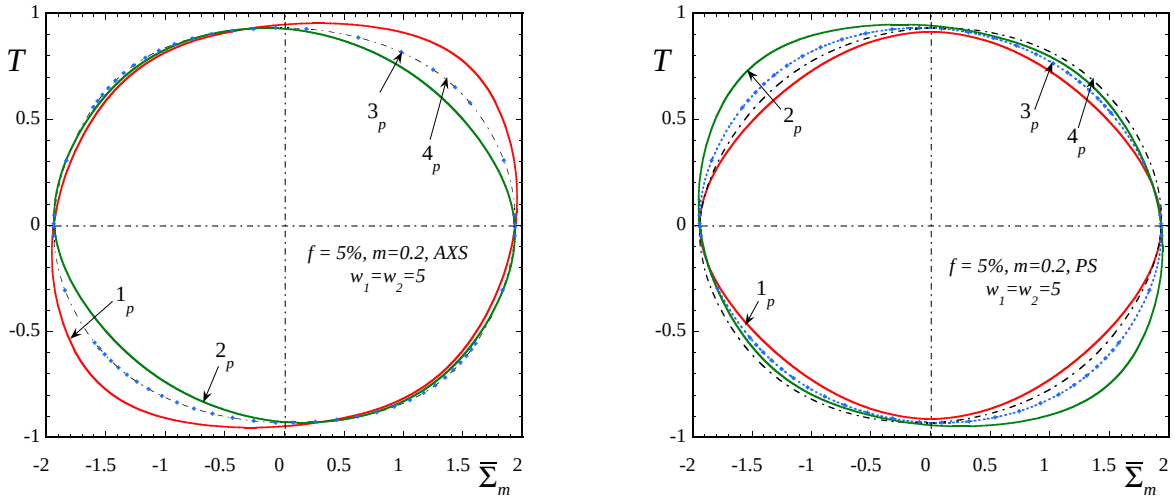

(a) (b)

Figure 6.18: Gauge surfaces on the $\overline{\Sigma}_m - T$ plane (T denotes a measure of the deviatoric stress $\overline{\boldsymbol{\Sigma}}'$, such that $|T| = \overline{\Sigma}_{eq}$) for anisotropic, porous materials made up of prolate spheroidal ($w_1 = w_2 = 5$) voids as determined by the SOM. The matrix phase is described by an exponent $m = 0.2$ ($n = 5$), while the porosity is $f = 5\%$. The curves involve different orientations of the major axis of the prolate voids as shown in Table 6.2, while the loading is: (a) axisymmetric about the 3−axis. (b) combination of in-plane ($1 - 2$ plane) shear with pressure.

In turn, Fig. 6.19b corresponding to in-plane shear—pressure loading is discussed next. In the context of this figure, we observe that, similarly to the Fig. 6.19a, the effect of the orientation of the voids on the overall response of the porous medium is quite significant. Note the difference exhibited by the several gauge curves at sufficiently high triaxial loadings (i.e., $\overline{\Sigma}_m \gg T$), where it is evident that misorientation of the voids may lead to softening or hardening, depending on the relative symmetry of the loading and the microstructure.

Table 6.3: Oblate voids: Orientation of principal axes

Cases	$\mathbf{n}^{(1)}$	$\mathbf{n}^{(2)}$	$\mathbf{n}^{(3)}$	ψ_1	ψ_2	ψ_3
1_o	–	–	$(0\,0\,1)$	0^o	0^o	0^o
2_o	–	–	$(0\,1\,0)$	90^o	0^o	0^o
3_o	–	–	$(0\,1\,1)$	-45^o	0^o	0^o
4_o	–	–	$(1\,0\,1)$	0^o	45^o	0^o

Ellipsoidal voids. Fig. 6.20 shows corresponding gauge curves for porous materials containing ellipsoidal voids with aspect ratios $w_1 = a_3/a_1 = 5$ and $w_2 = a_3/a_2 = 0.2$ (see Fig. 6.14). Note that in the context of this microstructural configuration, it is not sufficient to describe only the orientation of the major axis of the voids, which is aligned with $\mathbf{n}^{(2)}$ in this case (since $a_2 > a_3 > a_1$), but it is necessary to provide as well information about the orientation of the minor or middle axis. In fact, the minor and middle axes are aligned with $\mathbf{n}^{(1)}$ and $\mathbf{n}^{(3)}$, respectively. In Table 6.4, we present four

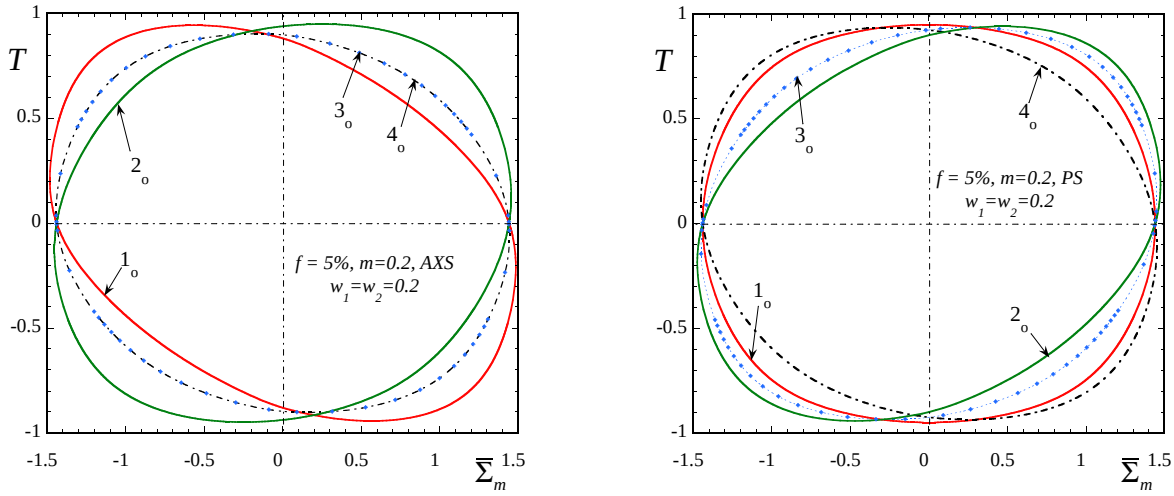

(a) (b)

Figure 6.19: Gauge surfaces on the $\overline{\Sigma}_m - T$ plane (T denotes a measure of the deviatoric stress $\overline{\boldsymbol{\Sigma}}'$, such that $|T| = \overline{\Sigma}_{eq}$) for anisotropic, porous materials made up of oblate spheroidal ($w_1 = w_2 = 0.2$) voids as determined by the SOM. The matrix phase is described by an exponent $m = 0.2$ ($n = 5$), while the porosity is $f = 5\%$. The curves involve different orientations of the major axis of the oblate voids as shown in Table 6.3, while the loading is: (a) axisymmetric about the $3-$axis. (b) combination of in-plane ($1-2$ plane) shear with pressure.

different orientations for the principal axes of the void, which are used in Fig. 6.20.

More specifically, in Fig. 6.20a, we consider an axisymmetric loading about the $\mathbf{e}^{(3)}-$axis defined by (6.45). As a consequence of the orthotropic symmetry of the void, none of the curves corresponding to the four cases considered here coincide. It is further emphasized that the effect of the orientation of the ellipsoidal voids on the effective behavior of the porous medium is rather significant, similar to the case of oblate voids.

Table 6.4: Ellipsoidal voids: Orientation of principal axes

Cases	$\mathbf{n}^{(1)}$	$\mathbf{n}^{(2)}$	$\mathbf{n}^{(3)}$	ψ_1	ψ_2	ψ_3
1_e	$(1\,0\,0)$	$(0\,1\,0)$	$(0\,0\,1)$	0^o	0^o	0^o
2_e	$(1\,0\,0)$	$(0\,0\,1)$	$(0\,\bar{1}\,0)$	90^o	0^o	0^o
3_e	$(1\,0\,0)$	$(0\,1\,1)$	$(0\,\bar{1}\,1)$	45^o	0^o	0^o
4_e	$(1\,\bar{1}\,0)$	$(1\,0\,1)$	$(0\,1\,0)$	0^o	45^o	0^o

In turn, looking at Fig. 6.20b corresponding to in-plane shear – pressure loading given by (6.46), we observe that the effective behavior of the porous medium is substantially different than the one predicted for axisymmetric loading. Moreover, it is interesting to remark that as a consequence of the microstructure (fully anisotropic) and the loading, the porous material exhibits completely different behaviors for all four orientations shown in Fig. 6.20b.

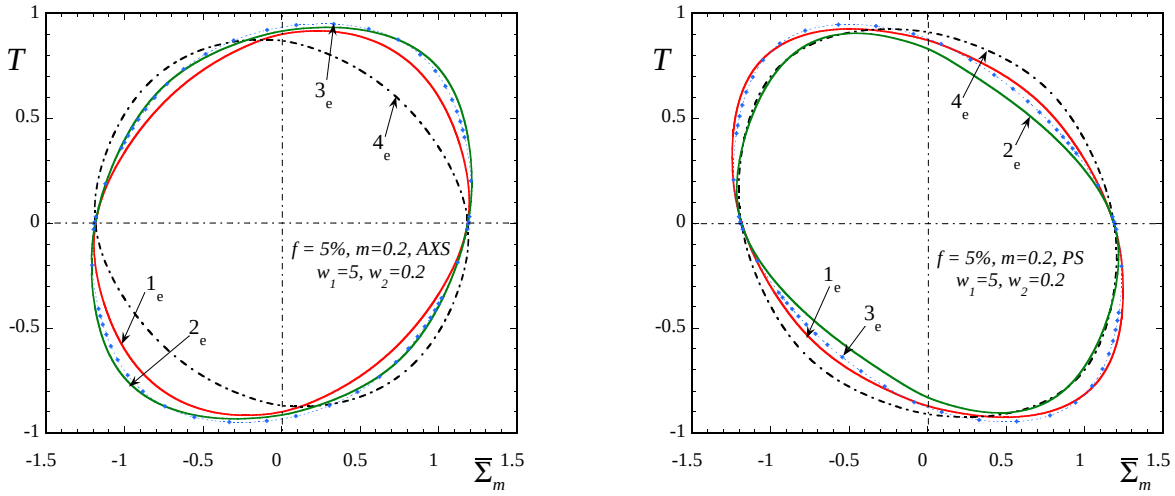

(a) (b)

Figure 6.20: Gauge surfaces on the $\overline{\Sigma}_m - T$ plane (T denotes a measure of the deviatoric stress $\overline{\mathbf{\Sigma}}'$, such that $|T| = \overline{\Sigma}_{eq}$) for anisotropic, porous materials made up of ellipsoidal ($w_1 = 5$, $w_2 = 0.2$) voids as determined by the SOM. The matrix phase is described by an exponent $m = 0.2$ ($n = 5$), while the porosity is $f = 5\%$. The curves involve different orientations of the principal axes of the ellipsoidal voids as shown in Table 6.4, while the loading is: (a) axisymmetric about the $3-$axis. (b) combination of in-plane ($1-2$ plane) shear with pressure.

6.5.3 Deviatoric planes for anisotropic porous media

In this subsection, we make an attempt to complement the results presented in the previous subsection by presenting cross-sections of the gauge surface in the deviatoric plane ($\Pi-$plane or octahedral plane), similarly to the cross-sections presented in the context of isotropic porous media (see Fig. 6.11). As already discussed in the beginning of this section, we assume that the principal directions of the macroscopic stress tensor coincide with the Cartesian system of reference defined by the three orthonormal vectors $\mathbf{e}^{(i)}$ with $i = 1, 2, 3$. In this connection, the gauge function is defined by (6.37) and the $\Pi-$plane is defined by considering a constant pressure, i.e., $\overline{\Sigma}_m = const$ and in-plane Cartesian coordinates defined by (6.40). For consistency with the isotropic results presented previously, we choose a constant pressure $\overline{\Sigma}_m = 0.9\,\overline{\Sigma}_m^H$, with $\overline{\Sigma}_m^H$ denoting the mean stress for purely hydrostatic loading for a given microstructural configuration as predicted by the SOM method. The determination of $\overline{\Sigma}_m^H$ (denoted alternatively in Chapter 2 as $\overline{\Sigma}_m^H\Big|_{som}$ to emphasize that it corresponds to the hydrostatic point as predicted by the SOM) is detailed in Appendix V of Chapter 2.

In what follows, we present cross-sections of the gauge surface on the $\Pi-$plane as predicted by the SOM, the VAR for the three microstructural configurations introduced in the context of Fig. 6.14, i.e., for (i) prolate voids with aspect ratios $w_1 = w_2 = 5$, (ii) oblate voids with aspect ratios $w_1 = w_2 = 0.2$ (the generalized FL model is also shown for the cases (i) and (ii)) and (iii) ellipsoidal voids $w_1 = 5$ and $w_2 = 0.2$. In addition, the principal axes of the voids are allowed to be misaligned with the principal loading directions, similar to the cases discussed in the previous subsection. For clarity, we also include a table together with each figure corresponding to the three aforementioned

microstructural configurations, which includes information about the orientation of the principal axes of the voids relative to the fixed frame of reference, as presented in the beginning of this section.

It is useful to present explicitly the values of $\overline{\Sigma}_m^H$ for the three aforementioned configurations, as predicted by the procedure described in Appendix V of Chapter 2. Thus, one finds for a porosity $f = 5\%$ and nonlinearity $m = 0.2$ (or $n = 5$) that

1. if $w_1 = w_2 = 5$ (prolate) : $\overline{\Sigma}_m^H = 1.93848$
2. if $w_1 = w_2 = 0.2$ (oblate) : $\overline{\Sigma}_m^H = 1.44014$
3. if $w_1 = 5$, $w_2 = 0.2$ (ellipsoid) : $\overline{\Sigma}_m^H = 1.18390$

In the following analysis, the above mentioned values will be used to define the cross-sections on the $\Pi-$plane, by considering a constant pressure $\overline{\Sigma}_m = 0.9\,\overline{\Sigma}_m^H$, as noted previously. It should be noted, however, that the above value is approximate and results from the criterion (2.199), which implies that the VAR and FL methods predict a different hydrostatic point, which is not exact as well. In this light, we choose as a reference hydrostatic point for arbitrary ellipsoidal microstructures the one delivered by the criterion (2.199).

Prolate voids. Fig. 6.21 shows SOM gauge curves on the $\Pi-$plane for a porous material consisting of prolate voids with aspect ratios $w_1 = w_2 = 5$. The continuous (and dashed) symmetry lines on the graph correspond to the three axisymmetric loading conditions aligned with the laboratory frame of reference. More specifically, Fig. 6.21a shows results for prolate voids whose principal axes are aligned with the principal loading directions. According to Table 6.5, the 1_p, 2_p and 3_p curves correspond to prolate voids, whose major (symmetry) axis is aligned with the $\mathbf{e}^{(3)}$, $\mathbf{e}^{(2)}$ and $\mathbf{e}^{(1)}$ directions, respectively.

Table 6.5: Prolate voids: Orientation of principal axes

Cases	$\mathbf{n}^{(1)}$	$\mathbf{n}^{(2)}$	$\mathbf{n}^{(3)}$	ψ_1	ψ_2	ψ_3
1_p	–	–	(0 0 1)	0^o	0^o	0^o
2_p	–	–	(0 1 0)	90^o	0^o	0^o
3_p	–	–	(1 0 0)	0^o	90^o	0^o
4_p	–	–	(0 1 1)	-45^o	0^o	0^o
5_p	–	–	(1 1 0)	0^o	90^o	45^o
6_p	–	–	(1 0 1)	0^o	45^o	0^o
7_p	–	–	(0 3 4)	34.35^o	0^o	0^o

As already expected, the form of the gauge curves is identical for these three cases, while the 2_p and 3_p curves can be obtained by $2\,\pi/3$ and $4\,\pi/3$ clockwise rotation of the 1_p curve about the axes origin. In addition, due to the spheroidal symmetry of the microstructure, the 1_p, 2_p and 3_p curves are symmetric about the $\overline{\Sigma}_3'-$, $\overline{\Sigma}_2'-$ and $\overline{\Sigma}_1'-$axis, respectively. A second important observation is linked to the fact that if axisymmetric loading conditions are considered transversely to the pore symmetry axis (e.g., look at 1_p curve when it crosses the positive $\overline{\Sigma}_2'-$axis), the effective behavior of

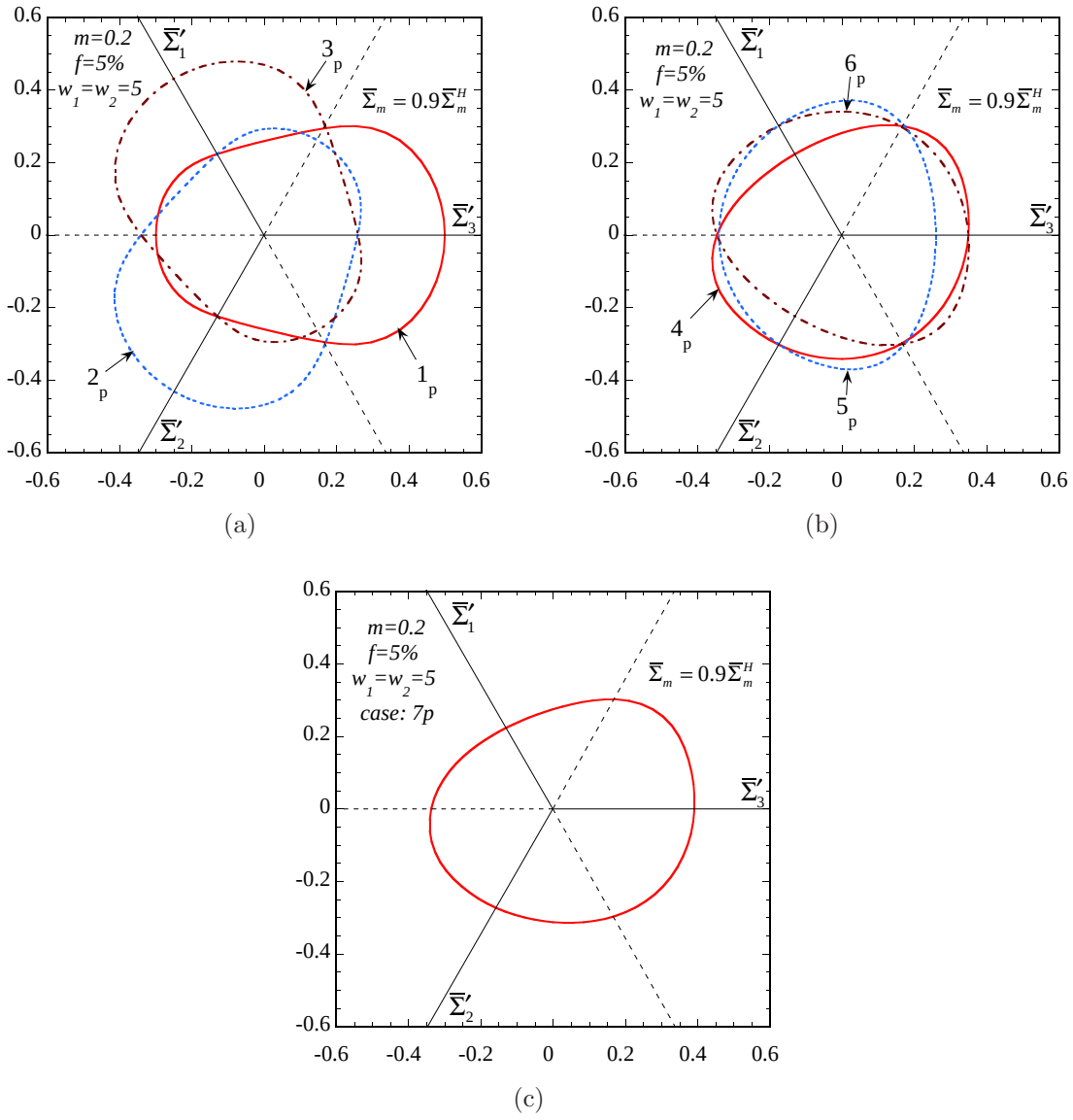

Figure 6.21: *SOM* cross-sections of the gauge surface on the $\Pi-$plane (or octahedral plane) for porous media consisting of prolate voids with aspect ratios $w_1 = w_2 = 5$, porosity $f = 5\%$ and nonlinearity $m = 0.2$ ($n = 5$). The cross-sections are defined by a constant pressure $\overline{\Sigma}_m = 0.9\overline{\Sigma}_m^H$ (with $\overline{\Sigma}_m^H$ denoting the mean stress for purely hydrostatic loading for a given microstructural configuration). The relevant graphs correspond to the cases that the pore symmetry axis is (a) aligned (1_p–3_p) and (b)-(c) misaligned (4_p–7_p) with the principal directions of the loading.

the material is significantly more compliant than in the case of axisymmetric loading along the pore symmetry axis (e.g., look at 1_p curve when it crosses the positive $\overline{\Sigma}_3'-$axis).

On the other hand, Fig. 6.21b shows gauge curves for porous media containing prolate voids whose principal axes are misaligned with the principal loading directions. According to According to Table 6.5, the curves 4_p, 5_p and 6_p correspond to the cases that the major (symmetry) axis of the voids lies in the $2-3$, $1-3$ and $1-2$ plane, respectively. Similar to the curves in part (a) of this figure, the 5_p and 6_p estimates can be obtained by $2\,\pi/3$ and $4\,\pi/3$ clockwise rotation of the 4_p curve about the

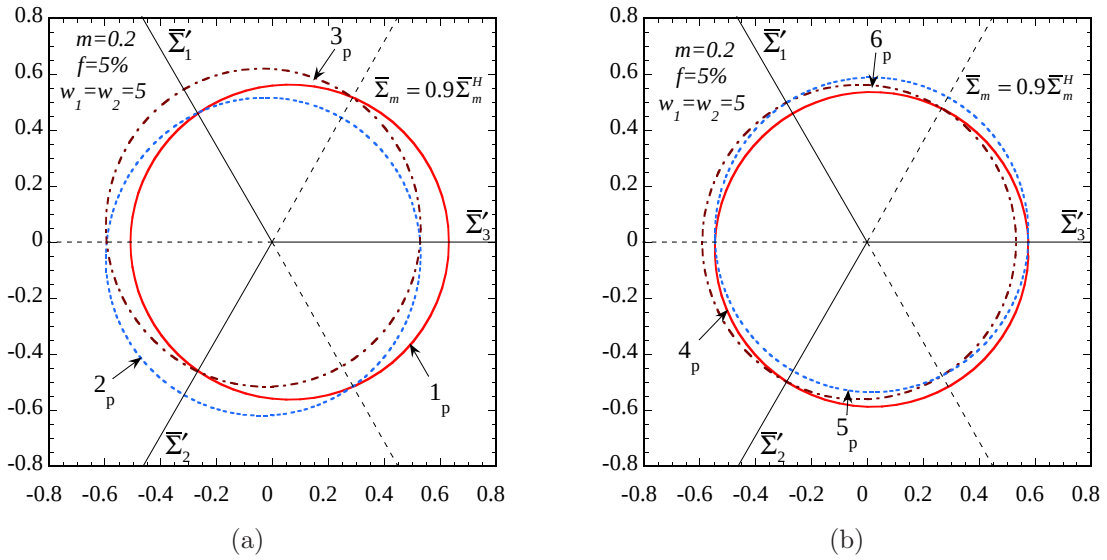

Figure 6.22: VAR cross-sections of the gauge surface on the $\Pi-$plane (or octahedral plane) for porous media consisting of prolate voids with aspect ratios $w_1 = w_2 = 5$, porosity $f = 5\%$ and nonlinearity $m = 0.2$ ($n = 5$). The cross-sections are defined by a constant pressure $\overline{\Sigma}_m = 0.9\overline{\Sigma}_m^H$ (with $\overline{\Sigma}_m^H$ denoting the mean stress for purely hydrostatic loading for a given microstructural configuration). The relevant graphs correspond to the cases that the principal directions of the void are (a) aligned and (b) misaligned with the principal directions of the loading.

axes origin. In addition, the 4_p, 5_p and 6_p curves are symmetric about the $\overline{\Sigma}_1'-$, $\overline{\Sigma}_3'-$ and $\overline{\Sigma}_2'-$axis, respectively. This is a direct consequence of the specific choice for the orientation of the symmetry axis of the voids relative to the principal loading directions. Note that the effective behavior of a porous medium with prolate voids, whose symmetry axis is not aligned with the principal loading directions, is, in general, *anisotropic* and thus no symmetry of the gauge surface on the $\Pi-$plane should be expected. Indeed, Fig. 6.21c verifies this observation, where we chose to show the 7_p gauge curve corresponding to prolate voids aligned in the direction (034). Finally, by comparing parts (a) and (b) of Fig. 6.21, we observe that the shape of the gauge curves and, consequently, the effective behavior of the porous medium becomes very different when the principal axes of the voids are misaligned with respect to the principal loading directions.

For completeness, Fig. 6.22 shows gauge curves on the $\Pi-$plane for a porous material consisting of prolate voids with aspect ratios $w_1 = w_2 = 5$, as predicted by the VAR method. As previously, the curves 1_p, 2_p and 3_p in Fig. 6.22a correspond to prolate voids, whose major (symmetry) axis is aligned with the $\mathbf{e}^{(3)}$, $\mathbf{e}^{(2)}$ and $\mathbf{e}^{(1)}$ directions, respectively. In turn, the curves 4_p, 5_p and 6_p in Fig. 6.22b correspond to the cases that the major (symmetry) axis of the voids lies in the $2-3$, $1-3$ and $1-2$ plane, respectively. A major observation in the context of this figure is related to the shape of the curves, which are found to remain elliptical in shape, in contrast with the SOM curves of Fig. 6.21. In addition, the VAR delivers stiffer estimates (note the scale in the plots) than the SOM method (a comparison between all the methods for a given loading and microstructure is presented later in this section). In addition, it is evident from Fig. 6.22 that the effect of the orientation of the voids is

not so strong by comparison with the corresponding effect observed in the context of the SOM.

Table 6.6: Oblate voids: Orientation of principal axes

Cases	$\mathbf{n}^{(1)}$	$\mathbf{n}^{(2)}$	$\mathbf{n}^{(3)}$	ψ_1	ψ_2	ψ_3
1_o	–	–	(0 0 1)	0^o	0^o	0^o
2_o	–	–	(0 1 0)	90^o	0^o	0^o
3_o	–	–	(1 0 0)	0^o	90^o	0^o
4_o	–	–	(0 1 1)	-45^o	0^o	0^o
5_o	–	–	(1 1 0)	0^o	90^o	45^o
6_o	–	–	(1 0 1)	0^o	45^o	0^o
7_o	–	–	(0 3 4)	34.35^o	0^o	0^o

Oblate voids. Similar to the prolate case, Fig. 6.23 shows SOM gauge curves on the $\Pi-$plane for a porous material consisting of oblate voids with aspect ratios $w_1 = w_2 = 0.2$. As before, the continuous (and dashed) symmetry lines on the graph correspond to the three axisymmetric loading conditions aligned with the laboratory frame of reference. In particular, Fig. 6.23a shows gauge curves for porous media containing oblate voids whose minor (symmetry) axis is aligned with the principal loading directions. In accord with Table 6.6, the curves 1_o, 2_o and 3_o correspond to the cases that the symmetry axis of the voids is aligned with the $\mathbf{e}^{(3)}$, $\mathbf{e}^{(2)}$ and $\mathbf{e}^{(1)}$ direction, respectively. Due to the spheroidal symmetry of the microstructure, the corresponding 1_o, 2_o and 3_o curves are symmetric about the $\overline{\Sigma}_3'-$, $\overline{\Sigma}_2'-$ and $\overline{\Sigma}_1'-$axis, respectively. Furthermore, the 2_o and 3_o curves can be obtained by $2\,\pi/3$ and $4\,\pi/3$ clockwise rotation of the 1_p curve about the axes origin. Nonetheless, the curves for oblate voids are significantly different in shape than the ones for prolate voids (Fig. 6.21a).

In turn, Fig. 6.23b shows gauge curves for porous materials consisting of oblate voids whose symmetry axis is misaligned with the principal loading directions. More specifically, the curves 4_o, 5_o and 6_o correspond to the cases that the symmetry axis of the voids lies in the $2-3$, $1-3$ and $1-2$ plane. Table 6.6 contains information about the orientation of the principal axes of the voids. In this case, the porous medium is still transversely isotropic about a direction that is not parallel to any of the three principal loading directions and, thus, the shape of the gauge curves is very different from those corresponding to the cases 1_o, 2_o and 3_o. Similar to the prolate case, the 4_o, 5_o and 6_o curves can be obtained by $2\,\pi/3$ and $4\,\pi/3$ clockwise rotation of the 1_p curve about the axes origin, whereas they are symmetric about the $\overline{\Sigma}_1'-$, $\overline{\Sigma}_3'-$ and $\overline{\Sigma}_2'-$axis, respectively. However, this is only due to the specific choice for the orientation of the symmetry axis of the voids relative to the principal loading directions. As already remarked in the context of prolate voids, when the pores are misaligned with the principal loading directions, the corresponding gauge curve is expected to exhibit no symmetry on the $\Pi-$plane. This is easily verified by showing in Fig. 6.23c the case 7_o of oblate voids whose symmetry axis is aligned in the direction (034).

On the other hand, Fig. 6.24 shows gauge curves on the $\Pi-$plane for a porous material consisting of oblate voids with aspect ratios $w_1 = w_2 = 0.2$, as predicted by the VAR method. In particular, the curves 1_o, 2_o and 3_o, shown in Fig. 6.24a, correspond to the cases that the symmetry axis of the

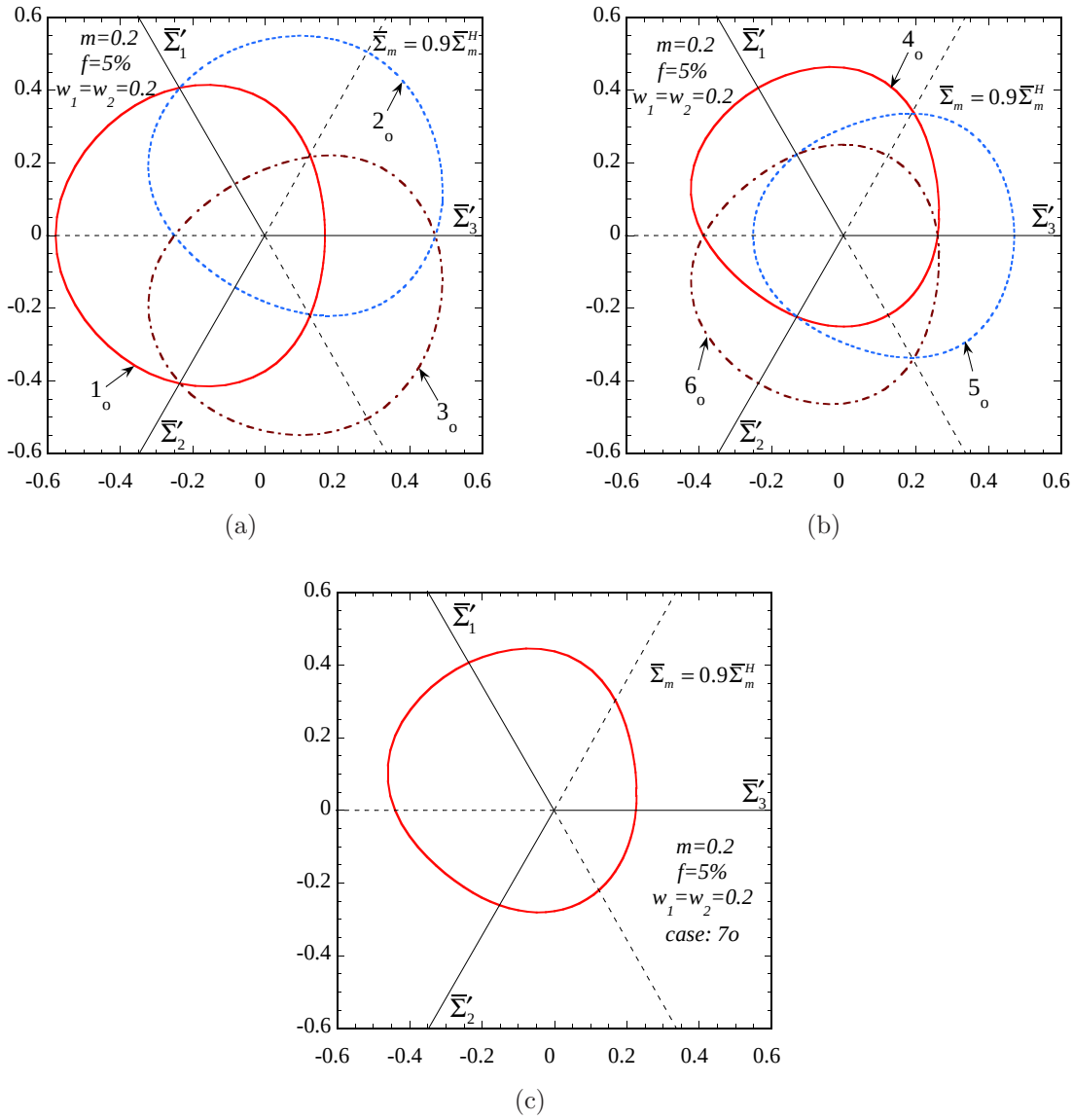

Figure 6.23: *SOM* cross-sections of the gauge surface on the Π−plane (or octahedral plane) for porous media consisting of oblate voids with aspect ratios $w_1 = w_2 = 0.2$, porosity $f = 5\%$ and nonlinearity $m = 0.2$ ($n = 5$). The cross-sections are defined by a constant pressure $\overline{\Sigma}_m = 0.9\overline{\Sigma}_m^H$ (with $\overline{\Sigma}_m^H$ denoting the mean stress for purely hydrostatic loading for a given microstructural configuration). The relevant graphs correspond to the cases that pore symmetry axis is (a) aligned (1_o–3_o) and (b)-(c) misaligned (4_o–7_o) with the principal directions of the loading.

voids is aligned with the $\mathbf{e}^{(3)}$, $\mathbf{e}^{(2)}$ and $\mathbf{e}^{(1)}$ direction, respectively, whereas the curves 4_o, 5_o and 6_o, shown in Fig. 6.24b, correspond to the cases that the symmetry axis of the voids lies in the $2-3$, $1-3$ and $1-2$ plane, respectively. Similar to the prolate configuration, the VAR curves remain also elliptical for oblate voids. However, the effect of the orientation of the oblate voids on the effective response of the porous medium is somewhat amplified, although not as significant as in the context of the *SOM* method in Fig. 6.23.

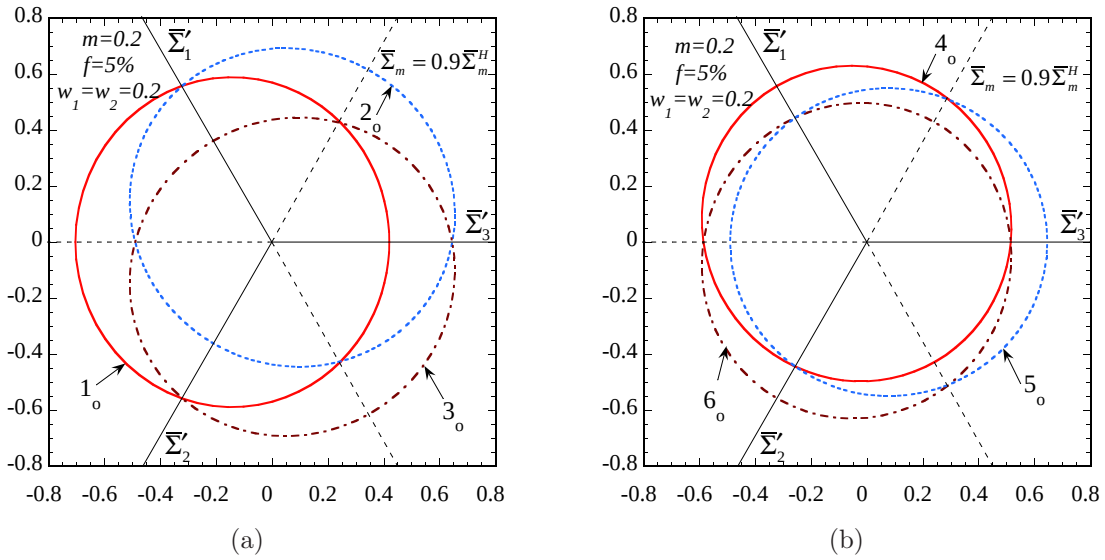

Figure 6.24: VAR cross-sections of the gauge surface on the $\Pi-$plane (or octahedral plane) for porous media consisting of oblate voids with aspect ratios $w_1 = w_2 = 0.2$, porosity $f = 5\%$ and nonlinearity $m = 0.2$ ($n = 5$). The cross-sections are defined by a constant pressure $\overline{\Sigma}_m = 0.9\overline{\Sigma}_m^H$ (with $\overline{\Sigma}_m^H$ denoting the mean stress for purely hydrostatic loading for a given microstructural configuration). The relevant graphs correspond to the cases that the principal directions of the void are (a) aligned and (b) misaligned with the principal directions of the loading.

Ellipsoidal voids. On the other hand, Fig. 6.25 shows SOM gauge curves for porous materials consisting of ellipsoidal voids with aspect ratios $w_1 = w_2 = 0.2$. In this case, the behavior of the material is orthotropic in a frame of reference defined by the orientation vectors of the principal axes of the voids, i.e., $\mathbf{n}^{(i)}$ (with $i = 1, 2, 3$). Unlike the previous two configurations involving spheroidal voids, in this case, it is necessary to describe the orientation of all three (or at least two) orientation vectors $\mathbf{n}^{(i)}$ (with $i = 1, 2, 3$) with respect to the unit vectors $\mathbf{e}^{(i)}$ (with $i = 1, 2, 3$). Thus, Table 6.7 includes the six cases studied in this work. More specifically, Fig. 6.25a presents gauge curves for voids whose principal axes are aligned with the principal loading directions. The main observation in the context of this figure is that the gauge curves 1_e, 2_e and 3_e do not exhibit any symmetry in contrast to the two previous cases involving spheroidal pore shapes. Nevertheless, these curves are all identical in shape, and for instance, the 2_e and 3_e estimates can be reproduced by $2\,\pi/3$ and $4\,\pi/3$ rotation of the 1_e estimate about the axes origin.

Fig. 6.25b shows corresponding curves for ellipsoidal voids whose principal axes are not aligned with the principal loading directions. As a consequence, the shape of the 4_e, 5_e and 6_e curves is substantially different than the ones shown for the 1_e, 2_e and 3_e curves in part (a) of this figure. An interesting observation that should be made in the context of Fig. 6.25b, is that the 4_e, 5_e and 6_e curves are symmetric about the $\overline{\Sigma}_1'-$, $\overline{\Sigma}_3'-$ and $\overline{\Sigma}_2'-$axis, respectively. This is in contrast with the corresponding curves in part (a) of this figure. This "unexpected" behavior reveals the complicated interaction between the loading conditions and the microstructure for the prediction of the effective behavior of the porous material. It is remarked that this state of microstructure involving ellipsoidal

Table 6.7: Ellipsoidal voids: Orientation of principal axes

Cases	$\mathbf{n}^{(1)}$	$\mathbf{n}^{(2)}$	$\mathbf{n}^{(3)}$	ψ_1	ψ_2	ψ_3
1_e	$(1\,0\,0)$	$(0\,1\,0)$	$(0\,0\,1)$	0^o	0^o	0^o
2_e	$(0\,0\,1)$	$(1\,0\,0)$	$(0\,1\,0)$	0^o	-90^o	-90^o
3_e	$(0\,1\,0)$	$(0\,0\,1)$	$(1\,0\,0)$	90^o	0^o	90^o
4_e	$(1\,0\,0)$	$(0\,1\,1)$	$(0\,\bar{1}\,1)$	45^o	0^o	0^o
5_e	$(0\,0\,\bar{1})$	$(1\,1\,0)$	$(1\,\bar{1}\,0)$	0^o	90^o	-45^o
6_e	$(0\,\bar{1}\,0)$	$(1\,0\,1)$	$(\bar{1}\,0\,1)$	45^o	0^o	90^o

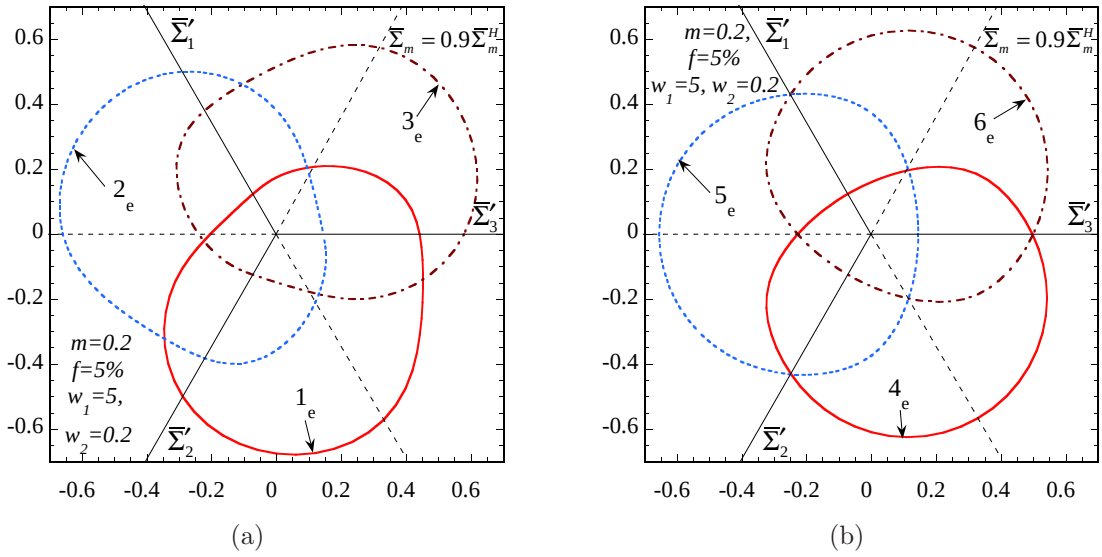

(a) (b)

Figure 6.25: *SOM* cross-sections of the gauge surface on the $\Pi-$plane (or octahedral plane) for porous media consisting of ellipsoidal voids with aspect ratios $w_1 = 5$ and $w_2 = 0.2$, porosity $f = 5\%$ and nonlinearity $m = 0.2$ ($n = 5$). The cross-sections are defined by a constant pressure $\bar{\Sigma}_m = 0.9\bar{\Sigma}^H_m$ (with $\bar{\Sigma}^H_m$ denoting the mean stress for purely hydrostatic loading for a given microstructural configuration). The relevant graphs correspond to the cases that the principal directions of the void are (a) aligned and (b) misaligned with the principal directions of the loading.

voids constitutes the most difficult case among the three microstructural configurations considered here, because of the different possible behaviors that can occur due to the nontrivial interaction between the microstructure and the loading conditions.

Finally, Fig. 6.26 shows VAR gauge curves for porous materials consisting of ellipsoidal voids with aspect ratios $w_1 = w_2 = 0.2$. The geometrical interpretation of the 1_e-6_e curves, shown in parts (a) and (b) of this figure is described in Table 6.7, where, as previously, the orientations of the principal axes of the voids $\mathbf{n}^{(i)}$ are shown with respect to the fixed unit vectors $\mathbf{e}^{(i)}$. In particular, it is observed that the VAR curves remain elliptical even in this case that the voids exhibit orthotropic symmetry. In addition, it is interesting to mention that although the effect of the orientation of the voids in each of part (a) and (b) is shown to be significant, it can be observed that the pair of the curves 1_e-4_e, $2_e - 5_e$ and 3_e-6_e exhibit very minor differences. Of course, by comparison of Fig. 6.25 and Fig. 6.26,

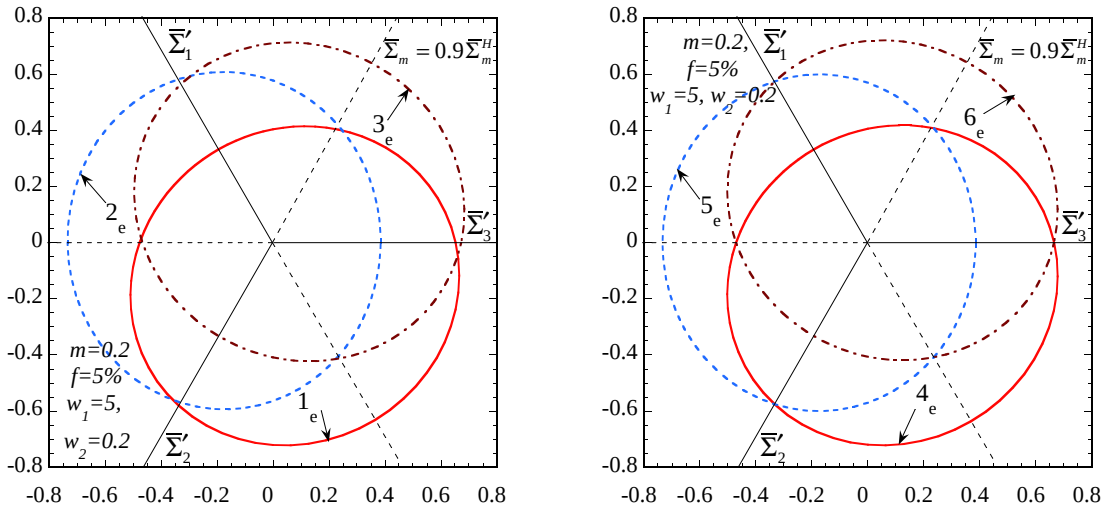

Figure 6.26: VAR cross-sections of the gauge surface on the $\Pi-$plane (or octahedral plane) for porous media consisting of ellipsoidal voids with aspect ratios $w_1 = 5$ and $w_2 = 0.2$, porosity $f = 5\%$ and nonlinearity $m = 0.2$ ($n = 5$). The cross-sections are defined by a constant pressure $\overline{\Sigma}_m = 0.9\overline{\Sigma}_m^H$ (with $\overline{\Sigma}_m^H$ denoting the mean stress for purely hydrostatic loading for a given microstructural configuration). The relevant graphs correspond to the cases that the principal directions of the void are (a) aligned and (b) misaligned with the principal directions of the loading.

it is evident that the VAR estimates are in fact much stiffer than the corresponding SOM estimates, which is already expected.

All models. In the following, we choose the cases 1_p, 1_o and 1_e, presented previously, and we plot the SOM and the VAR simultaneously. In addition, we include FL (Flandi and Leblond, 2005) gauge curves by making use of the extension of the FL model to arbitrary stress states, provided by these authors in the appendix of part I of their work. Since, this extension is not validated further by the authors, we just include these results without making further comments about the accuracy of this extension.

Thus, Fig. 6.27a shows SOM, VAR and FL gauge curves on the $\Pi-$plane for a porous medium consisting of prolate voids with aspect ratios $w_1 = w_2 = 5$, whose major axis is aligned with the $\mathbf{e}^{(3)}-$direction. The main observation in the context of this figure is that the VAR estimate is significantly stiffer than both the SOM and FL method. In addition, the FL curve seems to have an elliptical shape, similar to the elliptical shape of the VAR curve, in contrast with the SOM which exhibits a very non-elliptical shape, which is significantly flattened in certain directions. Nonetheless, all estimates are symmetric about the $\overline{\Sigma}_3'-$axis, which is a consequence of the transversely isotropic response of the porous medium under axisymmetric loading along the pore symmetry axis.

In turn, Fig. 6.27b shows corresponding SOM, VAR and FL gauge curves on the $\Pi-$plane for a porous medium consisting of oblate voids with aspect ratios $w_1 = w_2 = 0.2$, whose major axis is aligned with the $\mathbf{e}^{(3)}-$direction. Similar to part(a) of this figure, in part (b), the VAR estimate is found to be significantly stiffer than the SOM and the FL, particularly in the positive $\overline{\Sigma}_3'-$axis,

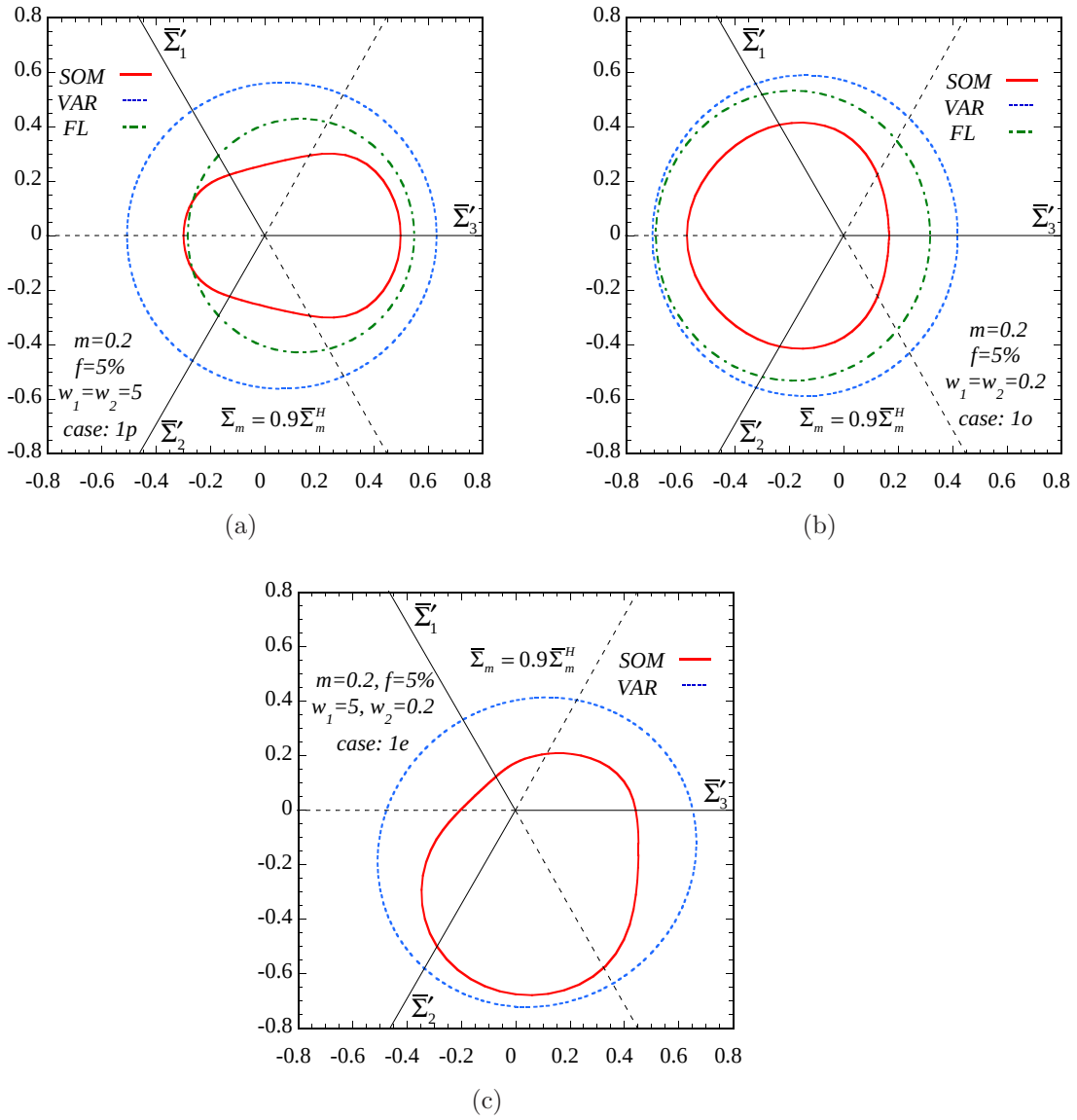

Figure 6.27: Collective SOM, VAR and FL results for voids with aspect ratios equal to (a) $w_1 = w_2 = 5$ (prolate), (b) $w_1 = w_2 = 0.2$ (oblate) and (c) $w_1 = 5$, $w_2 = 0.2$ (ellipsoids).

while all methods remain symmetric about this axis since the porous material is transversely isotropic about the pore symmetry axis (i.e., $\mathbf{e}^{(3)}-$axis) under axisymmetric loading about the 3−direction. In addition, the FL curve is very similar in shape with the VAR curve, in contrast with the SOM method, which exhibits a flattening in the positive $\overline{\Sigma}_3'-$axis.

Finally, Fig. 6.27c shows SOM and VAR gauge curves on the Π−plane for a porous medium consisting of ellipsoidal voids with aspect ratios $w_1 = 5$-$w_2 = 0.2$, whose principal axes are oriented according to the 1_e case in Table 6.7. It is emphasized, here, that the FL model cannot handle orthotropic microstructures (i.e., ellipsoidal voids with two different aspect ratios) and thus is not included in this figure. More specifically, the difference in the shape between the SOM and the VAR estimates is significant. Due to the orthotropic symmetry of the porous medium, the SOM curve exhibits no symmetry, whereas the VAR curve remains elliptical, which implies that it has two

axes of symmetry. However, those axes of symmetry in the VAR estimate do not coincide with any particular axes in the graph. In addition, the VAR estimate is significantly stiffer than the SOM estimate for all loadings considered here.

6.6 Concluding Remarks

In this chapter, we studied the instantaneous effective response of isotropic and anisotropic porous materials subjected to general loading conditions. The main conclusions can be separated in two main groups. The first one is related to isotropic porous media, whereas the second to anisotropic ones. In particular, the new "second-order" model, developed in section 2.6, makes use of a new prescription for the reference stress tensor, given by relation (2.202), which is such that the resulting "second-order" estimates reproduce exactly the behavior of the "composite-sphere assemblage" in the limit of hydrostatic loading and therefore coincides with the hydrostatic limit of Gurson's (1977) criterion for porous materials with an ideally-plastic matrix phase. This has as a consequence a significant improvement of this new model over the earlier "variational" method for the estimation of the effective behavior of isotropic and anisotropic porous materials.

More specifically, the "second-order" estimates have been compared with the Lee and Mear (1992c) estimates in the context of dilute porous media consisting of spheroidal (prolate or oblate) voids that are subjected to axisymmetric loading conditions aligned with the pore symmetry axes. The main conclusion of this section is that the "second-order" method was found to improve dramatically on the earlier "variational" method by being in good agreement with the Lee and Mear results for all nonlinearities, stress triaxialities and void shapes considered. On the other hand, the Lee and Mear estimates were found to predict lower values than the "second-order" model for the dilatational and the deviatoric part of the strain-rate, particularly at high stress triaxialities. As already discussed in section 4.6, the difference between the two models is possibly due to the fact that the dilute methods used by Lee and Mear require a very large number of terms in the Rayleigh-Ritz eigen-function expansion to achieve sufficient accuracy at high stress triaxialities and nonlinearities (Huang, 1991b). A possible reason for this difficulty in obtaining convergent results could be attributed to the fact that the range of validity of the dilute expansion for the effective stress potential of the porous medium, which was found to diminish to zero at high nonlinearities and purely hydrostatic loading (see subsection 3.2.5).

In turn, for finite porosities, the new second-order model was found to improve significantly on the earlier "variational" estimates of Ponte Castañeda (1991), discussed in section 2.5, especially at high stress triaxialities, low porosities and high nonlinearities, where the "variational" bound was known to be overly stiff. To establish this, the new "second-order" estimates were compared with exact results obtained by high-rank sequential laminates, discussed in section 3.4, and were found to be in very good agreement for the entire range of stress triaxialities and nonlinearities considered. By comparison, the Leblond et al. (1994) and the Gurson (1977) models were found to be stiffer than the "second-order" estimates in a significant range of the stress triaxialities.

In addition, both the "second-order" model and the sequential laminates were found to depend on

all three invariants of the macroscopic stress tensor. Interestingly, the effect of the third invariant was found to be non negligible even at moderate and high triaxialities and moderate porosities leading to an "asymmetric" response of the composite in the $\Pi-$plane (or octahedral plane). On the other hand, the Leblond et al. (1994), the Gurson (1977) and the "variational" model depend only on the first two invariants of the macroscopic stress tensor.

It is worth mentioning that even though the interest in this work is on small concentration of the vacuous phase, the above homogenization methods (i.e., "second-order" theory and "variational" bound) may be also applied for composites with high concentration of voids. For example, (Despois et al., 2006) have used the "variational" bound to fit experimental data in the context of metal foams. For such high-porosity materials, however, the improvements documented in this work relative to the earlier "variational" model are expected to be comparatively smaller. Moreover, it should be emphasized that the Willis type estimates for linear composites are expected to be sufficiently accurate for small and moderate concentrations of the inclusions (or voids in the present study). Thus, the application of the estimates presented in this chapter and the previous ones are expected to hold for porous media with high concentrations provided that we deal with closed-pore media. On the other hand, for very high porosities and open-pore materials appropriate linear schemes or numerical techniques (such as finite element calculations) should be used for foamed materials (Chen et al., 1999; Deshpande and Fleck, 1999; McCullough et al. 1999; Ashby, 2000; Despois et al., 2006; Conde et al., 2006; San Marchi and Mortensen, 2001;).

In turn, the "second-order" model has been compared with the recent Flandi and Leblond (2005) model in the case of transversely isotropic porous materials consisting of spheroidal voids subjected to axisymmetric loading directions aligned with the pore symmetry axis. The agreement of the two models was better for prolate than for oblate voids. However, it was shown that the effective behavior of the porous material is substantially different if it consists of ellipsoidal voids with two different aspect ratios. This last case can only be studied by the "second-order" method, which is capable of handling materials with more general ellipsoidal microstructures, in contrast with several earlier models, such as Flandi and Leblond (2005) (Gologanu et al., 1993; Gărăjeu et al., 2000; Monchiet et al., 2007) that are valid only for transversely isotropic microstructures and axisymmetric loading conditions aligned with the pore symmetry axis.

In addition, it was found that the applied load can also affect significantly the effective behavior of anisotropic porous media. In order to study the effect of the applied loading conditions, two different stress states were considered; an axisymmetric and an in-plane shear–pressure loading condition. The two conditions were compared for porous media consisting of prolate and ellipsoidal voids. In the case of prolate voids, the porous material was found to have a softer effective response when subjected to in-plane shear–pressure loading than in axisymmetric loading. On the other hand, the porous material with ellipsoidal voids exhibited a significantly different behavior when subjected to the two aforementioned loadings. Note that these curves for the two different loadings coincide in the purely hydrostatic loading as they should be, but the slope of the curves at these points is substantially different.

In the following, we studied the effect of the orientation of the voids on the effective response

of anisotropic porous media by making use of the "second-order" model developed in this study. It was found that in all cases considered, involving prolate, oblate and ellipsoidal voids, this effect can be significant and certainly cannot be neglected. Initially, we considered cross-section of the gauge surfaces on the meridional plane, i.e., on the $\overline{\Sigma}_m - \overline{\Sigma}_{eq}$ plane. As already expected, all the curves coincide at the hydrostatic point, as they should be. Nonetheless, the slope of the curves at this point can be very different indicating the importance of having a model that is able to distinguish between different orientations of the principal axes of the voids, even at high triaxial loading conditions.

Next, we have presented "second-order" curves for anisotropic microstructures on the $\Pi - plane$. In those cross-sections, the effect of the orientation of the voids relative to the principal directions of the loading was found to be very significant for the effective behavior of the porous material. In the same context, we were able to observe certain symmetries in the behavior of the porous medium, when the relative orientation of the voids and the loading yields certain symmetries on the effective response of the material. For instance, when the voids are spheroidal and the matrix phase isotropic, then the material is transversely isotropic in the direction parallel to the pore symmetry axis. However, if none of loading directions coincide with the pore symmetry axis then the effective behavior of the porous material is substantially different from the one that we would obtain if the loading and the pores were aligned. For further validation and comparison of the "second-order" estimates, we have shown corresponding results as predicted by the "variational" method, as well as the Flandi-Leblond (2005) model (only for spheroidal voids). The main conclusion drawn out of these comparisons is that the "second-order" curves exhibit very non-elliptical shapes, in contrast to the "variational" method, which remains elliptical for all configurations considered here. In turn, the Flandi-Leblond curves seem to remain elliptical, as well, however this has to be shown analytically. Of course, the "variational" estimates are significantly stiffer than both the "second-order" and the Flandi-Leblond models, as already expected.

In this connection, we conclude by emphasizing that the new "second-order" model is based on a rigorous variational principle, which has been generalized to more complex anisotropic microstructures (arbitrary pore shapes and orientation) and general, three-dimensional loadings, in contrast to the Gurson model which is restricted to isotropic microstructures, and the Leblond et al. (1994) (Gologanu et al., 1993,1994,1997; Gărăjeu et al., 2000; Flandi and Leblond, 2005) model which is valid only for axisymmetric loading conditions and transversely isotropic microstructures. Furthermore, the strategy followed in this work can be extended, in principle, to more general constitutive laws (non-power law) for the matrix phase. It is relevant to emphasize in this connection that our ultimate objective is to develop a *completely general* constitutive models for porous media with evolving anisotropy in the spirit of the earlier works of Ponte Castañeda and Zaidman (1994) and Kailasam and Ponte Castañeda (1998) in the context of the "variational" procedure (1991). Such an attempt will be presented in the following chapter.

Chapter 7

Evolution of microstructure: spherical and ellipsoidal voids

This chapter is concerned with the determination of the effective response and evolution of microstructure of random porous media subjected to general loading conditions. The "second-order" model (SOM) of Ponte Castañeda (2002a), discussed in section 2.6, is compared with the earlier "variational" model (VAR) of Ponte Castañeda (1991), discussed in section 2.5, the Lee and Mear (1994) (LM) method for dilute porous media (see subsection 3.2.4), unit-cell finite element calculations (FEM) (see subsection 3.5) and the recent model by Flandi and Leblond (2005) (FL) (see subsection 3.3) for several nonlinearities and triaxialities. The results discussed in the previous chapter will be applied in the present one, where we will make an attempt to study the importance of the various microstructural variables, introduced in section 2.2.1, for given loading conditions. It should be noted that the Lee and Mear and the finite element method, as well as the Flandi-Leblond model are valid only for porous media consisting of spheroidal voids subjected to axisymmetric loading conditions aligned with the pore symmetry axis. On the other hand, the "second-order" and the "variational" methods are valid for general ellipsoidal microstructures and loading conditions. For clarity, we include Fig. 7.1 to describe the microstructural variables involved in this section. Further details about the relevant microstructural variables are given in subsection 2.2.1.

7.1 Evolution laws for general ellipsoidal voids

In particular, we study the problem of porous materials consisting of ellipsoidal voids, subjected to general loading conditions. Due to the finite deformations, the initially spherical voids evolve into ellipsoidal ones with certain orientation in space. Thus, the relevant microstructural variables are the porosity f, the aspect ratios w_1 and w_2 and the orientation vectors $\mathbf{n}^{(i)}$ (with $i = 1, 2, 3$). The general evolution equations for these microstructural variables have been presented in section 2.7, and, for completeness, they are recalled briefly here:

Porosity. By making use of the incompressibility of the matrix phase, the evolution law for the porosity is obtained from the kinematical relations

$$\dot{f} = (1 - f)\overline{D}_{ii}, \quad i = 1, 2, 3, \tag{7.1}$$

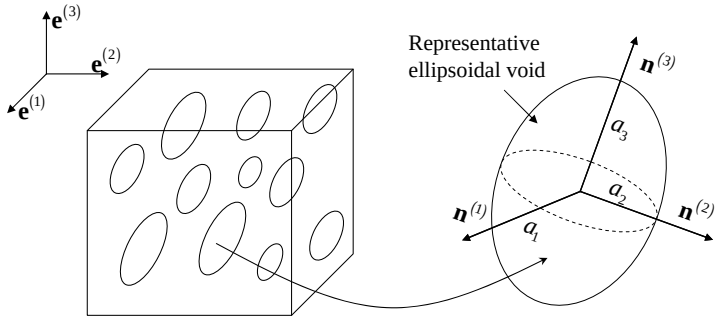

Figure 7.1: Representative ellipsoidal void in the case of spherical microstructures.

where $\overline{\boldsymbol{D}}$ is evaluated from relation (6.3) for the "variational" method and (6.14) for the "second-order" method.

Aspect ratios. The evolution of the aspect ratios of the ellipsoidal void is defined by

$$\dot{w}_i = w_i \left(\mathbf{n}^{(3)} \cdot \overline{\boldsymbol{D}}^{(2)} \, \mathbf{n}^{(3)} - \mathbf{n}^{(i)} \cdot \overline{\boldsymbol{D}}^{(2)} \, \mathbf{n}^{(i)} \right) = w_i \left(\mathbf{n}^{(3)} \otimes \mathbf{n}^{(3)} - \mathbf{n}^{(i)} \otimes \mathbf{n}^{(i)} \right) \cdot \overline{\boldsymbol{D}}^{(2)}, \tag{7.2}$$

(no sum on $i = 1, 2$). The average strain-rate in the void $\overline{\boldsymbol{D}}^{(2)}$ is computed by relation (6.4) for the "variational" method and (6.19) for the "second-order" method.

Orientation vectors. The evolution of the orientation vectors $\mathbf{n}^{(i)}$ is determined by the spin of the Eulerian axes of the ellipsoidal voids, or microstructural spin $\boldsymbol{\omega}$, via

$$\dot{\mathbf{n}}^{(i)} = \boldsymbol{\omega} \, \mathbf{n}^{(i)}, \quad i = 1, 2, 3. \tag{7.3}$$

The microstructural spin $\boldsymbol{\omega}$ is related to the average spin in the void, $\overline{\boldsymbol{\Omega}}^{(2)}$, and the average strain-rate in the void, $\overline{\boldsymbol{D}}^{(2)}$, and can be expressed in direct notation (Aravas and Ponte Castañeda, 2004) by

$$\boldsymbol{\omega} = \overline{\boldsymbol{\Omega}}^{(2)} + \frac{1}{2} \sum_{\substack{i,j=1 \\ i \neq j \\ w_i \neq w_j}}^{3} \frac{w_i^2 + w_j^2}{w_i^2 - w_j^2} \left[(\mathbf{n}^{(i)} \otimes \mathbf{n}^{(j)} + \mathbf{n}^{(j)} \otimes \mathbf{n}^{(i)}) \cdot \overline{\boldsymbol{D}}^{(2)} \right] \mathbf{n}^{(i)} \otimes \mathbf{n}^{(j)}, \tag{7.4}$$

with $w_3 = 1$. On the other hand, the Jaumann rate of the orientation vectors $\mathbf{n}^{(i)}$, denoted by $\overset{\triangledown}{\mathbf{n}}{}^{(i)}$ $(i = 1, 2, 3)$ is given by

$$\overset{\triangledown}{\mathbf{n}}{}^{(i)} = -\boldsymbol{\Omega}^p \, \mathbf{n}^{(i)} \qquad i = 1, 2, 3, \tag{7.5}$$

where $\boldsymbol{\Omega}^p = \overline{\boldsymbol{\Omega}} - \boldsymbol{\omega}$ is the plastic spin (Dafalias, 1985). The above definition is helpful for the computation of the Jaumann hardening rate in the context of ideal-plasticity. Note that the above evolution laws are valid for both the "variational" and the "second-order" method, whereas the computation of the phase average fields in the composite is the one that brings about the difference between the "variational" and the "second-order" estimates.

7.2 Dilute porous media

In this section, we present selective results, extracted by the Lee and Mear (1994) (LM) work, the "second-order" method (SOM) and finite element calculations (FEM) for the evolution of microstructure in porous media consisting of spheroidal voids that are subjected to axisymmetric loading conditions aligned with the pore symmetry axis. Thus, depending on the loading, the pores may take prolate or oblate shapes.

As already discussed in detail in chapters 4, 5 and 6, the LM estimates are valid for dilute porous media. On the other hand, it has been observed by Duva and Hutchinson (1984) and Duva (1986) that the dilute methods, such as the one of Lee and Mear (1994) under consideration here, cannot be used to deliver accurate estimates for small but finite concentrations of voids at high nonlinearities and stress triaxialities. For this reason, the SOM estimates are obtained for porosity $f_o = 10^{-6}$, which can be considered sufficiently small for the purpose of these comparisons. In turn, for validation of the two methods, i.e., the SOM and the LM, we include also results obtained by FEM calculations for porosity $f_o = 10^{-4}$. Although, this value is not as small as the one of $f_o = 10^{-6}$, it will be seen that the corresponding SOM results do not exhibit any differences for these two different values of f_o, indicating that even the value $f_o = 10^{-4}$ can be considered as dilute provided that the porosity remains at low values during the deformation process. This remark is made in order to emphasize that for sufficiently large triaxiality loadings, the porosity increases rapidly leading to non-dilute concentrations of voids. In this case, the comparisons between the LM, the SOM and the FEM are not meaningful and the estimates can diverge significantly from each other.

Next, the loading conditions considered here are the same defined in section 6.2, such that the remote non-zero components of the macroscopic stress tensor $\overline{\boldsymbol{\sigma}}$ are

$$\overline{\sigma}_{11} = \overline{\sigma}_{22} = T, \quad \overline{\sigma}_{33} = S. \tag{7.6}$$

Then, the stress triaxiality is defined in terms of S and T by

$$X_\Sigma = \frac{S + 2\,T}{3\,|S - T|} = \frac{S}{|S|}\,\frac{1 + 2\,T/S}{3\,|1 - T/S|}. \tag{7.7}$$

In the figures to follow, we use the ratio T/S as the loading parameter in the problem. The values used are $T/S = 0, 0.2, 0.4, 0.6$, which correspond to stress triaxiality $X_\Sigma = \pm 1/3, \pm 0.583, \pm 1, \pm 1.833$, respectively. Obviously for the values of T/S given previously, the sign of X_Σ depends on the sign of the normalized quantity $S/|S|$. For later use, it is pertinent to define here the remote axial strain-rate $\dot{\varepsilon}^\infty_{33}$ and strain ε^∞_{33} in the absence of voids, which take the form

$$\dot{\varepsilon}^\infty_{33} = \dot{\varepsilon}_o \left(\frac{\overline{\sigma}_{eq}}{\sigma_o}\right)^n \frac{S - T}{\overline{\sigma}_{eq}}, \quad \varepsilon^\infty_{33} = \int_t \dot{\varepsilon}^\infty_{33} \mathrm{d}t, \tag{7.8}$$

where σ_o is the flow stress of the matrix phase and $\dot{\varepsilon}_o$ is a reference strain-rate taken in the calculation to follow equal to unity.

Fig. 7.2 shows results for the evolution of the normalized porosity f/f_o for various stress ratios $T/S = 0, 0.2, 0.4, 0.6$, as a function of the remote axial strain ε^∞_{33} for a nonlinear exponent $n = 10$. In this figure, the SOM estimates are found to be in agreement with the LM results for all stress

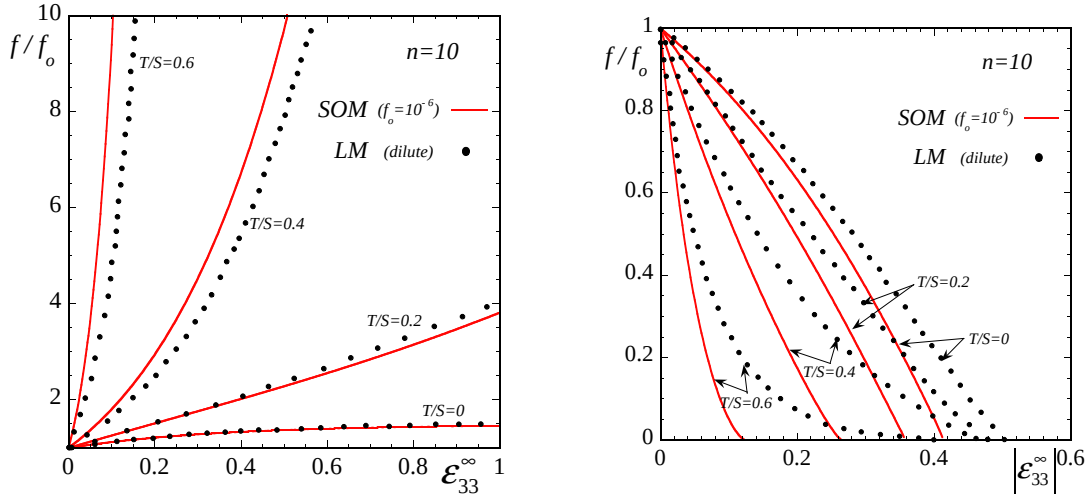

Figure 7.2: Results are shown for the evolution of the normalized porosity f/f_o as a function of the remote axial strain $\varepsilon_{33}^{\infty}$ for a dilute porous material consisting of initially spherical pores subjected to axisymmetric loading conditions. The matrix phase exhibits a viscoplastic behavior with an exponent $n = 5$. *SOM* and *LM* estimates are shown for (a) tensile and (b) compressive loading conditions for ratios of the in-plane stress components $T/S = 0, 0.2, 0.4, 0.6$ or $X_{\Sigma} = \pm 1/3, 0.583, 1, 1.833$.

ratios considered. In particular, Fig. 7.2a shows results for tensile loadings, i.e., $S/|S| > 0$, where it is found that by increasing the stress ratio T/S, the normalized porosity f/f_o grows rapidly taking very high values at small deformations. As already anticipated by the results presented in the previous chapters associated with dilute porous media, the *LM* method predicts lower values for f/f_o when compared with the *SOM* results, at sufficiently high stress triaxialities ($T/S = 0.4, 0.6$). In turn, Fig. 7.2b shows corresponding results for compressive loadings, i.e., $S/|S| < 0$. In that case, the voids collapse, i.e., the porosity closes down at finite strains, whereas the strain of the pore closure is strongly dependent on the stress ratio T/S. The results predicted by the *SOM* are found to be more compliant than the *LM* predictions. This observation is in accordance with the remark made in the context of Fig. 7.2a, i.e., that the *LM* is stiffer at high nonlinearities and triaxialities.

As already stated in the introduction of this section, in order to validate further the results obtained in the previous figure, we present in Fig. 7.3 results for the evolution of the normalized porosity f/f_o as predicted by the *SOM* and the *FEM* methods for porosities $f_o = 10^{-4}$, which are "compared" with the dilute estimates of Lee and Mear. The stress triaxialities considered here are the same used previously, i.e., $T/S = 0, 0.2, 0.4, 0.6$. First of all, we observe that the *FEM* estimates lie closer to the corresponding *SOM* results for both tensile and compressive loadings than to the *LM* predictions. In particular, the *FEM* results are more compliant than the *LM* estimates, which is in agreement with the observations made previously in the context of the *SOM* predictions. It is also important to recall here that contrary to the *FEM* calculations, the *LM* procedure assumes that the void evolves through a sequence of spheroidal shapes (see also Fleck and Hutchinson, 1986) during the deformation process, which constitutes an idealization that may

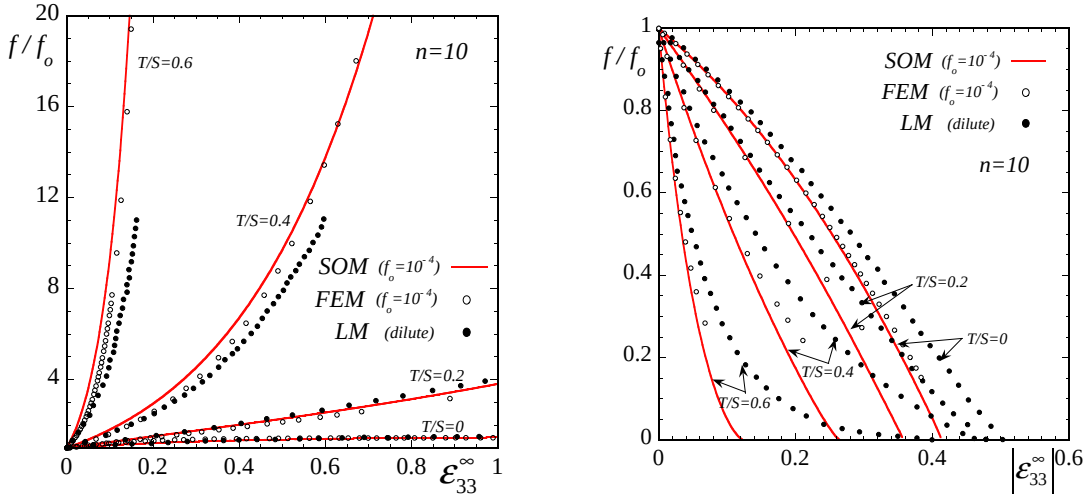

Figure 7.3: Results are shown for the evolution of the normalized porosity f/f_o as a function of the remote axial strain $\varepsilon_{33}^{\infty}$ for a dilute porous material consisting of initially spherical pores subjected to axisymmetric loading conditions. The matrix phase exhibits a viscoplastic behavior with an exponent $n = 5$. *SOM* and *LM* estimates are shown for (a) tensile and (b) compressive loading conditions for ratios of the in-plane stress components $T/S = 0, 0.2, 0.4, 0.6$ or $X_{\Sigma} = \pm 1/3, 0.583, 1, 1.833$.

become rough particularly at high stress triaxialities and nonlinearities. On the other hand, in the *SOM*, use is made of the average fields in the vacuous phase to compute an average *spheroidal* shape for the void. Obviously, all of the three procedures are different and, in general, are expected to lead to different estimates. However, it is evident from Fig. 5.3 and the results discussed in section 6.2, that the *LM* procedure could underestimate slightly the effective response of dilute porous media, particularly at high nonlinearities and stress triaxialities.

7.2.1 Effect of the initial pore shape

Finally, Fig. 7.4 presents results for the evolution of the normalized porosity f/f_o in dilute porous media subjected to axisymmetric compressive loadings with stress ratios $T/S = 0, 0.4$ and nonlinear exponent for the matrix phase $n = 5$, as a function of the remote axial strain $|\varepsilon_{33}^{\infty}|$ and the aspect ratio of the spheroidal voids w. In this figure, we consider porous media consisting of spherical voids ($w = 1$), prolate voids with aspect ratios $w = 3/2, 2$ and oblate voids with aspect ratios $w = 2/3, 1/2$. More specifically, Fig. 7.4a shows results for a stress ratio $T/S = 0$ with $S/|S| < 0$, i.e., uniaxial compression. The *SOM* estimates for f/f_o are in agreement with the *LM* results for all the aspect ratios considered here. Both methods predict a faster pore closure (i.e., $f/f_o \to 0$) in the case of oblate voids ($w = 2/3, 1/2$), than for prolate ones ($w = 3/2, 2$), which is intuitively expected. This result indicates that a porous material containing prolate voids is stiffer than oblate voids in the direction of the pore symmetry axis. Similar observations can be made in Fig. 7.4b, which corresponds to an axisymmetric compressive loading with higher stress ratio $T/S = 0.4$. As already expected, the *SOM* predicts a faster reduction of the normalized porosity f/f_o than the *LM* method at higher

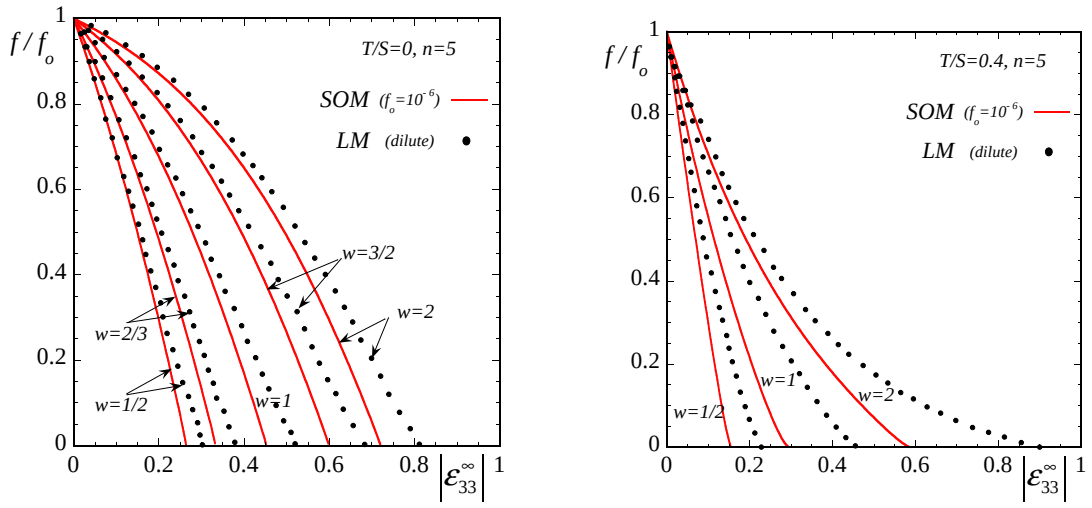

Figure 7.4: Results are shown for the evolution of the normalized porosity f/f_o as a function of the remote axial strain $\varepsilon_{33}^{\infty}$ for a dilute porous material consisting of spherical and spheroidal pores subjected to axisymmetric compressive loading conditions. The matrix phase exhibits a viscoplastic behavior with an exponent $n = 5$. SOM and LM estimates are shown for stress ratios (a) $T/S = 0$ and (b) $T/S = 0.4$ for spherical voids ($w = 1$), prolate voids with aspect ratios $w = 3/2, 2$ and oblate voids with aspect ratios $w = 2/3, 1/2$.

stress triaxialities. This result is consistent with the observations made previously, i.e., that the SOM method predicts a more compliant effective response for the porous material than the LM at high triaxialities and nonlinearities.

7.3 Axisymmetric loading conditions

In this section, we validate the "second-order" (SOM) and the "variational" (VAR) estimates by comparing them with unit-cell finite element calculations (FEM). For completeness, it is recalled that we consider a cylindrical unit-cell consisting of an initially spherical void with initial porosity $f_o = 0.01\%$. The unit-cell is subjected to periodic boundary conditions, as already discussed in section 3.5, such that the applied stress triaxiality X_Σ, remains constant during the deformation process. Furthermore, the loading is axisymmetric such that the initially spherical void evolves into a spheroidal void (i.e., the void has a circular cross-section on a specific plane). Several nonlinear exponents are used, i.e., $n = 1, 2, 4, 10$, while the material is subjected to both tensile and compressive loadings. The effect of the stress triaxiality and the nonlinearity on the evolution of the microstructure is studied in detail.

In this regard, for the calculations performed in this section, axisymmetric traction boundary conditions defined in (7.6) are applied, whereas the stress triaxiality X_Σ is given by (7.7). The values used in the following paragraphs are $X_\Sigma = \pm 1/3, \pm 1, \pm 3$, which correspond to stress ratio $T/S = 0, 0.4, 0.727$ (with $S/|S| \lesseqgtr 0$), respectively.

Next, provided that the major axis of the voids is aligned with the laboratory frame of reference

and the principal loading axes, the only relevant microstructural variables (see Fig. 7.1) are the porosity f and the aspect ratio $w = w_1 = w_2 = a_3/a_1 = a_3/a_2$, with $a_1 = a_2$ and a_3 denoting the lengths of the principal semi-axes of the spheroidal void. The cases $w > 1$ and $w < 1$ correspond to prolate and oblate spheroidal voids, respectively. In turn, the orientation of the void and thus the orientation vectors $\mathbf{n}^{(i)}$ (with $i = 1, 2, 3$) remain fixed during the deformation process.

7.3.1 Tensile loadings

Uniaxial tension loading with $X_\Sigma = 1/3$ ***or*** $T/S = 0$ ***with*** $S/|S| > 0$. Fig. 7.5 presents results for the evolution of the relevant microstructural variables for an initially isotropic porous medium subjected to uniaxial tension loading. The porosity f normalized by the initial porosity f_o, the aspect ratio w, and the macroscopic axial component of the strain-rate $\overline{D}_{33}$ normalized by the equivalent strain-rate in the absence of voids $\dot{\varepsilon}^{\infty}_{eq}$ are shown as a function of the nonlinear exponent $n = 1, 2, 4, 10$ and the total axial strain $\bar{\varepsilon}_{33}$. In Fig. 7.5a, the predictions of the SOM for the evolution of the porosity f are in very good agreement with the FEM results for all the nonlinearities considered. Similarly to the case of cylindrical voids, the main feature of this loading predicted by both the SOM and the FEM estimates, is that the porosity initially grows but finally it approaches an asymptote for sufficiently large strains. In Fig. 7.5b, the evolution of the aspect ratio w is shown for the four nonlinear exponents considered here. The SOM tends to overestimate slightly the evolution of the aspect ratio w, when compared with the corresponding FEM predictions. However, it is observed that the evolution of the aspect ratio does not depend strongly on the nonlinearity of the matrix phase, certainly much less than the corresponding evolution of the porosity. It should be noted here that the corresponding evolution curves obtained by the VAR method do not depend on the nonlinearity and they all coincide with the $n = 1$ curve. In this regard, the SOM is found to improve significantly on the earlier VAR method, especially at high nonlinearities. Finally, Fig. 7.5c shows the evolution of the normalized macroscopic axial strain-rate $\overline{D}_{33}/\dot{\varepsilon}^{\infty}_{eq}$. The agreement between the SOM and the FEM estimates is remarkable even at very high nonlinearities (i.e., $n = 10$). In contrast, the corresponding VAR results are found to underestimate the evolution of $\overline{D}_{33}/\dot{\varepsilon}^{\infty}_{eq}$, particularly at high nonlinearities.

For completeness, deformed (and superimposed undeformed) states of the relevant cross-section of the unit-cell are shown in Fig. 7.6 for several stages of the deformation process. In Fig. 7.6a and 7.6b, the matrix phase is described by an exponent $n = 1$, whereas in Fig. 7.6c and 7.6d by $n = 10$. In particular, Fig. 7.6a and 7.6c correspond to a total macroscopic strain $\sim 30\%$, where it is easily observed that for $n = 10$ the porosity and the aspect ratio take higher values than for $n = 1$. Similarly, Fig. 7.6b and 7.6d correspond to a total macroscopic strain $\sim 80\%$. An interesting remark in the context of this figure, is that the shape of the void remains almost ellipsoidal even in the nonlinear case $n = 10$, which implies that the fields in the vacuous phase are fairly uniform. In addition, it is easily observed that the elongation of the void occurs in the direction of the maximum principal stress.

Triaxial tension loading with $X_\Sigma = 1$ ***or*** $T/S = 0.4$ ***with*** $S/|S| > 0$. Fig. 7.7 shows results

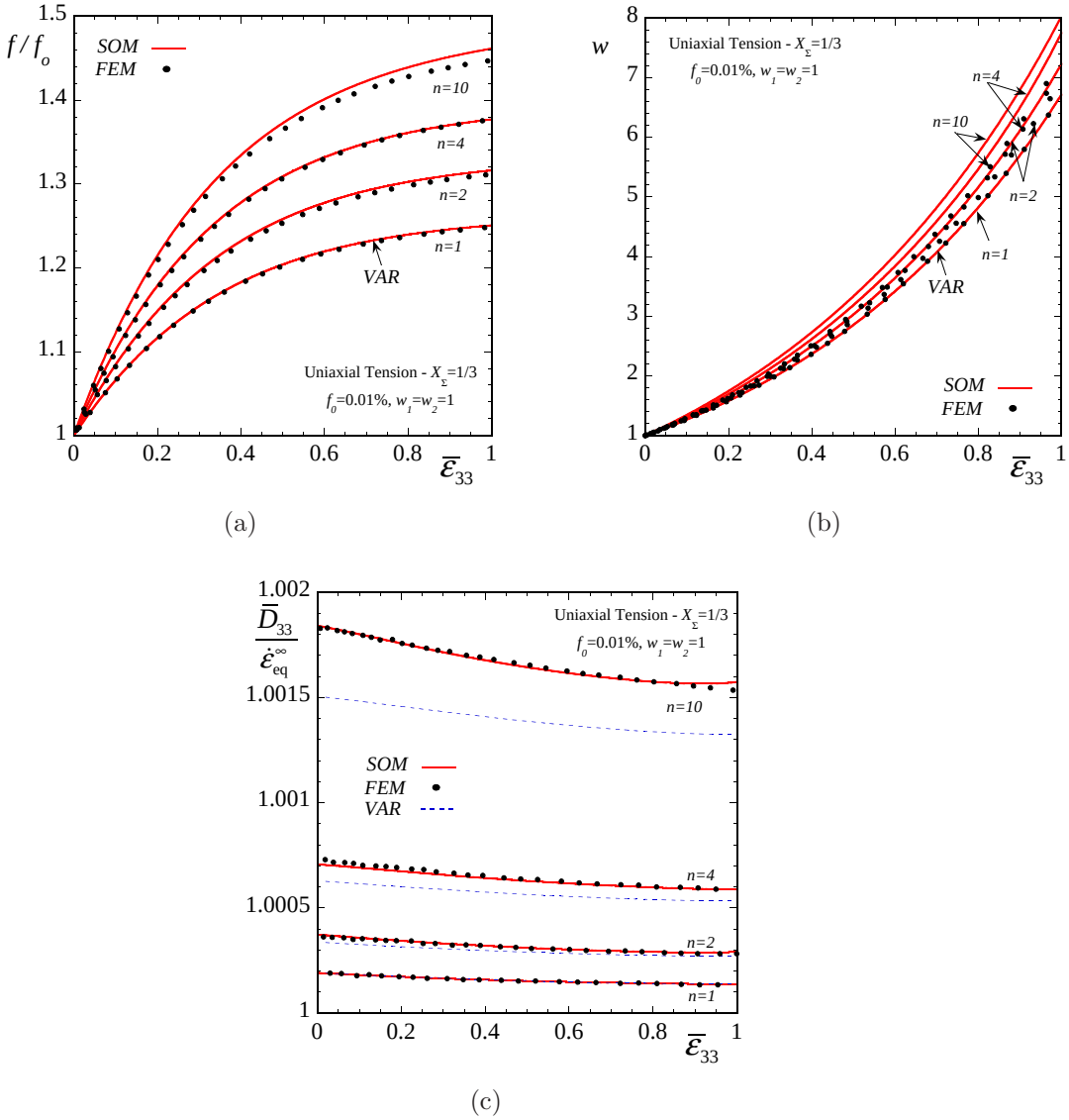

Figure 7.5: Results are shown for the evolution of the relevant microstructural and macroscopic variables for a porous material consisting of initially spherical pores embedded in a matrix with exponent $n = 1, 2, 4, 10$ as a function of the axial macroscopic strain $\bar{\varepsilon}_{33}$. The initial porosity is $f_o = 0.01\%$ and the material is subjected to axisymmetric uniaxial tension loading ($X_\Sigma = 1/3$ and $T/S = 0$ with $S/|S| > 0$) so that the voids become spheroidal in shape. SOM, FEM and VAR estimates are shown for the evolution of the (a) normalized porosity f/f_o, (b) the aspect ratio w and (c) the normalized axial strain-rate $\overline{D}_{33}/\dot{\varepsilon}^\infty_{eq}$ ($\dot{\varepsilon}^\infty_{eq}$ is the corresponding strain-rate in the absence of voids). The VAR estimate for the evolution of the porosity f/f_o and the aspect ratio w is found to be independent of the nonlinear exponent n and the corresponding predictions coincide with the $n = 1$ curves.

for the evolution of the relevant microstructural and macroscopic variables for an initially isotropic porous material subjected to triaxial tension with stress triaxiality $X_\Sigma = 1$. The normalized porosity f/f_o, the aspect ratio w, and the normalized macroscopic equivalent strain-rate $\overline{D}_{eq}/\dot{\varepsilon}^\infty_{eq}$ are shown as a function of the nonlinear exponent $n = 1, 2, 4, 10$ and the total equivalent strain $\bar{\varepsilon}_{eq}$. In Fig. 7.7a, the SOM estimates for the evolution of the porosity f are found to be in excellent agreement with

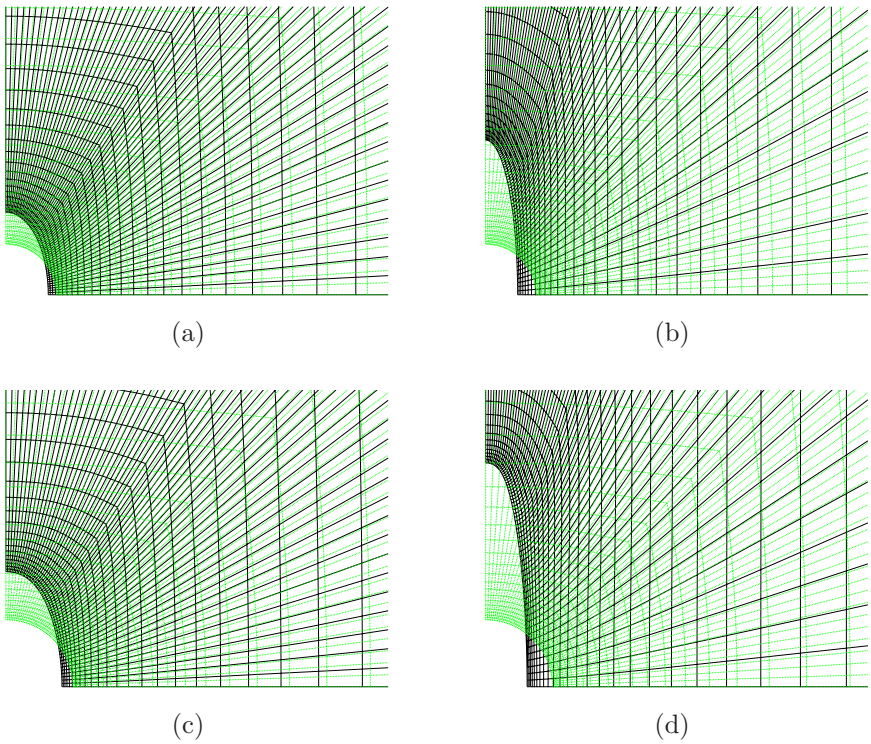

Figure 7.6: Deformed and undeformed contours for uniaxial tension loading with stress triaxiality $X_\Sigma = 1/3$. Part(a) and (b) correspond to an exponent $n = 1$ of the matrix phase for an axial deformation $\overline{\varepsilon}_{33} \sim 0.3$ and $\overline{\varepsilon}_{33} \sim 0.8$, respectively. In turn, parts (c) and (d) correspond to an exponent $n = 10$ and $\overline{\varepsilon}_{33} \sim 0.3$ and $\overline{\varepsilon}_{33} \sim 0.8$, respectively.

the corresponding FEM predictions especially at high nonlinearities $n > 4$. In contrast with the uniaxial tension loading, in the case of $X_\Sigma = 1$, the rate of growth of the porosity increases during the deformation process, such that for $\sim 80\%$ strain and nonlinearity $n = 10$ the initial porosity f_o has increased twenty times. On the other hand, in Fig. 7.7b, the aspect ratio w of the void is found to increase in a much slower rate than in the uniaxial tension loading. The SOM estimates overestimate the evolution of the aspect ratio when compared with the FEM results. However, the inaccurate prediction of the evolving aspect ratio by the SOM seems to leave unaffected the evolution of the normalized porosity f/f_o in Fig. 7.7a and certainly the normalized macroscopic strain-rate $\overline{D}_{eq}/\dot{\varepsilon}^{\infty}_{eq}$ in Fig. 7.7c, which is seen to be in very good agreement with the FEM results for all nonlinearities. This last observation implies that in the case of $X_\Sigma = 1$, the evolution of porosity controls the effective behavior of the porous medium. In contrast, the VAR estimates seriously underestimate the evolution of the porosity f/f_o (the VAR curves for the evolution of f/f_o and w coincide with the $n = 1$ curve for all nonlinearities), which has as a consequence the inaccurate prediction of the normalized macroscopic strain rate $\overline{D}_{eq}/\dot{\varepsilon}^{\infty}_{eq}$ and thus the effective behavior of the porous medium.

Triaxial tension loading with $X_\Sigma = 3$ ***or*** $T/S = 0.727$ ***with*** $S/|S| > 0$. Similarly to the previous case, Fig. 7.8 shows evolution plots for the normalized porosity f/f_o, the aspect ratio w and the normalized macroscopic equivalent strain-rate $\overline{D}_{eq}/\dot{\varepsilon}^{\infty}_{eq}$ as a function of the nonlinearity $n = 1, 2, 4, 10$ and the macroscopic equivalent strain $\overline{\varepsilon}_{eq}$ for an initially isotropic porous material

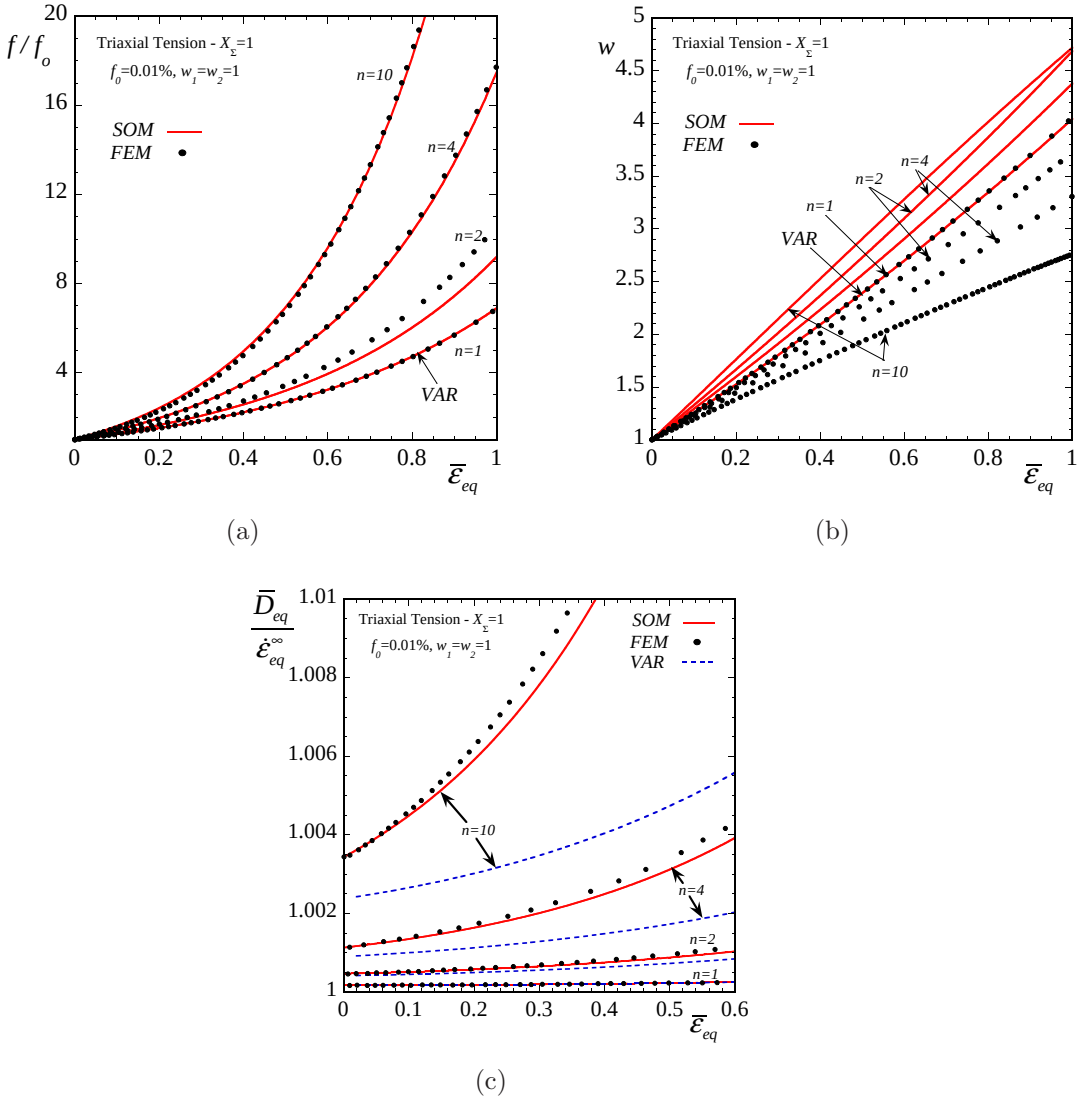

Figure 7.7: Results are shown for the evolution of the relevant microstructural and macroscopic variables for a porous material consisting of initially spherical pores embedded in a matrix with exponent $n = 1, 2, 4, 10$ as a function of the equivalent macroscopic strain $\overline{\varepsilon}_{eq}$. The initial porosity is $f_o = 0.01\%$ and the material is subjected to axisymmetric triaxial tension loading ($X_\Sigma = 1$ and $T/S = 0.4$ with $S/|S| > 0$) so that the voids become spheroidal in shape. SOM, FEM and VAR estimates are shown for the evolution of the (a) normalized porosity f/f_o, (b) the aspect ratio w and (c) the normalized axial strain-rate $\overline{D}_{eq}/\dot{\varepsilon}^{\infty}_{eq}$ ($\dot{\varepsilon}^{\infty}_{eq}$ is the corresponding strain-rate in the absence of voids). The VAR estimate for the evolution of the porosity f/f_o and the aspect ratio w is found to be independent of the nonlinear exponent n and the corresponding predictions coincide with the $n = 1$ curves.

subjected to high triaxiality loading with $X_\Sigma = 3$. In this high triaxiality loading, the evolution of the porosity f/f_o is expected to increase rapidly with the macroscopic strain $\overline{\varepsilon}_{eq}$, which is verified by the corresponding SOM and FEM estimates in Fig. 7.8a. The SOM and the FEM are in very good agreement in this case, while the SOM improves dramatically on the earlier VAR method, which is independent of the nonlinearity n and thus, all the VAR estimates coincide with the $n = 1$ curve.

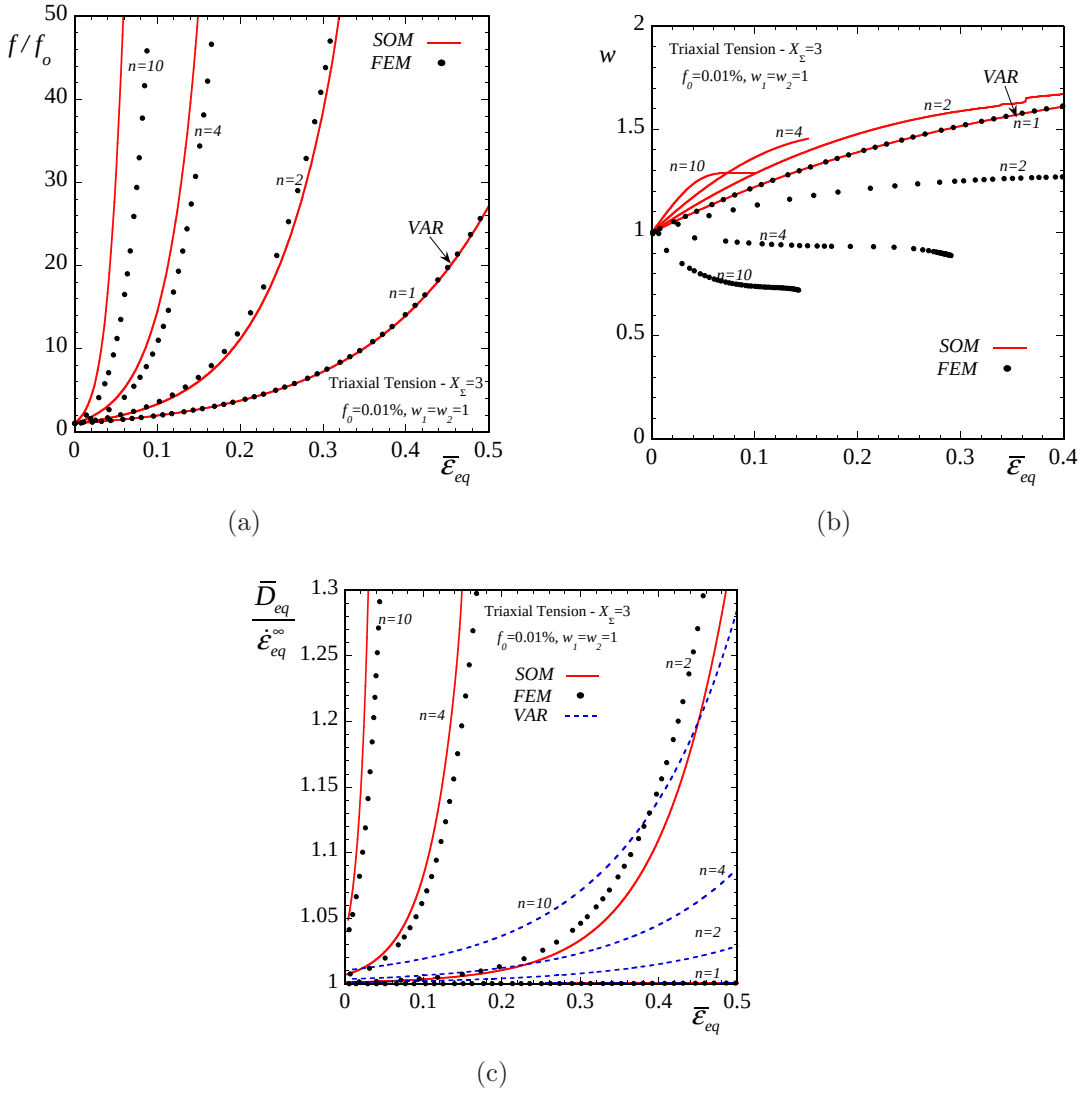

Figure 7.8: Results are shown for the evolution of the relevant microstructural and macroscopic variables for a porous material consisting of initially spherical pores embedded in a matrix with exponent $n = 1, 2, 4, 10$ as a function of the equivalent macroscopic strain $\overline{\varepsilon}_{eq}$. The initial porosity is $f_o = 0.01\%$ and the material is subjected to axisymmetric triaxial tension loading ($X_\Sigma = 3$ and $T/S = 0.727$ with $S/|S| > 0$) so that the voids become spheroidal in shape. SOM, FEM and VAR estimates are shown for the evolution of the (a) normalized porosity f/f_o, (b) the aspect ratio w and (c) the normalized axial strain-rate $\overline{D}_{eq}/\dot{\varepsilon}^{\infty}_{eq}$ ($\dot{\varepsilon}^{\infty}_{eq}$ is the corresponding strain-rate in the absence of voids). The VAR estimate for the evolution of the porosity f/f_o and the aspect ratio w is found to be independent of the nonlinear exponent n and the corresponding predictions coincide with the $n = 1$ curves.

Note that for $n = 10$, the initial porosity f_o increases approximately by *fifty* times after a total strain $\sim 5\%$, as predicted by the SOM and the FEM method. On the other hand, in Fig. 7.8b, the aspect ratio of the void w evolves only slightly, while remaining very close to its initial spherical shape. At this point, it is interesting to note that at sufficiently high nonlinearities $n > 4$ the void elongates in the direction transverse to the maximum principal stress (see that $w < 1$ for $n > 4$), as predicted by the FEM results. In other words, the initially spherical void evolves into an oblate void. This

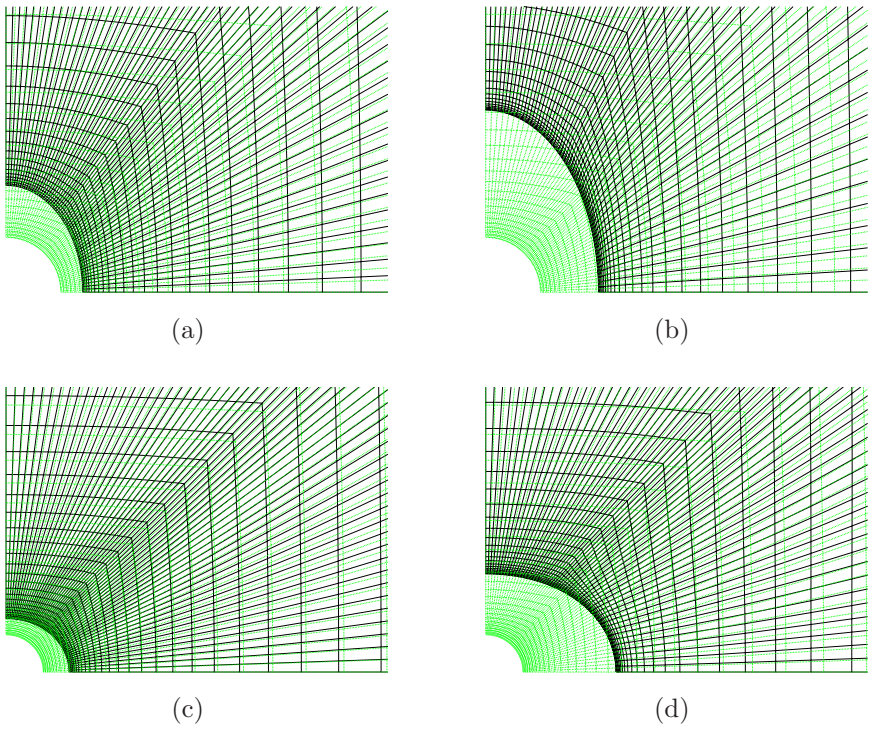

Figure 7.9: Deformed and undeformed contours for triaxial tension loading with stress triaxiality $X_\Sigma = 1$. Part(a) and (b) correspond to an exponent $n = 1$ of the matrix phase for a deformation $\overline{\varepsilon}_{eq} \sim 0.2$ and $\overline{\varepsilon}_{eq} \sim 0.4$, respectively. In turn, parts (c) and (d) correspond to an exponent $n = 10$ and $\overline{\varepsilon}_{eq} \sim 0.03$ and $\overline{\varepsilon}_{eq} \sim 0.06$, respectively.

interesting effect has initially been observed by Budiansky et al. (1982) and Fleck and Hutchinson (1986) in the dilute case. Such an effect can only be a direct consequence of the nonlinearity of the matrix phase and the high triaxiality loading, which induce a certain distribution of strains around the void resulting in this unexpected phenomenon. However, even though the SOM method is not able to capture this very nonlinear, "local" effect accurately, it remains in remarkable agreement with the FEM predictions for the normalized macroscopic strain-rate $\overline{D}_{eq}/\dot{\varepsilon}^{\infty}_{eq}$, as can be observed in Fig. 7.8c. This is a direct consequence of the fact that the SOM is able to predict accurately the evolution of porosity f/f_o, which clearly dominates over the evolution of the aspect ratio w. In contrast, the VAR estimates underestimate significantly the evolution of the porosity and thus the evolution of $\overline{D}_{eq}/\dot{\varepsilon}^{\infty}_{eq}$. The improvement of the SOM over the VAR estimates in this high triaxiality loading is attributed to the fact that the SOM is constructed such that it recovers the analytical CSA (composite sphere assemblage) result in purely hydrostatic loading, in contrast with the VAR method, which is too stiff in this case (see subsection 2.6.2).

It is interesting to include here the deformed meshes of the unit-cell for the linear $n = 1$ and nonlinear case $n = 10$, as shown in Fig. 7.9a,b and Fig. 7.9c,d, respectively. In particular, for the $n = 1$, the void is seen to elongate in the direction of the maximum principal stress (i.e., in the 3−direction). On the other hand, for $n = 10$, the void elongates transversely to the direction of the maximum principal stress. Nonetheless, it is worth noting that the porosity evolves with such a high

rate that dominates over the evolution of the shape of the void at high stress triaxialities.

7.3.2 Compressive loadings

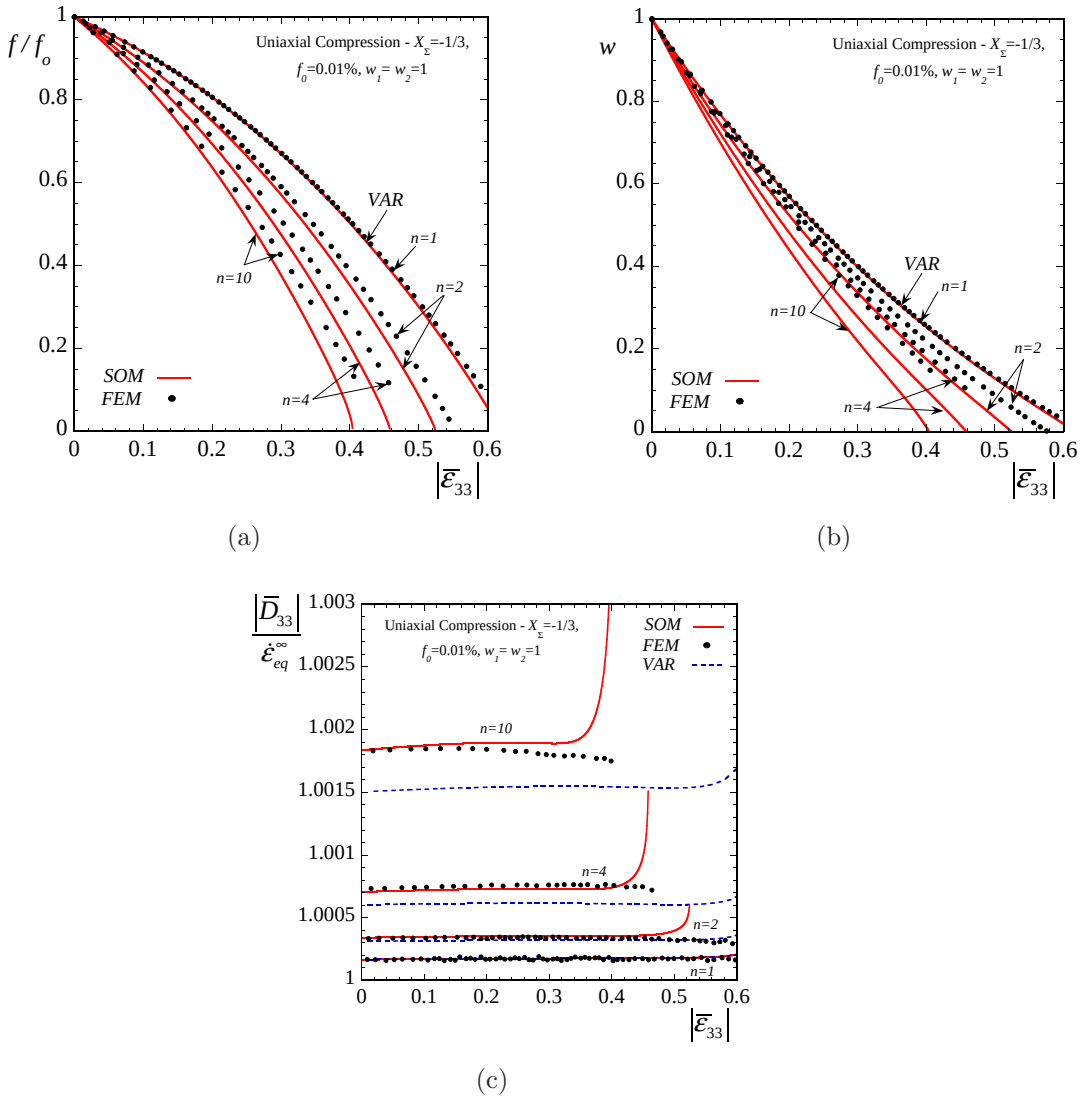

Figure 7.10: Results are shown for the evolution of the relevant microstructural and macroscopic variables for a porous material consisting of initially spherical pores embedded in a matrix with exponent $n = 1, 2, 4, 10$ as a function of the axial macroscopic strain $|\overline{\varepsilon}_{22}|$. The initial porosity is $f_o = 0.01\%$ and the material is subjected to axisymmetric triaxial compressive loadings ($X_\Sigma = -1/3$ and $T/S = 0$ with $S/|S| < 0$) so that the voids become spheroidal in shape. SOM, FEM and VAR estimates are shown for the evolution of the (a) normalized porosity f/f_o, (b) the aspect ratio w and (c) the normalized axial strain-rate $|\overline{D}_{33}|/\dot{\varepsilon}^\infty_{eq}$ ($\dot{\varepsilon}^\infty_{eq}$ is the corresponding strain-rate in the absence of voids). The VAR estimate for the evolution of the porosity f/f_o and the aspect ratio w is found to be independent of the nonlinear exponent n and the corresponding predictions coincide with the $n = 1$ curves.

Uniaxial compression loading with $X_\Sigma = -1/3$ ***or*** $T/S = 0$ ***with*** $S/|S| < 0$. Fig. 7.10 presents results for the evolution of the relevant microstructural and macroscopic variables for an

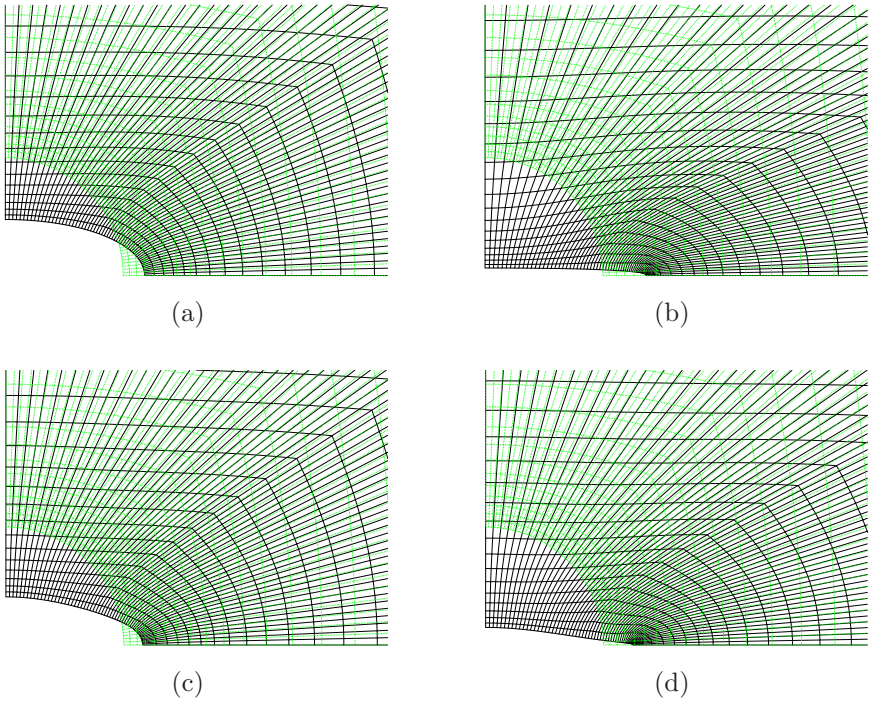

Figure 7.11: Deformed and undeformed contours for uniaxial compression loading with stress triaxiality $X_\Sigma = -1/3$. Part(a) and (b) correspond to an exponent $n = 1$ of the matrix phase for a deformation $|\bar{\varepsilon}_{33}| \sim 0.3$ and $|\bar{\varepsilon}_{33}| \sim 0.6$, respectively. In turn, parts (c) and (d) correspond to an exponent $n = 4$ and $|\bar{\varepsilon}_{33}| \sim 0.3$ and $|\bar{\varepsilon}_{33}| \sim 0.45$, respectively.

initially isotropic porous medium subjected to uniaxial compression loading. The normalized porosity f/f_o, the aspect ratio w, and the macroscopic axial component of the strain-rate $|\overline{D}_{33}|$ normalized by the equivalent strain-rate in the absence of voids $\dot{\varepsilon}^{\infty}_{eq}$ are shown as a function of the nonlinear exponent $n = 1, 2, 4, 10$ and the total axial strain $|\bar{\varepsilon}_{33}|$. In Fig. 7.10a, the SOM estimates for the normalized porosity f/f_o are found to be in good agreement with the corresponding FEM results, certainly better than the earlier VAR estimates that are independent of the nonlinearity and they all coincide with the $n = 1$ curve. As expected, both the SOM and the FEM models predict a sharp decrease of the porosity f/f_o at finite strains. As the nonlinearity increases, the point of zero porosity occurs at a lower strain $|\bar{\varepsilon}_{33}|$.

In turn, Fig. 7.10b shows corresponding estimates for the evolution of the aspect ratio w of the spheroidal void. Obviously, the initially spherical void evolves into an oblate spheroidal void which eventually becomes a pancake-shape crack ($w \to 0$). In this case, the SOM is found to overestimate the change in the aspect ratio w when compared with the FEM results which exhibit a very weak dependence on the nonlinear exponent n. It should be mentioned, however, that because of the strong nonlinearity of the matrix phase the void shape may deviate significantly from being a spheroid (see Fig. 7.11c,d). In this case, the void develops contact zones and special numerical care needs to be taken after this point in order to ensure material impenetrability. However, the objective of this work is not to perform with great accuracy the FEM calculations, rather than to provide a qualitative and, if possible, a quantitative comparison to the SOM estimates. For this reason, the FEM calculations

are terminated when the void develops these contact zones.

In order to complete the study of the porous material subjected to uniaxial compression, Fig. 7.10c shows corresponding curves for the normalized macroscopic axial strain-rate $|\overline{D}_{33}|/\dot{\varepsilon}^{\infty}_{eq}$. The SOM estimates are in good agreement with the corresponding FEM results, while they improve significantly on the earlier VAR estimates that are shown to underestimate the evolution of $\overline{D}_{33}/\dot{\varepsilon}^{\infty}_{eq}$, particularly at high nonlinearities. It is worth noting that both the SOM and the VAR estimates for $\overline{D}_{33}/\dot{\varepsilon}^{\infty}_{eq}$ exhibit a sharp increase. This is due to the rapid decrease of the aspect ratio w, which is found to close faster than the normalized porosity f/f_o. Conversely, if the porosity f/f_o decreased faster than w, as is the case for the corresponding loading in the cylindrical microstructures in Fig. 5.10, the macroscopic strain-rate $\overline{D}_{33}/\dot{\varepsilon}^{\infty}_{eq}$ would have a sharp decrease. In fact, this is the case for the compressive loadings to follow.

To make the aforementioned geometrical interpretations more clear, we include Fig 7.11 for uniaxial compression loading and for nonlinearities $n = 1, 4$. More specifically, in Fig 7.11a and 7.11b, deformed meshes are shown for the linear case $n = 1$ at two different deformation states. It is obvious in the context of this figure that in the linear case, the shape of the void remains strictly spheroidal even at very high compressive strains. On the other hand, for $n = 4$ the void remains ellipsoidal at relatively low strains (see Fig 7.11c), whereas, at higher strains, the void loses its concave shape and develops contact zones. In order to proceed further with the calculations, special care needs to be taken. However, as already mentioned in the previous paragraph, the focus in this study is not perform elaborate FEM calculations rather than to provide a quantitative validation to the SOM method.

Triaxial compression loading with $X_\Sigma = -1$ ***or*** $T/S = 0.4$ ***with*** $S/|S| < 0$. Fig. 7.12 shows evolution curves of the normalized porosity f/f_o, the aspect ratio w, and the normalized macroscopic equivalent strain-rate $|\overline{D}_{eq}|/\dot{\varepsilon}^{\infty}_{eq}$ for an initially isotropic porous medium subjected to triaxial compression loading with stress triaxiality $X_\Sigma = -1$ as a function of the total macroscopic equivalent strain $\overline{\varepsilon}_{eq}$. Fig. 7.12a shows evolution of the normalized porosity f/f_o as predicted by the SOM and the FEM methods for $n = 1, 2, 4$. In particular, the SOM is in quite good agreement with the FEM results, while it improves on the earlier VAR estimates, which are independent of the nonlinearity and hence they coincide with the $n = 1$ curve. It is worth noting that FEM results for $n = 10$ are not included here due to numerical difficulties.

Moreover, for the same reasons described in the case of uniaxial compression, where the void loses its concave shape at a certain deformation (see Fig. 7.13c,d), the FEM curve for $n = 4$ is cut off at a normalized porosity $f/f_o \sim 0.2$. In this connection, Fig. 7.12b shows corresponding results for the evolution of the aspect ratio w. The main observation in the context of this figure is that the FEM curves are shown to depend weakly on the nonlinear exponent n for this specific loading. In contrast the SOM estimates are found to overestimate the evolution of the aspect ratio when compared with the FEM results.

Even so, the corresponding SOM predictions for the normalized macroscopic strain-rate $\overline{D}_{eq}/\dot{\varepsilon}_{eq}$ are in good agreement with the FEM estimates for all the nonlinearities considered. Similarly to the case of $X_\Sigma = 1$, this last observation implies that the evolution of the aspect ratio w does not affect

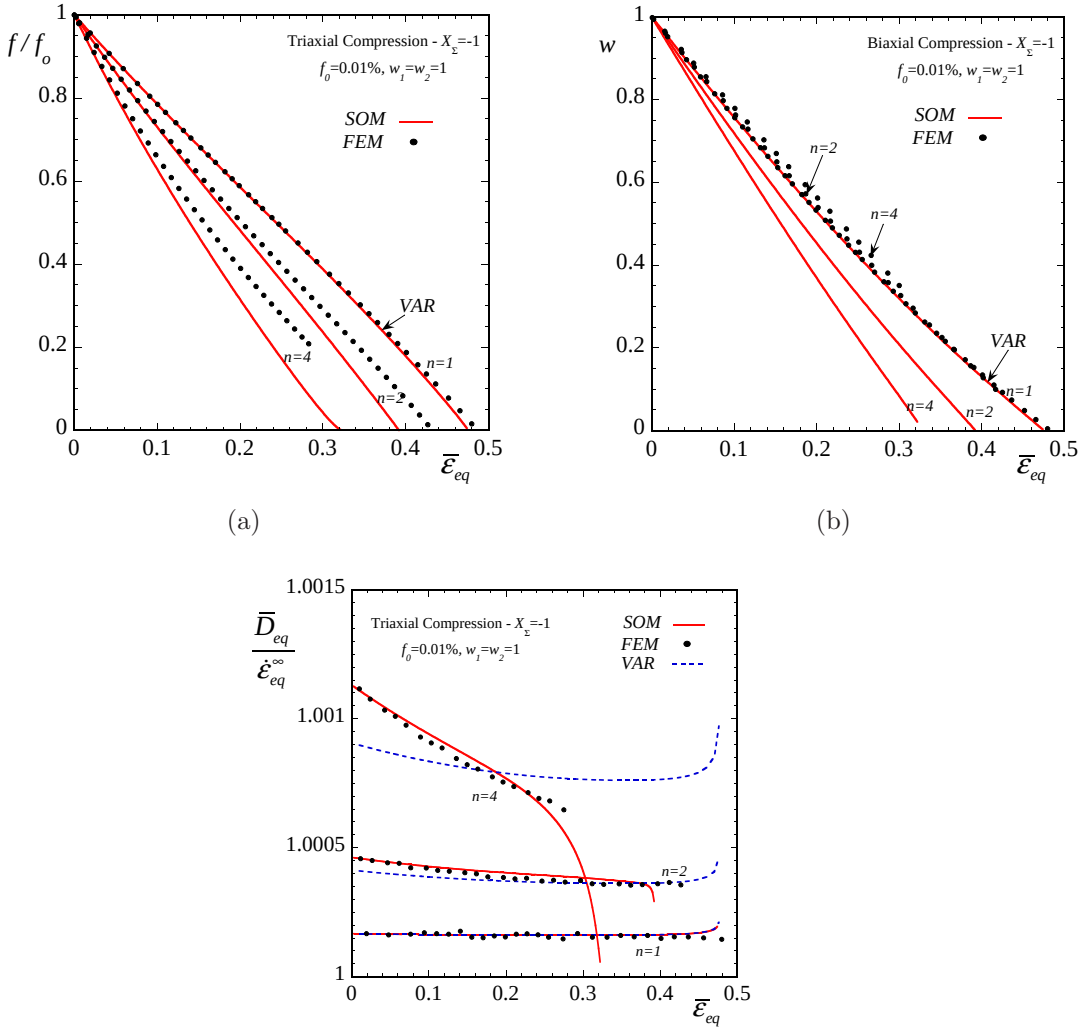

Figure 7.12: Results are shown for the evolution of the relevant microstructural and macroscopic variables for a porous material consisting of initially spherical pores embedded in a matrix with exponent $n = 1, 2, 4$ as a function of the equivalent macroscopic strain $\overline{\varepsilon}_{eq}$. The initial porosity is $f_o = 0.01\%$ and the material is subjected to axisymmetric triaxial compressive loading ($X_\Sigma = -1$ and $T/S = 0.4$ with $S/|S| < 0$) so that the voids become spheroidal in shape. SOM, FEM and VAR estimates are shown for the evolution of the (a) normalized porosity f/f_o, (b) the aspect ratio w and (c) the normalized axial strain-rate $\overline{D}_{eq}/\dot{\varepsilon}^{\infty}_{eq}$ ($\dot{\varepsilon}^{\infty}_{eq}$ is the corresponding strain-rate in the absence of voids). The VAR estimate for the evolution of the porosity f/f_o and the aspect ratio w is found to be independent of the nonlinear exponent n and the corresponding predictions coincide with the $n = 1$ curves.

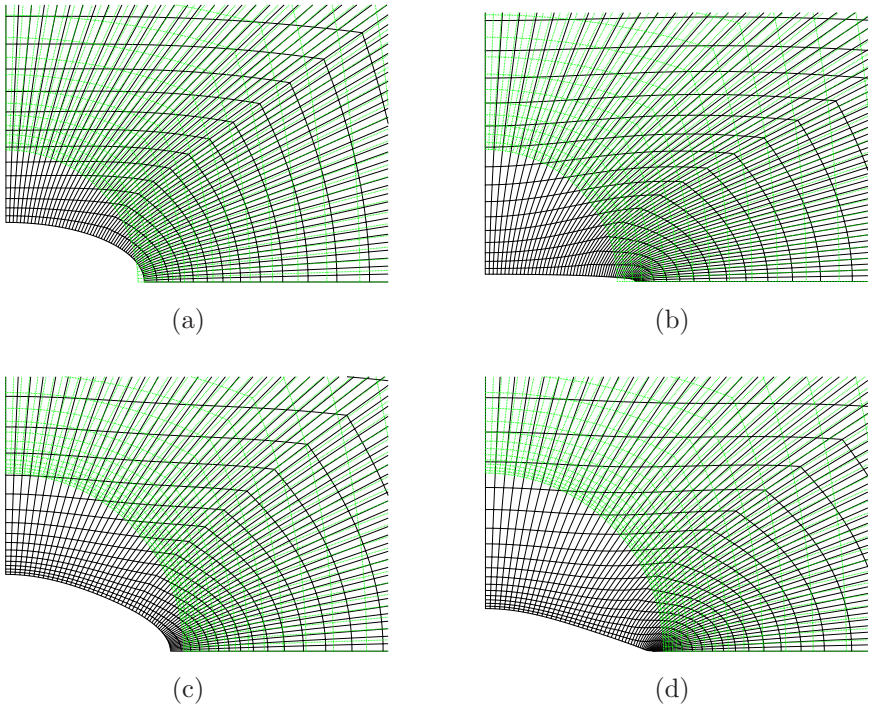

Figure 7.13: Deformed and undeformed contours for triaxial compression loading with stress triaxiality $X_\Sigma = -1$. Part(a) and (b) correspond to an exponent $n = 1$ of the matrix phase for a deformation $\overline{\varepsilon}_{eq} \sim 0.25$ and $\overline{\varepsilon}_{eq} \sim 0.45$, respectively. In turn, parts (c) and (d) correspond to an exponent $n = 4$ and $\overline{\varepsilon}_{eq} \sim 0.25$ and $\overline{\varepsilon}_{eq} \sim 0.35$, respectively.

the macroscopic behavior of the porous medium. Instead, the evolution of the porosity f/f_o is the dominant parameter in the problem. On the other hand, the VAR estimates severely underestimate the normalized macroscopic strain-rate $\overline{D}_{eq}/\dot{\varepsilon}_{eq}$, particularly at high nonlinearities. This is clearly due to the underestimation of the normalized porosity f/f_o in Fig. 7.12a. In addition, it is interesting to note that, while the VAR estimates for $\overline{D}_{eq}/\dot{\varepsilon}_{eq}$ show a sharp increase, the corresponding SOM results predict a sharp decrease. This qualitative difference between the two methods can be explained by noting that the VAR method predicts that the aspect ratio w goes faster to zero than the porosity f/f_o, whereas the opposite is true for the corresponding SOM result. Unfortunately, the FEM results are cut of before being able to extract such information.

Next, Fig. 7.13 shows deformed meshes of the unit-cell for nonlinearities $n = 1$ (parts (a) and (b)) and $n = 4$ (parts (c) and (d)). While the void remains strictly spheroidal in the linear case as shown in Fig. 7.13a and 7.13b, when $n = 4$, the void collapses at relatively low strains and after this point special care needs to be taken in order to continue further with the simulation of the unit-cell. This implies that estimating the effective response of porous media under compressive loadings is expected to be more sensitive than for tensile loadings.

Triaxial compression loading with $X_\Sigma = -3$ ***or*** $T/S = 0.727$ ***with*** $S/|S| < 0$. Fig. 7.14 shows evolution curves of the normalized porosity f/f_o, the aspect ratio w, and the normalized macroscopic equivalent strain-rate $|\overline{D}_{eq}|/\dot{\varepsilon}^{\infty}_{eq}$ for an initially isotropic porous medium subjected to triaxial compression loading with fixed stress triaxiality $X_\Sigma = -3$ as a function of the total macro-

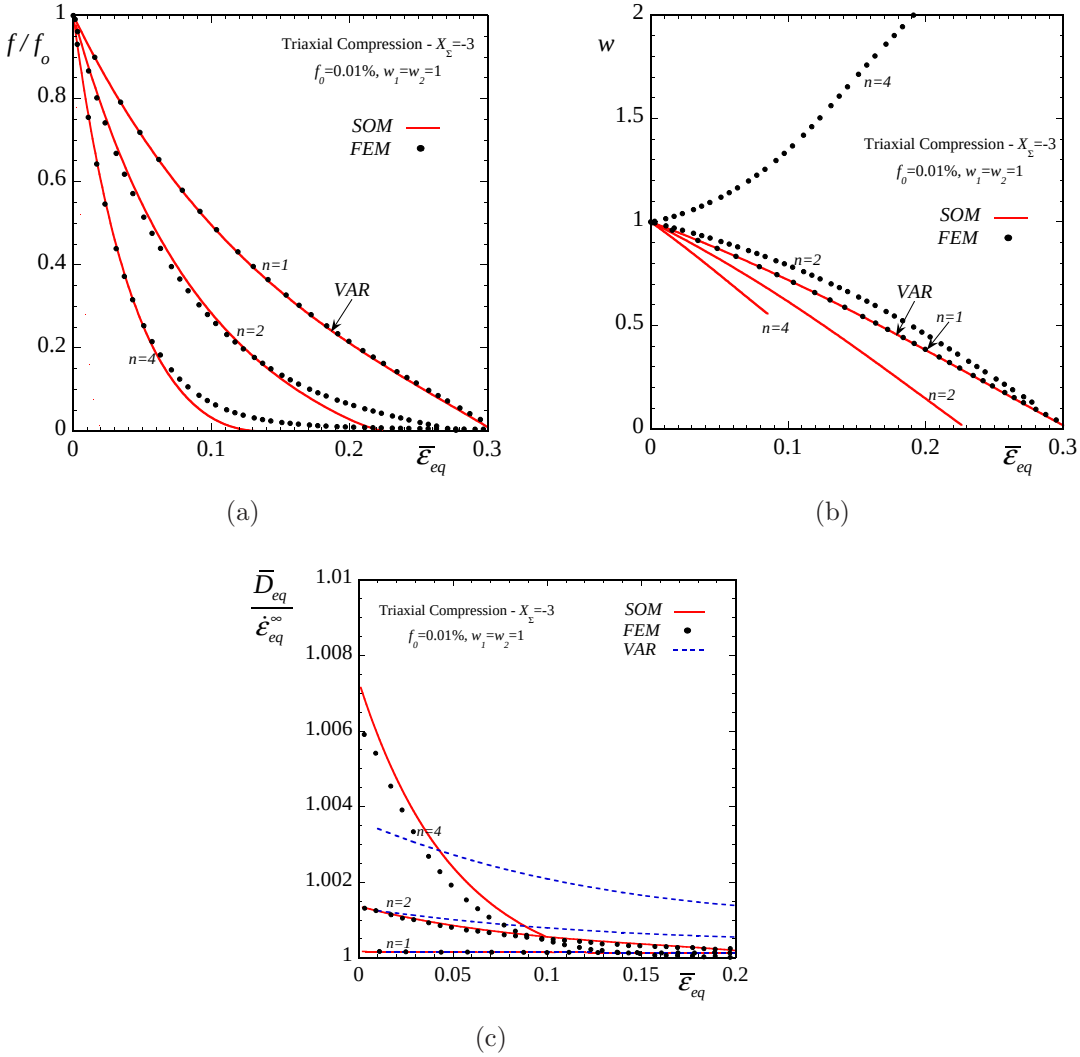

Figure 7.14: Results are shown for the evolution of the relevant microstructural and macroscopic variables for a porous material consisting of initially spherical pores embedded in a matrix with exponent $n = 1, 2, 4$ as a function of the equivalent macroscopic strain $\bar{\varepsilon}_{eq}$. The initial porosity is $f_o = 0.01\%$ and the material is subjected to axisymmetric triaxial compressive loading ($X_\Sigma = -3$ and $T/S = 0.727$ with $S/|S| < 0$) so that the voids become spheroidal in shape. SOM, FEM and VAR estimates are shown for the evolution of the (a) normalized porosity f/f_o, (b) the aspect ratio w and (c) the normalized axial strain-rate $\overline{D}_{eq}/\dot{\varepsilon}^{\infty}_{eq}$ ($\dot{\varepsilon}^{\infty}_{eq}$ is the corresponding strain-rate in the absence of voids). The VAR estimate for the evolution of the porosity f/f_o and the aspect ratio w is found to be independent of the nonlinear exponent n and the corresponding predictions coincide with the $n = 1$ curves.

scopic equivalent strain $\bar{\varepsilon}_{eq}$. Fig. 7.14a shows SOM and FEM estimates for the evolution of the normalized porosity f/f_o. Both methods are in very good agreement, at least up to $f/f_o \sim 0.1$. The main observation in the context of this figure is that both methods predict initially a sharp drop of the porosity, whereas for $f/f_o < 0.2$ the corresponding curves change slope so that the rate of decrease of the porosity becomes smaller. In turn, Fig. 7.14b shows corresponding curves for the evolution of the aspect ratio w, where the SOM estimate differs significantly from the corresponding

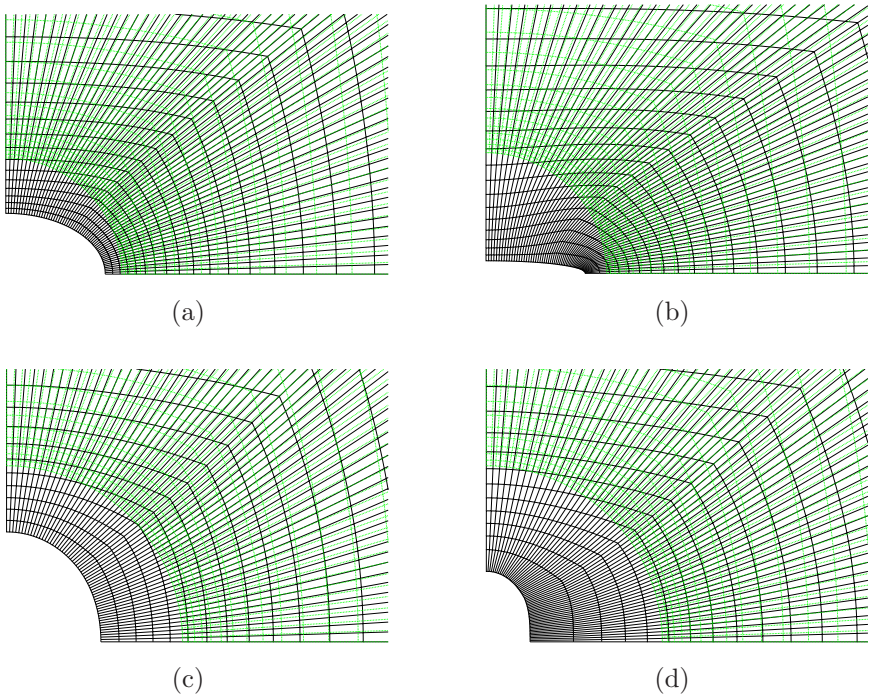

Figure 7.15: Deformed and undeformed contours for triaxial compression loading with stress triaxiality $X_\Sigma = -3$. Part(a) and (b) correspond to an exponent $n = 1$ of the matrix phase for a deformation $\bar{\varepsilon}_{eq} \sim 0.15$ and $\bar{\varepsilon}_{eq} \sim 0.27$, respectively. In turn, parts (c) and (d) correspond to an exponent $n = 4$ and $\bar{\varepsilon}_{eq} \sim 0.06$ and $\bar{\varepsilon}_{eq} \sim 0.14$, respectively.

FEM prediction. Similarly to the observations made in the context of Fig. 7.8b, the void elongates in the direction parallel to the maximum compressive stress, taking a prolate spheroidal shape (see Fig. 7.15). As already discussed previously for the case of $X_\Sigma = 3$, the SOM does not capture this effect here. However, it is interesting to observe that the corresponding SOM prediction for the normalized macroscopic strain-rate $\overline{D}_{eq}/\dot{\varepsilon}_{eq}$ is in remarkable agreement with the FEM results for all the nonlinearities considered. This observation simply implies that the evolution of the porosity f/f_o controls the effective response of the porous medium. On the contrary, the evolution of the aspect ratio w, albeit interesting in a *local* level, does not affect the behavior of the porous material in the macroscopic level. Finally note that the VAR estimates fail to capture even qualitatively the evolution of $\overline{D}_{eq}/\dot{\varepsilon}_{eq}$, particularly at high nonlinearities.

For completeness, Fig. 7.15 shows the deformed meshes of the unit-cell for $n = 1$ (parts (a) and (b)) and $n = 4$ (parts (c) and (d)). Looking at Fig. 7.15a and 7.15b, we observe that the porosity decreases during the deformation process, while the void shrinks in the direction of the maximum compressive stress. In contrast, for $n = 4$, we verify the observation initially made by Budiansky et al. (1982), where it was found that the void shrinks in the direction, which is parallel to the maximum compressive stress, inducing a prolate shape for the void, as shown in Fig. 7.15c and 7.15d. Note also the huge deformation of the elements in Fig. 7.15d, which probably implies that after this point, it is necessary to remesh the unit-cell for more accurate results.

7.3.3 Brief summary

In the previous subsections, we made an attempt to validate the SOM model for several nonlinearities and stress triaxialities by comparing it with FEM results. As a general remark, the SOM is capable of predicting with sufficient accuracy the evolution of the relevant microstructural and macroscopic variables in the context of initially isotropic porous media subjected to axisymmetric loading conditions.

In particular, the SOM has been studied for tensile loading conditions, which induce, in general, an increase of the initial porosity. While for lower stress triaxialities (e.g., uniaxial tension) the porosity evolves slightly, at high stress triaxialities the evolution of the porosity can be dramatic. As a consequence of the fact that the SOM is constructed to recover the analytical hydrostatic shell result (see relation (2.196)), it improves significantly on the earlier VAR estimates, which fail to provide even qualitative agreement with the FEM results at high stress triaxialities.

In addition, it has been shown that the SOM estimates for the evolution of the aspect ratio of the void shape are sufficiently accurate for low stress triaxialities and high nonlinearities, when compared with the FEM predictions. However, at high stress triaxialities and nonlinearities, the FEM predict an elongation of the void in the direction which is transverse to the maximum principal stress. Such a counterintuitive result has already been known in the literature since the early work of Budiansky et al. (1982). Nonetheless, this highly nonlinear phenomenon does not affect the macroscopic behavior of the porous material. In contrast, at high stress triaxialities the evolution of the porosity controls the effective response of the material. This is the main reason that the SOM delivers accurate results for the macroscopic strain-rates even though it fails to predict accurately the evolution of the aspect ratio at high stress triaxialities.

Similarly to the tensile loadings, the SOM has been validated under compressive loadings, where the evolution of porosity has been found to dominate over the evolution of the aspect ratio at high triaxial loadings. Furthermore, it is worth noting that under compressive loadings the FEM method requires special care when the porosity reaches low values. The reason for this lies in the large distortion of the elements observed in this case. Therein lies the importance of the homogenization methods that can provide estimates even at very low values of the porosity.

7.4 Comparison of existing models for spheroidal voids

In this section, the "second-order" method (SOM) is compared with the Flandi and Leblond (2005) model (FL), the "variational" method (VAR) and finite element calculations (FEM) for the determination of the evolution of microstructure in porous media consisting of initially spherical voids. As already discussed in detail in the previous section, this comparison is meaningful for sufficiently small porosities, i.e., $f_o = 0.01\%$ and axisymmetric loading conditions as defined by relation (7.6). In fact, we will make use of the previous results, where, now, we will also include the FL and the VAR model for all the microstructural variables. These methods are compared for a nonlinear exponent $n = 10$, and stress triaxialities $X_\Sigma = \pm 1/3, \pm 1, \pm 3$, which correspond to stress ratio $T/S = 0, 0.4, 0.727$ (with

$S/|S| \lesseqgtr 0$), respectively.

Before proceeding with the discussion of the results, it is important to emphasize that the FL results are obtained by making use of the value $q = 1.47$ instead of $q = 1$ for the parameter introduced in section 3.3. This parameter has been initially introduced by Tvergaard (1981) in the model of Gurson (1977) in order to achieve a better agreement between the numerical and approximate criteria. However, when $q \neq 1$, the FL model exhibits a softer behavior than the spherical shell under purely hydrostatic loading (see exact result (2.196)). On the other hand, if the value $q = 1$ is used in the calculations, the analytical hydrostatic result is recovered, but the corresponding predictions of the FL model become very stiff for moderate and high triaxialities (e.g., $X_\Sigma = 1,3$) and consequently they do not compare well with the FEM results. Such results will not be included in this study, instead the use of the value $q = 1.47$ will be used in accordance with the initial proposal of the authors in their published manuscript (Flandi and Leblond, 2005).

7.4.1 Tensile loadings: comparison between several models

In this subsection, we present corresponding results for tension loadings as predicted by the various methods discussed previously. In particular, we consider a porous material with initially spherical voids subjected to axisymmetric boundary conditions defined by relations (7.6).

Uniaxial tension loading with $X_\Sigma = 1/3$ ***or*** $T/S = 0$ ***with*** $S/|S| > 0$. First, the uniaxial tension loading is considered in Fig. 7.16, where the relevant evolution variables are shown as a function of the axial strain $\overline{\varepsilon}_{33}$ for a nonlinear exponent $n = 10$. The main observation in the context of this figure is that, for the evolution of the normalized porosity f/f_o, the SOM is in much better agreement with the FEM predictions than the FL and the VAR models. On the contrary, the SOM overestimates the evolution of the aspect ratio w, while the FL method is in very good agreement with the FEM results. The VAR method underestimates the evolution of w, as already expected. Looking at Fig. 7.16c, the SOM estimates for the normalized axial strain-rate $\overline{D}_{33}/\dot{\varepsilon}^{\infty}_{eq}$ ($\dot{\varepsilon}^{\infty}_{eq}$ is the strain-rate in the absence of voids) improve significantly on the VAR results by giving very good agreement with the FEM predictions. In contrast, the FL method exhibits a somewhat different qualitative behavior from the FEM and the SOM results.

Triaxial tension loading with $X_\Sigma = 1$ ***or*** $T/S = 0.4$ ***with*** $S/|S| > 0$. In the sequel, analogous evolution curves are shown for triaxial tension loading for a stress triaxiality $X_\Sigma = 1$. The evolution variables are plotted as a function of the total equivalent strain $\overline{\varepsilon}_{eq}$ for a nonlinear exponent $n = 10$. In Fig. 7.17a, the SOM and the FL estimates for the evolution of the normalized porosity f/f_o are in very good agreement with the FEM predictions. On the other hand, the VAR method underestimates significantly the evolution of the porosity f/f_o, as already expected. In turn, Fig. 7.17b shows corresponding curves for the evolution of the aspect ratio w, where the FL model is found to be in good agreement with FEM predictions. In contrast, the SOM and the VAR overestimate the evolution of w. Even so, the SOM estimates for the normalized equivalent macroscopic strain-rate $\overline{D}_{eq}/\dot{\varepsilon}^{\infty}_{eq}$ remain in good agreement with the FEM and the FL results. In contrast, the VAR method still provides a very poor estimate in this case, which is a direct consequence of the inaccurate pre-

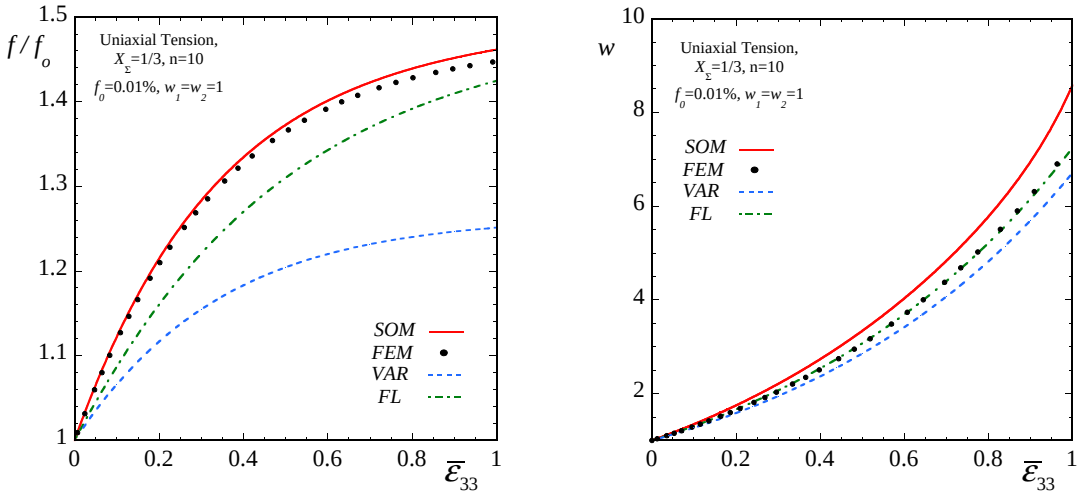

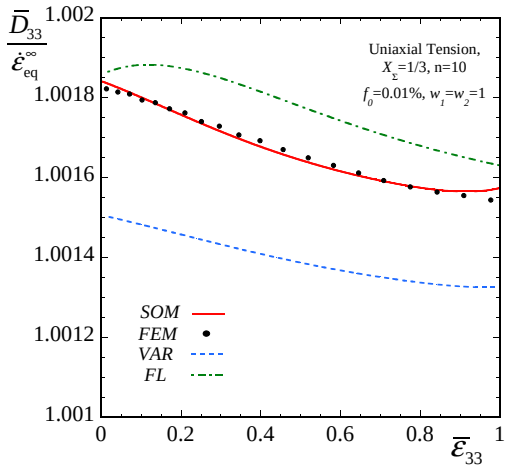

Figure 7.16: Results are shown for the evolution of the relevant microstructural and macroscopic variables for a porous material consisted of initially spherical pores embedded in a matrix with exponent $n = 10$ as a function of the axial macroscopic strain $\bar{\varepsilon}_{33}$. The initial porosity is $f_o = 0.01\%$ and the material is subjected to axisymmetric uniaxial tension loading ($X_\Sigma = 1/3$ and $T/S = 0$ with $S/|S| > 0$) so that the voids evolve into prolate spheroids with aspect ratio $w_1 = w_2 = w > 1$. The SOM and the VAR estimates are compared with FEM results and the recent Flandi-Leblond (2005) model (FL) for the evolution of the (a) porosity f, (b) the aspect ratio w and (c) the normalized axial strain-rate $\overline{D}_{33}/\dot{\varepsilon}^{\infty}_{eq}$ ($\dot{\varepsilon}^{\infty}_{eq}$ is the corresponding strain-rate in the absence of voids).

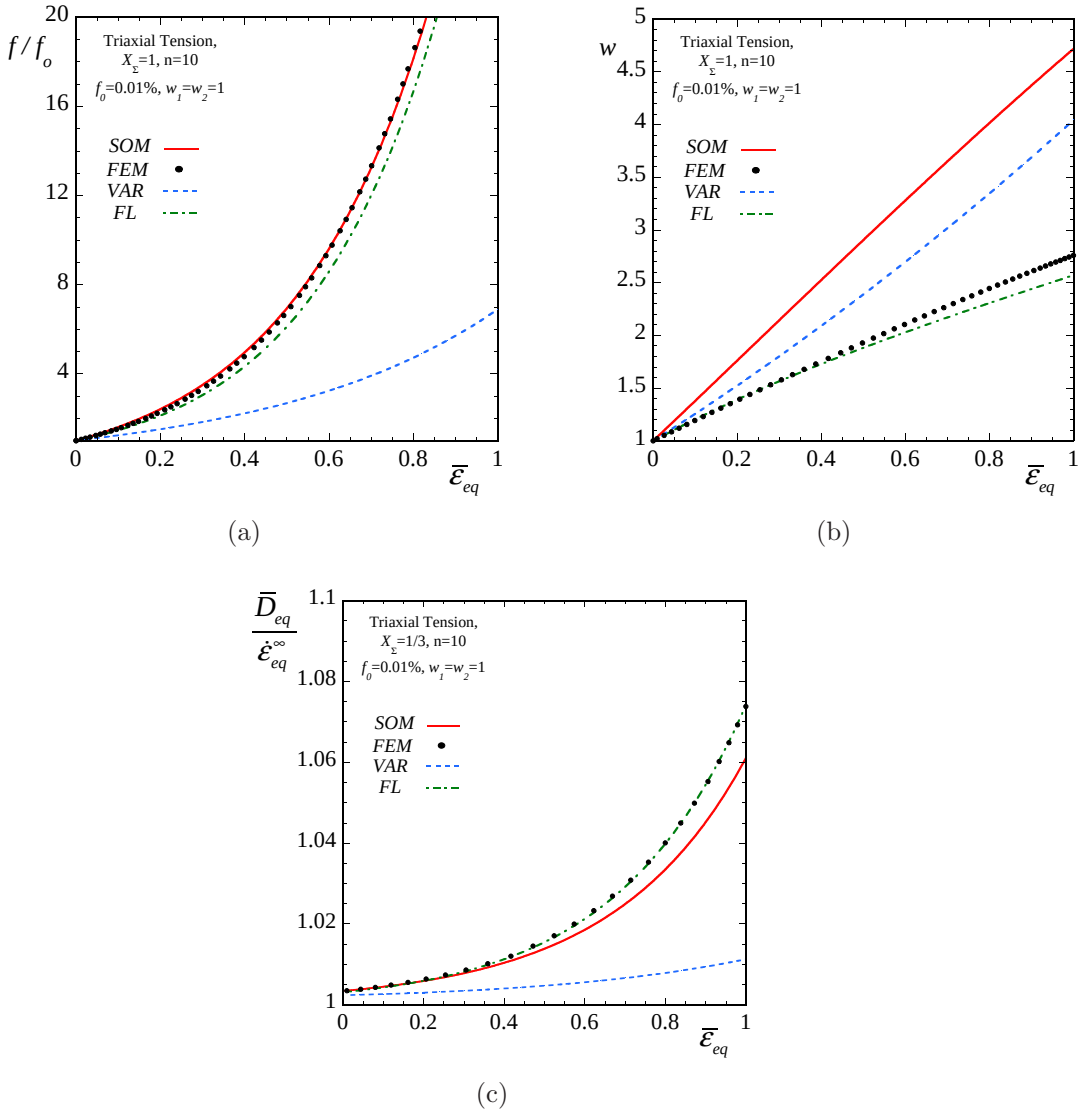

Figure 7.17: Results are shown for the evolution of the relevant microstructural and macroscopic variables for a porous material consisted of initially spherical pores embedded in a matrix with exponent $n = 10$ as a function of the axial macroscopic strain $\bar{\varepsilon}_{eq}$. The initial porosity is $f_o = 0.01\%$ and the material is subjected to axisymmetric triaxial tension loading ($X_\Sigma = 1$ and $T/S = 0.4$ with $S/|S| > 0$) so that the voids evolve into prolate spheroids with aspect ratio $w_1 = w_2 = w > 1$. The SOM and the VAR estimates are compared with FEM results and the recent Flandi-Leblond (2005) model (FL) for the evolution of the (a) porosity f, (b) the aspect ratio w and (c) the normalized axial strain-rate $\overline{D}_{eq}/\dot{\varepsilon}^{\infty}_{eq}$ ($\dot{\varepsilon}^{\infty}_{eq}$ is the corresponding strain-rate in the absence of voids).

diction of the evolution of the porosity. This result implies that the evolution of the porosity controls the effective response of the porous material at this moderate stress triaxiality, while the effect of the evolution of the aspect ratio w is minor in this case.

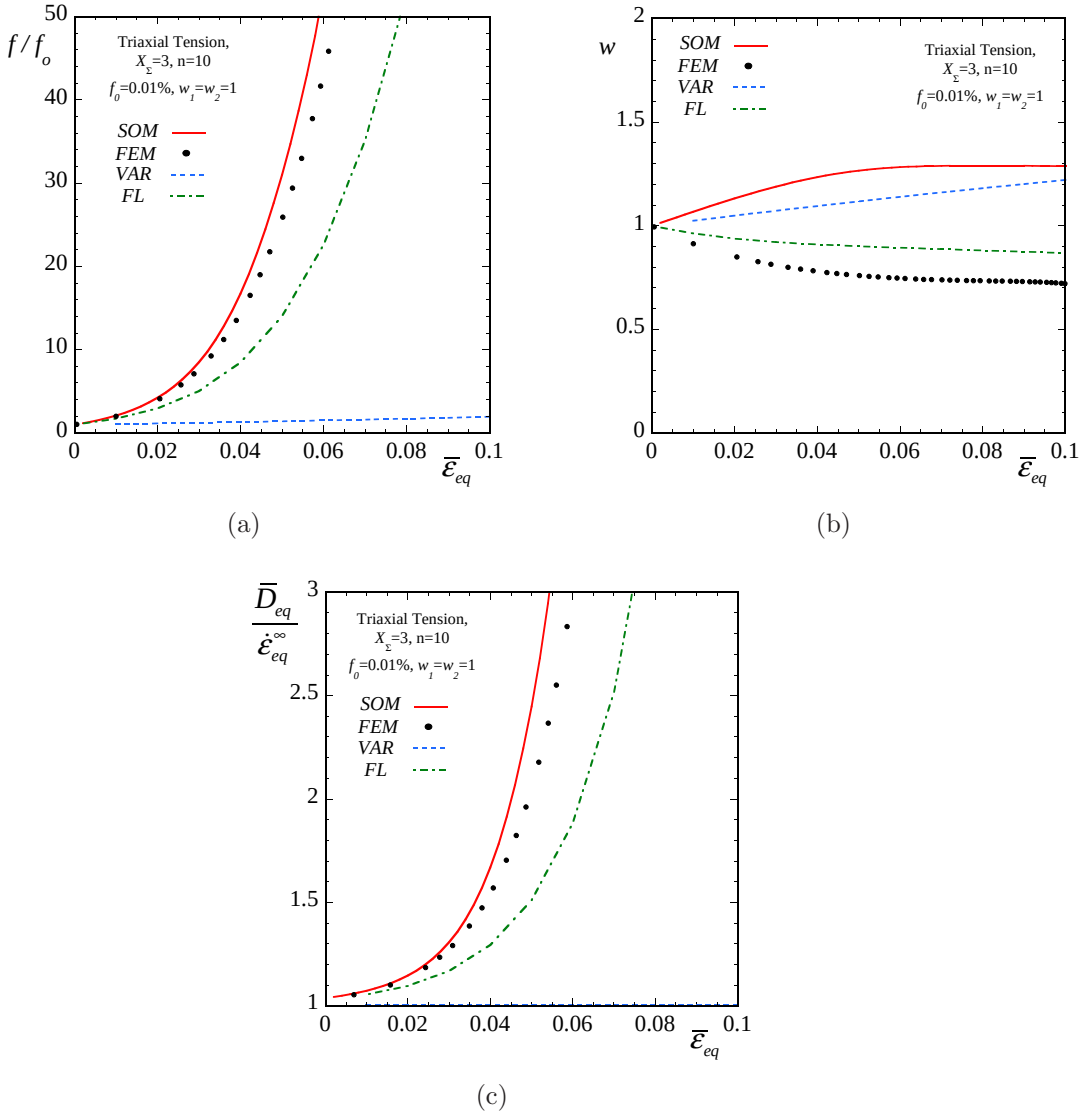

Figure 7.18: Results are shown for the evolution of the relevant microstructural and macroscopic variables for a porous material consisted of initially spherical pores embedded in a matrix with exponent $n = 10$ as a function of the axial macroscopic strain $\bar{\varepsilon}_{eq}$. The initial porosity is $f_o = 0.01\%$ and the material is subjected to axisymmetric triaxial tension loading ($X_\Sigma = 3$ and $T/S = 0.727$ with $S/|S| > 0$) so that the voids evolve into prolate spheroids with aspect ratio $w_1 = w_2 = w > 1$. The SOM and the VAR estimates are compared with FEM results and the recent Flandi-Leblond (2005) model (FL) for the evolution of the (a) porosity f, (b) the aspect ratio w and (c) the normalized axial strain-rate $\overline{D}_{eq}/\dot{\varepsilon}^{\infty}_{eq}$ ($\dot{\varepsilon}^{\infty}_{eq}$ is the corresponding strain-rate in the absence of voids).

Triaxial tension loading with $X_\Sigma = 3$ ***or*** $T/S = 0.727$ ***with*** $S/|S| > 0$. Finally, the series of evolution plots for tension loadings is completed by corresponding results for a stress triaxiality $X_\Sigma = 3$, as shown in Fig. 7.18. In this figure, it is obvious that the normalized porosity f/f_o evolves

rapidly, in contrast to the aspect ratio w, which takes values very close to unity, and hence remains almost spherical. In particular, the SOM is in very good agreement with the FEM predictions, while the FL tends to underestimate the evolution of the porosity f/f_o, although it is found to behave very well as far as the evolution of the aspect ratio w is concerned. As already discussed in the previous section, for this high triaxiality loading, the void tends to elongate in the direction transverse to the maximum principal stress, leading to an oblate shape for the void, as already discussed in the context of Fig. 7.8. This effect is captured by the FL model, which is found to be in qualitative agreement with the FEM results. On the other hand, even though the SOM does not predict accurately the evolution of w, it remains in good agreement with the FEM results, certainly better than the FL estimates, for the evolution of the equivalent macroscopic strain-rate $\overline{D}_{eq}/\dot{\varepsilon}^{\infty}_{eq}$. In contrast, the VAR method severely underestimates the evolution of the porosity f/f_o and as a consequence fails to predict accurately the evolution of the normalized macroscopic strain-rate $\overline{D}_{eq}/\dot{\varepsilon}^{\infty}_{eq}$ and thus the effective response of the porous medium. Similarly to the previous figure, the main conclusion in the context of this figure is that the evolution of the porosity f/f_o is predominant over the evolution of the aspect ratio w and hence, it controls the overall behavior of the composite.

7.4.2 Compressive loadings: comparison between several models

.

In this subsection, we present corresponding results for compression loadings. In particular, we consider a porous material with initially spherical voids subjected to axisymmetric loading conditions defined by relations (7.6).

Uniaxial Compression loading with $X_\Sigma = -1/3$ ***or*** $T/S = 0$ ***with*** $S/|S| < 0$. Initially, we consider uniaxial compression loading conditions ($X_\Sigma = -1/3$) with nonlinear exponent $n = 10$, as shown in Fig. 7.19. Part (a), provides comparisons of the various models for the evolution of the normalized porosity f/f_o as a function of the absolute macroscopic axial strain $|\bar{\varepsilon}_{33}|$. The main observation in the context of this figure is that, while the SOM, the FL and the FEM predictions are in good agreement during the whole deformation process (up to the closure of the porosity), the VAR method overestimates significantly the evolution of the porosity almost by $\sim 50\%$. On the contrary, in Fig. 7.19b, all the methods exhibit the same qualitative behavior for the evolution of the aspect ratio w. Nonetheless, they progressively deviate from each other, with the VAR estimate delivering the highest values for w. Fig.7.19c shows corresponding plots for the normalized macroscopic axial strain-rate $\overline{D}_{33}/\dot{\varepsilon}^{\infty}_{eq}$ ($\dot{\varepsilon}^{\infty}_{eq}$ is the strain-rate in the absence of voids). In this figure, the SOM and the FEM predictions are in very good agreement, whereas the corresponding FL results are found to be qualitatively different than the previous two methods. The VAR method, in turn, underestimates the evolution of $\overline{D}_{33}/\dot{\varepsilon}^{\infty}_{eq}$ as a consequence of the poor estimation for the evolution of the porosity.

Triaxial compression loading with $X_\Sigma = -1$ ***or*** $T/S = 0.4$ ***with*** $S/|S| < 0$. Fig. 7.20 provides evolution plots for a stress triaxiality $X_\Sigma = -1$ as a function of the equivalent macroscopic strain $\bar{\varepsilon}_{eq}$ for a nonlinear exponent $n = 4$. The main observation in the context of this figure is that, while initially the SOM and the FL predictions for the normalized porosity f/f_o are in very

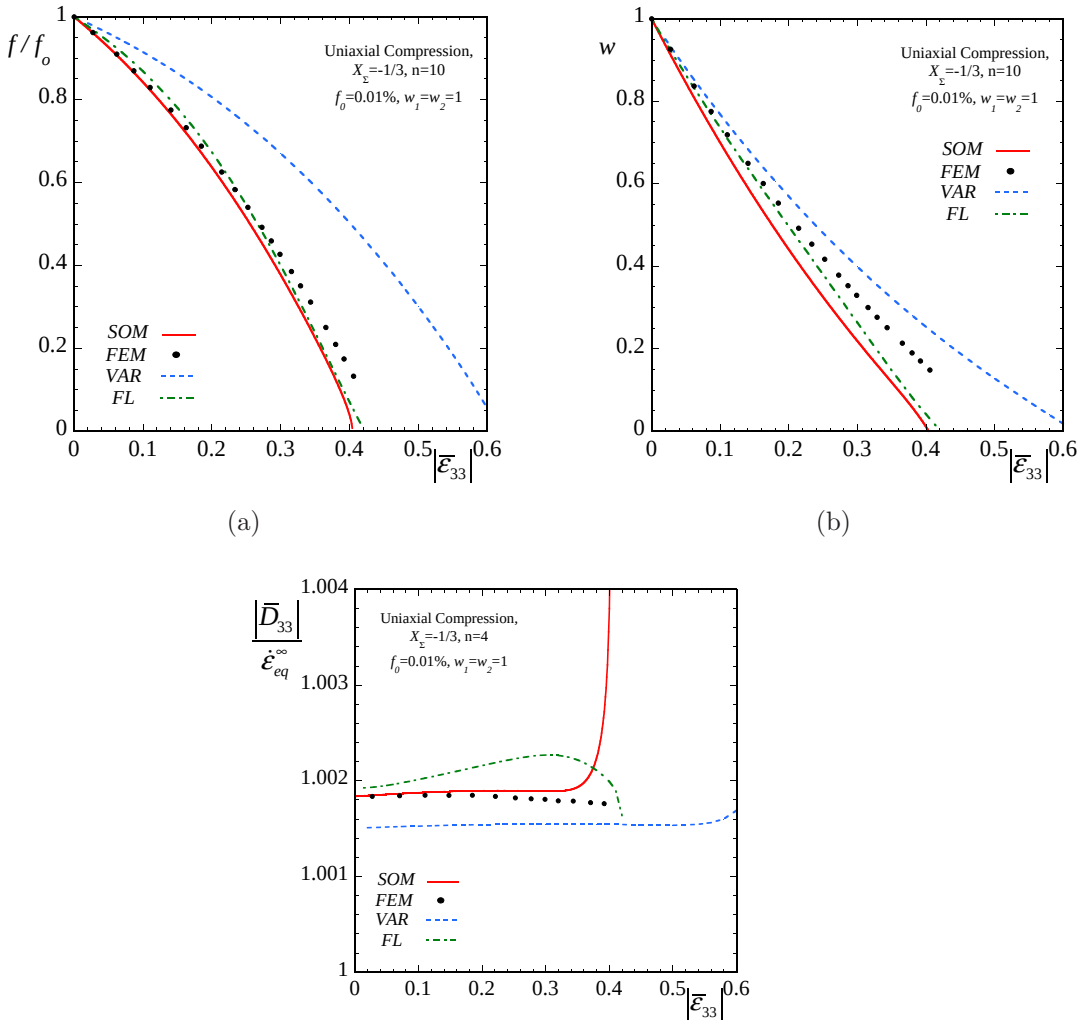

Figure 7.19: Results are shown for the evolution of the relevant microstructural and macroscopic variables for a porous material consisted of initially spherical pores embedded in a matrix with exponent $n = 10$ as a function of the axial macroscopic strain $|\bar{\varepsilon}_{33}|$. The initial porosity is $f_o = 0.01\%$ and the material is subjected to axisymmetric uniaxial compression loading ($X_\Sigma = -1/3$ and $T/S = 0$ with $S/|S| < 0$) so that the voids evolve into oblate spheroids with aspect ratio $w_1 = w_2 = w < 1$. The SOM and the VAR estimates are compared with FEM results and the recent Flandi-Leblond (2005) model (FL) for the evolution of the (a) porosity f, (b) the aspect ratio w and (c) the normalized axial strain-rate $\overline{D}_{33}/\dot{\varepsilon}^{\infty}_{eq}$ ($\dot{\varepsilon}^{\infty}_{eq}$ is the corresponding strain-rate in the absence of voids).

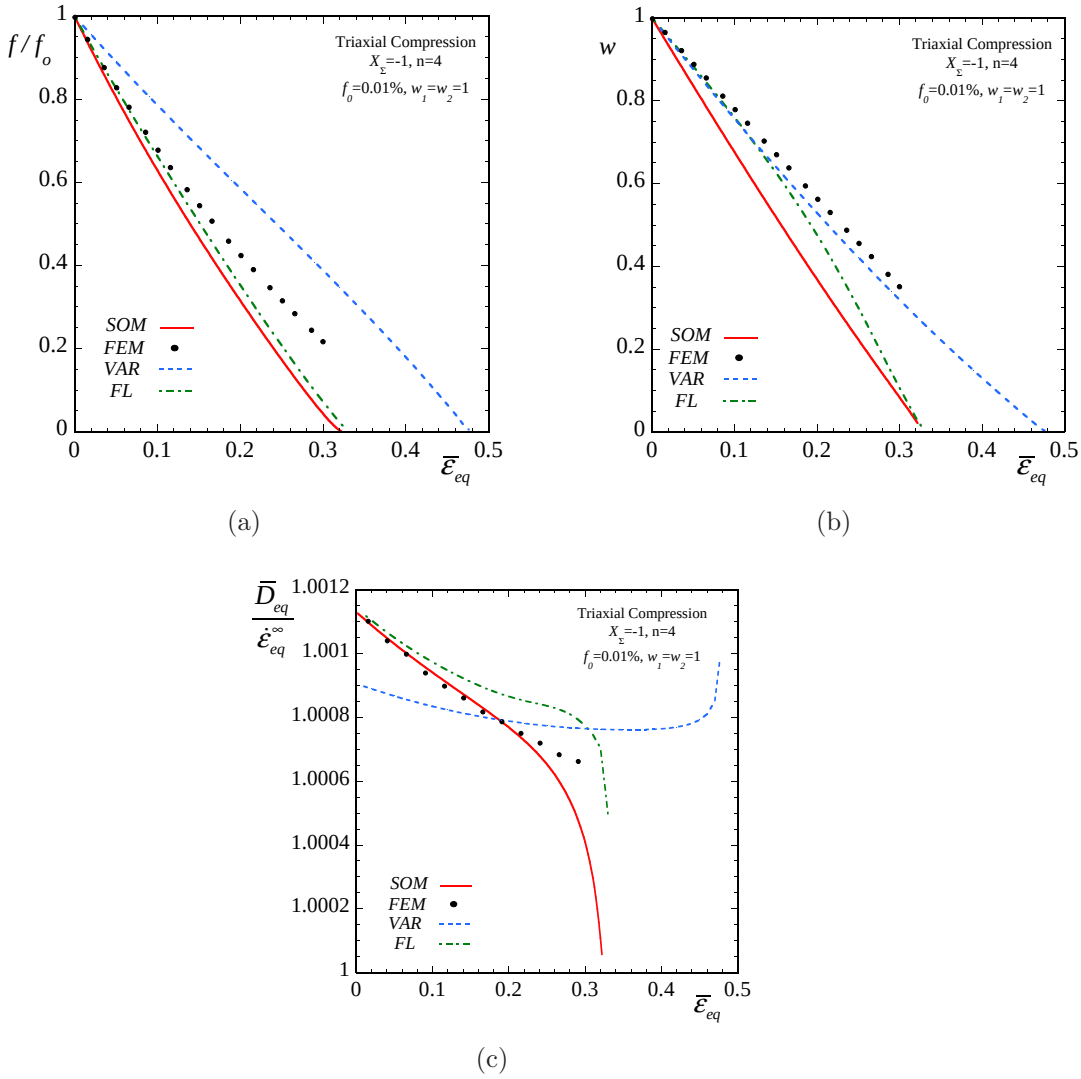

Figure 7.20: Results are shown for the evolution of the relevant microstructural and macroscopic variables for a porous material consisted of initially spherical pores embedded in a matrix with exponent $n = 4$ as a function of the axial macroscopic strain $\bar{\varepsilon}_{eq}$. The initial porosity is $f_o = 0.01\%$ and the material is subjected to axisymmetric triaxial compression loading ($X_\Sigma = 1$ and $T/S = 0.4$ with $S/|S| < 0$) so that the voids evolve into oblate spheroids with aspect ratio $w_1 = w_2 = w < 1$. The SOM and the VAR estimates are compared with FEM results and the recent Flandi-Leblond (2005) model (FL) for the evolution of the (a) porosity f, (b) the aspect ratio w and (c) the normalized axial strain-rate $\overline{D}_{eq}/\dot{\varepsilon}^{\infty}_{eq}$ ($\dot{\varepsilon}^{\infty}_{eq}$ is the corresponding strain-rate in the absence of voids).

good agreement with the FEM results, as the porosity decreases, the SOM and FL remain sharper predicting a closure of the porosity at strains $\sim 30\%$. In contrast, the FEM results — due to reasons already explained in the context of Fig. 7.12 — are abruptly cut off. This occurs because the void boundary in the FEM unit-cell calculation loses its concave shape and develops contact zones (see Fig. 7.13). This behavior is also observed in the corresponding FEM curve for the evolution of the aspect ratio w in Fig. 7.20b. In this figure, the VAR estimate is in better agreement with the FEM results than the rest of the methods. However, this agreement is believed to be a consequence of the loading conditions and the nonlinearity considered here. It is worth noting that although the FL estimate is initially in good agreement with the FEM and the VAR estimate, it deteriorates as the aspect ratio w becomes smaller and finally, approaches the corresponding SOM estimate.

The set of results for $X_\Sigma = -1$ is completed with the curve for the evolution of the normalized macroscopic equivalent strain-rate $\overline{D}_{eq}/\dot{\varepsilon}^{\infty}_{eq}$. It is interesting to note that despite the fact that the SOM provides the worst prediction than the rest of the methods for the evolution of the aspect ratio, it is in very good agreement with the FEM results for the evolution of $\overline{D}_{eq}/\dot{\varepsilon}^{\infty}_{eq}$. This is a direct consequence of the fact that the evolution of the void shape has a minor effect on the overall behavior of the porous medium, as already remarked in the context of high-triaxiality plots of the previous subsections. In contrast, the VAR estimate does not exhibit the same qualitative features with the SOM and the FL models in this last curve. Note the sharp change of the VAR curve upwards, contrary to the sharp decrease of the SOM and the FL curves. Definite conclusions cannot be drawn, however, for the FEM curve due to the cut off point. The sharp decrease of the $\overline{D}_{eq}/\dot{\varepsilon}^{\infty}_{eq}$ is due to the fact that the porosity f/f_o approaches the zero value faster than the aspect ratio w does. In contrast, in the VAR method, the aspect ratio w decreases faster than the porosity f/f_o and thus the slope of $\overline{D}_{eq}/\dot{\varepsilon}^{\infty}_{eq}$ exhibits a sharp increase.

Triaxial compression loading with $X_\Sigma = -3$ ***or*** $T/S = 0.727$ ***with*** $S/|S| < 0$. Finally, Fig. 7.21 shows evolution plots for a stress triaxiality $X_\Sigma = -3$ as a function of the equivalent macroscopic strain $\bar{\varepsilon}_{eq}$ for a nonlinear exponent $n = 4$. In particular, part (a) shows evolution of the normalized porosity f/f_o, where all but the VAR methods are in very good agreement. As already anticipated, for high triaxialities the VAR method overestimates the evolution of the porosity due to the lack of reproducing the exact hydrostatic solution of the spherical shell problem (compare relations (2.196) and (2.197)). In Fig. 7.21b, in turn, the various models deliver very different estimates for the evolution of the aspect ratio w, with the FL model being in closer agreement with the FEM results. This disagreement between the various methods is due to the fact that the void elongates in a direction parallel to the maximum compressive principal stress (see previous discussion for high triaxialities), leading to a prolate shape for the void. This is a "local" phenomenon that occurs at sufficiently high triaxialities and nonlinearities. However, it is interesting to note that even though the SOM provides a poor estimate for the aspect ratio w, it predicts with remarkable accuracy the normalized macroscopic equivalent strain-rate $\overline{D}_{eq}/\dot{\varepsilon}^{\infty}_{eq}$ when compared with the corresponding FEM and FL results. This "paradox" can be easily explained by the fact that for high triaxiality loadings the evolution of porosity f/f_o is so dramatic that it completely controls the effective behavior of the porous material, whereas the corresponding evolution of the aspect ratio w is significant only at

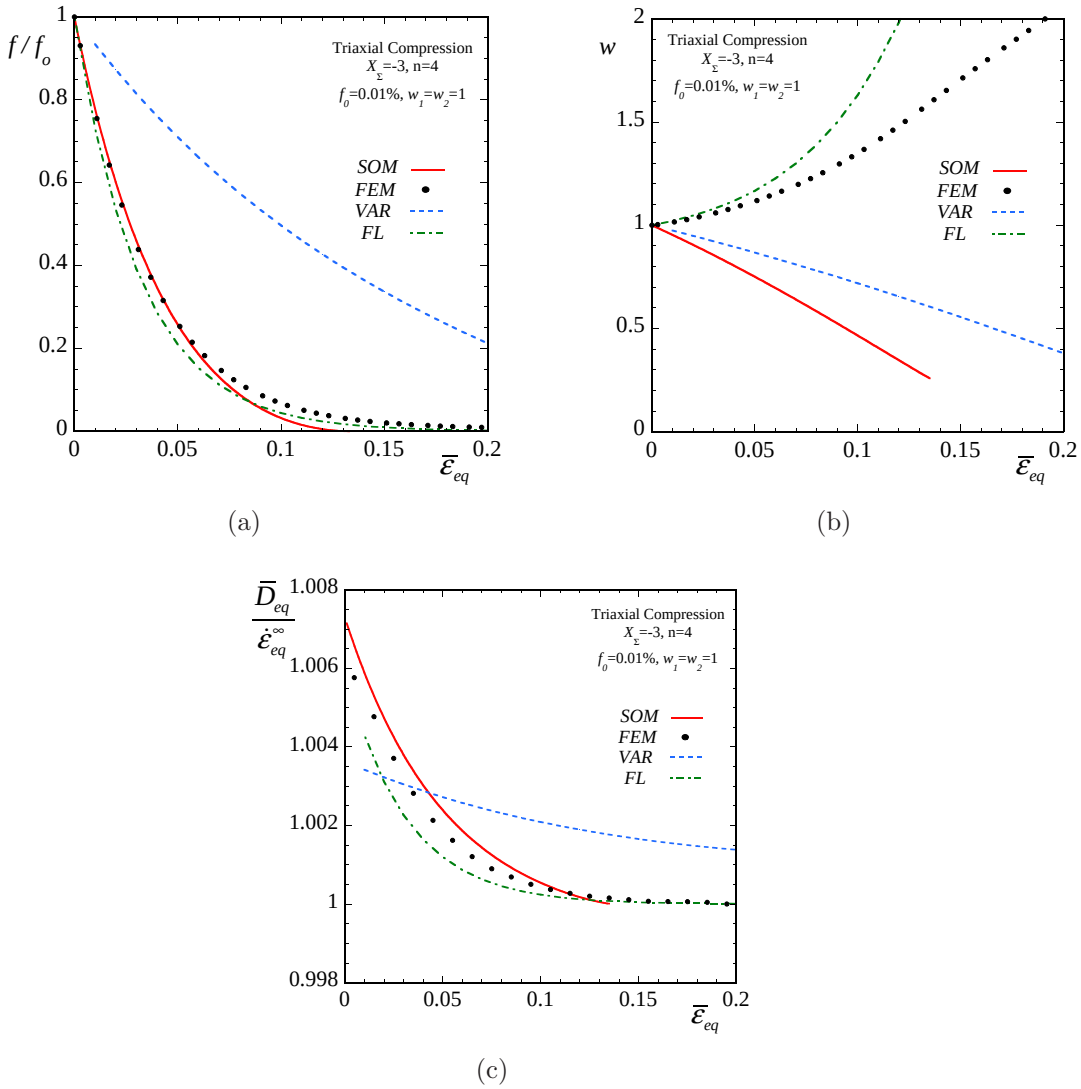

Figure 7.21: Results are shown for the evolution of the relevant microstructural and macroscopic variables for a porous material consisted of initially spherical pores embedded in a matrix with exponent $n = 4$ as a function of the axial macroscopic strain $\bar{\varepsilon}_{eq}$. The initial porosity is $f_o = 0.01\%$ and the material is subjected to axisymmetric triaxial compression loading ($X_\Sigma = 3$ and $T/S = 0.727$ with $S/|S| < 0$) so that the voids evolve into oblate spheroids with aspect ratio $w_1 = w_2 = w < 1$. The SOM and the VAR estimates are compared with FEM results and the recent Flandi-Leblond (2005) model (FL) for the evolution of the (a) porosity f, (b) the aspect ratio w and (c) the normalized axial strain-rate $\overline{D}_{eq}/\dot{\varepsilon}^{\infty}_{eq}$ ($\dot{\varepsilon}^{\infty}_{eq}$ is the corresponding strain-rate in the absence of voids).

a local level and thus does not affect the overall behavior of the composite. Of course, the VAR estimate provides poor estimates for the evolution of the porosity and consequently fails to predict accurately the evolution of $\overline{D}_{eq}/\dot{\varepsilon}^{\infty}_{eq}$ as well.

7.4.3 Brief summary

In the previous subsections, we compared the SOM model with the FL (Flandi and Leblond, 2005) and VAR model, and the FEM method for the estimation of the evolution of the relevant microstructural and macroscopic variables in porous materials containing initially spheroidal voids in small concentrations ($f_o = 0.01\%$) that are subjected to axisymmetric loading conditions with several stress triaxialities. For completeness, we have chosen to compare the various methods for a nonlinear exponent $n = 10$, where the behavior of the composite is highly nonlinear. A general remark in the context of this section, is that both the SOM and the FL methods can predict qualitatively and quantitatively the evolution of the microstructural and macroscopic variables when compared with the corresponding FEM results. In contrast, the VAR method is significantly stiffer than the rest of the methods, and although being in qualitative agreement with the FEM predictions in most of the cases, it fails to estimate accurately the evolution of the relevant variables, particularly at high stress triaxialities.

In particular, the SOM has been found to be in better agreement with the FEM results than the FL for lower stress triaxialities (such as uniaxial tension loading), especially for the evolution of the porosity and the macroscopic strain-rate. In contrast, the SOM has been found to be in less good agreement with the FEM and FL results for the evolution of the aspect ratio at high stress triaxialities. However, it has been noted that the evolution of the aspect ratio has only a minor effect on the effective behavior of the porous material at high triaxiality loadings. This is a direct consequence of the fact that the porosity evolves significantly when compared with the rate of change of the aspect ratio in this case. Thus, the effective behavior of the porous material is mainly controlled by the evolution of the porosity which induces a strong softening (hardening) at tensile (compressive) loading conditions. For this reason, the SOM and the FL predictions — even though very different for the evolution of the aspect ratio — are in good agreement with the FEM results for the evolution of the macroscopic strain-rate in the porous medium.

Finally, it is emphasized that in the previous subsections, we have validated the various models in the context of porous materials with initially spherical voids that are subjected to *axisymmetric* loading conditions, leading to voids with spheroidal shape. However, it is important to note that this type of loading and microstructural configurations, albeit very common ones, are very restrictive to draw general conclusions about the accuracy of these models. For this reason, we will attempt to study the effective behavior of initially *anisotropic* porous media subjected to various loading conditions in the following sections. Note that the SOM and the VAR methods are capable of handling more general microstructures and loading conditions (as already discussed in section 6.5), in contrast with the FL model which is valid only for spheroidal voids and axisymmetric loading conditions aligned with the pore symmetry axis.

7.5 Evolution in porous media with an ideally-plastic matrix phase

This section is concerned with the evolution of microstructure in porous materials consisting of "misoriented" spheroidal (prolate or oblate) voids subjected to tensile or compressive axisymmetric loading conditions, defined in (7.6). Thus, we consider spheroidal voids whose symmetry axis is oriented in three different directions. For simplicity, we consider rotations of the voids only about the $1-$axis by $\psi_1 = 45^o$ and $\psi_2 = 90^o$, while the aligned case $\psi_1 = 0^o$ is also considered. The rest of the angles are $\psi_2 = \psi_3 = 0^o$. Due to the axisymmetric loading conditions considered here, the angles ψ_2 and ψ_3 remain fixed during the deformation process. More general conditions could be considered, however, the problem would be to complicated to extract useful conclusions about the influence that the orientation of the voids exerts on the macroscopic behavior of such porous media.

The reasoning behind the study of such configurations is linked to the recent work of Nakajima (2007). In that work, the author constructed "lotus-type" porous metals made out of long voids aligned in a certain direction. In the sequel, these materials where subjected to compressive loads parallel and transverse to the major axis of the pores. Significant differences in the effective response of the porous material were found in those cases. In particular, when the loading direction was parallel to the axis of the voids, the author found that it is difficult to reduce the porosity sufficiently after 80% deformation. However, when compressive loading was applied transverse to the axis of the voids, the porous material exhibited much softer behavior and after 80% deformation the total porosity in the material was observed to be much smaller than in the previous case.

Although, we are still far from considering any type of quantitative comparison with these experimental evidence, it is interesting to study the above mentioned problem by making use of the "second-order" model (SOM) developed in this work in section 2.6. We expect that, at least in qualitative terms, the new SOM model is able to capture the main features of the previously described problem. For comparison, we will also include the Flandi and Leblond (2005) (FL) model, which can only be used in cases that the void will remain spheroidal during the deformation process. However, when the void symmetry relative to the loading is not preserved this last model cannot be used.

7.5.1 Tensile loadings: prolate voids

More specifically, tensile and compressive loading conditions are considered, while the stress triaxiality remains fixed during the deformation process. Fig. 7.22 shows evolution curves for porous media with an ideally-plastic matrix phase consisting of prolate voids with aspect ratio $w_1 = w_2 = 5$ and initial porosity $f_o = 5\%$, subjected to uniaxial tension loading ($X_\Sigma = 1/3$ or $T/S = 0$ with $S/|S| > 0$) as a function of the macroscopic equivalent strain $\bar{\varepsilon}_{eq}$. In Fig. 7.22a, when the orientation angle $\psi_1 = 0^o$, both the SOM and the FL models can be used to predict the effective response of the material. In fact, the evolution of the porosity f is not significant in the case of $\psi_1 = 0^o$. However, as the initial orientation of the voids changes, substantial differences in the evolution of f occur. While for $\psi_1 = 0^o$ and $\psi_1 = 45^o$ the growth of the voids is of the order of $\sim 1\%$ and $\sim 20\%$ over the initial

porosity f_o, respectively, the corresponding increase of f for $\psi_1 = 90^o$ is of the order of $\sim 120\%$ after a deformation of 100%.

The corresponding normalized equivalent macroscopic stress $\overline{\sigma}_{eq}/\sigma_o$ curves (σ_o is the flow stress of the matrix phase), shown in Fig. 7.22b, verify the findings of part (a) by predicting that the porous material is softer in the case of $\psi_1 = 90^o$ than in $\psi_1 = 0^o$. Moreover, while for $\psi_1 = 0^o$ the $\overline{\sigma}_{eq}/\sigma_o$ exhibits a slight hardening, as predicted by both the SOM and the FL models, the corresponding SOM curve for $\psi_1 = 90^o$ clearly shows softening of the material. In the intermediate case of $\psi_1 = 45^o$ the $\overline{\sigma}_{eq}/\sigma_o$ (σ_o is the flow stress of the matrix phase) initially increases, whereas, at higher strains ($\overline{\varepsilon}_{eq} > 60\%$), it decreases. This peculiar behavior is due to the misorientation of the voids relative to the loading directions, which, in turn, has as a consequence the spin of the voids, and their final alignment with the principal loading directions.

The rest of the two figures, part (c) and part (d) complete the set of the evolution curves. In particular, Fig. 7.22c shows the evolution of the aspect ratios w_1 and w_2 for these various angles considered here. For $\psi_1 = 0^o$, the void remains spheroidal during the deformation and thus both the SOM and the FL estimates are in good agreement predicting significant increase in $w_1 = w_2$. In turn, for $\psi_1 = 45^o$, the aspect ratios evolve in a different manner, with w_1 remaining always higher than the w_2. Nonetheless, both w_1 and w_2 finally increase to high values at sufficiently high strains. On the other hand, for $\psi_1 = 90^o$ the two aspect ratios decrease, with w_1 preserving approximately its initial value, while w_2 approaches the zero value asymptotically. In this regard, it is obvious that apart from the purely aligned case $\psi_1 = 0^o$, in the rest of the cases, the voids are expected to evolve in ellipsoidal shapes. Therein lies the main difference between the more general SOM and the FL method which can only handle spheroidal pore shapes. Finally, Fig. 7.22d shows the evolution of the angle ψ_1 in the case of initially oriented voids at $\psi_1 = 45^o$, where it is found to approach asymptotically the zero value. The interpretation of this is linked to the fact that because of the loading the voids try to align themselves with the direction of the maximum principal stress. It is noted that in the cases of $\psi_1 = 0^o$ and $\psi_1 = 90^o$, the orientation angle does not evolve, as expected. In summary, those results verify that the misorientation of the microstructure relative to the loading direction can have great impact on the effective response and possible failure of the porous material. Thus, while the FL method is accurate enough for spheroidal microstructures and axisymmetric loading conditions aligned with the pore symmetry axis, it is evident that it cannot be used to study more complex problems which require a more general description of the relevant microstructural variables.

For completeness, in Fig. 7.23, higher triaxiality loadings are considered, where evolution curves for porous media with an ideally-plastic matrix phase are shown as a function of the equivalent macroscopic strain $\overline{\varepsilon}_{eq}$ for initial porosity $f = 5\%$. It is worth noting that for purely hydrostatic loading, the effect of the orientation is expected to be minimal, however, it is interesting to see what is the effect of the misorientation of the microstructure at a moderate stress triaxiality such as the one used here, i.e., $X_\Sigma = 1$ or $T/S = 0.4$ with $S/|S| > 0$. Fig. 7.23a presents results for the evolution of the porosity f as predicted by the SOM and the FL models. The FL model refers to the case of $\psi_1 = 0^o$, as already discussed in the context of the previous figure. For this case, it is observed that the FL provides a much higher estimate for the evolution of the porosity f than the SOM method.

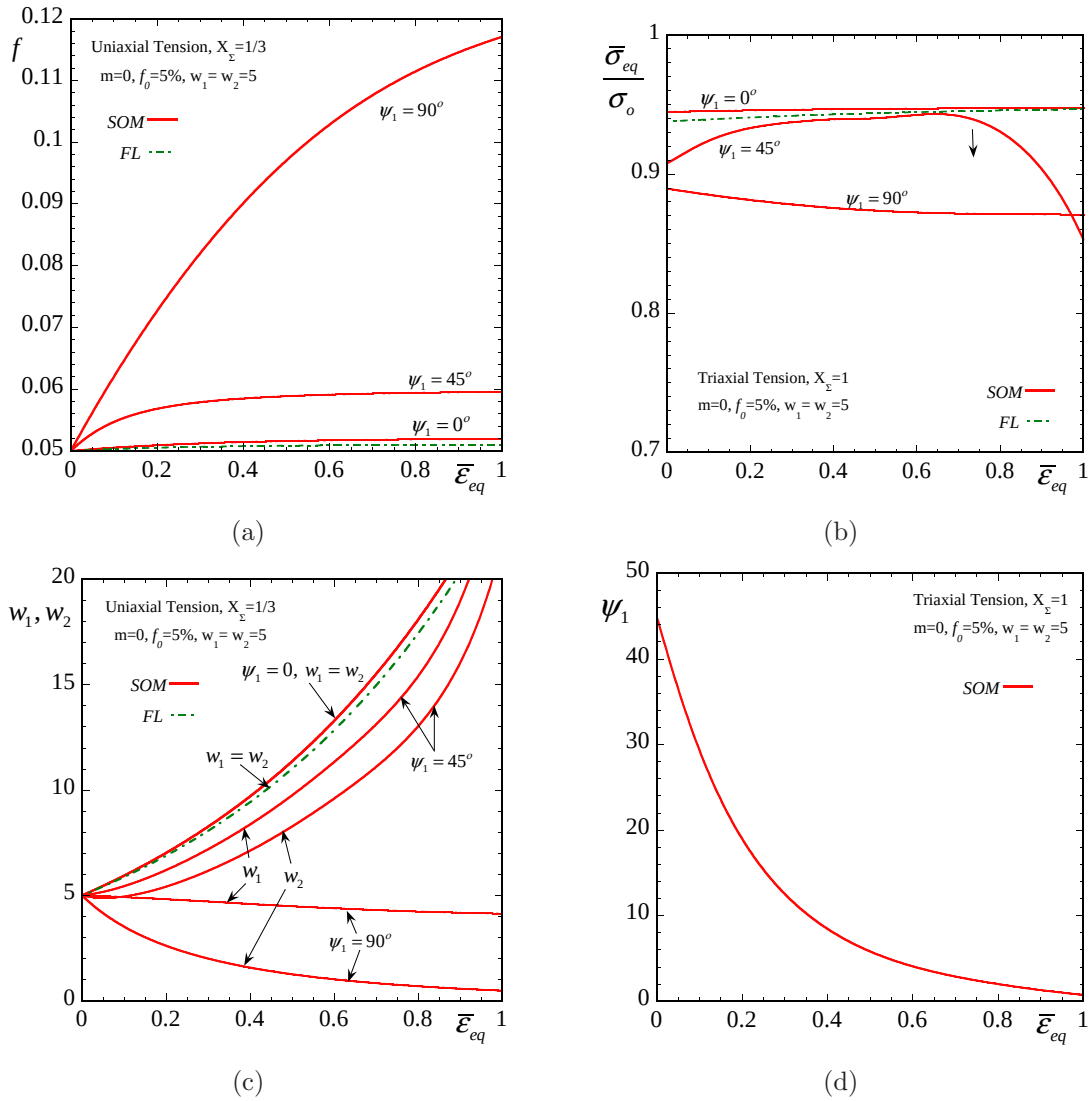

Figure 7.22: Results are shown for the evolution of the relevant microstructural and macroscopic variables for a porous material consisted of prolate voids with initial aspect ratio $w_1 = w_2 = 5$ and orientated in three different directions $\psi_1 = 0, 45, 90^o$, $\psi_2 = \psi_3 = 0$. The initial porosity is $f_o = 5\%$ and the matrix phase exhibits an ideally-plastic behavior. The composite is subjected to uniaxial tension loading conditions with fixed stress triaxiality, $X_\Sigma = 1/3$ or $T/S = 0$ with $S/|S| > 0$. *SOM* and *FL* (Flandi and Leblond, 2005) estimates are shown for the evolution of the (a) porosity f, (b) the macroscopic stress $\overline{\sigma}_{eq}/\sigma_o$ normalized by the yield stress of the matrix phase, (c) the aspect ratios w_1 and w_2, and (d) the orientation angle ψ_1.

It should be noted, however, that the *FL* results have been obtained by considering the parameter $q = 1.47$ (see section 3.3), which is introduced by the authors in order to approximate the behavior of a periodic microstructure and certainly, in the case of $f = 5\%$ the responses of "periodic" and "random" materials are very different. Thus this difference between the two models is attributed to this special parameter q. Nonetheless, it is remarkable to observe very different predictions for the various angles ψ_1. As already expected, the porosity evolves in a much higher rate in the case of $\psi_1 = 90^o$ than in $\psi_1 = 0^o$. In contrast, the porosity curves for $\psi_1 = 0^o$ and $\psi_1 = 45^o$ do not show

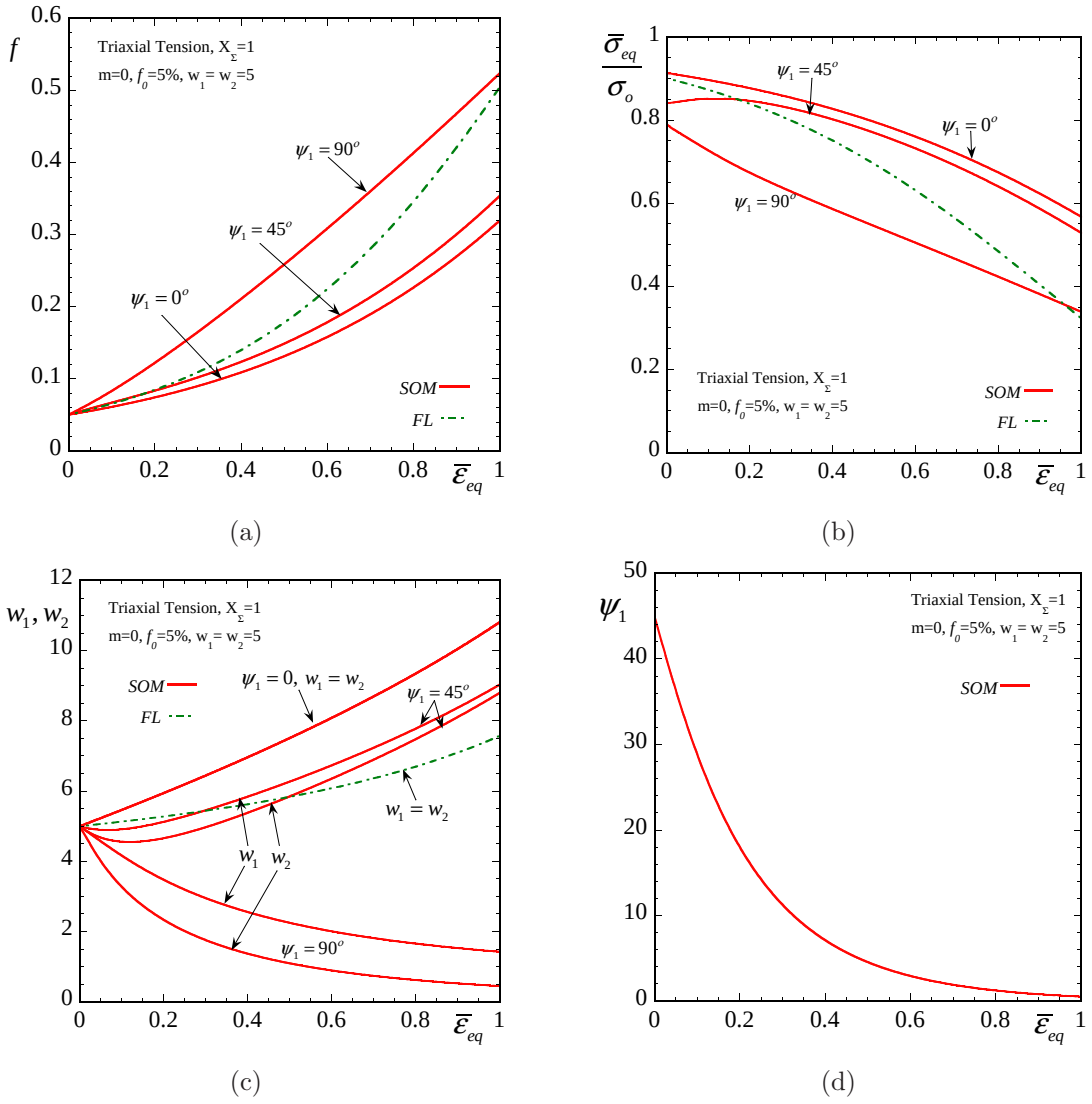

Figure 7.23: Results are shown for the evolution of the relevant microstructural and macroscopic variables for a porous material consisted of prolate voids with initial aspect ratio $w_1 = w_2 = 5$ and orientated in three different directions $\psi_1 = 0, 45, 90^o$, $\psi_2 = \psi_3 = 0$. The initial porosity is $f_o = 5\%$ and the matrix phase exhibits an ideally-plastic behavior. The composite is subjected to triaxial tension loading conditions with fixed stress triaxiality, $X_\Sigma = 1$ or $T/S = 0.4$ with $S/|S| > 0$. *SOM* and *FL* (Flandi and Leblond, 2005) estimates are shown for the evolution of the (a) porosity f, (b) the macroscopic stress $\overline{\sigma}_{eq}/\sigma_o$ normalized by the yield stress of the matrix phase, (c) the aspect ratios w_1 and w_2, and (d) the orientation angle ψ_1.

significant differences. Looking now at the normalized equivalent macroscopic stress $\overline{\sigma}_{eq}/\sigma_o$ curves, in Fig. 7.23b, the SOM predictions indicate that the porous material is stiffer for $\psi_1 = 0^o$ than for $\psi_1 = 90^o$. This is directly related to the increase of porosity which is a softening mechanism, described previously. In the case of $\psi_1 = 45^o$, though, the material exhibits an initial hardening, while at strains $\sim 20\%$ it starts softening. As already mentioned in the case of uniaxial tension this behavior is a direct consequence of the spin of the microstructure.

To complete the study of this figure, the evolution of the aspect ratios w_1 and w_2 and the orientation angle ψ_1, in Fig. 7.23c and Fig. 7.23d, respectively, is discussed next. For $\psi_1 = 0^o$, the voids remain prolate during the deformation and hence the two aspect ratios $w_1 = w_2$ are equal. In this case the SOM predicts higher aspect ratios than the FL model. In contrast, for $\psi_1 = 45^o$ and $\psi_1 = 90^o$ the initially prolate voids evolve into ellipsoidal voids, where the two aspect ratios w_1 and w_2 take different values. In this case, only SOM estimates are available. It is interesting to observe that, while for $\psi_1 = 0^o$ and $\psi_1 = 45^o$, the aspect ratios finally increase to a relatively high value, for $\psi_1 = 90^o$, w_1 and w_2 decrease to very low values. Finally, Fig. 7.23d shows the evolution of the orientation angle ψ_1 in the case that the voids are oriented initially at $\psi_1 = 45^o$. As already anticipated intuitively, the angle evolves asymptotically to $\psi_1 \to 0^o$, since the voids try to align themselves with the loading directions.

7.5.2 Compressive loadings: prolate voids

In this subsection, porous materials with an ideally-plastic matrix phase, discussed previously, are subjected to axisymmetric *compressive* loading conditions, as defined by (7.6). First, in Fig. 7.24, we consider uniaxial compression loading $X_\Sigma = -1/3$ (or $T/S = 0$ with $S/|S| < 0$) for porous materials consisting of prolate voids oriented at three different angles, $\psi_1 = 0^o, 45^o, 90^o$. The initial aspect ratios of the voids are $w_1 = w_2 = 5$ and the porosity $f_o = 5\%$. For the case of $\psi_1 = 0^o$, FL estimates are also included. In Fig. 7.24a, evolution curves for the porosity f are shown as a function of the equivalent macroscopic strain $\overline{\varepsilon}_{eq}$. The main observation in the context of this plot is that the effect of the misorientation of the voids relative to the loading directions has dramatic effects on the evolution of the porosity. Thus, while the SOM and the FL estimates for $\psi_1 = 0^o$ predict that the porosity is still finite at 100% deformation, for $\psi_1 = 45^o$ and $\psi_1 = 90^o$, f is found to become zero at strains $\sim 30\%$ and $\sim 40\%$, respectively. This has direct consequences on the prediction of the normalized macroscopic equivalent stress $\overline{\sigma}_{eq}/\sigma_o$ (σ_o is the flow stress of the matrix phase), in Fig. 7.24b, where it is observed that for $\psi_1 = 45^o$ and $\psi_1 = 90^o$, the effective response of the material is softer than for $\psi_1 = 0^o$. Furthermore, in the case of $\psi_1 = 45^o$, where the principal axes of the voids rotate during the deformation process, the corresponding SOM estimate shows an initial sharp drop in the stress, which may lead to possible unstable behaviors. In contrast, the FL model is valid only for $\psi_1 = 0^o$ and thus, incapable of predicting such behaviors that are related with the spin of the microstructure during the deformation process.

Next, Fig. 7.24c shows corresponding estimates for the evolution of the aspect ratios w_1 and w_2. As already anticipated, for the $\psi_1 = 0^o$ case, both the SOM and the FL models predict a

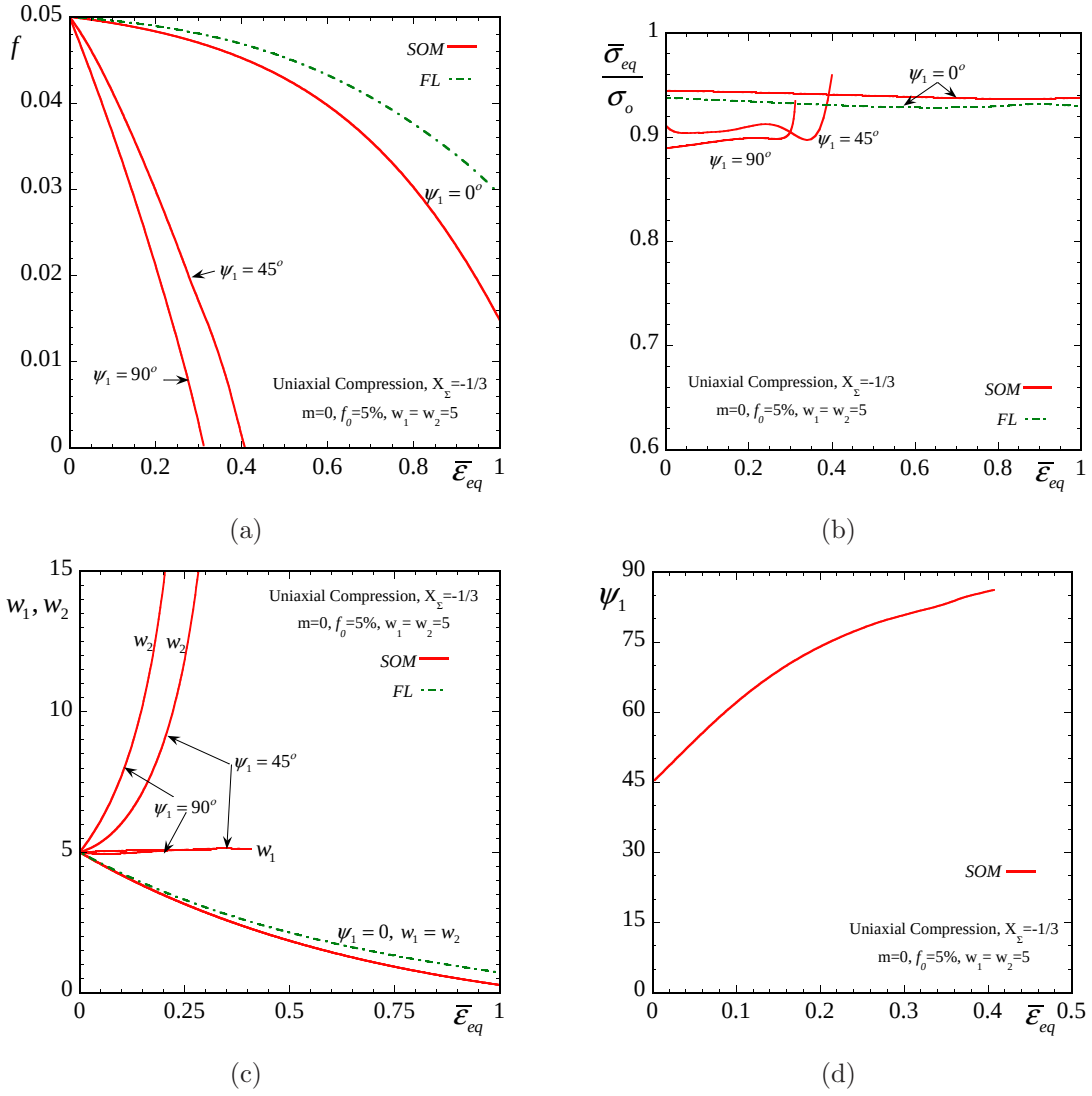

Figure 7.24: Results are shown for the evolution of the relevant microstructural and macroscopic variables for a porous material consisted of prolate voids with initial aspect ratio $w_1 = w_2 = 5$ and orientated in three different directions $\psi_1 = 0, 45, 90^o$, $\psi_2 = \psi_3 = 0$. The initial porosity is $f_o = 5\%$ and the matrix phase exhibits an ideally-plastic behavior. The composite is subjected to uniaxial compression loading conditions with fixed stress triaxiality, $X_\Sigma = -1/3$ or $T/S = 0$ with $S/|S| < 0$. *SOM* and *FL* (Flandi and Leblond, 2005) estimates are shown for the evolution of the (a) porosity f, (b) the macroscopic stress $\overline{\sigma}_{eq}/\sigma_o$ normalized by the yield stress of the matrix phase, (c) the aspect ratios w_1 and w_2, and (d) the orientation angle ψ_1.

decrease of the aspect ratios, while the initial spheroidal shape is preserved. Note, however, that when $w_1 = w_2$ becomes less than unity, the prolate voids become oblate. On the other hand, for $\psi_1 = 45^o$ and $\psi_1 = 90^o$, the initially spheroidal voids become ellipsoidal with two different aspect ratios, i.e., $w_1 \neq w_2$. In particular, w_2 grows faster in the case of $\psi_1 = 90^o$ than in $\psi_1 = 45^o$, whereas w_1 remains almost constant in both cases. In turn, Fig. 7.24d presents the corresponding evolution of the orientation angle ψ_1 as a function of $\overline{\varepsilon}_{eq}$, in the case that the voids are initially oriented at $\psi_1 = 45^o$. Here, the angle ψ_1 tends to evolve towards 90^o, but because of the fact that the porosity

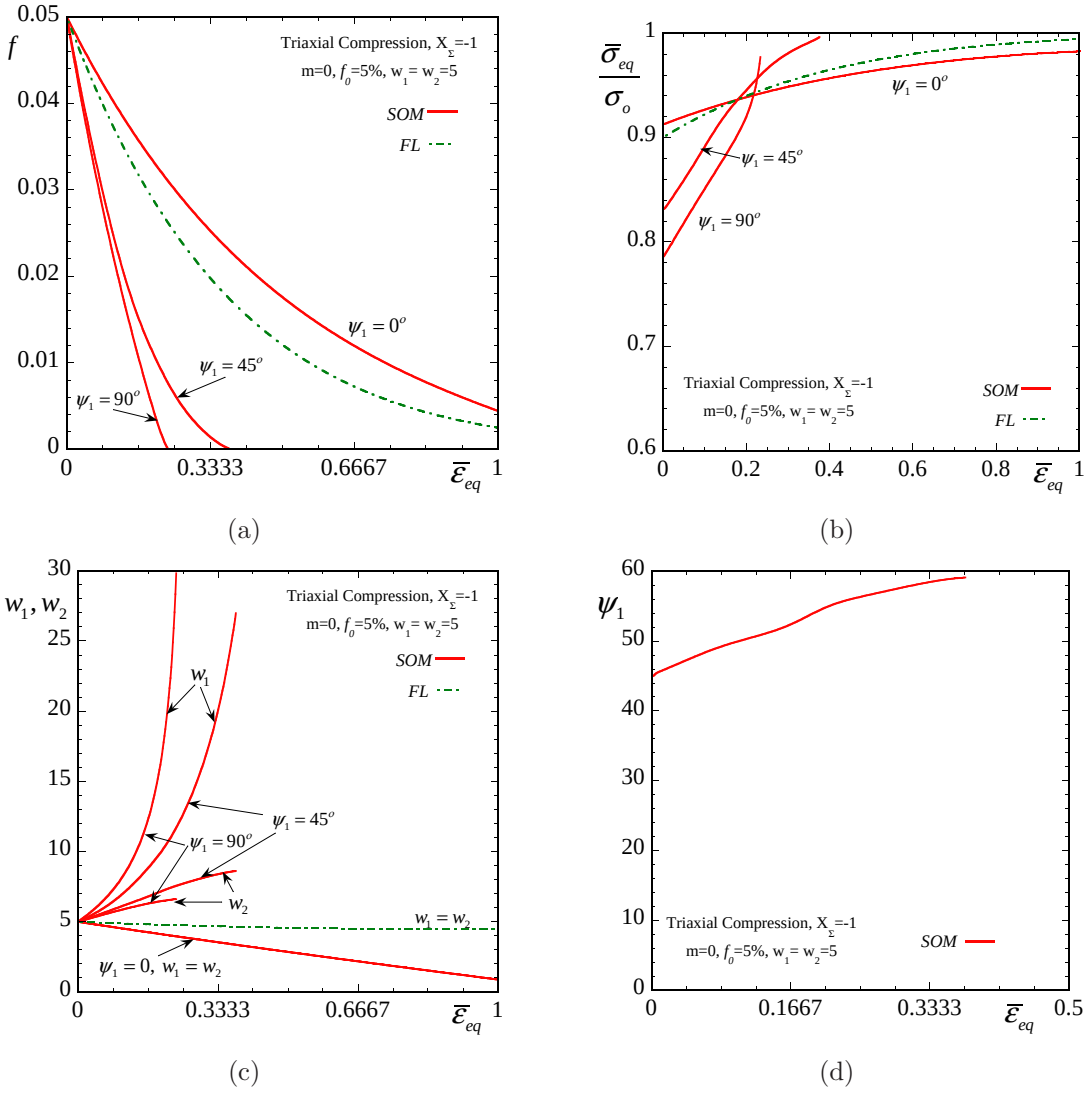

Figure 7.25: Results are shown for the evolution of the relevant microstructural and macroscopic variables for a porous material consisted of prolate voids with initial aspect ratio $w_1 = w_2 = 5$ and orientated in three different directions $\psi_1 = 0, 45, 90^o$, $\psi_2 = \psi_3 = 0$. The initial porosity is $f_o = 5\%$ and the matrix phase exhibits an ideally-plastic behavior. The composite is subjected to triaxial tension loading conditions with fixed stress triaxiality, $X_\Sigma = -1$ or $T/S = 0.4$ with $S/|S| < 0$. *SOM* and *FL* (Flandi and Leblond, 2005) estimates are shown for the evolution of the (a) porosity f, (b) the macroscopic stress $\overline{\sigma}_{eq}/\sigma_o$ normalized by the yield stress of the matrix phase, (c) the aspect ratios w_1 and w_2, and (d) the orientation angle ψ_1.

becomes zero at finite strain, the curve stops before this value is reached.

Finally, the set of results for porous materials with an ideally-plastic matrix phase consisting of initially prolate voids is completed by considering the case of axisymmetric compressive loading with fixed stress triaxiality $X_\Sigma = -1$ (or $T/S = 0.4$ with $S/|S| < 0$), as shown in Fig. 7.25. Similarly, to the previous case of uniaxial compression, in Fig. 7.25a, the evolution of porosity f for prolate voids aligned at $\psi_1 = 0^o$ exhibits significant differences when compared with the corresponding results for $\psi_1 = 45^o$ and $\psi_1 = 90^o$. While for $\psi_1 = 0^o$, both the *SOM* and the *FL* models predict finite porosity

at 100% deformation, for $\psi_1 = 45^o$ and $\psi_1 = 90^o$, the porosity becomes zero at much lower values of the $\overline{\varepsilon}_{eq}$ as predicted by the SOM. Because of this, the corresponding $\overline{\sigma}_{eq}/\sigma_o$ curves in Fig. 7.25b are very different for the three values of the initial orientation angle of the voids. In particular, for $\psi_1 = 45^o$ and $\psi_1 = 90^o$ the porous material exhibits a very strong hardening, although initially is softer than the $\psi_1 = 0^o$ case, where the SOM and the FL models are found to be in good agreement.

These results are complemented with corresponding estimates for the evolution of the aspect ratios w_1 and w_2 in Fig. 7.25c. This plot is rather complicated, however, the main observation in the context of this figure is that for $\psi_1 = 45^o$ and $\psi_1 = 90^o$, the initially prolate voids become ellipsoidal in shape with w_1 taking significantly higher values than w_2 in both cases. In contrast, for $\psi_1 = 0^o$, the voids remain spheroidal during the deformation process with the FL method predicting almost constant values for $w_1 = w_2 \sim 5$, while the SOM curve predicts sufficient decrease in $w_1 = w_2$. Finally, Fig. 7.25d illustrates the evolution of ψ_1 for the case that the voids are initially oriented at 45^o. Similarly to the uniaxial compression loading, the principal axes of the voids tend to align with the principal loading directions, and thus they rotate towards 90^o. However, due to the fact that the porosity becomes zero very fast they never reach this value.

7.5.3 Tensile loadings: oblate voids

For completeness, it is also important to consider porous materials that consist of oblate voids subjected to the previously mentioned axisymmetric loading conditions (see (7.6)). The oblate voids have initial aspect ratios $w_1 = w_2 = 0.2$ and they are oriented initially with three different angles, i.e., $\psi_1 = 0^o, 45^o, 90^o$ relative to the loading directions. The initial porosity is $f_o = 5\%$ and the rest of the orientation angles ψ_2 and ψ_3 are set for simplicity equal to zero. Moreover, because of the applied loading, ψ_2 and ψ_3 remain fixed during the deformation process, i.e., equal to zero. The conclusions that can be drawn by studying porous materials with oblate voids are similar to the ones in the previous subsection for prolate voids.

Fig. 7.26 shows evolution curves for porous media with an ideally-plastic matrix phase subjected to uniaxial tension loading with fixed stress triaxiality $X_\Sigma = 1/3$ (or $T/S = 0$ with $S/|S| > 0$) as a function of the macroscopic equivalent strain $\overline{\varepsilon}_{eq}$. In Fig. 7.26a, it is observed that for oblate voids aligned at $\psi_1 = 0^o$, the SOM and the FL estimates for the evolution of porosity f are in good agreement. In particular, for $\psi_1 = 0^o$, SOM and FL predict a very fast growth of the porosity, in contrast with the corresponding SOM estimates for $\psi_1 = 45^o$ and $\psi_1 = 90^o$, which predict relatively low values for f. This differences in the predictions for the evolution of the porosity are translated into significant differences between the corresponding estimates for the normalized equivalent macroscopic stress $\overline{\sigma}_{eq}/\sigma_o$ (σ_o is the flow stress of the matrix phase) in Fig. 7.26b. Here, the porous material is stiffer for $\psi_1 = 90^o$ and softer for $\psi_1 = 0^o$. For the intermediate value of $\psi_1 = 45^o$, the principal axes of the voids rotate during the deformation process. As a consequence, the porous medium initially exhibits a hardening, which changes to softening at higher values of the macroscopic equivalent strain $\overline{\varepsilon}_{eq}$.

Note that for $\psi_1 = 0$ the FL model predicts softer behavior for the porous material than the

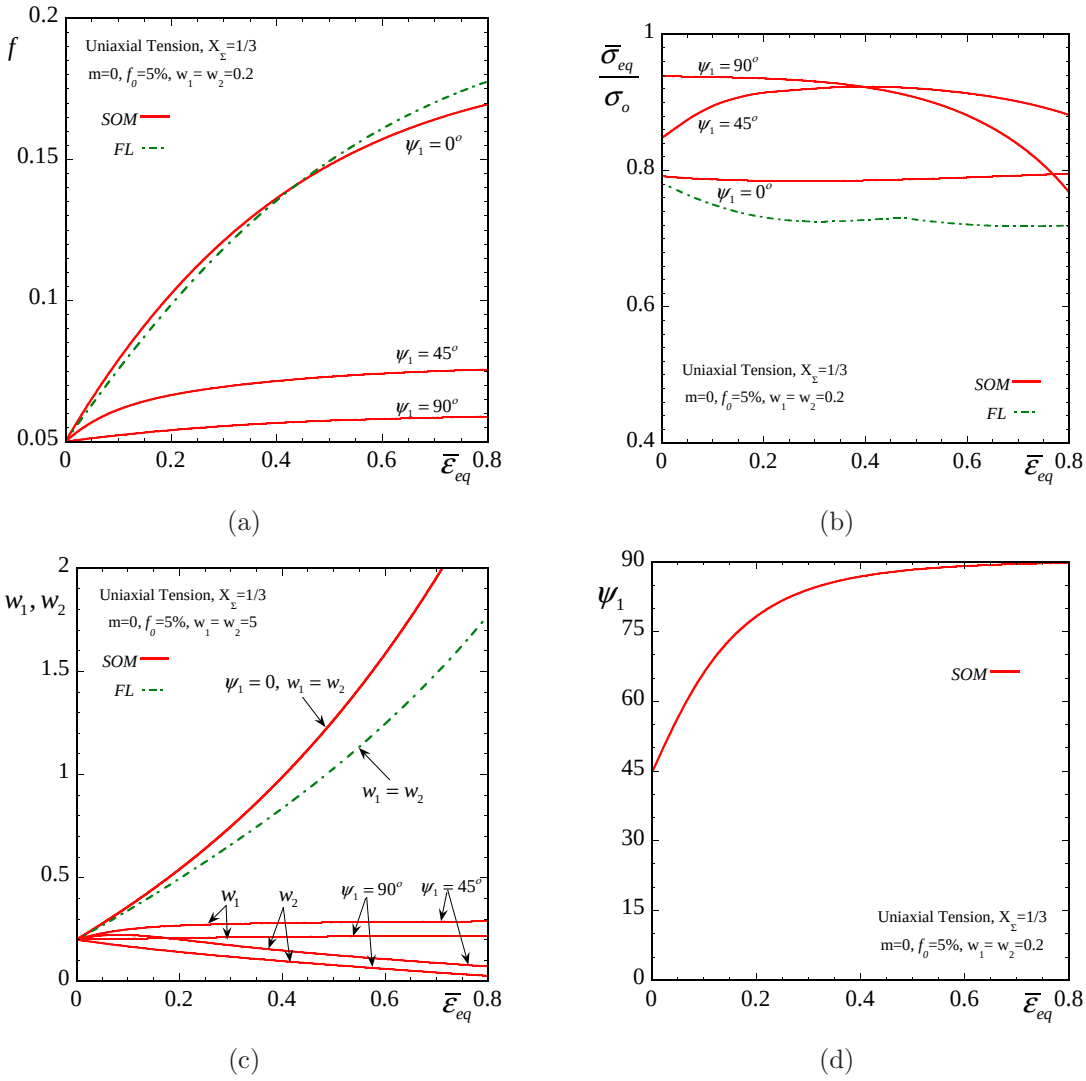

Figure 7.26: Results are shown for the evolution of the relevant microstructural and macroscopic variables for a porous material consisted of oblate voids with initial aspect ratio $w_1 = w_2 = 0.2$ and orientated in three different directions $\psi_1 = 0, 45, 90^o$, $\psi_2 = \psi_3 = 0$. The initial porosity is $f_o = 5\%$ and the matrix phase exhibits an ideally-plastic behavior. The composite is subjected to uniaxial tension loading conditions with fixed stress triaxiality, $X_\Sigma = 1/3$. *SOM* and *FL* (Flandi and Leblond, 2005) estimates are shown for the evolution of the (a) porosity f, (b) the macroscopic stress $\overline{\sigma}_{eq}/\sigma_o$ normalized by the yield stress of the matrix phase, (c) the aspect ratios w_1 and w_2, and (d) the orientation angle ψ_1.

SOM model. This can be explained by looking at the evolution of the aspect ratios w_1 and w_2 in Fig. 7.26c. For $\psi_1 = 0^o$ the *FL* predicts a slower rate of increase for the aspect ratios than the *SOM*, which in connection with the increase of the porosity, implies an initial softer response for the porous material when compared with the corresponding *SOM* estimates. In turn, when $\psi_1 = 45^o$ and $\psi_1 = 90^o$ the aspect ratios take very low values. In addition, w_1 and w_2 evolve in a different manner so that the initially oblate voids become ellipsoidal during the deformation process. Finally, Fig. 7.26d concludes the set of figures for this specific loading. In this figure, the evolution of the angle ψ_1 is presented for porous materials with oblate voids initially oriented at $\psi_1 = 45^o$ as a function

of the macroscopic equivalent strain $\overline{\varepsilon}_{eq}$. As already anticipated, the voids tend to align with the principal loading directions and hence ψ_1 approaches the asymptotic value of 90^o.

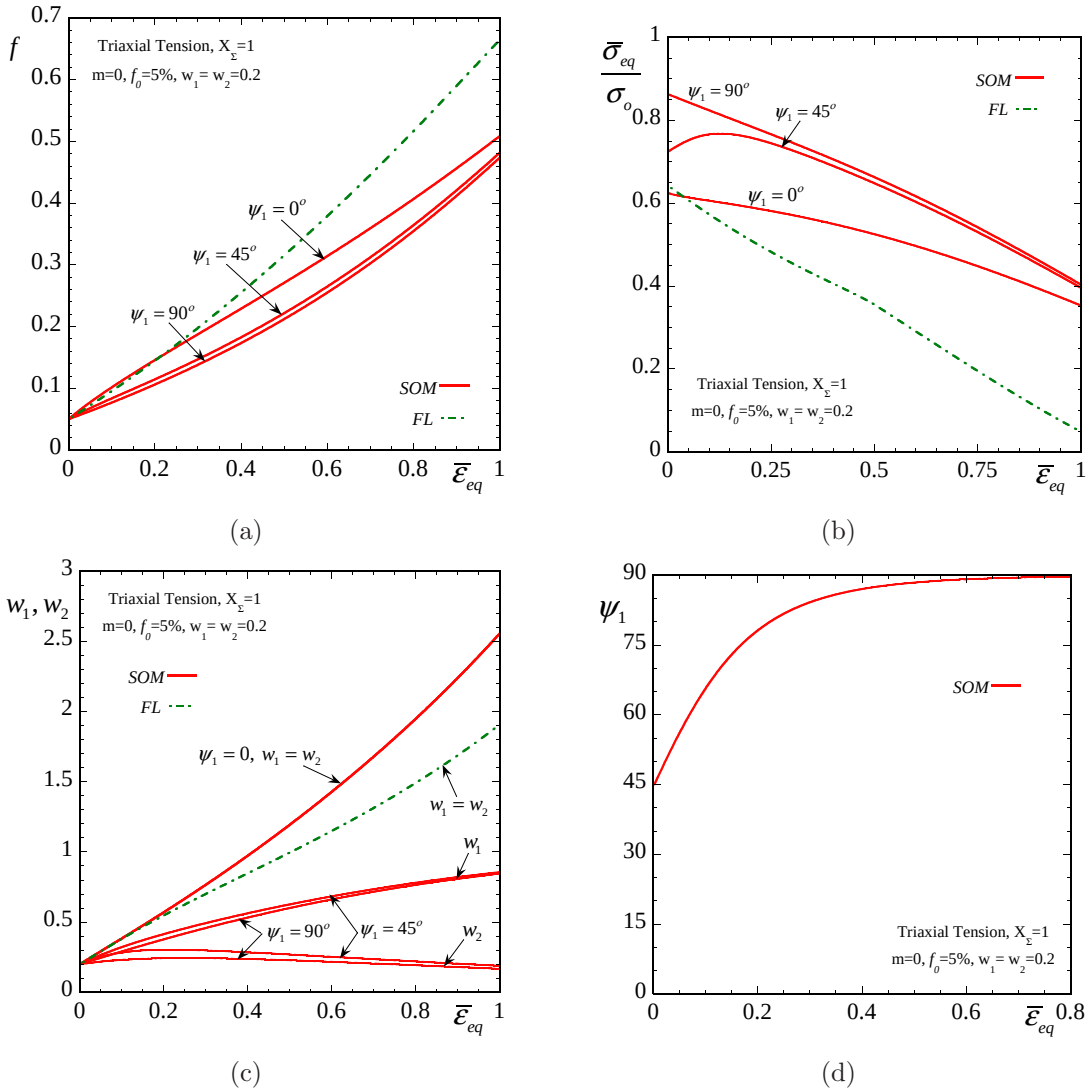

Figure 7.27: Results are shown for the evolution of the relevant microstructural and macroscopic variables for a porous material consisted of oblate voids with initial aspect ratio $w_1 = w_2 = 0.2$ and orientated in three different directions $\psi_1 = 0, 45, 90^o$, $\psi_2 = \psi_3 = 0$. The initial porosity is $f_o = 5\%$ and the matrix phase exhibits an ideally-plastic behavior. The composite is subjected to triaxial tension loading conditions with fixed stress triaxiality, $X_\Sigma = 1$. *SOM* and *FL* (Flandi and Leblond, 2005) estimates are shown for the evolution of the (a) porosity f, (b) the macroscopic stress $\overline{\sigma}_{eq}/\sigma_o$ normalized by the yield stress of the matrix phase, (c) the aspect ratios w_1 and w_2, and (d) the orientation angle ψ_1.

Next, we consider triaxial loadings with fixed stress triaxiality $X_\Sigma = 1$ (or $T/S = 0.4$ with $S/|S| > 0$), as shown in Fig. 7.27. Part (a) of this figure presents *SOM* and *FL* estimates for the evolution of porosity f as a function of the equivalent macroscopic strain $\overline{\varepsilon}_{eq}$. The *SOM* curves that correspond to $\psi_1 = 45^o$ and $\psi_1 = 90^o$ are almost identical, while the $\psi_1 = 0^o$ curve is slightly higher than the previous ones. However, an interesting observation in the context of this figure is that the

different orientation angles of the voids do not affect significantly the evolution of porosity. On the other hand, the evolution of the normalized macroscopic equivalent stress $\overline{\sigma}_{eq}/\sigma_o$, shown in Fig. 7.27b, depends strongly on the angle ψ_1. For instance, the SOM estimate for $\psi_1 = 0^o$ and $\psi_1 = 90^o$ differ by almost $\sim 35\%$, although in both cases the porous medium exhibits the same qualitative behavior, namely softening. In contrast, for $\psi_1 = 45^o$, the porous material initially hardens and then softens. This is due to the spin of the voids in this case. The FL model, finally, shows very strong softening compared to the rest of the estimates, as a consequence of the fact that it predicts high rates of growth for the porosity during the deformation process.

With regard to the evolution of the aspect ratios w_1 and w_2 in Fig. 7.27c, the SOM and the FL are in qualitative agreement for the $\psi_1 = 0^o$ curve, with the latter taking lower values than the earlier one for the entire deformation process. On the other hand, for $\psi_1 = 45^o$ and $\psi_1 = 90^o$, the aspect ratios evolve similarly. In particular, w_1 increases to a value close to unity, while w_2 remains close to its initial value 0.2. This last results implies that even at this moderate triaxiality, the initially oblate voids evolve into ellipsoidal ones with significant differences in the two aspect ratios. In turn, Fig. 7.27d illustrates the evolution of the orientation angle ψ_1, which starts from the initial value of 45^o, and approaches asymptotically the value of 90^o. As already concluded in the previous figures, this result implies that the major axis of the voids tend to align with the principal loading directions.

7.5.4 Compressive loadings: oblate voids

In this subsection, the porous materials with an ideally-plastic matrix phase, discussed previously, are subjected to axisymmetric *compressive* loading conditions, as defined by (7.6). More specifically, Fig. 7.28 presents evolution curves for porous media with an ideally-plastic matrix phase subjected to uniaxial compression loading with fixed stress triaxiality $X_\Sigma = -1/3$ (or $T/S = 0$ with $S/|S| < 0$) as a function of the macroscopic equivalent strain $\overline{\varepsilon}_{eq}$. Looking at Fig. 7.28a, the corresponding estimates for the evolution of the porosity f, as predicted by the SOM and the FL (only for $\psi_1 = 0$), are remarkably different for the various angles ψ_1. The effect of the orientation of the voids is very strong in this case, since for $\psi_1 = 0^o$ and $\psi_1 = 45^o$ the porosity becomes zero at very low strains ($\overline{\varepsilon}_{eq} \sim 15\%$), whereas for $\psi_1 = 90^o$ the voids close down at strains $\overline{\varepsilon}_{eq} \sim 90\%$. Making use of these observations in the context of the evolution of porosity, it is relevant to look at the corresponding curves for the normalized macroscopic equivalent $\overline{\sigma}_{eq}/\sigma_o$ (σ_o denotes the flow stress of the matrix phase) in Fig. 7.28b. Here, the porous material is initially much softer for the case of $\psi_1 = 0^o$ and $\psi_1 = 45^o$ than for $\psi_1 = 90^o$. However, as the porosity approaches the zero value, the porous medium hardens rapidly, which is illustrated by the sharp change of the slope in the $\psi_1 = 0^o$ and $\psi_1 = 45^o$ curves for $\overline{\sigma}_{eq}/\sigma_o$. On the other hand, the corresponding estimate for $\psi_1 = 90^o$ shows a very slight hardening. It is important to note here that for $\psi_1 = 0^o$ and $\psi_1 = 90^o$ the SOM predicts hardening of the porous material during the entire deformation process. In contrast, the corresponding estimates for the $\psi_1 = 45^o$ curve exhibit a very strong softening initially, before they start increasing rapidly at a strain $\sim 15\%$, which implies the hardening of the porous medium. This is a direct consequence of the spin of the microstructure that occurs for $\psi_1 = 45^o$, in contrast with the $\psi_1 = 0^o$ and $\psi_1 = 90^o$

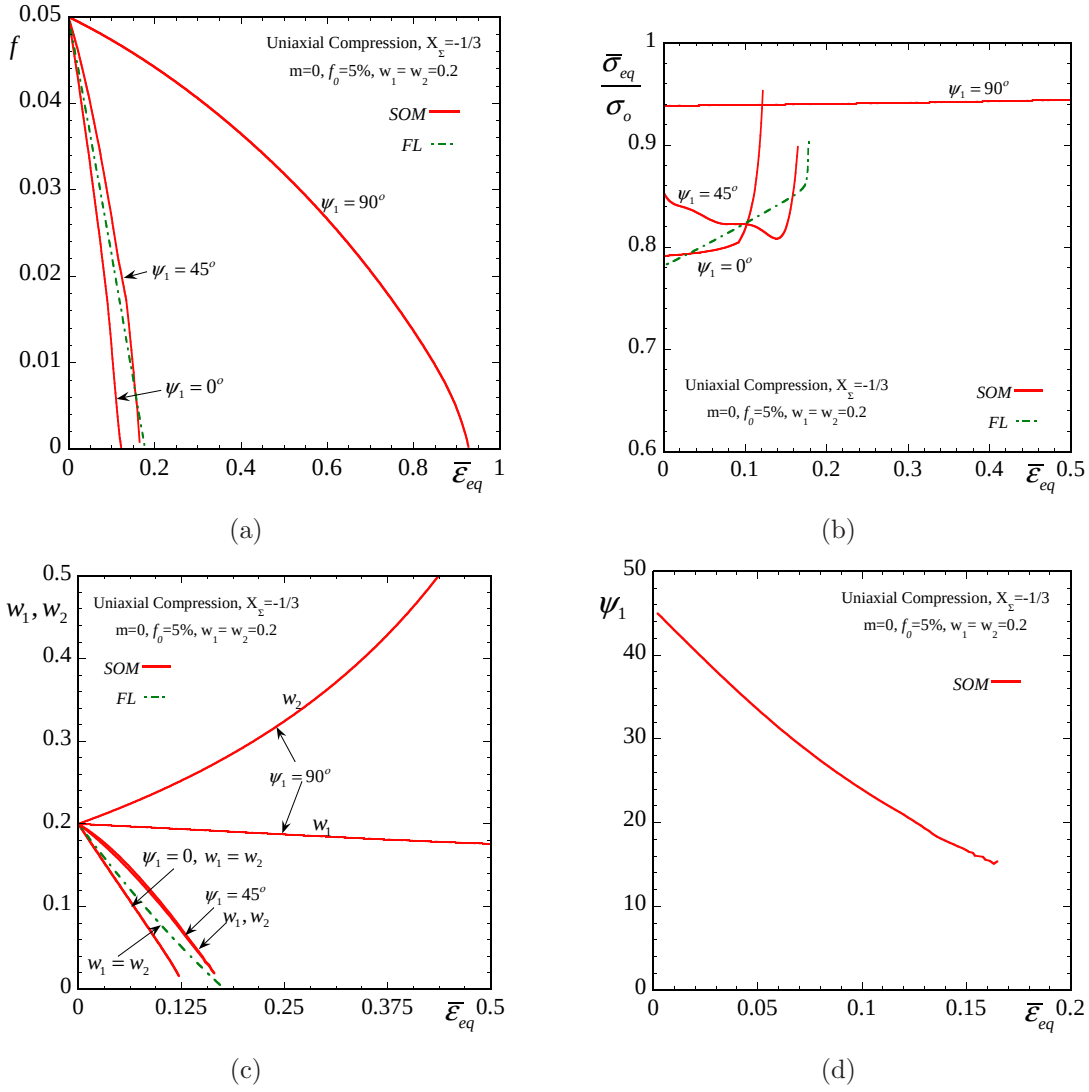

Figure 7.28: Results are shown for the evolution of the relevant microstructural and macroscopic variables for a porous material consisted of oblate voids with initial aspect ratio $w_1 = w_2 = 0.2$ and orientated in three different directions $\psi_1 = 0, 45, 90^o$, $\psi_2 = \psi_3 = 0$. The initial porosity is $f_o = 5\%$ and the matrix phase exhibits an ideally-plastic behavior. The composite is subjected to uniaxial compression loading conditions with fixed stress triaxiality, $X_\Sigma = -1/3$. *SOM* and *FL* (Flandi and Leblond, 2005) estimates are shown for the evolution of the (a) porosity f, (b) the macroscopic stress $\overline{\sigma}_{eq}/\sigma_o$ normalized by the yield stress of the matrix phase, (c) the aspect ratios w_1 and w_2, and (d) the orientation angle ψ_1.

configurations, where the principal axes of the voids remain fixed during the deformation process.

Next, Fig. 7.28c presents results for the evolution of the aspect ratios w_1 and w_2. As already expected, for $\psi_1 = 0$ and $\psi_1 = 45^o$ the aspect ratios drop rapidly to zero. On the other hand, for $\psi_1 = 90^o$, w_1 remains almost constant, close to unity, whereas w_2 grows fast to higher values. Finally, Fig. 7.28d shows the change of the orientation angle ψ_1, when the voids are initially oriented to $\psi_1 = 45^o$. The angle ψ_1 approaches progressively the zero value, since the voids try to align themselves with the principal loading directions. However, the closure of the porosity occurs before

ψ_1 reaches this asymptotic value.

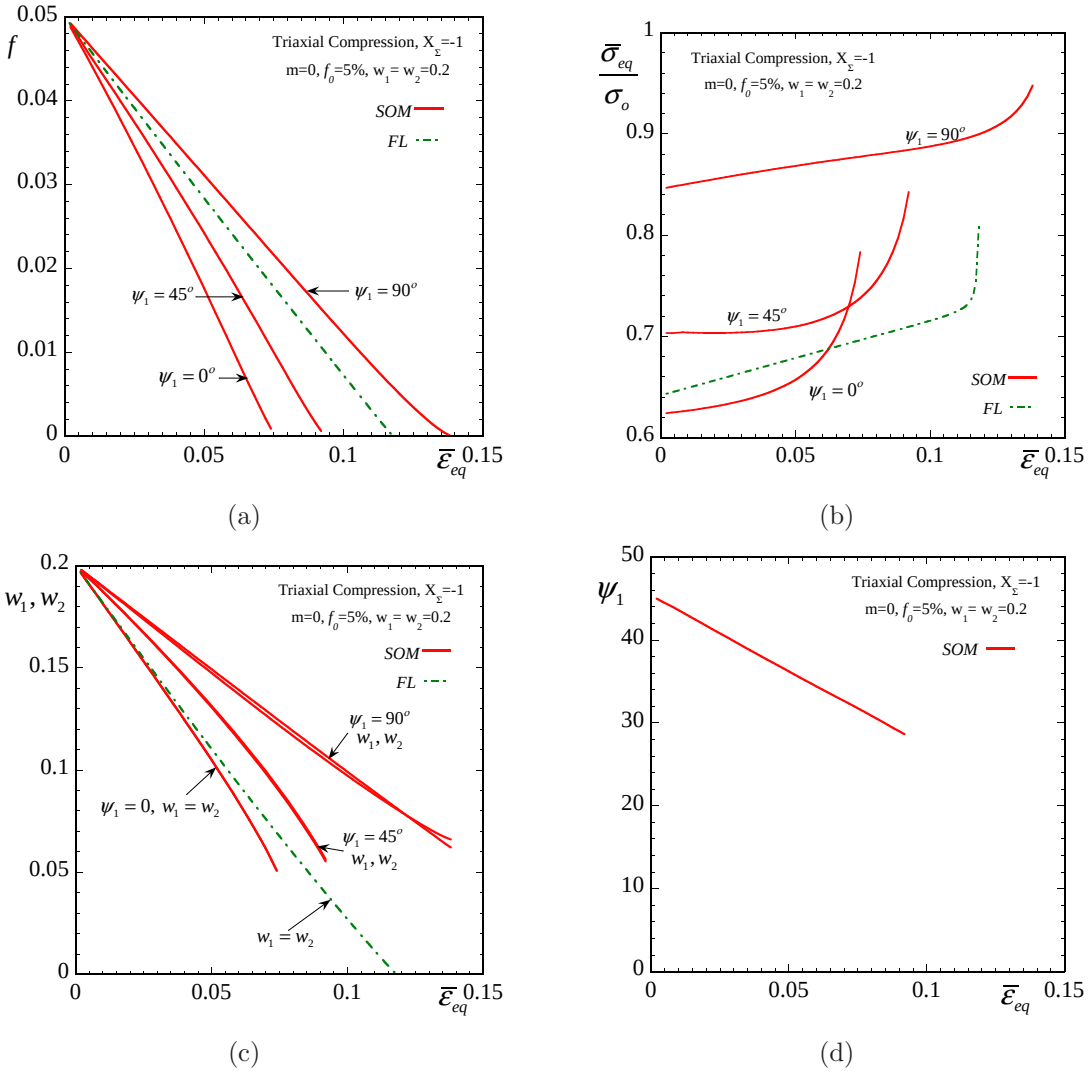

Figure 7.29: Results are shown for the evolution of the relevant microstructural and macroscopic variables for a porous material consisted of oblate voids with initial aspect ratio $w_1 = w_2 = 0.2$ and orientated in three different directions $\psi_1 = 0, 45, 90^o$, $\psi_2 = \psi_3 = 0$. The initial porosity is $f_o = 5\%$ and the matrix phase exhibits an ideally-plastic behavior. The composite is subjected to triaxial compression loading conditions with fixed stress triaxiality, $X_\Sigma = -1$. *SOM* and *FL* (Flandi and Leblond, 2005) estimates are shown for the evolution of the (a) porosity f, (b) the macroscopic stress $\overline{\sigma}_{eq}/\sigma_o$ normalized by the yield stress of the matrix phase, (c) the aspect ratios w_1 and w_2, and (d) the orientation angle ψ_1.

Finally, we discuss the case of triaxial compression with fixed stress triaxiality $X_\Sigma = -1$ (or $T/S = 0.4$ with $S/|S| < 0$). Fig. 7.29a presents *SOM* and *FL* estimates for the evolution of porosity f as a function of the equivalent macroscopic strain $\overline{\varepsilon}_{eq}$. The *FL* curve corresponds to the case of oblate voids with $\psi_1 = 0^o$. The main observation in the context of this figure is that all the curves predict a very sharp drop of the porosity f (note that the scale of the $\overline{\varepsilon}_{eq}$ axis is blown up). Similarly to the $X_\Sigma = 1$ predictions, the evolution of porosity is found to depend slightly on the orientation angle ψ_1. On the contrary, the corresponding normalized equivalent macroscopic stress

$\overline{\sigma}_{eq}/\sigma_o$ in Fig. 7.29b, shows a much stronger dependence on ψ_1. Even though all the curves predict a progressive hardening of the porous medium, the $\psi_1 = 90^o$ estimate is significantly higher than the corresponding $\psi_1 = 0^o$ and $\psi_1 = 45^o$ curves. Of course the FL estimate lies closer to the $\psi_1 = 0^o$ result of the SOM. In all the cases, the $\overline{\sigma}_{eq}/\sigma_o$ curves exhibit a sharp increase, which is linked to the closure of the porosity, and thus the hardening of the porous material.

Fig. 7.29c, in turn, shows the corresponding estimates for the evolution of the aspect ratios w_1 and w_2. In this figure, the SOM estimate for $\psi_1 = 0^o$ and the relevant FL predictions are in good agreement. It is also interesting to note that, for $\psi_1 = 45^o$ and $\psi_1 = 90^o$, the aspect ratios remain almost identical, i.e., $w_1 \backsimeq w_2$, which implies that the initially oblate voids preserve their shape during the deformation process. Finally, Fig. 7.29d shows the evolution of ψ_1, which starts at 45^o, but because of the early closure of the porosity, the ψ_1 curve is not able to reach any asymptotic value, which is intuitively the zero value in this case.

7.5.5 Brief summary

In summary, the SOM and FL estimates have been used to predict the evolution of the microstructure in porous media with an ideally-plastic matrix phase consisting of initially prolate or oblate voids, whose principal axes were assumed to be aligned and misoriented with the applied loading directions. For simplicity, we considered only rotations of the voids around the $1-$axis, while the loading was axisymmetric about the $3-$direction. Even in these particular cases, there has been found that the misorientation of the voids can have a crucial effect on the macroscopic response of the material. In this regard, it has been shown that the SOM model is able to to explain qualitatively [‡] experimental evidence presented in the beginning of the section. On the other hand, the FL model is valid only for spheroidal voids and axisymmetric loading conditions that preserve the alignment of the microstructure and the loading during the deformation, and thus is not capable of handling these more general microstructural and loading conditions.

Furthermore, it is important to mention that in cases that the porosity decreases rapidly due to compressive loadings, which is a hardening mechanism, the porous medium could exhibit strong softening due to the spin of the microstructure. This certainly implies that the material may become unstable in those cases. In addition, the voids exhibit a tendency to align themselves with the principal loading directions, which is intuitively expected. Indeed, the SOM method predicts such a behavior for all the loadings presented in this section. In the following section, we examine possible development of instabilities in porous media with an ideally-plastic matrix phase when subjected to plane-strain loading conditions.

[‡] We have no definite experimental or numerical results to perform a quantitative study.

7.6 Plane-strain loading for porous media with an ideally-plastic matrix phase: instabilities

In this section, we make use of the "second-order" (SOM) and the "variational" (VAR) method to study the effective response and possible development of instabilities in porous materials with an ideally-plastic matrix phase consisting of initially spherical voids subjected to plane-strain loading conditions. As already discussed in section 2.9, these materials can lose ellipticity and thus become unstable. Similar to the two-dimensional case discussed in section 5.4, we will consider loadings that do not induce a change in the orientation of the principal axes of the voids. The reason for this is that the computation of the effective Jaumann hardening rate, introduced in relation (2.318) can be simplified considerably, since in this case the Jaumann rates and the standard time derivatives of the relevant quantities coincide.

"Variational" method. Thus following the analysis presented in subsection 2.8.1 (and section 6.1) for ideally-plastic materials, the Jaumann hardening rate, delivered by the "variational" method (VAR), is written as

$$H_J = H = -\left\{ q_f \frac{\partial \widetilde{\Phi}_{var}}{\partial f} + \sum_{i=1}^{2} q_w^{(i)} \frac{\partial \widetilde{\Phi}_{var}}{\partial w_i} \right\}, \tag{7.9}$$

where $\widetilde{\Phi}_{var}$ is the effective yield condition defined in (6.5). In turn, the functions q_f and $q_w^{(i)}$ have been derived in relations (2.241) and (2.242), such that

$$q_f(\overline{\boldsymbol{\sigma}};\, f,\, w_1,\, w_2) = (1-f)\, \frac{\partial \widetilde{\Phi}_{var}}{\partial \overline{\sigma}_{jj}}, \qquad j = 1,2,3, \tag{7.10}$$

and

$$q_w^{(i)}(\overline{\boldsymbol{\sigma}};\, f,\, w_1,\, w_2) = w_a \left(\mathbf{n}^{(3)}\, \mathbf{n}^{(3)} - \mathbf{n}^{(i)}\, \mathbf{n}^{(i)} \right) \cdot \frac{3}{(1-f)^2} \widehat{\mathbf{Q}}^{-1} \frac{\overline{\boldsymbol{\sigma}}}{\sigma_o}, \qquad i = 1,2, \tag{7.11}$$

with no sum on i. Furthermore, $\widehat{\mathbf{Q}} = \frac{1}{\mu}\mathbf{Q}$ has been defined in the context of relation (6.2) and is independent of the shear moduli μ (see Appendix IV of chapter 2). In turn, the computation of $\mathbf{Q}$ (see (2.59)) is performed numerically and its calculation is detailed in Appendix I of chapter 2. Note that in this case, the use of $\mathbf{n}^{(i)}$ is somewhat redundant in the sense that we considered that the principal axes of the voids are aligned with the axes of the laboratory frame, i.e., $\mathbf{n}^{(1)} = \mathbf{e}^{(1)}$, $\mathbf{n}^{(2)} = \mathbf{e}^{(2)}$ and $\mathbf{n}^{(3)} = \mathbf{e}^{(3)}$.

"Second-order" method. Next following the analysis presented in subsection 2.8.2 (and section 6.1) for ideally-plastic materials, the Jaumann hardening rate, delivered by the "second-order" method (SOM), is written as

$$H_J = H = -\left\{ y_f \frac{\partial \widetilde{\Phi}_{som}}{\partial f} + \sum_{i=1}^{2} y_w^{(i)} \frac{\partial \widetilde{\Phi}_{som}}{\partial w_i} \right\}, \tag{7.12}$$

where $\widetilde{\Phi}_{som}$ is the effective yield condition defined in (6.21). In turn, the functions y_f and $y_w^{(i)}$ are given by

$$y_f(\overline{\boldsymbol{\sigma}};\, f,\, w_1,\, w_2) = (1-f)\, \frac{\partial \widetilde{\Phi}_{som}}{\partial \overline{\sigma}_{jj}}, \qquad j = 1,2,3, \tag{7.13}$$

and

$$y_w^{(i)}(\overline{\boldsymbol{\sigma}};\, f,\, w_1,\, w_2) = w \left(\mathbf{n}^{(3)}\, \mathbf{n}^{(3)} - \mathbf{n}^{(i)}\, \mathbf{n}^{(i)} \right) \cdot \frac{3}{1-f} \mathbf{K} \left(\frac{3}{1-f}\, \widehat{\mathbf{Q}}(k)^{-1}\, \frac{\overline{\boldsymbol{\sigma}}}{\sigma_o} - \boldsymbol{\mathcal{M}}(k)\, \frac{\check{\boldsymbol{\sigma}}}{\sigma_o} \right), \tag{7.14}$$

with $i = 1, 2$ and no sum on i. In addition, $\mathbf{E}$ and $\mathbf{F}$ are given by (4.24), whereas $\widehat{\mathbf{Q}} = \frac{1}{\mu}\mathbf{Q}$ is a function of the anisotropy ratio k but is independent of the shear moduli μ (see Appendix IV of chapter 2). In turn, the computation of $\mathbf{Q}$ (see (2.59)) is performed numerically and its calculation is detailed in Appendix I of chapter 2. The evaluation of the anisotropy ratio k has been described in relation (6.22). Similar to the previous case, the principal axes of the voids are considered to be aligned with the axes of the laboratory frame, i.e., $\mathbf{n}^{(1)} = \mathbf{e}^{(1)}$, $\mathbf{n}^{(2)} = \mathbf{e}^{(2)}$ and $\mathbf{n}^{(3)} = \mathbf{e}^{(3)}$.

Now, the only non-zero components of the strain-rate and stress tensor are $\overline{D}_{11}$, $\overline{D}_{22}$, $\overline{\sigma}_{11}$, $\overline{\sigma}_{22}$ and $\overline{\sigma}_{33}$, respectively. We recall here the definitions for the mean stress $\overline{\sigma}_m$ and the equivalent stress $\overline{\sigma}_{eq}$

$$\overline{\sigma}_{eq} = \frac{1}{\sqrt{2}}\sqrt{(\overline{\sigma}_{11} - \overline{\sigma}_{22})^2 + (\overline{\sigma}_{11} - \overline{\sigma}_{33})^2 + (\overline{\sigma}_{33} - \overline{\sigma}_{11})^2}, \qquad \overline{\sigma}_m = \frac{\overline{\sigma}_{11} + \overline{\sigma}_{22} + \overline{\sigma}_{33}}{3}, \tag{7.15}$$

as well as for the stress triaxiality X_Σ,

$$X_\Sigma = \frac{\overline{\sigma}_m}{\overline{\sigma}_{eq}}. \tag{7.16}$$

In this application, we are interested for loadings with fixed stress triaxiality X_Σ during the deformation process. Hence, the known quantities in the problem are:

$$\overline{D}_{11} = 1, \quad \overline{D}_{33} = 0, \quad X_\Sigma = \text{given}. \tag{7.17}$$

The previous three relations need to be satisfied together with the effective yield condition $\widetilde{\Phi}(\overline{\boldsymbol{\sigma}}) = 0$ (see relation (6.5) and (6.21)). Thus, the unknowns of the problem are

$$\overline{\sigma}_{11}, \quad \overline{\sigma}_{22}, \quad \overline{\sigma}_{33}, \quad \dot{\Lambda}. \tag{7.18}$$

It is worth mentioning that we have arbitrarily made the choice of $\overline{D}_{11} = 1$ and $\overline{D}_{33} = 0$, while different options could also be considered. Nonetheless, since the porous medium is initially isotropic, the choice of the plane-strain direction is arbitrary and does not affect the final result, which in this case is the prediction of the shear localization instability. On the other hand, if we consider anisotropic porous media that consist of initially ellipsoidal voids with aspect ratios $w_1 \neq 1$ or $w_2 \neq 1$, then the specific choice of the plane-strain direction is crucial. For simplicity, we will consider only porous media that are initially isotropic in this work.

The sufficient conditions for shear localization are given by relations (2.320) and (2.321). The first condition is related to the determination of the critical hardening rate H_{cr}. For the previously described loading, the critical hardening rate can be shown to be $H_{cr} = 0$ (Rice, 1976). The second condition (2.321) simply yields that there should exist a non-deforming surface in the deformation field. Because of the plane-strain character of the problem this is satisfied trivially. Hence, the only condition sufficient for shear localization is the zero hardening rate. In the following paragraphs, we will study the possibility of shear localization in the case of fixed stress triaxiality loading.

Fig. 7.30 shows evolution curves for the porosity f, the aspect ratios w_1 and w_2, the hardening rate H and the equivalent stress $\overline{\sigma}_{eq}$ normalized by the flow stress in the matrix phase σ_o as a function of the stress triaxiality ($X_\Sigma = -0.05, 0.4$) and the macroscopic strain $\overline{\varepsilon}_{eq}$ for initial porosity $f_o = 10\%$.

More specifically, Fig. 7.30a shows the evolution of porosity f as predicted by the SOM and the VAR methods. For $X_\Sigma = -0.05$, the SOM predicts a faster decrease in the porosity than the VAR

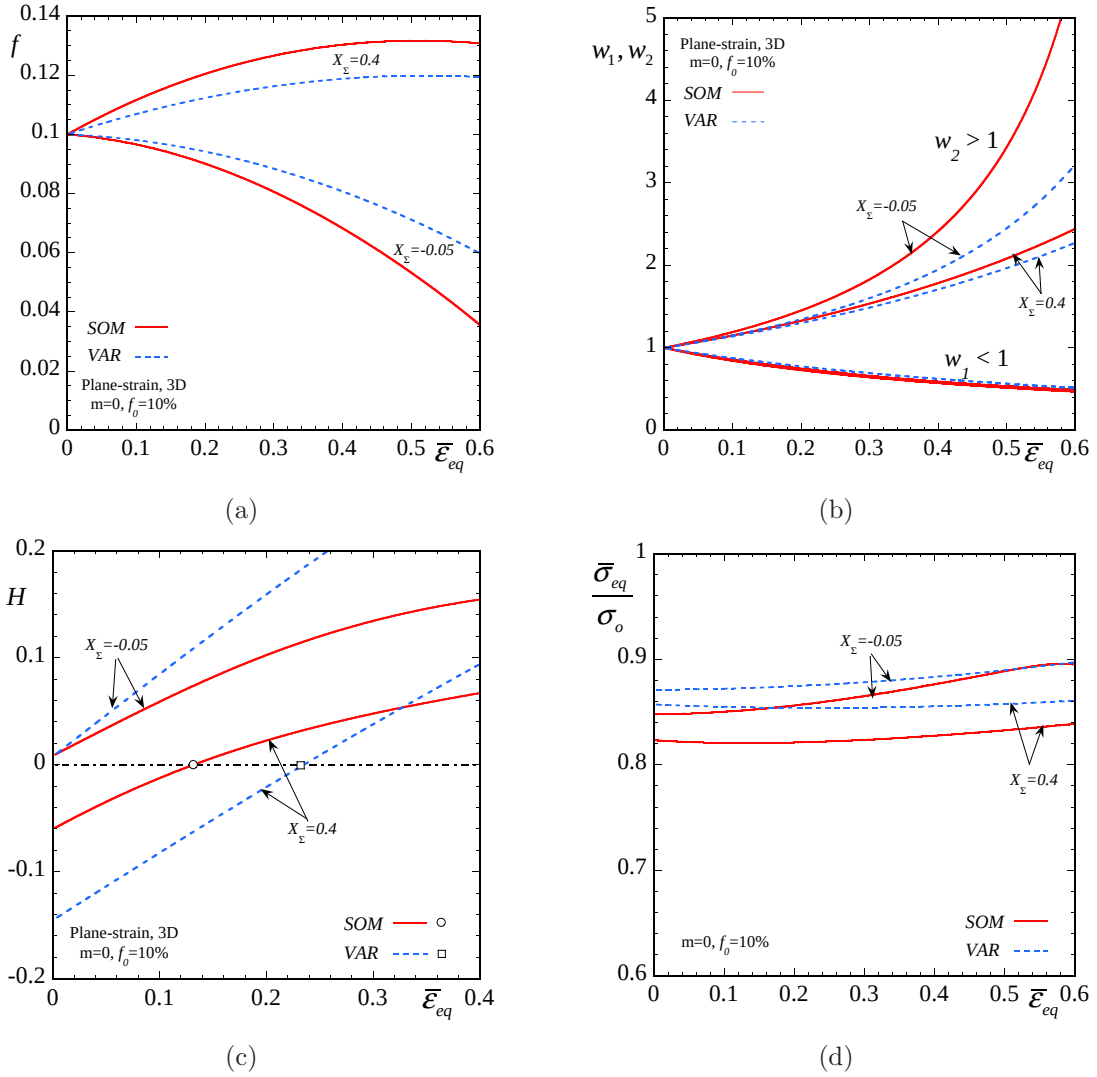

Figure 7.30: Results are shown for the evolution of the relevant microstructural and macroscopic variables for a porous material consisted of initially spherical pores with initial porosity $f_o = 10\%$. The matrix phase exhibits an ideally-plastic behavior, while the composite is subjected to plane-strain loading conditions with fixed stress triaxiality, $X_\Sigma = -0.05, 0.4$. *SOM* and *VAR* estimates are shown for the evolution of the (a) porosity f, (b) the aspect ratio w, (c) the normalized, macroscopic equivalent stress $\bar{\sigma}_{eq}/\sigma_o$ (σ_o denotes the flow stress of the matrix phase), and (d) the hardening rate of the composite as a function of the macroscopic, equivalent strain $\bar{\varepsilon}_{eq}$. In (d) the symbols ∘ and □ denote the loss of ellipticity for the porous medium as predicted by the *SOM* and the *VAR*, respectively.

method, and thus a faster hardening of the porous medium. On the other hand, in Fig. 7.30b, the corresponding *SOM* estimates for the evolution of the aspect ratios w_1 and w_2 indicate that the material softens faster in the direction of the applied loading (this is explained by the sharp increase of w_2 and decrease of w_1). In contrast, the rate of change of the aspect ratios predicted by the *VAR* method is lower than the one of the *SOM*. These two contradicting mechanisms, i.e., evolution of porosity and aspect ratios, when they are combined together, they yield an overall hardening of the porous medium, which is illustrated by the initial positive hardening rate H in Fig. 7.30c, for both

methods. This geometrical hardening of the porous medium continues as the deformation progresses, and as a consequence, the material does not exhibit instabilities, which is deduced by observing that H never crosses zero. In Fig. 7.30d, the corresponding normalized equivalent macroscopic stress $\overline{\sigma}_{eq}/\sigma_o$ just verifies this observations, while the SOM exhibits initially softer behavior than the corresponding VAR estimate.

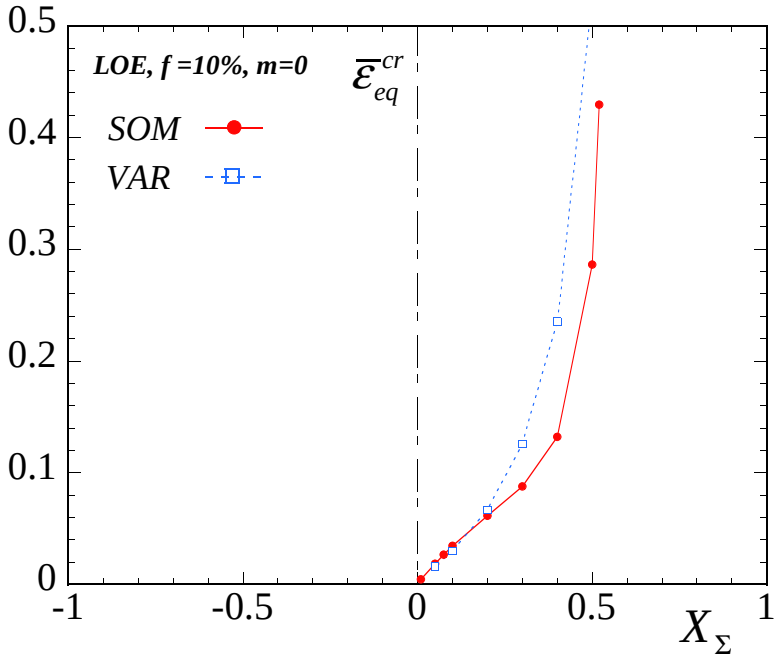

Figure 7.31: Macroscopic onset-of-failure curves as predicted by the SOM and VAR calculations, for an initially isotropic porous medium with ideally-plastic matrix phase and initial porosity $f_o = 10\%$. The plot shows the critical equivalent strain $\overline{\varepsilon}^{cr}_{eq}$ as a function of the applied stress triaxiality X_Σ.

On the other hand, for $X_\Sigma = 0.4$, the corresponding SOM estimate predicts an initially positive rate of growth of the porosity f, whereas at a finite strain (e.g., $\overline{\varepsilon}_{eq} \sim 50\%$), it starts slowly to decrease. The same observation is also true for the VAR estimate with the only difference that the growth of f is smaller than in the SOM case. Note that the increase of the porosity is a softening mechanism. On the other hand, the fast rate of change in the aspect ratios results in the hardening of the material in the direction of the applied loading. This is true for both the SOM and the VAR methods, with the difference that in the SOM the rate of change of w_1 and w_2 is higher than in the VAR. In contrast to the previous case, the porous material exhibits an initial softening, which evolves into hardening at a finite strain. This is shown in Fig. 7.30c, where for both the SOM and the VAR the corresponding curve for H crosses zero. Note that the symbols $\circ$ and $\square$ indicate the critical strain-rate that H becomes zero as predicted by the SOM and the VAR models respectively. As already mentioned before, when $H = 0$ the porous material material may become unstable. Obviously, both the SOM and the VAR methods predict such shear localization instabilities, however, the critical strain where the instability occurs is different. In Fig. 7.30d, the corresponding macroscopic equivalent stress $\overline{\sigma}_{eq}/\sigma_o$ simply verifies the previous conclusions. It is noted, though, that the VAR predicts a stiffer

response (higher values for $\overline{\sigma}_{eq}/\sigma_o$) for the porous composite than the SOM.

The procedure of identifying an instability point, described previously, can be repeated for the entire range of stress triaxialities $X_\Sigma \in (-\infty, +\infty)$. Thus, Fig. 7.31 is a map of these instability points. In particular, the critical strain $\overline{\varepsilon}_{eq}^{cr}$, where the instability occurs, is plotted as a function of the stress triaxiality X_Σ. It is interesting to note that despite the many differences exhibited by the SOM and the VAR methods for the prediction of the evolution of the porosity and the aspect ratios (see Fig. 7.30), the corresponding instability map is very similar. In fact, the SOM predicts instabilities at lower values of the deformation when compared to the VAR method. It should be emphasized at this point that, the FL (Flandi and Leblond, (2005)) model is not capable of predicting this type of instabilities due to the fact that it cannot consider plane-strain loading conditions.

7.7 Concluding remarks

In this chapter, we have studied the important problem of estimating the evolution of microstructure in porous media consisting of spherical or ellipsoidal voids subjected to general loading conditions. It is apparent that the combinations of loading conditions and microstructural configurations are countless. For this reason, we had to choose among the many possible loadings and microstructures, a representative and, at the same time, a simple combination of the relevant variables so that we can extract useful information on the effective response of porous media when subjected to finite deformations. In particular, the new "second-order" model, discussed in section 2.6, has been compared with results extracted by the Lee and Mear (1994) study for dilute porous media, as well as with unit-cell finite element calculations for axisymmetric loading conditions such that the alignment of the principal axes of the voids and the principal loading directions is preserved. For comparison, the "variational" method and the recent Flandi and Leblond (2005) model were also included in this study. The "variational" method, as already expected by earlier studies (Ponte Castañeda and Zaidman, 1994; Kailasam and Ponte Castañeda, 1998) and the discussion made in the context of the previous chapter, delivers much stiffer estimates than the "second-order" method especially at high stress triaxialities. On the other hand, the Flandi-Leblond model is constructed only for transversely isotropic porous materials (i.e., spheroidal voids) subjected to axisymmetric loading conditions such that the transverse isotropy of the material is preserved during the deformation process. Thus, this last model has been used to compare with the "second-order" estimates in the cases that it is applicable.

Firstly, the "second-order" model has been compared with corresponding estimates by Lee and Mear (1994) in the case of dilute porous media consisting of spheroidal voids subjected to axisymmetric tensile or compressive loading conditions aligned with the pore symmetry axis. The main conclusion in the context of this comparison was that the "second-order" model is in good agreement with the Lee and Mear method. However, it is interesting to note that the Lee and Mear estimates predict a stiffer effective response for the porous material than the "second-order" model leading to lower or higher values for the porosity at tensile or compressive loadings, respectively. To explain this differences between the two models, we have included finite element unit-cell results, where it

was found that the "second-order" predictions lie closer to the finite element results than the Lee and Mear estimates do. The reason for this was attributed to the fact that the Lee and Mear procedure makes use of the assumption that the void evolves through a sequence of spheroidal shapes (see also Fleck and Hutchinson, 1986) during the deformation process, which constitutes an idealization that may become rough when compared with finite element calculations where the void is allowed to deform in a non-spheroidal shape.

Moreover, it is also important to mention that, according to Huang (1991b), in the method used by Lee and Mear to predict the evolution of microstructure in dilute porous media, a very large number of terms needs to be considered in the Rayleigh-Ritz eigen-function expansion to achieve sufficient accuracy at high stress triaxialities and nonlinearities. In this regard, the author believes that similar to the case of cylindrical pores, these two aforementioned observations could explain the fact that the Lee and Mear technique predicts lower values for the evolution of porosity.

On a separate subsection, we studied the effect of the initial shape of the voids on evolution of porosity under compressive loadings. In this regard, both the "second-order" and the Lee and Mear (1999) methods were found to be in good agreement for the prediction of the evolution of the porosity. In particular, both methods predict that if a compressive load is applied along the symmetry axis of the spheroidal void, then the materials containing oblate voids are more compliant than the ones comprising prolate voids leading to a fast closure of the porosity. In contrast, when the voids are prolate the porosity still goes to zero but with a much slower rate than in the case of oblate voids.

In the sequel, the "second-order" method has been compared with unit-cell finite element results for a wide range of stress triaxialities ($X_\Sigma = \pm 1/3, \pm 1, \pm 3$ or $T/S = 0, 0.4, 0.727$ with $S/|S| \leqslant 0$) and low initial porosities $f_o = 0.01\%$. The "second-order" model was found to improve significantly on the earlier "variational" method, which was shown to underestimate (overestimate) the evolution of porosity when the porous medium is subjected to tension (compression) loadings. Although, at high triaxialities and nonlinearities the "second-order" model overestimates the evolution of the aspect ratio, the corresponding predictions for the macroscopic equivalent strain-rate are in very good agreement with the finite element results. This is due to the fact that the evolution of porosity dominates over the evolution of the aspect ratios of the voids and thus controls the effective behavior of the porous medium. In this regard then, it is safe to say that the "second-order" method is capable of estimating with very high accuracy the macroscopic behavior of porous media that are subjected to this special, albeit important, axisymmetric loading condition, for the entire range of stress triaxialities and nonlinearities.

For completeness, these results have been compared in a separate section with the Flandi-Leblond (2005) model for a high nonlinearity (nonlinear exponent of the matrix phase $n = 10$) and for all the aforementioned triaxialities. The main conclusion that comes out of this comparison is that both models provide accurate estimates for the determination of the effective response of a porous medium. The "second-order" method delivers better results for the evolution of the porosity and the macroscopic strain-rate, particularly for low stress triaxialities. On the other hand, the Flandi-Leblond model can capture nonlinear effects of the evolution of the aspect ratio of the voids. This effect was initially discussed by Budiansky et al. (1982) and Fleck and Hutchinson (1986). These

authors found that at sufficiently high triaxialities and nonlinearities the voids elongate in a direction that is transverse to the maximum principal strain or stress. Nonetheless, it is also important to emphasize that in this study it has been shown that this counterintuitive elongation of the void is a *local* phenomenon and thus, does not affect the macroscopic behavior of the composite, which is mainly controlled by the evolution of the porosity at high stress triaxialities.

In the following, we have studied the problem of estimating the evolution of microstructure in porous media with an ideally-plastic matrix phase and spheroidal voids whose principal axes do not coincide with the principal loading directions. For simplicity, we have considered initially prolate and oblate voids rotated around the $1-$axis and axisymmetric loading conditions with the maximum tensile or compressive principal stress aligned with the $3-$axis. When the major axis of the voids was aligned with the loading at 0^o, the Flandi-Leblond model was also used to provide estimates for the evolution of the relevant microstructural variables. However, when the voids are considered misaligned with the loading directions the Flandi-Leblond model was not valid and only "second-order" estimates were shown. The main conclusion in the context of these examples is that the initial orientation of the voids relative to the applied loading can have dramatic effects on the effective response of the porous medium. Interestingly, we observed that even though the porosity may decrease significantly during the deformation process, which implies that the porous medium may harden, because of the rotation (or spin) of the microstructure the material exhibits strong softening. We further noted that the initially misoriented voids tend to spin in order to align their principal axes with the principal loading directions.

Then, the "second-order" and the "variational" methods have been used to predict possible shear localization instabilities for porous media with an ideally-plastic matrix phase and initially spherical voids subjected to plane-strain loading conditions with fixed stress triaxiality. An important conclusion that results from the study of this problem is that the various microstructural variables interact in very complicated ways such that the final response of the material may exhibit overall geometrical softening or hardening. This evolution of the microstructural variables then leads to shear localization instabilities as presented by Rice (1976). In particular, we have studied the evolution of microstructure for initially isotropic porous media with porosity $f_o = 10\%$ for two different stress triaxialities $X_\Sigma = -0.05, 0.4$. For the first one, both the "second-order" and the "variational" models did not predict a shear localization instability. In this particular case, the material always hardens during the deformation process. On the other hand, for $X_\Sigma = 0.4$ the porous medium initially exhibits a softening which evolves into hardening during the deformation. This change in the effective response of the porous material is translated into a change of sign for the corresponding hardening rate H, which, in turn, implies that the material may lose stability at this point (Rice, 1976). Then, we have complemented this study with a complete map of the instability points as a function of the stress triaxiality. In that plot, it was interesting to observe that the "second-order" and the "variational" predictions exhibited a very similar qualitative behavior by predicting instabilities only in the positive triaxiality regime. However, the "second-order" has been found to predict shear localization at a lower macroscopic equivalent strain than the "variational" method. It is further noted that the Flandi-Leblond model cannot be used for plane-strain loading conditions and for this reason was not

included in this study.

As a closing remark, it is emphasized that the new "second-order" model is based on a rigorous variational principle which is valid for general ellipsoidal microstructures and loading conditions. It has been shown that the response of a porous material depends strongly on the orientation of the microstructure relative to the loading directions. This last conclusion amplifies the significance of having general models that are able to take into account this microstructural effects, in contrast with earlier models that can only deal with simple microstructures and loading conditions (i.e., spheroidal microstructures and axisymmetric loading conditions aligned with the pore symmetry axis). It should be mentioned that the "variational" method is also able to deal with general microstructures, where it provides relatively good qualitative agreement with the finite element calculations and the new "second-order" model. However, the "variational" method is overly stiff for high triaxialities and this prohibits its use in several applications where the applied pressures are high.

Chapter 8

Closure

In this thesis, homogenization-based constitutive models have been developed for viscoplastic two phase materials, and particularly porous materials subjected to finite deformations. These constitutive models have the capability of handling the nonlinear response of the local phases, microstructural information, such as the volume fraction, shape, orientation and distribution of the phases in a given two-phase system, as well as the evolution of these microstructural and macroscopic variables along a given loading path. Incorporating the evolution of the microstructure and the effective response of the material in these models allows us to predict possible development of macroscopic instabilities, such as shear localization, which occur due to the geometrical softening or hardening of the medium during the deformation process.

The proposed constitutive models, discussed in this work, are based on two nonlinear homogenization methods:

- the "variational" method (VAR) of Ponte Castañeda(1991),
- the "second-order" method (SOM) of Ponte Castañeda (2002a).

It is noted that the "variational method has been given an interpretation as "modified secant method" by Suquet (1995). Both of the aforementioned nonlinear homogenization methods are based on the construction of a "linear comparison composite" (LCC). The reason for such a construction is linked to the fact that there exist several *linear* homogenization methods in the literature, that are capable of dealing with $N-$phase systems, such as the Hashin-Shtrikman bounds (1963), the Willis estimates (1977, 1978), as well as the Ponte Castañeda and Willis (1995) results for ellipsoidal particulate microstructures. In turn, these linear estimates can be used to deliver estimates for the nonlinear composite via the construction of the LCC. It is important to point out that, in spite of the fact that the homogenization is carried out at the level of the LCC, these methods have the capability of accounting for the nonlinear behavior of the phases by letting the moduli of the phases in the LCC depend on the nonlinear properties of the phases in the original nonlinear composite.

Motivated by several experiments and applications, special attention has been given to viscoplastic composites, and particularly porous media with "particulate" microstructures and isotropic phases. General expressions have been presented for the effective stress potential, as well as for the phase average and second moments of the fields of two-phase composites consisting of ellipsoidal inclusions

(or voids for the case of porous media) distributed randomly in a matrix phase. It is remarked that spherical or cylindrical inclusions, cracks and laminated microstructures can be recovered as limiting cases of the ellipsoidal inclusions.

For completeness, we have studied first the problem of homogenization in two-phase composites consisting of linearly viscous and "thermo-viscous" phases. Within this class of linear composites with "particulate" microstructures, use has been made of the Willis estimates (1978) to obtain expressions for the effective behavior of the composite. Further specialization of these general expressions has been provided for the limiting case of a linearly viscous and "thermo-viscous" porous materials. Having established rigorous estimates and bounds for this class of linear composites, we have proceeded with the discussion of the "variational" and "second-order" nonlinear homogenization methods in the general context of two-phase viscoplastic systems, which were later specialized for viscoplastic porous media. A key difference between the "variational" and the "second-order" method is the type of the LCC used. More specifically, the "variational" method makes use of an *isotropic* LCC, which leads to rigorous lower bounds for the effective stress potential of the composite. These bounds can be shown to be optimal. On the other hand, the LCC within the "second-order" method is *anisotropic*. The anisotropy of the LCC can be viewed as a necessary feature when dealing with viscoplastic composites. The key for this explanation is associated with the fact that the local incremental response of nonlinear materials, and particularly viscoplastic ones, is *anisotropic*. Thus, one expects that by allowing the LCC to be anisotropic would reveal many of the nonlinear features of the local phases. Indeed, this is the case in our problem, particularly for low triaxiality loadings.

However, when the interest is on viscoplastic porous materials and high triaxiality loadings (or purely hydrostatic loadings), both the "variational" and the "second-order" (in the original formulation of Ponte Castañeda (2002a) and later by Idiart and Ponte Castañeda (2005)) methods overestimate significantly the effective response of the porous medium, particularly at low and moderate volume fractions of the porous phase (or porosity). Nonetheless, it is emphasized that it has not yet been possible to fully optimize the "second-order" method, in terms of all the parameters involved in this technique, especially with respect to the "reference" second-order stress tensor. In this work, we have made an attempt to propose a more general reference stress tensor that would improve the hydrostatic behavior of the "second-order" method, while preserving the capability of handling completely general loadings and ellipsoidal microstructures. To achieve that, we made use of the exact hydrostatic solution for the "composite sphere or cylinder assemblage" microstructure of Hashin (1962), to compute the reference stress tensor. In the sequel, this choice has been approximately generalized for more general ellipsoidal microstructures and loading conditions. In this manner, we managed to bridge the *gap* between the earlier "variational" method and the recent "second-order" method, at least in the context of viscoplastic porous media.

In order to validate and compare the new "second-order" model, we have included in our study several models for porous viscoplastic media proposed in the past thirty years in the literature. In this regard, Chapter 3 deals with the discussion of these methods and models. These studies can be divided into four main categories. The first group is related with the methodologies introduced by McClintock (1968), Rice and Tracey (1969) and Budiansky et al. (1982) in the context of *dilute*

viscoplastic porous media. These methods are based on a dilute approximation of the effective stress potential up to the first order in the volume fraction of the pores. In addition to that these models require the choice of a stream function, which leads to a proposed velocity field that ultimately minimizes the energy function of the dilute medium. Initially, these studies were restricted to the instantaneous response of dilute porous media consisting of spherical voids subjected to high triaxiality loadings. These techniques have been developed later by Fleck and Hutchinson (1986) and Lee and Mear (1992b,c; 1994; 1999) to account for cylindrical voids with elliptical cross-section, as well as for spheroidal voids with prolate or oblate shape subjected to axisymmetric loading conditions aligned with the pore symmetry axis. However, these models are based on a choice of a stream function, which poses limitations in the applicability of these approximations to two-dimensional problems or three-dimensional ones with certain symmetries, such as the one of spheroidal voids and axisymmetric loadings (aligned with the pore symmetry axis). In addition to this, the range of the validity of the expansion of the effective stress potential about the porosity diminishes to zero at high nonlinearities and stress triaxialities. This possibly explains the observations made by Huang (1991b), who found that a large number of terms needs to be considered in the representation of the stream function for convergence of the results at high nonlinearities and stress triaxialities. As a consequence, these methods can lead to underestimation of the dilatation rate of the void.

A second group of studies, related to viscoplastic porous materials, is associated with the well-known work of Gurson (1977), who made use of the exact solution for a shell (spherical or cylindrical cavity) under hydrostatic loadings, suitably modified, to obtain estimates for the effective behavior of porous solids with an ideally-plastic matrix phase and isotropic or transversely isotropic distributions of porosity. This model has been successfully extended to spheroidal voids and axisymmetric loading conditions (aligned with the symmetry of the void) by Gologanu et al. (1993, 1994, 1997). In the sequel, Leblond et al. (1994) extended the Gurson model to account for a more general viscoplastic behavior for the matrix phase. A series of works followed after that, including the studies of Gărăjeu et al. (2000), Flandi and Leblond (2005a,b) and Monchiet et al. (2007), which made use of trial velocity fields to obtain approximate estimates for the effective behavior of viscoplastic porous media. Nonetheless, all these methods are restricted to porous media consisting of spheroidal voids subjected to axisymmetric loading conditions (aligned with the pore symmetry axis). In contrast, the aforementioned nonlinear homogenization methods are based on a rigorous variational principle and thus are capable of dealing with more general ellipsoidal microstructures and loading conditions.

A third group of studies on viscoplastic porous media is related to the class of "sequentially laminated" microstructures. One of the main features of these composites, is that in the linear case, they are identical (Frankfort and Mura, 1986; Milton, 2002) to the Willis estimates (1978) for particulate microstructures used in this work to solve for the LCC. In this connection, the *nonlinear* sequential laminates are particularly appropriate to assess the accuracy of the "second-order" method and, in general, of any LCC-based homogenization method (such as the "variational" method), on condition that the Willis estimates be used for the LCC. It can be observed (deBotton and Hariton, 2002) that as the rank of the lamination increases, the material becomes isotropic. In this study, we made use of these *isotropic* high-rank laminates to compare with corresponding estimates obtained by

the "second-order" and the "variational" method. It should also be emphasized that recently Idiart (2007) has shown that when the high-rank sequential laminates are subjected to purely hydrostatic loading, they recover the composite sphere or cylinder assemblage solution. This result makes these materials an ideal test case for the homogenization methods studied in this thesis.

Finally, a fourth group of studies on viscoplastic porous media deals with the numerical computation of the fields in a periodic unit-cell consisting of a single void by making use of the well-known finite element method. However, the problem we are interested in is the one of random porous media. For this reason, a very small porosity (0.01%) has been used in the finite element calculations in order for the comparison with the nonlinear homogenization methods to be meaningful. For simplicity, we have studied porous media consisting of cylindrical voids subjected to plane-strain loading conditions, as well as of spherical voids subjected to axisymmetric loading conditions.

In the sequel of this thesis, Chapters 4 through 7 have dealt with the application of the above discussed methods in the context of viscoplastic porous materials. To be precise, Chapters 4 and 5 deal with the estimation of the effective behavior and evolution of microstructure in porous media consisting of cylindrical voids subjected to plane-strain loading conditions. The possibility of instabilities has also been addressed in this context. In turn, Chapters 6 and 7 are related to the determination of the effective behavior and evolution of microstructure in porous media consisting of spherical or ellipsoidal voids subjected to general loading conditions. In what follows, we summarize the main results obtained in these chapters.

Chapter 4 deals with the estimation of the effective behavior of porous materials consisting of aligned cylindrical voids with circular or elliptical voids distributed randomly and isotropically in an isotropic viscoplastic matrix. The material is subjected to plane-strain loading conditions. One of the main results of this chapter was that the "second-order" model, proposed in this work, improves dramatically on the earlier "variational" method, particularly at high stress triaxialities and nonlinearities. As already pointed out previously, the new "second-order" model is constructed such that it recovers the exact solution for a shell (cylindrical cavity in this case) under hydrostatic loadings. As a consequence, the "second-order" estimates are found to be in good agreement with corresponding results obtained by Fleck and Hutchinson (1986) and Lee and Mear (1992b) for the dilatation rate and the deviatoric part of the macroscopic strain-rate in dilute porous media. Furthermore, the "second-order" is found to be in very good agreement, for all nonlinearities, porosities and triaxialities considered, with corresponding results obtained by the high-rank laminates in the case of isotropic porous material with finite volume fraction of voids. Lastly, the "second-order" model has been used to estimate the effective behavior of porous media consisting of cylindrical voids with elliptical cross-section, where it was found that the effect of the porosity and the shape of the void may induce contradicting effects. For instance, elongation of the pore leads to geometrical hardening (softening) in the direction parallel (transverse) to its major axis, whereas increase of the porosity leads to softening and vice versa. Combination of these effects may lead to hardening in certain directions and softening in others.

In Chapter 5, use is made of the results of chapter 4 to predict the evolution of microstructure and the macroscopic behavior of porous media with cylindrical voids subjected to finite plane-strain

deformation. The new "second-order" model, as well as the "variational" method have been compared with corresponding results obtained by the Lee and Mear (1999) method (for dilute porous media) and unit-cell finite element calculations. In this connection, the "second-order" estimates were found to improve significantly on the earlier "variational" method by being in remarkable agreement with the Lee and Mear results in the dilute case, and the finite element predictions for finite, but still small, porosities for all nonlinearities and stress triaxialities considered. In particular, one of the main improvements of the "second-order" model is linked to the use of the anisotropic LCC as opposed to the isotropic LCC in the "variational" method. A second improvement of the "second-order" method against the "variational" method is associated with the accurate prediction of the evolution of porosity at high stress triaxialities. This has been achieved by choosing the "reference" stress tensor such that the "second-order" method recovers the analytical shell result in hydrostatic loadings. In this regard then, the "second-order" method has been used to predict shear localization instabilities in porous solids with an ideally-plastic matrix phase. For comparison reasons, the "variational" method and the Gurson model were also used. It has been observed that for the loadings considered (aligned loadings which induce no rotation of the principal axes of the pores), the Gurson model did not predict instabilities, while the "second-order" model was more unstable than the "variational" method. However, it is interesting to remark that the "second-order" model was in qualitative agreement with the "variational" method for the prediction of instabilities in porous solids with ideally-plastic matrix phase.

In contrast to Chapter 4 and 5, where two-dimensional model problems were studied in order to gain insight on the behavior of viscoplastic porous media, Chapters 6 and 7 deal with more realistic three-dimensional microstructures and loadings. More specifically, in Chapter 6, we have studied the effective behavior of isotropic and anisotropic viscoplastic porous media when subjected to more general loading conditions. One of the main results in the context of isotropic porous media is related to the fact that the "second-order" method and the sequential laminates were found to depend on all three invariants of the macroscopic stress tensor. Interestingly, the effect of the third invariant was found to be non negligible even at moderate and high triaxialities and moderate porosities leading to an "asymmetric" response of the composite in the $\Pi-$plane. On the other hand, the Leblond et al. (1994), the Gurson (1977) and the "variational" model depend only on the first two invariants of the macroscopic stress tensor. In the sequel, the "second-order" method has been compared with corresponding estimates obtained by the Flandi and Leblond (2005a) model for spheroidal (prolate and oblate) voids subjected to axisymmetric loading conditions. The agreement of the two methods was relatively good for these two cases.

In addition to these special cases, the "second-order" method has also been used to predict the effective behavior of porous materials with ellipsoidal voids subjected to more general loading conditions, not necessarily aligned with the principal axes of the voids. The main conclusion that came out of this chapter was that the misorientation of the microstructure relative to the principal loading directions can lead to significant softening or hardening of the material in certain directions. To study this effect in a more complete way, we have included cross-sections of the effective stress potential (or gauge surface) on the $\Pi-$plane (or octahedral plane). The resulting gauge curves

exhibited very different shapes, which were found to depend strongly on the shape of the voids, as well as on the relative orientation of the principal axes of the voids with respect to the principal loading directions. Furthermore, the effective behavior of a porous medium consisting of spheroidal voids has been shown to be completely different to the one of a porous material with ellipsoidal voids under the same loading conditions.

Finally, in Chapter 7, we have made use of the previous results to predict the evolution of microstructure in porous media consisting of spherical or ellipsoidal voids. The "second-order" method has been initially compared with corresponding results by Lee and Mear (1994) for dilute porous materials, where both methods delivered very similar results regarding the evolution of the porosity under several stress triaxialities. Next, the "second-order" and the "variational" methods have been compared with finite element predictions and results obtained by the Flandi and Leblond (2005b) model for porous media with initially spherical pores subjected to axisymmetric loading conditions. The main result of this comparison was that both the "second-order" and the Flandi and Leblond (2005a) models were in good agreement with the finite element predictions for all stress triaxialities considered. The "second-order" method delivers better results for the evolution of the porosity and the macroscopic strain-rate, particularly for low stress triaxialities. On the other hand, the Flandi-Leblond model can capture nonlinear effects of the evolution of the aspect ratio of the voids. This effect was initially discussed by Budiansky et al. (1982) and Fleck and Hutchinson (1986). These authors found that the voids elongate in a direction that is transverse to the maximum principal strain or stress at sufficiently high triaxialities and nonlinearities. Nonetheless, it is also important to emphasize that in this study it has been shown that this counterintuitive elongation of the void is a *local* phenomenon and thus, does not affect the macroscopic behavior of the composite, which is mainly controlled by the evolution of the porosity at high stress triaxialities.

Based on experimental evidence by Nakajima (2007), we have used the "second-order" method to study the evolution of the relevant microstructural and macroscopic variables in lotus-type porous metals. These materials consist of aligned elongated pores in a certain direction such that their initial response is transversely isotropic. It has been observed experimentally that if one performs a uniaxial compression test parallel to the symmetry axis of the voids the remaining porosity after 80% deformation is still significant. On the other hand if one applies the same load transversely to the pore symmetry axis the remaining porosity reduces dramatically. Interestingly, although expected, the "second-order" method has been able to predict such a qualitative behavior for a material consisting of prolate or oblate voids oriented in different angles. For completeness, the "second-order" and the "variational" models have then been used to predict shear localization instabilities in porous media consisting of initially spherical voids that are subjected to plane-strain loading conditions. Both the "second-order" and the "variational" methods were found to predict instabilities at low stress triaxialities, with the first one delivering unstable behaviors at lower strains than the second one. However, it should be mentioned that the porous media considered here are expected to become less unstable if the ideally-plastic assumption for the behavior of the matrix is relaxed by introducing hardening effects.

In summary, the new "second-order" model, developed in this thesis, has been shown to deliver

accurate estimates for viscoplastic porous media with general ellipsoidal microstructures subjected to general loading conditions. This new model is the continuation of a series of studies in the context of porous media, which manages to bridge the gap between various homogenization methods developed in the last years in the context of porous power-law materials. The main improvement of this new model against the previous versions of the "second-order" and the "variational" methods, is associated with the fact that it is constructed to recover the exact shell result under hydrostatic loading conditions. This allows the use of this method to solve several problems of interest, where the porous medium is subjected to high stress triaxiality loadings leading to a significant increase of the porosity and thus to failure of the material. Another advantage of this new model is linked to the fact that it is based on a rigorous variational principle which is valid for general ellipsoidal microstructures and loading conditions, in contrast with earlier models that can only deal with simple microstructures and loading conditions (i.e., spheroidal microstructures and axisymmetric loading conditions aligned with the pore symmetry axis). Lastly, the model is simple enough to be implemented in standard finite element packages to solve structural problems of interest.

At this stage, it is important to address some of the future directions associated with the results presented in this thesis. First of all, the present version of the "second-order" model is based on an ad-hoc prescription for the "reference" stress tensor. This choice requires the computation of two factors, which are related to the effective behavior of the porous material at purely hydrostatic loadings. It would be really useful if we could define a reference stress tensor that depends only in one factor leading to simplification of the calculations that need to be performed. Moreover, when the behavior of the porous material is not isotropic, there are no available exact results for hydrostatic pressure loadings, and for this reason, we had to introduce approximations for the computation of the reference stress tensor in this case. This approximation has led to a conservative prediction of the effective behavior of the porous material, particularly for ellipsoidal voids with very different aspect ratios. Although, this is not a bad feature of the method, especially in terms of designing, it would be interesting to investigate further this problem in this direction, as it would provide even more accurate results than the ones presented here. In addition, it has already been identified that the new "second-order" model does not predict accurately the evolution of the shape of the voids at sufficiently high stress triaxialities. Although to this end, it has been shown that the aspect ratio has only a minor effect on the effective behavior of the material, it would be interesting to examine further the reason for this inaccuracy and possibly propose a solution to this. This would allow us to study coalescence of voids for arbitrary loading conditions.

Another important remark is that the new "second-order" model has been applied in the context of porous solids with viscoplastic and ideally-plastic matrix phase. However, in real life applications, the mechanical behavior of the materials under consideration exhibit also elastic effects. Thus, it would be of great interest to be able to incorporate elastic effects in the above described models, which would allow the study of "elasto-plastic" porous materials. This can now be accomplished by making use of the recently proposed variational procedure by Lahellec and Suquet (2007a,b,c) to obtain estimates for the effective response and evolution of microstructure in elasto-plastic or elasto-viscoplastic porous media. The use of this procedure would allow us to solve more realistic problems

(such as metal fatigue), where a non-monotonic load is applied leading to unloading and unstable behaviors in the porous material. In addition, the model could then be implemented to standard finite element packages for solving real life applications such as rolling or extrusion of metals, ductile fracture and necking of specimens.

Finally, new lotus-type porous materials have been developed recently by Nakajima (2007), which are proposed for various bio-applications such as implants at regions of fractured bone or as superior dental prosthetics. One of the important reasons for using such materials is related to the fact that bone tissue is able to grow inside the porous phase of the metal, and thus allow the material interact more efficiently with the bio-environment. However, it is essential to be able to provide estimates for the mechanical behavior of such materials, since in most of the cases mentioned previously, they are subjected to complicated loading conditions leading to failure. The methods developed previously could ultimately provide qualitative and hopefully quantitative understanding of the mechanical behavior of such materials. It should also be mentioned that these materials possess lightweight and superior mechanical properties, and thus they could be used in several prospective applications such as mechanical parts of airplanes, automobiles, etc.

Bibliography

[1] Aravas, N. (1987). On the numerical integration of a class of pressure-dependent plasticity models. *Int. J. Num. Meth. Eng.* 24, 1395-1416.

[2] Aravas, N. (1992). Finite elastoplastic transformations of transversely isotropic metals. *Int. J. Solids Struct.* 29, 2137-2157.

[3] Aravas, N., Cheng C., Ponte Castañeda, P. (1995). Steady-state creep of fiber reinforced composites: constitutive equations and computational issues. *Int. J. Solids Structures* 32, 2219–2244.

[4] Aravas, N., Ponte Castañeda, P. (2004). Numerical methods for porous metals with deformation-induced anisotropy. *Comput. Methods Appl. Mech. Engng.* 193, 3767–3805.

[5] Ashby, M.F., Evans, A.G., Fleck, N.A., Gibson, L.J., Hutchinson, J.W., Wadley, H.N.G. (2000). Metal Foams: A Design Guide. Butterworth-Heinemann. ISBN 0 7506 7219 6.

[6] Bao, G., Hutchinson, J., McMeeking, R. (1991). Particle reinforcement of ductile matrices against plastic flow and creep. *Acta Metall. Mater.* 39, 1871–1882.

[7] Bensoussan, A, Lions, J. L., Papanicolaou, G. (1978). Asymptotic analysis for periodic structures. North Holland.

[8] Beran, M. (1965). Use of the variational approach to determine bounds for the effective permittivity of random media. *Nuovo Cimento* 38, 771–782.

[9] Berveiller, M., Zaoui A. (1979). An extensions of the self-consistent scheme to plastically-flowing polycrystals. *J. Mech. Phys. Solids* 26, 325–344.

[10] Bilger, N., Auslender F., Bornert, M., Masson, R. (2002). New bounds and estimates for porous media with rigid perfectly plastic matrix, *C. R. Mecanique* 330 127–132.

[11] N. Bilger, F. Auslender, M. Bornert, J.-C. Michel, H. Moulinec, P. Suquet and A. Zaoui, (2005). Effect of a nonuniform distribution of voids on the plastic response of voided materials: a computational and statistical analysis, *Int. J. Solids Struct.* 29 517–538.

[12] Bornert, M., Masson, R., Ponte Castañeda, P., Zaoui, A. (2001). Second-order estimates for the effective behaviour of viscoplastic polycrystalline materials. *J. Mech. Phys. Solids* 49, 2737–2764.

[13] Bornert, M., Stolz C. and Zaoui A., 1996. Morphologically representative pattern-based bounding in elasticity. J. Mech. Phys. Solids 44, 307331.

[14] Bouchitte, G., Suquet, P. (1991). Homogenization, plasticity and yield design. G. Dal Maso and G. F. Dell'Antonio, eds., Composite Media and Homogenization Theory, 107–133.

[15] Budiansky, B. (1965). On the elastic moduli of some heterogeneous materials. *J. Mech. Phys. Solids* 13, 223–227.

[16] Budiansky, B., Hutchinson, J. W., Slutsky, S. (1982). Void growth and collapse in viscous solids. *Mechanics of Solids, The Rodney Hill 60th aniversary Volume*, Hopkins, H. G. and Sewell, M. J., eds., Pergamon Press Oxford 13–45.

[17] Chen, C., Lu, T.J., Fleck, N. A. (1999). Effect of imperfections on the yielding of two-dimensional foams. *J. Mech. Phys. Solids, 47* (11), 2235-2272.

[18] Cheng, H., Gupta, K. C. (1989). A historical note on finite rotations. *J. Appl. Mech.* 56, 139145.

[19] Conde, Y., Despois, J.-F., Goodall, R., Marmottant, A., Salvo, L., San Marchi, C., Mortensen, A., (2006). Replication processing of highly porous materials. *Adv. Eng. Mater.*, 8(9), 795-803.

[20] Dafalias, Y., F. (1985). The plastic spin. *J. Appl. Mech.* 52, 865–871.

[21] Dafalias, Y., F., Rashid, M., M. (1989). The effects of plastic spin on anisotropic material behavior. *Int. J. Plasticity* 5, 227–246.

[22] Danas, K., Idiart, M.I., Ponte Castañeda, P., (2008a). A homogenization-based constitutive model for two-dimensional viscoplastic porous media. C. R. Mecanique 336, 79-90.

[23] Danas, K., Idiart, M.I., Ponte Castañeda, P., (2008b). Homogenization-based constitutive model for isotropic viscoplastic porous media. *Int. J. Solids Struct.*, in press.

[24] deBotton, G. (2005). Transversely isotropic sequentially laminated composites in finite elasticity. *J. Mech. Phys. Solids* 53, 1334–1361.

[25] deBotton, G., Hariton, I. (2002). High-rank nonlinear sequentially laminated composites and their possible tendency towards isotropic behavior. *J. Mech. Phys. Solids* 50, 2577–2595.

[26] deBotton, G., Ponte Castañeda, P. (1992). On the ductility of laminated materials. *Int. J. Solids Struct.* 29, 2329–2353.

[27] Deshpande, V.S., Fleck, N. A. (1999). Isotropic constitutive models for metallic foams. *J. Mech. Phys. Solids*, 48(6-7), 1253-1283.

[28] Despois, J.F., Mueller R., Mortensen A., (2006). Uniaxial deformation of microcellular metals. *Acta Mater.* 54, 4129–4142.

[29] Drucker, D.C., (1966). The continuum theory of plasticity on the macroscale and the microscale. *J. Mater.* 1, 873910.

[30] Duva, J. M., Hutchinson, J. W. (1984). Constitutive potentials for dilutely voided nonlinear materials. *Mech. Mater.* 3, 41–54.

[31] Duva, J. M. (1986). A constitutive description of nonlinear materials containing voids. *Mech. Mater.* 5, 137–144.

[32] Eshelby, J. D. (1957). The determination of the elastic field of an ellipsoidal inclusion and related problems. *Proc. R. Soc. Lond.* A 241, 376–396.

[33] L. Flandi, J. B. Leblond, (2005a). A new model for porous nonlinear viscous solids incorporating void shape effects – I: Theory, *Eur. J. Mech. A/Solids* 24, 537–551.

[34] L. Flandi, J. -B. Leblond, (2005b). A new model for porous nonlinear viscous solids incorporating void shape effects – I: Numerical validation, *Eur. J. Mech. A/Solids* 24, 552–571.

[35] Fleck, N. A., Hutchinson, J. W. (1986). Void growth in shear. *Proc. R. Soc. Lond.* A 407, 435–458.

[36] Francfort, G., Murat, F. (1986). Homogenization and optimal bounds in linear elasticity. *Arch. Rat. Mech. Anal.* 94, 307–334.

[37] Gărăjeu, M., Michel, J. -C., Suquet, P. (2000). A micromechanical approach of damage in viscoplastic materials by evolution in size, shape and distribution of voids. *Comp. Methods Appl. Mech. Engrg.* 183, 223–246.

[38] Gilormini, P., Michel, J.-C. (1998) Finite element solution of the problem of a spherical inhomogeneity in an infinite power-law viscous matrix. *Eur. J. Mech. A/Solids* 17, 725–740.

[39] Gologanu, M., Leblond, J. -B., Devaux, J. (1993). Approximate models for ductile metalscontaining non-spherical voids – case of axisymmetric prolate ellipsoidal cavities. *J. Mech. Phys. Solids* 41, 1723–1754.

[40] Gologanu, M., Leblond, J. -B., Devaux, J. (1994). Approximate models for ductile metalscontaining non-spherical voids – case of axisymmetric oblate ellipsoidal cavities. *ASME J. Engrg. Materials Technol.* 116, 290–297.

[41] Gologanu, M., Leblond, J. -B., Devaux, J. (1997). Recent extensions of Gurson's model for porous ductile metals, Suquet, P. (Ed.), Continuum micromechanics. In: CISM lectures series. Springer, New York, 61–130.

[42] Gurson, A. L. (1977). Continuum theory of ductile rupture by void nucleation and growth. *J. Engng. Mater. Technol.* 99, 2–15.

[43] Hashin Z. (1962). The elastic moduli of heterogeneous materials. *J. Appl. Mech*, 143–150.

[44] Hashin, Z., Shtrikman, S. (1962a). On some variational principles in anisotropic and nonhomogeneous elasticity. *J. Mech. Phys. Solids* 10, 335–342.

[45] Hashin, Z., Shtrikman, S. (1962b). A variational approach to the theory of the elastic behavior of polycrystals. *J. Mech. Phys. Solids* 10, 343–352.

[46] Hashin, Z., Shtrikman, S. (1963). A variational approach to the theory of the elastic behavior of multiphase materials. *J. Mech. Phys. Solids* 11, 127–140.

[47] Hershey, A. V. (1954). The elasticity of an isotropic aggregate of anisotropic cubic crystals. *ASME J. Appl. Mech.* 21, 236–240.

[48] Hill, R. (1952). The elastic behavior of a crystalline aggregate. *Proc. Phys. Soc. Lond.* A 65, 349–354.

[49] Hill, R. (1956). New horizons in the mechanics of solids. *J. Mech. Phys. Solids* 5, 66–74.

[50] Hill, R. (1963). Elastic properties of reinforced solids: some theoretical principles. *J. Mech. Phys. Solids* 11, 127–140.

[51] Hill, R. (1965a). Continuum micro-mechanics of elastoplastic polycrystals. *J. Mech. Phys. Solids* 13, 89–101.

[52] Hill, R. (1965b). A self-consistent mechanics of composite materials. *J. Mech. Phys. Solids* 13, 213–222.

[53] Hill, R. (1978). Aspects of invariance in solids mechanics. *Advances in Applied Mechanics* 18, (ed.C-S Yih), Academic Press, New York, 1–75.

[54] Huang, R., (1991). Accurate dilatation rates for spherical voidsin triaxial stress fields. *J. Appl. Mech.* 58, 1084–1086.

[55] Huang, R., Hutchinson, J., W., Tvergaard, V., (1991). Cavitation instabilities in elastic-plastic solids. *J. Mech. Phys. Solids* 39, 223–241.

[56] Hutchinson, J. W., (1976). Bounds and self-consistent estimates for creep of polycrystalline materials. *Proc. R. Soc. Lond.* A 348, 101–127.

[57] Idiart, M., I. (2006). Macroscopic behavior and field statistics in viscoplastic composites, Ph.D. thesis, University of Pennsylvania.

[58] Idiart, M., I., (2007). Nonlinear sequential laminates reproducing hollow sphere assemblages. *C. R. Mecanique* 335, 363-368.

[59] Idiart, M., I., Danas, K., Ponte Castañeda, P. (2006). Second-order estimates for nonlinear composites and application to isotropic constituents. *C.R. Mecanique 334*, 575–581.

[60] Idiart, M., I., Ponte Castañeda, P. (2005). Second-order estimates for nonlinear isotropic composites with spherical pores and rigid particles, *C.R. Mecanique 333*, 147–154.

[61] Idiart, M. I., Ponte Castañeda, P. (2006) Variational linear comparison bounds for nonlinear composites with anisotropic phases. I. General results. *Proc. R. Soc. Lond. A* 463, 907-924.

[62] Idiart, M., I., Ponte Castañeda, P. (2007). Field statistics in nonlinear composites. I: Theory. *Proc. R. Soc. Lond.* A 463, 183–202.

[63] Kachanov, L., M., (1971). Foundations of the Theory of Plasticity. North-Holland, Amsterdam.

[64] Kailasam, M., (1998). A general constitutive theory for particulate composites and porous materials with evolving microstructures. Ph.D.thesis, University of Pennsylvania.

[65] Kailasam, M., Ponte Castañeda, P. (1998). A general constitutive theory for linear and nonlinear particulate media with microstructure evolution. *J. Mech. Phys. Solids* 46, 427–465.

[66] Kailasam, M., Aravas, N., Ponte Castañeda, P. (2000). Porous metals with developing anisotropy: Constitutive models, computational issues and applications to deformation processing. *CMES, Tech Science Press* 1, 105–118.

[67] Kröner, E. (1958). Berechnung der elastischen konstanten des vielkristalls aus den konstanten des einkristalls. *Z. Physik* 151, 504–518.

[68] Kröner, E. (1977). Bounds for effective elastic moduli of disordered materials. *J. Mech. Phys. Solids* 25, 137–155.

[69] Laws, N. (1973). On the thermostatics of composite materials. *J. Mech. Phys. Solids* 21, 9–17.

[70] Lahellec, N., Suquet, P. (2007a). Effective behavior of linear viscoelastic composites: a time-integration approach. *Int. J. Solids Struct.* 44, 507–529

[71] Lahellec, N., Suquet, P. (2007c). On the effective behavior of nonlinear inelastic composites: I. Incremental variational principles. *J. Mech. Phys. Solids* 55, 1932–1963.

[72] Lahellec, N., Suquet, P. (2007c). On the effective behavior of nonlinear inelastic composites: II. A second-order procedure. *J. Mech. Phys. Solids* 55, 1964–1992.

[73] Leblond, J. -B., Perrin, G., Suquet, P. (1994). Exact results and approximate models for porous viscoplastic solids. *Int. J. Plasticity* 10 (1994) 213–235.

[74] Lee, B. J., Mear, M. E. (1991a). Effect of inclusion shape on the stiffenes of non-linear two phase composite. *J. Mech. Phys. Solids* 39, 627–649.

[75] Lee, B. J., Mear, M. E. (1991b). Effect of inclusion shape on the stiffenes of isotropic and transversely isotropic two phase composite. *Int. J. Solids Struct.* 28, 975–1001.

[76] Lee, B. J., Mear, M. E. (1992a). Effective propesrties of power-law solids containing elliptical inhomogeneities. Part I: Rigid inclusions. *Mech. Mater.* 13, 313–335.

[77] Lee, B. J., Mear, M. E. (1992b). Effective propesrties of power-law solids containing elliptical inhomogeneities. Part II: Voids. *Mech. Mater.* 13, 337–356.

[78] Lee, B. J., Mear, M. E. (1992c). Axisymmetric deformation of power-law solids containing a dilute concentration of aligned spheroidal voids. *J. Mech. Phys. Solids* 40, 1805–1836.

[79] Lee, B. J., Mear, M. E. (1994). Studies of the growth and collapse of voids in viscous solids. *J. Eng. Mat. Tech.* 116, 348–358.

[80] Lee, B. J., Mear, M. E. (1999). Evolution of elliptical voids in power-law viscous solids. *Mech. Mater.* 31, 9–28.

[81] Levin, V.M. (1967). Thermal expansion coefficients of heterogeneous materials. *Mekh. Tverd. Tela.* 2, 8394.

[82] Lopez-Pamies, O., Ponte Castañeda, P., (2007). Homogenization-based constitutive models for porous elastomers and implications for macroscopic instabilities: IAnalysis. *J. Mech. Phys. Solids*, submitted for publication.

[83] Lubliner J. (1990). Plasticity Theory. Macmillan Publishing Company.

[84] Mariani, S., Corigliano, A. (2001). Anisotropic behavior of porous, ductile media. *Int. J. Solids Struct.* 38, 2427–2451.

[85] Masson, R. (2008). New explicit expressions of the Hill polarization tensor for general anisotropic elastic solids. *Int. J. Solids Struct.* 45, 757–769.

[86] McClintock, F. A. (1968). A criterion by for ductile fracture by growth of holes. *Trans. ASME, Series E, J. Appl. Mech.* 35, 363–371.

[87] McCullough, K Y G, Fleck, N A, Ashby, M F. (1999). Uniaxial stress-strain behaviour of aluminium alloy foams. *Acta Materialia, 47(8)*, 2323-2330.

[88] McElwain, D.L.S., Roberts, A.P., Wilkins, A.H. (2006). Yield criterion for porous materials subjected to complex stress states. *Acta Mater.* 54, 1995–2002.

[89] Michel, J. C., Moulinec, H., Suquet, P. (1999). Effective properties of composite material with periodic microstructure: a computational approach. *Comput. Methods Appl. Mech. Engrg.* 172, 109–143.

[90] Michel, J.C., Suquet, P. (1992). The constitutive law of nonlinear viscous and porous materials. *J. Mech. Phys. Solids* 40, 783 – 812.

[91] Milton, G. W. (1982). Bounds on the elastic and transport properties of two-component composites. *J. Mech. Phys. Solids* 30, 177 – 191.

[92] Milton, G. W. (2002). *The Theory of Composites.* Cambridge University Press.

[93] Monchiet, V., Charkaluk, E., Kondo, D. (2007). An improvement of Gurson-type models of porous materials by using Eshelby-like trial velocity fields. *C. R. Mecanique* 335, 32–41.

[94] Mori, T., Tanaka, K. (1973). Average stress in matrix and average elastic energy of materials with misfitting inclusions. *Acta Metall.* 21, 571–574.

[95] Mura, T., (1987). Micromechanics of Defects in Solids, Second, revised edition, Kluwer, Dordrecht.

[96] Nakajima, H. (2007). Fabrication, properties and application of porous metals with directional pores. *Progress in Materials Science* 52, 10911173.

[97] Needleman, A. (1972). Void growth in an elastic plastic medium. *J. Appl. Mech.* 39, 964–970.

[98] Needleman, A., Tvergaard, V., Van der Giessen, E. (1995). Evolution of void shape and size in creeping solids. *Int. J. Damage Mechanics* 4, 134–152.

[99] Nebozhyn, M. V., Ponte Castañeda, P. (1999). The second-order procedure: exact vs approximate results for isotropic, two-phase composites. *J. Mech. Phys. Solids* 47, 2171–2185.

[100] Ogden, R. (1984). Nonlinear elastic Deformations, Ellis Horwood Series in Mathematics and its Applications, Halsted Press, New York.

[101] Pastor, J., Ponte Castañeda, P. (2002). Yield criteria for porous media in plane strain: second-order estimates versus numerical results, *C. R. Mecanique* 330, 741–747.

[102] Perrin, G., Leblond, J.-B., (1990). Analytical study of a hollow sphere made of plastic porous material and subjected to hydrostatic tension application to some problems in ductile fracture of metals. *Int. J. Plasticity* 6, 677699.

[103] Perrin, G., Leblond, J.-B., (2000). Accelerated void growth in porous ductile solids containing two populations of cavities. *Int. J. Plasticity* 16, 91120.

[104] Pellegrini, Y.-P., (2002). Plasticity criterion for porous medium with cylindrical void. *C. R. Mecanique* 330, 763768.

[105] Ponte Castañeda, P. (1991). The effective mechanical properties of nonlinear isotropic composites. *J. Mech. Phys. Solids* 39, 45–71.

[106] Ponte Castañeda, P. (1992a). New variational principles in plasticity and their application to composite materials. *J. Mech. Phys. Solids* 40, 1757–1788.

[107] Ponte Castañeda, P. (1992b). Bounds and estimates for the properties of nonlinear heterogeneous systems. *Phil. Trans. R. Soc. Lond.* A 340, 531–567.

[108] Ponte Castañeda, P. (1996). Exact second-order estimates for the effective mechanical properties of nonlinear composite materials. *J. Mech. Phys. Solids* 44, 827–862.

[109] Ponte Castañeda, P. (1997). Nonlinear composite materials: Effective constitutive behavior and microstructure evolution, Suquet, P. (Ed.), Continuum micromechanics. In: CISM lectures series. Springer, New York, 61–130.

[110] Ponte Castañeda, P. (2001). Second-order theory for nonlinear composite dielectrics incorporating field fluctuations. *Phys. Rev. B* 64, 214205.

[111] Ponte Castañeda, P. (2002a). Second-order homogenization estimates for nonlinear composites incorporating field fluctuations. I. Theory. *J. Mech. Phys. Solids* 50, 737–757.

[112] Ponte Castañeda, P. (2002b). Second-order homogenization estimates for nonlinear composites incorporating field fluctuations. II. Applications. *J. Mech. Phys. Solids* 50, 759–782.

[113] Ponte Castañeda, P. (2006). Heterogenous materials *Ecole Polytechnique editions.*

[114] Ponte Castañeda, P., Nebozhyn, M. V. (1997). Variational estimates of the self-consistent type for the effective behaviour of some model nonlinear polycrystals. *Proc. R. Soc. Lond.* A 453, 2715–2724.

[115] Ponte Castañeda, P., Suquet, P. (1995). On the effective mechanical behavior of weakly inhomogeneous nonlinear materials. *Eur. J. Mech. A/Solids* 2, 205–236.

[116] Ponte Castañeda, P., Suquet, P. (1998). Nonlinear composites. *Adv. Appl. Mech.* 34, 171–302.

[117] Ponte Castañeda, P., Suquet, P. (2001). Nonlinear composites and microstructure evolution. In: Aref, H., Phillips, J. W. (Eds.), *Proceedings of the 20th International Congress of Theoretical and Applied Mechanics* (ICTAM 2000). Kluwer Academic Publishers, Dordrecht, The Netherlands, 253273.

[118] Ponte Castañeda, P., Willis, J. R. (1988). On the overall properties of nonlinearly viscous composites. *Proc. R. Soc. Lond.* A 416, 217–244.

[119] Ponte Castañeda, P., Willis, J. R. (1995). The effect of spatial distribution on the effective behavior of composite materials and cracked media. *J. Mech. Phys. Solids* 43, 1919–1951.

[120] Ponte Castañeda, P., Willis, J. R. (1999). Variational second-order estimates for nonlinear composites. *Proc. R. Soc. London* 455, 1799–1811.

[121] Ponte Castañeda, P., Zaidman, M. (1994). Constitutive models for porous materials with evolving microstructure. *J. Mech. Phys. Solids* 42, 1459–1497.

[122] Ponte Castañeda, P., Zaidman, M. (1996). The finite deformation of nopnlinear composite materials–I. Instanteneous constitutive relations. *Int. J. Solids Struct.* 33, 1271–1286.

[123] Rice, J. R. (1976). The localization of plastic deformation. *Proceedings of the*14^{th} *International Congress of Theoretical and Applied Mechanics*, W. T. Koiter, ed., North-Holland Publiching Company, 207-220.

[124] Rice, J. R., Tracey, D. M. (1969). On the ductile enlargement of voids in triaxial fields. *J. Mech. Phys. Solids* 17, 201–217.

[125] Reuss, A. (1929). Calculation of the flow limits of mixed crystals on the basis of the plasticity of the monocrystals. *Z. Angew. Math. Mech.* 9, 49–58.

[126] Sab, K. (1992). On the homogenization and the simulation of random materials. *Eur. J. Mech., A/Solids* 11, 585–607.

[127] Sab, K. (1994a). Homogenization of non-linear random media by a duality method. Application to plasticity. *Asymptotic Analysis* 9, 311–336.

[128] Sab, K., (1994b). Evaluation of the effective strength of a plate with random holes. *C.R. Acad. Sci. Paris II* 319, 491497.

[129] Saff, E. B., Kuijlaars, A. B. J. (1997) Distributing many points on a sphere. *The Mathematical Intelligencer* 19, 5–11.

[130] San Marchi, C., Mortensen A., (2001). Deformation of open-cell aluminium foam. *Acta Mater.* 49, 3959–3969.

[131] Sanchez-Palencia, E. (1970). Equations aux dérivées partielles. Solutions périodiques par rapport aux variables d' espace et applications. *C. R. Acad. Sc. Paris* 271, 1129–1132.

[132] Shtern, M.B., Maidanyuk, A.P., Cocks, A., 2002a. Effect of the third invariant on the effective reaction of plastic porous bodies. I. Behavior of a porous material unit cell and generalized rule of normality. Powder Metallurgy and Metal Ceramics 41, 329–335.

[133] Shtern, M.B., Maidanyuk, A.P., Cocks, A., 2002b. Effect of the third invariant on the effective reaction of plastic porous bodies. II. Loading surface of porous bodies whose properties are sensitive to a triaxial stressed state. Powder Metallurgy and Metal Ceramics 41, 347–354.

[134] Suquet, P. (1983). Analyse limite et homgénéisation. *C. R. Acad. Sci. Paris* II 296, 1355–1358.

[135] Suquet, P. (1987). Elements of homogenization for inelastic solids. in Homogenization Techniques for Composite Media (Edited by E. Sanchez Palencia and A. Zaoui), Lecture Notes in Physics, Vol. 272, pp. 193-278. Springer-Verlag, Berlin, Germany.

[136] Suquet, P. (1990). A simplified method for the prediction of homogenized elastic properties of composites with periodic microstructure. *C. R. Mecanique* 311, 769–774.

[137] Suquet, P. (1993). Overall potentials and extremal surfaces of power law or ideally plastic materials. *J. Mech. Phys. Solids* 41, 981–1002.

[138] Suquet, P. (1995). Overall properties of nonlinear composites: a modified secant moduli theory and its link with Ponte Castañeda's nonlinear variational procedure. *C. R. Acad. Sci. Paris II* 320, 563–571.

[139] Suquet, P., Ponte Castañeda, P. (1993). Small-contrast perturbation expansions for the effective properties of nonlinear composites. *C. R. Acad. Sci. Paris II* 317, 1512–1522.

[140] Talbot, D. R. S., Willis, J.R. (1983). Variational principles for inhomogeneous nonlinear media. *IMA J. Appl. Math.* 35, 39–54.

[141] Talbot, D. R. S., Willis, J.R. (1992). Some simple explicit bounds for the overall behavior of nonlinear composites. *Int. J. Solids Struct.* 29, 1981–1987.

[142] Tartar, L. (1979). Estimations fines de coefficients homogénéisés. *Lecture Notes in Mathematics, Springer Verlag* 704, 364–373.

[143] Taylor, G. I. (1938). Plastic strains in metals. *J. Inst. Metals* 62, 307–324.

[144] Tvergaard, V.,(1981). Influence of voids on shear band instabilities under plane strain conditions. *Int. J. Fracture* 17, 389407.

[145] Voigt, W. (1889). Ueber die bezienhung zwischen den beiden elastitäts-constanten isotroper/ *Ann. Physik* 38, 573–588.

[146] Willis, J.R. (1977). Bounds and self-consistent estimates for the overall moduli of anisotropic composites. *J. Mech. Phys. Solids* 25, 185–202.

[147] Willis, J.R. (1978). Variational principles and bounds for the overall properties of composites. *Continuum Models and Discrete Systems* 2, (ed. J. Provan), 185–212.

[148] Willis, J.R. (1981). Variational and related methods for the overall properties of composites. *Adv. Appl. Mech* 21, 1–78.

[149] Willis, J.R. (1982). Elasticity theory of composites. *Mechanics of Solids, The Rodney Hill 60th aniversary Volume*, Hopkins, H. G. and Sewell, M. J., eds., Pergamon Press, Oxford 653–686.

[150] Willis, J.R. (1983). The overall elastic response of composite materials. *J. Appl. Mech.* 50, 1202–1209.

[151] Willis, J.R. (1991). On methods for bounding the overall properties of nonlinear composites. *J. Mech. Phys. Solids* 39, 73–86.

[152] Willis, J.R. (1992). On methods for bounding the overall properties of nonlinear composites: correction and addition. *J. Mech. Phys. Solids* 40, 441–445.

[153] Zaidman, M., Ponte Castañeda, P. (1996). The finite deformation of nopnlinear composite materials–II. Evolution of the microstructure. *Int. J. Solids Struct.* 33, 1271–1286.